# Advanced Nanotechnologies for the Central Nervous System : design, Optimization, Application, and Scale-up

Ilaria Ottonelli

COLLEGE ED BIOLOGIE DOCTORAL SANTE PAYS DE LA LOIRE

université angers (2)

# THESE DE DOCTORAT

DE
L'UNIVERSITÉ D'ANGERS
SOUS LE SCEAU DE
LA COMUE ANGERS – LE MANS

ECOLE DOCTORALE N° 605
*Biologie-Santé*
Spécialité : Pharmacie

Par
**Ilaria OTTONELLI**

## Advanced Nanotechnologies for the Central Nervous System

Design, Optimization, Application, and Scale-up

**Thèse présentée et soutenue à Modena (Italie), le 19/05/2023**
**Unité de recherche :** CRCI2NA Nantes Angers, équipe 5 GLIAD

**Rapporteurs avant soutenance** :

Monsieur Gert FRICKER, Professeur Université de Heidelberg, Allemagne
Madame Francesca RE, Professeur Université de Milano Bicocca, Italie

**Composition du Jury :**

Président : Monsieur Stefano FUMAGALLI, Professeur Université de Firenze, Italie
Examinateurs : Monsieur Emmanuel GARCION, Directeur de Recherche – Inserm, Université d'Angers
Madame Maria RUZZENE, Professeur Université de Padova, Italie
Dir. de thèse : Monsieur Frank BOURY, Professeur des Universités Université d'Angers
Co-dir. de thèse : Monsieur Giovanni TOSI, Professeur Université de Modena, Italie
Madame Barbara RUOZI, Professeur Université de Modena, Italie

**Università degli Studi di Modena e Reggio Emilia**

Dipartimento di Scienze Biomediche, Metaboliche, e Neuroscienze

Dottorato di ricerca in Clinical and Experimental Medicine (CEM) –

Medicina Clinica e Sperimentale

**Ciclo XXXV**

Curriculum ***Nanomedicine, Medicinal and Pharmaceutical Sciences***

# Advanced Nanotechnologies for the Central Nervous System: Design, Optimization, Application, and Scale-up

*in collaboration with Université d'Angers, France*

***Ilaria Ottonelli***

Matricola #**149061**

Tutor: Prof. Giovanni Tosi

Co-Tutor: Prof. Frank Boury

Co-cotutor: Prof. Barbara Ruozi

Coordinatore del Corso di Dottorato: Prof. Marco Vinceti

*Success is a staircase, not a doorway*

*- Dorothy Walters*

# TABLE OF CONTENT

# ABSTRACT

Nanotechnologies, such as nanoparticles (NPs) and nanomedicines (NMeds), have emerged as promising tools for the treatment and diagnosis of pathologies of the central nervous system. Features such as: a small tunable size, the ability to protect sensitive molecules, a high drug loading capacity, tunable drug release, specific targeting, and biodegradability, make them a prime choice for hard-to-treat diseases; however, these advanced technologies require in-depth optimizations from design, production, administration, and scale-up to meet the selective criteria needed to go from benchtop to bedside.

The first factor to be considered when designing NPs is the core material composition, such as polymers and lipids: not only must they be biocompatible and biodegradable, but also compatible with the drug loaded. Polymers and lipids can be chemically modified to have specific properties, such as solubility, pH-sensitivity, or enzyme degradation. Another major advantage of NMeds is their ability to protect sensitive molecules from degradation. In fact, often peptides, proteins, and nucleic acids are used as therapeutic molecules against a variety of diseases, but they suffer from rapid degradation in biological environments. Here, NMeds can reduce the loss of molecules, thus increasing the therapeutic efficacy of these systems. Independent of both the matrix material and the chosen biological active molecule, a major barrier is the delivery of the NMeds to the desired site. The Blood-brain barrier's (BBB) natural protective effect makes the delivery to the brain extremely difficult. NMeds can be engineered with targeting ligands with high affinity and specificity, allowing for BBB crossing, and specific delivery to diseased cells. Once delivered to the specific diseased site, further optimized delivery systems can allow for the controlled release of the drug over time at the active site. This is necessary to increase the pharmaceutical potential of the drug by decreasing the necessary dose, allowing for less invasive treatments. The creation of these multifaceted nanotechnology systems is a daunting task.

Moreover, while many of the standard protocols that are used in a research lab allow for the fine tuning of such attributes, they are often difficult to translate to larger scale production processes. In recent years, microfluidic technology has become much more mainstream and can permit the automation and adaptation of these protocols to GMP standard practices. The conversion from benchtop to microfluidic protocols, however, is still an arduous task in order to guarantee that the nano systems have a similar makeup, characteristics, and functionality when dosed.

In my PhD project, my work revolved around finding solutions to the problems that can occur when designing nanotechnologies for different drugs, disease states, and applications. Peer-reviewed articles which have been accepted in competitive journals demonstrate my thesis work and the barriers overcome: synthesis and optimization of a novel PLGA-chitosan hybrid material, improving the stability of enzymes loaded in PLGA NPs, targeting the BBB and Glioblastoma by adding various targeting ligands, controlling drug release from NMeds using gel scaffolds, microfluidic scale-up, and the identification of the formation of the protein corona on different NMeds. All of these individual enhancements and optimizations will further improve the understanding of nanotechnology, and how to overcome the barriers that are currently blocking the production of marketable products to cure hard to treat diseases.

# RIASSUNTO

Le nanotecnologie farmaceutiche, come nanoparticelle (NPs) e nanomedicine (NMeds), sono strumenti promettenti per il trattamento e la diagnosi delle patologie del sistema nervoso centrale. Le loro caratteristiche, quali la piccola dimensione, la capacità di proteggere le molecole sensibili, un'elevata capacità di caricamento del farmaco, il rilascio controllato di farmaci, il targeting specifico, e la biodegradabilità, le rendono perfette per malattie difficili da trattare. Tuttavia, queste tecnologie avanzate richiedono ottimizzazioni approfondite a partire dalla progettazione, produzione, amministrazione e fino allo scale-up per poter passare dal laboratorio al paziente.

Il primo fattore da considerare quando si progettano NPs è il materiale, come polimeri e lipidi: non solo devono essere biocompatibili e biodegradabili, ma anche compatibili con il farmaco caricato. I polimeri e i lipidi possono essere modificati chimicamente per avere proprietà specifiche, come la solubilità, la sensibilità al pH o la degradazione enzimatica. Un altro grande vantaggio delle NMeds è la loro capacità di proteggere molecole sensibili dalla degradazione. Spesso infatti peptidi, proteine e acidi nucleici sono usati come molecole terapeutiche contro una varietà di malattie, ma vengono rapidamente degradati negli ambienti biologici. Qui, le nanotecnologie possono ridurre la perdita di farmaco, aumentando così l'efficacia terapeutica. Indipendentemente sia dal materiale della matrice che dal principio attivo, una barriera importante è la consegna delle NMeds al sito desiderato. L'effetto protettivo naturale della barriera ematoencefalica (BEE) rende estremamente difficile la veicolazione di farmaci al cervello. Le NMeds possono essere funzionalizzate con ligandi con alta affinità e specificità, che permettono di attraversare la BEE e colpire solo le cellule malate. Una volta consegnato al sito specifico della malattia, NMeds ulteriormente ottimizzate possono consentire il rilascio controllato del farmaco nel tempo nel sito attivo. Ciò è necessario per aumentare il potenziale farmaceutico del farmaco diminuendo la dose necessaria

e consentendo trattamenti meno invasivi. La creazione di questi sistemi nanotecnologici sfaccettati è molto complessa. Sfortunatamente, mentre molti dei protocolli standard utilizzati in un laboratorio di ricerca consentono la messa a punto di tali attributi, sono spesso difficili da tradurre in processi di produzione su larga scala. Negli ultimi anni, la tecnologia della microfluidica è diventata molto più diffusa e può consentire l'automazione e l'adattamento di questi protocolli alle pratiche standard GMP. La conversione da protocolli da banco a protocolli microfluidici, tuttavia, è ancora un compito arduo al fine di garantire che i nanosistemi abbiano una composizione, caratteristiche e funzionalità simili ai classici una volta somministrati.

Nel mio progetto di dottorato, mi sono concentrata sulla ricerca di soluzioni ai problemi che possono verificarsi durante la progettazione di nanotecnologie per diversi farmaci, patologie e applicazioni. Articoli peer-reviewed che sono stati accettati in riviste indicizzate dimostrano il mio lavoro di tesi: sintesi e ottimizzazione di un nuovo materiale ibrido PLGA-chitosano, miglioramento della stabilità enzimi formulati in NPs polimeriche, targeting della BEE e di glioblastoma con ligandi mirati, controllo del rilascio di farmaci da nanomedicine tramite idrogel, scale-up microfluidico, e l'identificazione della formazione della protein corona su diversi nanosistemi. Tutti questi miglioramenti e ottimizzazioni individuali miglioreranno ulteriormente la comprensione della nanotecnologia e come superare le barriere che attualmente bloccano la produzione di prodotti commercializzabili per curare malattie difficili da trattare.

# INTRODUCTION

## Nanotechnology and Nanoparticles

Over the centuries, medicine has continued to improve lives. Diseases have been cured and more and more therapeutic compounds have been discovered, leading to the improvement of life expectancy to almost 73 years old compared to that of 45 in the 1950's [1]. Together with the increased number of therapeutic molecules available, though, an increased number of issues linked to these therapeutics was evidenced, such as poor bioavailability, harsh side effects, and non-specific toxicity. To this end, Nanotechnology has become a forerunner in the medical field offering new and innovative ways to boost drug delivery approaches by both ameliorating the therapeutic profiles of molecules and improving therapeutic options for hard-to-treat diseases [2–6]. Nanotechnology offers the benefits of improving drug solubility, stability, bioavailability, and the option to control their release and target the cargo to a specific organ or cell. These advantages could bring back to light the therapeutic potential of many drugs that were rejected due to poor solubility or toxicity. The variety of possible nanotechnology vehicles is vast, ranging from small drug conjugates, pro-drugs, inorganic nanoparticles, viral delivery systems, and the highly studied and popular lipidic and polymeric Nanoparticles (NPs) [7–10]. Each system presents advantages and limitations in drug loading capacity, protective capabilities, length of treatment, and toxicity. Thanks to the deep research conducted in the last decades, these variations can be finely tuned, by critically choosing the core material, the methodology of production, the surface functionalization, and the overall physical-chemical properties of the final formulation, thus making nanotechnology the most versatile and promising possibility for future treatments (Figure 1) [11,12].

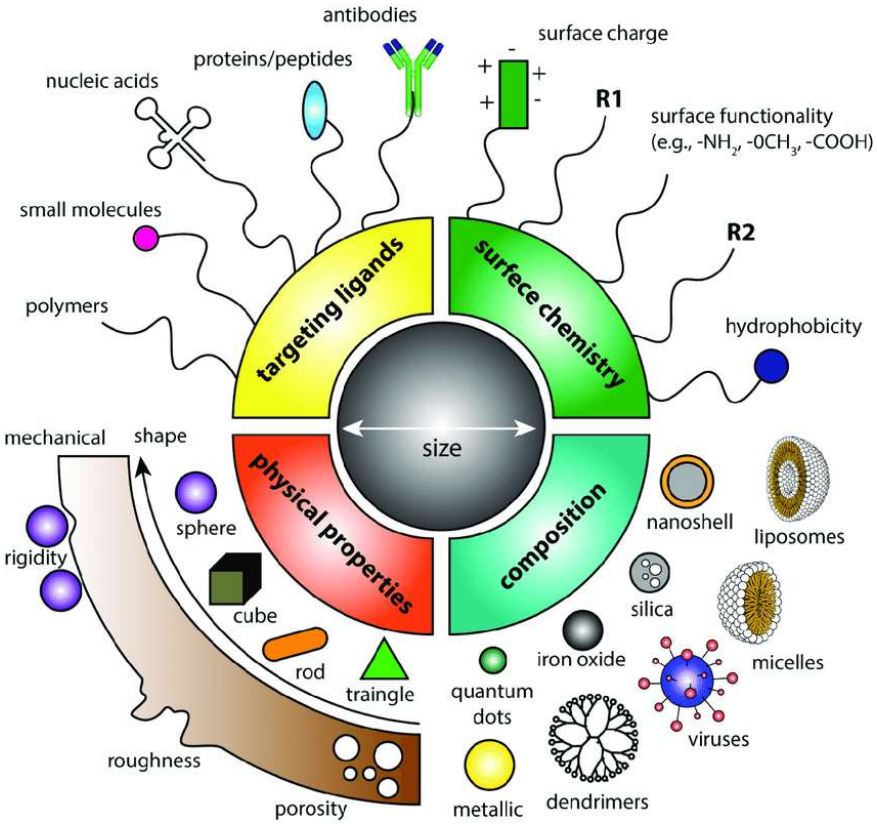


**Figure 1.** Graphical representation of some of the main characteristics that must be taken into consideration during the design of nanoparticles (from [13]).

## Selection or design of the core material

The core material is often used as a first parameter to describe Nanotechnologies. In fact, with all of the possible variables in the design and synthesis of various nanotechnologies, the material in which these systems are designed is of critical importance. In the field of Nanotechnologies, inorganic and organic nanoparticles (NPs) have taken the spotlight thanks to their various advantages [14–16]. Inorganic NPs, such as Gold, Silver, and Silica, have shown great potential for drug loading and theranostic purposes, thanks to an exceptionally high reproducibility [17–19]. Unfortunately, their non-biodegradability often results in the accumulation of these NPs in clearance organs such as the kidney, spleen, liver, and lungs, thus leading to toxicity or organ failure [20–22]. Organic NPs, on the other hand, can be produced with biodegradable materials, reducing toxicity issues linked to accumulation in the body (Figure 2). The first class of materials used to produce biodegradable NPs was lipids, with the formulation of liposomes in the early '90s. Lipids, comprising natural and synthetic phospholipids, fatty acids, fatty esters, etc., are widely used to produce a variety of lipidic NPs, the most renowned being liposomes, solid lipid nanoparticles, and lipid nanoclusters. While advantageous for their biodegradability, biocompatibility, and versatility, as demonstrated by the numerous products approved for clinical use, their applications are often limited by lack of stability during storage, due to aggregation of the NPs or limited control on drug retention [23–26].

Polymers can be introduced to overcome the limitations of lipidic NPs. Natural polymers, such as cellulose, agarose, chitosan, and hyaluronic acid, are widely used to produce NPs thanks to their availability, low cost, and biocompatibility; however, a major drawback in the use of natural polymers is the poor control on their characteristics, as they are often mixtures of molecules with different degrees of substitution, ramification, molecular weight, etc. Hence, synthetic polymers are often the prime choice to design polymeric NPs, with a vast database of di-block, triblock, linear, and hyper-branched polymers to choose from [27–31].

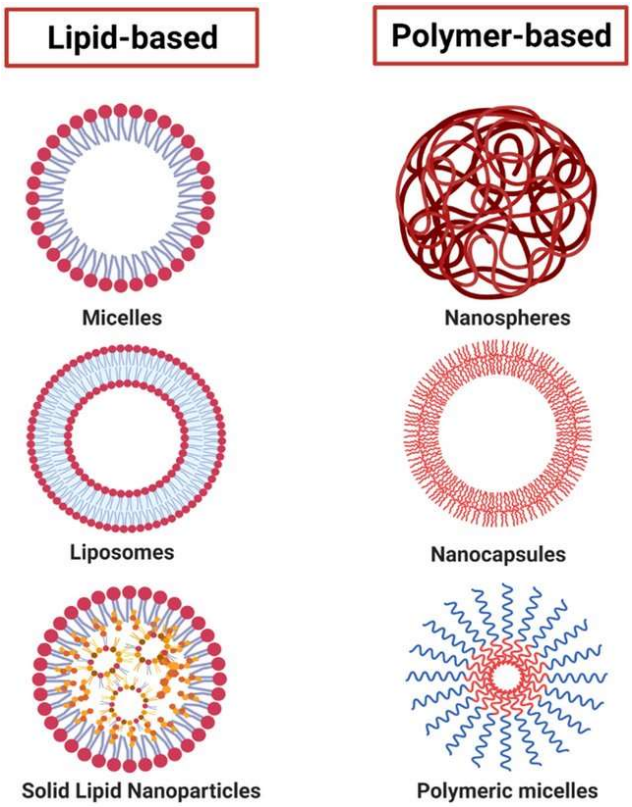


**Figure 2**. Examples of different structures for organic NPs, depending on the material used (from [32]).

Among synthetic polymers for NP production, polymers of lactic and glycolic acid are by far one of the most used. The major advantage of poly lactic acid (PLA) and copolymers of lactic and glycolic acid (PLGA) is their metabolic degradation in vivo in their monomers, which are completely biodegradable and enter the Krebs cycle, resulting in a minimal toxicity for the body. Moreover, it is possible to tune the time needed for degradation by adjusting the percentage of glycolic acid, as it decreases linearly with the amount of glycolic acid in the copolymer. Another paramount feature of PLA and PLGA lies in their acidic termination, that allows for easy surface functionalization, as will be discussed further in following sections [33–38].

Another possibility recently investigated to take advantage of the properties of both polymers and lipids, is the formulation of hybrid NPs. These peculiar nanotechnology systems are generally composed by a mixture of polymers and lipids, that can arrange in different structures such as a matrix sphere, or a core-

shell structure, depending on the single components and the method of production. What is particularly interesting about these hybrid systems is their possibility to combine the great biocompatibility of lipids, with the structural stability and easy tunability of polymers, creating a device with improved features compared to the "pure" counterparts. It is also noteworthy that the possibilities for hybrid NPs are infinite, thanks to the use of a variety of lipids, polymers, but also inorganic materials, thus leading to new possible applications for almost any kind of disease [39–43].

A limiting step in the use of complex systems such as hybrid NPs often lies in the difficult quantification of the single components used. In fact, it is often difficult to separate lipids from polymers, which is a necessary step to precisely quantify the amount of each material that actually takes part in the final structure of the NPs. To reduce this problem, it is possible to exploit the properties of two different materials by conjugating them in a single molecule. This possibility has been largely explored with the polymer PEG (polyethylene glycol), which has been covalently bound to a variety of phospholipids or polymers with the aim of conferring them a more hydrophilic and less reactive surface [44–48]. PEGylation has been used in the last few decades to produce NPs with reduced immunogenicity, longer half-life, and improved efficacy, as also demonstrated by the Covid-19 vaccine; however, a few concerns have been recently raised linked to possible induction of immune reactions after long-term treatments [49–52].

By chemically conjugating molecules with different properties, it is possible to produce novel materials that result in NPs with improved features. For example, it is possible to promote the self assembly of a hydrophilic polymer by covalently binding to it a lipidic molecule, or a hydrophobic polymer. This is what we investigated in Chapter 1, where a project about chemical conjugation of PLGA and Chitosan is presented. The novel PLGA-Chitosan conjugate presented properties from both starting materials that would further allow for enhanced drug loading, high biodegradability, and overall improved therapeutic options.

## The importance of the cargo

Selection and design of the core material of NPs is important for their biological interaction, biodistribution, and biocompatibility, but first and foremost their compatibility with the drug of choice [53]. In fact, the selection of which type of therapeutic is to be delivered drastically changes the characteristics that are needed in the nanotechnology system. In this respect, the size, charge, and material used come into play, and a balance must be found to address characteristics needed for the type of drug molecule, the disease, and the methodology used. When all these parameters are taken into consideration, it is possible to optimize the loading content while ensuring the stability and deliverability of the molecule to the desired site. Overall, NPs are versatile tools that can load a variety of therapeutic agents. While small molecules are attractive for the ease of encapsulating large quantities, they exhibit a mono-effect with one molecule creating one outcome. Moreover, many small molecule drug candidates show high toxicity, low solubility, low specificity, and low bioavailability, making it necessary to use a nanotechnology system in order to enhance their administration [54].

Beyond small molecules, it is also possible to protect and deliver larger, biological therapeutics such as peptides, proteins, enzymes, or genetic material. These biological molecules are advantageous as they are often natural and are more specific for target cell processes. Thus, they are currently on the rise as therapeutic molecules. Enzymes in particular are large proteins with a particular 3-D structure that allows for the turnover of substrates, the lack of or misfolding of enzymes being linked to a variety of diseases [55–57].

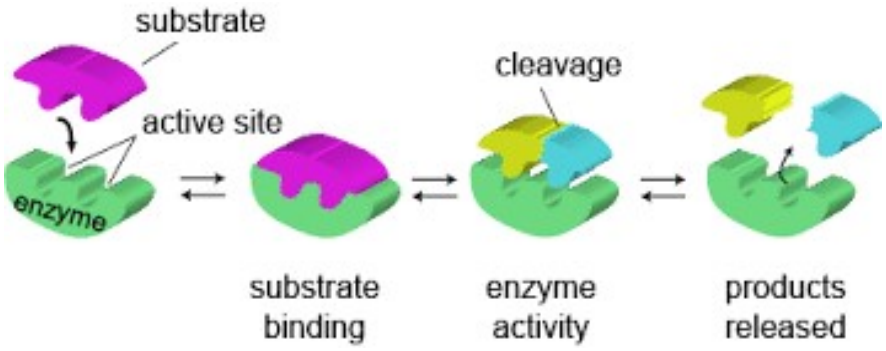


**Figure 3.** Schematic representation of an enzymatic reaction (from [58])

Enzymes can turnover their substrate many times after administration, prolonging their activity and therapeutic efficacy (Figure 3); however, they also have large drawbacks when administered. The 3-dimensional aspect of the enzyme is critical to its function, but also means that it is much more susceptible to biological inactivation. Interactions with proteins in the blood, pH sensitivity, lack of biodistribution, and the inability to pass most organ or cellular barriers are major limitations to the free dosing of enzymes [59–63]. These deficits could be overcome with nanotechnology systems. Nanosystems, and NPs in particular, can encapsulate enzymes to protect their 3-D structure and improve their delivery to have long lasting effects. Furthermore, the idea of nanoreactors has been recently investigated, where the delivery system loaded with an enzyme can selectively allow the reagent to enter, convert it in a safe environment, and release the product for long term delivery [64–68].

Loading enzymes into a nanotechnology system requires more attention compared to small molecules. Many of the most commonly utilized methods for the production of NPs rely on heat, organic solvents, sonication, long time frames, or general conditions that can lead to a drastic loss of enzyme activity. This problem is still a major leading problem in the efficacious delivery of enzymes for therapeutic treatments in patients [69–71]. Therefore, it is often necessary to modify the protocols by adding stabilizing agents during formulation in order to improve the encapsulation and maintain enzyme activity, to ensure the therapeutic potential of the encapsulated enzyme. This idea is presented in

Chapter 3, where the stabilizing effect of two additives, namely BSA and Tween, was investigated during formulation of the enzyme ß-Glucosidase into PLGA NPs.

Finally, genetic material can be used as a therapeutic agent, as it is able to produce large numbers of therapeutic proteins or enzymes with a single administration. DNA, though, must reach the nucleus, making it harder to deliver. On the other hand, siRNA and mRNA are very promising and do not require nuclear delivery, but they are much more susceptible to protective enzymes against foreign genetic material getting into the cells [72–77].

The large size of plasmid DNA, the natural defense system of the body to filter out (liver, spleens, kidneys) or eliminate foreign genetic material (such as from viruses) via an immune response, and the intracellular delivery to the nucleus of the afflicted cells make it necessary to protect genetic material with a nanotechnological delivery system. In the last decade, there has been a huge undertaking to solve this problem with viral, inorganic, lipidic, or polymeric systems [78–84]. Each system shows advantages and disadvantages for DNA delivery, such as the high encapsulation of genetic material in polyplex (charge-based complexation) and cationic systems, but they often suffer from stability or storage issues. For this reason, new and intricate systems are still being designed to incorporate genetic materials, protecting them for degradation and allowing for specific targeting, addressing the important features such as stability, encapsulation, and delivery into a singular system.

## Targeting

The intelligent design of nanoparticles does not end at the selection of components (material, drug, surfactants, stabilizers etc) and their formation into a 3-D delivery system. Even if the particles can be loaded with the drug and safely injected into the bloodstream, they must arrive, accumulate, and release their payload at the site of interest in order to be effective and without creating systemic toxicity. For this reason, NPs must be designed to reach their specific target. Targeting can be accomplished via numerous methods: 1) Physical, 2) Passive targeting utilizing natural biological phenomena, 3) or active targeting with targeting ligands [85].

Physical targeting is one of the most direct and sure ways to deliver nanotechnologies to the site of interest. This type of targeting can be achieved via direct injections at the site, the use of implants, or the use of physical stimuli to deliver and/or activate the NPs in the desired location by using ultrasound, heat, light, magnetism, or electric current [86–91]. While extremely effective, these methods have several drawbacks. Direct injections are high risk in certain tissues (such as the brain) due to the localized damage caused, and implants are generally highly invasive due to the need for surgery. Moreover, patient compliance is often a problem as these techniques can be painful and therefore they are poorly tolerated. Furthermore, the activating stimuli must be specific and localized, requiring special instrumentation or surgery to have access to the desired tissue (in terms of some light activated NPs) (Figure 4).

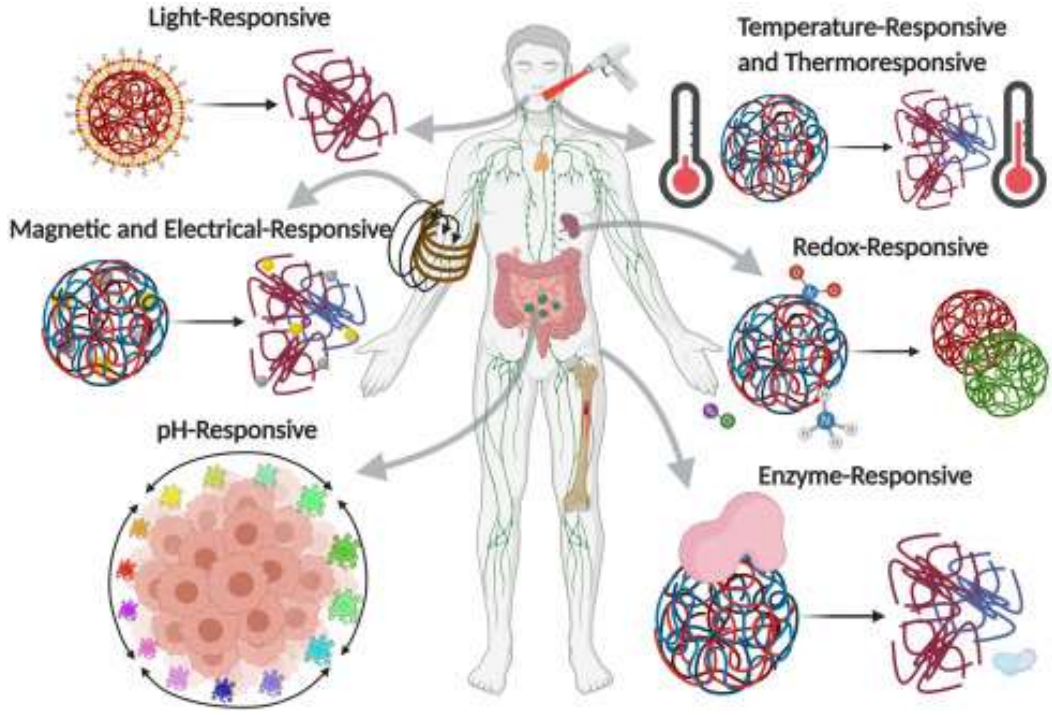


**Figure 4.** Examples of physical targeting of NPs with the use of external stimuli (from [92]).

Passive targeting exploits natural biological characteristics to deliver NPs to a specific target after administration [93]. The first pass clearance organs (liver, kidneys, and spleen) usually show an increased uptake of any drug delivery vehicle due to their primary function of filtering the blood. While functional, this process is poorly controllable and the systemic biodistribution throughout these organs is a major drawback as toxicity will still be observed. A similar example is the enhanced permeation and retention (EPR) effect [94–96]. The EPR effect occurs due to the fast formation of new capillaries and break down of the junctions of vascular endothelium during tumor growth. Endothelial cells normally allow for the passage of small molecules from the bloodstream to the tissues, having fenestrations of a few nanometers. During the fast growth of tumors, these fenestrations tend to increase in size up to 500 nm [97]. As a consequence, NPs will be able to pass the gaps of the endothelium and become trapped in the tumor environment [98,99]. Here, NPs can release their cargo upon degradation directly in the vicinity of the tumor. This effect is even further improved by the fact that

the fast growing tumor cells tend to uptake and metabolize much more material than nearby healthy cells. A similar effect has also been seen in other types of diseases other than cancer such as inflammatory diseases, hypertension, and ischemia/reperfusion injury [100,101]. While this effect has shown great results in research settings, it is highly disputed for effectiveness in humans as many researchers evidenced that the phenomenon is not as effective in humans, and therefore the results in smaller research animals is unrealistically elevated [102–104]. Another example of passive targeting is using NPs that activate the immune response to target macrophages and lymphocytes [105–108]. By having an immunogenic effect, immune cells naturally uptake the NPs to remove them from the bloodstream, leading to the uptake of the pharmaceutical compounds as well. Notwithstanding the possibility of designing NPs to exploit passive targeting by tuning their size, hydrophobicity, charge, or adding adjuvant molecules, these routes are often inadequate to create a functional delivery system, and their use is limited to a few applications.

Because of the non-specific results of passive targeting, active targeting strategies have led the way to improve specific delivery, decrease required doses, and limit off-target toxicity of NPs [109,110]. In fact, the possibility of engineering the surface of NPs with targeting ligands has been explored. Several ligands targeting organs, tissues, cell surface proteins, intracellular organelles, or specific pathways have been discovered, but their selection and use must be carefully controlled in order to optimize their potential [111]. There are several characteristics that separate the most promising targeting ligands from their less effective counterparts. Selectivity is the first crucial criteria for any ligand. If a ligand's receptor or target is located throughout the body, the targeting effect will be masqueraded by the off-target uptake. Therefore, a targeting ligand will be most successful if its ligand is located, or drastically overexpressed, in the desired target tissue or cell. An exception to this rule would be for ligands that allow the crossing of the Blood Brain Barrier (BBB). In fact, many BBB targeting ligands do not follow the specificity criterion, but their effect is still relevant due to the intrinsic difficulty to enter the CNS.

Equally important to the selectivity of the ligand, NP ligands must also present a high affinity for their receptor. Due to the small size and short interaction time between the receptor and the targeted NP in the bloodstream, a low affinity would hamper the interaction, leading to poor efficacy. Fortunately, another effect occurs with targeted NPs called multivalency effect, i.e. the improved affinity of a ligand for its receptor when more than one ligand on the surface of NPs can simultaneously bind to multiple receptors on the target cell [112–116]. While this advantageous effect has been often demonstrated *in vitro*, it is very difficult to quantify its impact on the targeting efficacy, as it would require a precise characterization of the amount and distribution of the ligand on the surface of the NP. Since this type of analysis is still poorly optimized, it is often overlooked at, solely indicating whether the ligand allows for the targeting or not.

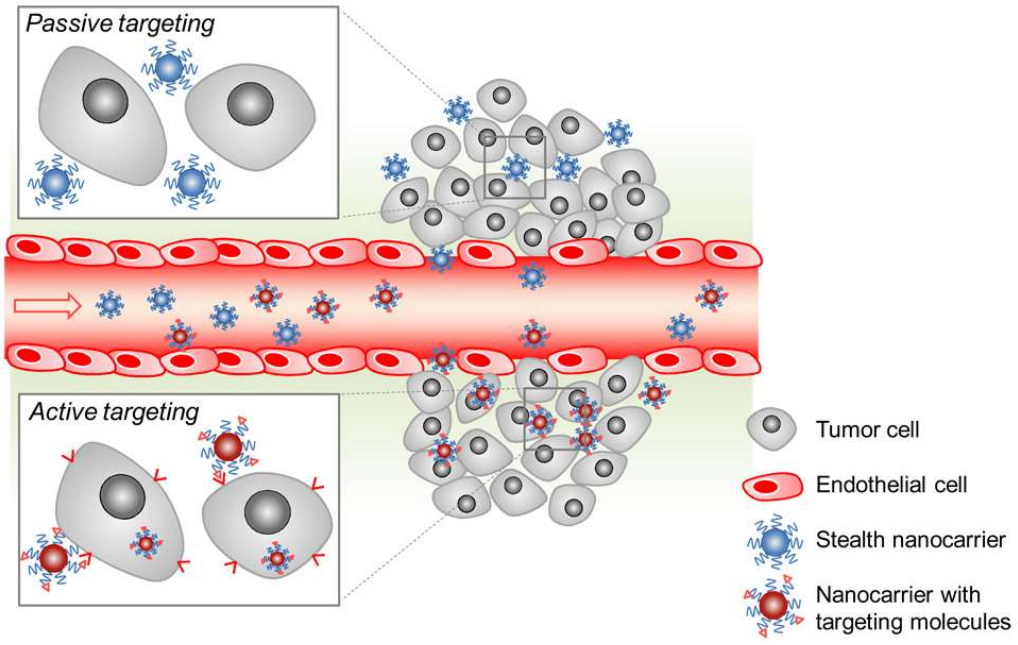


**Figure 5.** Graphical representation of the difference between active and passive targeting strategies for NPs (from [117]).

Selecting a ligand with high specificity and affinity is very important, but the characteristics of the ligand's interaction with its receptor, and the effect of the interaction are also pertinent. This has been a concept in the literature for decades. Many ligands with high specificity and affinity bind their cell membrane receptors

and create an internal pathway cascade, but NPs are not internalized. This could be a good effect, as the activated cell pathway might allow to increase the susceptibility of the cell to the drug released by the NP attached to the cell surface, leading to improved therapeutic effects; however, if the NP needs to be internalized for the drug to have a therapeutic effect, this is a roadblock. The same idea can also be translated to transport across barriers, such as the BBB. If the ligand and receptor remain blocked in the vascular lumen, the NP will not cross the membrane and will remain ineffective to target CNS disease. Therefore, it is very important to know the function of the ligand and its biological fate after interaction with its receptor, in order to understand if it could be useful as a targeting ligand [118–127]. The idea of internalization of NPs is even further complicated by size restrictions. In fact, literature evidence suggests that each ligand has a size restriction for the maximum size cargo that it is able to transport into a cell or across a membrane. This is a very difficult factor to take into consideration and is very difficult to ascertain through laboratory experiments; however, it is critical in the selection of ligands as even if a ligand works for a smaller nanotechnology system, a similar but slightly larger system could block all beneficial effects making the ligand useless [95,103,128,129].

When utilizing a ligand for BBB crossing, another parameter must be considered: what exactly are we trying to target. While the question might seem banal, the specific targeting of brain diseases is often overshadowed by the successful crossing of the BBB. Many hard-to-treat diseases are labeled as such due to being in a hard-to-reach organ, or due to the difficulty of diagnosis and treatment at early stages. Getting the NPs across the BBB is difficult due to its tight junctions, selective receptors, and efflux transporters, but is sufficient for early-stage diagnosis, and to minimize off-target effects; however, it is also important to have a disease-specific ligand in order to generate a therapeutic effect. Ligands that directly target the cells of interest are growing as a research field, leading to two possible options: 1) Decorating NPs with different ligands for each different effect [130], or 2) finding ligands that have more than one effect, directly leading to the

ultimate desired outcome [112]. The first option allows to directly select each ligand for its optimal efficiency and effect, but drastically complicates the synthesis or modification of the surface of the NPs. This is due to not only the need to have different chemical reactions and protecting groups to ensure that both ligands can be bound to the same surface, but also greatly complicates the quantification of the ligands and characterization of the surface. The second option is clearly more favored, but the possibility of a ligand to have both organ and diseased cell specific delivery is much less likely and harder to find and demonstrate.

Numerous ligands have taken the spotlight for organ and disease specific delivery ranging from peptides, antibodies, aptamers, or small molecules, each of them presenting advantages and disadvantages [131–134]. Small molecules are easy to synthesize and modify, but they show poor specificity for their target. Aptamers on the other hand can be more specific, but they are very sensitive to microenvironmental conditions and tend to be rapidly cleared from the tissue. The most specific ligands among these classes are antibodies, thanks to their 3D structure; however, their use is limited by their high cost and potential immunogenicity. To date, the ligands with the most promising balance for effective applications are peptides, which present good specificity, low cost, and easy synthesis (Table 1).

**Table 1.** Examples of ligands used for active targeting of NPs.

| | **Ligand** | **NP type** | **Target** | **Ref** |
|---|---|---|---|---|
| Peptides | EphA2-targeting peptide | Liposomes | osteosarcoma | [135] |
| | CPKSNNGVC | PLGA NPs | colorectal cancer | [136] |
| | VHPK | poly(ß-amino)esther NPs | inflamed endothelial cells | [137] |
| | g7 | PLGA NPs | BBB | [138] |
| | a6 | micelles | multiple myeloma | [139] |
| Aptamers | PrPC aptamer | gold NPs | colorectal cancer | [140] |

| | | | | |
|---|---|---|---|---|
| | AS1411 | PLGA-PEG | lung cancer | [141] |
| | A10 | PLGA-PEG | prostate cancer | [142] |
| | A6 | hybrid DSPE-PEG PLGA NPs | breast cancer | [143] |
| | Wy5a | PLGA-PEG | prostate cancer | [144] |
| Antibodies | Anti-CD105 | MnO NPs | breast tumor | [145] |
| | Anti-CD3 | protein NPs | T-Cells | [146] |
| | Anti-EGFR | gold NPs | breast tumor | [147] |
| | Anti-CD38 | SLNs | lymphoma | [148] |
| | OX-26 | PLGA NPs | BBB | [149] |
| Small molecules | Folate | lipoplex | leukemia | [150] |
| | BPA | polymeric micelles | melanoma | [151] |
| | lactoferrin | graphene oxide NPs | Glioma | [152] |
| | glucose | gold NPs | breast cancer | [153] |
| | alendronate | liposomes | bone | [154] |

In Chapter 3, research articles on targeted NPs are presented. Here, polymeric or hybrid NPs were surface functionalized with different ligands that were demonstrated to allow for the BBB crossing. Moreover, one ligand was demonstrated to be cell specific on glioblastoma cells, paving the way for the development of a more specific NP against glioblastoma multiforme.

### Controlled Release

One of the advantages of using NPs is the possibility to control the release kinetics of loaded drugs, thanks to properties of the core material composing the NP and strategies of drug loading (Figure 6).

Drug release from matrix NPs, where the active molecule is homogeneously dispersed in the material composing the core, is controlled by the characteristics of the matrix. Depending on the polymers or lipids used, the NP might present or

create hydrophilic pores that promote drug release by diffusion. This effect is more frequent for hydrophilic polymers, such as cellulose or chitosan, while lipids and hydrophobic polymers can generally ensure a slower release due to less interaction with biological fluids. A second mechanism of drug release is linked to the degradation of the matrix. In case of non-biodegradable polymers, drug release will be only controlled by diffusion, generating a more controlled system that has the drawback of accumulating in the tissues. Biodegradable NPs, on the other hand, release the drug by degradation of the polymer; thus, control on the degradation rate of the core material is key to tune the release profile of loaded drug. To do so, the molecular weight and the crystallinity of the molecules are two crucial parameters, where an increase in either of them will lead to a slower degradation, hence a more controlled release. Crystallinity is often reported to be a major issue in the controlled release of therapeutics from solid lipid nanoparticles. In fact, this type of NPs are often deemed as poorly stable, as the solid lipids in the matrix tend to reorganize during storage to their more stable crystalline form, thus expelling the drug from the matrix in the storage medium and hampering the controlled release [155–158].

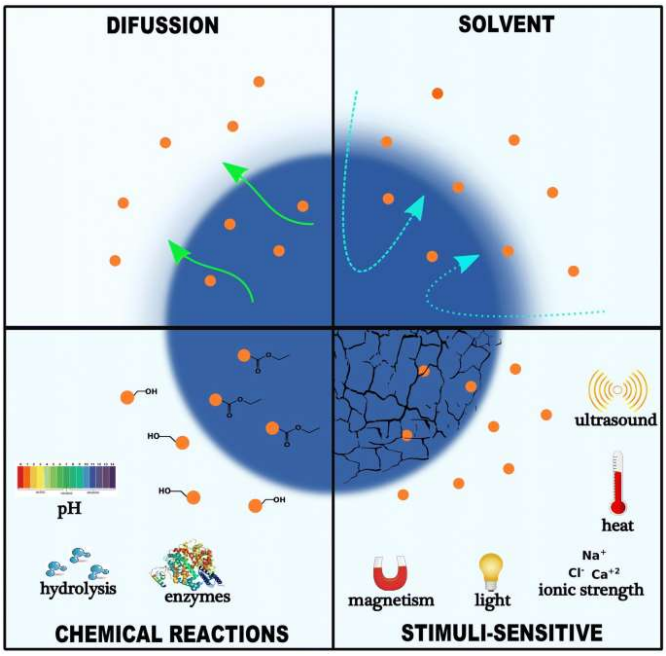


**Figure 6.** Graphical representation of the main mechanisms driving drug release from NPs (from [159]).

To achieve controlled release, strategies only based on the molecular weight, spatial organization, and crystallinity of the matrix component might be insufficient, and poorly tunable. Another possibility is to retard the release by introducing a stimuli-responsive mechanism. Delayed release after a stimulus such as pH, light, ultrasound, or enzymes usually follows the design idea of prodrug design. In this case, the drug is generally chemically linked to the core material of the NP via a sensitive linker, which can only be disrupted in certain conditions. This strategy, which can be combined with passive or active cell targeting, and with all the considerations mentioned above for the progressive release, can also improve specific drug delivery, as the linker can be only cleaved at the target site [160–164]. One prime example where this idea was investigated is the tumor microenvironment. The acidic pH and the presence of overexpressed enzymes are both factors that were taken advantage of by covalently conjugating cytotoxic drugs to the NPs, that would be only released in the tumor vicinity [165–167]. Similarly, nanobubbles were developed for the administration of drugs, and the drug release was ensured by the application of ultrasounds with an external device [168,169].

Finally, a last strategy can be applied to control and prolong the release of a therapeutic agent from a NP system: embedding NPs into an implantable scaffold. Biocompatible scaffolds, such as hydrogels, xerogels, or biotechnological structures, are now on the rise as promising tools for wound healing, tissue regeneration, and also organ substitutes. By systematically optimizing and controlling the characteristics of these scaffolds it is possible to control their formation, density, hydrophobicity, and degradation kinetics. These characteristics can also have a drastic effect on pharmaceutical profiles. In fact, implantable scaffolds can be loaded either with drugs such as small molecules, growth factors, chemotactic molecules, or even with previously formulated NPs [170–174]. The advantage of loading NPs into a scaffold is the possibility to take advantage of the characteristics of NPs, such as the protection of sensitive molecules, improved solubility and biocompatibility, and specific targeting.

Moreover, the controlled release of drugs from the NPs can further be optimized by tuning the properties of the implantable scaffold, leading to a finely controlled prolonged release that can be used to improve long-term treatments [175–180].

This strategy was investigated in Chapter 4, where hybrid NPs were loaded into an injectable hydrogel for sustained release of active molecules to the retina. The system, composed of hyaluronic acid and poloxamer 407, demonstrated the ability to be liquid at 4°C and to form a hydrogel over 35°C, representing the administration in vivo via intravitreal injection, and to delay the release of embedded NPs for up to 36 h after injection.

## Scalability

The production of nanoparticles has had huge success in the literature and to treat diseases both *in vitro* and *in vivo* models; however, many benchtop methods for small scale production are not adaptable to the large scale-up needed for cheap and fast commercialized production [181–185]. The need for methodology that allows for the minimization of solvents, expensive additives, and time, while increasing reproducibility and automation of Good Manufacturing Processes (GMP) qualified production is critical. The recent pandemic of Covid-19 demonstrated how critical this point is in the research field. The need for high throughput screening and production have led to the emergence and improvement of microfluidic technologies for drug screening, infection screening, and production protocols [186–189]. The industrial success of these techniques has led to an explosion of both home-made, 3-D printed, and industrially produced microfluidic devices [190–194].

Microfluidic technology is based on the controlled mixing of two or more different solutions into a device with microchannels. The channels can be optimized to have different geometries, dimensions, and materials, in order to be versatile for the production of a variety of nanosystems. In particular, microfluidic devices have been largely optimized for the production of liposomes, by simply mixing an organic solution of lipids with an aqueous buffer that might contain the drug (Figure 7). Similarly to standard techniques for liposome production, phospholipids will spontaneously self-assemble into vesicles, but the microchannel allows for a fine control on the nucleation that leads to the formation of highly homogeneous, small unilamellar liposomes [195–199]. This simple, single-step approach can be directly combined with a purification process, often using tangential flow filtration, creating a system that is easily scalable and usable by pharmaceutical companies. In fact, this happened for the production of the Covid-19 vaccine, where companies like Pfizer and Biontech exploited a

microfluidic technology to produce an mRNA-loaded liposome for global distribution and in such a short time [200,201].

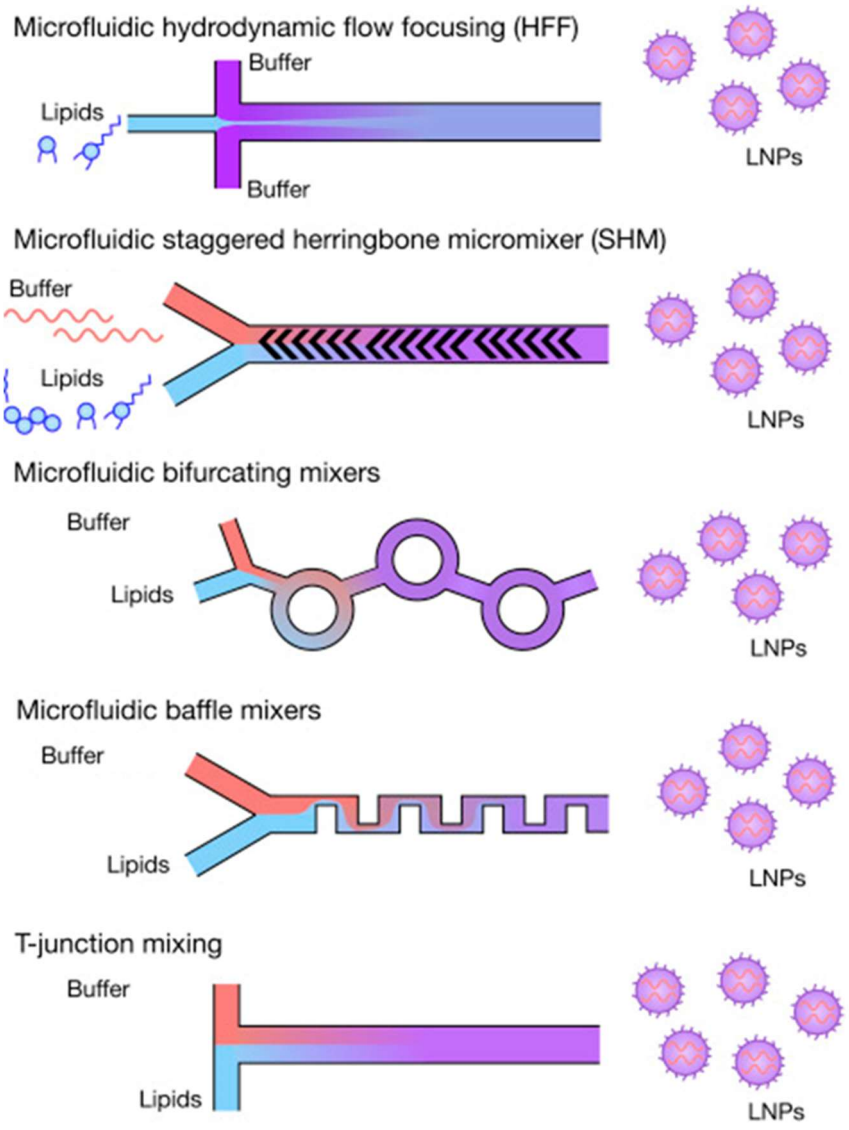


**Figure 7**. Examples of different geometries used for the fabrication of NPs with a microfluidic device (adapted from [202]).

While these systems have hit the spotlight with their many advantages, there are still some issues that need to be addressed. By optimizing the setting of the technology, it is also crucial to analyze whether the resulting NPs maintain the same characteristics of the already optimized products. In fact, while transferring benchtop protocols to microfluidic devices could help improve reproducibility and production rates, it is of paramount importance to ensure that not only the chemico-physical properties (size, PDI, surface charge) are suitable, but also the

structure and organization. Several researchers show that NPs, and in particular liposomes, can be formulated with identical properties compared to their benchtop brethren; however, this study is more complicated for polymeric and hybrid systems, less prone to spontaneous self-assemble, where the composition, morphology, and biological effects can vary depending on the production conditions [203,204]. So while the GMP production and automation of these systems can be considered a huge step in the right direction for improved use of NPs, a huge amount of time and effort must go into demonstrating that they will lead to clinically suitable NPs that not only are reproducible from the small lab scale, but also can ensure the same *in vitro* and *in vivo* results.

This issue was analyzed in the work reported in Chapter 5. Here, the production of hybrid NPs, already optimized and demonstrated to be efficient *in vivo* against Huntington's disease, was optimized using a microfluidic device. Results were compared to the NPs obtained by benchtop methods, revealing that chemico-physical and compositional features are insufficient to determine whether these two systems are equivalent, as demonstrated by a greatly different behavior when tested for storage stability.

## Biological fate of Nanoparticles

Unfortunately, even optimizing all the previously described variables of nanotechnology delivery systems, the last barrier to an effective therapeutic strategy lies in its passage throughout the body. NPs have become notorious, and are being heavily studied for their stability and reactions with biological environments and how this can affect their biodistribution and, ultimately, their biological fate. It is well known that any injected therapeutic, especially NPs, have biological consequences that could include toxicity and the activation of the immune system; however, the true story is more complicated than that. Immediately upon administration and entrance into the bloodstream, NPs have been shown to quickly and intimately react with the numerous blood components. As previously discussed, the system must be designed to not activate the immune or clotting response, nor should they be rapidly degraded by blood enzymes; however, interactions with the hundreds of different blood proteins is inevitable. This interaction forms a protein layer around the system coined as the "protein corona" (PC) [205–207]. Independent of the type of material, size, and zeta potential, blood proteins will rapidly be attracted to and interact with the surface of the nanosystem. While these interactions are inevitable, which and how much of each protein is highly variable, and dependent on the same properties of the NPs. The proteins with the highest affinity to the surface of the delivery system make up a closely associated and stable layer called the hard corona. Outside of this layer, are interactions with a much more dynamic layer of other proteins that make up the weakly bound soft corona (Figure 8). These two layers that comprise the entire protein corona have been demonstrated to show important and decisive effects in the biodistribution of NPs. In fact, the presence of certain classes of proteins, such as transport proteins, cytokines, complement factors, or immunoglobulins can determine a stealth effect for the NPs that bear them, or induce a reaction leading to elimination of the NPs and toxicity [208–214].

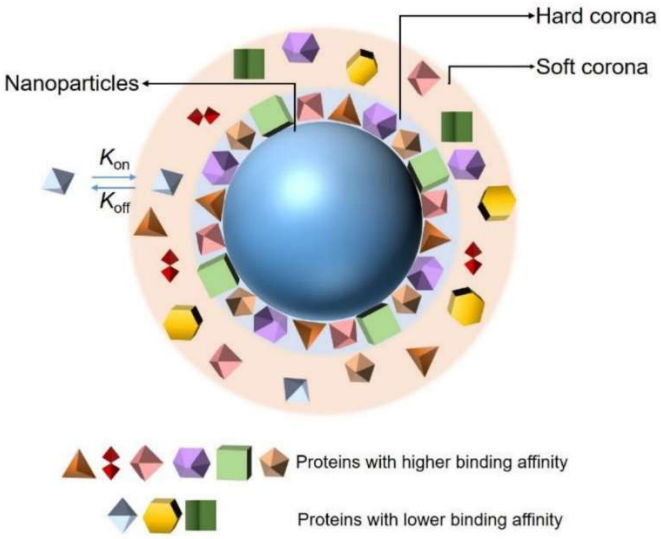


**Figure 8**. Schematic representation of the formation of the protein corona on the surface of NPs after administration (from [215]).

The most complicated aspect of the PC is that it is very diverse, and has been shown to be different for each type of nanosystem [216]. Major differences have been shown between distinctly different systems such as inorganic (gold, silver, silicon etc) compared to lipidic, compared to polymeric systems; however, even minor changes in the characteristics of the system can have drastic effects. Only considering polymeric systems, substantial differences have been seen depending on the size, zeta potential, and the presence of surface modifications, such as PEGylation or the addition of targeting ligands. These differences in the amount and quality of the proteins of the PC can promote the removal of NPs by the first pass clearance organs (liver, spleen, kidneys), toxicity, immune response activation, eventually affecting biodistribution, targeting ability, and uptake in the cells by possibly interfering with the correct interaction between a surface ligand and its receptor [217]. On one hand, some researchers have proposed to take advantage of the formation of the PC by creating an artificial PC *in vitro* before administration. By coating NPs with large inert proteins such as albumin, which can normally make up for the major part of the PC, it is possible to reduce the interaction of the NP with proteins in the bloodstream, enhancing the possibility to control their fate [218,219]. On the other hand, an in-depth investigation of the features of NPs that drive PC formation, the impact that each protein can have on

the NPs' fate, and the significant amount of each protein to have a biological effect is still missing in the literature [220]. In fact, this intricate and complicated process is dependent on so many minor variables that it must be evaluated for each individual delivery system, as minor changes can lead to drastic differences in the biological distribution and therapeutic effect of the systems.

In chapter 6, a research about the composition of the PC of three different NPs is reported. In this work, polymeric, lipidic, and hybrid formulations were incubated with plasma, and the composition of the different PCs was analyzed and compared. Our research evidenced how the literature lacks a comprehensive investigation on the mechanism driving PC formation, as in our case the two NPs that seemed the most similar from a chemico-physical point of view were the two with the most different PC.

Another phenomenon that doesn't receive the proper attention is the trafficking of NPs via Tunneling Nanotubes (TNTs), which could hamper the efficacy of the most carefully optimized NPs in terms of core material, stabilizers, targeting ligands, drug release profile, and protein corona formation [221–225]. TNTs are connections spontaneously formed between cells, often as a response to stressing stimuli. These bridges are formed by cell membrane and allow for the exchange of almost any kind of cytoplasmic material, such as ions, proteins, enzymes, organelles, and NPs [226]. Exchange of NPs between cells via TNTs could be a double-edge sword: on one hand, this could help spread treatment to a larger portion of the target organ, enhancing therapeutic efficacy. On the other hand, TNTs can also be formed between cells of different types, and the transportation of drug-loaded NPs from a target cell to a non-target cell would lead to unnecessary toxicity [227,228].

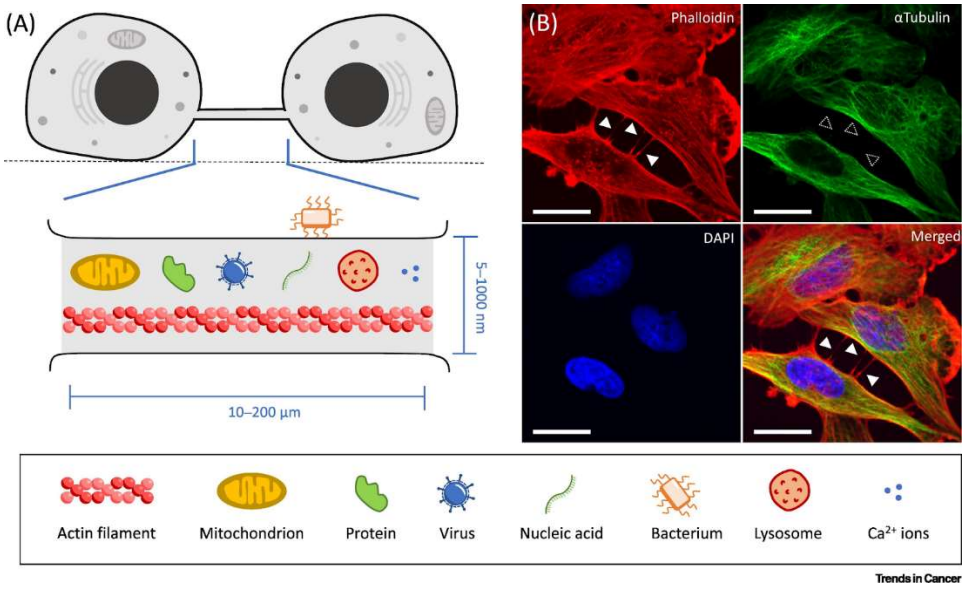


**Figure 9.** A) Graphical representation and B) confocal imaging of Tunneling Nanotubes, and examples of different materials that can be exchanged via TNTs (from [228]).

A major limitation in the study of the exchange of NPs via TNTs is the fact that TNTs were only discovered in the early 2000s. These constructs are still novel, and the mechanisms that drive their formation are still poorly understood. However, in the last few years, many researchers have observed that TNTs are a major player in the effective targeting of NPs, but a comprehensive study on how to selectively promote TNTs formation by tuning NPs' properties is still missing. This is the main focus of the literature research reported at the end of Chapter 6, where the most important investigations about NP transport via TNTs were compared to highlight the areas that still need to be addressed in the field.

# AIM OF THE STUDY

Advances in nanoparticles for medical applications have made leaps and bounds to improve modern treatments and lead to novel therapeutic options for hard-to-treat diseases. The selection and design of the core matrix and investigation on their assembly into nanostructures has led to a vast array of possible therapeutic delivery systems; however, most have not come to fruition as a viable cure of a disease. The reason for this limitation is their complexity. The number of variables that must all be optimized and fall into line to create a fully functional therapeutic system is a daunting task ranging from: selection of the core material, selection and quantification of the additives, optimization of the formulation techniques, selection of an appropriate drug molecule, stabilization of the drug during production, and modification of the system with targeting ligands to have cell specific affinity for diseased cells over healthy cells. Notwithstanding the improvements linked to these factors, their upscaling for industrial production and their biological fate after administration are still two limiting factors of the use of nanoparticles as therapeutic drug delivery systems.

This thesis focuses on projects that made up the work throughout my doctoral thesis to improve different aspects of nanoparticle design and optimization. Early projects worked on the synthesis of a novel hybrid polymer (PLGA-chitosan) to improve the range of therapeutics normally compatible with polymeric cores for improved formulation of small molecules, hydrophilic molecules, and genetic material. This work then expanded into drug compatibility, investigating the possibility of enzyme delivery. While the catalytic production of products is a major advantage in enzyme delivery, its delicate 3-D nature makes it hard to protect, encapsulate, and deliver to the diseased site. To this end, optimizations were performed to conserve enzyme activity during the formulation process of nanoparticles by using protective agents such as BSA and Tween, different molecules with distinct protective properties.

With optimizations of the core structure and stabilization of the therapeutic agent underway, it was important to also look into targeting moieties. A novel deltorphan-derived peptide was tested for its ability to pass the BBB, while a known ligand (ANG-2) was tested for its ability to transport a therapeutic agent into the brain. In another work, the efficacy of a BBB-penetrating peptide was demonstrated in vivo by delivering Cholesterol to the brain of Huntington's Disease mice. Moreover, novel ligands for the BBB, but linked to glioblastoma multiforme cell pathways, were tested for their ability to target both the BBB and enter specifically into cancerous cells over healthy astrocytes.

The possibility to prolong the release of therapeutic molecules from nanoparticles was investigated with the optimization of an injectable hydrogel. The system, loaded with retinal targeted hybrid nanoparticles, was optimized to be injectable in the vitreous and to form a stable hydrogel after administration due to temperature sensitivity. This complex system was able to delay the release of NPs from the hydrogel matrix, which could help ameliorate the current strategies for retinal delivery of therapeutics.

To ensure that any positive results would have a chance to pass from bench top methodology to industrial production and commercialization, microfluidic techniques were adapted to try to produce NPs with similar characteristics as those produced in small scale by benchtop protocols, highlighting how this aspect still needs to be properly addressed in the literature.

Finally, the interaction of NPs with the biological environment was analyzed. On one hand, the effect of changing the matrix composition of NPs on the protein corona and their biological fate was investigated. Polymeric-, lipidic-, and hybrid nanoparticles were, for the first time, analyzed for the composition of their HC and SC when incubated in Plasma to determine what changes can be made to improve their biocompatibility and risk of creating an immunogenic effect. Lastly, an evaluation of current literature about the interaction of NPs with Tunneling Nanotubes, their exchange via TNTs, and possible consequences was performed.

Nanotechnology delivery systems are incredibly complicated and elegant systems that require huge amounts of research and know-how to push existing candidates towards a functional and utilizable therapeutic option. Each step from design, synthesis, formulation, targeting, in vivo studies and upscaling is as important as the previous and each requires extreme precision and control to create a functional therapeutic system. The studies presented in this thesis demonstrate the small steps moved towards the creation of effective nanotechnology options against hard-to-treat diseases, altogether making a giant leap towards effective nanotherapeutic treatments in the future.

# CHAPTER 1

# Design of the Core Material

# Investigating novel syntheses of a series of unique hybrid PLGA-chitosan polymers for potential therapeutic delivery applications

**Jason Thomas Duskey [1,2], Cecilia Baraldi [3], Maria Cristina Gamberini [3], Ilaria Ottonelli [1,4], Federica Da Ros [1], Giovanni Tosi [1], Flavio Forni [1], Maria Angela Vandelli [1], Barbara Ruozi [1]**

[1] Nanotech Lab, Department of Life Sciences, University of Modena and Reggio Emilia, Italy

[2] Umberto Veronesi Foundation, Milano, Italy

[3] Department of Life Sciences, University of Modena and Reggio Emilia, Italy

[4] Clinical and Experimental Medicine PhD Program, University of Modena and Reggio Emilia, Modena, Italy

*Polymers* 2020, 12, 823, doi:10.3390/polym12040823

This article belongs to the Special Issue: "Polymeric Carriers for Biomedical and Nanomedicine Application"

Received: 10 March 2020

Revised: 26 March 2020

Accepted: 30 March 2020

Published: 4 April 2020

## Abstract

Discovering new materials to aid in the therapeutic delivery of drugs is in high demand. PLGA, a FDA approved polymer, is well known in the literature to form films or nanoparticles that can load, protect, and deliver drug molecules; however, its incompatibility with certain drugs (due to hydrophilicity or charge repulsion interactions) limits its use. Combining PLGA or other polymers such as polycaprolactone with other safe and positively charged molecules, such as chitosan, has been sought after to make hybrid systems that are more flexible in terms of loading ability, but often the reactions for polymer coupling use harsh conditions, films, unpurified products, or create a single unoptimized product. In this work, we aimed to investigate possible innovative improvements regarding two synthetic procedures. Two methods were attempted and analytically compared using nuclear magnetic resonance (NMR), fourier-transform infrared spectroscopy (FT-IR), and dynamic scanning calorimetry (DSC) to furnish pure, homogenous, and tunable PLGA-chitosan hybrid polymers. These were fully characterized by analytical methods. A series of hybrids was produced that could be used to increase the suitability of PLGA with previously non-compatible drug molecules.

## 1. Introduction

The discovery of effective therapeutic drugs is becoming increasingly difficult as seen by the drastic decline of new therapeutics accepted for public use each year. This is seen even with advances in structure activity relationship (SAR) studies [229], computer simulations of target structures (specific binding sequences and shape elucidation) [230], and high throughput screening methodology [231]. Novel surfaces and delivery nanosystems have taken the spotlight as the leading hope to advance new drugs from research into and beyond clinical studies by overcoming factors such as: lack of solubility, poor stability, poor biodistribution, immune response activation, off-target affects, and poor accumulation at the target site. Polymeric and lipid formulations have been taken advantage of to create fine-tuned systems to include targeting [232–234], triggerable activation (heat, light, reactive oxygen species (ROS), pH) [235–237], and varied uptake mechanisms to deliver pharmaceutics against numerous diseases [238–240].

In this respect, poly(lactic-co-glycolic acid) (PLGA) is of high interest due to the fact that it is: (1) FDA approved; (2) chemico-physically tunable to match biodistribution or loading needs; (3) capable of producing both nanosystems or polymeric scaffolds; (4) chemically modifiable to include stealthing moieties (polyethylene glycol, PEG) and/or targeting ligands. All of these aspects have been widely exploited in production of PLGA nanoparticles (NPs) for the possible cure of a plethora of diseases [138,241–245].

While PLGA NPs display many advantages in drug formulation, in comparison with cationic bio/polymers, they can suffer poor encapsulation efficiency when loading negatively-charged molecules. For example, while cationic bio/polymers (i.e., chitosan, cationic lipids, poly-ethylenimine, etc.) [246] can ionically bind negatively-charged DNA and form polyplexes, repulsion between the negatively-charged gene material and PLGA leads to negligible loading efficiencies. In this view, production of a co-polymer including chemical features needed for controlled release, absence of charge repulsion, and stable loading within the

protective hybrid polymer assembly could be the correct answer to these limitations.

Previously, attempts to overcome these limitations were investigated in various ways. First, by surface engineering negatively-charged NPs (such as PLGA) with cationic molecules in order to allow DNA absorption onto the surface [247–250]. While this approach could improve theoretical loading of gene material or other positively-charged molecules onto polymeric NPs, the stability of the exposed drugs in a biological environment and control of their release are still lacking. Secondly, a synthesis of chitosan on a PLGA film for adsorption of hydrophilic molecules of chitosan for protein loading [251]. While in this study loading was improved, the reaction was only monitored based on time and the film remained intact throughout all analysis and the presence of absorbed but not reacted chitosan could be present. By creating a controlled synthesis of hybrid polymers, it would be possible to include improved encapsulation of drugs into PLGA assemblies, improving encapsulation of the molecule as well as protecting it within the structure from desorption in the blood and degradation. Furthermore, systematically synthesizing series of hybrid polymers could allow for tunability to include controlled release kinetics and degradation kinetics of the molecules as well.

Therefore, in this research we attempt two different synthetic methods to create a pure hybrid PLGA-chitosan polymer series: solid phase synthesis on a film (adapted from Li et al. [251]), or in solution chemical reaction (adopted from a reaction to react chitosan to polycaprolactone [252]). This will allow for the synthesize of a unique series of PLGA-chitosan hybrid polymers with tailored and tunable physico-chemical characteristics that could be used to expand the use of PLGA delivery systems of currently incompatible drugs or environments and in a variety of drug delivery assemblies to treat a larger range of disease states.

## 2. Materials and Methods

### *2.1. Materials*

Poly (d,l-lactide-co-glycolide) acid [PLGA RG-503H 50:50, inherent viscosity in 0.1% (w/v) chloroform ($CHCl_3$) at 25 °C = 0.38 $dLg^{-1}$] was used as received from the manufacturer (Boehringer-Ingelheim, Ingelheim am Rhein, Germany). According to the experimental titration results of the carboxylic end of the polymers (4.94 mg potassium hydroxide (KOH)/g polymer) the molecular weight of RG-503H was calculated to be 11,000 Da. Low Molecular Weight chitosan, (mw 14,000) was purchased from Sigma Aldrich (Sigma Aldrich, Milano, Italy). All the solvents were of analytical grade, and all other chemicals and media were used as received from the manufacturers, and unless otherwise indicated, obtained from Sigma-Aldrich (Sigma Aldrich, Milano, Italy).

### *2.2. Solid Phase Synthesis of PLGA-Chitosan Co-Polymer*

The solid phase reaction of PLGA and chitosan was performed following the method of A.D. Li et al. with minor modifications (Scheme 1) [251]. Briefly, a PLGA solution (50 mg) was weighed into a round bottom flask and solubilized in 5 mL dicloromethane (DCM) and dried by rotary evaporation to create a thin film. The film was then washed for 1 h with 5 mL 6 w/v% NaOH (sodium hydroxide). This solution was discarded and the film was gently washed three times with 10 mL dilute HCl (hydrochloric acid 10%) followed by three more times with distilled water. The film was then completely covered in a solution containing N-Hydroxysuccinimide (NHS, 10 $mgmL^{-1}$) and 1-Ethyl-3-(3-dimethylaminopropyl) carbodiimide (EDC, 10 $mgmL^{-1}$) and reacted for another 6 h at room temperature in order to activate the acid group of PLGA with the NHS ester to promote the amide coupling with the amine of chitosan. This solution was discarded and the film was ultimately covered by a solution of 80 mL (reaction in round bottom flask) chitosan of 25 $mgmL^{-1}$ (pH 3.5). Remarkably, to achieve this pH value in which the chitosan becomes more soluble with decreasing pH it becomes highly viscous, HCl

(1N) was added dropwise and stirred vigorously for several minutes between each additional drop. Therefore, rigorous stirring for several minutes is needed in order to ensure the added HCl is dispersed uniformly throughout the solution and to avoid pockets of extreme acidity. After reacting for 48 h, the chitosan solution became much more transparent and less dense. The same procedure up to this point was also performed on a film on the surface of a glass petri dish (diameter 10 cm) with the following changes: the PLGA (150 mg) in 9 mL DCM evenly dispersed over the surface of the petri dish was left to evaporate at room temperature under a chemical hood overnight instead of on a rotary evaporator. The volumes required to cover the film with ~1 cm of each solution were decreased: NaOH 15 mL, EDC 15 mL (10 $mgmL^{-1}$), NHS (15 mL 15 mL (10 $mgmL^{-1}$), chitosan 15 mL (25 $mgmL^{-1}$, pH 3.5). This decrease in volume was possible because unlike in the round bottom flask where a large volume is needed to fill in the 3D spherical space, on a flat surface the volume needed to cover the film is a much smaller cylindrical cross-section of the round bottom flask (1 cm thick cylinder). All material from the round bottom or petri dish was poured into a separation funnel and the reaction vessel was washed 3 × with water followed by 3 × with DCM (10 mL each), in order to remove products and starting material that are soluble in aqueous or organic solvents, and added to the separatory funnel. After allowing the extraction to separate for 1 h at room temperature in the separation funnel, three distinct layers formed during separation: a clear DCM layer, a middle white emulsion, and the yellow chitosan solution. The three layers were separated into separate containers and lyophilized to calculate a percent yield and further characterization.

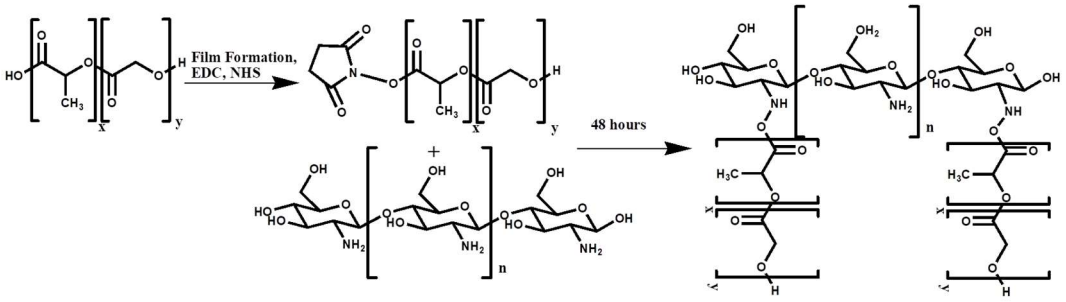


**Scheme 1.** Solid phase reaction of PLGA film with chitosan.

*2.3. Characterization Protocols of PLGA-Chitosan Co-Polymer in Solid-Phase.*

Characterization of chitosan-PLGA co-polymer was achieved by analysis in FTIR, and by NMR. The FT-IR spectra were recorded by a Vertex 70 (Bruker Optics, Ettlingen, Germany) FT-IR spectrophotometer, equipped with a deuterium triglycine sulphate (DTGS) detector (Bruker Optics, Ettlingen, Germany). Setting parameters are: resolution 4 $cm^{-1}$; apodization weak. The spectral range was 4000–600 $cm^{-1}$ with 32 scans for each spectrum. The ATR spectra were recorded using the Golden-Gate accessory (Golden Gate™ Single Reflection Diamond ATR Series MkII).

1H NMR and 13C samples of the solid phase reactions were run on a Bruker 600 mHz NMR (Bruker, Milano, Italy). Simply, 4 mg of sample were dissolved in deuterated water with 1% v/v deuterated acetic acid added (Chitosan, 700 uL), or deuterated dimethylsulfoxide (DMSO) (PLGA-chitosan product, 700 uL), scanned 40 (1H) or 3000 (13C) times and analyzed by Bruker Top Spin software (Bruker, Milano, Italy).

*2.4. Reaction of Chitosan and PLGA in Solution*

To perform the conjugation between chitosan and PLGA in organic solution, an organic soluble SDS-chitosan salt was formed (Scheme 2). In particular, adapting a protocol published by Cai et al. [252], a solution of chitosan (200 mg) in 2% v/v) acetic acid was precipitated with SDS (Sodium dodecyl sulfate 560 mg) in a rapport

of 1:100 for 2 h. The reaction was centrifuged for 10 min at 10,000 rpm in an ALC PK121 multispeed centrifuge (Concordia, Modena, Italy), the supernatant was discarded, and the precipitate was dried in a desiccator under negative pressure overnight. Simultaneously, PLGA was activated for reaction with chitosan by means of NHS-DDC technology. The covalent binding between the carboxy terminus of the polymer PLGA RG503H and the terminal amine of the peptide has been formed by standard methods, namely the activation of the carboxy group of PLGA by means of an ester with N-hydroxysuccinimide in the presence of dicyclohexylcarbodiimide, and the subsequent formation of an amidic linkage with the N-terminus of the unprotected peptide. Thus, to a solution of PLGA RG503H (1.00 g, 88 μmol) in anhydrous dioxane (5 mL), DCC (dicyclohexylcarbodiimide. 19.0 mg, 93 μmol) and N-hydroxysuccinimide (NHS, 11.0 mg, 93 μmol) were added, and the mixture was stirred for 4 h at 20 °C. After, the dicyclohexylurea was filtered away and the solution was decanted into cold anhydrous diethyl ether. The insoluble polymer was collected and purified by dissolution in DCM, followed by precipitation by the addition of anhydrous diethyl ether, then dried under reduced pressure. The content of NHS groups reacted with PLGA RG503H was determined by 1H-NMR spectroscopy (DPX 200; Bruker, Rheinstetten, Germany) in DMSO-d6, from the relative peak area of the multiplet at 2.95 ppm and of the multiplet at 1.80–1.60 ppm, corresponding to the protons of the N-succinimide and those of the methyl groups of the polymer, respectively, and resulted to be 49 μmol NHS/g of polymer. After having obtained both polymers, a fixed amount (50 mg) of the chitosan salt was then solubilized in anhydrous dimethylformamide (DMF, 10 mL) and reacted with different amounts (10, 50, or 240 mg) of activated PLGA-NHS (corresponding to ratio 1:5, 1:1, 5:1 chitosan: PLGA, respectively) and reacted for 48 h.

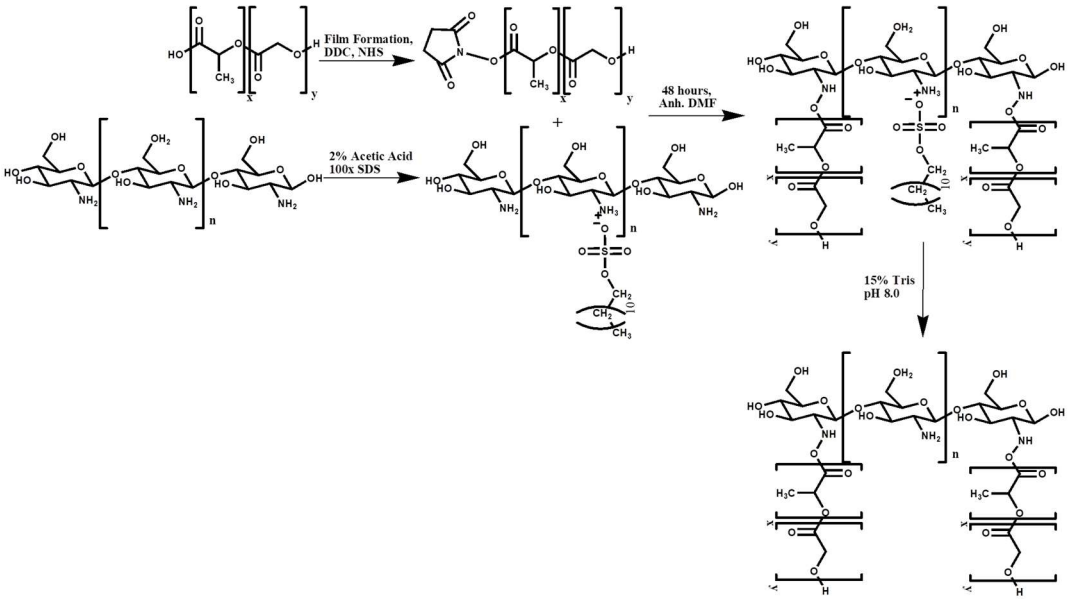


**Scheme 2.** Solution Phase Reaction using DMF soluble chitosan-SDS salt.

All the products were purified and isolated by means of centrifugation at 12,000 rpm for 10 min to remove any precipitated material during the reaction. The supernatant was then dried by rotoevaporation to yield a white/yellow powder containing the PLGA-chitosan/SDS salt conjugate. The SDS was then removed from the conjugate, which led to a precipitation of the final product by incubation in 50 mL 15% TRIS pH 8.0 for 48 h. The precipitate was then centrifuged at 12,000 rpm with an ALC PK121 multispeed centrifuge and the supernatant was decanted away. The final product was then dried by lyophilization and stored in a desiccator at room temperature until analysis. Solubility of the samples was tested by weighing 1 mg of each product and testing its ability to dissolve in DMSO or acetic acid (2% v/v) of concentrations of 200 $ugmL^{-1}$.

*2.5. Characterization Protocols of PLGA-Chitosan Co-Polymer in Solution*

FTIR was described as previously described. The FT-IR spectra were recorded by a Vertex 70 (Bruker Optics, Ettlingen, Germany) FT-IR spectrophotometer, equipped with a deuterium triglycine sulphate (DTGS) detector. Setting

parameters are: resolution 4 $cm^{-1}$; apodization weak. The spectral range was 4000–600 $cm^{-1}$ with 32 scans for each spectrum. The ATR spectra were recorded using the Golden-Gate accessory (Golden Gate™ Single Reflection Diamond ATR Series MkII).

After purification, NMR spectra were acquired at 300 K using an AVANCE III HD 600 Bruker spectrometer, equipped with a 2.5 mm H/X CPMAS probe operating at 600.13 and 150.90 MHz for 1H and 13C, respectively (Bruker, Milano, Italy). Samples were packed into 2.5 mm zirconia rotors and spun at the magic angle. 13C NMR spectra were obtained using a standard pulse sequence for cross polarization (CP), at 16 kHz magic angle spinning (MAS) rate. The relevant acquisition parameters for CP-MAS 13C NMR spectra were: 45 kHz spectral width, 10 s relaxation delay, 2.5 μs 1H 90° pulse, 62.5 kHz radio frequency field strength for Hartmann–Hahn match, 2k data points, and 2k scans. All chemical shifts were referenced by adjusting the spectrometer field to the value corresponding to 38.48 ppm chemical shift for the deshielded line of the adamantane 13C NMR spectrum.

Dynamic scanning Calorimetry of DSC was performed on a Netzsch Phox DSC 200 PC using the Netzsch Proteus analysis software (NETZSCH-Gerätebau GmbH, Selb, Germany). Samples were precisely weighed between 2–4 mg each into NETZSCH DSC-crucibles (Al; 25 uL) and sealed with their appropriate lids. An empty crucible was used as the reference sample. Samples were analyzed with the following thermometric gradient: 2 min isothermal gradient to standardize the starting point at 15 °C, 15–320 °C over 38 min increasing at 10 °C per minute, with a 2 min isothermal section.

## 3. Results

The most direct method of conjugating PLGA and chitosan is an amid bond formation between the amine on chitosan and the carboxylic acid of PLGA (Scheme 1). Functionally however, this reaction is complicated due to the extreme difference in solubility between the two molecules. Previous attempts reacted chitosan in solution with a PLGA film to create a positively-charged surface aiming to create nanofibers without the need for purification [251]. Another researcher produced the hybrid PLGA-chitosan polymer for the creation of nanoparticles, but it required harsh conditions (concentrated nitric acid) [253]. Therefore, to create a pure, reproducible, and controllable hybrid polymer that could be used in solution for NP formation, a reaction was performed under milder conditions on a PLGA film created by evaporating PLGA on a surface activating it with EDC and NHS and reacting it with a large excess of chitosan. After 48 h, the chitosan solution was removed and the product was purified in a biphasic solution of 0.1% acetic acid (PLGA-chitosan product) and DCM (non-reacted PLGA). Initial reactions were performed in a round bottom flask; however, to make the reaction greener by decreasing the ratio of surface area:volume (to decrease amount of solvent and reactants needed to cover the PLGA film), reactions were performed in a flat petri dish. This simple change not only decreased reaction volume (80 mL to 10 mL), but it also increased the % yield from ~25% to 50%.

Characterization of the product was performed by FTIR spectroscopy (a common technique for investigating interactions between polymers) and NMR. General FTIR points of interest for the reaction arise in the broad band between 3450 and 3200 $cm^{-1}$ (νOH + νNH) and two weak peaks at 2940 $cm^{-1}$ and 2890 $cm^{-1}$ (νCH2) (Figure S1, top panel). More critical for the identification of the conjugation of PLGA to chitosan are the major characteristic absorption bands at around 1648 and 1588 $cm^{-1}$, corresponding to amide I (νC=O) and amide II (δNH + νCN) of the residual N-acetyl groups. Under the band centered at 1585 $cm^{-1}$, the contribution of δNH2 is also hidden, which overlaps the amide II peak [254]. Pure PLGA

exhibits the strong characteristic adsorption peaks at 1170 and 1090 $cm^{-1}$ (νCOC, ether), 1130 $cm^{-1}$ (ϱCH3), 1452, 1390, and 745 $cm^{-1}$ (δCH), and peaks 3020 and 2930 $cm^{-1}$, which were attributed to νCH2 from glycolic acid portion, and νCH3 from the lactic acid portion. The most notable peak to discern the presence of PLGA arises at 1749 cm−1 (νC=O, ester) (Figure S1, bottom panel) [255]. FTIR analysis of the product showed that the mild acetic acid conditions did not result in the covalent linkage between PLGA and chitosan (Figure 1). While a shift in the amid bonds at 1648 and 1588 $cm^{-1}$ were observed, the new peaks did not correspond to further amid bond creation, but instead showed the resemblance of the formation of a chitosan salt [256] with bands further downfield at 1627 and 1517 $cm^{-1}$. Also, only a small emergence of a peak indicating the presence of the C=O of PLGA at 1748 $cm^{-1}$, but instead a peak at 1703 $cm^{-1}$ indicating the appearance of an acid was observed.

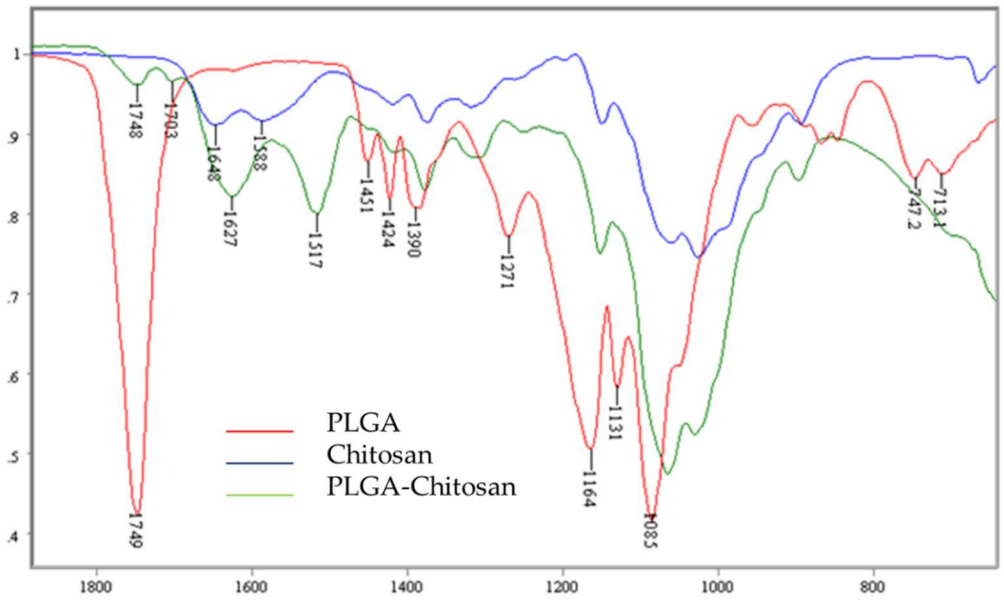


**Figure 1.** FT-IR/ATR spectra of unmodified poly lactic-co-glycolic acid (**red**), unmodified chitosan (**blue**), and PLGA-chitosan product (**green**).

NMR analysis confirms the poor reaction results. 1H NMR of the product and the chitosan control show little to no difference with the H2 peak at 3 ppm and the H3-6 peaks as a broad series of peaks at 3.5–4 ppm. These peaks corresponded to the

literature precedence of the 13C NMR peaks of the main carbon ring at ~ C1 (100 ppm), C3-5 (73–85 ppm), and C2,6 (55–60 ppm). However, the normal peaks expected for the PLGA C=O (170 ppm) or CH3 (1.5 ppm and 15 ppm 13C) or its degradation products (glycolic and lactic acid) are not present (Figure 2). Only small fragment peaks that do not cross correlate upon 2D analysis (Figure S2). Degradation of the PLGA into small fragments during the reaction would explain the FTIR results showing the formation of a small acid peak. It also could explain the amid bond shifts to that of the salt formation as small negatively-charged acidic degradation products could lead to a salt formation with the free amine of chitosan.

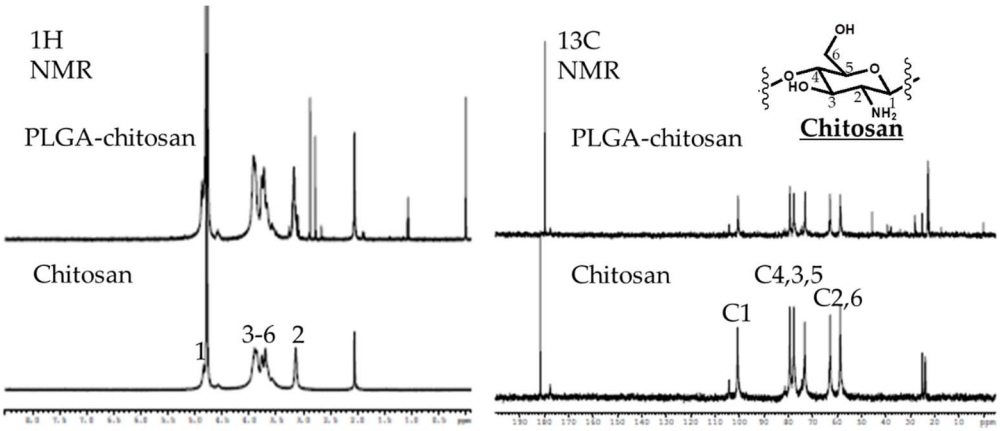


**Figure 2.** 600 MHz NMR Proton (**left panel**) and Carbon (**Right Panel**) analysis. Numbers indicate the Carbons (C1-6) of the chitosan ring structure or their respective hydrogens as depicted in the structure (Top right).

While the reaction of PLGA and chitosan is found in the literature, it is often performed with harsh conditions on gels or without purification. Using a solid phase reaction with mild reaction conditions did not prove successful. This ruled out this method as a viable option to create a controlled series of hybrid polymer variants for further characterization; therefore, more stable and controllable methodology was pursued.

The mild reaction conditions led to a lack of product formation. To overcome this, an alternate method was adapted in which chitosan is precipitated as an SDS salt

in order to improve its solubility in organic solutions (DMSO, choloroform, and DMF) [252].

This intermediate was then conjugated to PLGA-NHS in anhydrous DMF. To test the flexibility of the reaction, and to analyze the physical characteristics of various PLGA-chitosan hybrid polymers, a series of three reactions was performed: (1) an excess of chitosan in a 5:1 molar ration, (2) 1:1 chitosan: PLGA and (3) 1 chitosan: 5 PLGA (Table 1). The latter corresponds to an average of one PLGA being available for each sugar unit of chitosan. After reacting activated PLGA with chitosan-SDS for 48 h, the salt was dissociated in Tris 15% pH 8 for 48 h. The percent yield of the reactions increased proportionally with the increasing rapport of PLGA: chitosan in the reaction as shown in Table 1 (55%, 75%, and 82%). The solubility of the products also suggested an increased PLGA attachment due to the decreasing solubility in 2% acetic acid (*v*/*v*).

**Table 1.** Solution phase reaction conditions of PLGA and Chitosan-SDS.

| Reaction | Chitosan-SDS (mg Chitosan) | PLGA-NHS (mg) | % recovery | PLGA:chitosan in initial reaction solution (mol) | Solubility in Acetic Acid [a] |
|---|---|---|---|---|---|
| 1 | 50 | 10 | 55 | 1:5 | soluble |
| 2 | 50 | 50 | 75 | 1:1 | semi soluble |
| 3 | 50 | 240 | 82 | 5:1 | Not soluble |

a. 200 ug/mL 2% v/v

The conjugation of PLGA to chitosan again was analyzed by FTIR, and 13C NMR in solid state (due to the differences in solubility between the products). The PLGA and chitosan starting materials were identical to as described previously (Figure 1, Figure S1). In a PLGA concentration dependent manner, the progressive appearance and intensification of the band at 1755 cm−1, indicating the presence of PLGA (ester C=O stretching), can be observed (Figure 3). Unlike the solid-state reaction, bands indicating a chitosan salt formation were not observed (including the presence of the chitosan-SDS salt formation (1624 and 1523 cm−1)) (Figure S3). Instead, there was a clear and concentration dependent (based on initial PLGA amounts), shift indicating amid bond formation (Figure 3). This was confirmed by

observing the amide I and II peaks (1650 and 1585 $cm^{-1}$) shift to 1633 $cm^{-1}$ (amide I) and 1548 $cm^{-1}$ (amide II) (Figure 3). As compared with pure chitosan, the δNH contribution of the primary amine for the band at 1580 cm−1 decreases or even disappears, because of a change of primary amine in the chitosan chain into amide groups, as already attested in the literature [257]. The displacement of the band from 1586 cm−1 (chitosan) to 1549 cm−1 (PLGA-chitosan) suggests that the grafting reaction occurred mainly by the reaction between the −NH2 chitosan groups and −COOH PLGA groups. Furthermore, the band at 3184 cm−1 progressively increases, associated with NH stretching of the secondary amide (Figure 3 inset).

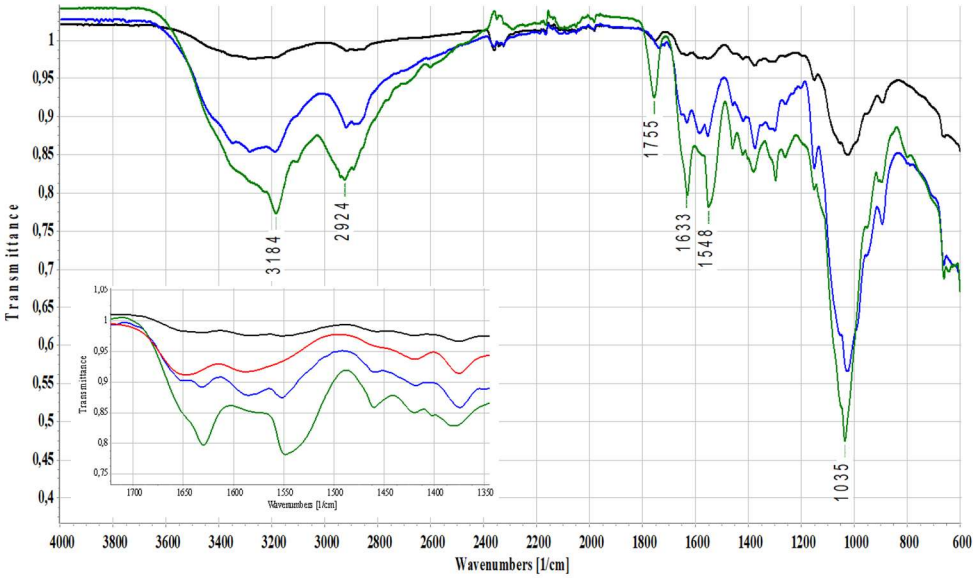


**Figure 3.** FTIR scan of PLGA-chitosan hybrid products of the reactions synthesized with different molar rapport of PLGA:chitosan of reaction (1) 1:5. black (2) 1:1. blue (3) 5:1. green, and (4) pure chitosan (red inset).

NMR analysis was used to support the FTIR findings (Figure 4). The solid-state NMR of pure chitosan showed the characteristic broad singlet at 100 ppm (carbon 1) along with two broad multiplet peaks between 50 pp, (carbon 2–5) and 90 ppm (carbon 6) in accordance with literature precedence (Figure 4 purple box) [258]. The pure PLGA exhibits the CH and CH2 peaks at 70 and 60 ppm, respectively, as well as the CH3 peak at 15 ppm and C=O peak at 170 ppm (Figure 4, orange boxes).

In all reactions, the iconic peaks of the chitosan can be seen. In all three reactions, the PLGA peak corresponding to the CH2 is hidden under the chitosan (purple box) and residual TRIS salt (blue box) peaks from 50–75 ppm, but the emergence of the CH peak at 70 ppm is observed (Figure 4, Figure S4). More evident however; is that by increasing the initial amount of PLGA in the reaction, the peak corresponding to C=O at 170 ppm (indicated by a star) as well as that of the CH3 group (indicated by an @) are seen to directly increase in intensity (Figure 4 orange boxes). It is important to note that SDS, and Chitosan-SDS salt (peaks 20–40 ppm) are not present in any of the samples indicating full removal of the salt back to the original chitosan structure in the product (Figure S4, red box). NMR analysis showed constant and equal NMR spectra across multiple product samples indicating the homogeneity and controllability of each product.

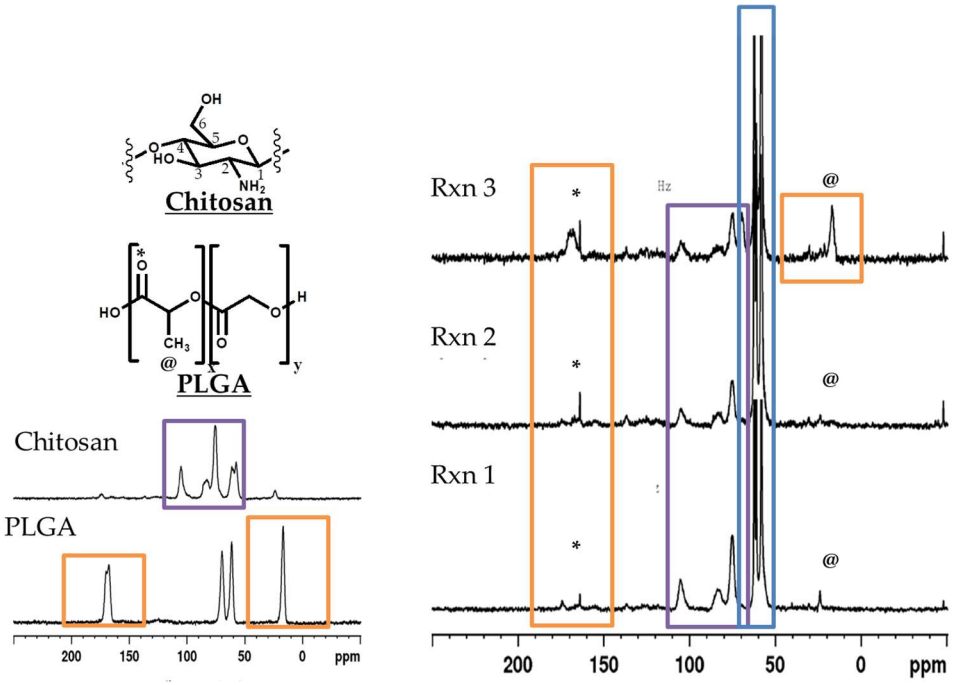


**Figure 4.** Solid state 13C NMR analysis with highlighted peaks of interest: chitosan (**purple**), PLGA (**orange**), TRIS salt (**blue**). Numbers indicate the Carbons (C1-6) of the chitosan ring structure or their respective hydrogens as depicted in the structure (Top left), * indicates the carbon of the PLGA carbonyl peak, and @ indicating the PLGA methyl group.

To further validate the conjugation of PLGA to chitosan, DSC analysis was performed (Figure 5). The transitional peak of PLGA was seen at 50 °C along with

an endothermic transition during its degradation between 280–380 °C. The chitosan control shows the liberation of the water entrapped between the chitosan chains at 115 °C along with an exothermic transition at approximately 300 °C reasoned to be the degradation of the chitosan ring structures permitting 3-D rotation. Analysis of the polymer samples showed a shift in all transitional states dependent on the concentration of PLGA in the initial reaction solution. With increasing amounts of PLGA, the transitional phase at 50 °C disappeared due to the loss of the glass transition when bound to chitosan. In a physical mixture of PLGA and chitosan however this transition was still observed (Figure S5). Secondly, a shift to higher temperatures of the water loss from 120 °C to 150 °C in sample 3 (with the most PLGA) exhibiting numerous peaks in this range. The energy required to remove the water associated with the chitosan chains is increased by the increased encumbrance of PLGA. Finally, the disappearance of the transition peak at around 290 °C caused by the bulky PLGA sterically hindering the free rotation of the chitosan chains as well as cancellation of the endothermic (PLGA) and exothermic (Chitosan) energies were observed supporting the FTIR and NMR data of the presence of increasing amounts of PLGA chemically linked to the chitosan chain. To ensure these changes were not caused by the presence of the chitosan-sds salt, a sample was also analyzed showing none of the characteristics of the polymer products (Figure S5).

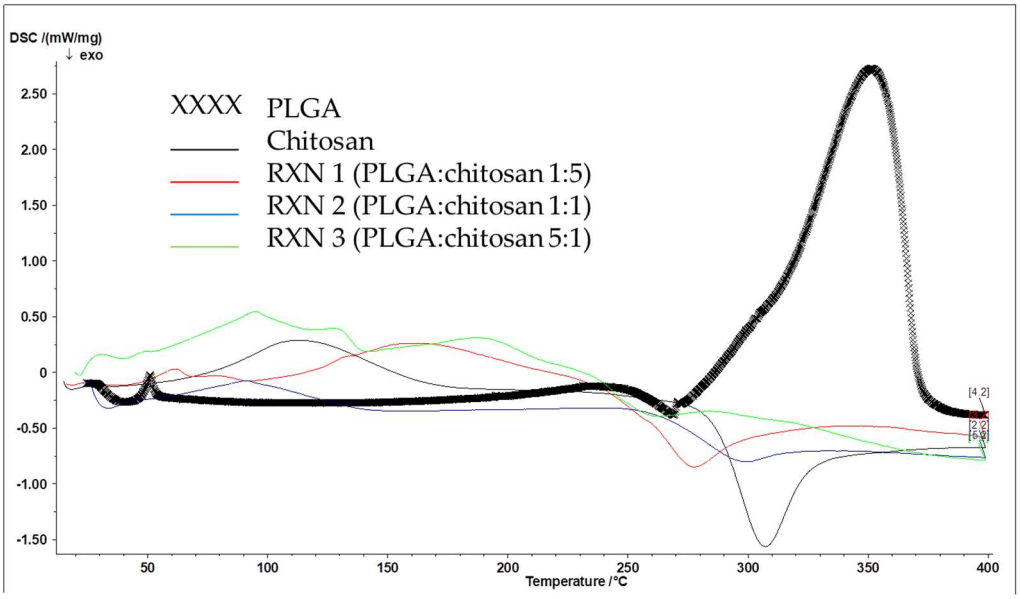


**Figure 5.** Dynamic scanning calorimetry analysi: PLGA (**black crosses**), chitosan (**black line**), and the three PLGA-chitosan reaction products based on PLGA:chitosan molar rapport: (1) 1:5 (**red**) (2) 1:1 (**blue**) and (3) 5:1 (**green**).

These three series of analysis not only demonstrate the formation of the hybrid polymer series using mild reaction conditions, but also show the versatility of the reaction in its ability to be stoichiometric controlled to create a uniform product unlike that seen by the solid-state reaction. The formation of the chitosan-SDS made it optimal for the reaction in organic solvents with PLGA. By varying the ration of PLGA in the reaction conditions from a 1:5 excess of chitosan, to 1:1, and finally to 5:1 excess of PLGA, it was possible to create a variation of hybrid polymers. The hybrid series was not only verified by the analytical characterizations, but also by the difference of solubility of the product. Controlling the reaction in a stoichiometric controlled manner to create such clean and reproducible product, hybrid polymers greatly increases the translatability and feasible uses of these polymers in drug delivery purposes.

## 4. Discussion and Conclusions

Finding new materials to stabilize molecules with poor stability, solubility, or biocompatibility properties is necessary to continue advancing new disease treatment methods with "critical" but non-compatible drugs. PLGA offers a very promising base material as it is FDA approved and has been used extensively to specifically target drugs to diseases as NPs or as site specific delivery agents inserted as a film but is limited in loading positively-charged molecules.

Creating new co-polymers in a constant and controlled manner offers an increasing utility of PLGA assemblies for a broader range of potential drug candidates in which it is currently non-compatible. To this end, two reaction methods were attempted to conjugate negatively-charged PLGA to the positively-charged chitosan to form a series of novel co-polymers. Previous works have attempted to make chitosan hybrid polymers using harsh reaction conditions (nitric acid), PLGA films, or in solution (to make polycaprolactone hybrid polymers) in a non-purified and uncontrollable manner. To truly benefit from these types of hybrid polymers, the reaction must be reproducible, controllable, create a series of pure homogenous products that can be selected dependent on the therapeutic need.

Data indicated that solid-phase synthesis using a PLGA film and mild reaction conditions was insufficient to create PLGA-chitosan hybrid polymers, but instead led to a salt formation with degradation products in solution. However, by utilizing an SDS salting out reaction to create a chitosan SDS intermediate that is soluble in organic solvents, a series of PLGA-chitosan co-polymers with different molar ratios were produced.

Remarkably, this reaction was able to furnish a unique series of pure and reproducible PLGA-chitosan hybrids with various molar rapport and solubilities. This controlled synthesis method makes these hybrids prime candidates for protection and delivery of a wide range of previously non-combatable drugs either as NPs formed through chitosan self-assembly techniques (for those still soluble in

acidic solutions) or for the encapsulation in stable and non-toxic films for long-term controlled release (for those insoluble in biological solutions).

These preliminary results could pave the way to further advances in the application of PLGA-based nanotherapeutics, expanding the tunability of the core polymer structure to be better suited for a wider range of drugs candidates to be loaded, protected, and delivered to diseased cells improving their potency and efficacy.

## 5. Supplementary Material

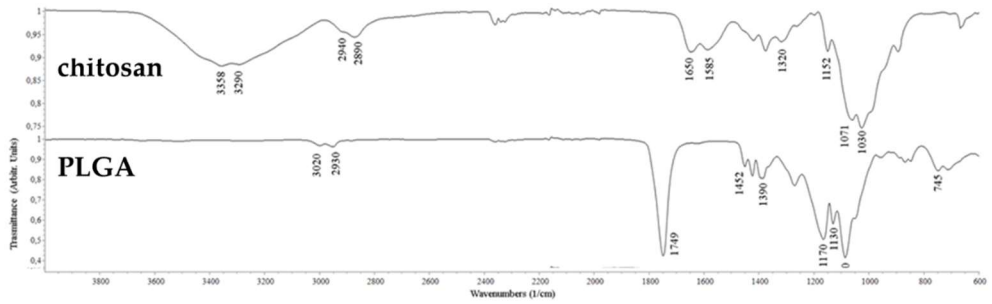


**Figure S1**: Full FTIR Scan of PLGA and chitosan polymers.

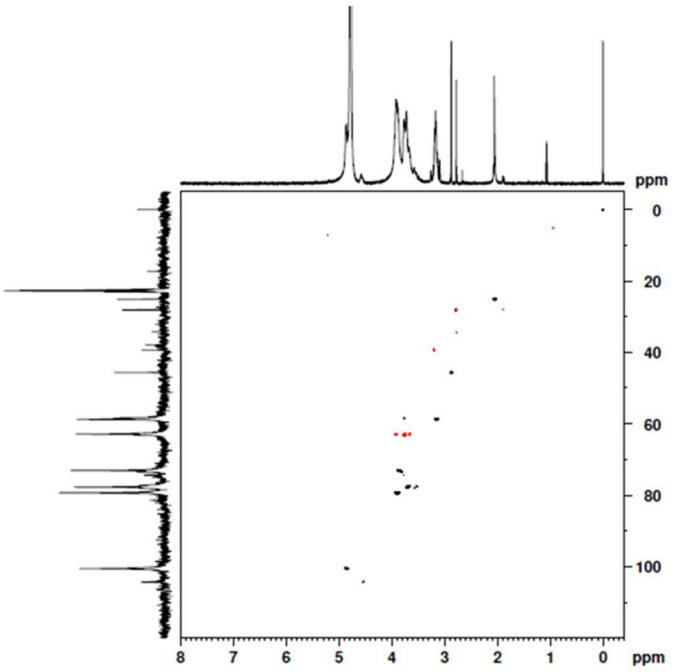


**Figure S2:** 2D NMR correlation analysis of the 1H and 13C PLGA-chitosan reaction product.

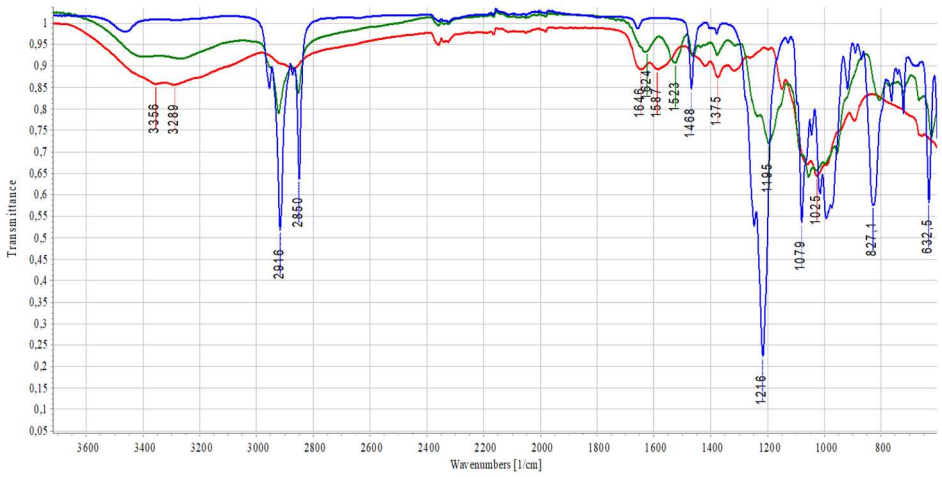


**Figure S3:** FTIR analysis of chitosan control (Red), chitosan-SDS salt (green) and SDS salt (blue).

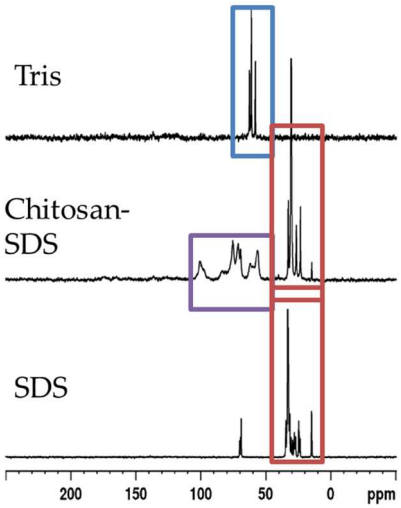


**Figure S4**: Solid state 13C NMR analysis with highlighted peaks of interest: chitosan (purple), SDS (red), TRIS salt (blue).

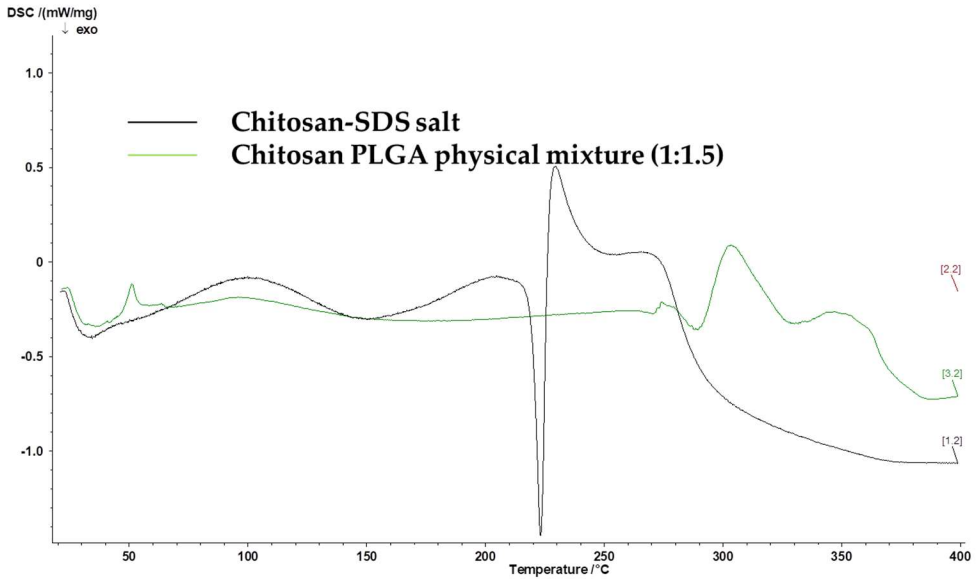


**Figure S5:** Dynamic scanning calorimetry analysis: chitosan-SDS salt (black line), chitosan : PLGA 1:1.5 physical mixture (green line).

# CHAPTER 2

# Stabilization of Sensitive Drugs

# Enzyme Stability in Nanoparticle Preparations Part 1: Bovine Serum Albumin Improves Enzyme Function

**Jason Thomas Duskey [1,2], Federica da Ros [1,3], Ilaria Ottonelli [1,4], Barbara Zambelli [5], Maria Angela Vandelli [1], Giovanni Tosi [1] and Barbara Ruozi [1]**

[1] Nanotech Lab, Te.Far.T.I., Department. Life Sciences, University of Modena and Reggio Emilia, 41125, Modena, Italy

[2] Fondazione Umberto Veronesi, 20122 Milano, Italy

[3] STEM Cell Lab, University of Milan, 20133, Milano, Italy

[4] Clinical and Experimental Medicine PhD Program, University of Modena and Reggio Emilia, 41125, Modena, Italy

[5] Laboratory of Bioinorganic Chemistry, Department of Pharmacy and Biotechnology, University of Bologna, 40127, Bologna, Italy

*Molecules* 2020, *25*, 4593, doi:10.3390/molecules25204593

This article belongs to the Special Issue: "25th Anniversary of Molecules—Recent Advances in Nanochemistry"

Received: 10 September 2020

Revised: 29 September 2020

Accepted: 6 October 2020

Published: 9 October 2020

## Abstract

Enzymes have gained attention for their role in numerous disease states, calling for research for their efficient delivery. Loading enzymes into polymeric nanoparticles to improve biodistribution, stability, and targeting in vivo has led the field with promising results, but these enzymes still suffer from a degradation effect during the formulation process that leads to lower kinetics and specific activity leading to a loss of therapeutic potential. Stabilizers, such as bovine serum albumin (BSA), can be beneficial, but the knowledge and understanding of their interaction with enzymes are not fully elucidated. To this end, the interaction of BSA with a model enzyme B-Glu, part of the hydrolase class and linked to Gaucher disease, was analyzed. To quantify the natural interaction of beta-glucosidase (B-Glu,) and BSA in solution, isothermal titration calorimetry (ITC) analysis was performed. Afterwards, polymeric nanoparticles encapsulating these complexes were fully characterized, and the encapsulation efficiency, activity of the encapsulated enzyme, and release kinetics of the enzyme were compared. ITC results showed that a natural binding of 1:1 was seen between B-Glu and BSA. Complex concentrations did not affect nanoparticle characteristics which maintained a size between 250 and 350 nm, but increased loading capacity (from 6% to 30%), enzyme activity, and extended-release kinetics (from less than one day to six days) were observed for particles containing higher B-Glu:BSA ratios. These results highlight the importance of understanding enzyme:stabilizer interactions in various nanoparticle systems to improve not only enzyme activity but also biodistribution and release kinetics for improved therapeutic effects. These results will be critical to fully characterize and compare the effect of stabilizers, such as BSA with other, more relevant therapeutic enzymes for central nervous system (CNS) disease treatments.

## 1. Introduction

Numerous proteins and peptides have received worldwide approval as therapeutic agents from regulatory authorities, and several hundred more are being tested in clinical trials. Among therapeutic proteins, enzymes represent a small but rapidly growing market due to their potential application in curing important, rare, and deadly diseases. For example, enzyme replacement therapy (ERT) is undoubtedly the most promising therapeutic approach for mucopolysaccharidosis (MPSs), as well as for some other forms of lysosomal storage disorders (LSDs) such as Gaucher disease [259], Fabry disease [260], and Pompe disease [261], in which remarkable clinical benefits are currently obtained [262]. Unfortunately, clinical applications of these macromolecules are hampered by numerous obstacles to their successful delivery and targeting. Enzymes frequently exhibit a rapid decrease in enzyme kinetics and specific activity due to their destabilization and short half-lives in serum, requiring frequent administration to maintain therapeutic levels. Also, improving their biodistribution remains a striking challenge as there is often poor accumulation in the pathological sites (especially in the central nervous system (CNS), bone, cartilage, cornea, and heart) [138,233]. A possible solution to these limitations lies on tailored delivery of enzymes by means of biodegradable and biocompatible nanomedicines (NMeds). Different NMeds, including polymeric micelles, liposomes, and polymer- and lipid-based nanoparticles (NPs) [263] have been exploited for enzyme encapsulation as they are able to protect enzymes from undesired immunologic reactions and biodegradation, to ameliorate the biodistribution of the enzyme, to improve the pharmacological response, and to modulate enzyme release at the target site limiting undesirable side-effects [264,265]. In this field, polymeric NPs, particularly those made of polylactide-co-glycolic acid (PLGA), have attracted considerable interest over the last few years as versatile tools for enzymatic delivery [266–268]. While many promising results have been described, frequently authors declare a certain criticism related to the

formulation aspect of enzyme-loaded NP formulations due to both low loading efficiency and the maintenance of the enzymatic activity [232,269].

Generally, in the function of the physico-chemical properties of the enzyme and the characteristics of the desired PLGA NPs, several techniques including nanoprecipitation, emulsion, sonication, extrusion and other stressful mechanical and chemical processes are employed during the preparation process. In particular, double emulsion water-oil-water protocols (also known as w/o/w techniques) have been widely tested for the encapsulation of hydrophilic molecules, such as therapeutic proteins and enzymes. This technique imposes substantial stresses on the chemical integrity and the native three-dimensional structure of proteins [270,271]. For example, protein inactivation and aggregation at the water/organic interface, probably due to interfacial adsorption followed by protein unfolding and aggregation, is one of the most detrimental events when applying this technique precluding the use of NPs [272]. Similarly, the application of ultrasonic energy to obtain nano-emulsions is important to consider as a critical process parameter. The complex physical and chemical phenomena that occur during the cavitation process (with extreme localized temperatures and pressures generated) can alter the molecular structure and cause potential surface charge changes in the enzyme [273].

Another critical methodology that significantly stresses the enzyme includes the freeze-drying process (such as lyophilization), applied to concentrate the enzyme and to allow stable storage of the NPs over time as was observed in our preliminary studies and confirmed in other literature sources [138,274].

To limit or solve the problems of enzyme encapsulation into polymeric NPs, the addition of a stabilizer such as polyols, sugars, inorganic salts, surfactants, and polymers [275,276] to protect enzymes by masking them from denaturation and to prevent protein inactivation during process manipulation have been reported [271]. Another approach to stabilize enzymes against emulsification stress is based on the addition of bovine serum albumin (BSA). The high solubility of albumin

(up to 40% w/v) at pH 7.4, its stability at pH values of 4 to 9, and temperature variations (up to 60 °C when heated for 10 h) without any deleterious effects make it an attractive macromolecular stabilizer [277–280]. As an example, Chang and co-workers demonstrated that BSA was able to stabilize an enzyme by promoting hydrophobic interactions and increasing the viscosity of the enzyme solution [281]; however, this must be carefully balanced as increasing the protein concentration and viscosity increases the probability of aggregation which could lead to decreased enzyme availability or non-uniform NP formation [282].

Considering the need for a better understanding of the protective effect of BSA on enzymes, we rationally studied the complexation between beta-glucosidase (B-GLU), a model enzyme that falls in the hydrolase enzyme class and is linked to the LSD Gaucher, with a stabilizer (BSA), combining this strategy with a modulate delivery through polymeric nanoparticles (PLGA NPs) to optimize the formulation strategy aiming to stabilize an enzyme, preserve its activity, and modulate release at the target site. To this aim, we characterized the interaction between B-GLU and BSA in solution using microscopy and ITC analysis to discover the interaction characteristics of the BSA stabilizer and the enzyme. We then evaluated the effect of using stabilized BSA:enzyme complexes in nanoparticle formation by means of a full chemico-physical characterization (charge, size, enzyme loading, activity, and release), followed by enzyme activity and release studies to establish if the addition of BSA:stabilizer complexes to a formulation would lead to more therapeutically relevant enzyme-based nanomedicines.

## 2. Results

### *2.1. BSA/B-GLU Interaction*

To better understand how BSA promotes the stabilization effects on B-GLU in aqueous solutions, titration of B-GLU with BSA was studied through isothermal titration calorimetry (ITC). The interaction of B-GLU with BSA is an exothermic reaction, as indicated by negative peaks following each addition of BSA into the enzyme solution (Figure 1 left). The heat of the B-GLU dilution was negligible (Figure 1 left, orange curve), while a minor endothermic heat of dilution for BSA was visible for the first two additions (Figure 1 Left, blue curve), which were discarded from the data analysis. Integrated heat data (Figure 1 right) showed a single inflexion point, which likely indicated a single binding event. Accordingly, the data were fitted (GoF = 50.81%) using a scheme involving a single binding site (N = 1.23 ± 0.01), providing an affinity constant KA = (5.3 ± 0.9) × 105 M−1 (KD = 1.9 ± 0.3 μM). The reaction is entropically driven with very small enthalpic contribution and favourable entropic values (ΔH = −0.26 ± 0.09 kcal mol−1 and ΔS = +25.4 cal mol−1 K−1). In particular, the stoichiometry of the complex between BSA and B-GLU is characterized by a molar ratio close to 1:1.

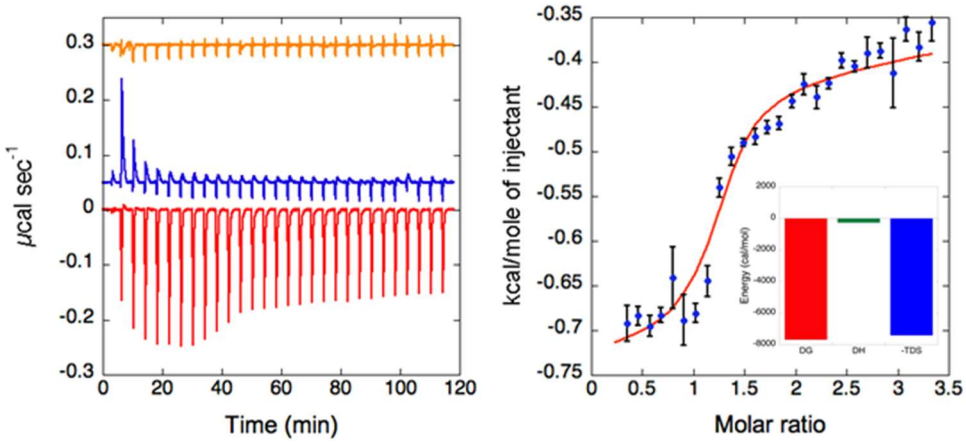


**Figure 1.** Isothermal titration calorimetry (ITC) analysis of the bovine serum albumin: beta-glucosidase (BSA:B-GLU) complex: (Left) Raw titration data of BSA titrated over B-GLU in PBS buffer pH 6 (red trace), BSA titrated over PBS buffer pH 6 (blue trace) and of PBS buffer pH 6 titrated over B-GLU (66 μM, orange trace). (Right) Binding isotherm of BSA titration over B-GLU obtained by integrating raw data for the protein titration and subtracting the corresponding control. The blue dots represent the experimental data, and the red curve represents the fit of the data using an

independent sites approach using the software Affinimeter. In the inset, the thermodynamic signature is reported.

To further characterize the complex formation, solutions of different BSA:B-GLU molar ratios ranging from 2:1 to 40:1 (high excess of surfactant) were prepared and analyzed (concentration of B-GLU 10 mg/mL to simulate conditions of the aqueous phase during formulation). The excess of BSA in respect to the enzyme molarity was necessary to assure at least the partial saturation of the B-GLU:BSA binding at the nM concentrations used for these experiments, which were distant from the value of the dissociation constant measured by ITC. Photon Correlation Spectroscopy (PCS) was applied to 2:1 (Complex 1), 10:1 (Complex 2), 20:1 (Complex 3) BSA:B-GLU molar ratio (Table 1). Unfortunately, the high viscosity of 3 nM BSA solution, used to obtain 40:1 (Complex 4) BSA:B-GLU molar ratio hindered reliable results by this method. The size distribution of free B-GLU shows the presence of a predominant peak (80% of the sample) of about 10 nm, most likely representing the globular form of the enzyme and minor amounts of larger structures with a diameter > 100 nm. BSA solutions corresponding to the concentrations used in the complexations (0.15, 0.75, 1.5, and 3 nM; Complexes 1–4, respectively) were also tested in the absence of the enzyme, showing a reproducible bimodal distribution with a predominant component of about 2–3 nm (60% of samples) and a secondary peak of about 20–38 nm (30–40% of the sample), probably due to aggregation. This finding is in line with other data present in literature, which showed differences in size depending on pH values: in particular, a primary peak, with a particle diameter ranging from 2 to 4 nm was found in solutions with pH 4–9 (compact spheroid particle), while the diameter increased at pH < 4 (extended form) [283,284]. The co-presence of BSA and B-GLU created a more complex dimensional distribution, with a significant increase of polydispersity; in particular, the 3 nm fraction decreased proportionally with an increased molar ratio of BSA to B-GLU (from 50% to 16%), corresponding to the increased contribution of larger structures (diameter > 50 nm) suggesting the re-

organization of proteins in solution. However, a noteworthy observation, was that the activity of the enzyme appeared to be unaffected by the increased presence of BSA (~16,000 pmol product/ug B-GLU). Unfortunately, the high viscosity of a 3 nM BSA solution hindered reliable results by this method.

**Table 1**. Chemico-physical properties and activity of BSA:B-GLU complex.

| | **PDI[a] (S.D.)** | **Peak 1 nm ± S.D. (% ± S.D.)** | **Peak 2 nm ± S.D. (% ± S.D.)** | **Peak 3 nm ± S.D. (% ± S.D.)** | **Zpot[b] mV (S.D.)** | **pmol Product/ug B-GLU (Activity at pH 6.7 ± S.D.)** |
|---|---|---|---|---|---|---|
| B-GLU | 0.31 ± 0.04 | 9.5 ± 0.9 (78 ± 12) | 144 ± 45 (24 ± 14) | / | | 16662 ± 800 |
| BSA solution (0.15 nM) | 0.28 ± 0.01 | 3.1± 0.1 (77 ± 3) | 19 ± 3 (18 ± 2) | 102 ± 25 (5 ± 2) | −20 ± 2 | |
| BSA solution (0.75 nM) | 0.33 ± 0.02 | 2.7 ± 0.4 (56 ± 9) | 32 ± 7 (45 ± 11) | / | −19 ± 5 | |
| BSA solution (1.5 nM) | 0.38 ± 0.03 | 2.4 ± 0.4 (61 ± 12) | 38 ± 3 (43 ± 7) | / | −13 ± 3 | |
| BSA/B-GLU 2:1 mol mol | 0.34 ± 0.01 | 3.5 ± 0.3 (46 ± 8) | | 288 ± 34 (53 ± 12) | −16 ± 1 | 16253 ± 775 |
| BSA/B-GLU 10:1 mol mol | 0.51 ± 0.04 | 2.5 ± 0.5 (25 ± 11) | 62 ± 6 (48 ± 14) | 241 ± 45 (25 ± 13) | −18 ± 4 | 16588 ± 675 |
| BSA/B-GLU 20:1 mol mol | 0.62 ± 0.05 | 2.3 ± 0.4 (16 ± 12) | 73 ± 5 (42 ± 12) | 369 ± 68 (41 ± 7) | −16 ± 3 | 17532 ± 943 |

The structure of all enzyme:BSA solutions were analyzed using atomic force microscopy (AFM). When the molar ratio between BSA and B-GLU was lower than 20:1 very small structures (diameter of about 20 nm) with a slightly collapsed

spherical shape were observed on the mica substrate (Figure 2A–C). On the contrary, the mixtures of BSA:B-GLU 40:1 molar ratio gave the formation of irregular and heterogeneous structures, with large amounts of background signal (Figure 2D).

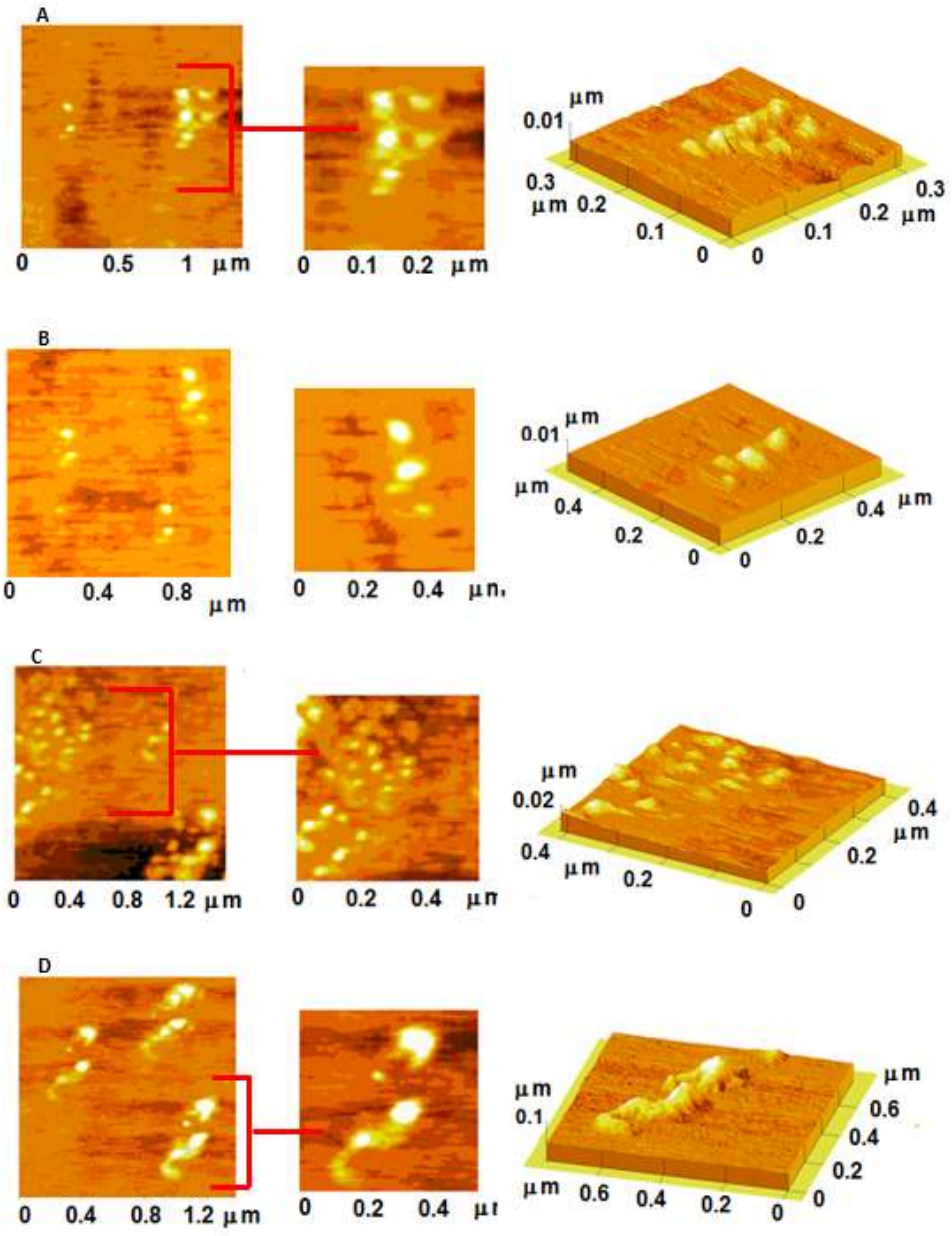


**Figure 2**. Atomic force microscopy (AFM) images of BSA:B-GLU complexes: 2:1 (panel A), 10:1 (panel B), 20:1 (panel C) and 40:1 (panel D).

*2.2. NPs Loaded with BSA:B-GLU Complexes*

B-GLU complexed with BSA, along with control samples, were formulated in PLGA NPs by means of a double emulsion (w/o/w) process. The chemical-physical properties of control samples (empty NPs, NPs formulated in BSA solution without B-GLU, and NPs loaded with B-GLU without BSA), and NPs loaded with BSA:B-GLU complexes are reported in Table 2. Control NPs without enzyme-containing BSA at concentrations of 0.15, 0.75, 1.5, and 3 nM (corresponding to the concentrations of complexes 1–4, respectively) exhibited homogenous NPs with an increase in size from 185 to 265 nm with increasing concentrations of BSA, a stable negative surface charge (around −20 mV) and a PDI always ~ 0.02 with the exception of the sample containing 3 nM BSA in which the PDI increased to 0.2, probably due to the higher viscosity of the suspension leading to variation in NP formation. Other control samples, namely B-Glu NPs prepared in the absence of BSA, formed 190 nm particles with a surface charge of −24 mV with good homogeneity as confirmed by small PDI values (0.017).

**Table 2**. Physico-chemical properties of nanoparticles (NPs).

| **Samples** | **Z-Average nm ± S.D.** | **PDI [a] ± S.D.** | **D(i)50 nm ± S.D.** | **D(i)90 nm ± S.D.** | **AFM Diameternm ± S.D.** | **ζ-pot mV ± S.D.** | **Yield% [b] ± S.D.** | **LC% ± S.D.** | **EE% ± S.D.** |
|---|---|---|---|---|---|---|---|---|---|
| NPs | 194 ± 17 | 0.06 ± 0.02 | 200 ± 16 | 311 ± 20 | 320 ± 47 | −21 ± 3 | 86.2 ± 2.1 | | |
| NPs B-GLU | 199 ± 28 | 0.17 ± 0.04 | 221 ± 26 | 376 ± 42 | 311 ± 69 | −24 ± 6 | 77.6 ± 3.3 | 0.6 ± 0.1 | 5.7 ± 0.9 |
| NPs/BSA (0.15 nM) | 185 ± 11 | 0.07 ± 0.02 | 189 ± 24 | 267 ± 21 | 215 ± 77 | −19 ± 3 | 72.2 ± 3.1 | | |
| NPs/Complex**1** | 234 ± 19 | 0.21 ± 0.01 | 227 ± 12 | 365 ± 25 | 302 ± 34 | −19 ± 2 | 69.2 ± 4.1 | 0.7 ± 0.3 | 6.8 ± 2 |
| NPs/BSA (0.75 nM) | 229 ± 21 | 0.09 ± 0.01 | 205 ± 20 | 297 ± 12 | 265 ± 67 | −22 ± 3 | 61.2 ± 2.3 | | |
| NPs/Complex**2** | 222 ± 17 | 0.11 ± 0.03 | 208 ± 19 | 332 ± 21 | 365 ± 76 | −25 ± 3 | 59.1 ± 2.6 | 3.1 ± 1.9 | 31 ± 7 |

| | | | | | | | | | |
|---|---|---|---|---|---|---|---|---|---|
| NPs/BSA (1.5 nM) | 234 ± 14 | 0.10 ± 0.02 | 209 ± 11 | 318 ± 11 | 318 ± 51 | −23 ± 3 | 56.9 ± 2.4 | | |
| NPs/Complex**3** | 243 ± 31 | 0.14 ± 0.02 | 215 ± 11 | 339 ± 14 | 375 ± 64 | −20 ± 3 | 51.1 ± 2.2 | 3.9 ± 1.4 | 38.7 ± 4 |
| NPs/BSA (3 nm) | 265 ± 67 | 0.27 ± 0.09 | 221 ± 12 | 401 ± 21 | / | −23 ± 6 | 41.3 ± 3.1 | | |
| NPs/Complex**4** | 266 ± 72 | 0.31 ± 0.09 | 253 ± 19 | 443 ± 16 | / | −22 ± 7 | 33.6 ± 7.2 | 1.2 ± 0.4 | 11 ± 5 |

NPs loaded with BSA:B-GLU complex showed a slight increase of both the mean diameter (from 180 to 230 nm) and the heterogeneity of the population (from 0.06 to 0.15), with the exception of Complex 4 (40:1) which showed both polymodal and polydisperse population of structures. Zeta potential of all samples was unaffected.

These values were supported by AFM measurements (Figure 3); NPs prepared in the presence of BSA (with or without B-GLU) tend to aggregate more on mica compared with PLGA NPs without stabilizer. Moreover, high concentrations of BSA in the formulation (BSA 3 nM and related NPs/Complex 4) were highly viscous and strongly hampered the approach with the sample, leading to artefacts in the analysis. Similarly, the interaction between the sample and the substrate as well as the continuous movement of the tip on the sample can drag particles on the support [285]. When the analysis was possible, the diameters obtained by AFM image processing resulted in higher values compared with the PCS data and the heights of the NPs were not found to correlate with diameter: this finding was probably connected to the water evaporation entailed in the AFM sample preparation influencing the NP size. Taken together, the AFM analyses generally confirm the heterogeneity of samples with a diameter of NPs ranging from 200 to 1000 nm.

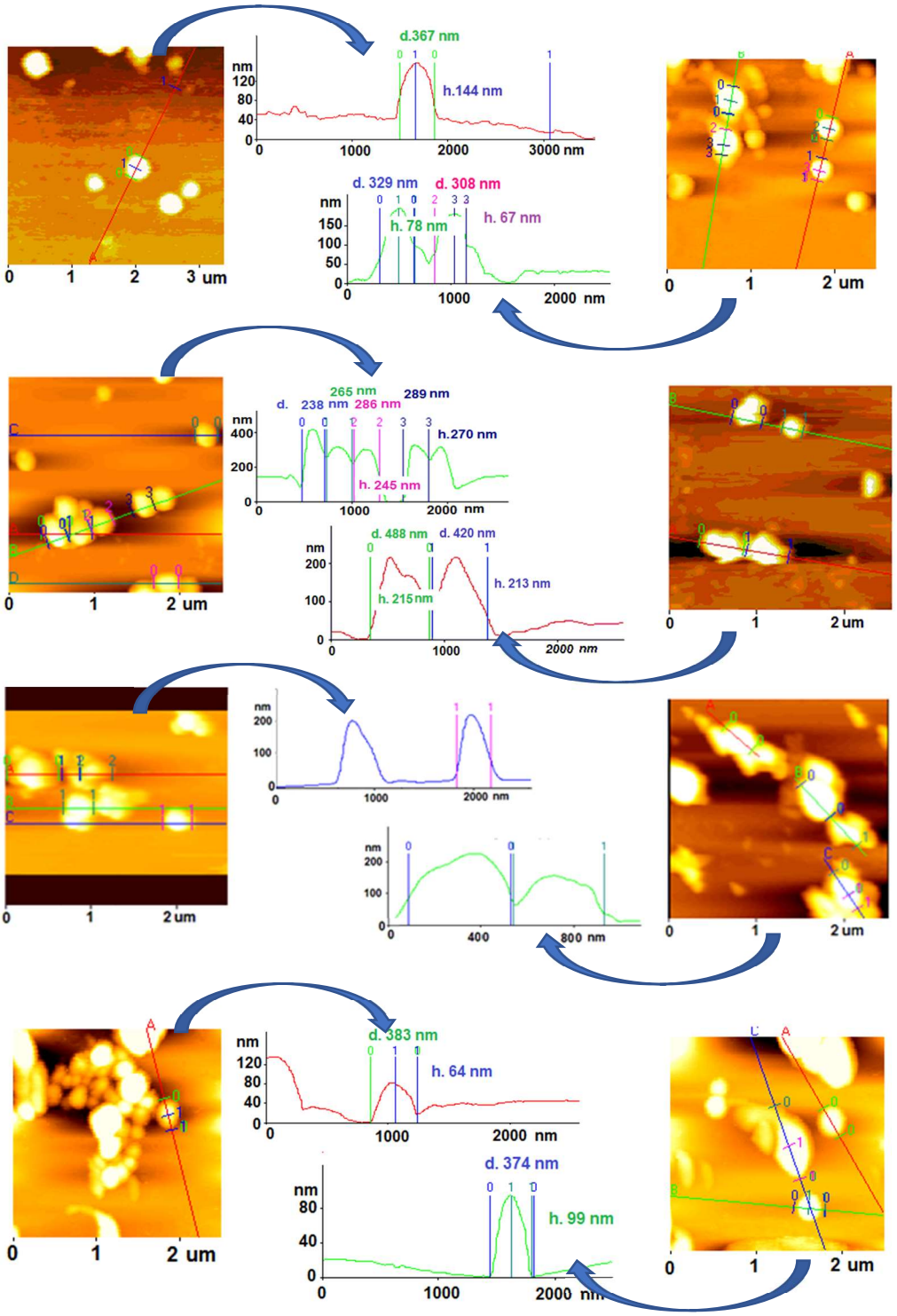


**Figure 3**. AFM images of the different NP preparations (a) NPs, (a1) NPs/B-GLU, (b) NPs/BSA 0,15 nM, (b1) NPs/Complex 1, (c) NPs/BSA 0,75 nM, (c1) NPs/Complex 2, (d) NPs/BSA 1,5 nM, (d1) NPs/Complex 3. Note: All NPs containing BSA:enzyme complex were produced with 5 mg B-Glu. The control samples are highlighted in grey.

Regarding pharmaceutical characterization, the presence of BSA:B-GLU complex in the NP preparations led to a strong variation on the percent yield of the NP recovery and encapsulation efficiency of the enzyme. In fact, the yield decreased proportionally with the increase of BSA concentration in the sample (from 80% to 30%). We hypothesized that this dramatic reduction in yield could be due to the relevant surfactant effect of both BSA and polyvinyl alcohol (PVA) on the suspension of NPs, leading to a less effective centrifugation outcome. In fact, the emulsifier action of BSA (in the inner aqueous phase) together with PVA (present in outer aqueous phase) could favour a reduction of both the dimension of the NPs and the interfacial tension leading to a very stable NPs suspension in the aqueous medium even after purification by centrifugation.

Remarkably, the most relevant outcome connected to the BSA concentration variation used to stabilize B-GLU was the enzyme encapsulation efficiency (Table 2). Without BSA, only a poor amount of B-GLU was efficiently loaded into NPs, namely 0.6% considering loading capacity (LC) and close to 6% considering encapsulation efficiency (EE). Similar encapsulation values were recorded (LC close to 0.7% and EE close to 7%) when incorporating the complex formed using the conditions" defined by the optimal molar ratio between BSA:B-GLU as suggested by titration studies (2:1). Notably, when the concentration of BSA in the formed complex was increased above these values, particularly with a molar ratio BSA:B-GLU 20:1 (Complex 3), encapsulation remarkably increased with LC 4% (4 mg B-GLU/100 mg of NPs) and EE 40%.

A further increase in BSA (BSA:B-GLU 40:1 mom:mol) did not correspond to an increase in encapsulation (LC 1.2% and EE 11%), which could be related to possible aggregation or too high viscosity of solution leading to a loss in encapsulation efficiency.

*2.3. B-Glu Release Study: Enzymatic Activity*

The release of B-GLU from NPs was evaluated in buffered solutions considered biologically relevant: pH 7.4 to mimic the environment upon systemic administration in the blood plasma and pH 4.5 to mimic endocytotic intracellular trafficking once taken up by cells [286–289]. The analysis of enzyme release becomes complicated due to the variability not only in the amount of enzyme released but in the activity remaining of the enzyme once released. This is further complicated by the competitive actions of enzyme release/activity and enzyme degradation once in free solution over time. Therefore, to characterize the global effect, enzyme release was analyzed considering the percent and activity of enzyme released (Figure 4) was quantified by enzyme activity per mg of nanoparticles (Figure 5).

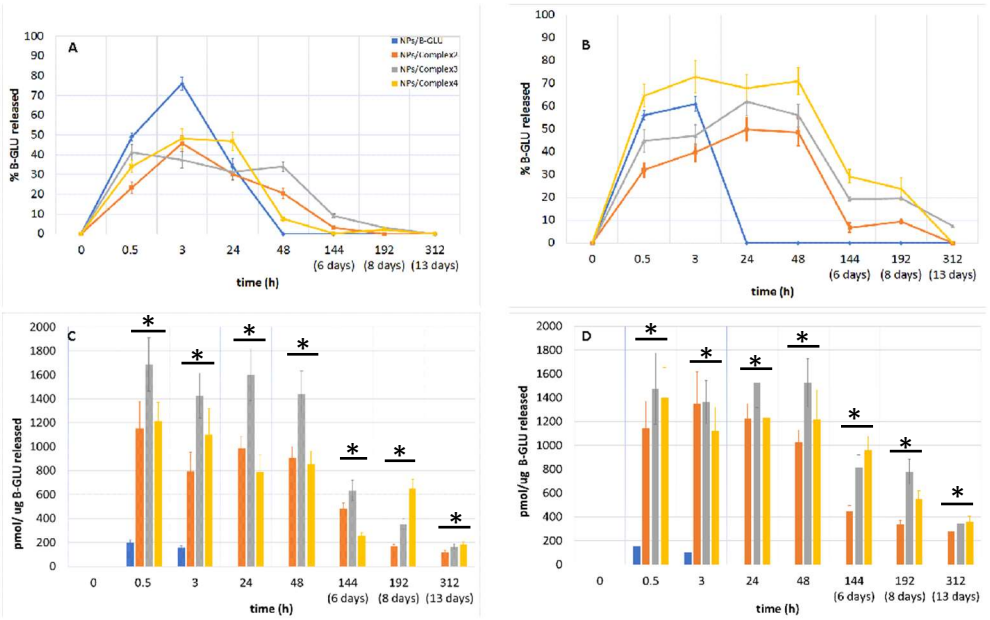


**Figure 4.** % of B-Glu released quantified by HPLC analysis at (A) pH 7.4 and (B) pH 4.5. The activity of enzyme/ug of B-Glu released from NPs at (C) pH 7.4 and (D) pH 4.5. * $p < 0.05$ vs. control NPs.

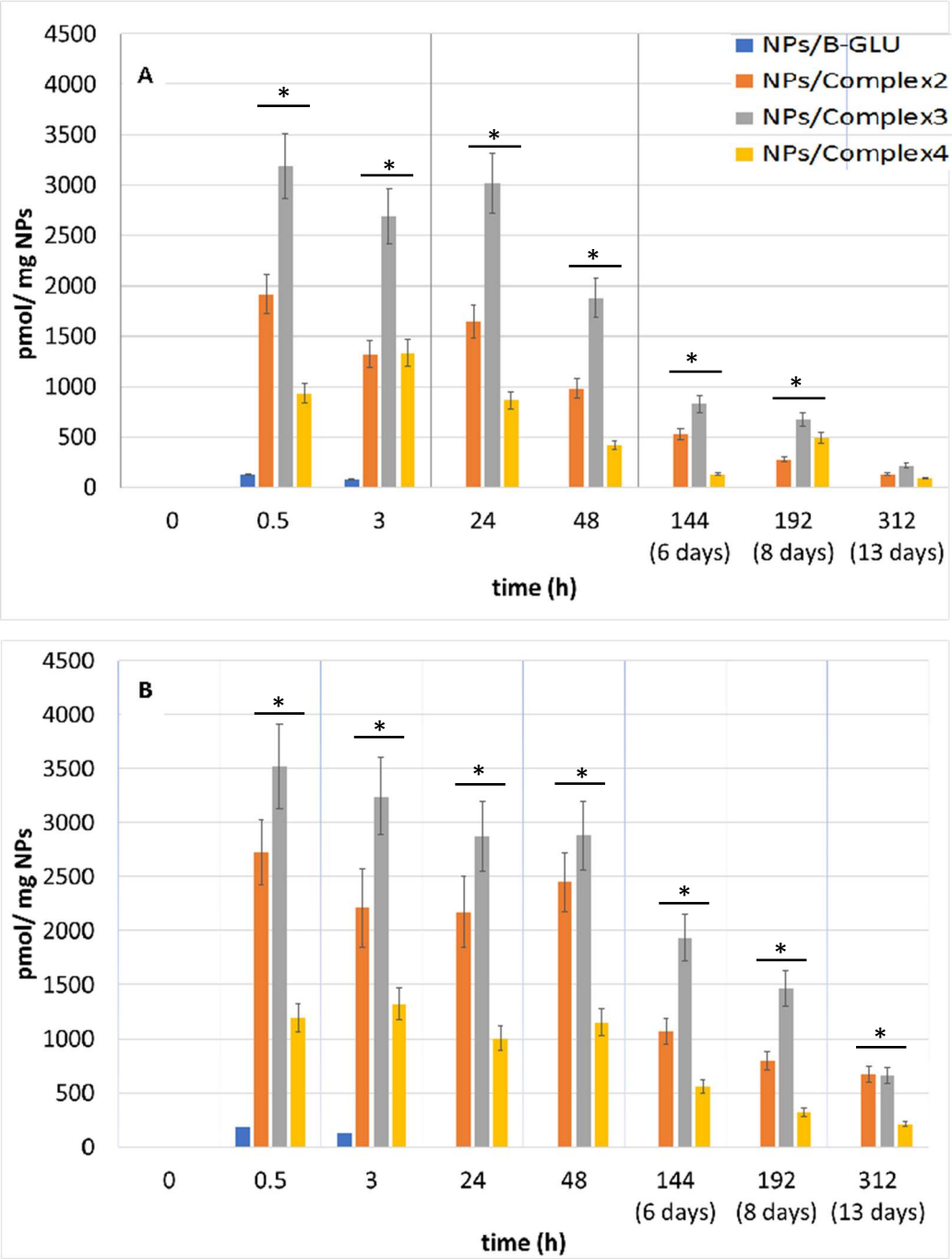


**Figure 5**. B-GLU activity per mg of NPs: (A) pH 7.4 and (B) pH 4.5. * $p < 0.05$ vs. control NPs.

The release of the enzyme from NPs at pH 7.4 and 4.5 was quantified by HPLC analysis (Figure 4A,B, respectively). In a pH 7.4 environment, B-GLU release from NPs without BSA as a stabilizer showed an almost complete burst release of ~80% over the first 3 h with no enzyme detectable at longer time points. On the contrary,

NPs containing BSA:B-GLU complex exhibited a remarkably lower percentage of burst release with a slower maintained release of enzyme up until 48 h independent of which complex was used, and even as long as 144 h in the case of Complex 2 (Figure 4A).

More striking, the enzyme released from the NPs lacking BSA was almost completely inactive at both pH values tested (Figure 4C,D), even at short time points (300 pmol/ug B-GLU), where the majority of the enzyme was released by HPLC analysis, with no activity seen at longer time points suggesting complete enzyme degradation. NPs containing BSA:B-GLU complexes show significantly more activity than the enzyme released by NPs/B-GLU without BSA (at both pH). However, at short time points (3 h) the enzymatic activity (evaluated considering the pmol of product transformed by enzyme) of B-GLU released was between 5-fold (complexes 2 and 4) and 8-fold (complex 3) higher than that of the enzyme released from NPs without BSA. Previous studies have shown that other LSD linked enzymes in a physiological pH solution, for 10 h at 37 °C, undergo destabilization with a loss of activity of about 40% [287,290,291]. This explains why in the experiments carried out both at pH 7.4 and 4.5 almost all enzyme amount can be quantified (80%) before degradation begins in the first 10 h and affects the kinetics and the complete release of BSA:B-GLU complex loaded into NPs over the 13 days of the experiment is never achieved as the degraded enzyme quantities were not quantifiable by HPLC.

More importantly, the activity remained close to maximal levels out to 48 h both at pH 7.4 and 4.5. Even after 48 h, enzyme activity was still detectable and decreased steadily over 13 days, with a more rapid decline at pH 7.4 respective to pH 4.5. Preservation of enzyme activity is more remarkable when considering NPs/Complex 3, which showed maximal observ with respect to ed encapsulation efficiency (EE 40%, Table 2). These two results indicate not only that the BSA:B-GLU complex is able to promote a prolonged release profile, but also stabilizes the

enzyme in solution allowing a more therapeutically relevant activity profile over time.

When the enzyme activity was reported with respect to a weighed quantity of NPs (Figure 5A,B), the observed results showed similar kinetics and overall evaluations. In particular, maximal activity during the first 24 of the experiment, with a rapid decrease for NPs without BSA, and a slower decline for those containing the BSA-BGLU complex were observed.

## 3. Discussion

Delivery of therapeutic proteins has gained great interest for the treatment of a number of diseases such as lysosomal storage disorders. More specifically, enzyme delivery possesses extraordinary therapeutic potential if properly formulated due to the fact that by exploiting this approach, enzymes can lead to prolonged and stable effects. In fact, achieving enzyme stability in the blood and targeted delivery still remains a challenge and a limiting step in order to move forward to clinical applications. To this end, nanoformulations could be reasonably considered as a resolutive strategy as it can achieve both specific targeting to disease sites and afford pharmaceutical advantages such as proper enzyme stabilization to protect pharmacological activity. Since BSA was shown to have a protective effect on enzymes, in this work, we exploited that effect to better characterize and understand the protective effect of complexes between BSA and B-GLU. The complex formation between BSA and B-GLU was found to be an exothermal reaction with a 1:1 molar ratio and an affinity in the μM range. When formulated into PLGA NPs, the very low concentrations of the enzyme needed for the encapsulation required an excess of BSA for complex formation. Results clearly indicated that a BSA:B-GLU ratio of 10:1 is the most efficient to achieve good performances in terms of encapsulation efficiency. An increasing concentration of BSA to 20:1 molar ratio was also considered: while it, unfortunately, led to a decreased recovery yield, it positively affected the encapsulation by dramatically increasing enzyme loading per mg of NPs. On the other hand, a further increase of BSA concentration (BSA:B-GLU 40:1) did not correspond to an increase in encapsulation, likely due to aggregation or too high viscosity of the solution that prevented an optimal condition for the reaction to occur.

Most importantly, the BSA:B-GLU complex stabilized the enzyme, slowing down its release from the NPs and extending its quantifiable activity up to more than ten days in a physiologically relevant environment.

In conclusion, a proper design of a strategy based on the optimization of enzymes stabilization could have dramatic effects in the field by increasing enzyme delivery as well as creating more stable, potentially long-term treatments. This will lead to a better understanding and the ability to compare various therapeutic enzymes for an increased therapeutic potential by limiting dose requirements, toxicity and off-target effects in order to cure previously untreatable diseases.

## 4. Materials and Methods

### *4.1. Materials*

Poly(D,L-lactide-co-glycolide) (PLGA,RG503H,MW ≅ 11,000) was used as received from the manufacturer (Boehringer-Ingelheim, Ingelheim am Rhein, Germany). Bovine Serum Albumin (BSA, 66 KDa), B-Glucosidase (B-GLU, MW 135 KDa) and polyvinyl alcohol (PVA, MW 15,000) were purchased from (Sigma-Aldrich, Milan, Italy). A MilliQ water system (Millipore, Bedford, MA, USA), supplied with distilled water, provided high-purity water (18 MO). All other chemicals were of analytical grade.

### *4.2. BSA:B-GLU Complexes*

BSA:B-GLU complexes were prepared by adding B-GLU (5 mg) into a BSA solution at different concentrations (0.15, 0.75, 1.5, and 3 nM) in 500 uL MilliQ water.

### *4.3. NPs Preparation*

NPs were obtained by a double emulsion method (w1/o/w2), adopted to increase the loading of hydrophilic molecules [292–294]. Briefly, 0.5 mL B glucosidase (5 mg) in an aqueous solution with or without BSA (0.15, 0.75, 1.5 and 3 nM) was emulsified in polymer solution (50 mg of PLGA in 2.5 mL CH2Cl2) under cooling (5 °C) by using a probe sonicator (MicrosonUltrasonic cell disruptor, Misonix Inc. Farmingdale, NY, USA) at 80 W for 45 s to obtain a w/o emulsion (first inner emulsion). The first inner emulsion was rapidly added to 12 mL of 1% (w:v) PVA aqueous solution and the w/o/w emulsion was formed under sonication (80 W for 45 s) at 5 °C. The formulation was mechanically stirred (1500 rpm) for at least 1 h (RW20DZM, Janke and Kunkel, IKA-Labortechnik, Staufen, Germany) at room temperature (RT) until complete evaporation of the organic solvent was achieved and finally purified by Hi-Speed Refrigerated Centrifugation (Beckman J21, Beckman Coulter, Indianapolis, IN, USA) at 16,000 rpm for 10 min at 5 °C. The supernatant was discarded, and the NPs were washed several times and re-

suspended in 4 mL Milliq water. From the NP resuspension, 1 mL was lyophilized and weighed for a percent yield recovery (see below).

*4.4. Characterization of BSA:B-GLU Complexes and NPs*

4.4.1. ITC Titration (Protein: Enzyme Interaction)

An ITC titration of the BSA and B-GLU interaction was evaluated at 25 °C using a high-sensitivity VP-isothermal titration calorimetry (ITC) microcalorimeter (Malvern Panalytical, Malvern, UK). The reference cell was filled with deionized water. The B-GLU solution was prepared by re-suspending 50 mg of protein powder in the reaction buffer (PBS, pH 6). A BSA stock solution at 25% w/v concentration was passed on a PD SpinTrap G-25 (Ge Healthcare) pre-equilibrated with reaction buffer. The protein was eluted at a concentration of 13% w/v and subsequently diluted to 1 mM with the reaction buffer to load the ITC syringe. Each experiment started with a small injection of 1–2 μL of BSA water solution, which was discarded from the analysis of the integrated data in order to avoid artefacts due to diffusion through the injection port occurring during the long equilibration period locally affecting the protein concentration near the syringe needle tip. The first addition was added only after baseline stability had been achieved. In each individual titration, 10 μL of 1 mM BSA solution was injected into a solution of 66 μM B-GLU using a computer-controlled 310-μL microsyringe. To allow the system to reach equilibrium, a 300 s delay was applied between each ligand injection. Control experiments obtained by titrating BSA into the reaction buffer or by titrating the reaction buffer into a B-GLU solution were performed. Integrated heat data obtained for each titration were fitted using a nonlinear least-squares minimization algorithm to a theoretical titration curve, using AFFINImeter (https://www.affinimeter.com/app/index.php/auth/login), using the independent sites approach. N (stoichiometry), ΔH (reaction enthalpy change, cal mol−1) and KA (binding constant, M−1) were the thermodynamic fitting parameters. The parameter Qdil (heat of dilution, cal mol−1) was also adjusted as fitting parameters. The reaction entropy was calculated using the relationships ΔG

= −RTlnKA (R = 1.9872 cal mol−1 K−1, T = 298 K) and ΔG = ΔH − TΔS. The reliability of the obtained fits was evaluated using the Goodness of Fit (GoF) parameter provided by the software.

### 4.4.2. AFM Analyses

Morphology of both BSA:B-GLU Complexes and NPs were evaluated by means of atomic force microscope (AFM, Park Instruments, Sunnyvale, CA, USA) analysis at RT. (about 25 °C) operating in air and in non-contact mode using triangular silicon tips. The resonant frequencies of the cantilever were found to be about 160 kHz. Before the analysis, a drop (20 μL) of the complexes or water-diluted NP suspensions (about 0.01 mg/mL) were applied to a small mica disk (1 cm × 1 cm); after 2 min, the excess water was removed using a paper filter. The topographical images obtained, also called "height" images, were flattened using second-order fitting to remove sample tilt.

### 4.4.3. Photon Correlation Spectroscopy (PCS) Analyses

The Mean particle size (Z-Average) and polydispersity index (PDI) of all samples (BSA:B-GLU Complexes and NPs) were determined at 25 °C by PCS using a Zetasizer Nano ZS (Malvern, UK; Laser 4 mW He–Ne, 633 nm, Laser attenuator Automatic, transmission 100–0.0003%, Detector Avalanche photodiode, Q.E. > 50% at 633 nm, T = 25 °C). The results were normalized with respect to a polystyrene standard suspension. The zeta potential (ζ-pot) was measured by using the same equipment with a combination of laser Doppler velocimetry and phase analysis light scattering (PALS). All the data are expressed as means of at least three individual preparation lots measured in triplicate.

### 4.4.4. Yield

A defined amount of purified NPs (around 10 mg) was freeze-dried (−60 °C, 1 × 10−3 mm/Hg for 48 h; LyoLab 3000, Heto-Holten, Allerod, Denmark) and the yield (Yield%) was calculated as follows:

Yield (%) = ((mg of freeze-dried sample)/(mg PLGA + mg of enzyme used for preparation)) × 100

*4.5. Quantification of Loaded Enzyme and Enzymatic Activity*

4.5.1. Enzyme Entrapment Efficiency (EE) and Loading Capacity (LC)

To quantify the amount of enzyme-Glu loaded into the NPs, an exact amount of freeze-dried loaded NPs (10 mg) was dissolved in DCM (1 mL). Then, MilliQ water (2 mL) (in which enzyme, but not PLGA, is soluble) was added. The mixture was electromagnetic stirring for at least an hour to allow complete evaporation of the organic solvent and polymer precipitation. The suspension was filtered (acetate cellulose filters, porosity 0.20 μm, Sartorius), and the amount of B-GLU in aqueous solution was quantified by analyzing 50 μL of the solution by RP-HPLC. The HPLC apparatus (JASCO Europe, Cremella, Italy) comprised a Model PU-2089 Plus pump provided with an injection valve with a 50 μL sample loop (Jasco, Model 7725i) with a C8 analytical column (Aeris™ 3.6 μm WIDEPORE XB-C8 200 Å, Phenomenex, Bologna, Italy). Solutions and mobile phases were freshly prepared before each. Elution was obtained using a gradient consisting of A [0.1% trifluoroacetic acid in MilliQ water (pH ~ 2)] and B (0.1% trifluoroacetic acid in acetonitrile) where the % of B was increased from 20–80 over 11 min at a flow rate of 1.2 mL/min. After the run was complete, 5 min was allowed at 20% B to re-equilibrate the column before the subsequent injection. All analyses were carried out under isothermal conditions at 70 °C (Column Heater, model 7971, Jones Chromatography). The eluent absorbance was monitored at 210 nm using a UV detector (Jasco UV-1575), and the chromatographic peak area was integrated and converted to a concentration of B-Glu based on a standard curve using the same

methodology. Linearity of the standard calibration curve was achieved in the range of 30–400 μg/mL (y = 44391x – 22.476 R2 = 0.99).

The entrapment efficiency (EE) and the loading capacity (LC), expressed as a percentage, were calculated using the following formulas:

$EE\% = D/Td \times 100$

$LC\% = D/W \times 100$

where D is the amount of B-GLU loaded in the NPs, Td is the amount of B-GLU used for the preparation, and W is the weight of the NPs (polymer + enzyme).

All the data are expressed as the mean of at least three sample analyses.

### 4.5.2. Quantification of Enzyme Activity

B-GLU activity was assayed by the microtiter plate method using the substrate 4-metilumbrelliferil-β-D-glucopiranoside. A reaction mixture of 100 uL containing 45 uL sample, 25 uL 4-metilumbrelliferil-β-D-glucopiranoside (2 mg/mL) substrate, and 25 uL Mc Ilvain buffer 4× pH 6 (monobasic phosphate 0.8 M, citric acid 0.4 M), and 5 uL water MilliQ was incubated under stirring (170 rpm) at 37 °C for 1 h. The reaction was stopped by adding 190 uL of glycine solution (250 mM, pH 10.7) to 10 ul of reaction solution; the product of the enzymatic reaction was monitored by using a fluorimeter, (Synergy HTX Multi-Mode Reader, BioTek, Winooski, VM, USA) with excitation lambda et 365 and the emission lambda at 488 nm. One unit of B-GLU activity was expressed as the amount of enzyme required to release one picomole of product under assay conditions and calculated based on a standard curve created on the same plate and same day by diluting a standard solution of 4-MU (5 uM) 0, 2, 5, 10, and 15 μL to a final volume of 200 in stop buffer.

Homogenate was diluted with millQ water to 2 mg/mL and sonicated, and GCase activity was determined in samples (20 μg protein) by hydrolysis of 5 mM 4-methylumbelliferyl-β-D-glucopyranoside in Mc IIvaine buffer (pH 5.4) in the

presence of 22 mM sodium taurocholate at 37 °C for 1 h. The reaction was stopped by addition of 0.25 M glycine (pH 10.4), and 4-methylumbelliferone fluorescence was measured at 365 nm excitation, 450 nm emission [111,295].

### *4.6. Release Studies*

Each sample (10 mg of lyophilized NPs) was re-suspended in an Eppendorf tube with 1 mL of buffer (PBS pH 7.4 or acetate buffer pH 4.5). The tube was closed and placed in a water bath (thermomix bu B. Braun, Milano, Italy) heated to 37 ± 0.1 °C, under stirring. At fixed time intervals (30 min, 3 h, 24 h, 48 h, 6 days, 8 days, or 13 days) samples were centrifuged (Spectrafuge 24D centrifuge, Edison, NJ USA at 13,300 rpm for 10 min to separate the NPs (pellet) from the released B-GLU (supernatant). The supernatant was filtered (cellulose acetate 0.20 μm), the precise volume was measured and divided into two aliquots which were processed by (1) HPLC analysis and (2) enzymatic activity as previously described.

### *4.7. Statistical Analysis*

Statistical analysis was performed using the Student T Test where * $p < 0.05$ .

Samples were analysed in triplicate on three independent formulation (N = 3).

# Tween® Preserves Enzyme Activity and Stability in PLGA Nanoparticles

**Jason Thomas Duskey [1], Ilaria Ottonelli [1,2], Arianna Rinaldi [1,2], Irene Parmeggiani [1], Barbara Zambelli [3], Leon Z. Wang [4], Robert K. Prud'homme [4], Maria Angela Vandelli [1], Giovanni Tosi [1], and Barbara Ruozi [1]**

[1] Nanotech Lab, Te.Far.T.I., Department of Life Sciences, University of Modena and Reggio Emilia, 41125 Modena, Italy

[2] Clinical and Experimental Medicine PhD Program, University of Modena and Reggio Emilia, 41125 Modena, Italy

[3] Laboratory of Bioinorganic Chemistry, Department of Pharmacy and Biotechnology, University of Bologna, 40127 Bologna, Italy

[4] Department Chemical and Biological Engineering, Princeton University, Princeton, NJ 08544, USA

Nanomaterials 2021, 11, 2946, doi:10.3390/nano11112946

Academic Editor: José das Neves

Received: 31 August 2021

Accepted: 28 October 2021

Published: 3 November 2021

## Abstract

Enzymes, as natural and potentially long-term treatment options, have become one of the most sought-after pharmaceutical molecules to be delivered with nanoparticles (NPs); however, their instability during formulation often leads to underwhelming results. Various molecules, including the Tween® polysorbate series, have demonstrated enzyme activity protection but are often used uncontrolled without optimization. Here, poly(lactic-co-glycolic) acid (PLGA) NPs loaded with β-glucosidase (β-Glu) solutions containing Tween® 20, 60, or 80 were compared. Mixing the enzyme with Tween® pre-formulation had no effect on particle size or physical characteristics, but increased the amount of enzyme loaded. More importantly, NPs made with Tween® 20:enzyme solutions maintained significantly higher enzyme activity. Therefore, Tween® 20:enzyme solutions ranging from 60:1 to 2419:1 mol:mol were further analyzed. Isothermal titration calorimetry analysis demonstrated low affinity and unquantifiable binding between Tween® 20 and β-Glu. Incorporating these solutions in NPs showed no effect on size, zeta potential, or morphology. The amount of enzyme and Tween® 20 in the NPs was constant for all samples, but a trend towards higher activity with higher molar rapports of Tween® 20:β-Glu was observed. Finally, a burst release from NPs in the first hour with Tween®:β-Glu solutions was the same as free enzyme, but the enzyme remained active longer in solution. These results highlight the importance of stabilizers during NP formulation and how optimizing their use to stabilize an enzyme can help researchers design more efficient and effective enzyme loaded NPs.

## 1. Introduction

Enzymes have taken the scene as promising pharmaceutical agents to treat numerous rare and deadly diseases worldwide, including pathologies of the central nervous system (CNS) [138,232,233,296,297]. Enzyme replacement therapy (ERT), which is based on the periodic administration of specific enzymes, is currently the most suitable therapy for difficult-to-treat diseases caused by a deficit in enzymes, such as lysosomal storage disorders (LSDs) [298–301]. However, therapeutic application of enzymes is still hampered by several obstacles that limit their clinical benefits because these macromolecules frequently fail in crossing biological barriers such as the blood brain barrier (BBB), and do not reach therapeutic concentrations in the target tissues [232,233,297,302–305]. Moreover, they show immunogenicity, short half-lives in blood circulation, and a rapid loss of specific activity/therapeutic potential. This calls for extensive research in ways to protect and prolong enzyme circulation in the blood. Moreover, many of the diseases caused by a lack of a functional enzyme, such as β-glucosidase (β-Glu) in Gaucher disease, require the enzyme not only to be protected, but also to be delivered to the CNS, where the majority of the damage is done. Therefore, new therapeutic strategies are urgently required to compensate for the deficit of enzymes in order to enable their safe delivery and accumulation in diseased cells.

To overcome these problems, the idea of enzyme encapsulation into tailored nanoparticles (NPs) represents one of the most attractive strategies. Among current advances in developed NPs, polymer-based NPs have gained increasing attention as biocompatible, biodegradable, targeted, and versatile platforms [306–312] for the delivery of a wide array of therapeutic molecules ranging from small molecules [237,313–315], peptides [241,316–318], proteins and enzymes [138,233,236,240,319], and genetic material [320–322]. The encapsulation of enzymes into polymeric NPs offer several advantages compared to conventional enzyme-based therapy, including: (i) stabilizing and protecting the enzyme; (ii) improving biological activity; (iii) possibility of targeted delivery; (iv) controlling

the enzyme release kinetics; (v) improving therapeutic efficacy and safety [264,302,323]. In particular, Poly(D,L-lactide-co-glycolide) (PLGA), a U.S. Food and Drug Administration (FDA)-approved polymer that can self-assemble into NPs has been of high interest [324–326]. This is because it is capable of encapsulating large molecules such as proteins and enzymes [327–331] and has also been demonstrated to have the capacity to transport large cargo across the BBB by adding targeting ligands [138,332–334]. This makes PLGA NPs a prime option to overcome many of these barriers for ERT treatment.

Despite these numerous advantages, the formulation process exposes the enzyme to physicochemical stresses which can alter the native conformation of the enzyme and inhibit its biological activity. For instance, the double emulsion water-oil-water technique, which is widely used for the encapsulation of enzymes into PLGA NPs, can cause protein unfolding and aggregation at the water/organic interface [272]. Various other stress conditions, including the use of organic solvents, exposure to highly energetic processes (e.g., sonication or freeze-drying), and high temperatures, frequently determine a loss of enzymatic activity. Therefore, it is necessary to develop new strategies that avoid or minimize the loss of enzyme activity during encapsulation into polymeric NPs [271,335].

One possible approach to prevent the loss of enzyme activity in solution or during formulative steps lies in the addition of stabilizers such as sugars [271,336–338], emulsifiers [339,340], and serum albumins [341–343]. Specific examples include: (1) Yun et al. used rabbit serum albumin in PLGA NPs encapsulating superoxide dismutase showing acceptable enzyme activity in vitro and in vivo [333]; (2) Osman et al. who tested PLGA NPs encapsulating DNaseI with the addition of hydroxypropyl-β-cyclodextrin (shown in other literature as an enzyme stabilizer [344]) [345]; (3) Atkins et al. that covalently linked the surfactant alkyl-glycolic acid ethoxylate to the surface of hen egg-white lysozyme to form a single enzyme NP with a surfactant shell which led to an up to 7-fold increase of enzyme activity in solution [346]; however, while offering protective features, these stabilizers can

impact the physicochemical characteristics (size, morphology, and zeta potential), encapsulation efficiency of the pharmaceutic, and the pharmaceutical properties (release kinetics, biodistribution, cell uptake, etc.) of the NPs [347,348]; 4) Another work used bovine serum albumin (BSA) and its ability to stabilize β-Glu during the formulation process [341]. BSA significantly enhanced loading capacity from 6% to 30%, and was shown to quantifiably directly bind to the enzyme (studied by isothermal titration calorimetry (ITC)) forming complexes in solution. This translated to an equal stabilization of the enzyme activity due to a BSA:β-Glu enzyme complex and a higher loading content of enzyme in the NPs. Moreover, the direct complexation of the two affected release kinetics from the PLGA matrix, shifting the release from an immediate burst release over 3 h (enzyme alone) to an extended release over 6 days [341].

The polysorbates or Tween® emulsifiers are another series of compounds that have been studied in the literature for their ability to influence the loading of pharmaceutics in NPs as well as for having stabilizing effects on enzymes [339,340,349]; however, there is little evidence of how the type and amount of Tween® can affect enzyme stability in NPs. In this regard, understanding the effect of these variables on the NP characteristics is important to optimize the formulation strategy to increase the stability of the enzyme, and modulate its release while maintaining high activity.

This work focused on elucidating if Tween® can have a stabilizing effect on a model enzyme during the formulation process into safe and biodegradable NPs. To this end, we combined β-Glu, the same model enzyme linked to the LSD Gaucher [350] used in our previous work with the stabilizer BSA [341], with Tween® stabilizers and loaded them into PLGA NPs. It was determined if the type and amount of Tween® (Tween® 20, 60 and 80) in the enzyme solution affects the enzyme stability during NP formation.

The comparison of enzyme activity suggested that Tween® 20 mixed in solution with β-Glu to form PLGA NPs led to the most promising results. Therefore,

Tween® 20:enzyme solutions at various molar ratios (ranging from 60:1 to 2419:1) were analyzed using ITC. After formulation of the solution mixtures into polymeric NPs, full characterization of each batch was performed to evaluate their physico-chemical characteristics, including the analysis of size, surface charge, morphology (atomic force microscopy (AFM) and scanning electron microscopy-field emission gun (SEM-FEG) analysis), loading capacity and encapsulation efficiency, and enzymatic activity. In particular, the quantity of Tween® 20 and β-Glu in the PLGA NPs was measured and how it affected enzyme activity and release. Finally, the effect of combining different stabilizers was analyzed. These studies underline the importance of stabilizers to preserve high enzyme activity and possibly modulate release kinetics for improved ERT.

## 2. Materials and Methods

### *2.1. Materials*

PLGA (Poly(D,L-lactide-co-glycolide), RG503H, MW ≅ 11,000) was purchased from (Evonik, Essen, Germany) and used as received. β-Glucosidase (β-Glu, MW 135 KDa), Tween® 20, 60, 80 (100%, guaranteed less than 3% water), and poly(vinyl alcohol) (PVA, MW 15,000), bovine serum albumin (BSA, 66 KDa, >98% pure), dichloromethane (DCM), 4-methylumbrelliferyl-β-D-glucopyranoside, and 4-methylumbelliferone (4-MU) were purchased from Sigma-Aldrich (Milan, Italy). MilliQ water was purified by a Millipore system (Millipore, Bedford, MA, USA). Analytical grade reagents were used for all other purposes unless otherwise noted.

### *2.2. NP Formulation*

Tween®:β-Glu mixtures were prepared by dissolving 5 mg of β-Glu with Tween® and diluting to a final volume of 500 μL with MilliQ. To analyze the various Tween® s, the molar ratio of Tween®:β-Glu was held constant at 2248:1 (corresponding to 20% *v*/*v* in water). Tween® 20:β-Glu solutions were formed similarly using different molar rapports of Tween® 20 to β-Glu to create solution 1–4, with solution 0 being a control of β-Glu without Tween® 20 (Table 1).

In the case of PLGA encapsulating BSA:β-Glu or Tween® 20:BSA:β-Glu solutions, the same procedure was followed but with the addition of 50 mg of BSA (20:1 BSA:β-Glu molar ratio) in the first aqueous phase before the double emulsion formulation.

**Table 1.** Tween® 20:β-Glucosidase solutions.

| Tween® 20:β-Glu* Solution n. | % v/v (Tween®20/Water) | Tween® 20 (μmol) | Tween® 20:β-Glu (mol:mol) |
|---|---|---|---|
| **0** | 0 | 0 | 0 |
| **1** | 0.5 | 2.2 | 60:1 |
| **2** | 5.0 | 22.4 | 605:1 |
| **3** | 10.0 | 44.8 | 1209:1 |
| **4** | 20.0 | 89.6 | 2419:1 |

* β-Glu was held constant in each solution mixture (5 mg, 37 nmol). * Total volume of the aqueous phase (MilliQ water and Tween® 20) was held constant at 500 μL.

PLGA NPs were produced utilizing the double emulsion method (w1/o/w2) [341,351]. The preformed Tween®:β-Glu solutions (Table 1) were added to the organic polymer solution (50 mg of PLGA in 2.5 mL of DCM) and the first emulsion (w/o) was obtained by sonicating on ice (amplitude 54%, 80 W) for 45 sec using a probe sonicator (SLPe, Branson, Milan, Italy). The first emulsion was added to 8 mL of a 1% (*w*/*v*) PVA and sonicated on ice (80 W for 45 sec) to obtain the final w1/o/w2 emulsion.

All formulations were mechanically stirred (RW 20 DZM, Janke & Kunkel, IKA Lab, Sigma Aldrich, Milan, Italy), at 1400 rpm, for 2 h at room temperature (RT) to evaporate the organic solvent. Finally, the NPs were purified by centrifugation (Multispeed Centrifuge PK 121, ALC, Bodanchimica, Cagliari, Italy) at 9,700 rpm for 10 min to remove the residual PVA and enzyme from the solution. The supernatant was discarded and the NPs were resuspended in 4 mL MilliQ water with the aid of a Vortex mixer (Velp Scientifica, Monza Brianza, Italy) and sonication bath (30 sec cycles until complete resuspension). The percent yield was calculated by lyophilizing 0.5 mL of the resuspended NPs (LyoLab 3000, Heto, Milan, Italy) and weighing the amount of NPs recovered. The lyophilized NPs were also used to extract and quantify the amount of Tween® and enzyme loaded

into the NPs (See Methods 2.6–2.8). The remaining NP suspension was aliquoted in 1 mL samples and stored at 4 °C.

*2.3. ITC Analysis*

As previously published [341], the possible interaction between Tween®20 and β-Glu was performed by ITC (25 °C), using a high-sensitivity VP-isothermal titration calorimetry microcalorimeter (Malvern Panalytical, Malvern, UK). 50 mg of β-Glu were solubilized in phosphate buffer saline (PBS, pH 6, 37 μM). 0.5 mM Tween® was passed on a pre-equilibrated PD SpinTrap G-25 (GE Healthcare, Chicago, IL, USA) and the reference cell was filled with MilliQ water. The Tween® (13% *w*/*v*) was eluted and diluted to 1 mM with PBS and loaded into the ITC syringe. 1–2 μL of the Tween® water solution were injected and discarded from the data at the beginning of each experiment to avoid artifacts in the injection port during equilibration. Once stabilized, the first addition was added. Each titration consisted of an injection of 10 μL Tween® (0.5 mM) into a 37 μM β-Glu solution via a computer-controlled 310 μL microsyringe. A 300 sec delay was incorporated to allow for equilibration between titration injections. Titrations of Tween® 20 into PBS or PBS into β-Glu solutions were used as controls. Integrated heat data were fitted using a nonlinear least-squares minimization algorithm to a theoretical titration curve, using AFFINImeter (V2.1802.5, Edificio Emprendia, Campus Vida, Campostela, Spain) through the independent sites approach for each titration. The thermodynamic fitting parameters consisted of ΔH (cal $mol^{-1}$ change in reaction enthalpy), N (stoichiometry), and KA ($M^{-1}$, binding constant). The parameter Qdil (heat of dilution, J $mol^{-1}$) was also adjusted as a fitting parameter. The relationships $\Delta G = -RTlnKA$ ($R = 8.314$ $J^{-1}$ $mol^{-1}$ $K^{-1}$, $T = 298$ K) and $\Delta G = \Delta H - T\Delta S$ were used to calculate the reaction entropy. Goodness of fit (GoF) was used to evaluate the reliability of the obtained fits based on software provided parameters.

*2.4. Size and Zeta Potential Analysis*

The mean particle size (Z-Average) and polydispersity index (PDI) of all samples were determined by photon correlation spectroscopy (PCS) analysis, using a Zetasizer Nano ZS (Malvern, Milan, Italy; laser 4 mW He–Ne, 633 nm, laser attenuator automatic, transmission 100–0.0003%, detector avalanche photodiode, Q.E. > 50% at 633 nm, T = 25 °C).

All samples were diluted before being analyzed: 10 μL of purified NPs suspension were diluted with MilliQ water to 1 mL to arrive at a final concentration of ~0.1 mg/mL. At least three individual NP formulations were prepared and analyzed to yield a mean for each data set.

The zeta potential (ζ-pot) was measured using a Zetasizer Nano ZS (Malvern, Milan Italy) with a combination of laser doppler velocimetry and a patented phase analysis light scattering method (M3-PALS). The same samples subjected to PCS (0.1 mg/mL) were analyzed using DTS1070 ζ-pot cuvettes and expressed as the mean of at least three individual NP preparations.

*2.5. Microscopy Analysis*

Atomic force microscopy (AFM, Park Instruments, Sunnyvale, CA, USA) was used to evaluate the morphology of NPs formulated with Tween®:enzyme solutions. Analyses were performed using triangular silicon tips at 25 °C in air and in non-contact mode. The cantilever resonant frequencies were set at ~160 kHz. Water-diluted NPs (20 μL, ~0.01 mg/mL) were added to a small mica disk (1 cm × 1 cm), let dry for 2 min and the excess solution was removed. The topographical images were flattened using second-order fitting to remove sample tilt.

The same samples were also imaged by scanning electron microscopy field emission gun (SEM-FEG). Briefly, a drop of a water-diluted suspension of the samples (about 0.01 mg/mL) was placed on a 200-mesh copper grid (TABB Laboratories Equipment, Berks, UK), allowed to adsorb, and the suspension

surplus was removed by filter paper. All grids were analyzed using a Nova NanoSEM 450 (FEI, Hillsboro, OR, USA) electron microscope operating at 30 kV using a SEM II detector in field-free mode.

*2.6. Weight Yield*

Purified NPs (0.5 mL) were freeze-dried and weighed (−60 °C, $1 \times 10^{-3}$ mm/Hg for 8 h; LyoLab 3000, Heto-Holten, Allerod, Denmark), and the yield% was calculated as follows:

$$Yield(\%) = \frac{freeze - dried\ sample\ (mg)}{PLGA\ (mg) + \ enzyme\ used\ for\ preparation(mg)} \times 100$$

*2.7. Quantification of β-Glu in PLGA NPs*

To quantify the β-Glu encapsulated in the NPs, a volume of 0.5 mL of purified NP suspension was freeze-dried, weighed, added with DCM (0.25 mL) and subjected to agitation with Vortex mixing (ZX4 Advanced IR Vortex Mixer, Velp, Usmate, Italy) for 30 sec to dissolve the PLGA. Then, the enzyme was extracted using 250 μL MilliQ in which the PLGA is insoluble. These samples were centrifuged (Spectrafuge 24D Labnet International Inc., Edison, NJ, USA) at 10,000 rpm for 2 min, to properly separate the aqueous from organic phase. 50 μL of the aqueous phase containing the enzyme were injected and quantified by reverse-phase high performance liquid chromatography (RP-HPLC) (Figure S1A).

As previously described [341] the HPLC (JASCO Europe, Cremella, Italy) was comprised of a Model PU-2089 Plus pump and a 50 μL sample loop (Jasco, Model 7725i) and fitted with an AerisTM C8 analytical column (3.6 μm WIDEPORE XB-C8 200 Å, Phenomenex, Bologna, Italy). The gradient consisted of a biphasic system using A [0.1% *v*/*v* trifluoroacetic acid in MilliQ water (pH~2)] and B [0.1% *v*/*v* trifluoroacetic acid in acetonitrile] where B was increased from 20 to 80% over

6 min (1.2 mL/min) under isothermal conditions at 70 °C (model 7971 Column Heater, Jones Chromatography, Rheinfelden, Germany). The absorbance was monitored at 210 nm using a UV detector (Jasco UV-1575, Carpi, Italy).The peak area was integrated, and a standard curve ranging from 20 to 1600 μg/mL (y = 40538x + 4330.9, $R^2$ = 0.99) was used to calculate the β-Glu concentration.

The entrapment efficiency (EE%) and the loading capacity (LC%) were calculated as follows:

$$EE\% = \frac{\beta Glu_{(NPs)}}{\beta Glu_{total}} \times 100$$

$$LC\% = \frac{\beta Glu_{(NPs)}}{NP_{total}} \times 100$$

where $\beta Glu_{(NPs)}$ indicates the amount (mg) of βGlu loaded in the NPs, $\beta Glu_{(total)}$ refers to the amount (mg) of β-Glu originally used in the formulation, and $NP_{(total)}$ the amount (mg) of NPs recovered. All data were calculated using three individual formulations for each sample type.

*2.8. Quantification of Tween® in PLGA NPs*

To determine the amount of Tween® 20 incorporated into or absorbed onto the NPs, the Tween® 20 was extracted from the NPs and analyzed by HPLC-evaporative light scattering detector (ELSD) analysis by modifying a previously published protocol [352].

A weighed amount of NPs (about 10 mg) was dissolved in 1 mL of DCM and vortexed for 20 sec to solubilize the PLGA. To extract Tween® 20, 1 mL of MilliQ water was added to the DCM suspension and vortexed again. Samples were stirred (Multistirrer, Magnetic Stirrer Velp Scientifica, Monza Brianza, Italy) to evaporate the DCM, and precipitate the PLGA. The volume of the resulting suspension was adjusted to 1.5 mL with MilliQ water and centrifuged (Spectrafuge 24D, Edison, NJ, USA) at 13,000 rpm for 3 min to pellet the PLGA. The supernatant was then analyzed by ELSD-HPLC (20 μL injection volume) (Figure S1B). Tween®

20 quantification was carried out on a 1260 Infinity II HPLC system (Agilent, Milano, Italy) with a fixed flow rate of 1.2 mL/min at RT, coupled with two detectors: 1) a UV detector (1260 variable wavelength detector (VWD)) set at $\lambda$ = 210 nm; 2) an ELSD system 1260 Infinity II (settings: evap. = 45 °C; neb. = 45 °C; gas = 1.60 SLM). A C8 (Phenomenex®) analytical column was used, and elution was obtained using a gradient consisting of A [MilliQ water] and B [acetonitrile]. The mobile phase gradient was optimized as follows:

- 0–5 min: 0–0% B
- 5–10 min: 0–60% B
- 10–15 min: 60–80% B
- 15–17 min: 80–0% B

A calibration curve was obtained using the same methodology (y = 0.101x − 1.1858, $R^2$ = 0.9932), and linearity was achieved from 2.5 to 15 μg injected in 20 μL.

Tween® 20 content and the mol:mol ratio Tween®20:β-Glu were calculated as follows:

$$Tween® \ 20 \ Content = \frac{mg \ Tween®20}{mg \ NPs} \times 100$$

$$molar \ ratio \ Tween® \ 20: \beta - Glu = \frac{mol \ Tween® \ 20 \ in \ the \ NPs}{mol \ of \ enzyme \ in \ NPs}$$

*2.9. β-Glu Activity Assay*

The activity of β-Glu was assessed using the substrate 4-methylumbrelliferyl-β-D-glucopyranoside. One hundred μL containing 45 μL of NPs or supernatant, 25 μL 4· McIlvain buffer pH 6 (0.4 M citric acid, 0.8 M monobasic phosphate), 5 μL water MilliQ, and 25 μL 4-methylumbrelliferyl-β-D-glucopyranoside (2 mg/mL) substrate were incubated for 1 h in a 96-well plate under agitation at 170 rpm and heated to 37 °C. Each sample underwent a 1:50 dilution with MilliQ water and the reaction was stopped by adding 10 μL to 190 μL of glycine "stop buffer" solution

(250 mM, pH 10.7) in a separate 96-well plate; the enzymatic product (4-MU) was measured by a fluorimeter (Synergy HTX Multi-Mode Reader, BioTek, Winooski, VT, USA) ex:em 365:488 nm. β-Glu activity was expressed as pmol of the product, 4 MU, per hour per μg of enzyme. Quantification was calculated using an internal standard curve produced on the same 96-well plate using 0, 2, 5, 10, 20, 50, 100 μL of a known 4MU solution (5 μM) diluted in "stop buffer" (250 mM glycine, pH 10.7) to a final volume of 200 μL. Control samples included NP resuspension buffer (MilliQ water), as well as empty NPs (NPs formulated without enzyme), Tween® solutions at the concentrations found in the NPs, and BSA solutions equal to those present in the NPs. These controls did not show an increased background compared to the water sample alone and were not considered.

*2.10. Enzyme Release Assay*

The effect of Tween® 20 on the release profile and activity of β-Glu from the PLGA NPs was analyzed in two different biologically relevant conditions: pH 7.4 (PBS) to simulate systemic release and pH 4.5 (acetate buffer) to simulate the lysosomal environment. Individual samples for each time point of PLGA NPs encapsulating β-Glu or Tween® 20:β-Glu solutions were analyzed from 1 h to 14 days at each pH. NP suspensions (0.9 mL) were buffered with 0.1 mL of release buffer (PBS 10x or acetate buffer 10x) in Eppendorf tubes (final volume 1 mL in 1· concentrated buffer). Samples were incubated in a heated bath (ISCO GTR 2000, Optolab, Concordia Sulla Secchia, Italy) at 37 °C under electromagnetic stirring. At each time point (1 h, 3 h, 6 h, 24 h, 72 h, 7 days, and 14 days) corresponding samples were centrifuged (Spectrafuge 24D centrifuge, Edison, NJ, USA) at 13,300 rpm for 7 min in order to separate NPs as a pellet. An aliquot of the supernatant (45 μL) containing the released enzyme was tested for enzyme activity. The remainder (960 μL) was freeze-dried, re-suspended with 0.1 mL MilliQ water (with the aid of a vortex mixer) and quantified by RP-HPLC analysis as previously described.

*2.11. Statistical Analysis*

Statistical analysis in all assays was performed using the Student T Test where * $p < 0.05$ and ** $p < 0.01$ as indicated in each figure (Table 2, Figures 1, 4, and 6). All statistical analyses (Z-Average, ζ-pot, PDI, %EE, enzyme activity and release) were performed in triplicate on three independent samples or NP formulation (N = 3) and the standard deviation (S.D.) from the mean of the three separate samples is represented by a "±" or error bars.

## 3. Results

Tween® is a trademarked line of surfactants which have been shown in the literature to help NP formation and stabilize enzymes [339,340,349,353–355]. Therefore, an initial study was performed to compare the formulation of the model enzyme β-Glu mixed in solution with the Tween® series of surfactants, which differ in their chemical structure, as their sorbitan-derived core is esterified respectively with lauric (Tween®20), stearic (Tween®60), or monooleic acid (Tween®80). The aim was to determine which variant poses the highest potential for formulating and preserving enzyme activity in PLGA NPs. β-Glu mixed in solution with each different Tween® in the aqueous phase before formulation with the double emulsion method did not produce any difference in size or ζ-pot of the NPs compared to empty PLGA NPs or those containing free β-Glu, resulting unanimously with monodisperse particles ranging from 177 to 208 nm with low PDI < 0.2 and a negative surface charge of the NPs ranging from −16 to −23 mV (Table 2).

**Table 2.** Effect of Tween® Type Comparison on Nanoparticle Characteristics.

| Sample † | Z-Average nm ± S.D. | PDI ± S.D. | ζ-pot mV ± S.D. | Yield% ± S.D. | LC% ± S.D. | EE% ± S.D. |
|---|---|---|---|---|---|---|
| **Empty NPs** | 190 ± 15 | 0.06 ± 0.01 | -20 ± 3 | 85.1 ± 3.1 | / | / |
| **NPs β-Glu** | 199 ± 25 | 0.09 ± 0.02 | -22 ± 6 | 82.5 ± 6.8 | 0.4 ± 0.1 | 3.9 ± 1.5 |
| **NPs_Tween® 20:β-Glu** | 198 ± 33 | 0.09 ± 0.06 | -16 ± 7 | 75.9 ± 2.3 | 0.9 ± 0.1 | 7.8 ± 1.9* |
| **NPs_Tween® 60:β-Glu** | 177 ± 44 | 0.05 ± 0.04 | -23 ± 7 | 78.2 ± 1.8 | 0.8 ± 0.1 | 5.6 ± 2.6 |
| **NPs_Tween® 80:β-Glu** | 208 ± 23 | 0.22 ± 0.03 | -20 ± 4 | 72.7 ± 5.4 | 0.5 ± 0.1 | 5.4 ± 2.2 |

† the ratio of Tween®:β-Glu was held constant, mol:mol 2248:1. * statistically significant compared to NPs β-Glu, $p = 0.049$.

The fact that the different Tween®s had little effect on the NP self-assembly process is not surprising, given that they have previously been used in the literature for this purpose. Further analyzing the NP characteristics, varying the type of Tween®

did not affect the %yield of the NPs; however, statistical analysis showed that while each Tween® was not significantly different from each other ($p$ = 0.23), even though all three showed slightly improved %EE compared to control NPs with only β-Glu, only NPs containing Tween®20 were significantly higher than the ones without Tween® (3.9 and 7.8 respectively, $p$ = 0.049) (Table 2). Similarly to the increase in %EE a higher enzyme activity was also observed. All NPs with Tween®:β-Glu significantly outperformed the control NPs which contained β-Glu without Tween®. Interestingly, while the %EE was not significantly different between NPs with the different Tweens®, the enzyme activity did show variation. Here it is important to note that activity of β-Glu within the intact NPs was quantified to avoid using organic solvents that could potentially damage the enzyme during extraction; however, control samples showed that PLGA did not interfere with a direct comparison of NPs containing enzyme with or without Tween®. In this case, the presence of Tween® 20 in the enzyme solution led to NPs that statistically outperformed its other Tween® counterparts in terms of preserved enzyme activity (Figure 1). These results closely resemble the protective effect of Tween® 20 on β-Glu when disposed to the same stresses (organic solvent, sonication, and centrifugation) without the presence of PLGA. While Tween® 20 has no effect on the free enzyme, it stabilizes the enzyme when stressed leading to retention of ~40% of its activity compared to only 10% for the un-stabilized enzyme under stress (Figure S2). Because the major barrier to effective ERT is delivering a therapeutically relevant amount of enzyme to the diseased site, the improved %EE and activity of Tween® 20 merit further studies to better understand the correlation between Tween® 20 and enzyme stabilization and therefore only Tween® 20 was chosen for more in depth studies.

Due to the improved features of Tween® 20:β-Glu solution mixtures in the formulation of PLGA NPs, a more detailed study of the solution and its incorporation into the NPs during formulation was performed. To this end, 5 different Tween®:β-Glu solutions (Solutions 0–5) were analyzed ranging in a

mol:mol ratio of 60–2419:1, where solution 0 was designated as a control with no Tween® but only β-Glu.

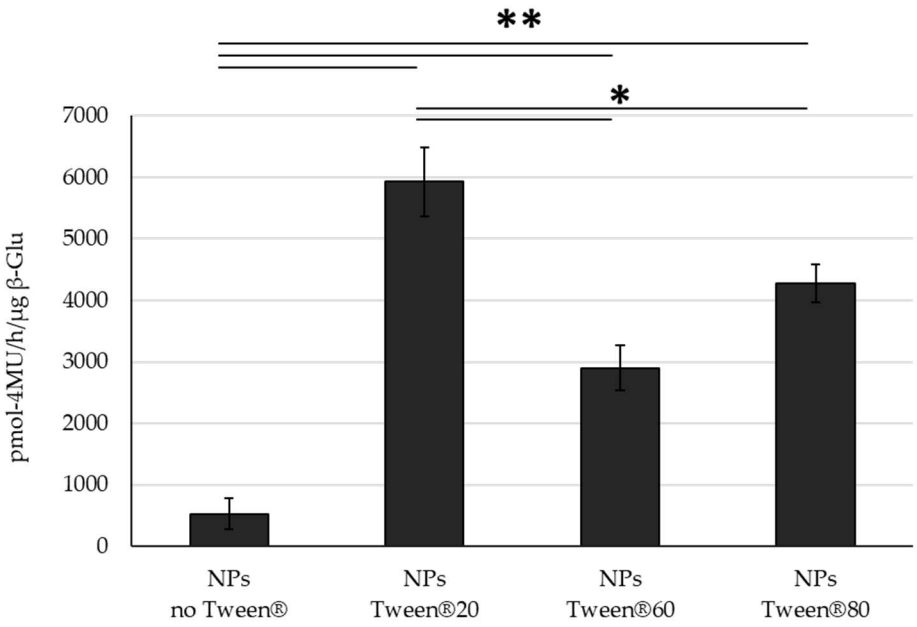


**Figure 1.** Activity Comparison. Activity of β-Glu mixed with Tween® 20, 60, 80 and encapsulated into PLGA NPs. Statistical analysis was performed using the Student T test where * $p < 0.05$, ** $p < 0.01$ and N = 3 individual NP formulations for each type.

The total volume of all mixtures and the amount of enzyme were held constant at 500 µL and 5mg respectively (solution compositions are described more in detail in Methods Section 2.2 (Table 1)). Contrary to the previously published results using BSA:β-Glu complexes [341] that showed small nanosized structures upon complexation with a range from ~9–60 nm, Tween®:β-Glu mixtures analyzed by PCS showed erratic results due to the non-homogeneity of the sample, as highlighted by PDI values ranging from 0.35 to 0.80, suggesting poor or uncontrolled complexation. Here the ζ-pot reached neutral values around 2 ± 2 mV. (Table 3).

**Table 3.** Characteristics of Tween® 20:β-Glucosidase Solutions.

| Tween®20:β-Glu Solution n. | Z-Average nm ± S.D. | PDI ± S.D. | Peak 1 nm ± S.D. (% ± S.D.) | Peak 2 nm ± S.D. (% ± S.D.) | Peak 3 nm ± S.D. (% ± S.D.) | ζ-pot mV ± S.D. |
|---|---|---|---|---|---|---|
| **0** | 792 ± 27 | 0.65 ± 0.11 | 78 ± 12 (80 ± 4) | 144 ± 45 (15 ± 5) | / | -2.21 ± 4 |
| **1** | 932 ± 225 | 0.79 ± 0.06 | 564 ± 200 (73 ± 11) | 1185 ± 3120 (20 ± 3) | 602 ± 915 (5 ± 3) | 2.27 ± 3 |
| **2** | 636 ± 23 | 0.71 ± 0.09 | 521 ± 275 (60 ± 5) | 36 ± 46 (38 ± 8) | 3470 ± 2453 (2 ± 2) | 2.12 ± 2 |
| **3** | 114 ± 60 | 0.35 ± 0.09 | 9 ± 1 (65 ± 7) | 529 ± 11 (34 ± 7) | 5125 ± 191 (8 ± 4) | 2.13 ± 1 |
| **4** | 116 ± 47 | 0.49 ± 0.14 | 281 ± 470 (59 ± 8) | 936 ± 935 (30 ± 9) | 3218 ± 1697 (10 ± 8) | 2.14 ± 1 |

This unquantifiable binding between Tween® 20 and β-Glu was also supported by ITC. In this study, Tween® 20 (0.5 mM) was titrated over β-Glu (37 μM) (Figure 2). Similar to the PCS analyses, ITC suggested a weak binding interaction with the fit of the data indicating the presence of a single binding event with N = 0.62 ± 0.08 Ka = 6 ± 1 × 104, ΔH = 3.8 ± 0.4 kJ $mol^{-1}$, ΔS = 79.9 J $mol^{-1}$ $K^{-1}$. The relatively low binding constant provided a c value of 1, lower than the optimal one (c = M × KA × N), which indicated that the conditions used could provide only a suboptimal sigmoidicity of the binding isotherm, without a clear inflection point. In theory, the value of "c" could be improved by increasing the enzyme and surfactant concentrations. However, this was not a possibility in this case as doubling the Tween® 20 concentration in the titration syringe led to a high heat of dilution for the detergent, which increased the signal-to-noise-ratio and masked the heat of binding. For this reason, the stoichiometry of the reaction could not be reliably derived from the fit under the conditions used. In the hypothesis of a 1:1 binding event, the dissociation constant can be calculated as 17 ± 3 μM. The derived

thermodynamic signature shows both favorable enthalpic and entropic values, with a prevalence of the entropic term. This is likely due to the hydrophobic nature of the interaction between the detergent and the enzyme. Hydrophobic interactions are indeed usually entropy-driven, as water molecules, previously organized around the hydrophobic surfaces, are released into the bulk of the solution. It is important to note that during titration, the Tween® 20 concentration in the sample cell is lower than the critical micellar concentration (cmc), indicating that it represents the enzyme interaction with single molecules of the detergent.

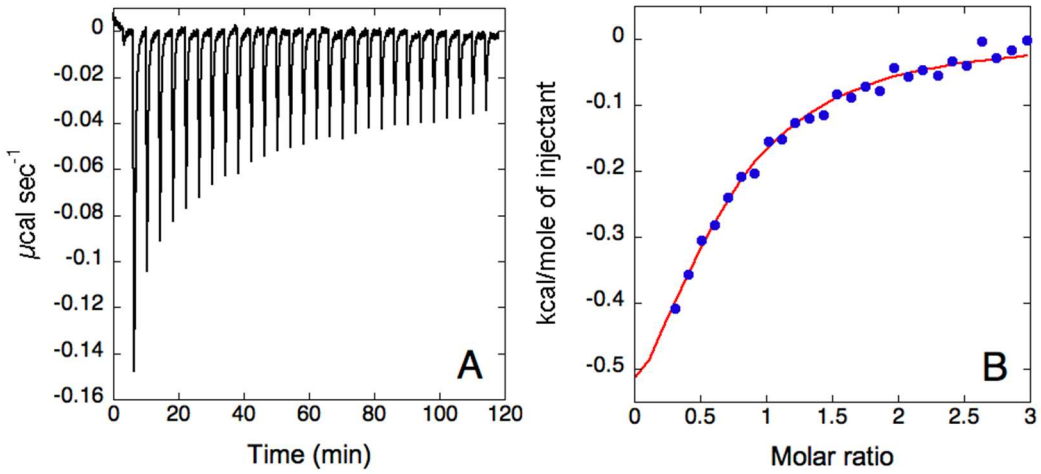


**Figure 2.** Isothermal titration calorimetry analysis of Tween® 20 and β-glucosidase. (**A**) Raw titration data of Tween® 20 (0.5 mM) titrated over β-Glu (37 µM) in PBS buffer, pH 6. (**B**) Binding isotherm of Tween® 20 titration over β-Glu, obtained by integrating raw data for the protein titration. The blue dots represent the experimental data and the red curve represents the fit of the data using a single set of sites model.

The ITC data of Tween® 20:β-Glu solution mixtures suggested that the stabilizing effect did not arrive from a strong quantifiable complexation with the enzyme β-Glu, but from an effect during the formulation of the NPs. This also supports the almost neutral zeta potential with large errors along with the lack of distinct nano sized self-assemblies in solution. To better evaluate the stabilizing effect of Tween® 20 on the enzyme each solution mixture was used to formulate β-Glu-PLGA NPs and were characterized for Z-Average, ζ-pot, %yield, %LC and %EE (Table 4).

As expected based on the initial study, varying the molar rapport of Tween® 20: β-Glu had no significant effect on the physico-chemical characteristics of the NPs. Each NP formulation had a comparable Z-Average, PDI, and ζ-pot (~190 nm, PDI < 0.1, and −18 mV) as that without stabilizer. There was a slight difference in %EE among the samples, with Solution 2 showing the highest encapsulation at 11.1%; however, the %EE was statistically higher for NPs formulated with all of solution mixtures when compared to the control sample without Tween® even though the differences between each mixture were not statistically significant.

**Table 4.** Physical characterization and loading content of Tween®20:β-Glucosidase solutions in PLGA NPs.

| | **Z-Average nm ± S.D.** | **PDI ± S.D.** | **AFM Diameter nm ± S.D.** | **ζ-pot mV ± S.D.** | **Yield% ± S.D.** | **LC% ± S.D.** | **EE% ± S.D.** |
|---|---|---|---|---|---|---|---|
| **Empty NPs** | 190 ± 15 | 0.06 ± 0.01 | 320 ± 47 | −20 ± 3 | 85.1 ± 3.1 | / | / |
| **NPs_Solution0** | 199 ± 25 | 0.09 ± 0.02 | 311 ± 69 | −22 ± 6 | 82.5 ± 6.8 | 0.4 ± 0.1 | 3.9 ± 1.5 |
| **NPs_Solution1** | 185 ± 24 | 0.08 ± 0.03 | 173 ± 41 | -16 ± 5 | 72.7 ± 5.5 | 1.1 ± 0.0 | 9.7 ± 1.2 |
| **NPs_Solution2** | 188 ± 13 | 0.08 ± 0.01 | 142 ± 39 | -16 ± 10 | 73.9 ± 4.3 | 1.0 ± 0.1 | 11.1 ± 1.2 |
| **NPs_Solution3** | 191 ± 23 | 0.08 ± 0.02 | 150 ± 26 | -16 ± 7 | 81.8 ± 3.6 | 0.8 ± 0.1 | 8.4 ± 4.0 |
| **NPs_Solution4** | 198 ± 33 | 0.09 ± 0.06 | 270 ± 31 | -16 ± 7 | 75.9 ± 2.3 | 0.9 ± 0.1 | 7.8 ± 2.5 |

To further analyze the morphology and self-assembly of each NP, AFM and SEM-FEG analysis were performed (Figures 3 and S3). AFM analysis demonstrated that all Tween® 20-enzyme solutions were incorporated into NPs ranging from 150 to 300 nm with some aggregates reaching 500 nm, as seen with NPs encapsulating Solution 3. Analyzing the images, it was seen that with the higher amount of Tween® (Solution 4) more uniform spherical NPs were formed (Figure S1).

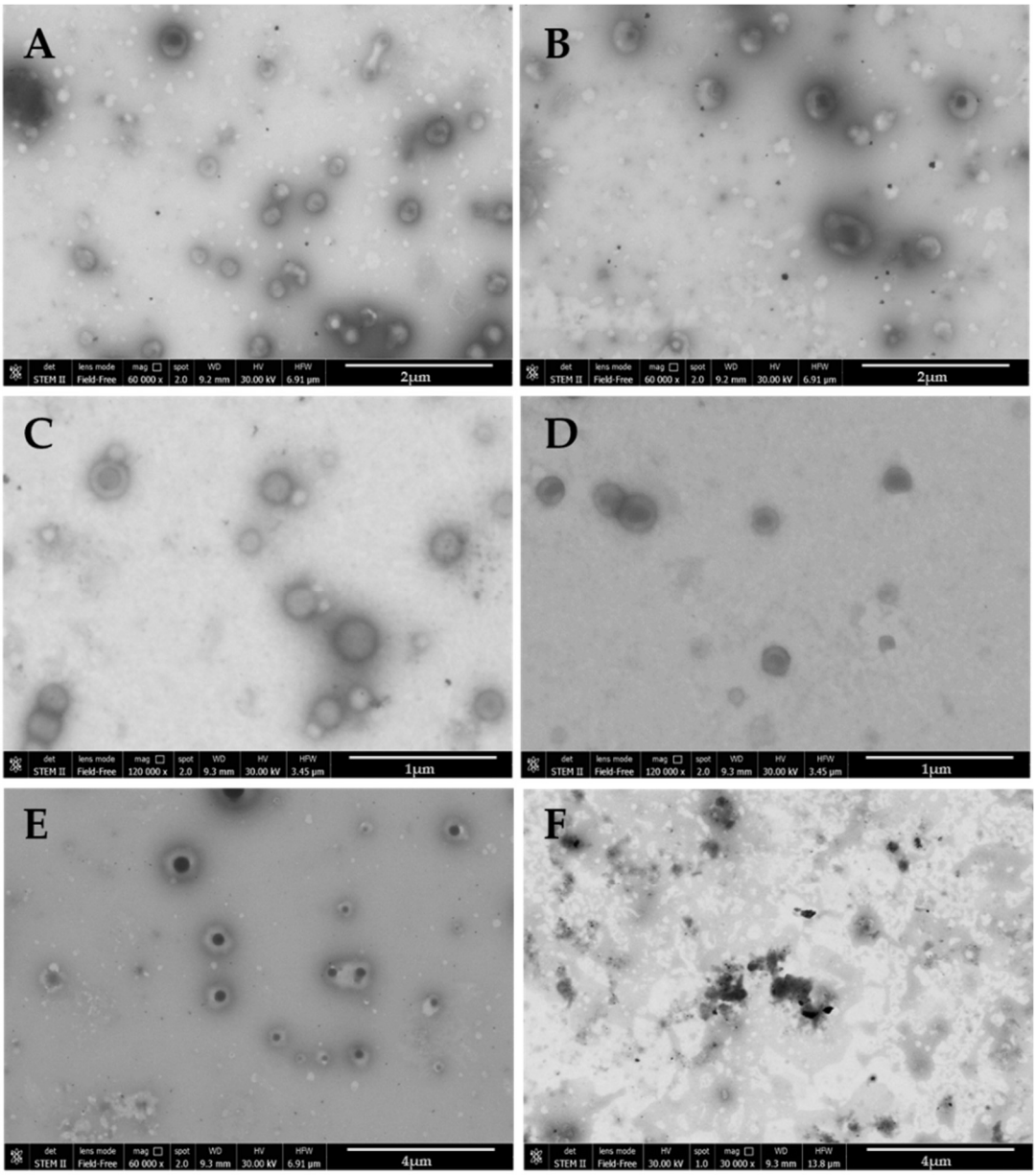


**Figure 3.** SEM-FEG Nanoparticle images; (**A**) NPs PLGA:Solution0; (**B**) NPs PLGA:Solution1, (**C**) NPs PLGA:Solution2; (**D**) NPs PLGA:Solution3; (**E**) NPs PLGA:Solution4; (**F**) Solution Tween®20: β-Glu non-formulated. Note: all formulations contain 5 mg β-Glu.

SEM-FEG analysis supported these findings where all images showed spherical NPs ranging from 150 to 300 nm. With this microscopic method, however, the double emulsion containing Tween® is more apparent. Increasing the amount of Tween® led to the NPs becoming more uniform and presenting a halo around the denser core (Figure 4E). Further supporting the ITC data, Solution 4 was analyzed in solution pre-formulation and no self-assemblies were identifiable (Figure 3F).

To determine if these structural differences were caused directly by a variation in the amount of Tween® 20 incorporated into the NPs, a quantification of Tween® 20 content was performed by ELSD-HPLC, following a protocol modified from a previously published article (Table 5) [352]. While the HPLC-ELSD technique allowed for the quantification of the Tween® in the NPs, reverse phase columns are incompatible with the polymer PLGA, meaning no structural information could be provided of intact NPs. Therefore, Tween® 20 was extracted from the NPs using an organic solvent, to destroy the 3D-assembly, and an aqueous solvent was used to solubilize and quantify the Tween® to determine if there is a correlation between the physical characteristics and the presence of Tween® 20. Interestingly, the amount of total Tween® 20 incorporated into the NPs remained constant independently from the Tweeen®20:enzyme solution mixture encapsulated, despite the increased amount of surfactant in the initial aqueous solution (~9 mg/100 mg NPs). This is an interesting result because even over such large differences in the amount of Tween® 20 in the aqueous phase (0.5–20% *v*/*v*), there appeared to be a saturation effect where the PLGA NPs have an incorporation limit of ~ 10% of the total mass of the NPs. This means, the only difference in final Tween® 20 amount can be observed in the ratio of Tween®:β-Glu (increasing from 841:1 to 1560:1) due to the difference in %EE and final %yield.

**Table 5.** Quantification of Tween® 20 content in Nanoparticles formulated with solutions 1–4.

| Samples | Tween® 20 content mg Tween® 20/100mg NPs | β-Glu content mg β-Glu/100 mg NPs | Tween® 20:β-Glu mol/mol |
|---|---|---|---|
| **NPs_Solution1** | 9.4 ± 0.3 | 1.1 ± 0.0 | 844 |
| **NPs_Solution2** | 9.3 ± 0.2 | 1.0 ± 0.1 | 872 |
| **NPs_Solution3** | 9.3 ± 0.1 | 0.8 ± 0.1 | 1233 |
| **NPs_Solution4** | 9.7 ± 0.6 | 0.9 ± 0.1 | 1560 |

While the increased amount of Tween® 20 appeared to form more homogenous NPs according to the microscopic analysis, the constant PCS results, and amount of Tween® 20 in the NPs was directly translated to the activity in the NPs. While all Tween® 20:enzyme solution mixtures yielded NPs with higher activity respective to those without Tween® 20, the difference between the various mixtures was insignificant, showing only a slight trend towards higher activity correlated to a higher amount of Tween® 20 in the initial solution, as well as the trend towards higher Tween® 20:β-Glu molar rapports (Figure 4, Table 5).

While interesting, this brings up another question as to why, even when the amount of residual Tween® 20 remains constant (~9.5%) in the final composition of NPs, the trend towards a higher molar rapport of Tween® 20:β-Glu also led to a trend towards higher activity. One possible conclusion would be that the protective effect is completely ascribed to stabilization from the stresses in solution. To study if the presence of Tween® 20 affects the release and activity of the enzyme from the NPs, the release profile was studied at the biologically relevant pHs of 7.4 (representing blood circulation) and 4.5 (lysosome).

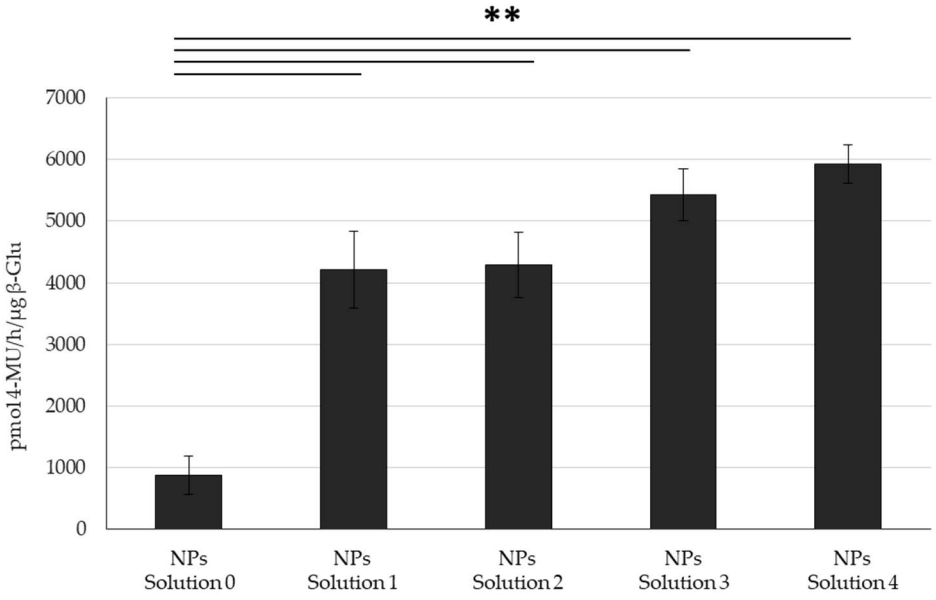


**Figure 4.** Activity Comparison. Activity of β-GluTween®20 solutions at different molar ratios (Solutions 1-4) and encapsulated into PLGA NPs. Statistical analysis was performed using the Student *t* test where ** $p < 0.01$ and N = 3 individual NP formulations of each type.

Unfortunately, a detailed analysis of the release kinetics using the Peppas model was not feasible due to the equilibrium of the release of enzyme from the NPs and the subsequent loss of enzyme activity in the supernatant, making it unquantifiable by HPLC, over time; therefore, we looked at each timepoint individually to measure both intact and active released enzyme. As previously seen in the article looking at β-Glu stabilization with BSA [341], enzyme loaded NPs with no stabilizer not only showed maximum release within 3 h at both pHs with a release of ~ 61% at pH 7.4 and 21.3% at pH 4.5 of the total enzyme content, but showed very little enzyme activity peaking at 200 pmol 4-MU/h/μg β-Glu. The difference in total amounts of recovered enzyme could be due to the instability of the enzyme in solution leading to lower quantification yields (Figure 5, Grey bars). The NPs formulated with Solution 4 showed very different results. A maximum release (62.7% at pH 4.5 and 80% at pH 7.4) was still observed within 24 h; however, two interesting observations were made. First, the released enzyme remained stable and measurable by HPLC even out to between 7 and 14 days (Figures 5A,B, black bars). Secondly, and in accordance with the first observation, the more stabilized enzyme retained activity at much higher levels and for longer times than the enzyme encapsulated alone. This is interesting because the results indicating low\poor complexation between Tween® 20 and enzyme still led to stabilization in solution after being released in some way. One possible hypothesis for this still relates back to the stabilization of the NPs during formulation. More homogenous and constant NP formation could protect the enzyme from stresses such as solvent contact and sonication. These stresses could negatively impact the 3-D structure of the enzyme, leading it to be more susceptible to physical changes that lead to a loss of activity once released in biologically relevant conditions. Another hypothesis could be the "sacrificial lamb" effect: this would explain both the protection of the enzyme in solution under stress during formulation, but also explain as to why when the enzyme is released (presumably together with the incorporated Tween® 20), it is protected long term and retains its activity.

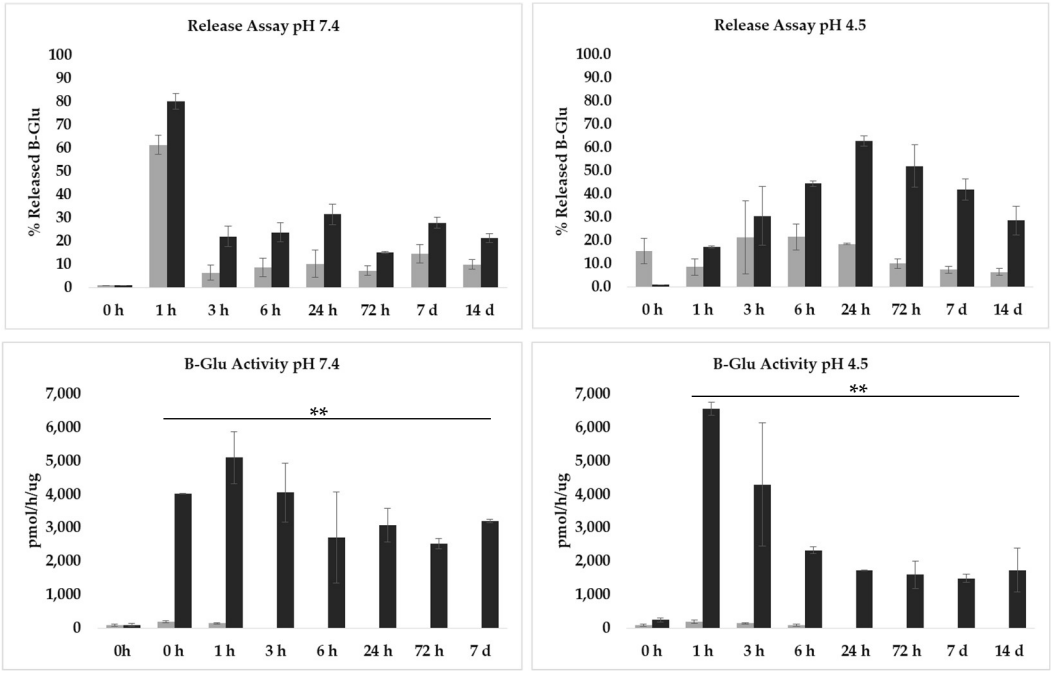


**Figure 5.** Quantification of the release and enzyme activity of β-glucosidase from the nanoparticles. Grey: control Solution 0 NPs (no Tween®20). Black: Solution 4 NPs (with Tween®20). (**A**) %Release of β-Glu at pH 7.4, (**B**) %Release of β-Glu at pH 4.5, (**C**) Activity of released β-Glu at pH 7.4, (**D**) Activity of released β-Glu at pH 4.5. Analysis of N = 3 separate NP formulations.
** $p < 0.01$ NPs with Tween 20 vs. NPs without Tween 20 per each timepoint.

Due to the differences in interaction, loading efficiency and release profiles between Tween® 20:enzyme solutions and BSA:enzyme complexes formulated into PLGA NPs, it was hypothesized that these two stabilizing molecules work by different (but still undefined) mechanisms. To this end it was tested to see if they could complement each other maintaining even higher levels of enzyme activity respective as each individually. Controls on stressed enzyme or stabilized enzyme under stress show this effect in solution (Figure S2) and therefore, studies during NP formulation were tested. NPs encapsulating BSA:β-Glu Complex (molar rapport 20:1), Tween® 20:β-Glu Solution 4, and a BSA:Tween® 20:β-Glu mixture solution (with the molar ratios of enzyme to BSA and Tween® 20 equal to that of the individual formulations) were compared. NPs formulated with BSA:Enzyme, Tween® 20:Enzyme, or BSA:Tween® 20:Enzyme solutions were purified by centrifugation to remove any stabilizer or free enzyme in the supernatant. The intact NPs were then tested directly for the amount of β-Glu activity present. This was then normalized to the amount of enzyme encapsulated for each NP type

based on an extraction and quantification of the amount of enzyme present. The combination of both stabilizers showed similar sizes (216 nm) and ζ-pot (−15 mV) as when formulated with only one of them. The %EE of BSA:Tween®:β-Glu was increased as previously seen with the BSA:β-Glu complex but not to the same extent (14 and 25%, respectively). Ultimately the combination of both stabilizers together in the formulation led to retention of a statistically higher enzyme activity in the NPs, an effect that appeared to be additive compared to NPs with the individual stabilizers (Figure 6).

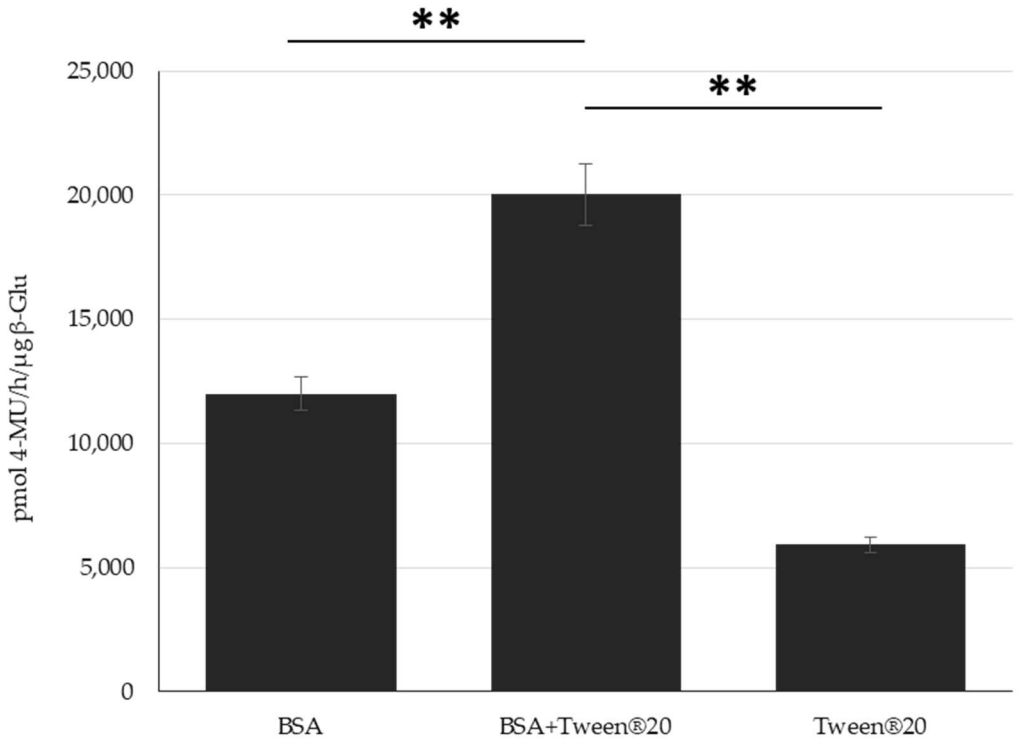


**Figure 6.** Combination Stabilization. Measurement of the β-Glu Activity in NPs formulated with: BSA:Enzyme, Tween®20:Enzyme, or BSA:Tween® 20:Enzyme solution.. Statistical analysis was performed using the Student t test where, ** $p < 0.01$ and measured for N = 3 individual NP formulations of each type.

## 4. Discussion

Hard to treat diseases are plaguing science at the moment with very few functional cures being approved to treat them. Nanomedicine has paved the way to creating new and improved treatments due to their ability to be targeted to certain organs, tissues, or cells, and to encapsulate and protect a wide variety of pharmaceutical molecules. Many diseases such as LSDs are caused by poor functioning or lack of enzymes which has led to a boom in research for ERT; however, enzyme administration has been a major bottleneck due to their delicate 3D structure required to maintain activity and lack of bioavailability when dosed in the blood [356–358]. Even with the improved prospects of encapsulating enzymes in NPs, the formulation process is known to deteriorate the enzyme, causing a loss of activity. For these reasons stabilizers are added to help maintain enzyme activity during encapsulation, but how they affect the enzyme and the formulations has not been described in detail in the literature. In fact, Tween® is often used in enzyme particle formulations or during enzyme release assays without taking into consideration its potential stabilizing effect on the enzyme and its activity [359–362]. In this article, we expand on previous works looking at the complexation of BSA with β-Glu for improved activity by comparing the commercially available Tween® series which has also been used in NP preparation.

Here polysorbates (more specifically Tween® 20) demonstrated an efficient stabilizing effect of β-Glu in PLGA NPs. But it is very important to highlight the differences from the recently published work of the same type regarding BSA [341]. While BSA showed a direct interaction with the enzyme, Tween® 20 did not. This highlights how the different stabilizers can affect an enzyme's potential in different ways: BSA led to higher loading content and enzyme encapsulation (LC%–%EE) and the complexation also affected enzyme release, while Tween® 20 did not show direct interaction with the enzyme, did not increase LC% or %EE to the same extent, and had no direct effect on the release kinetics. This strongly suggests a difference in mechanism where BSA directly stabilizes the enzyme

during complexation prior formulation, while Tween® has a much more global effect on the NP formation and stabilization throughout the formulative process. Characterizations of how stabilizers help maintaining high levels of enzyme activity also include studies on the oligomeric state of the enzyme. Even in recent years this topic is being published in the literature with high interest and not completely understood as results show differences in the oligomer state being dependent on numerous factors such as the stabilizer, inhibitor, and also origins of the β-Glu. Studies looking at β-Glu derived from *Aspergillus niger* demonstrate that surfactants can change the equilibrium versus the monomer increasing its activity by 60% [363]. On the other hand, β-Glu from *Spodoptera frugiperda* and almond demonstrate higher activity in the homodimer form of the enzyme [364,365]. Aim of this study was to analyze whether Tween® had the same complexation rate of BSA, however advanced studies including x-ray crystallography, NMR, high-res electron microscopy or small angle neutron scattering are needed.

This difference between the two stabilizing mechanisms was further supported by the fact that these two effects could be complementary by using both stabilizers simultaneously to formulate enzyme loaded NPs with even more therapeutic potential. Having the knowledge and ability to combine stabilizers to increase enzyme loading into the NPs while maintaining its activity is key to the future of NP based ERT. While enzyme offer the advantage of higher long-term product turnover, PLGA NPs in the literature often demonstrate low encapsulation rates as seen in this work (0.4 mg/100 mg NPs), and the loss of activity during formulation is one of biggest inhibiting factors for their successful use. This 10-fold increase from 0.4 to 3.9 mg/100 mg using BSA as a stabilizer in enzyme NPs is a notable difference. This is similar to the 8 fold increase in activity of Tween® 20:β-Glu NPs compared to non-stabilized NPs (approximately 6000 pmol 4-MU/h/μg β-Glu compared to 800 respectively) even without the increase in %LC. While combining the two stabilizers did not lead to the expected 20-fold increase, it did lead to a substantially improved result over each stabilizer by itself, which could

break through the barrier of successful NP based ERT: literature precedence suggests that even small but highly active enzyme doses can lead to pathology corrections in vivo, paving the way for NP based therapies that ensure the delivery of active enzyme in a more bio-compatible and therapeutic manner to.

These results compared to the BSA stabilization results introduce a very interesting topic in the field of NP enzyme delivery: enzyme stabilization must be characterized more completely. This is because the appropriate selection or mixture of multiple stabilizers with different mechanisms significantly improve NP based ERT pharmaceutics in different ways, i.e., binding, stabilizing, increasing loading efficiency, or increasing both NP and enzyme stabilization. This seems to be an obvious statement but one that is drastically missing from the field in the literature. Too often, these types of stabilizers are taken for granted and used without quantification or optimization. This stems directly from the fact that most of these compounds are known to help stabilize the NP formulation or enzyme in some manner but are used as general constituents and not considered as direct players. This is highlighted by numerous citations where the presence of these stabilizers will go undiscussed, uncharacterized/unquantified, or without demonstrating the mode in which it affords increased enzyme activity potential for therapeutic delivery, or even more grave, NP systems will often be tested without the proper controls lacking the stabilizer to show its importance in the system [319,322,353–355,366].

This more in-depth characterization and quantification of stabilizers in NP systems is important from a characterization and understanding standpoint but becomes even more relevant when thinking about its possible biological effects. Tween® as a surfactant is known to have potential cell membrane destabilizing effects and cell toxicity. Therefore, when unquantified and uncontrolled, this stabilizer could have devastating effects upon translation to clinical use [367–371]. In this study, we demonstrated that NPs formulated with various rapports of Tween® 20:β-Glu and increasing amounts of Tween® 20 had a constant incorporation of 9 mg Tween®/100

mg of NPs. This is critical information because it ensures that both in vitro, where our standard NP doses arrive at a maximum of 100 μg (9 μg Tween®) per well of cells, and for in vivo mice studies, in which we dose up to 20 mg/kg of NPs (45 μg Tween®), the amount of Tween® administered within the NPs is lower than literature values for polysorbate toxicity; however, while this low amount is good for evading toxicity, it is yet to be tested in vivo if this amount is enough to maintain the enhanced BBB crossing potential of NPs with a polysorbate shell, as also described in the literature [372,373].

## 5. Conclusions

The results reported in this research article, in conjunction with previous published enzyme stabilization results, highlight the need to characterize the effects of different additives when discussing enzyme delivery. This is because while certain combinations of stabilizers could lead to additive effects further increasing therapeutic potential, it is not certain if two stabilizers that have the same mode of stabilization will be complementary. Therefore, interest in the mode of action of these stabilizers found abundantly in the literature should not be taken for granted as is, and further studies are needed to find potential combined systems. These new systems, that have already been demonstrated to be able to efficiently deliver enzymes in vitro and in vivo, have the potential to offer a much more effective therapy which a much higher acceptance rate than the current aggressive and invasive ERT approaches to treat enzyme-based diseases.

## 6. Supplementary material

**Table SI1**. List of the abbreviations used in the main text

% = percentage

° C = Degrees Celsius

AFM = Atomic Force Microscopy

BBB = Blood Brain Barrier

BSA = Bovine Serum Albumin

CNS = Central Nervous System

DCM = dichloromethane

EE = entrapment efficiency

ELSD = Evaporative Light Scattering Detector

ERT = Enzyme Replacement Therapy

GoF = Goodness of Fit

h = hours

ITC = Isothermal titration calorimetry

J= joules

K = kelvin

KA = binding constant

kHz = kilohertz

LC = loading capacity

ln = logarithm

LSDs = Lysosomal Storage Disorders

mg = milligram

mg/mL = milligram per milliliter

min = minute

mL/min = milliliter per minute

mm/Hg = millimeters of mercury

mM= millimolar

mol = mole

MU = 4-Methylumbelliferone

nm = nanometer

NP = Nanoparticle

p = p-value

PBS = Phosphate-buffered saline

PCS = Photon Correlation Spectroscopy

PDI= polydispersity index

PLGA = Poly(D, L-lactide-co-glycolide)

pmol = picomole

PVA = poly(vinyl alcohol)

R = gas constant (8.314 J $K^{-1}mol^{-1}$)

RP-HPLC = Reversed-Phase High-Performance Liquid Chromatography

rpm = revolutions per minute

RT = room temperature

s = second

S.D. = standard deviation

SEM-FEG = Scanning Electron Microscopy Field emission Gun

T = temperature in Kelvin

VWD = Variable wavelength detector

β-Glu = β-Glucosidase

ΔG = Gibbs Free Energy

ΔH = enthalpy change

ζ-pot = zeta potential

μg = microgram

μg/mL = microgram per milliliter

μL = microliter

μM = micromolar

**Figure SI1**. AFM images of the different NP preparations: a) NPs PLGA:Complex0, b) NPs PLGA:Complex1, c) NPs PLGA:Complex2, d) NPs PLGA:Complex3, e) NPs PLGA:Complex4. Note: all formulations contain 5 mg β-Glu.

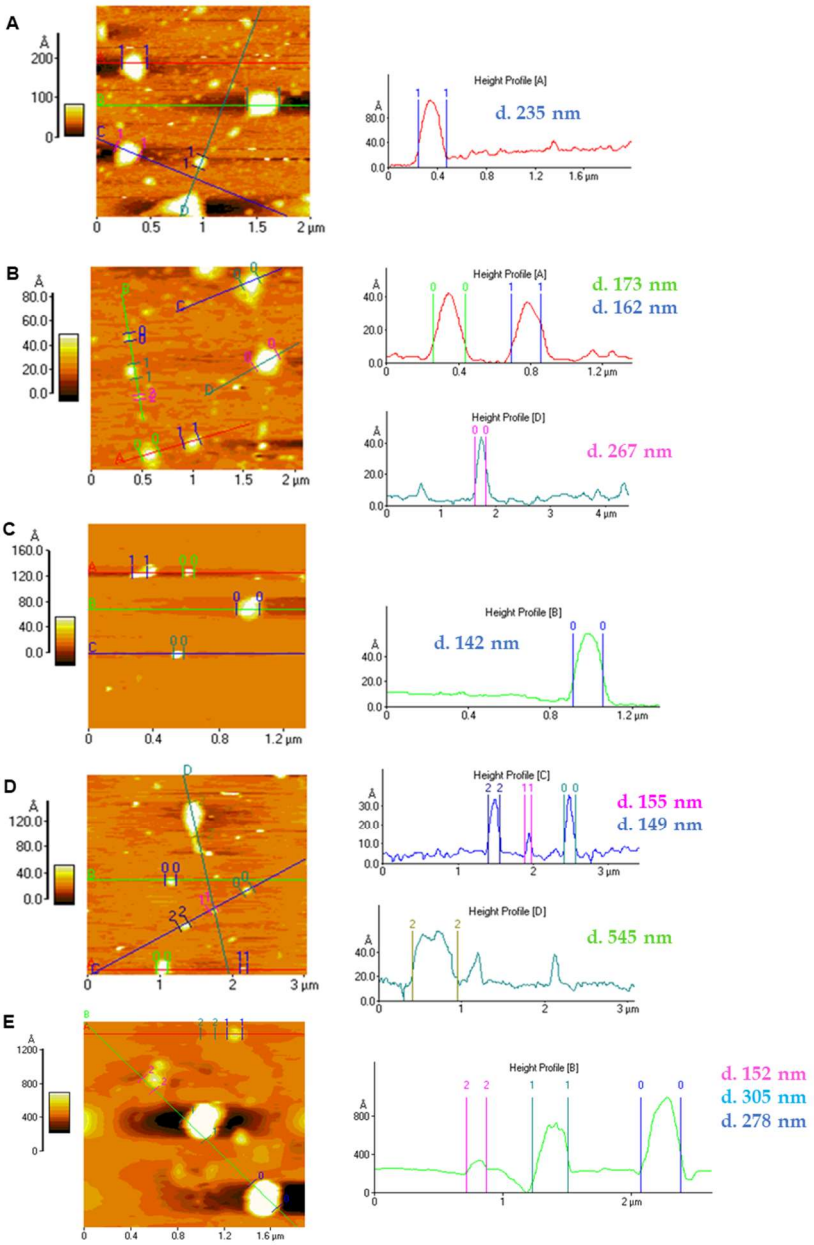

# CHAPTER 3

# Targeting

# Novel peptide-conjugated nanomedicines for brain targeting: in vivo evidences

**Jason Thomas Duskey [1,2], Ilaria Ottonelli [1,3], Federica Da Ros [1,4], Antonietta Vilella [5], Michele Zoli [5], Sandra Kovachka [6], Francesca Spyrakis [6], Maria Angela Vandelli [1], Flavio Forni [1], Giovanni Tosi [1], Barbara Ruozi [1]**

[1] Nanotech Lab, Te.Far.T.I., Dept. Life Sciences, University of Modena and Reggio Emilia, Italy, 41125

[2] Umberto Veronesi Foundation, Milan, Italy, 20122

[3] Clinical and Experimental Medicine PhD Program, University of Modena and Reggio Emilia, Modena, Italy, 41125

[4] STEM Cell Lab, University of Milan, Italy, 20133

[5] Department of Biomedical, Metabolic and Neural Sciences, University of Modena and Reggio Emilia, Italy, 41125

[6] Department of Drug Science and Technology, University of Turin, Italy, 10125

*Nanomedicine: Nanotechnology, Biology and Medicine* 2020, *28*, 102226, doi:10.1016/j.nano.2020.102226.

Revised 22 April 2020

Available online 29 May 2020

Version of Record 5 July 2020

## Abstract

Central Nervous System (CNS) compartments remain one of the most difficult districts for drug delivery. This is due to the presence of the Blood Brain Barrier (BBB) that hampers 90% of drug passage, dramatically requiring non-invasive treatment strategies. Here, for the first time, the use of opioid-derived deltorphin-derivative peptides to drive biodegradable and biocompatible polymeric (i.e. poly-lactide-co-glycolide, PLGA) nanomedicines delivery across the BBB was described. Opioid-derived peptides were covalently conjugated to furnish activated polymers which were further used for fluorescently tagged nanoformulations. Beyond reporting production, formulation methodology and full physico-chemical characterization, in vivo tests generated clear proof of BBB-crossing and CNS targeting by engineered nanomedicines opening the research to further applications of drug delivery and targeting in CNS disease models.


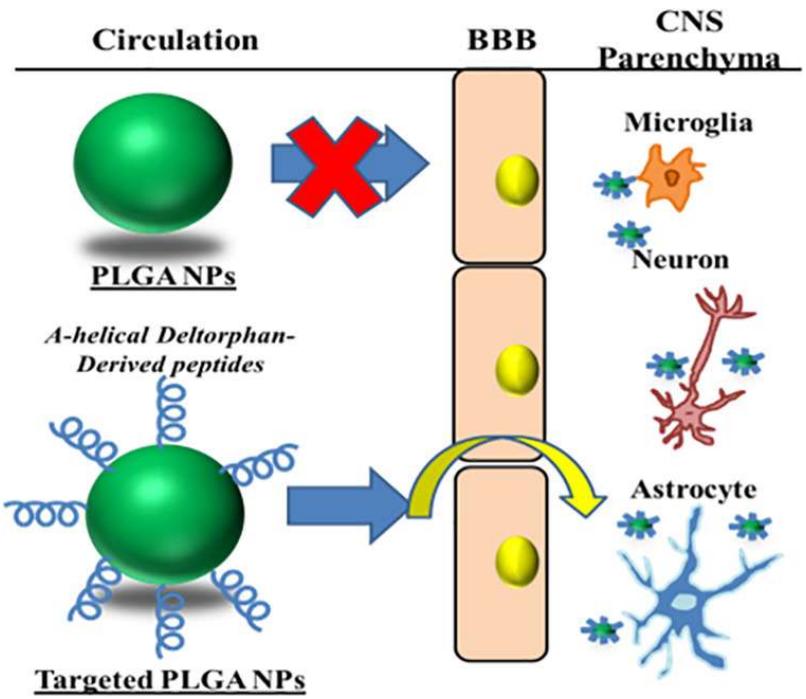

## 1. Introduction

The Blood-Brain Barrier (BBB) represents the major obstacle for drug delivery to the Central Nervous System (CNS) since more than 90% of active molecules are unable to cross [374]. Thus, neuro-pathologies up to now are considered as "difficult-to-treat" with poor prognosis and treatment options. Non-invasive technologies capable of assuring efficacious drug delivery to the brain are highly required, and thus is one of the hottest fields in neurological research. Amongst the numerous approaches attempted for selective access to the CNS [375], nanomedicine-based strategies are leading the research with cutting edge technology combining novel solutions for i) controlled drug delivery ii) specific tailoring for unique diseases and iii) surface engineering with the most suitable and selective ligands for BBB crossing pathways [232,296,351,376–378]. Regarding point 3, a plethora of ligand types (peptides, antibodies, surfactants, etc.) for BBB crossing, usually, covalently conjugated to nanomedicines, have been investigated in vivo and in vitro [379]. Amongst them, specific amphipathic peptides (i.e. opioid peptides) showed strongly enhanced rates of BBB crossing [380,381], thus stimulating endothelial cell uptake mechanisms [382,383]. Moreover, it has been shown that glycosylation could improve BBB crossing of peptides and even drug delivery systems [384]. In this view, opioid-derived peptides were able to transport poly-lactide-co-glycolide (PLGA) nanoparticles (NPs) loaded with various drugs at a very high percent (more than 10% of injected doses) to the CNS in relevant animal models [138,332,385]. This ability is highly attributed to their peculiar conformation which stimulate interaction with BBB endothelial cells and endocytosis pathways for accessing CNS [381,386]. Deltorphin peptides and their derivatives (glycosylated or not) share this unique structure [387] and have been broadly pointed out with evidential proof-of-evidence to have CNS activity and BBB crossing abilities. This and the fact that the deltorphin receptors are non-saturable permits engineered NPs to reach higher percentages in the CNS after systemic administration [388]. In order to exploit these unique properties of deltorphins to find efficacious solutions for BBB crossing and drug delivery to the

CNS in vivo, novel deltorphin derived hepta-peptides by slightly modifying the original aminoacidic sequences by substituting Tyr, responsible for the opioid effect [389], with Gly were synthesized. These peptides were characterized to ensure retention of the peptide's conformation critical for its ability to interaction with brain endothelial cells and cross the BBB. These novel heptapeptides were then covalently conjugated to polymeric NPS, fully characterized for their physico-chemical properties and further tested in vivo for the ability to drive the polymeric NPs across the BBB and reach the CNS by systemic and non-invasive administration in mouse models.

## 2. Results And Discussion

### *2.1 Polymer/Nanoparticles Synthesis and Characterization*

The deltorphan peptide and its glycosylated form (ODP, OGDP respectively) were synthesized substituting the Tyr, which is responsible for the opioid effect, with Gly (DP and GDP) (Table I).

**Table I.** Deltorphan parent peptide and derivative sequences

| Deltorphan Peptides | Abbreviation | Sequence |
|---|---|---|
| **Original Parent Peptide** | ODP | Tyr-(D)Ala-Phe-Asp-Val-Val-Gly-$NH_2$ |
| **Derivative peptide** | DP | Gly-(D)Ala-Phe-Asp-Val-Val-Gly-$NH_2$ |
| **Original Glycosylated peptide** | OGDP | Tyr-(D)Ala-Phe-Asn[β-GlcNAc(Ac)3]-Val-Val-Gly-$NH_2$ |
| **Glycosylated Derivative** | GDP | Gly-(D)Ala-Phe-Asn(β-GlcNAc-OH)-Asp-Val-Val-Gly-$NH_2$ |

DP and GluDP were submitted to 50 ns-long MD simulations to investigate their conformational space and the most stable states assumed in water solutions. Both peptides explore open and folded conformations, with a significant prevalence for the latter. The phi, psi and omega dihedrals, as well as the alpha 1, 2 and 3 angles (Figure 1) have been calculated and tracked along the simulations. The average values of all the angles for each peptide all along the trajectories are reported (Table II). The dihedral mean values have been also reported in a standard Ramachandran plot, to possibly identify a prominent secondary structure conformation.

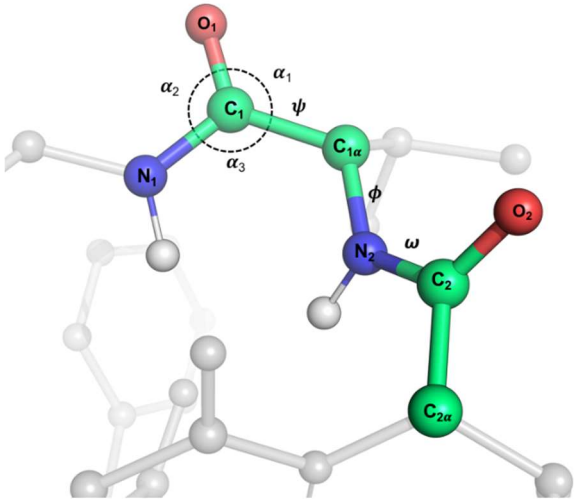


**Figure 1**. $\alpha_1$: angle formed by $O_1$-$C_1$-$C_\alpha$; $\alpha_2$: angle formed by $N_1$-$C_1$-$O_1$; $\alpha_3$: angle formed by $N_1$-$C_1$-$C_\alpha$; phi ($\phi$): angle formed by $C_1$-$C_\alpha$-$N_2$-$C_2$; psi ($\psi$): angle formed by $N_1$-$C_1$-$C_\alpha$-$N_2$; omega (**ω**): angle formed by $C_\alpha$-$N_2$-$C_2$- $C_{2\alpha}$.

**Table II**. Overall average dihedral values calculated for the entire peptides along the 50 ns-long during MD simulations. The more explicative omega distribution is reported in Figure S2-S5.

| | **phi ($\phi$)** | **psi ($\psi$)** | **omega (ω)** | **$\alpha_1$** | **$\alpha_2$** | **$\alpha_3$** |
|---|---|---|---|---|---|---|
| **DP** | -50,43° | -6,61° | 11,21° | 121,43° | 124,53° | 118,04° |
| **GluDP** | -51,02° | 33,69° | -3,29° | 122,13° | 117,39° | 118,79° |
| **ODP** | 3,94° | -12,04° | -10,32° | 123,72° | 117,45° | 118,52° |
| **OGluDP** | -53,14° | 0,66° | 2,83° | 123,33° | 117,25° | 118,67° |

As shown, DP falls at the border between the most-favoured and the additional allowed right-handed $\alpha$-helix region (Figure 2). GluDP is slightly further away from the most-favoured region, lying at the border between the additional allowed and the generously allowed right handed $\alpha$-helix region. The conformation of the two peptides in a $\alpha$-helix-shaped conformation, as extracted by the MD simulations is reported (Figure 3).

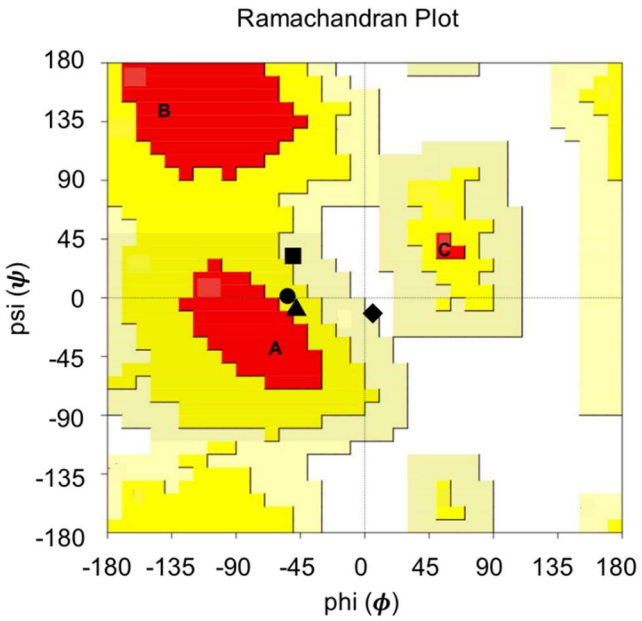


**Figure 2**. Dihedral overall average values during MD simulation: ▲DP; ■ GluDP; ◆ ODP; ● OGluDP. (Ramachandran plot generated in ProCheck software. Red region: most favoured (A)-right handed ***α***-helix, B)-***β***-sheet, C) left handed-***α*** helix), yellow region: additional allowed, light yellow region: generously allowed and white region: disallowed.

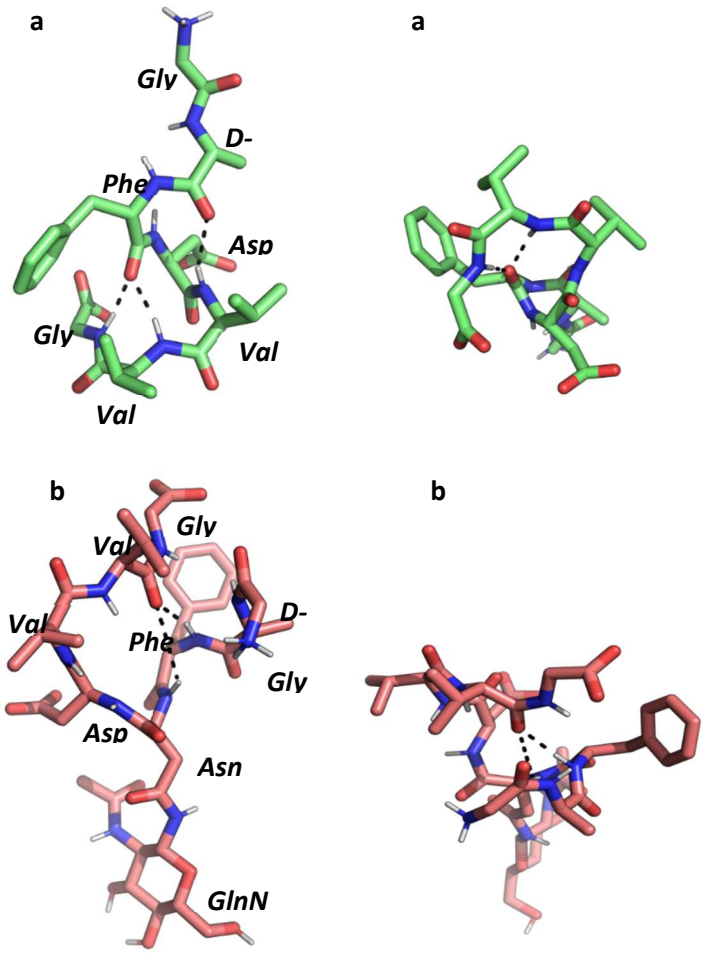


**Figure 3.** Folded conformations obtained for the DP and GluDP peptides by means of Molecular Dynamics simulations. a. DP frontal view. a'. DP vertical view. Phi and Psi average values are -57.10° and -6.61°, respectively. b. GluDP frontal view. b' GluDP vertical view. Phi and Psi average values are -69.29° and 34.72°, respectively. The peptides are shown in capped sticks, the intramolecular hydrogen bonds as black dashed lines.

To further check the simulations capacity to cover the available conformational space we extended the trajectory for GluDP, up to 700 ns, considered quite long for the simulation time of a small molecule [390]. The same results were obtained, thus confirming the suitability of the technique. For comparison, the conformation of the original peptides ODP (Tyr-D-Ala-Phe-Asp-Val-Val-Gly-$NH_2$) and OGluDP (Tyr-D-Ala-Phe-[β-GlcNAc(Ac)3]Asn-Val-Val-Gly-$NH_2$), known to have an opioid analgesic effect, was also investigated. The average dihedral and angle values are reported in Table 1 and the average conformation plotted in the Ramachandran

graph (Figure 2). While OGluDP lies close to DP, in the additional allowed region for right handed $\boldsymbol{\alpha}$-helix, ODP is located at the border between the generously allowed and the disallowed region.

These results support previous findings, according to which deltorphyn-derived peptides prefer to assume and maintain collapsed, generally $\boldsymbol{\alpha}$-helix-shaped, conformations which seem to be pivotal in BBB crossing [391]. The graphs showing the dihedrals value and the dihedral plots for all the analysed peptides are reported in the Supporting Information (Figure S2-S6).

Regarding polymeric conjugation, PLGA was conjugated to each peptide as shown by the presence of relevant NMR peaks assessed to be close to 20% of the peptides conjugated to PLGA (Figure S7A and S7B). These conjugated polymers were used in all preparations which produced NPS with a high production yield of more than 90%. The NPs were featured by comparable sizes (close to 250 nm) independent of peptide presence, and a consistently negative surface charge ranging from -20 mV to -40mV dependant on the peptide surface engineering (Table III). Shape and morphology were also assessed by STEM analysis confirming the formation of spherical NPs with homogenous surfaces and morphologies independent of the presence or lack of surface engineering (Figure 4).

**Table III**. Chemico-physical characterization of NPs. Size values are expressed in nm. Zeta potential values are expressed in mV. PDI means polydispersity index, namely with values between 0 and 1. The lower the PDI value, the higher homogeneicity in the NP population. Values of SD are expressed in brackets. Each analysis was assessed in triplicate per analysed batch.

| Sample name | Size (SD) | PDI | Zeta Potential (SD) |
|---|---|---|---|
| **NPs** | 225 (12) | 0.27 (0.01) | -20 (5) |
| **DP-NPs** | 249 (10) | 0.18 (0.03) | -34 (4) |
| **Glu-DP-NPs** | 259 (21) | 0.23 (0.02) | -29 (5) |

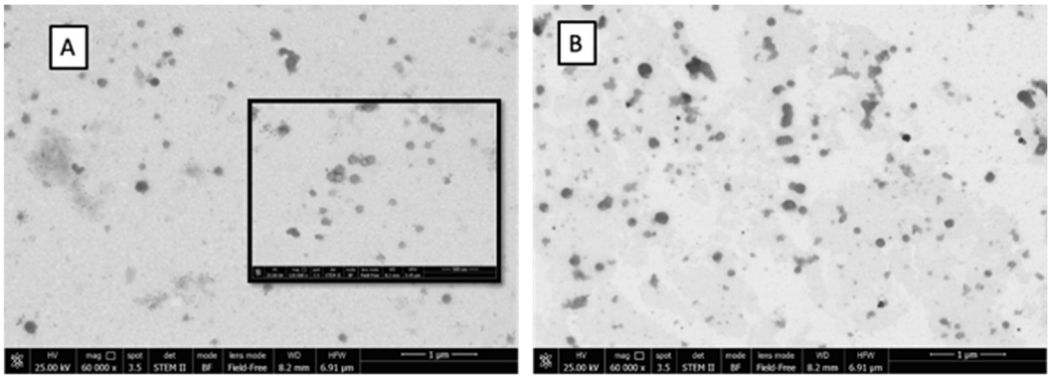


**Figure 4.** STEM images of Glu-DP-NPs (A) and DP-NPs (B). In the box, images of Glu-DP-NPs at higher magnification.

*2.2 In vivo readouts*

*In vivo* confocal miscroscopy sample analysis described that un-modified control NPs are detected in the brain to a very low extent (Figure S8), in line with previous data obtained [386,392–394]. On the contrary, the presence of engineered NPs within the brain parenchyma (highlighted by red spots due to Cy5 fluorescence), with particular focus on hippocampal dentate gyrus, is seen. Results demonstrated that both Glu-DP-NPs and DP-NPs are able to cross the BBB and distribute in the CNS parenchyma independent on whether the NPs are modified with the glycosylated or non-glycosylated peptide (Figure 5 and 6).

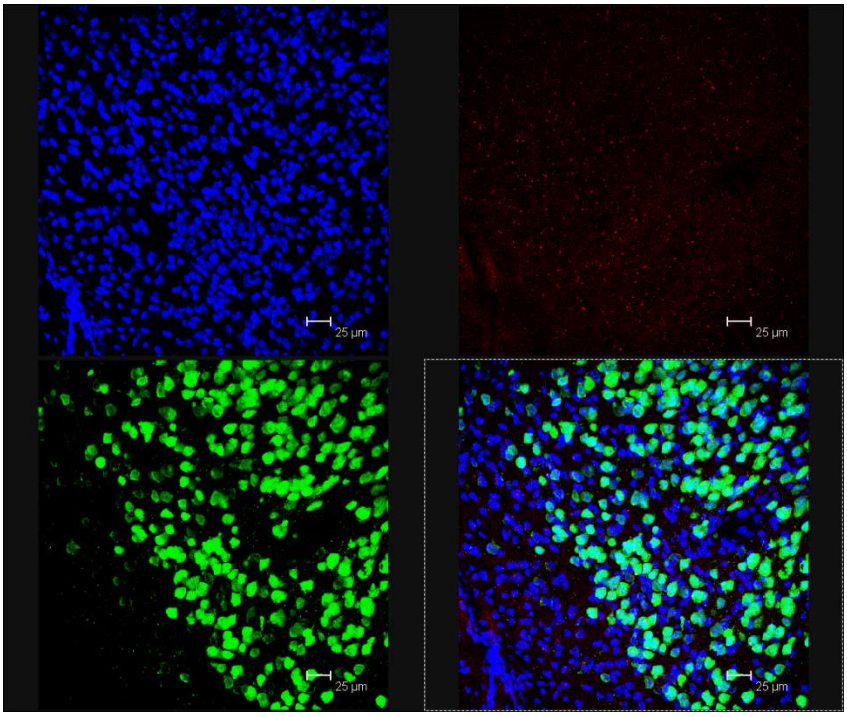


**Figure 5.** Representative confocal image of brain parenchyma after systemic administration of DP-NPs. Nucleus are stained with DAPI (blue signals), Neurons are stained with NEUN (green signals) and DP-NPs are tagged with Cy5 (red signals).

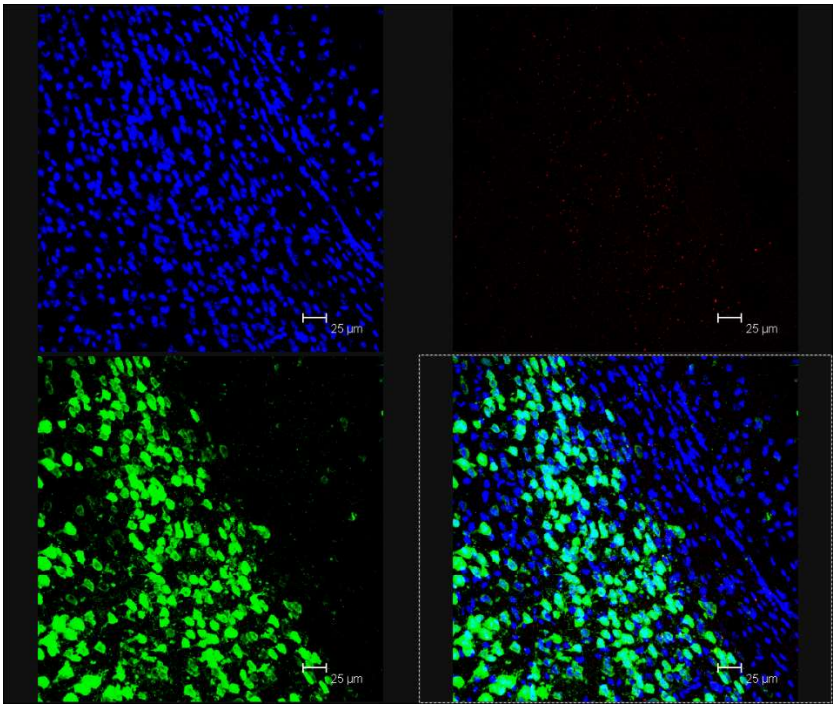


**Figure 6.** Representative confocal image of brain parenchyma after systemic administration of Glu-DP-NPs. Nucleus are stained with DAPI (blue signals), Neurons are stained with NEUN (green signals) and DP-NPs are tagged with Cy5 (red signals).

At a semi-quantitative level of analysis, a marked difference in NP numbers was demonstrated for Glu-DP-NPs in respect to DP-NPs calculated by the higher number presence and signal intensity (Figure 7). Taken together, these results suggest that glycosylation of the peptide on the NP (Glu-DP-NP treated mice) is able to facilitate higher amounts of BBB crossing into the CNS compared to those treated with NPs with the non-glycosylated peptide (DP-NP treated mice).

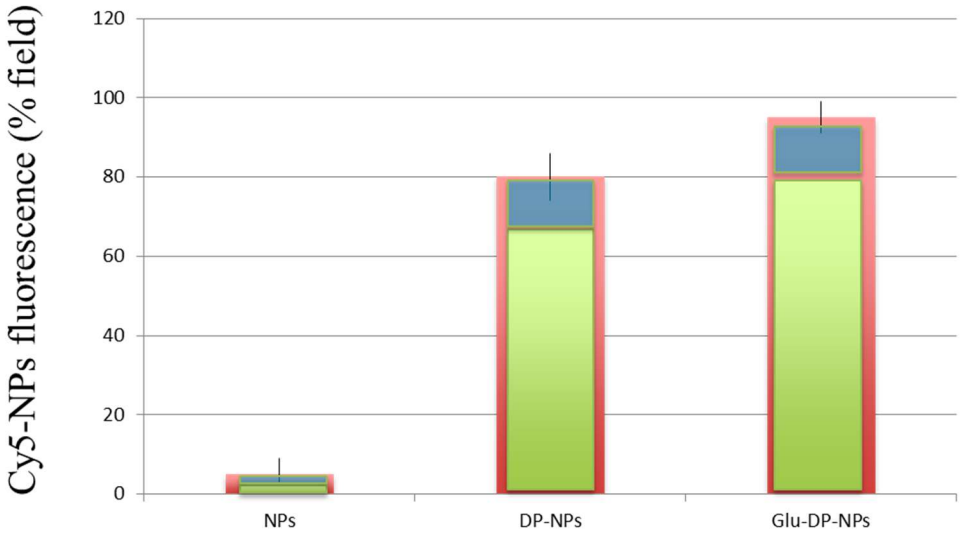


**Figure 7.** Semiquantitative analysis of CY5-NPs signals % per field. The value represents the mean of significant signals selected from background using the threshold function and the field area % calculated. For each treatment, 10 cells per section in 3 animals were analysed. Red bars indicated the total red signals meaning labelled NPs, green bars indicated the percentage of red signals co-localizing with DAPI and NEUN positive signals; blue bars represent the percentage of red signals co-localizing with DAPI signals.

Co-localization images also demonstrated that DP-NPs and Glu-DP-NPs (depicted by the red spots) are not only in close contact with NeuN positive neurons but also with other brain cells (Neun negative), probably astrocytes or microglia.

The analysis of IBA1 stained samples (Figure S9A-D) clearly showed that only in rare cases were both NP type (Glu-DP or DP NPs) co-localized with microglia signals, demonstrating a more relevant tropism to neurons in respect to other cell types. In fact, semiquantitative analysis revealed that close to 70% and 80% of DP-NPs and Glu-DP-NPs respectively preferentially accumulated in neurons (Figure

7). This confirms the tropism of NPs modified with the novel deltorphan peptides (Glu-DP or DP Nps) for these cell types as was seen with the parent-opiod peptide modified NPs previously [395].

Notably, at a higher magnification, the presence of engineered NPs is lacking within brain capillaries, probably indicating that the process of endo-transcytosis is complete as soon as 6 hrs after systemic administration (Figures S10 and S11).

## 3. Conclusion

Novel peptides are highly required to transport engineered nanomedicines across the BBB, enter the CNS, and trigger endocytic pathways where they are needed to release active molecules. Opioid peptides, in particular deltorphines, were shown to i) cross the BBB and ii) stimulate endocytosis after interaction with brain endothelial cells.

Previous data demonstrated that 7-8 aminoacid peptide sequences could be enough to trigger endocytic pathways and that peptide conformation, alpha-helix-like being better, could play a major role in their efficacy of promoting CNS entrance [382,386,391,396,397].

Our preliminary experiments demonstrated for the first time that two novel deltorphin-derived peptides, featured by $\boldsymbol{\alpha}$-helix-shaped conformations, conjugated to PLGA are able to efficiently drive engineered NPs to across the BBB after systemic administration in healthy animals. These readouts confirmed previous hypotheses on the role of opioid-derived peptides in promoting strong interactions with the BBB and triggering transcytosis dominated transport of 150 nm carriers into the brain parenchyma [386].

Deltorphin targeted NPs (Glu-DP-, DP-Nps) were able to not only cross the BBB, but also be up-taken primarily by neurons and to a low extent by other brain cells (such as glial cells). Further experiments devoted to a deeper analysis on the NP tropisms to the different cell types and brain areas identified as pathological target sites (i.e. striatum or cortex which are deeply involved in certain neurodegenerative diseases), will help in better understanding possible and novel scenarios.

Furthermore, beyond confirming the ability of deltorphin derivative peptides to cross, and transport polymeric NPs across, the BBB, these results also highlight and support the possible role of peptide glycosylation in improving BBB crossing as hypothesized in previous reports [382,393,396,397].

As a final consideration, most BBB crossing strategies are based on surface engineering of nanomedicines with ligands which target saturable-receptors (transferrin receptor, insulin receptor, etc.) imposing a "maximum transport" limit [398]. Non-saturable receptors, as is thought to be the deltorphin peptide receptors [399], would be more than favorable in terms of increased efficiency in CNS targeting and drug delivery.

Taken together, these results could pave the way to a new research path on opioid-derived peptides featured by specific helix-like conformation as possible ligands to engineer nanomedicines for CNS drug targeting and delivery.

## 4. Experimental Section

### *4.1 Materials*

Poly (D,L-lactide-co-glycolide) acid [PLGA RG-503H 50:50, inherent viscosity in 0.1% (w/v) $CHCl_3$ at 25°C = 0.38 $dLg^{-1}$] was used as received from the manufacturer (Boehringer-Ingelheim, Ingelheim am Rhein, Germany). According to the experimental titration results of the carboxylic end of the polymers (4.94 mg KOH/g polymer) the molecular weight of RG-503H was calculated to be 11,000 Da. Peptides Gly-(D)Ala-Phe-Asp-Val-Val-Gly and Gly-(D)Ala-Phe-Asn(GlcNAc-Beta-OH)-Asp-Val-Val-Gly] were obtained from Mimotopes (Springvale Rd Mulgrave, Victoria, Australia) and differs from parent peptides in terms of Tyr substitution ([Tyr-(D)Ala-Phe-Asp-Val-Val-Gly-$NH_2$ and Tyr-(D)Ala-Phe-Asn[b-GlcNAc(Ac)3]-Val-Val-Gly-$NH_2$]). Pluronic F68 (molecular weight of 8500-9000 Da) was purchased from Sigma-Aldrich. Primary antibodies were purchased from Synaptic Systems (NEUN and IBA1). Secondary goat anti-mouse AlexaFluor 488 conjugated antibodies were purchased from Invitrogen. Fetal bovine serum (FBS), and phosphate-buffered saline (PBS) were purchased from Euroclone Celbio (Milan, Italy). All solvents were of analytical grade, and all other chemicals and media were used as received from the manufacturers, and unless otherwise indicated, obtained from Sigma-Aldrich.

### *4.2 Animals*

For *in vivo* testing, juvenile C57BL/6 mice were used. The authors state that they have obtained appropriate institutional review board approval or have followed the principles outlined in the Declaration of Helsinki for all human or animal experimental investigations. The experiments were carried out in accordance with the European Communities Council Directives of 24 November 1986 (86/609/EEC) for experimental care.

*4.3 Peptide conformation study*

The conformation assumed by the peptides was investigated by means of Molecular Dynamics simulations. The original and newly derived non-glycosilated deltorphin-derived peptide [DP: Gly-(D)Ala-Phe-Asp-Val-Val-Gly] and the glycosilated deltorphin-derived peptide [GluDP: Gly-(D)Ala-Phe-Asn(GlcNAc-Beta-OH)-Asp-Val-Val-Gly] were parameterized using the ab initio RESP-charge-fitting methodology, as implemented in the BiKi Life Science software suite (http://www.bikitech.com) [400,401]. Also, the MD simulation setup was performed using the BiKi Life Science software suite (http://www.bikitech.com). Gromacs 4.6.1 was used to run MD simulations [390]. The TIP3P model was employed for water modelling. The solvated system was first minimized by 5000 steps of steepest descent and then equilibrated in four subsequent steps: 100 ps in NVT ensemble at 100 K, 100 ps in NVT ensemble at 200 K, 100 ps in NVT ensemble at 300 K, and a 1 ns long NPT simulation to reach the pressure equilibrium condition. The integration step was equal to 1 fs. The Verlet cutoff scheme, the Bussi−Parrinello thermostat, LINCS for the constraints (all bonds), and the particle mesh Ewald for electrostatics, with a short-range cutoff of 11 Å, were applied. The production runs were carried out in the NVT ensemble at 300 K without any restraint for 50 ns and no restrain was applied. For each peptide two replicas were run, upon reassigning velocities. The first replica of GluDP was extended up to 750 ns, to check the conformational stability and the reliability of the shorter simulations.

*4.4 Synthesis and characterization of Deltorphin-derived peptide PLGA conjugates*

As previously described [395], amide formation to covalently bind the carboxy terminus of the polymer PLGA RG503H and terminal amine of the peptides were formed using standard peptide coupling methods by means of N-hydroxysuccinimide (NHS) and dicyclohexylcarbodiimide (DCC) chemistry (Table SI and SII). In brief, to a solution of PLGA RG503H (1.00 g, 88 μmol) in

anhydrous dioxane (15 mL) at 4°C in an ice bath, DCC (19.0 mg, 93 μmol) and NHS (11.0 mg, 93 μmol) were added, and the mixture was returned to room temperature and stirred for 4 h at 20°C. Then, the dicyclohexylurea byproduct (DCU) was filtered away and the solution was decanted into cold anhydrous ether (200 mL) and left to precipitate for 2 hrs. The insoluble polymer was collected and purified by dissolution in $CH_2Cl_2$, followed by re-precipitation in anhydrous diethyl ether overnight. The ether was decanted and the product was dried under reduced pressure. The content of NHS groups reacted with PLGA RG503H was determined by 1H-NMR spectroscopy (DPX 200; Bruker, Rheinstetten, Germany) in DMSO-d6, from the relative peak area of the multiplet at 2.95 ppm (protons of the N-succinimide) and multiplet at 1.80–1.60 ppm (methyl groups of the polymer), and resulted to be 49 μmol NHS/g of polymer. The NHS activated polymer was dissolved in anhydrous DMSO (5 mL) and triethylamine (17 μL, 120 μmol) was added, followed by the addition of DP or GDP (80 μmol), under stirring. After 6 hrs at r.t., the conjugated peptide-polymer product was precipitatedby adding 200 mL diethyl ether. The precipitated polymer-peptide conjugate was collected and purified by dissolution in $CH_2Cl_2$ followed by another precipitation in $CH_3OH$ (200 mL). The $CH_3OH$ was decanted and the product was dried under reduced pressure overnight. Quantification of the extent of conjugation was performed using 1H-NMR (FT-NMR AVANCE400, Brucker Biospin) in DMSO-d6. With this procedure, the spectra of non-glycosilated deltorphin-derived peptide conjugated with PLGA (DP-PLGA) and glycosilated deltorphin-derived peptide conjugate (GluDP-PLGA) were obtained and the amount of peptide conjugated to the polymer was calculated by integrating the peak area of the signals at 7.2–7.5 ppm (aromatic protons of Phe) in relation to the multiplet at 1.80–1.60 ppm (methyl groups of the polymer) (Figure S7).

*4.5 Synthesis and characterization of PLGA-CY5*

PLGA-Cy5 was synthesized referring to an already optimized protocol whereby PLGA carboxy group is activated by means of an ester with N-hydroxysuccinimide (NHS), in presence of dicyclohexylcarbodiimide (DCC), and finally linked to the amino group of cyanine-5-amine by an amidic linkage. In detail (chart and table I supplementary information), PLGA RG503H (1 g, 88 μmol) was solubilized into anhydrous dioxane (15 mL) under magnetic stirring and 10°C with the aid of a cold water bath. N-hydroxysuccinimide (12 mg) and dicyclohexylcarbodiimide (22 mg) were then added and ice bath was removed to carry out the reaction at room temperature for 4 hours.

The suspension was filtered under reduced pressure to remove the precipitate (by-product: dicyclohexylurea, DCU) and the activated polymer was precipitated with anhydrous ether (200 mL directly into the flask), re-suspended in 2 ml of dioxane and re-precipitated with ether (total volume 200 mL). The product obtained was then solubilized in DCM, transferred into a round bottom evaporating flask and evaporated to dryness by means of a rotary evaporator (Büchi R114) then stored in a desiccator under reduced pressure overnight.

The activated polymer PLGA-NHS (1 g) was solubilized into anhydrous dimethyl sulfoxide (DMSO) (5 mL) in a round bottom flask under magnetically stirring while the cyanine 5 amine (43 mg) was solubilized separately in anhydrous DMSO (2 mL) and added to the former (chart and table II supplementary). TEA (14 μL) was added to reach pH 7-8 and the reaction was allowed to continue for 7 hours at room temperature. The mixture was added drop wised into a flask containing ether (50 mL) to precipitate the product (visible oil on the bottom of the flask) and, after 2 hours, the ether was decanted. The oil (i.e. PLGA-Cy5) was re-solubilized in DCM (2 mL) and a few drops of ether saturated with HCl were added to neutralize the excess TEA. Methanol (50 mL) was finally added and the product was left precipitate overnight. The turbid blue solution obtained was centrifuged at 10000 rpm for 10 minutes (ALC multispeed centrifuge PK 121) to separate the

product (pellet) which was solubilized with few mL of DCM and transferred into a flask; the supernatant was centrifuged at 9000 rpm for 5 minutes to separate the product still in suspension. This process was repeated six times and all the product solubilized in DCM was collected into the flask, re-precipitated with methanol and centrifuged. The pellet was finally solubilized with DCM, transferred into a round bottom flask and evaporated to dryness (Büchi R114). The structure of the conjugated polymer obtained (2 mg dissolved into 750 uL $CDCl_3$) was analysed by means of $H^1$-NMR spectroscopy (Brucker 400 Ultrashield, 40 scans) and the spectrum obtained, processed by Topspin software, was compared to the spectra obtained from both reagents (PLGA and cyanine 5 amine) in $CDCl_3$. All the products were characterized by NMR, as shown in supplementary figure 1 with confirmation of formation of final product PLGA-Cy5.

*4.6 Engineered NPs production*

To obtain polymeric NPs (PLGA, GluDP-NPs, DP-NPs) 50 mg of the polymer mixtures (Table III), were dissolved in acetone (4 mL). This organic phase was added dropwise into an aqueous solution of Pluronic F68 3% w/v (12,5 mL). After magnetically stirring the solution at room temperature for 15 min, the organic solvent was removed at 30°C under reduced pressure using a Rotavapor-Buchi R 114. The solution was then centrifuged at 14,000 RPM for 15 minutes at 4°C using a Spectrafuge ™ 24D microcentrifuge. The supernatant was discarded and the pellet was resuspended 4 mL of MilliQ water and 1:1 w/w trehalose was added as a cryoprotectant. NPs were then stored at -20°C until use. In order to obtain easily-traceable NPs, in each polymer mixture a fixed percentage (5% w/w) of PLGA-CY5 was inserted.

**Table IV**. Polymeric composition of the different PLGA-based NPs.

| Sample name | Polymeric mixture | Ratio of the polymeric mixture (w/w) |
|---|---|---|
| **NPs** | PLGA:PLGA-CY5 | 95:5 |
| **DP-NPs** | PLGA: DP-PLGA: PLGA-CY5 | 90:5:5 |
| **Glu-DP-NPs** | PLGA: Glu-DP-PLGA: PLGA-CY5 | 90:5:5 |

*4.7 Characterization of NPs*

The mean diameter (Z-average), the size distribution [expressed as D(50) and D(90)] and the polydispersity index (PDI) of the samples were determined at 25°C by Photon Correlation Spectroscopy (PCS) using a Zetasizer Nano ZS (Malvern, Malvern, UK; Laser 4 mW He–Ne, 633 nm, laser attenuator automatic, transmission 100–0.0003%, detector avalanche photodiode, Q.E. >50% at 633 nm). For each formulation, the mean diameter and PDI were calculated as the mean of three replicate measurements of three different batches (9 measurements). The zeta potential (z-potential) was measured using the same equipment with a combination of laser Doppler velocimetry and phase analysis light scattering (PALS). Z-potential data were collected as the average of 10 measurements. Scanning transmission electron microscope characterization was performed on a drop of the water suspension sample (about 0.05 mg/ml) placed on a 200-mesh formvar copper grid (TABB Laboratories Equipment, Berks, UK) using a Nova Nano SEM 450 (FEI Co., OR, USA) (acceleration voltage 30 KV) with a scanning transmission electron microscope II detector.

*4.8 Animal Testing and immunohistochemistry of brain sections*

GluDP-, DP- and control-NPs were diluted in a saline solution (1 mg of NPs$mL^{-1}$), dosed in C57BL6J mice with a single intraperitoneal injection of 200 μg of NPs (6 animals per group). The animals were sacrificed at 6 hrs, which was chosen due to previous literature precedence with similar opioid engineered NPS (max accumulation within 2 hrs to 5 days post injection) to be sufficient to access the CNS and show possible tropism [402]. For histological processing, animals were anesthetized with isoflurane until a loss of reflexes was observed. Intracardial perfusion was performed with 4% PBS-paraformaldehyde (100 mL 10 $min^{-1}$) preceded by an infusion of 50 mL of 0,9% NaCl saline containing heparin sodium (5000$UL^{-1}$); the organs (brain, liver, spleen and kidneys) were dissected out. The

brains were post-fixed in the same PBS-paraformaldehyde solution for 12 hr, rinsed in 15% sucrose in PBS for approximately 12 hrs and then in 30% sucrose in PBS for 1 day. The brains were frozen using dry ice, and coronal 50 μm thick sections series were cut via a cryotome, washed three times in cold 1x PBS and stored at -20°C in a glycerol-PBS solution until use. As a control, a fresh saline solution was also i.p. injected with the same procedure in 6 fresh mice. Brain sections were processed for multiple immunofluorescence histochemistry according to the following protocol. After five washes with 1x PBS pH 7.4 for 10 min, blocking was performed for 1 hr at room temperature in a 1x PBS solution containing 0.1% Triton X100 and 1% bovine serum albumin (BSA). Incubation with primary antibody as described in materials (NEUN for neuron staining and IBA1 for microglia) diluted in 0.3% Triton X100, 1% normal serum (NS) and 1x PBS was performed overnight at 4°C. After three washes in PBS / 0.1% Triton X100, incubation with goat anti mouse Alexa488 (1:200) secondary antibody in 0.2% Triton X100, 1% NS and PBS was carried out for 90 min at RT. After washing three times with PBS for 10 min, brain sections were placed on gelatinised glass slides, dried, incubated with DAPI, and mounted for confocal microscopy analysis.

*4.9 Confocal Analysis of Brain Samples*

Confocal analysis was performed with a Leica DM IRE 2 (Bannockburn, IL, USA); Leica Confocal System: scan head multiband 3 channels Leica TCS SP2 with AOBS, laser diode blu COH (405 nm / 25 mW), Laser Ar (458 nm / 5 mW) (476 nm / 5 mW) (488 nm / 20 mW) (496 nm / 5 mW) (514 nm / 20 mW), Laser HeNe (543 nm / 1.2 mW), Laser HeNe (594 nm) (Orange), Laser HeNe (633 nm / 102 mW). In particular, NPs (due to their labeling with Cy5) were clearly visible by excitation using the 633 nm laser with an emission readout at 650 nm, while staining of DAPI, NEUN or IBA1 were detected using different wavelengths. Semi-quantitative measurement of NPs was performed on confocal images by means of image analysis software (ImageJ) using established protocols for statistical evaluation

performed by using Student's t-test [403]. Briefly, NPs profiles were selected from background using the threshold function and the field area % was calculated. For each treatment, 10 cells per section in 3 animals were analysed.

## 5. Supplementary Material

*5.1 Synthesis and characterization of PLGA-CY5*

First step: activation of PLGA RG503H

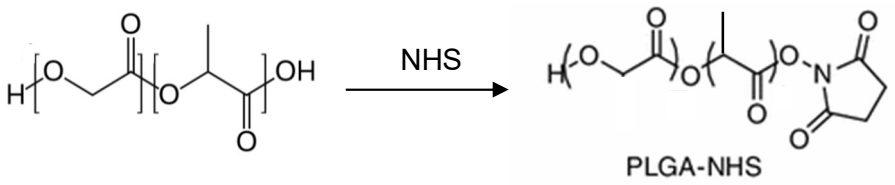


**Table S1**. Summary of the reagents used to synthesize PLGA-Cy5 (first step)

| Substance | Molecular weight | Moles | Quantity |
|---|---|---|---|
| PLGA RG503H | 11000 | 88 μmol | 1 g |
| NHS | 115,09 | 105,6 μmol | 12 mg |
| DCC | 206,33 | 105,6 μmol | 22 mg |
| Anhydrous dioxane | | | 15 ml |
| Anhydrous ether | | | 200 ml |

Second step: derivatization of the activated polymer

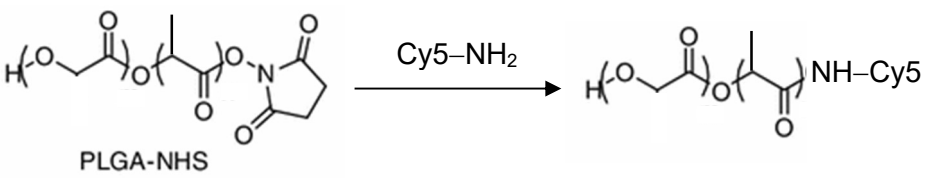

**Table S2**: summary of the reagents used to synthesize PLGA-Cy5 (second step)

| Substance | Molecular weight | Moles | Quantity |
|---|---|---|---|
| PLGA-NHS | | 88 µmol | 1 g |
| Cyanine 5 amine | 653,77 | 66 µmol | 43 mg |
| TEA | 101,19 | 99 µmol | 14 µL |
| Anhydrous DMSO | | | 5 + 2 ml |

Characterization of PLGA-Cy5: The final product was characterized by $^{1}$H-NMR spectroscopy and compared to the spectra of the reagents.

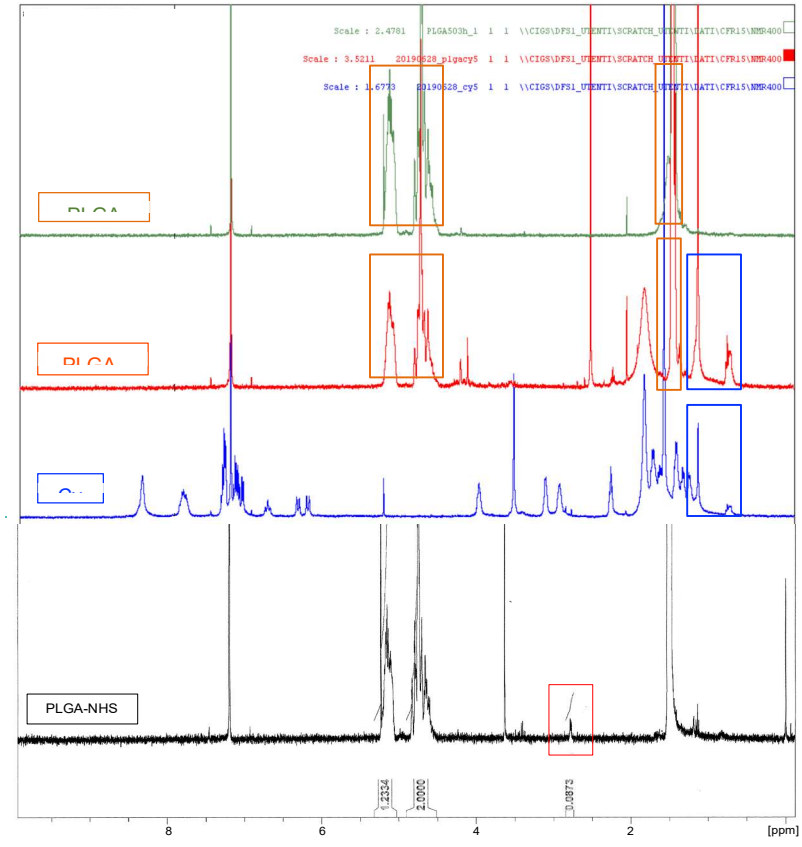


Figure S1: 1H-NMR spectra of the product (PLGA-Cy5), reagents (PLGA 503H and Cy5) and intermediate (PLGA-NHS) of the reaction. In details, the 1H-NMR spectrum of the final product PLGA-Cy5 shows the signals characteristics of PLGA in the regions 4.5-5.5 ppm and 1.5 ppm (fig. 1, supplementary, orange boxes) together with the signals characteristic of Cy5 in the region 0-1.25 ppm (fig.1 supplementary, blue boxes). The signal characteristic of the intermediate product of the reaction, i.e. activated PLGA (PLGA-NHS), at ppm 2,5-3 is not present in the spectrum of the final product, demonstrating the occurred formation of the amidic linkage between PLGA and Cy5 amine.

## 5.2 Molecular Dynamics simulations

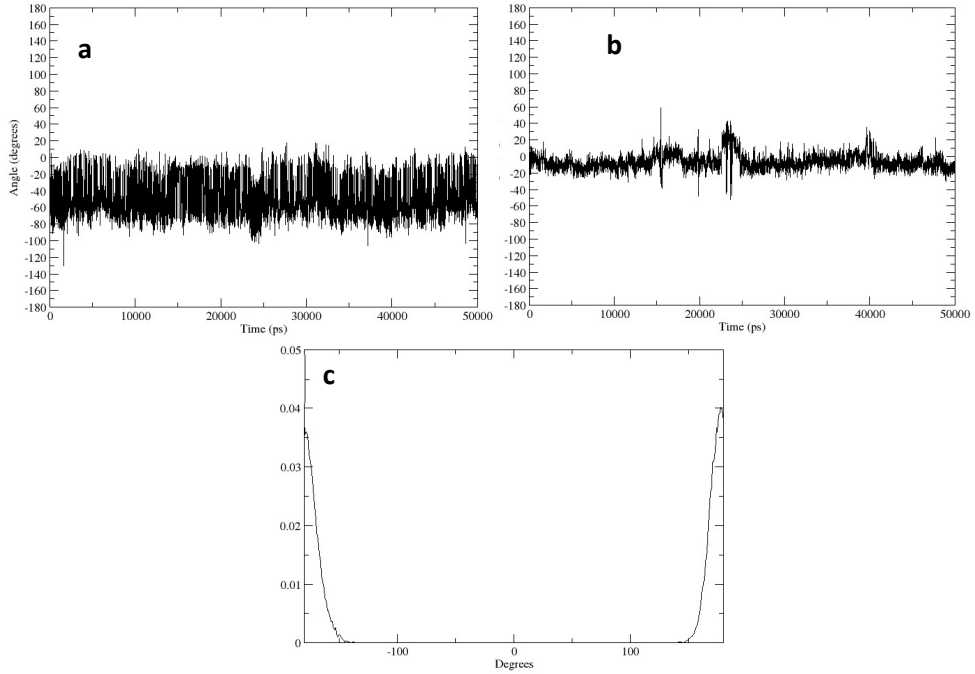


**Figure S2**. Phi (a) and Psi (b) dihedral average values along the 50 ns-long MD simulation for the DP peptide. (c). Distribution of the omega dihedral.

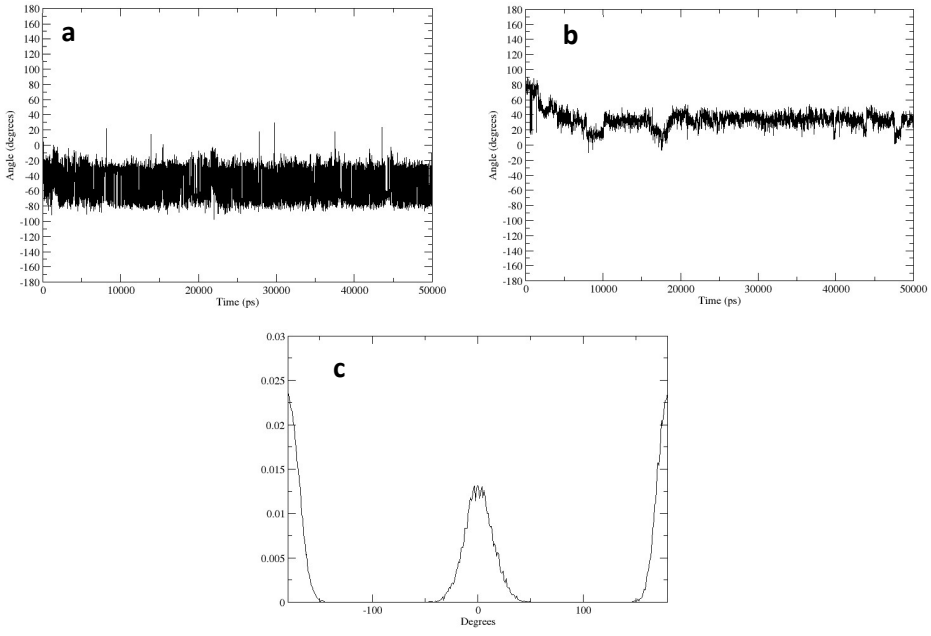


**Figure S3**. Phi (a) and Psi (b) dihedral average values along the 50 ns-long MD simulation for the GluDP peptide. (c). Distribution of the omega dihedral.

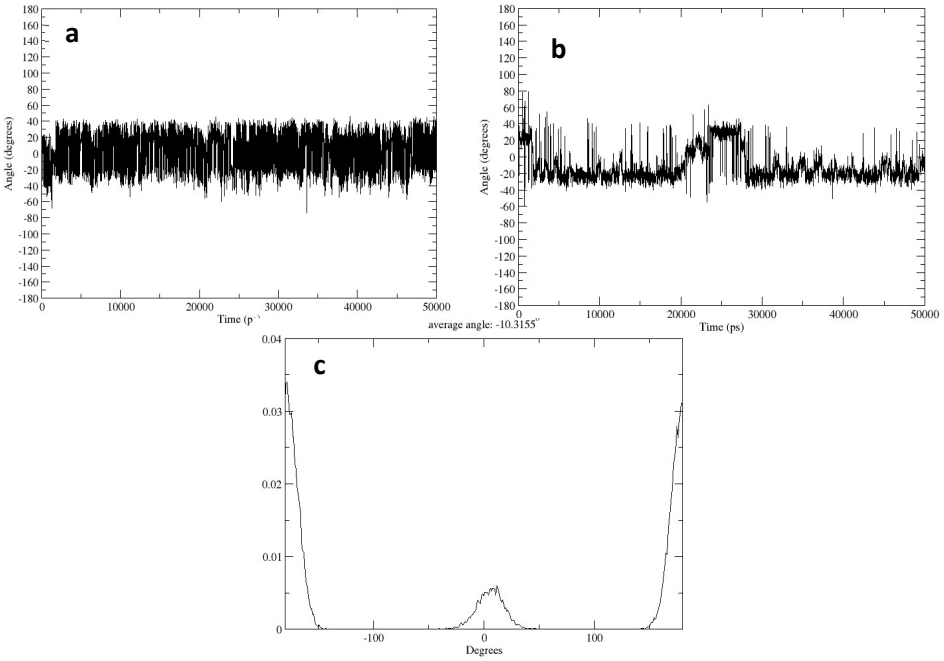


**Figure S4**. Phi (a) and Psi (b) dihedral average values along the 50 ns-long MD simulation for the ODP peptide. (c). Distribution of the omega dihedral.

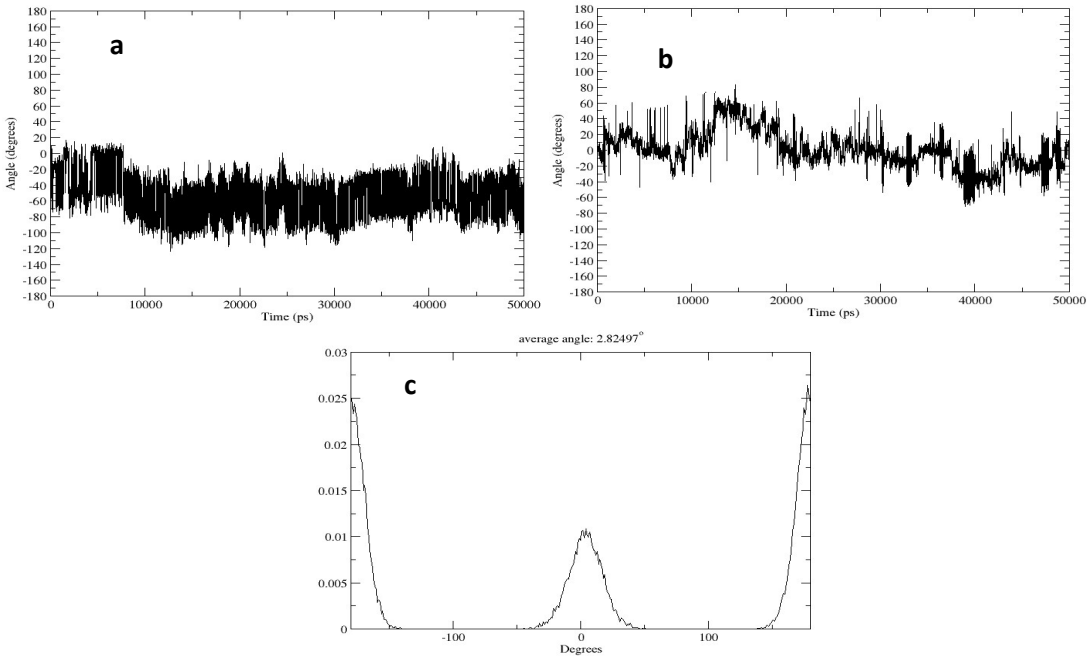


**Figure S5**. Phi (a) and Psi (b) dihedral average values along the 50 ns-long MD simulation for the OGluDP peptide. (c). Distribution of the omega dihedral.

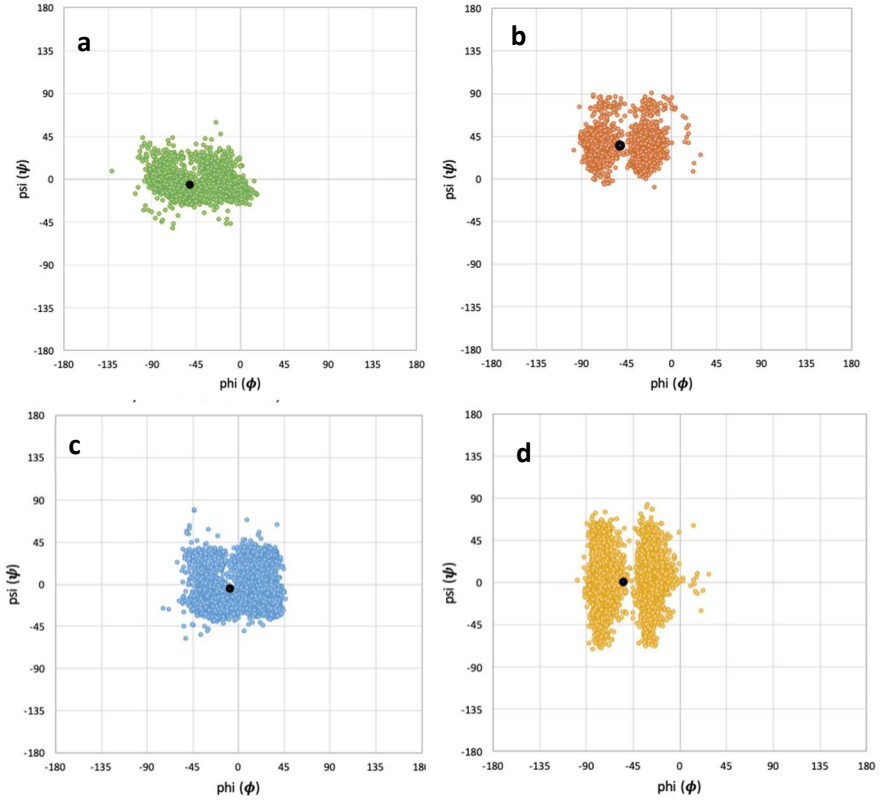


**Figure S6.** Phi/Psi dihedral values calculated for each frame of the 50 ns-long MD simulations run for the DP (a), GluDP (b), ODP (c) and OGluDP (d) peptides. The average value is shown by the black sphere.

## *5.3 DP-PLGA and Glu-DP-PLGA NMR Analysis*

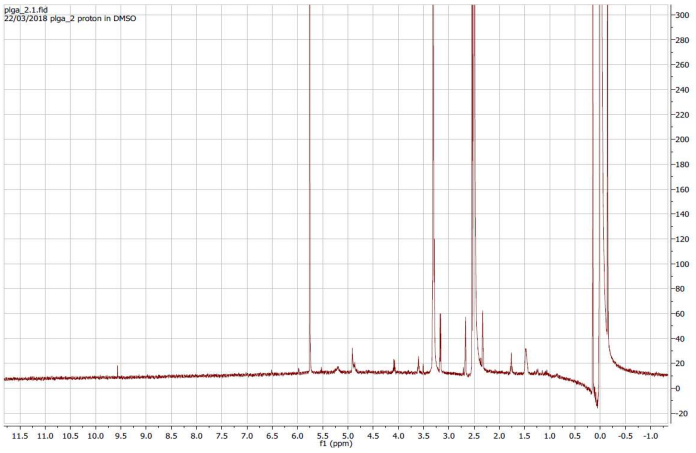


**Figure S7A.** H1-NMR analysis of DP-PLGA in DMSO.

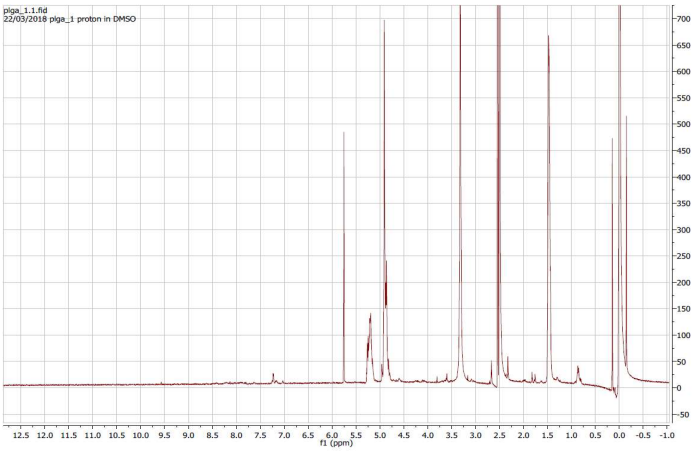


**Figure S7B.** H1-NMR analysis of Glu-DP-PLGA in DMSO.

## *5.4 Confocal Analysis*

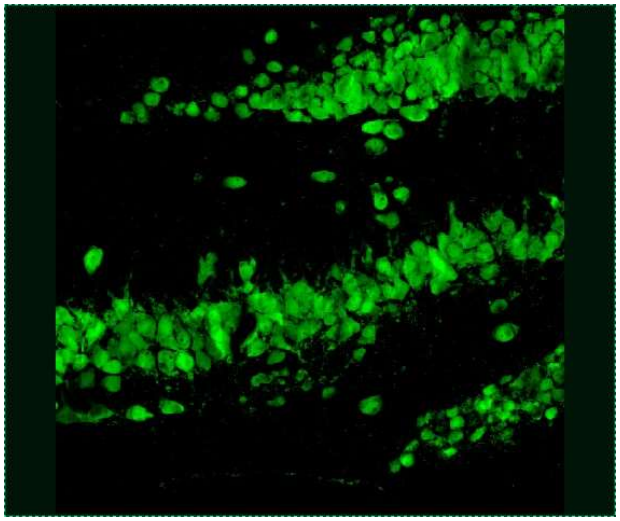

**Figure S8**. control ip injection, sacrifice time: 6hr; Staining : Neurons ( NEUN 488)

Few NPs (red spots) were present and negligible with respect to other samples

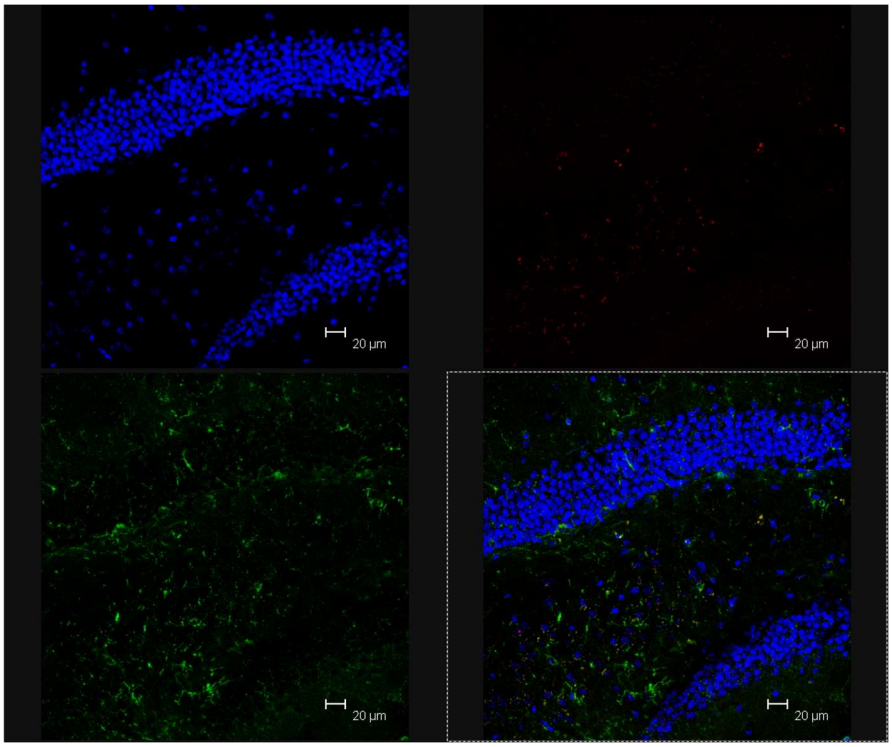


**Figure S9A.** DP-NPs, ip injection, sacrifice time: 6hr; Staining : Nucleus (DAPI) microglia (IBA1 488) NPs (Cy5).

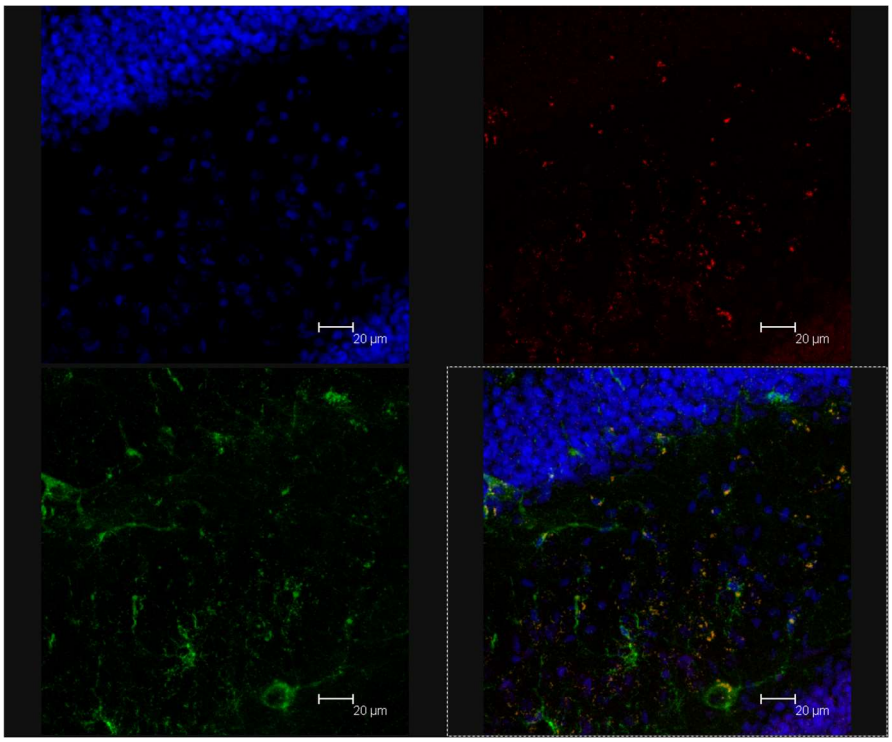


**Figure S9B.** DP-NPs, ip injection, sacrifice time: 6hr; Staining : Nucleus (DAPI) microglia (IBA1 488) NPs (Cy5), higher magnification.

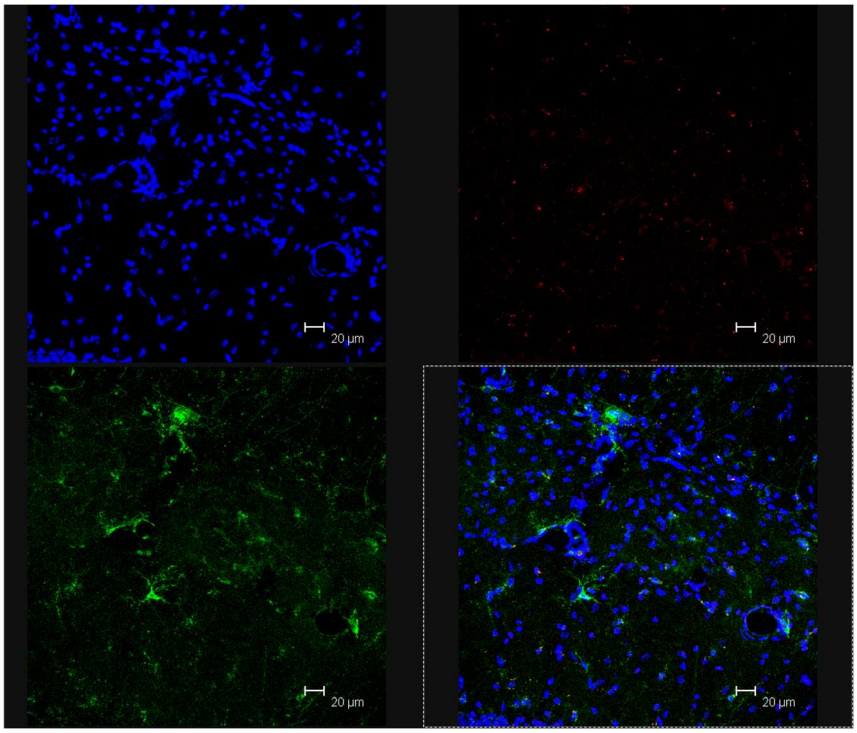


**Figure S9C.** Glu-DP-NPs, ip injection, sacrifice time: 6hr; Staining : Nucleus (DAPI) microglia (IBA1 488) NPs (Cy5).

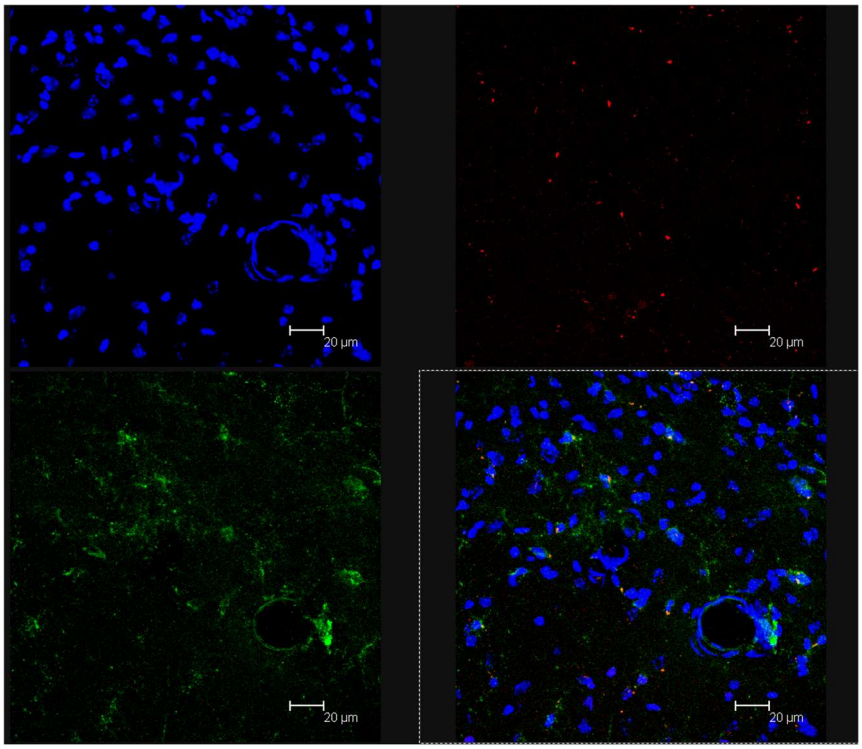


**Figure S9D.** Glu-DP-NPs, ip injection, sacrifice time: 6hr; Staining : Nucleus (DAPI) microglia (IBA1 488) NPs (Cy5), higher magnification.

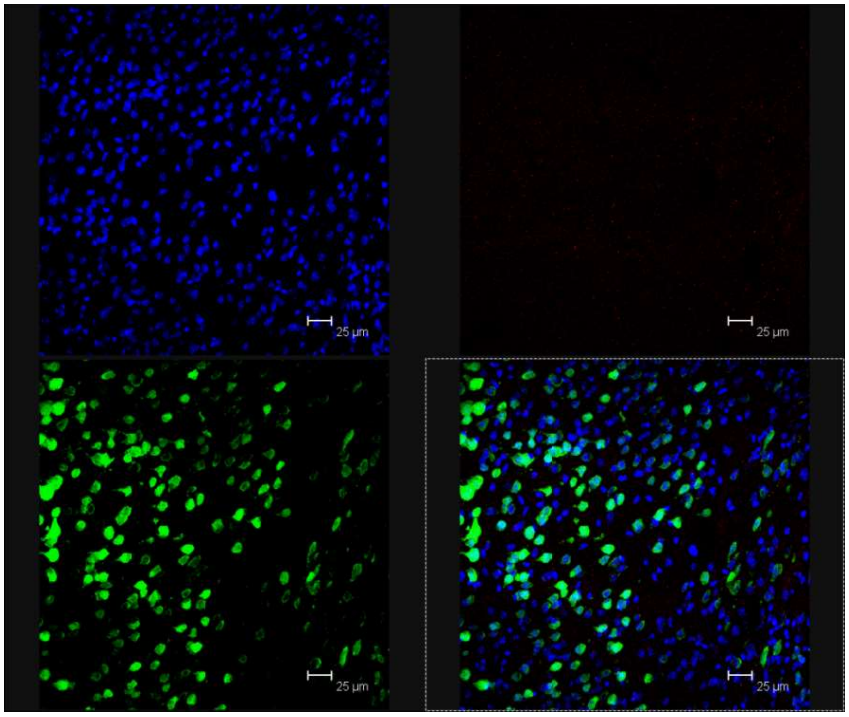


**Figure S10A**. DP-NPs, ip injection, sacrifice time: 6hr; Staining : Nucleus (DAPI) Neurons (NEUN 488) NPs (Cy5).

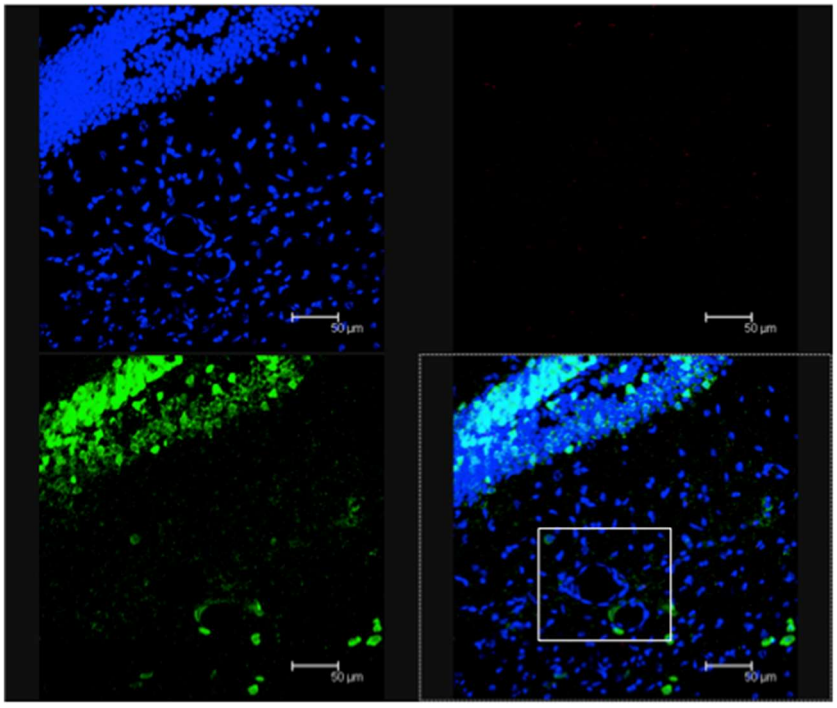


**Figure S10B**. DP-NPs, ip injection, sacrifice time: 6hr; Staining : Nucleus (DAPI) Neurons (NEUN 488) NPs (Cy5). Brain microvessels are highlighted within the white box.

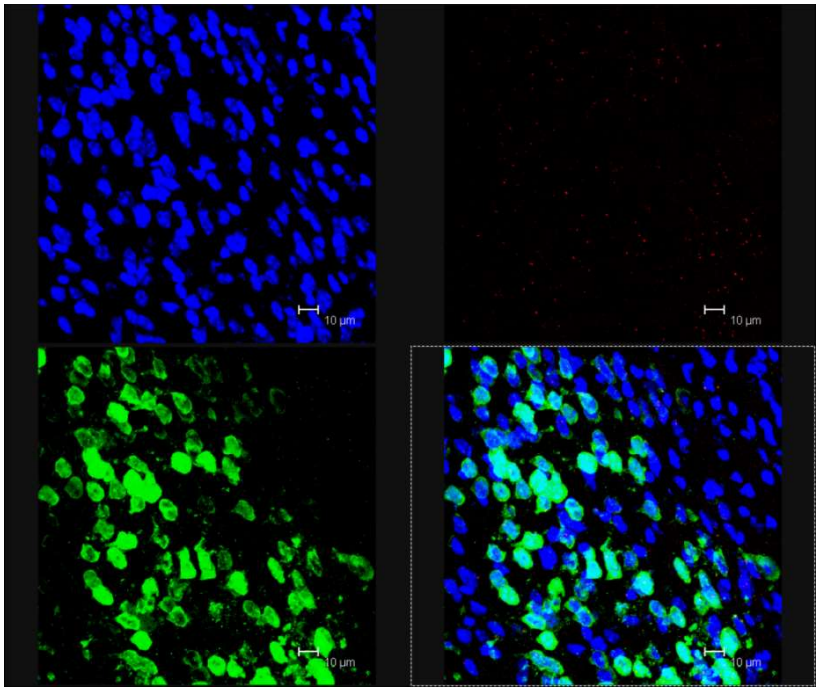


**Figure S11A.** Glu-DP-NPs, ip injection, sacrifice time: 6hr; Staining : Nucleus (DAPI) Neurons (NEUN 488) NPs (Cy5).

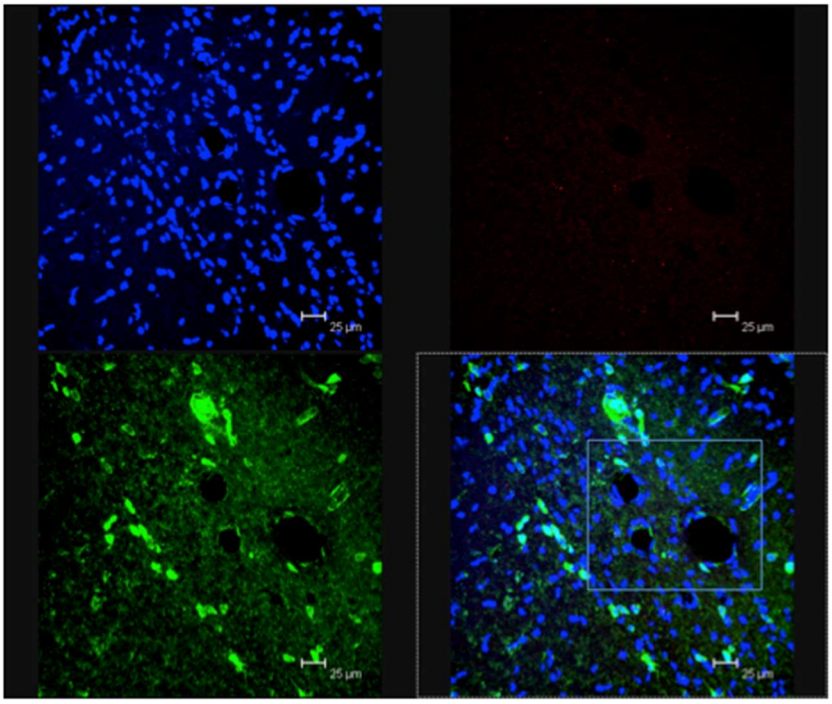


**Figure S11B.** Glu-DP-NPs, ip injection, sacrifice time: 6hr; Staining : Nucleus (DAPI) Neurons (NEUN 488) NPs (Cy5). Brain microvessels are highlighted within the white box.

# PLGA-PEG-Ang–2 Nanoparticles for Blood–Brain Barrier Crossing: Proof-of-Concept Study

**Gina P. Hoyos-Ceballos [1], Barbara Ruozi [2], Ilaria Ottonelli [2,3], Federica Da Ros [2], Maria Angela Vandelli [2], Flavio Forni [2], Eleonora Daini [4], Antonietta Vilella [4], Michele Zoli [4], Giovanni Tosi [2], Jason T. Duskey [2], and Betty L. López-Osorio [1]**

[1] Grupo de Investigación Ciencia de los Materiales, Instituto de Química, Facultad de Ciencias Exactas y Naturales, Universidad de Antioquia, Calle 62 No. 52–59, Medellín 050015, Colombia
[2] Department of Life Sciences, University of Modena and Reggio Emilia, 41124 Modena, Italy
[3] Clinical and Experimental Medicine PhD Program, University of Modena and Reggio Emilia, Modena, Italy, 41125
[4] Department of Biomedical, Metabolic and Neural Science, University of Modena and Reggio Emilia, 41124 Modena, Italy

*Pharmaceutics* 2020, *12*, 72, doi:10.3390/pharmaceutics12010072

Received: 29 November 2019

Accepted: 14 January 2020

Published: 17 January 2020

## Abstract

The treatment of diseases that affect the central nervous system (CNS) represents a great research challenge due to the restriction imposed by the blood–brain barrier (BBB) to allow the passage of drugs into the brain. However, the use of modified nanomedicines engineered with different ligands that can be recognized by receptors expressed in the BBB offers a favorable alternative for this purpose. In this work, a BBB-penetrating peptide, angiopep-2 (Ang–2), was conjugated to poly(lactic-co-glycolic acid) (PLGA)-based nanoparticles through pre- and post-formulation strategies. Then, their ability to cross the BBB was qualitatively assessed on an animal model. Proof-of-concept studies with fluorescent and confocal microscopy studies highlighted that the brain-targeted PLGA nanoparticles were able to cross the BBB and accumulated in neuronal cells, thus showing a promising brain drug delivery system.

## 1. Introduction

Discovering new methods to treat diseases is becoming increasingly complicated because of the numerous natural biological barriers in our bodies such as opsonization by proteins in the blood, first-pass clearance organs, and the immune response [404,405]. The difficulty of overcoming these barriers to create a cure is exponentially increased when trying to deliver pharmaceutics across the blood–brain barrier (BBB) [406,407]. This is due to the brains increased security including tight junctions, low molecule diffusion rates, efflux transporters, and difficulty in reaching sufficient drug exposure in the brain compartment [408]. Nanomedicine has been the leading field in surpassing these barriers to deliver drugs to the brain. This is because their physico-chemical characteristics can be controlled to improve drug solubility, compatibility in BBB interactions, and can be targeted using ligands specific to improve delivery into the brain [409–411]. A very promising targeting ligand for the delivery of nanomedicines into the brain is Angiopep-2 (Ang–2), a 19 amino acid peptide (TFFYGGSRGKRNNFKTEEY-OH) which binds the low-density lipoprotein receptor-related protein 1 (LRP1), which is widely expressed throughout the central nervous system (CNS) (by endothelial cells on the basolateral surface, neuroblasts, microglia, astrocytes, and neurons) [412–415]. This ligand has been highly sought after in its use to deliver nanomedicines to the brain because of its ability to activate transcytosis across the BBB, as well as its upregulation in human glioma cells [416–418]. To this end, Ang–2 has been conjugated to numerous nanocarrier types in order to improve BBB crossing, including liposomes, tandem micelles, PEG-PCL, solid lipid nanoparticles, dendrigraft poly-l lysine, and poly-amidoamine dendrimers to deliver various active compounds (Coumarin, docetaxel, siRNA, etc.) [419–422]. Poly(lactic-co-glycolic acid) (PLGA) is an FDA approved polymer that can self-assemble into nanoparticles, with selectable features including the size, shape, charge, and drug loading capacity as a function of the formulation parameters. Moreover, literature extensively reported its ability to encapsulate, protect, and deliver a wide range of bioactive compounds (small molecules, proteins, enzymes, etc.) [423–425].

However, only a few studies indicated that PLGA-based nanoparticles modified with Ang–2 could be a promising active brain-targeting drug delivery system [416,417,421,426,427]. In this work, we focused on creating and characterizing targeted Ang–2 PLGA nanoparticles (NPs); the surface was engineered by conjugating Ang–2 directly to the polymer, and nanoformulation was then gained, or with post-formulation anchorage to NP through the conjugation of the thiol-containing cysteine added to the Ang–2 and a maleimide containing PLGA. These NPs were then characterized for their amount of Ang–2 bound to the NPs and tested in vivo for their ability to pass the BBB and enter into the brain parenchyma. Moreover, technological and methodological procedures to produce engineered nanomedicines proposed in our work are quite simple and easy to be adapted from brain delivery of other potential drugs, therefore spreading the possibility of application in other brain diseases.

## 2. Materials and Methods

### *2.1. Materials*

Poly(lactic-co-glycolic acid) of molecular weight 24–38 kDa (PLGA 50:50) and Pluronic F127® were purchased from Sigma-Aldrich (Milan, Italy). The PLGA-b-PEG copolymer was previously obtained through the modification of PLGA with mPEG-NH2 (MW: 5000 Da) [425]. The PLGA (Resomer 503 H) derivatized with the fluorophore Cy5 was obtained by the Laboratory of Nanomedicine and Pharmaceutical Technology of the University of Modena and Reggio Emilia (Modena, Italy) as previously reported [428]. The PLGA-Mal (MW: 20 kDa) was purchased from Nanosoft Biotechnology (Lewisville, TX, USA). The modified Angiopeptide-2 with a cysteine end group (CTFFYGGSRGKRNNFKTEEY), referred to from now as Ang–2, was synthesized by the company GenScript (MerckMillipore, Oregon City, OR, USA). The ultrapure water was supplied by a Milli-Q® water purification system (Synergy® UV, Darmstadt, Germany). All the solvents and other reactive products were also of a high degree of purity (>95%) and used as purchased without modification, unless otherwise stated.

### *2.2. Animals*

For the in vivo tests, C57BL/6 mice were used. The experiments were carried out in accordance with the European Communities Council Directives of 24 November 1986 (86/609/EEC) for experimental care.

### *2.3. Synthesis and Characterization of PLGA Conjugate with the Ang–2*

The conjugation between Ang–2 and PLGA was carried out by reacting the maleimide group, present on the glycolic acid terminus of the PLGA chains, with the cysteine thiol group originating from the peptide, as shown in Figure 1 [407,429]. Briefly, 20 mg of PLGA-Mal together with 1.2 mg of the peptide (molar ratio PLGA-Mal/Ang–2 2:1) were dissolved in 4 mL anhydrous dimethyl sulfoxide

(DMSO). After 15 h of reaction under constant agitation, the modified polymer was precipitated by adding diethyl ether [395]. Finally, the polymer was dried under reduced pressure and stored for characterization and use in the preparation of nanoparticles [393].

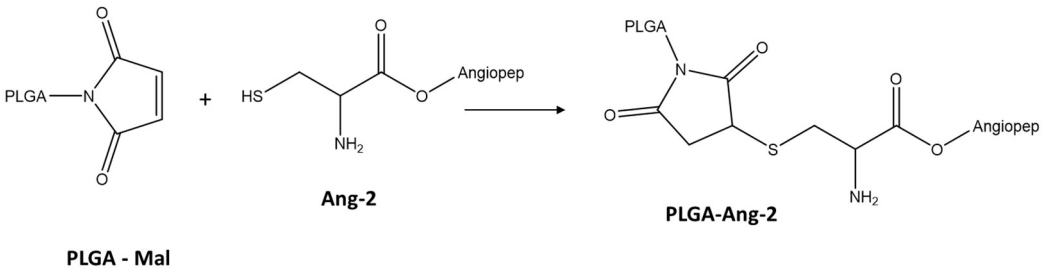


**Figure 1**. Scheme of PLGA functionalization with Ang–2.

Modified PLGA products (PLGA-Ang–2) were analyzed by 1H-NMR to confirm the presence of Ang–2. The conjugate and control samples (3 mg) were dissolved in deuterated DMSO (0.5 µL), and the spectrum was obtained in a Bruker 400 MHz spectrometer.

*2.4. Preparation of PLGA Nanoparticles Functionalized with Ang–2 (Ang–2-NPs)*

For comparative purposes, the polymer nanoparticles were obtained through the nanoprecipitation method using two different conjugation strategies: pre and post-functionalization (Figure 2) [430].

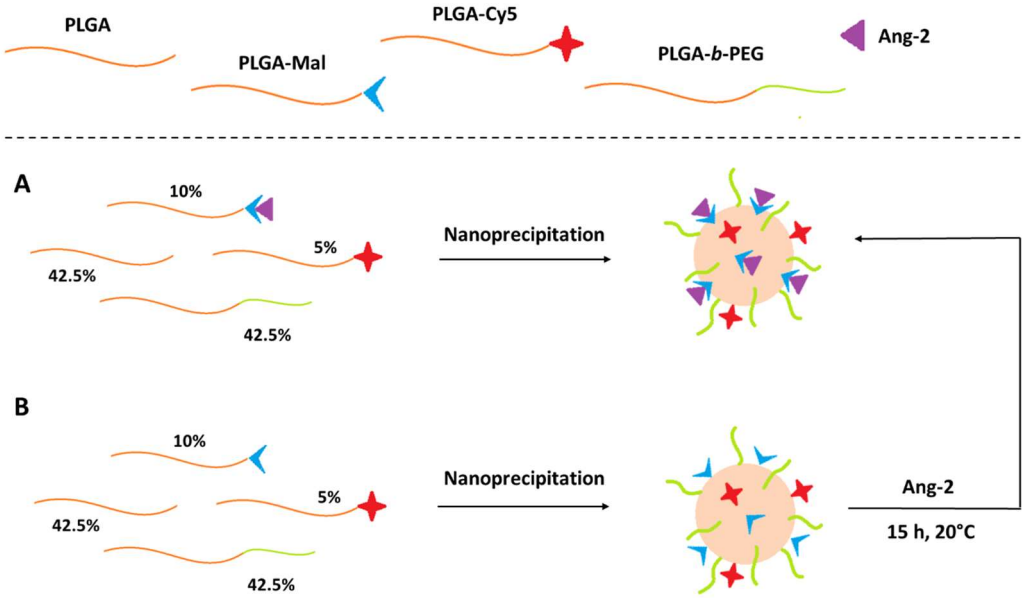


**Figure 2.** Schematic representation of the modification of PLGA/PLGA-*b*-PEG nanoparticles with Ang–2 through (**A**) pre-functionalization and (**B**) post-functionalization.

The pre-formulation functionalized nanoparticles (pre-formulation Ang–2 NPs) were prepared from mixtures with the following composition: PLGA (42.5%), PLGA-*b*-PEG (42.5%), PLGA-Cy5 (5%), and PLGA-Ang–2 (10%, synthesized as described above). An exact amount (10 mg) of the mixture was dissolved in 2 mL of acetone and subsequently added dropwise to 4 mL of a PF127 solution (1.0% *w*/*v*). Finally, the organic solvent was removed under reduced pressure using a rotary evaporator and purified as described in Section 2.5.

Post-formulation functionalized nanoparticles (post-formulation Ang–2 NPs) were prepared as previously described for pre-formulation Ang–2 NPs but using a modified polymer mixture: PLGA (45%), PLGA-*b*-PEG (45%), and PLGA-Mal (10%). After purification and resuspension, the nanoparticles obtained were subsequently modified through covalent binding with Ang–2 in different PLGA-Mal/Ang–2 molar ratios (3:1, 2:1, and 1:1). For this modification, the corresponding amount of Ang–2 was dissolved in an aqueous solution, added to the NPs suspension, and reacted under constant stirring for 15 h [410,430,431]. Finally, Cy5 fluorescently labeled nanoparticles were prepared with the following

composition: PLGA (42.5%), PLGA-*b*-PEG (42.5%), PLGA-Cy5 (5%), and PLGA-Mal (10%), and they were post modified (PLGA-Mal/Ang–2 molar ratio 2:1) in order to carry out in vivo tests. Nanoparticles without PLGA-Mal were prepared as controls.

### *2.5. Purification of Nanoparticles*

For removal and quantification of free Ang–2 from the post-formulation Ang–2 NPs, the suspensions obtained were centrifuged for 15 min at a speed of 13,500 rpm using a Spectrafuge™ 24D microcentrifuge (LabNet, Woodbridge, NJ, USA). The supernatant was removed by decantation, and the solid was resuspended in Milli-Q water (MerckMillipore, Oregon City, OR, USA). The Ang–2-NP suspension was then stored in the refrigerator for further analysis.

### *2.6. Characterization of Nanoparticles*

#### 2.6.1. Distribution of Particle Size and Zeta Potential

Particle size, polydispersity index and zeta potential measurements were carried out on a Zetasizer Nano ZS (Malvern Instrument, Worcestershire, UK) at 25 °C, after purification of the NPs. The experiments were performed in triplicate, and the results are reported as the mean value ± standard deviation.

#### 2.6.2. HPLC Quantification of Ang–2 in Post-Functionalized Nanoparticles

The quantification of Ang–2 conjugated after NP formation (post-formulation) was carried out indirectly by quantifying the amount of free Ang–2 that remained in the supernatant after NP purification using high-performance liquid chromatography (HPLC). A 500 μL aliquot of supernatant was left at RT for 72 h until complete dimerization was achieved, and 50 μL was injected onto a C8 column (Aeris™ WIDEPORE XB-C8, 150 × 4.6 mm, 3.6 μm) using a gradient

method where the mobile phases consisted of 0.1% trifluoroacetic acid (TFA) in water (solution A) and 0.1% TFA in acetonitrile (ACN) (solution B), where solution B was increased from 10% to 35% over 12 min with a flow of 1.2 mL/min. The amount of Ang–2 in the supernatant was determined with a standard curve designed by integrating the peak of interest using a UV detector monitoring $\lambda$ = 215 nm (linear in the range of 1–50 μg/mL and a correlation coefficient of 0.9991). The difference between the initial amount of peptide added to the formulation and the amount quantified in the supernatant allowed the calculation of the percentage of peptide bound to the NPs.

### *2.7. In Vivo Tests: Brain Uptake of the Nanoparticles*

#### 2.7.1. Animal Handling Protocols and Sample Preparation for Systemic Injection of Post-Functionalized Ang–2 NPs

The post-formulation procedure lead to the production of post-formulation Ang–2 NPs (or as a control, fresh saline solution lacing NPs), which were suspended in a saline solution and injected i.p. (100 μL, 1 mg/mL) into C57Bl6 mice (female and male, weight close to 25 g). As control, unmodified NPs were also administered. After 1 or 4 h, the mice were sacrificed for histological processing: each mouse was anesthetized with chloral hydrate (400 mg/kg, i.p.) and underwent intracardial perfusion with an infusion of 50 mL of 0.9% NaCl saline containing heparin sodium (5000 U/L) followed with 4% paraformaldehyde and 0.2% picric acid in phosphate-buffered saline (PBS) (70 mL/7 min) ensued by extraction of the brain. The brains were post-fixed in the same solution for 12 h, rinsed with increasing concentrations of sucrose in PBS over 1.5 d, and frozen using dry ice. Coronal sections (50 μm thick) were cut at a cryotome, washed in cold 1× PBS, and stored at −20 °C in a glycerol-PBS solution until used.

#### 2.7.2. Immunohistochemistry of Brain Sections

Brain sections were processed for multiple immunofluorescence histochemistry according to published protocol (ref). Neuronal nuclear antigen (NeuN) (Millipore, USA) from DAKO was used as the primary antibody, and goat anti-mouse Alexa488 (1:200) or goat anti-rabbit Alexa488 (1:200) were used as secondary antibodies.

### 2.7.3. Confocal Analysis

Confocal analysis was performed with a Leica DM IRE 2 (Bannockburn, IL, USA); Leica Confocal System: scan head multiband 3 channels Leica TCS SP2 with Acousto-Optical Beam Splitter (AOBS) laser diode blu (405 nm/25 mW), Laser Ar (458 nm/5 mW) (476 nm/5 mW) (488 nm/20 mW) (496 nm/5 mW) (514 nm/20 mW), Laser HeNe (543 nm/1.2 mW), Laser HeNe (594 nm) (orange), and Laser HeNe (633 nm/102 mW). In particular, NPs (due to their labeling with Cy5) were clearly visible by excitation with the 633 nm laser with an emission readout at 650 nm, while staining of NeuN and other immunohistochemistry tags were detected using 488 and 500 nm excitation and emission wavelengths, respectively.

## 3. Results and Discussion

### *3.1. Quantification of Ang–2 on Modified PLGA by 1H-NMR*

The 1H-NMR spectra of PLGA-Mal, Ang–2, and the PLGA modified with Ang–2 (PLGA-Ang–2) are presented in Figure 3. The intense signals observed at δ = 4.9 and 5.2 ppm in the PLGA-Mal and PLGA-Ang–2 spectra correspond to the methylene (–CH2) and methine (–CH) groups of the PLGA. On the other hand, the signals observed in the PLGA-Ang–2 spectrum around δ = 7.0 ppm are attributed to the aromatic protons present in the amino acids phenylalanine (Phe) and tyrosine (Tyr) of the peptide, thus confirming the polymer functionalization [393].

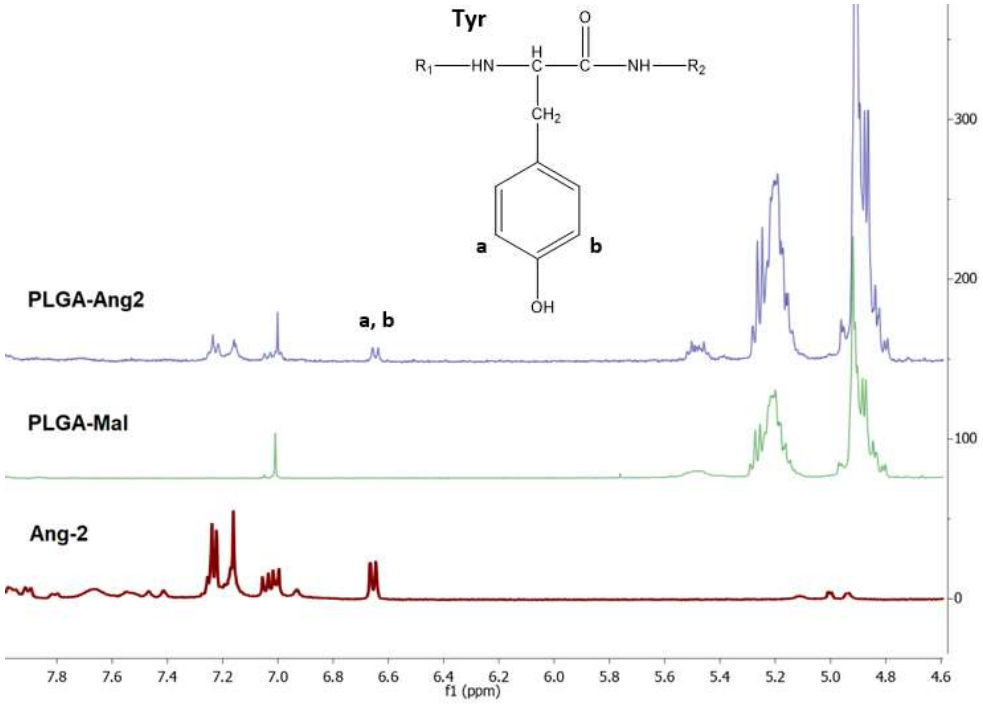


**Figure 3.** [1]H-NMR spectra of PLGA-Mal, Ang–2, and PLGA-Ang2 obtained in deuterated DMSO.

The functionalization degree of PLGA with Ang–2 was calculated from the ratio between the area of the doublet observed at δ = 6.65, corresponding to aromatic protons of Tyr, and the area of the signal observed at δ = 1.5, corresponding to the protons of the methyl groups (–CH3) of PLGA. In Equation (1), the obtained Ang–

2/PLGA relation is shown, where ai corresponds to the integrated area under the signals of the 1H-NMR spectrum for the respective fractions, mi corresponds to the number of protons corresponding to each signal, and ni is the number of repetition units of the fraction i. This calculation indicates that for every PLGA there is 0.51 units of Ang–2 (2:1 PLGA/Ang–2). The modified polymer was used to prepare the pre-functionalized nanoparticles.

$$\frac{Ang-2}{PLGA} = \frac{a_{Ang-2}\ /m_{Ang-2}}{(a_{Ang-2}\ /m_{Ang-2}) + (a_{CH_3}/(m_{CH_3}\ x\ n_{CH_3}))}$$

$$= \frac{4/4}{(4/4)\ + (795.29/(3\ x\ 278))} = 0.51$$

*3.2. HPLC Quantification of Ang–2 in Post-Functionalized Nanoparticles*

Because of the incompatibility of PLGA with HPLC analysis, the amount of Ang–2 bound to the post-functionalized nanoparticles was determined indirectly from the supernatant obtained during the purification process using a calibration curve previously constructed from a standard solution of the peptide. In the chromatograms obtained for the supernatant, two peaks were detected at 2.7 and 3.4 min of retention. By analyzing this solution over time, it is possible to observe the time-dependent transformation of the first eluted peak into the second, as shown in Figure 4. This conversion of the product can be explained by disulfide bond formation (dimerization) of the Ang–2 peptide N-terminal cysteines [432]. Since the formation of the Ang–2 dimer is spontaneous, the complete conversion of the monomer to the dimer was allowed, and the dimer calibration curve was constructed to carry out the quantification of the free Ang–2.

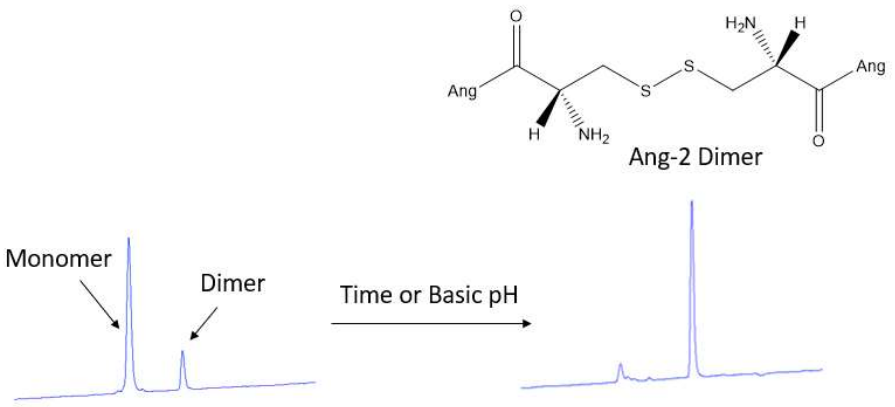


**Figure 4**. Chromatographic analysis obtained for the monomer (2.4 min) and the Ang–2 dimer (3.4 min) after 72 h at room temperature or adding a tris buffer solution at pH 9 only to quickly check the dimer formation.

Table 1 shows the amount of Ang–2 bound to the nanoparticles for the different ratios of PLGA-Mal/Ang–2 studied (3:1, 2:1, and 1:1). It was observed that even when PLGA-Mal was not used in the formulation (no reaction should occur between Ang–2 and PLGA), part of the Ang–2 remained bound to the nanoparticles. This is due to the nonspecific adsorption of the peptide to the NP surface. On the other hand, the amount of Ang–2 bound to the NPs increased significantly ($P < 0.05$) with the presence of PLGA-Mal in the formulation, which suggests the covalent binding of this peptide with the polymer. Finally, and as expected, an increase in the amount of Ang–2 per grams of NP was observed by increasing the amount of initial peptide added to the formulation.

**Table 1**. Amount of Ang–2 bound to the nanoparticles determined through HPLC for three different PLGA-Mal/Ang–2 ratios. The controls correspond to nanoparticles with the same amount of Ang–2 as the experiment, but without the presence of PLGA-Mal. Values represent mean ± standard deviation (n = 3 experiments). * and ** show statistically significant differences ($P < 0.05$) between the label samples.

| Initial amount PLGA-Mal : Ang-2 | µg Ang-2 / g NPs | Final molar ratio Ang-2/PLGA-Mal |
|---|---|---|
| Control (3:1) | 1.65 ± 0.60 | |
| 3:1 | 3.06 ± 0.11 | 0.25 ± 0.01 |
| Control (2:1) | 2.59 ± 0.71* | |

| | | |
|---|---|---|
| 2:1 | 4.42 ± 0.74* | 0.37 ± 0.06 |
| Control (1:1) | 4.24 ± 0.71** | |
| 1:1 | 8.78 ± 1.93** | 0.73 ± 0.23 |

*3.3. Size Distribution and Zeta Potential of Pre- and Post-Functionalized Ang2-NPs*

The pre- and post-functionalized Ang2-NPs were characterized through particle size, polydispersity index, and zeta potential measurements. For comparative purposes, the values of these variables for NPs without Ang–2 were also determined (Table 2). For all prepared NPs, monomodal and homogeneous dispersions were obtained (PDI ≤ 0.1); however, it was observed that the conjugation of Ang–2 to the nanoparticles through either strategy led to an increase in particle size compared to non-functionalized nanoparticles ($P < 0.05$), which could be related to the presence of peptide onto NPs. The zeta potential values were lower than −20 mV for all formulations because of the negative surface charge related with the carboxylic groups of the PLGA.

**Table 2.** Particle size, polydispersity index, and zeta potential of PLGA-b-PEG nanoparticles pre- and post-functionalized with Ang–2.

| PLGA-*b*-PEG **Formulations** | **Particle Size (nm)** | **PDI** | **Zeta Potential (mV)** |
|---|---|---|---|
| Non-functionalized NPs | 136.3 ± 6.8 | 0.06 ± 0.01 | -27.4 ± 2.7 |
| Pre-Formulation ANG-2 NPs | 166.4 ± 2.4 | 0.08 ± 0.04 | -26.2 ± 0.9 |
| Post-Formulation ANG-2 NPs | 177.3 ± 12.7 | 0.10 ± 0.01 | -21.9 ± 3.4 |

*3.4. In Vivo Brain Distribution of ANG-2 NPs*

To demonstrate the ability for modified nanoparticles to cross the blood–brain barrier and reach various brain areas, 100 μL of post-formulation Ang–2 NP suspension (1 mg/mL) was i.p. injected into C57BL/6 mice. After one or four hours, the mice were sacrificed and the brain was removed and histologically stained for the presence of cell nuclei (DAPI) and neuronal cells (neuronal nuclear antigen, NeuN). Representative results were already visible, qualitatively demonstrating penetration of the Ang–2-NPs across the BBB at 1 h (data not shown), similar to

those results obtained at 4 h. With respect to control samples (unmodified labeled NPs) not showing significant signals related to NPs (Figure S1), the presence of Ang–2 NPs was uniform throughout the dentate gyrus, cortex, and hippocampus (Figure 5A, red channel), suggesting a robust, uniform passage of the NPs across the BBB. The clear accumulation of Ang–2 NPs in brain parenchyma is remarkable in consideration of the inability of unmodified NPs and modified NPs used as controls (data not shown) to cross BBB alone (data not shown), which was also broadly assessed from other outputs in literature of NPs of similar composition and size [431,433]. In analyzing the images, Ang–2-NPs colocalized with the various cell types present in the brain, evidenced only with DAPI, but were often also in close proximity to the neuronal cells (Figure 5B, red and yellow arrows respectively). This is interesting because it could indicate a different mode of cell uptake than what has been seen previously for PLGA NPs targeted with the simil-opioid peptide ligand g7 [395,423,434] that are broadly up-taken only by neurons. Moreover, further studies will be required to better elucidate the mechanism of Ang–2 NP entrance in the brain or in the cells, for instance by blocking endo-transcytosis or the clathrin/caveolin uptake process, and therefore to draft a complete hypothesis on BBB-crossing pathways and neuron uptake of these kinds of NPs. Transcytosis pathways, therefore, could not be evidenced with these remarkable but preliminary experiments.

(A)

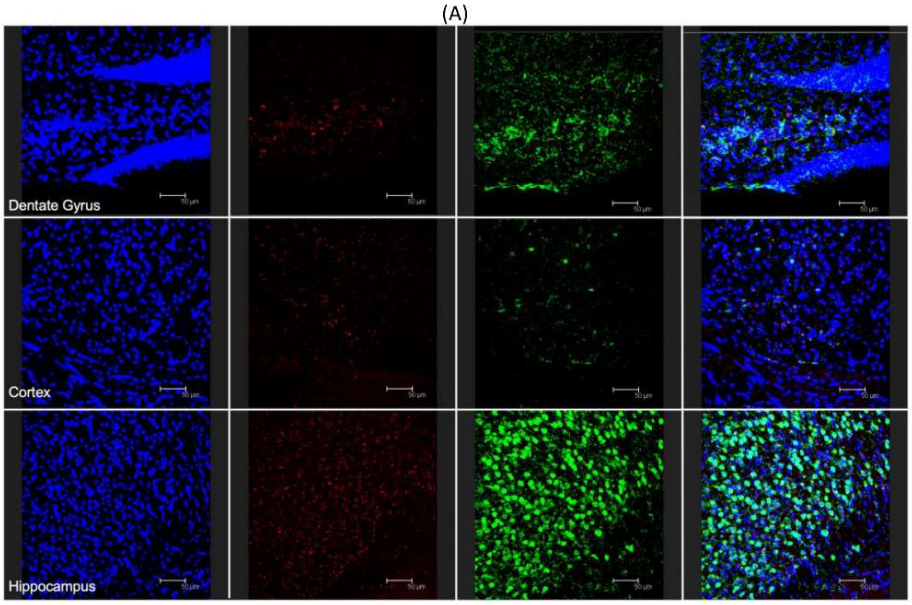
Dentate Gyrus
Cortex
Hippocampus

(B)

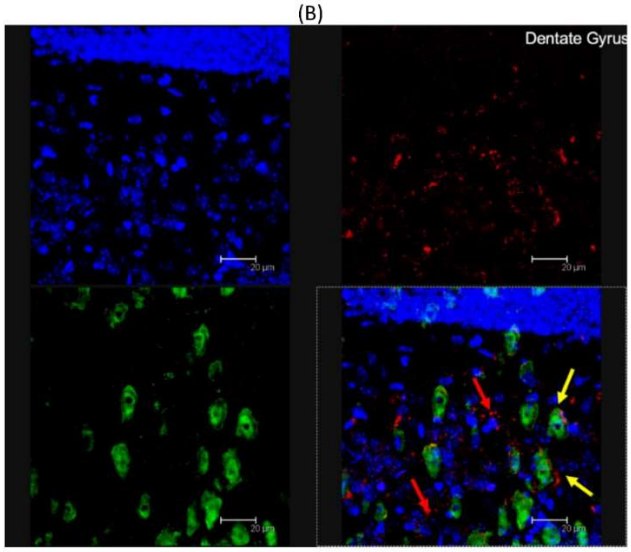
Dentate Gyrus

(C)

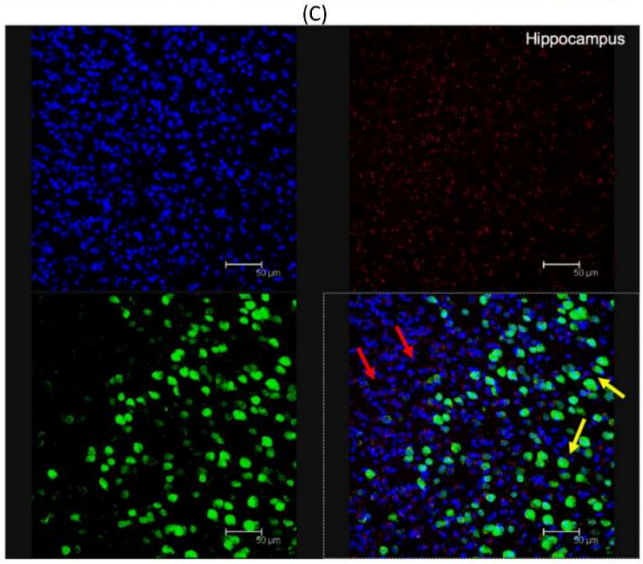
Hippocampus

**Figure 5.** (A) Fluorescent microscopy analysis of Ang–2-NP brain distribution: cross section of the dentate gyrus, cortex, and hippocampus stained with DAPI (blue channel), Cy5- labeled ang-2-NPs (red channel), and NEUN (green channel). (B) Magnified analysis of the dentate gyrus. (C) Magnified analysis of hippocampus. In both images (B,C), colocalization with (red arrows) NEUN negative stained cells and colocalization with neurons (yellow arrows) are identified. All images are representative of the average analysis, and scale bars in (A–C) are set at 50, 20, and 50 μm, respectively.

## 4. Conclusions

In summary, in this work, Ang–2 NPs were prepared by nanoprecipitation using pre- and post-formulation strategies and using PF127 as a stabilizer. With both methodologies, we obtained NPs with sizes lower than 200 nm, compatible with systemic administration and to enable possible BBB crossing. Furthermore, brain accumulation was, for the first time, confirmed through in vivo analysis, where we observed the localization of this kind of nanoparticle within the brain cells, highlighting in particular the neuron accumulation in different brain areas (i.e., cortex and hippocampus). In fact, even if Ang–2 is not new in the CNS targeting panorama, previous papers dealt with experiments on different polymers used in production of nanomedicines (as caprolactone [419], a mixture of mesoporous silica PLGA-based NPs [435]), or different nanocarrier architectures, as in the use of micelles [436]. In any paper, besides some in vivo experiments on BBB crossing, data on cell tropism and clear brain visualization are not often reported. Therefore, the formulations presented in the current paper could be used as carriers of different drugs to the CNS, thus increasing the alternatives for the treatment of brain diseases.

## 5. Supplementary Material

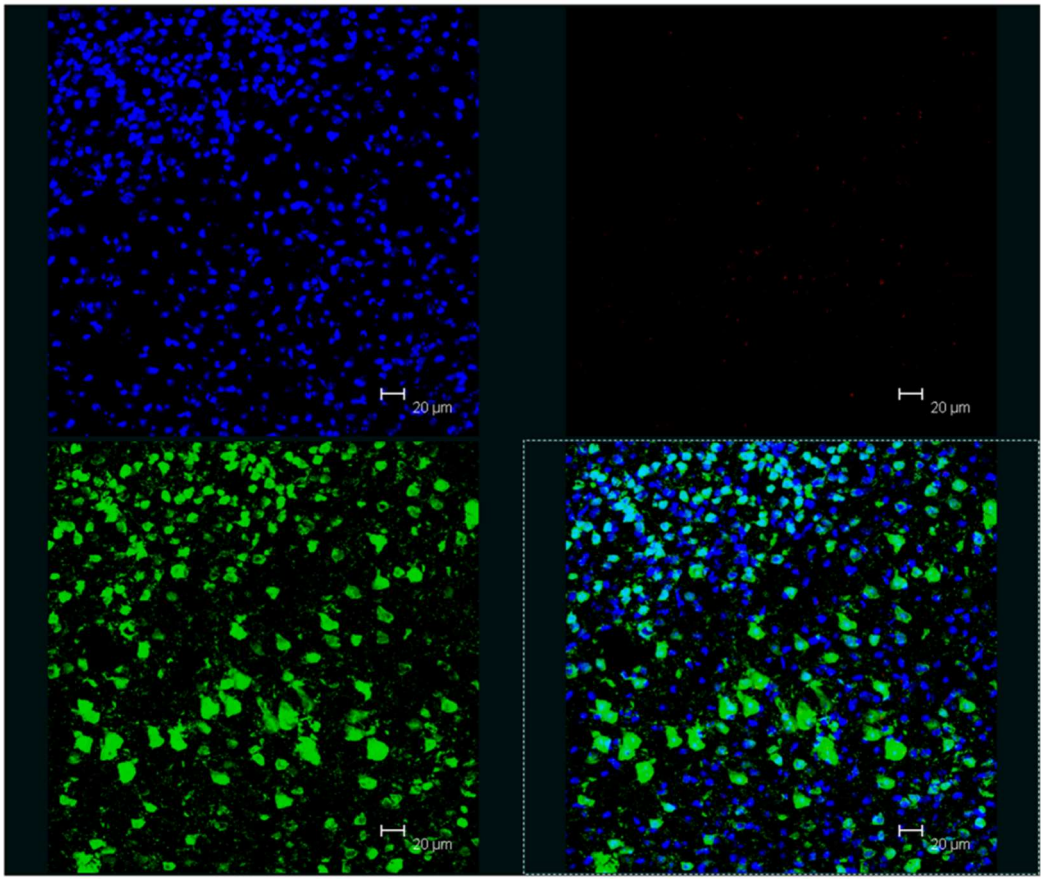


**Figure S1**. Fluorescent microscopy analysis of non-functionalized NP brain distribution. Staining with DAPI (blue channel), Cy5 fluorescence (red channel), and NEUN (green channel).

# Insights into kinetics, release, and behavioral effects of brain-targeted hybrid nanoparticles for cholesterol delivery in Huntington's disease

**Giulia Birolini [1,2], Marta Valenza [1,2], Ilaria Ottonelli [3,4], Alice Passoni [5], Monica Favagrossa [5], Jason T. Duskey [3,6], Mauro Bombaci [2], Maria Angela Vandelli [3], Laura Colombo [5], Renzo Bagnati [5], Claudio Caccia [7], Valerio Leoni [8], Franco Taroni [7], Flavio Forni [3], Barbara Ruozi [3], Mario Salmona [5], Giovanni Tosi [3], Elena Cattaneo [1,2]**

[1] Department of Biosciences, University of Milan, via G. Celoria 26, 20133 Milan, Italy

[2] Istituto Nazionale di Genetica Molecolare "Romeo ed Enrica Invernizzi", via F. Sforza 35, 20122 Milan, Italy

[3] Nanotech Lab, Te.Far.T.I. Center, Department of Life Sciences, University of Modena and Reggio Emilia, Via G. Campi, 103, 41125 Modena, Italy

[4] Clinical and Experimental Medicine PhD Program, University of Modena and Reggio Emilia, via G. Campi 289, 411214 Modena, Italy

[5] Istituto di Ricerche Farmacologiche Mario Negri IRCCS, via Mario Negri 2, 20156 Milan, Italy

[6] Umberto Veronesi Foundation, 20122 Milan, Italy

[7] Unit of Medical Genetics and Neurogenetics, Fondazione I.R.C.C.S. Istituto Neurologico Carlo Besta, Via Celoria 11, 20131 Milan, Italy

[8] Laboratory of Clinical Pathology, Hospital of Desio, ASST-Monza, School of Medicine and Surgery, University of Milano-Bicocca, Via Cadore 48, 20900 Monza, Italy

*Journal of Controlled Release* 2021, *330*, 587–598, doi:10.1016/j.jconrel.2020.12.051.

Received 28 October 2020

Revised 23 December 2020

Accepted 28 December 2020

Available online 5 January 2021

Version of Record 10 January 2021

## Abstract

Supplementing brain cholesterol is emerging as a potential treatment for Huntington's disease (HD), a genetic neurodegenerative disorder characterized, among other abnormalities, by inefficient brain cholesterol biosynthesis. However, delivering cholesterol to the brain is challenging due to the blood-brain barrier (BBB), which prevents it from reaching the striatum, especially, with therapeutically relevant doses.

Here we describe the distribution, kinetics, release, and safety of novel hybrid polymeric nanoparticles made of PLGA and cholesterol which were modified with an heptapeptide (g7) for BBB transit (hybrid-g7-NPs-chol). We show that these NPs rapidly reach the brain and target neural cells. Moreover, deuterium-labeled cholesterol from hybrid-g7-NPs-chol is released in a controlled manner within the brain and accumulates over time, while being rapidly removed from peripheral tissues and plasma. We confirm that systemic and repeated injections of the new hybrid-g7-NPs-chol enhanced endogenous cholesterol biosynthesis, prevented cognitive decline, and ameliorated motor defects in HD animals, without any inflammatory reaction.

In summary, this study provides insights about the benefits and safety of cholesterol delivery through advanced brain-permeable nanoparticles for HD treatment.


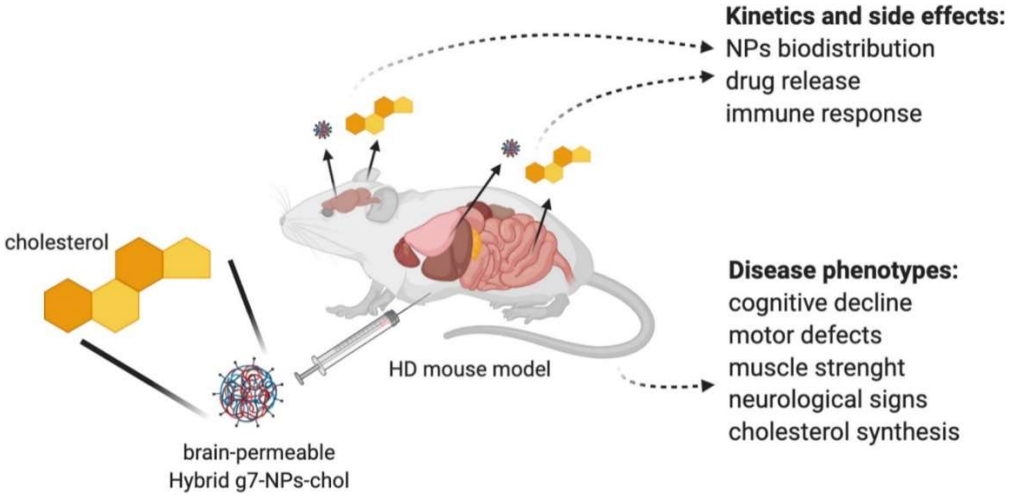

## 1. Introduction

Targeting the brain with therapeutic agents is made difficult by the blood-brain barrier (BBB). Current strategies to circumvent this problem include temporary BBB disruption, conjugation of brain-permeable ligands to the drug of interest, intranasal delivery, or direct delivery of molecules into the brain by means of invasive strategies [437]. Among them, nanocarriers [438] decorated on their surface with brain-targeting ligands [439,440] are emerging because of their non-invasiveness. Polymeric nanoparticles (NPs) made of the FDA-approved polymer poly (D,L-lactide-*co*-glycolide) (PLGA) and surface-engineered with the g7 glycopeptide (Gly-L-Phe-D-Thr-Gly-L-Phe-L-Leu-L-Ser(O-beta-D-glucose)-CONH2) are reported to transport molecules into the CNS after their systemic administration in rodents [392]. g7 stimulates membrane curvature and, following endocytosis of the whole carrier at the BBB, it promotes BBB transit by multiple pathways [386]. Previous studies indicate that about 10% of the injected g7-NP reaches the brain [288,386,393,395,402,441].

This system has been applied to deliver drugs to cope with Huntington's disease (HD), an adult-onset, neurodegenerative genetic disorder caused by a CAG repeat expansion in the gene encoding the Huntingtin (HTT) protein. Individuals carrying the mutation develop motor defects, cognitive decline, and psychiatric disturbances. Neuronal dysfunction precedes neurodegeneration, which mainly affects the medium-spiny neurons (MSNs) of the striatum and the cortical neurons [442]. One pathway found to be affected in HD involves brain cholesterol. Peripheral cholesterol is not able to cross the BBB and locally synthesized brain cholesterol is implicated in synapses formation, maintenance and activity, and optimal neurotransmitter release [443,444]. Brain cholesterol biosynthesis and content are reduced across several rodent models of HD [445–450] and altered brain cholesterol homeostasis is also measurable in HD patients starting from pre-symptomatic stages through the circulating level of the brain-specific cholesterol catabolite 24-hydroxycholesterol (24S-OHC) [451,452]. This dysfunction implies a

lower availability of newly synthetized cholesterol and its metabolites in the HD brain with detrimental consequences for neuronal and synaptic activities [449,450,453]. Accordingly, strategies aimed at delivering cholesterol to the HD brain proved to be effective [385,454]. In particular, in a first study, systemic injections of PLGA-g7-NPs loaded with cholesterol (PLGA-g7-NPs-chol) were found to prevent synaptic and cognitive defects in a transgenic mouse model of HD [385]. In a subsequent study, cholesterol was infused for 4 weeks into the striatum of HD mice through osmotic mini-pumps, a well-characterized system for controlled drug administration. This led to the identification of the optimal dose of cholesterol needed to restore synaptic and neuropathological features and reverse motor and cognitive abnormalities in HD mice [454]. Recently, the effectiveness of nose-to-brain delivery of cholesterol to the HD brain has also been tested [455]. In the first study with PLGA-g7-NPs-chol, the amount of cholesterol delivered to the brain was sub-optimal compared with the dose identified with osmotic mini-pumps. Although it is difficult to directly compare these systems due to different mechanisms of cholesterol release, it has been estimated that this type of NPs provides the brain with approximately 2 μg of cholesterol in each systemic injection [385], while approximately 13 μg of cholesterol per day was infused into the striatum with mini-pumps, enabling maximum benefit in HD mice after 4 weeks of treatment [454].

The development of a more efficient, non-invasive, brain-targeted cholesterol-based therapy for HD patients requires an optimized generation of NPs with improved pharmaceutical properties. In particular, in this study we tested the therapeutic value of new nanoparticles whose formulation process, structural characteristics, and drug loading capacity have been enhanced.

These NPs, herein named hybrid-g7-NPs-chol, were prepared using a novel formulation that efficiently combines materials (g7-PLGA, PLGA, and cholesterol as starting materials for formulation) [351], using nanoprecipitation (MIX-N) or single emulsion (MIX-SE) with surfactants such as Pluronic F68 in MIX-N and

polyvinyl alcohol (PVA) in MIX-SE. This study therefore aimed to investigate the distribution of hybrid-g7-NPs-chol in different brain regions, peripheral tissues, and the circulation, and the kinetics of cholesterol release, the benefits to animals' behavior. Potential side effects which might emerge following chronic treatment in HD mice were also investigated.

## 2. Method section

*2.1. Production and characterization of hybrid-g7-NPs-chol*

Starting from already published results [351,385], we produced hybrid NPs using a nanoprecipitation method (N) and simple emulsion (SE). Following previous readouts on the polymer ratio to be used in formulation [138], 1:1 *w*/w ration between PLGA and Cholesterol was adopted. In details, all hybrid nanoparticles were formulated starting from 50 mg of a mixture of Cholesterol (Sigma-Aldrich, Milan, Italy), PLGA (PLGA R503H Evonik, Essen, Germany) and PLGA-g7 in a weight ratio of 1:0.8:0.2 (25 mg Chol, 20 mg PLGA, 5 mg PLGA-g7).

PLGA-g7 was synthesized *via* amide formation in the Nanotech Laboratory of the University of Modena and Reggio Emilia, following a previously described protocol [395,428]. PLGA is a synthetic polymer approved by the US Food and Drug Administration (FDA) and European Medicine Agency (EMA) for biomedical devices. PLGA has a very high biodegradability (Mundargi et al. J. Control. Release 2009): it enters into the Krebs cycle and it is degraded by non-enzymatic hydrolysis leading to the formation of lactic acid, glycolic acid, $CO_2$ and $H_2O$. Up to now, no clear data on the degradation rate of PLGA within the brain is available, but the data relating to PLGA clearance in degradation are strongly related to MW and composition of the polymer and in particular the PLGA used in this paper is described to be degrade within a range of 3–4 weeks [243,456,457]. Pure g7 was purchased from Mimotopes (Clayton, Victoria, Australia).

To obtain MIX-N, Chol and PLGA mixture was dissolved in acetone (4 mL). The organic phase was then added dropwise into 50 mL of a 0.5% (*w*/*v*) Pluronic-F68 aqueous solution at 45 °C under magnetic stirring (1300 rpm). After 20 min, the organic solvent was removed at 30 °C under reduced pressure (10 mmHg). The MIX-NPs were recovered and purified three times by an ultracentrifugation process carried out at 14,500 rpm for 10 min (4 °C; Sorvall RC28S, Dupont, Brussels, Belgium) to remove the unformed material and the free surfactant fraction in the solution. The obtained MIX-NPs were re-suspended

in 3 mL of a 0.2% (*w*/*v*) Pluronic-F68 aqueous solution at room temperature and gently sonicated until completely resuspended.

As cryoprotectant, 150 mg of threalose (Sigma-Aldrich, Milan, Italy) dissolved in 0,5 mL of 0.2% Pluronic-F68 solution were added to the NPs suspension before flash freezing with dry ice and methanol bath. NPs were stored at −20 °C until use.

To obtain MIX-SE, Chol:PLGA mixture were dissolved in dichloromethane (4 mL) and emulsified in 20 mL of 1% (*w*/*v*) PVA aqueous solution by sonication (Microson Ultrasonic cell disruptor, Misonix Inc. Farmingdale, NY, USA) (80 W over 1 min) under cooling (5 °C). Then, the O/W emulsion was stirred for at least 3 h (1300 rpm; RW20DZM, IKALabortechnik, Staufen, Germany) at r.t. to allow the solvent evaporation. The MIX-SE were collected and purified by ultracentrifugation as previously described for MIX-N, and stored at 4 °C before the use.

Fluorescently labeled MIX NPs were produced with the same protocol described in 1.1.1, adding 2% in weight of Cy5 derived PLGA and 2% in weight of Bodipy-Cholesterol (Avanti, Alabama, USA). Cy5-PLGA was synthesized in the Nanotech Laboratory of the University of Modena and Reggio Emilia using a protocol published in [428]. The total composition was a mixture of Chol:Chol-Bodipy:PLGA:PLGA-Cy5:PLGA-g7 in weight ratio of 0.96:0.04:0.76:0.04:0.2 (24 mg Chol, 1 mg Chol-Bodipy, 19 mg PLGA, 1 mg PLGA-Cy5, 5 mg PLGA-g7). After centrifugation, NPs were resuspended in an aqueous solution of Pluronic-F68 2% and added of threalose as previously reported before flash freezing.

g7-NPs-d6-Chol were obtained using the same protocol described in paragraph 1.1.1. For the formulation, 50 mg of a mixture of D6 Chol:PLGA:PLGA-g7 in weight ratio of 1:0.8:0.2 (25 mg D6 Chol, 20 mg PLGA, 5 mg PLGA-g7) were used.

*2.2. Production of PLGA-g7-NPs loaded with cholesterol*

PLGA-g7-NPs-chol were produced as reported in [385], confirming technological and pharmaceutical features as described in Table S1 as shown before.

*2.3. Chemico-physical and morphological characterization*

100 μL of each type of NPs suspension was freeze-dried (−60 °C, 1 · 10–3 mm/Hg for 48 h; LyoLab 3000, Heto-Holten, Allerod, Denmark) and the yield (Yield%) was calculate as follows:

Yield (%) = [(mg of freeze dried MIX-N or MIX-SE)/(mgPLGA+mg Chol)] × 100.

Mean particle size (Z-Average) and polydispersity index (PDI) of the samples were determined using a Zetasizer Nano ZS (Malvern, UK; Laser 4 mW HeNe, 633 nm, Laser attenuator Automatic, transmission 100–0.0003%, Detector Avalanche photodiode, Q.E. > 50% at 633 nm). Samples were diluted in MilliQ water at about 0.1 mg/mL. The results were also expressed as intensity distribution, i.e. the size 10% [D(10)], 50% [D(50)] and 90% [D(90)], below which all the MIX NPs are placed. The zeta potential (ζ-pot l) was measured using the same equipment with a combination of laser Doppler velocimetry and phase analysis light scattering (PALS). All data are expressed as means of at least three determinations carried out for each prepared lot (three lots for each sample).

The morphology of the samples was evaluated by atomic force microscopy (AFM) (Park Instruments, Sunnyvale, CA, USA) and scanning transmission electron microscopy (STEM) as reported in [351], confirming the same results as reported in supplementary Fig. S1. AFM analysis were conducted at about 20 °C operating in air and in non-contact mode using a commercial silicon tip-cantilever (high resolution noncontact "GOLDEN" Silicon Cantilevers NSG-11, NT-MDT, tip radius 10 nm; Zelenograd, Moscow, Russia) with stiffness of about 40 Nm − 1 and a resonance frequency around 160 kHz. A drop of each hybrid NPs suspension was diluted with distilled water (about 1:5 *v*/v) before application on a

small mica disk (1 cm × 1 cm). After 2 min, the excess of distilled water was removed using a paper filter and the sample analyzed. Two kinds of images were obtained: the first is a topographical image and the second is indicated as "error signal". This error signal is obtained by comparing two signals: the first one representing the amplitude of the vibrations of the cantilever, and the second the amplitude of a reference point. The images obtained by this method show small superficial variations of the samples. Images were processed and analyzed using software from Gwyddion (Department of Nanometrology, Czech Metrology Institute, Brno, Czech Republic).

The internal structure/architecture of the samples was analyzed by scanning transmission electron microscopy (STEM). Briefly, a drop of a water-diluted suspension of the samples (about 0.03 mg/mL) was placed on a 200-mesh copper grid (TABB Laboratories Equipment, Berks, UK), allowed to adsorb, and the suspension surplus was removed by filter paper. All grids were analyzed using a Nova NanoSEM 450 (FEI, Oregon, USA) transmission electron microscope operating at 30 kV using a STEM II detector in Field free mode.

To quantify the amount of cholesterol hybrid-g7-NPs-chol, NPs previously lyophilized to calculate the yield (~1 mg) were dissolved in chloroform (0.3 mL), followed by addition of isopropyl alcohol (0.6 mL) to precipitate the polymer. The mixture was vortexed (15 Hz for 1 min; ZX3, VelpScientifica, Usmate, Italy) and then filtered (polytetrafluoroethylene filter, porosity 0.20 μm, Sartorius). The amount of Chol in the sample was quantified by RP-HPLC using an HPLC apparatus comprised a Model PU980 pump provided with an injection valve with a 50 μL sample loop (Model 7725i Jasco) and an UV detector at 210 nm (UV975, Jasco). Chromatography separation was carried out on a Syncronics C18 (250 × 4.6 mm; porosity 5 μm; Thermo Fisher Scientific, Waltham, MA, USA) at r.t. and with a flow rate of 1.2 mL/min, operating in an isocratic mode using 50:50 *v*/v acetonitrile:ethanol as mobile phase. The solvents of the mobile phase were filtered through 0.45 μm hydrophilic polypropylene membrane filters

(Sartorius) before their use. Chromatographic peak areas of the standard solutions were collected and used for the generation of calibration curves. Linearity was assumed in the range of 50–500 μg/mL (r2 = 0.99). All data are expressed as the mean of at least three determinations.

The chemico-physical properties, concentration and cholesterol amount in g7-NPs used in this work are described in Table S1 along with morphological analysis with AFM and STEM (Fig. S1).

*2.4. Colony management*

All animal experiments were approved and carried out in accordance with Italian Governing Law (D.lgs 26/2014; Authorization n.581/2019-PR issued July 29, 2019 by Ministry of Health); the NIH Guide for the Care and Use of Laboratory Animals (2011 edition) and EU directives and guidelines (EEC Council Directive 2010/63/UE).

Our R6/2 colony lifespan was approximately of 12–13 weeks and only males were used to maintain it [458]. Transgenic 6-week-old R6/2 males were mated with wild type females (B6CBAF1/J, purchased from Charles River). CAG repeat length that could affect strain productivity, general behavior, litter size, pup survival, genotype frequency, phenotype was monitored every 6 months with a range between 150 and 180 CAGs.

Mice were weaned and then genotyped at 3 weeks of age (+/− 3 days) and they were housed under standard conditions in enriched cage (22 ± 1 °C, 60% relative humidity, 12 h light/dark schedule, 3–4 mice/cage, with food and water *ad libitum*).

*2.5. Mice treatments*

For biodistribution studies, cholesterol release study and quantitative analysis, 7-week-old wt or R6/2 mice were treated with 1, 2 or 3 ip injections. For chronic experiments, R6/2 mice were treated with 2 ip injections at week, from 5 to 9 weeks

of age. Wt and R6/2 littermates treated with saline solution was used as controls. In all the experiments, mice received 660 μg of cholesterol in each injection.

*2.6. Immunohistochemistry and image acquisition*

Animals were deeply anesthetized with Avertin 2.5% and transcardially perfused with PFA 4%. Brains, lungs and liver were collected in PFA 4% for 2 h and then in 30% sucrose to prevent ice crystal damage during freezing in OCT. 15 μm-thick brain coronal sections or lung and liver sections were counterstained with the nuclear dye Hoechst 33258 (1:10.000, Invitrogen) and then mounted under cover slips using Vectashield (Vector Laboratories). To study the co-localization of g7-NPs-chol_2.0 with neuronal and glial markers, 15 μm-thick brain coronal sections were incubated with the following primary antibodies for 3 h at RT: rabbit anti-DARPP32 (1:100, Cell Signaling, 2306); mouse anti-NeuN (1:100, Millipore, MAB377); rabbit anti-GFAP (1:250, Dako, Z0334); rabbit anti-IBA1 (1:100, Wako, 019–1971). Anti-rabbit Alexa Fluor 488-conjugated goat secondary antibodies (1:500; Invitrogen) or anti-mouse Alexa Fluor 488-conjugated goat secondary antibodies (1:500; Invitrogen) were used for detection (1 h at RT). Sections were counterstained with the nuclear dye Hoechst 33258 (1:10.000, Invitrogen) and then mounted under cover slips using Vectashield (Vector Laboratories).

Images were acquired the following day with a confocal microscope (Leica SP5). Laser intensity and detector gain were maintained constant for all images and 3-z steps images were acquired at 40×. To quantify hybrid g7-NPs-chol in different tissues, ImageJ software was used to measure the fluorescence of Cy5 ($n = 4$ images/mouse/tissue).

To quantify the released bodipy cholesterol from g7-NPs-chol_2.0, Volocity software was used using the plug-in "find objects" and "calculate object correlation" ($n = 6$ images/mouse/tissue).

*2.7. Liquid chromatography-mass spectrometry (LC-MS) analysis for d6-chol*

A recently validated method was used [455]. Briefly, 50 μL of plasma was diluted with 200 μL of ethanol containing 200 ng of beta-sitosterol, used as internal standard. Samples were vortexed and centrifuged at 13200 rpm for 15 min and aliquots of the supernatants were injected directly into the LC-MS system. Forty milligrams of each brain area and peripheral tissue were homogenized in 1 mL of ethanol/water 4:1 (*v*/v), containing 500 ng of internal standard. Homogenates were centrifuged for 15 min at 13200 rpm at 4 °C, and aliquots of the supernatants were injected into the LC-MS system. D6-chol levels were determined using a 1200 Series HPLC system (Agilent Technologies, Santa Clara, CA, U.S.A.) interfaced to an API 5500 triple quadrupole mass spectrometer (Sciex, Thornhill, Ontario, Canada). The mass spectrometer was equipped with an atmospheric pressure chemical ionization (APCI) source operating in positive ion and multiple reaction monitoring (MRM) mode to measure the product ions obtained in a collision cell from the protonated $[M - H_2O]^+$ ions of the analytes. The transitions identified during the optimization of the method were *m*/*z* 375.3–152.1 (quantification transition) and *m*/*z* 375.3–167.1 (qualification transition) for D6-chol; *m*/*z* 397.3–147.1 (quantification transition) and *m*/*z* 397.3–161.1 (qualification transition) for β-sitosterol (IS). D6-chol and beta-sitosterol were separated on a Gemini C18 column (50 × 2 mm; 5 μm particle size), using an isocratic gradient in 100% methanol at 35 °C.

*2.8. Gas chromatography-mass spectrometry (GC–MS) analysis for neutral sterols*

To a screw-capped vial sealed with a Teflon-lined septum were added 50 μL of homogenates together with 500 ng of D4-lathosterol (CDN Isotopes, Canada), 500 ng of D6-desmosterol (Avantipolar Lipids, USA), and 100 ng of D6-lanosterol (Avantipolar Lipids, USA) as internal standards, 50 μL of butylated hydroxytoluene (BHT) (5 g/L) and 25 μL of EDTA (10 g/L). Argon was flushed through to remove air. Alkaline hydrolysis was allowed to proceed at room

temperature (22 °C) for 1 h in the presence of 1 M ethanolic potassium hydroxide solution under magnetic stirring. After hydrolysis, the neutral sterols (lathosterol, desmosterol and lanosterol) were extracted twice with 5 ml of hexane. The organic solvents were evaporated under a gentle stream of nitrogen and converted into trimethylsilyl ethers with BSTFA-1% TMCS (Cerilliant, USA) at 70 °C for 60 min. Analysis was performed by gas chromatography - mass spectrometry (GC–MS) on a Clarus 600 gas chromatograph (Perkin Elmer, USA) equipped with Elite-5MS capillary column (30 m, 0.32 mm, 0.25 μm. Perkin Elmer, USA) connected to Clarus 600C mass spectrometer (Perkin Elmer, USA). The oven temperature program was as follows: initial temperature 180 °C was held for 1 min, followed by a linear ramp of 20 °C/min to 270 °C, and then a linear ramp of 5 °C/min to 290 °C, which was held for 10 min. Helium was used as carrier gas at a flow rate of 1 mL/min and 1 μL of sample was injected in splitless mode. Mass spectrometric data were acquired in selected ion monitoring mode. Peak integration was performed manually. Sterols were quantified against internal standards, using standard curves for the listed sterols.

*2.9. Behavioral tests*

Mice behavior was evaluated at 9 and 11 weeks of age.

Rotarod test: mice were tested over three consecutive days. Firstly, animals were trained on a rotating bar at 4 rpm for 5 min (apparatus model 47,600, Ugo Basile). One hour later, mice were tested for three consecutive accelerating trials of 5 min with the rotarod speed linearly increasing from 4 to 40 rpm. The latency to fall from the rod was recorded for each trial and averaged.

Activity Cage test: animals were placed in an arena (25 cm × 25 cm) (2Biological Instrument) and allowed to freely move for an hour in presence of a low-intensity white light source. Movements were assessed by an automated tracking system (Actitrack software, 2Biological Instrument) connected to infrared sensors surrounding the arena. Total distance travelled, mean velocity speed, and numbers

of rearings were analyzed. The % of time that mice explored the periphery or the center area of the was evaluated as a measure of anxiety-like behavior.

Novel Object Recognition (NOR) test: in the habituation stage, mice were placed into an empty non-reflective arena (44 × 44 × 44 cm) for 10 min. In the familiarization stage, two identical objects (A′ and A″) were presented to each animal for 10 min. The day after, during the test stage, animals were exposed to one familiar object (A′) and a new object (B) for 10 min. All phases of the test were conducted with a low-intensity white light source. The index of discrimination was calculated as (time exploring the novel object−time exploring the familiar object)/(time exploring both objects) × 100. Mice exploring less than 7 s. were excluded from the analysis due to their inability to perform the task.

Paw clasping test: animals were suspended by the tail for 30 s and the clasping phenotype was graded according to the following scale: level 0, no clasping; level 1, clasping of the forelimbs only or both fore- and hindlimbs once or twice; and level 2, clasping of both fore- and hindlimbs more than three times or more than 5 s.

Grip strength test: animals were lifted by the tail, lowered towards the grip (Ugo Basile) and gently pulled straight back with consistent force until they released its grip. The forelimb grip force, measured in grams, was recorded. The test was repeated for 5 times, and measures were averaged.

*2.10. Bio-Plex*

Animals were deeply anesthetized with Avertin 2.5% to collect blood which was centrifuged at 13.000 rpm at 4 °C for 15 min to obtain the plasma. Striatum, cortex, and liver were isolated and frozen. 10 mg of striatum, cortex and liver were homogenize using a tissue grinder in 1 mL of lysing solution according to manufacturer instructions (Bio-Plex® Cell Lysis Kit, Biorad, #171304011). The lysate was frozen at −80 °C, sonicated at 40% for 20 s and centrifuged at 4.500 *rcf* at

4 °C for 4 min to collect the supernatant. The supernatant was quantified using DC™ Protein Assay Kit I (Biorad, #5000111) and samples were diluted to a final concentration of 500 μg/mL. To perform the Bio-Plex assay, 150 μL of assay buffer were added to 150 μL of samples.

Concerning the plasma, samples were centrifuged at 1.500 rcf at 4 °C for 5 min. 60 μL of assay buffer and 120 μL of sample diluent were added to 60 μL of plasma.

All samples were tested for the following cytokines using the Bio-Plex Pro Mouse Cytokine 23-plex Assay: IL-1$\alpha$, IL-1β, IL-2, IL-3, IL-4, IL-5, IL-6, IL-9, IL-10, IL-12 (p40), IL-12 (p70), IL-13, IL-17A, Eotaxin, G-CSF, GM-CSF, IFN-$\gamma$, KC, MCP-1 (MCAF), MIP-1$\alpha$, MIP-1β, RANTES, TNF-$\alpha$, (Biorad, #M60009RDPD) according to manufacturer instructions and detected using Bioplex™ 200 System (Bio-Rad). The concentration of each cytokine was calculated through calibration curve (individual for each cytokine), determined independently for each experiment, by Bioplex Manager™ software 4.1.

### *2.11. Statistics*

Prism 8 (GraphPad software) was used to perform statistical analyses. G-power software was used to pre-determine group allocation, data collection and all related analyses. For animal studies, mice were assigned randomly, and sex was balanced in the various experimental groups; animals from the same litter were divided in different experimental groups; blinding of the investigator was applied to *in vivo* procedures and all data collection. Grubbs' test was applied to identify outliers. For each set of data to be compared, we determined whether data were normally distributed or not to select parametric or not parametric statistical tests. The specific statistical test used is indicated in the legend of all results figures. Table S3 summarizes all the trials and read-outs performed.

## 3. Results and discussion

### *3.1. Localization of hybrid-g7-NPs-chol MIX-N and MIX-SE* in vivo

The characteristics of both hybrid-g7-NPs-chol MIX-N and MIX-SE were in line with those described in previous studies [351,385] in terms of size, homogeneity, surface charge, cholesterol content, and morphology (Table S1 and Fig. S1). The maximal percentages of cholesterol present in hybrid-g7-NPs-chol MIX-N and MIX-SE were 32.7 ± 2% and 41.5 ± 1.5%, respectively, reaching a cholesterol content which is around 40 times higher than that of PLGA-g7-NPs-chol [385]. This drug delivery system is therefore expected to deliver to the HD brain a therapeutic dose of cholesterol closer to that identified with the osmotic mini-pumps [454], while being less invasive and more translatable.

The hybrid-g7-NPs-chol MIX-N and MIX-SE were first tested in 7-week-old wild-type (wt) mice to verify their uptake and distribution in vivo. To this aim, animals were treated with a single or multiple (3) intraperitoneal (ip) injections of hybrid-g7-NPs-chol MIX-N or MIX-SE labeled with cyanine 5 (Cy5) and sacrificed at different time points (4 h, 24 h, 1 week, 2 weeks) following the last ip injection (Fig. 1(a)). Fluorescence analysis was then performed on brain and peripheral slices to analyze the localization of the Cy5-labeled hybrid-NPs-Chol signals of both MIXs (Fig. 1(b) and (c); Fig. S2). Four hours after a single ip injection, Cy5 signal was detected in the striatum, cortex (Fig. 1(b) and (c)), and hippocampus, as well as in lung and liver (Fig. 1(b) and (c) and Fig. S2(a) and S2(b)), indicating that BBB transit was rapid. Quantification of Cy5 signals revealed that the clearance of both MIXs in peripheral tissues were quite rapid, at least in lung and somewhat less so in liver, since the Cy5 signals decreased markedly 24 h after the ip injection (Fig. S2). Importantly, NPs were accumulating in the brain over time, as evidenced by the Cy5-NPs signal being present at 24 h, 1 week, and 2 weeks after ip injection (Fig. 1(b) and (c); Fig. S2), and strengthening following multiple injections (Fig. 1(b) and (c); Fig. S2). High-magnification confocal images indicated the presence of hybrid-g7-NPs-chol in different neuronal and glial cell types as demonstrated by the

colocalization of the signals from Cy5 (NPs) and DARPP32 (marker of striatal medium spiny neurons), GFAP (marker of astrocytes), and IBA1 (marker of microglia) (Fig. 1(d)). Although the biodistributions of MIX-N and MIX-SE were similar, the latter showed higher aggregation in liver, a finding that was more evident after multiple ip injections but which disappeared after 1 week (Fig. S2(b)).

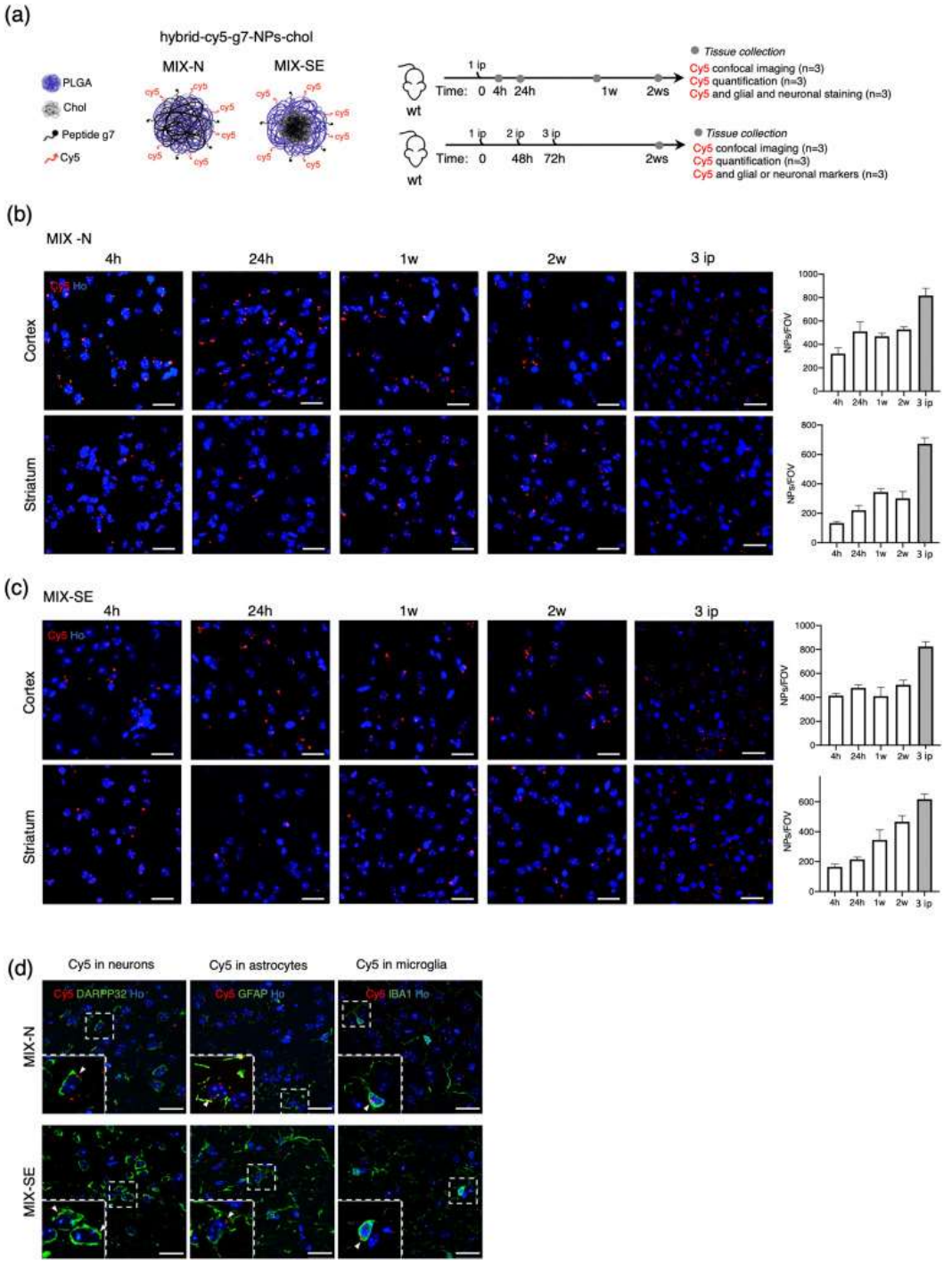


**Fig. 1.** (a) Experimental paradigm used in the study. Wild-type (wt) mice (n = 2 mice/MIX/time point) were treated with a single or multiple intraperitoneal (ip) injection of hybrid-Cy5-g7-NPs-chol (MIX-N or MIX-SE) and sacrificed at different time points. Brain, liver, and lung were collected for distribution analysis. (b) and (c) Representative confocal images of coronal slices containing cortex and striatum from wt mice that received 1 or 3 ip injections of hybrid-Cy5-g7-NPs-chol (MIX-N in (b) or MIX-SE in (c)) and sacrificed after 4 h, 24 h, 1 week, and 2 weeks with relative quantification. (d) Representative confocal images of immunostaining for DARPP32, GFAP, and IBA1 (green) on coronal sections of brains isolated from wt mice after receiving ip-injected hybrid-Cy5-g7-NPs-chol labeled with Cy5 (red) and sacrificed 2 weeks after the injection. White arrowheads indicate

intracellular g7-NPs. Hoechst was used to counterstain nuclei (Ho, blue). Scale bar is 30 μm. Data are expressed as the number of g7-NPs per field of view ± standard error of the mean.

Overall, these results demonstrate that hybrid-g7-NPs-chol rapidly reach the brain and accumulate over time within target cells.

*3.2. Cholesterol delivery and intracellular release*

To track cholesterol delivery and intracellular release from hybrid-g7-NPs-chol, we performed specific experiments using g7-NPs-chol covalently labeled with Cy5 and loaded with the fluorescent analogue bodipy cholesterol (hybrid-Cy5-g7-NPs-bodipy-chol). Seven-week-old wt and HD mice (R6/2 model) [458] were treated with a single ip injection of hybrid-Cy5-g7-NPs-bodipy-chol MIX-N or MIX-SE and sacrificed at 24 h and 2 weeks after the ip injection (Fig. 2(a)). Following confocal analysis in brain slices, we analyzed the colocalization of red spots (Cy5, NPs) and the green signal (bodipy cholesterol) to evaluate bodipy cholesterol release from the new formulations. We show that 24 h after a single ip injection of hybrid-Cy5-g7-NPs-bodipy-chol, Cy5 and bodipy-chol signals nicely colocalized in striatum and cortex, as indicated by the scatterplot of red and green pixel intensities (Fig. 2(b) and (c)). Importantly, analysis performed 2 weeks after ip injection revealed a partial separation between Cy5 and bodipy-chol signals (Fig. 2(b) and (c)), indicating a slow and progressive release of cholesterol over time. In contrast, cholesterol release in the liver of mice treated with MIX-N was faster than in the brain. In fact, a complete overlap of red and green signal was found 24 h after the ip injection, while 2 weeks after the ip injection all the exogenous cholesterol was released from NPs (Fig. S3). By comparing the overlap coefficient between Cy5 and bodipy signals (Table S2), we found that approximately 30% of bodipy-chol no longer colocalized with Cy5-NPs in cortex and striatum starting from 2 weeks after ip injection, suggesting a progressive release from hybrid-g7-NPs-chol in the brain, in parallel with a reduction in Cy5 signal, probably due to polymer degradation. In contrast, 2 weeks after ip injection, about 90% of bodipy-cholesterol no longer colocalized with Cy5-NPs in the liver (Table S2). No

differences in cholesterol release kinetics were found between wt and HD mice, indicating that cholesterol release over-time did not depend on mouse genotype (Table S2). We also conclude that MIX-N and MIX-SE NPs had similar biodistribution profiles and kinetics of cholesterol release. Notably, as MIX-N showed less aggregation in liver and, more importantly, as the surfactant present in the formulation (Pluronic F68) is approved by the FDA [459], we decided to proceed by testing only this kind of NPs in subsequent studies.

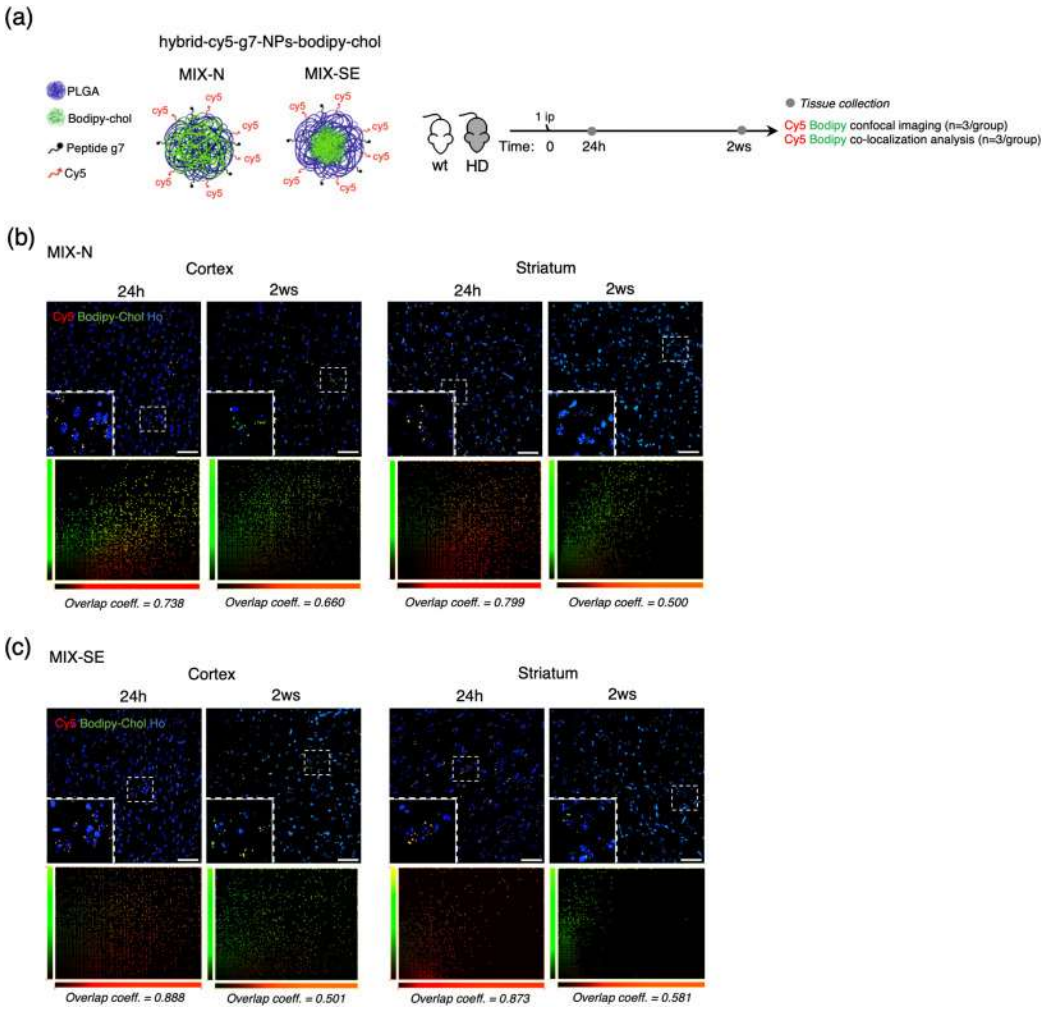


**Fig. 2.** (a) Experimental paradigm used in the study. Wild-type and R6/2 mice (n = 3 mice/genotype/MIX/time point) were treated with a single ip injection of hybrid-Cy5-g7-NPs-bodipy-chol (MIX-N or MIX-SE) and sacrificed at different time points. Brain and liver were collected for the analysis. (b) and (c) Representative confocal images of brain slices from R6/2 mice after ip injection of hybrid-Cy5-g7-NPs-bodipy-chol (MIX-N in (b) or MIX-SE in (c)) and sacrificed after 24 h or 2 weeks and relative co-localization of bodipy-chol and g7-NPs. Hoechst was used to counterstain nuclei (Ho, blue). Scale bar is 50 μm.

*3.3. Kinetics of cholesterol delivery to different organs*

Next, to study the kinetics of exogenous cholesterol delivery and to quantify the total amount of cholesterol delivered in vivo, we performed two experiments using only MIX-N hybrid-g7-NPs-chol loaded with cholesterol labeled with six deuterium atoms (d6-chol) (hybrid-g7-NPs-d6-chol).

In the first experiment, 7-week-old HD mice were treated with a single ip injection of hybrid-g7-NPs-d6-chol and sacrificed at 30 min, 6 h, 24 h, 1 week, and 2 weeks after the ip injection (Fig. 3(a)). Blood, kidney, lung, liver, cortex, striatum, and cerebellum were collected to measure the amount of d6-chol in the different tissues using liquid chromatography mass spectrometry (LC-MS), starting from 6 h after the ip injection (Fig. 3(b)). We show that starting from 24 h after the treatment, the content of d6-chol increased in the brain tissues over a 2-week period, a finding which is indicative of its slow and progressive release from the NPs (Fig. 3(b)). In contrast, in the liver, d6-chol was rapidly released 30 min after ip injection and rapidly degraded over time. In lung and kidney, NPs were detected around 6 h after the ip injection, the peak of d6-chol release occurred 1 week after the ip injection, after which it was rapidly eliminated (Fig. 3(c)). In plasma, the maximum amount of d6-chol was detected 24 h after the ip injection (Fig. 3(c)). Importantly, this concentration (317,67 ng/mL +/− 635,34) is around 4.000 times lower than the concentration of cholesterol that is present in mouse blood (128 mg/100 mL).

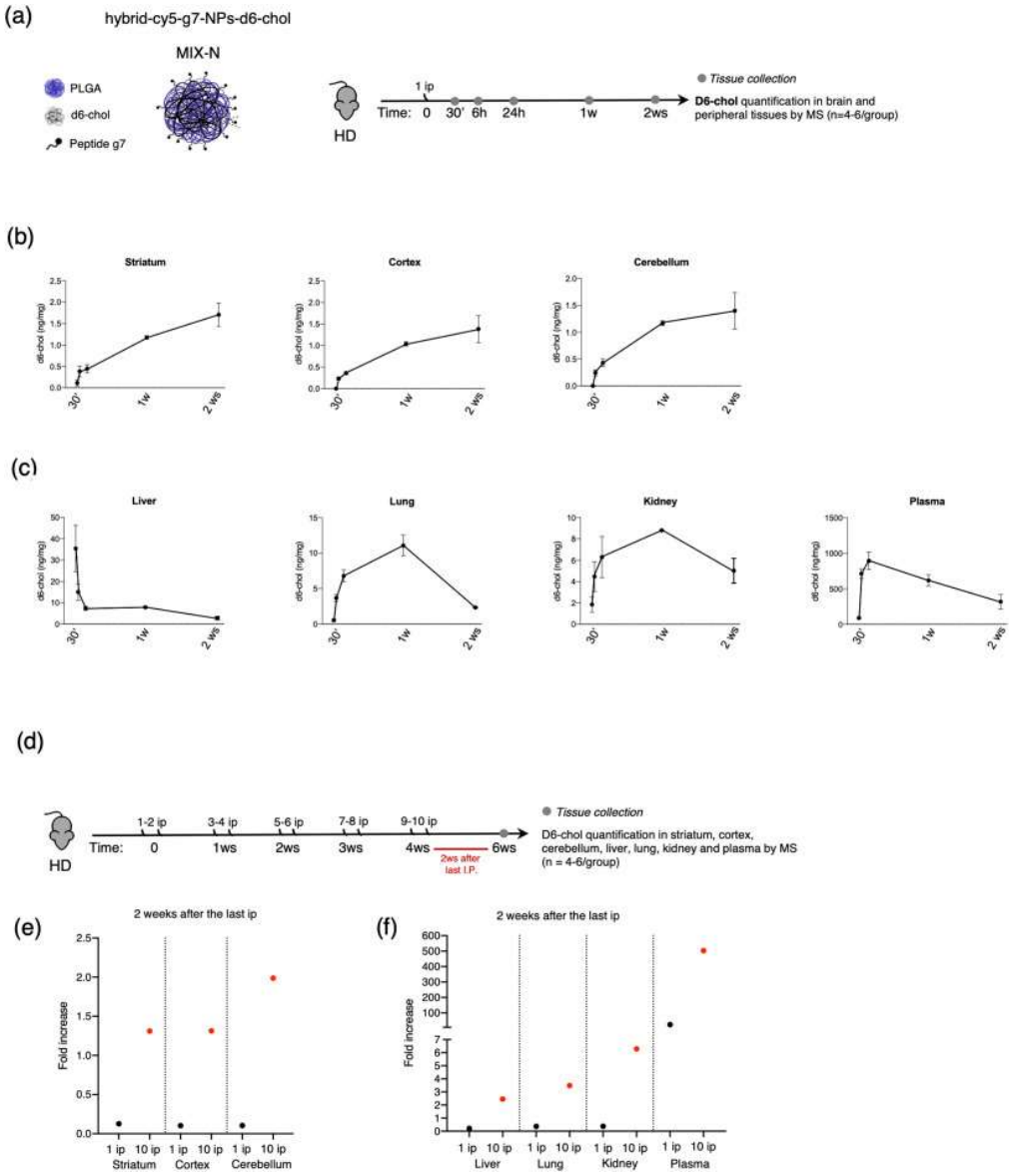


**Fig. 3**. (a) Experimental paradigm used in the study. R6/2 mice were treated with a single ip injection of hybrid-g7-NPs-d6-chol (MIX-N) and sacrificed at different time points. Striatum, cortex, cerebellum, liver, lung, kidney, plasma, and liver were collected for mass spectrometry analysis (n = 3 mice/time point). (b) and (c) Levels of d6-chol in striatum, cortex, cerebellum (b), liver, lung, kidney, and plasma (c) measured by LC-MS. (d) Experimental paradigm used in the study. R6/2 mice were treated with hybrid-g7-NPs-d6-chol (MIX-N) from 5 weeks of age to 9 weeks of age with 2 ip injections/week and sacrificed 2 weeks after the last ip injection. Striatum, cortex, cerebellum, liver, lung, kidney, and plasma and liver were collected for mass spectrometry analysis (n = 3 mice). (e) and (f) Levels of d6-chol in striatum, cortex, cerebellum (e), liver, lung, kidney, and plasma (f) measured by LC-MS (red dots). Black dots refer to the measurement represented in Fig. 3B–C. Data are expressed as means ± standard error of the mean.

In a second experiment, to quantify cholesterol delivered with the therapeutic regimen of interest, HD mice were treated from 5 to 9 weeks of age with 2 ip

injections/week and sacrificed 2 weeks after the last ip injection (Fig. 3(d)). MS analysis revealed that the concentration of d6-chol measured in each tissue following 10 ip injections was around 10 times the concentration of d6-chol measured 2 weeks after a single ip injection (Fig. 3(d) and (e)), indicating that the exogenous cholesterol accumulated in all tissues, even if with different kinetics.

These results demonstrated that the kinetics of cholesterol release differed between brain, plasma, and peripheral tissues and that this delivery system allows a slow release and accumulation of cholesterol in different brain regions where it becomes available to cells over time. Moreover, the fast elimination of cholesterol from blood and peripheral tissues potentially avoids systemic side effects after chronic treatment. Finally, these data combined with the data obtained with bodipy-chol (Fig. 2(b) and (c)), support furtherly the hypothesis that the release of cholesterol from NPs is progressive and slow.

*3.4. Enhancement of cholesterol synthesis in the HD mouse brain*

We have recently demonstrated that a therapeutically relevant dose of cholesterol delivered to the striatum through osmotic mini-pumps indirectly stimulated endogenous cholesterol synthesis, leading to the reversal of both motor and cognitive abnormalities in HD mice [454]. In contrast, lower doses delivered to the striatum through osmotic mini-pumps [454] or to the brain via PLGA-g7-NPs-chol [385] led to a complete rescue of cognitive decline without significant change in endogenous brain cholesterol biosynthesis or in motor performance.

Since hybrid-g7-NPs-chol [351], with their hybrid structure, are able to carry a larger amount of cholesterol than the previously used PLGA-g7-NPs-chol [385], we sought to test whether the increased amount of cholesterol in hybrid-g7-NPs-chol was sufficient to stimulate endogenous cholesterol synthesis in the diseased brain. As surrogate markers of cholesterol biosynthesis, we quantified cholesterol precursors (lanosterol, lathosterol, desmosterol) by isotopic dilution gas-chromatography mass spectrometry (ID-MS) in the striata of HD mice after a

chronic treatment. Accordingly, HD mice from 5 to 9 weeks of age were treated with PLGA-g7-NPs-chol or with hybrid-g7-NPs-chol with 2 ip injections/week and sacrificed 2 weeks after the last ip injection (Fig. 4(a)). As expected, robust deficits of lanosterol, lathosterol, and desmosterol were evident in striatum from HD mice treated with saline compared with wt littermates (Fig. 4(b)–(d)), confirming previous results [446–448,450]. Of note, significant increases in lanosterol and desmosterol levels were found in striatal tissues of HD mice treated with hybrid-g7-NPs-chol compared with those treated with PLGA-g7-NPs-chol (Fig. 4(b)–(d)).

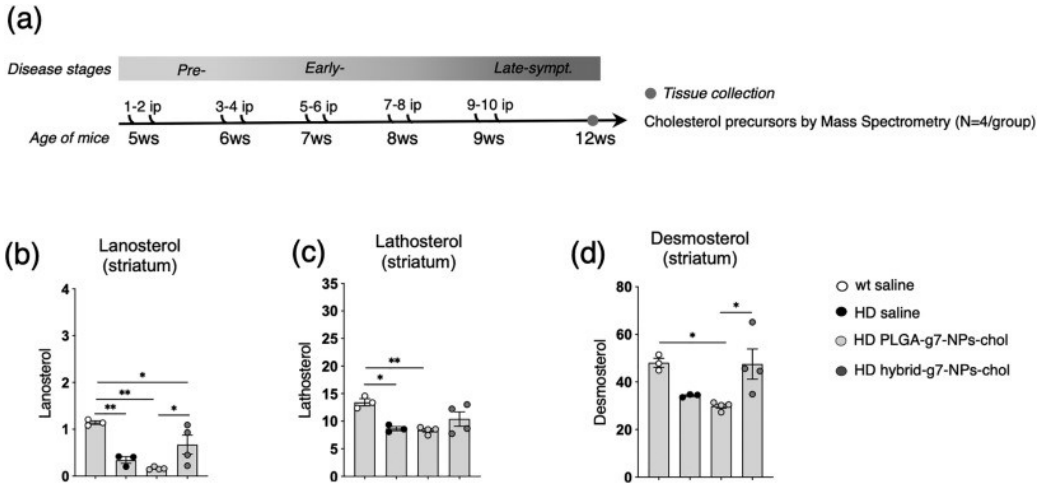


**Fig. 4.** (a) Experimental paradigm used in the study. R6/2 mice were treated with PLGA-g7-NPs-chol and hybrid-g7-NPs-chol from 5 weeks of age to 9 weeks of age with 2 ip injections/week. Wt and R6/2 littermates were treated with saline solution as controls. Striatum and cortex were collected at 11 weeks of age for mass spectrometry analysis (n = 3–4 mice/group). (b), (c), and (d): Lanosterol (b), lathosterol (c), and desmosterol (d) levels measured by GC–MS in the striatum of wt saline, R6/2 saline, R6/2 + PLGA-g7-NPs-chol, and R6/2 + hybrid-g7-NPs-chol mice at 11 weeks of age (n = 3–4 mice/group). Data are expressed as means ± standard error of the mean. Each dot corresponds to the value obtained from each animal. Statistics: one-way ANOVA with Newman–Keuls post-hoc test (*p < 0.05; **p < 0.01; ***p < 0.001).

Taken together, these results suggest that the hybrid-g7-NPs-chol transport and release in the brain more cholesterol compared with PLGA-g7-NPs-chol and that the dose is able to enhance endogenous cholesterol biosynthesis in HD mice.

### *3.5. Effects on cognition, locomotion, and strength*

To assess the power of hybrid-g7-NPs-chol to counteract motor and cognitive defects in HD mice, hybrid-g7-NPs-chol were ip injected into R6/2 mice with the same experimental paradigm described in Fig. 4(a) and their motor and cognitive performance were compared with those of R6/2 and wt mice treated with saline solution.

First, we analyzed motor coordination by evaluating the latency of mice to fall when tested on a rotating bar with accelerating speed in the rotarod test. Starting from 8 weeks of age, HD mice exhibited a progressive deterioration in motor coordination, as shown by the shorter latency to fall compared with wt controls. Systemic and chronic administration of hybrid-g7-NPs-chol did not rescue this defect in HD mice (Fig. 5(a)).

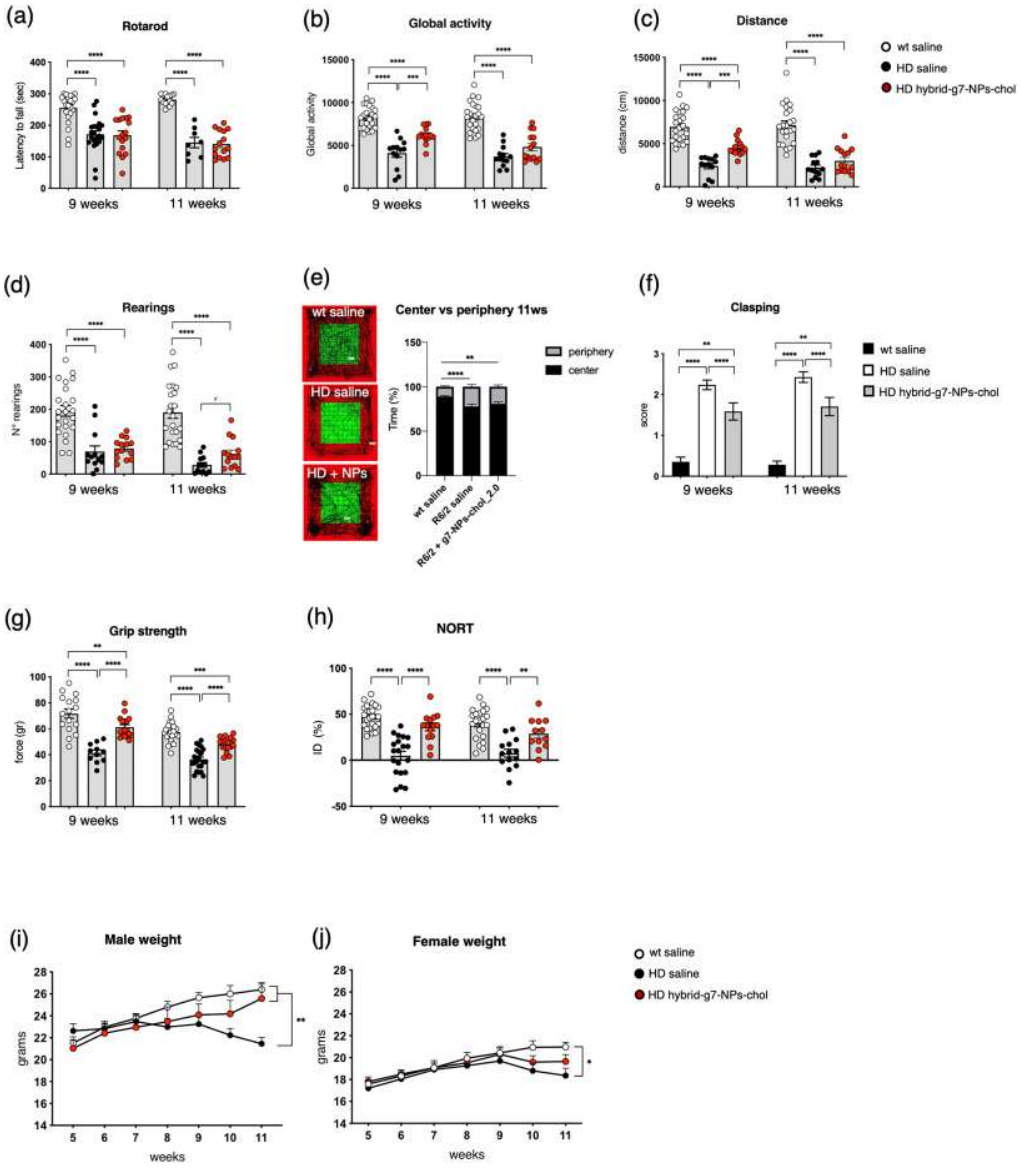


**Fig. 5.** (a) Latency to falling (seconds) from an accelerating rotarod at 8 and 10 weeks of age in wt saline (n = 24–25), R6/2 saline (n = 15–17), and R6/2 + hybrid-g7-NPs-chol (n = 17) treated mice. (b), (c), (d), (e) and (f): Global motor activity (b), total distance travelled (c), and number of rearings (d) in an open-field test at 9 and 11 weeks of age in wt saline (n = 24–25), R6/2 saline (n = 15–17), and R6/2 + hybrid-g7-NPs-chol (n = 17) mice. (e) Representative track plots generated from the open-field test from wt saline (n = 24–25), R6/2 saline (n = 15–17), and R6/2 + hybrid-g7-NPs-chol (n = 17) mice and relative quantification of the times spent in the center and in the periphery (%) of the arena at 11 weeks of age. (f) Grip strength (grams) at 9 and 11 weeks of age in wt saline (n = 16–24), R6/2 saline (n = 11–22), and R6/2 + hybrid-g7-NPs-chol (n = 17) mice. (g) Paw clasping at 9 and 11 weeks of age in wt saline (n = 25), R6/2 saline (n = 22), and R6/2 + hybrid-g7-NPs-chol (n = 17) mice. (h) Discrimination index (DI %) in the novel object recognition test of wt saline (n = 22–23), R6/2 saline (n = 13–19), and R6/2 + hybrid-g7-NPs-chol (n = 10–13) mice at 9 and 11 weeks of age. DI above zero indicates a preference for the novel object; DI below zero indicates a preference for the familiar object. (i) and (j) Body weight (grams) of male (i) and female (j) mice at different time points. Data are from three independent trials and shown as scatterplot graphs with means ± standard error. Each dot corresponds to the value obtained from each animal. Statistics: one-way ANOVA with Newman–Keuls post-hoc test (*p < 0.05; **p < 0.01; ****p < 0.0001; ***p < 0.001) or unpaired Student t-test (#p < 0.05; ##p < 0.01).

To further test the animals' motor abilities, we analyzed spontaneous locomotory activity in the activity cage test. During disease progression, HD mice showed a severe hypokinetic phenotype as demonstrated by reduced global activity, total distance travelled, and number of rearings compared with wt mice, at both 9 and 11 weeks of age. At 9 weeks, HD mice treated with hybrid-g7-NPs-chol had greater global activity and total distance travelled compared with HD mice treated with saline, even if they did not reach the performance observed in wt mice. Moreover, these differences were lost at 11 weeks of age, suggesting that the amount of cholesterol delivered in the brain was not sufficient to counteract motor deficits at a late symptomatic time point, when the HD phenotype worsens (Fig. 5(b) and (c)). When we looked at the number of rearings, no rescue was measured in HD mice treated with hybrid-g7-NPs-chol (Fig. 5(d)). As a measure of anxiety-like behavior, the time that mice spent exploring the periphery or center area of the arena during the activity cage test was also evaluated (Fig. 5(e)). HD animals spent more time in the periphery compared with wt mice, indicating anxiety-related behavior. Cholesterol delivery did not rescue this phenotype (Fig. 5(e)).

As a marker of disease progression, we measured hind-limb clasping with the paw clasping test, a test widely used to measure neurological features in several mouse models of neurodegeneration. In HD mice treated with hybrid-g7-NPs-chol, this phenotype was ameliorated (Fig. 5(f)).

To study neuromuscular functions and strength, we determined the force developed by the mice using the grip-strength test. Muscular strength was reduced in HD mice from 9 weeks of age and it was completely rescued by hybrid-g7-NPs-chol at both 9 and 11 weeks of age (Fig. 5(g)).

Furthermore, we found that 44% of the analyzed R6/2 animals treated with saline suffered from epileptic seizures, while only 18% of R6/2 mice injected with hybrid-g7-NPs-chol were affected.

Finally, to evaluate cognitive function we performed the novel object recognition (NOR) test. As expected, long-term memory declined during disease progression in HD mice, with a marked impairment in the ability to discriminate novel and familiar objects at 11 weeks of age. HD mice treated with hybrid-g7-NPs-chol performed similarly to wt mice, indicating that this treatment completely prevented cognitive decline in these animals (Fig. 5(h)). Weight loss was observed in R6/2 mice starting from a late time point (10 weeks of age). Remarkably, this parameter was rescued in male R6/2 mice treated with hybrid-g7-NPs-chol (Fig. 5(i) and (j)).

Collectively, these results indicate that the dose of cholesterol delivered and released in the brain with chronic treatment was sufficient to prevent cognitive decline over time and ameliorate some motor defects at 9 weeks of age. However, the fast and aggressive phenotype of this HD mouse model did not allow us to evaluate the long-term effect of this treatment when all cholesterol is released from the NPs, which may require several weeks.

*3.6. Assessment of markers of inflammation, a possible side effect*

To explore any eventual side effects of chronic administration of hybrid-g7-NPs-chol, we next sought to analyze the inflammation status of treated mice. Cytokines, chemokines, and growth factors are cell-signaling proteins that mediate a wide range of physiological responses including immunity and inflammation, and are also associated with a spectrum of neurodegenerative diseases [460,461]. Through the simultaneous detection of 23 analytes in a single well of a 96-well microplate, we analyzed the inflammation status of striatum, cortex, liver, and plasma from HD mice treated with saline or with hybrid-g7-NPs-chol. In general, we did not observe gross changes in the levels of the analytes analyzed, except for an increase in IL-2 in the striatum and a decrease in eotaxin in cortex and in IL-1a and IL2 in plasma of R6/2 mice treated with hybrid-g7-NPs-chol compared with R6/2 mice treated with saline (Table 1). These findings suggest

that chronic treatment with hybrid-g7-NPs-chol is safe in R6/2 mice. Moreover, observation of the mice during chronic administration regimens did not reveal any cases of mortality in the treated and control groups and no signs of abnormal behavioral reactions and general clinical symptoms were detected.

Overall, these results suggest that chronic administration of hybrid-g7-NPs-chol does not lead to side effects in HD mice.

**Table 1**. Inflammatory response of HD mice following systemic and chronic injection of hybrid g7-NPs-chol.

| Analyte | Striatum | | Cortex | | Liver | | Plasma | |
|---|---|---|---|---|---|---|---|---|
| | fold-change | | fold-change | | fold-change | | fold-change | |
| | Mean ± SEM | p-value | Mean ± SEM | p-value | Mean ± SEM | p-value | Mean ± SEM | p-value |
| IL-1a | 1,010 ± 0,025 | 0,9348 | 0,927 ± 0,033 | 0,3884 | 0,976 ± 0,111 | 0,8622 | **0,212 ± 0,032** | **0,0078 **** |
| IL-1b | 1,055 ± 0,200 | 0,8435 | 0,747 ± 0,134 | 0,3254 | 1,088 ± 0,184 | 0,7466 | 0,920 ± 0,381 | 0,8608 |
| IL-2 | **1,415 ± 0,076** | **0,0081 **** | 0,708 ± 0,013 | 0,1058 | 1,159 ± 0,179 | 0,4831 | **0,398 ± 0,081** | **0,0467 *** |
| IL-3 | 1,012 ± 0,298 | 0,9739 | 0,771 ± 0,097 | 0,2840 | 1,031 ± 0,038 | 0,7151 | N/D | |
| IL-4 | 0,632 ± 0,110 | 0,5871 | 1,472 ± 0,499 | 0,4103 | 0,744 ± 0,182 | 0,4333 | 0,429 ± 0,184 | 0,3575 |
| IL-5 | 1,264 ± 0,165 | 0,5834 | 1,276 ± 0,561 | 0,6831 | 0,924 ± 0,158 | 0,7211 | 0,330 ± 0,085 | 0,1610 |
| IL-6 | 1,061 ± 0,132 | 0,7723 | 1,019 ± 0,102 | 0,9132 | 0,889 ± 0,133 | 0,5446 | N/D | |
| IL-9 | 0,789 ± 0,143 | 0,4046 | 0,836 ± 0,145 | 0,5136 | 0,900 ± 0,112 | 0,6095 | N/D | |
| IL-10 | 1,020 ± 0,291 | 0,9593 | 0,677 ± 0,123 | 0,1301 | 1,109 ± 0,354 | 0,8100 | 1,175 ± 0,002 | 0,1610 |
| IL-12 (p40) | 1,666 ± 0,435 | 0,2450 | 0,667 ± 0,176 | 0,3861 | 1,843 ± 0,113 | 0,1025 | 0,921 ± 0,236 | 0,8124 |
| IL-12 (p70) | 0,944 ± 0,242 | 0,8601 | 0,798 ± 0,138 | 0,3859 | 0,803 ± 0,116 | 0,4620 | N/D | |
| IL-13 | 0,950 ± 0,072 | 0,5667 | 0,835 ± 0,069 | 0,2902 | 0,977 ± 0,097 | 0,8460 | 1,099 ± 0,152 | 0,5886 |
| IL-17 | 1,345 ± 0,414 | 0,5198 | 0,892 ± 0,125 | 0,2902 | 1,194 ± 0,104 | 0,3108 | 1,345 ± 0,414 | 0,5198 |
| Eotaxin | 1,695 ± 0,359 | 0,1447 | **0,447 ± 0,078** | **0,0228 *** | 0,958 ± 0,215 | 0,8927 | 0,809 ± 0,195 | 0,5637 |
| G-CSF | 0,943 ± 0,203 | 0,8490 | 0,914 ± 0,153 | 0,6571 | 1,001 ± 0,120 | 0,9970 | 0,987 ± 0,148 | 0,9529 |
| GM-CSF | 1,025 ± 0,222 | 0,9314 | 1,060 ± 0,220 | 0,8302 | 1,090 ± 0,080 | 0,4218 | 0,724 ± 0,188 | 0,2956 |
| ING-gamma | 1,413 ± 0,272 | 0,2607 | 0,899 ± 0,102 | 0,5404 | 1,155 ± 0,184 | 0,4968 | 0,749 ± 0,322 | 0,7225 |
| KC | 1,337 ± 0,302 | 0,3446 | 1,340 ± 0,169 | 0,1438 | 0,988 ± 0,313 | 0,9742 | 0,489 ± 0,086 | 0,1494 |
| MCP-1 | 0,947 ± 0,375 | 0,9216 | 0,907 ± 0,196 | 0,8058 | 1,657 ± 0,414 | 0,2082 | 1,365 ± 0,689 | 0,7636 |
| MIP-1a | 1,133 ± 0,326 | 0,7593 | 0,816 ± 0,138 | 0,4708 | 1,065 ± 0,126 | 0,6874 | 0,525 ± 0,222 | 0,5987 |
| MIP-1b | 1,511 ± 0,186 | 0,1488 | 0,731 ± 0,137 | 0,3533 | 0,920 ± 0,192 | 0,7806 | 0,614 ± 0,452 | 0,4762 |
| Ranteg | 1,010 ± 0,075 | 0,9520 | 1,020 ± 0,134 | 0,9271 | 0,882 ± 0,087 | 0,5915 | 0,998 ± 0,231 | 0,9954 |
| TNF-a | 1,173 ± 0,276 | 0,6227 | 0,854 ± 0,249 | 0,6447 | 1,100 ± 0,352 | 0,8135 | 0,851 ± 0,371 | 0,8106 |

*data expressed as fold-change (HD mice treated with hybrid-g7-NPs-chol vs HD mice treated with saline solution)*

## 4. Conclusion

Previous studies pointed out the benefits of strategies aimed at delivering cholesterol to the HD brain [385,454], but defining the dose of cholesterol that reaches the brain is critical to a complete understanding of the power and limits of the approach. With the aim of developing a new and non-invasive strategy closer to clinical application, hybrid-g7-NPs-chol were produced with improved chemical and physical properties and increased cholesterol content [351]. Here, we characterized hybrid-g7-NPs-chol in vivo in a transgenic mouse model of HD. We demonstrated that hybrid-g7-NPs-chol are taken up and reach different cell types in the brain, and that they accumulate over time and are able to release cholesterol, which becomes available for neuronal functions. Importantly, NPs are rapidly degraded in the plasma and in peripheral tissues without a detectable inflammatory response. These systems can be optimized further in order to transport not only cholesterol but other molecules that can be useful in treating HD and other brain pathologies, or even used with different routes of administration [455]. Finally, we highlighted the utility of cholesterol as a model drug with which to define delivery systems based on NPs.

## 5. Supplementary Material

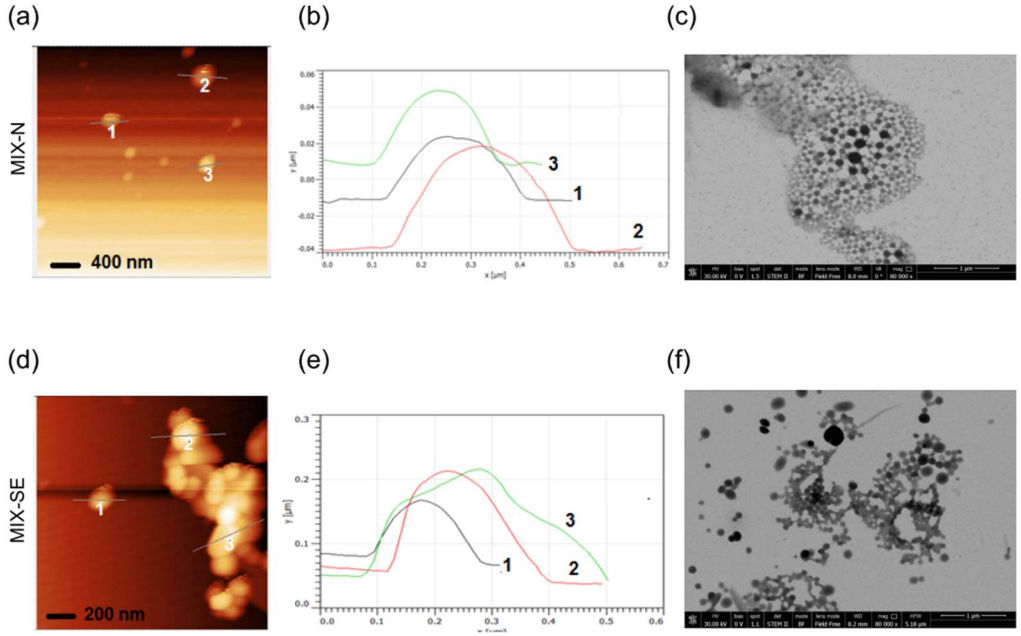


**Figure S1.** (a), (b) and (c) Atomic Force Microscopy (AFM) image (a) with relative analyses of profiles (b) and Scanning Transmission Electron microscopy (STEM) image (c) of MIX-N NPs. (d), (e) and (f) AFM image (d) with relative analyses of profiles (e) and STEM image (f) of MIX-SE NPs.

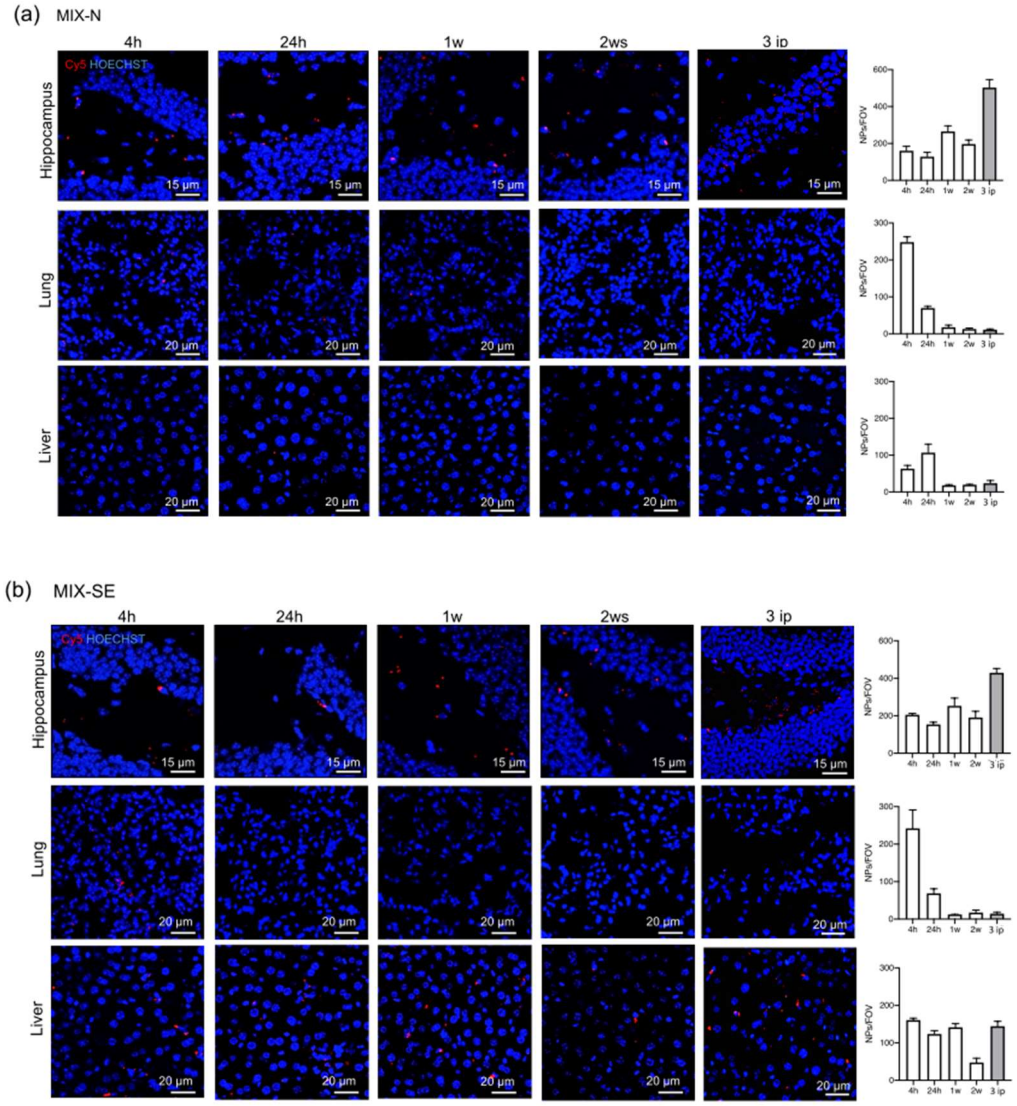


**Figure S2**. (a) and (b). Representative confocal images of hippocampus, lung, and liver slices from wt mice that received 1 or 3 ip injection hybrid-Cy5-g7-NPs-chol (MIX-N in (a) or MIX-SE in (b)) and sacrificed after 4h, 24h, 1w, and 2w with relative quantification. Hoechst were used to counterstain nuclei (Ho, blue). Data are expressed as the number of g7-NPs-chol for 1 field of view ± standard error of the mean.

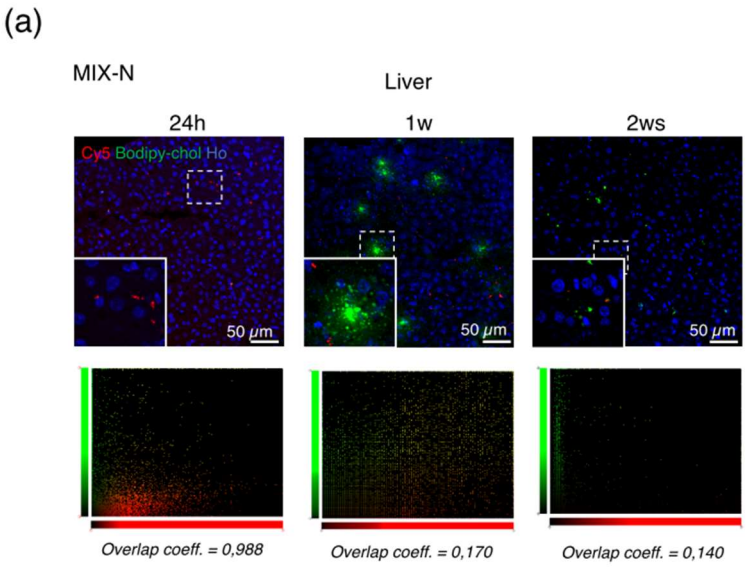


**Figure S3**. Representative confocal image of liver slices from R6/2 mice ip injected with hybrid- Cy5-g7-NPs-bodipy-chol (MIX-N) and sacrificed after 24 h, 1 week or 2 weeks and relative co-localization of bodipy-chol and g7-NPs.

**Table S1**. Chemico-physical properties of NPs involved in the study and produced with different composition. In brackets SD. PDI stands for Polydispersity index, with values between 0 and 1. Lower is the PDI values, higher is the homogeneity of the sample in terms of size distribution. Amount of cholesterol is expressed in mg.

| Type | Sample Name | | Size (nm) | PDI | Zeta Potential (mV) | Chol Content (mg Chol/100mg NPs) | Concentration (mg/mL) | In vivo experiments and analyes |
|---|---|---|---|---|---|---|---|---|
| PLGA | PLGA-g7-NPs-chol | | 180 (15) | 0.05 (0.02) | -22 (4) | 0.9 (0.1) | 9 | Mass spectrometry analysis |
| Hybrid | Cy5-g7-NPs-chol | *MIX-N* | 230 (12) | 0.16 (0.1) | -20 (5) | 28 (3) | 6,7 | Bio-distribution |
| | | *MIX-SE* | 250 (14) | 0.13 (0.5) | -20 (5) | 31 (3) | 7,4 | Bio-distribution |
| | Cy5-g7-NPs-Bodipy-chol | *MIX-N* | 303 (4) | 0.25 (0,02) | -25 (4) | 32 (4) | 8,5 | qualitative studies of chol release |
| | | *MIX-SE* | 270 (15) | 0.16 (0.5) | -19 (6) | 26 (5) | 8,8 | qualitative studies of chol release |
| | g7-NPs-d6-chol | *MIX-N* | 166 (4) | 0.22 (0,1) | -42 (1) | 24 (1) | 8,4 | d6-chol quantification by mass spectrometry |
| | g7-NPs-chol | *MIX-N* | 240 (14) | 0,24 (0,04) | -25 (3) | 30 (5) | 8,6 | Mass spectrometry and behavioural analysis |

**Table S2**. Cholesterol release from hybrid-Cy5-g7-NPs-bodipy-chol: overlap coefficient.

| genotype | time after ip injection | overlap coefficient (MIX-N) | | | overlap coefficient (MIX-SE) | | |
|---|---|---|---|---|---|---|---|
| | | Cortex | Striatum | Liver | Cortex | Striatum | Liver |
| wt mice | 24h | 0,829 | 0,873 | 0,840 | 0,708 | 0,828 | N/D |
| | 2ws | 0,667 | 0,544 | 0,055 | 0,542 | 0,647 | N/D |
| R6/2 mice | 24h | 0,738 | 0,799 | 0,988 | 0,888 | 0,873 | N/D |
| | 2ws | 0,660 | 0,500 | 0,140 | 0,501 | 0,581 | N/D |

**Table S3**. Summary of all the trial performed and the animals used in this study.

| Trial number and date | Experimental groups | Bio-distribution | Chol release: quantitative analysis | Chol release: quantitative analysis | Mass spectrometry analysis | Behavioral analysis | Bioplex analysis |
|---|---|---|---|---|---|---|---|
| | | N mice | N mice | N mice | N mice | N mice | N mice |
| 1 - September 2017 | wt + hybrid-cy5-g7-NPs-chol MIX-N | 10 | | | | | |
| | wt + hybrid-cy5-g7-NPs-chol MIX-SE | 10 | | | | | |
| 2 - November 2017 | wt + hybrid-cy5-g7-NPs-chol MIX-N | 10 | | | | | |
| | wt + hybrid-cy5-g7-NPs-chol MIX-SE | 10 | | | | | |
| 3 - February 2018 | wt + hybrid-cy5-g7-NPs-bodipy-chol MIX-N | | 9 | | | | |
| | wt + hybrid-cy5-g7-NPs-bodipy-chol MIX-SE | | 9 | | | | |
| | R6/2 + hybrid-cy5-g7-NPs-bodipy-chol MIX-N | | 9 | | | | |
| | R6/2 + hybrid-cy5-g7-NPs-bodipy-chol MIX-SE | | 9 | | | | |
| 4 - May 2018 | R6/2 + hybrid-g7-NPs-d6-chol MIX-N | | | 21 | | | |
| 5 - January 2019 | wt saline | | | | 3 | 10 | |
| | R6/2 saline | | | | 3 | 8 | |
| | R6/2 + hybrid-g7-NPs-chol | | | | 3 | 10 | |
| 6 - November 2019 | wt saline | | | | | 5 | |
| | R6/2 saline | | | | | 4 | 4 |
| | R6/2 + PLGA-g7-NPs-chol | | | | | 10 | |
| | R6/2 + hybrid-g7-NPs-chol | | | | | 7 | 5 |

# Glioblastoma Multiforme Selective Nanomedicines for Improved Anti-cancer Treatments

**Jason Thomas Duskey[1], Arianna Rinaldi[1,2], Ilaria Ottonelli[1,2], Riccardo Caraffi[1], Chiara Alessia De Benedictis[3], Ann Katrin Sauer[3,4,5], Giovanni Tosi[1], Maria Angela Vandelli[1], Barbara Ruozi[1*], and Andreas Martin Grabrucker[3,4,5*]**

[1] Nanotech Lab, Te.Far.T.I., Department of Life Sciences, University of Modena and Reggio Emilia, 41125, Modena, Italy

[2] Clinical and Experimental Medicine PhD Program, University of Modena and Reggio Emilia, 41125, Modena, Italy

[3] Department of Biological Sciences, University of Limerick, V94 T9PX Limerick, Ireland

[4] Bernal Institute, University of Limerick, V94 T9PX Limerick, Ireland

[5] Health Research Institute (HRI), University of Limerick, V94 T9PX Limerick, Ireland

*Pharmaceutics* **2022**, *14*, 1450, doi:10.3390/pharmaceutics14071450.

Received: 2 June 2022

Accepted: 8 July 2022

Published: 12 July 2022

## Abstract

Glioblastoma Multiforme (GBM) is a devastating disease with a low survival rate and few efficacious treatment options. The fast growth, late diagnostics, and off-target toxicity of currently used drugs represent major barriers that need to be overcome to provide a viable cure. Nanomedicines (NMeds) offer a way to overcome these pitfalls by protecting and loading drugs, increasing blood half-life, and being targetable with specific ligands on their surface. In this study, the FDA-approved polymer poly (lactic-co-glycolic) acid was used to optimise NMeds that were surface modified with a series of potential GBM-specific ligands. The NMeds were fully characterised for their physical and chemical properties, and then in vitro testing was performed to evaluate cell uptake and GBM cell specificity. While all targeted NMeds showed improved uptake, only those decorated with the-cell surface vimentin antibody M08 showed specificity for GBM over healthy cells. Finally, the most promising targeted NMed candidate was loaded with the well-known chemotherapeutic, paclitaxel, to confirm targeting and therapeutic effects inC6 GBM cells. These results demonstrate the importance of using well-optimised NMeds targeted with novel ligands to advance delivery and pharmaceutical effects against diseased cells while minimising the risk for nearby healthy cells.

## 1. Introduction

Glioblastoma Multiforme (GBM) is an incredibly devastating disease that is immediately considered a grade 4 cancer diagnosis due to its very high motility and growth rate [462–465]. GBM affects approximately 17,000 people annually, creating vast amounts of healthcare and treatment costs for patients and their families that have been estimated at up to $250,000 per patient [466,467]. After diagnosis, currently accepted treatments include surgical tumour resection followed by radiotherapy and concomitant chemotherapy with temozolomide (TMZ) [468,469]. Unfortunately, studies show that even with this combined approach, less than 25% of patients survive more than two years [470,471]. The major limitations of these treatments lie in the significant side effects of the chemotherapeutics and the inability of those drugs to selectively eliminate residual GBM cells, which often leads to recurrences. In this view, nanomedicine (NMed) delivery systems offer crucial advantages. NMeds can be formulated to improve the solubility, biodistribution, and bioavailability of previously incompatible chemotherapeutics [40,341,348,472]. Moreover, targeted NMeds hold a considerable advantage over other traditional delivery methods. A rapidly increasing number of studies are being published searching for novel ligands to be incorporated onto the surface of NMeds to achieve specific delivery to organs [241,314,473,474], cells [475,476], or even intracellular locations [477–479], with several studies focusing on permeating the Blood Brain Barrier (BBB) for brain targeting [480–485]. When designing NMeds for GBM targeting, there are several barriers to overcome. For a ligand to be GBM specific, it should not only be able to target GBM cells but also to deliver the cargo across the BBB. At the same time, delivering toxic anticancer drugs to the brain often leads to severe toxicity and can drastically affect the healthy cells (astrocytes, neurons, etc.) and disrupt proper brain functions [486–491]. Thus, identifying a ligand that is non-saturable, capable of transporting nano-sized cargo, and has high affinity and specificity for GBM could significantly increase the therapeutic potential and lower the off-target toxicity of NMeds loaded with chemotherapeutic agents.

Based on the most recent literature, several ligands that have shown potential for brain targeting can also be evaluated regarding their tropism for specific cell populations such as brain cancer and GBM [386,492–494]. This work aimed to evaluate the targeting potential of different surface-decorated NMeds to determine their specificity and ability to deliver nano-sized cargo to GBM cells. Thus, four ligands were tested: two peptides, g7 and AAVF, and two monoclonal antibodies, M08J and M08. The peptides g7 and AAVF are already published for their BBB crossing potential. The g7 peptide (sequence GFtGFLS[O-ß-D-Glucose]) is an opioid receptor ligand that, when attached to the surface of NMed, has been demonstrated to cross the BBB at up to 10% of the injected dose and improve the brain delivery of a variety of therapeutic molecules [138,314,332,386,395]. The peptide AAVF (sequence FVVGQSY) is a short peptide from the adeno-associated virus protein coat, which was found through phage display studies and has recently been shown to have potential BBB targeting effects [495–498]. While this is already a huge bonus for the delivery of pharmaceutics across the BBB, these ligands have been demonstrated to have the potential for GBM specificity as well, but more thorough evaluations are required [499–502]. The two antibodies, M08J and M08, are two commercially available isoforms of Cell Surface Vimentin (CSV) antibodies that have different activities due to non-disclosed proprietary reasons [503]. CSV is an intermediate filament protein that is naturally expressed in numerous cell types such as lymphocytes, macrophages, and fibroblasts etc., and it was found to be important in epithelial–mesenchymal transition (EMT) [504,505]. Further evidence has also linked CSV to tumour growth, evidenced by its upregulation in various cancer types ranging from oral cancer, breast cancer, colon cancer, prostate cancer etc [505–509]. The presence of CSV in brain cancer and model cell lines has also been shown for numerous tumours in the CNS; however, the amounts of CSV are highly dependent on cell type, patient, and also treatment regimens [510–513]. While CSV is often upregulated in GBM, it has also been shown to be expressed at high levels in the brain endothelium cells,

suggesting that these ligands could help in both BBB crossing and specifically targeting GBM cells [513–516].

To evaluate their targeting potential, polymeric NMeds composed of the biodegradable and biocompatible polymer poly(D,L-lactic-co-glycolic) acid (PLGA) were optimised and fully characterised for improved surface modification with the ligands. The formulation and surface modification protocols were further optimised to reduce reagent loss and make the formulation and modification more "green". Optimised surface decorated NMeds were then tested *in vitro* to assess their cell uptake in GBM (C6) and healthy astrocyte (DI TNC1) cell cultures, as well as their effect on cell viability. Co-culture experiments further demonstrated the targeting capacity of these ligand-targeted NMeds and their effects on cell growth. Finally, the most promising targeted NMed candidate was loaded with the anticancer drug paclitaxel (PTX) to evaluate its anti-cancer effect on GBM cells. These results revealed the potential of NMeds with the novel ligands to enhance transport, cell uptake, and specificity to GBM cells. This improvement could greatly increase the chances of creating a functional therapeutic that minimises damage to the nearby cells in the central nervous system (CNS) while increasing chemotherapeutic effectiveness.

## 2. Materials and Methods

### *2.1 Materials*

Resomer® RG 503H Poly(D,L-lactide-co-glycolic) acid 50:50 (PLGA) MW 11000-12000 was purchased from Evonik (Essen, Germany). 4-Morpholineethanesulfonic acid (MES, MW 195.24), N-(3-Dimethylaminopropyl)-N′-ethylcarbodiimide (EDC, MW 155.24), N-Hydroxysuccinimide (NHS, MW 115.09); Pluronic® F68, D-(+)-Trehalose dihydrate (MW 378.33), acetone, acetonitrile (ACN), barium chloride ($BaCl_2$), and iodine ($I_2$) were purchased from Sigma-Aldrich (Milan, Italy). 1-[6-(6-aminohexylamino)-6-oxohexyl]-3,3-dimethyl-2-[(1E,3E,5E)-5-(1,3,3-trimethylindolin-2-ylidene)penta-1,3-dienyl]-3H-indolium chloride hydrochloride (Cy5 amine, MW 653.77) was purchased from Lumiprobe (Hannover, Germany). PAAVF peptide (MW 943.47) was purchased from GenScript (Piscataway, New Jersey, USA). The g7 peptide (MW 888.97) was purchased from Mimotopes Pty Ltd (Mulgrave, Victoria, Australia). Cell Surface Vimentin (CSV) monoclonal antibody, clone 84-1, H00007431-M08 (M08) and Cell Surface Vimentin (CSV) monoclonal antibody, clone 84-1, H00007431-M08J (M08J), were purchased from Abnova (Taipei, Taiwan). Dichloromethane (DCM), trifluoroacetic acid (TFA), and potassium iodide (KI) were purchased from Carlo Erba (Milan, Italy). Hydrochloric acid 36% (HCl) was purchased from Avantor (Radnor Township, Pennsylvania, USA). Paclitaxel (PTX, MW 853.906, CAS 33069-62-4) was purchased from Selleckchem (Houston, TX, USA). MilliQ water was purified by a Millipore system (Millipore, Bedford, MA, USA). All chemicals used were of analytical grade. If not otherwise mentioned, all other chemicals and reagents were purchased from Sigma Aldrich (Milan, Italy).

*2.2. NMed formulation*

2.2.1 Synthesis of PLGA-Cy5

PLGA was conjugated to Cyanine 5 (Cy5) via an amide bond formation using an already optimised protocol [235,428]. Briefly, PLGA (1 g, 88 μmol) was solubilized in anhydrous dioxane (15 mL) under magnetic stirring at 10 °C. The PLGA was activated by added NHS (12 mg) and DCC (22 mg) and left to react at room temperature for 4 h. The by-product, dicyclohexylurea, was removed by paper filtration, and cyanine 5 amine (43 mg) was added to the purified activated polymer. The pH was adjusted to 7-8 with TEA, and the reaction was allowed to continue for 7 h at room temperature. Next, the conjugated polymer was purified by precipitation in ether. The basic pH was neutralised by the addition of ether saturated with HCl. Finally, the polymer was precipitated in methanol overnight, followed by several steps of centrifugation at 10,000 rpm for 10 min (ALC multispeed centrifuge PK 121) to separate the product. The PLGA-Cy5 product was stored at -20°C for future use.

2.2.2 Optimisation of the NMed formulations

PLGA NMeds were formulated via the nanoprecipitation technique. First, PLGA and the PLGA-Cy5 conjugate were solubilised in 4 ml of acetone and vortexed (total polymer weight = 50 mg) (Advanced Vortex Mixer ZX3, Velp® Scientifica). This solution was added dropwise into a beaker containing 12.5 ml of Pluronic® F68 under magnetic stirring (Multistirrer, Magnetic Stirrer Velp® Scientifica, Usmate Velate, Italy) for 2 hours at room temperature. The NMed suspension was purified by centrifugation at 9,700 rpm for 10 minutes and resuspended in 4 mL of Pluronic® F68 1.5% w/v. The NMed suspensions were stored at 4°C for further analysis.

This general method was used to optimise the amount of PLGA-Cy5, ranging from 0.1 – 4% w/w of total PLGA. Further optimizations were then performed by

maintaining the amount of PLGA-Cy5 constant at 0.2% w/w while varying the amount of Pluronic® F68 concentration in the aqueous phase (12.5 mL) from 0 – 3% w/v. Finally, as previously indicated, the purified by centrifugation and the NMeds were resuspended in 4 mL of 1.5% w/v Pluronic® F68.

*2.3. Optimisation of the post-modification surface modification reaction*

Reaction of the ligands to the NMed surface was performed in 0.1 M MES at pH 4.9. To achieve this composition, NMeds were initially centrifuged after formulation and resuspended in MES solution 0.1 M; however, this method required two centrifugation steps which hampered the NMed stability and led to aggregation. To overcome this, the first centrifugation was avoided by adding 2 mL of MES solution 5X (0.5 M) directly to the NMed suspension (10 mL, approx. 4 mg/mL) to achieve a final concentration of 100 mM pH 4.9. To the buffered NMed suspension, 300 mg of EDC were added and left to react for 10 min, followed by the addition of 100 mg of NHS. This reaction was left stirring at room temperature for 20 minutes, and the activated NMeds were characterised for their physicochemical characteristics, weight yield %, and % residual surfactant.

To complete the post-modification reaction, 1 or 10 μg of each ligand, g7, AAVF, M08J, or M08, were added to the activated NMed suspension(10 μg / 40 mg NMeds). The reaction was maintained stirring for 1.5 hours at room temperature. The suspension of surface-modified NMeds was purified by centrifugation for 10 minutes at 9,700 rpm to form a pellet. The supernatant was discarded, and the pellet was resuspended in 4 mL of Pluronic® F68 1.5% w/v and stored at 4 - 8°C until used.

*2.4. NMed characterisation*

2.4.1 Size and Zeta Potential Analysis

The particle size, Polydispersity Index (PDI), and Z-potential were measured by diluting 10 μL of the purified NMeds in 1 mL of MilliQ water (final concentration of 0.01 mg/mL) and analysed using Photon Correlation Spectroscopy (PCS): Laser 4 mW He–Ne, 633 nm, Laser attenuator Automatic, transmission 100–0.0003%, Detector Avalanche photodiode, Q.E. > 50% at 633 nm, T = 25°C (Zetasizer Nano ZS, Malvern, Malvern, UK). All samples were analysed in triplicate of at least three independent NMed formulations.

2.4.2 Microscopy analysis by AFM

The morphology of the targeted NMeds was evaluated by Atomic Force Microscopy (AFM, Park Instruments, Sunnyvale, CA, USA) at RT operating in air and non-contact mode using triangular silicon tips. The resonant frequencies of the cantilever were found to be in the range of 160 kHz. Before the analysis, the NMeds were diluted to 0.01 mg/mL, applied to a small mica disk (1 cm × 1 cm), and analysed after removing the excess solution. The topographical images were flattened using second-order fitting to remove sample tilt.

2.4.3 Weight yield

Purified NMed aliquots of 0.5 mL were lyophilised (LyoLab 3000, Heto-Holten, ThermoFisher Scientific, Waltham, MA) in pre-weighed Eppendorf tubes, and the weight yield % was calculated as follows:

yield % = ((mg product - mg Pluronic® F68 used in resuspension)/mg total PLGA) * 100

2.4.4 Pluronic® F68 quantification

The residual amount of Pluronic® F68 remaining in the formulated NMeds was evaluated using a previously published colourimetric method [517]. NMeds were solubilized in 0.5 mL of DCM and then slowly added to 10 mL of water. The organic solvent was evaporated by stirring at room temperature to precipitate the PLGA, which was then removed by filtration (cellulose nitrate filter, porosity 0.45 m, Sartorius, Firenze, Italy). 2 mL of the aqueous solution were treated with 2 mL of 0.5% w/v $BaCl_2$ in HCl 1 N and 0.5 mL of $I_2$/KI (0.05 M/0.15 M). This mixture was incubated for 10 minutes in the dark. Then the Pluronic® F68 concentration was calculated using a spectrophotometer (Model V530, Jasco, Cremella, Italy) measuring the absorbance at 540 nm, using a calibration curve made from stock solutions of Pluronic® F68 prepared under the same experimental conditions. Linearity was found in the range of 4 – 48 μg/mL of Pluronic® F68 ($R^2$ = 0.9927). Due to the sensitivity of the $I_2$/KI aqueous solution to heat and light, the standard curve was calculated fresh each day. The analysis was performed in triplicate on three different NMed formulations. The residual Pluronic® F68 was calculated as follows:

% residual Pluronic® F68 = (quantified mg Pluronic® F68/mg NMeds) * 100

### 2.4.5. Storage Stability

NMed suspensions were aliquoted (50 μL), stored at 4°C, frozen at -20°C, or lyophilised over 3 weeks. Frozen and lyophilized samples were supplemented with the cryoprotectant trehalose at ratios ranging from 0.1 - 3 w/w of the NMeds. After 3 weeks, the samples were thawed, brought to room temperature, and analysed for size, PDI, and Z-potential.

### 2.4.6 Paclitaxel NMed formulations

Paclitaxel (PTX) loaded PLGA NMeds were formulated using a modified protocol from the previous nanoprecipitation (without the presence of PLGA-Cy5). First,

PTX (0.5 mg) was solubilized in 1 mL of acetone and added to 50 mg of PLGA solubilized in 3 ml of acetone to arrive at 4 mL. The solution was vortexed (Advanced Vortex Mixer ZX3, Velp® Scientifica) and added dropwise into a beaker containing 12.5 ml of Pluronic® F68 1.5% w/v, and the acetone was evaporated by magnetic stirring (Multistirrer, Magnetic Stirrer Velp® Scientifica) for 2 hours at RT. Following formation, the NMeds were either modified with M08 as previously described using the post-modification method or subjected to a mock post-modification reaction without M08 in the solution (non-modified). The NMeds were purified by centrifugation at 9,700 rpm for 10 minutes, resuspended in 4 mL of Pluronic® F68 1.5% w/v, and analysed for size, PDI, and Z-potential as previously described.

The amount of PTX in the NMeds was quantified using HPLC analysis (Jasco Europe, Cremella, Italy): the system consisted of a PU-2089 Pump with a 50 µL sample loop (model 775i). The column used for analysis was a 5HC-C18 250x4.6 mm (Agilent, Cernusco sul Naviglio, Italy). The mobile phases consisted of: A) $H_2O$ + 0.1% (v/v) TFA and B) ACN. The optimised gradient consisted of increasing phase B from 50-90% ACN over 10 minutes which yielded to a PTX retention time of 7 min. The absorbance was monitored at 210 nm using a UV detector (Jasco UV-1575). NMeds (~ 2 mg) were lyophilized, and the paclitaxel was liberated from the NMeds by adding 0.5 mL DCM and 0.5 mL of ACN. The solution was then magnetically stirred until all the DCM evaporated, precipitating the PLGA. ACN was then added to arrive at a final volume of 1 mL, and 50 µL were injected into the HPLC. The encapsulation efficiency of PTX (% EE) and loading content (% LC) were calculated using a standard curve calculated with pure PTX in ACN. The following formulas were used:

% EE = (measured PTX / feeding PTX) * 100

% LC = (measured PTX / amount of NMeds analysed) * 100

*2.5. In vitro studies*

2.5.1 Cell culture

C6 Rat GBM cells (ATCC/LGC Standards, UK) were cultured in Ham's F-12K medium with 20% FBS and 1% penicillin/streptomycin (Sigma Aldrich/Merck Life Science, Ireland). DI TNC1 Rat Astrocyte cells (ATCC/LGC Standards, UK) were grown in DMEM High Glucose medium with 10% FBS and 1% penicillin/streptomycin. All cell lines were kept at 37°C and 5% $CO_2$.

2.5.2 NMed uptake studies in C6 cells

C6 cells were seeded at a density of 30,000 cells on PLL-coated glass coverslips inserted in a 24 well plate and grown overnight. Calcein-AM dye was prepared in a stock solution of 33.51 mM in DMSO and used at a final working concentration of 3 μM in an F12-K medium. The cells were incubated with Calcein-AM for 30 min at 37°C, after which the staining solution was removed and replaced with fresh media.

Control (non-targeted) and targeted NMeds (with 1 μg or 10 μg of ligand) were added to the cell media at the final concentrations of 25, 50, or 100 μg/mL. After either 3 or 24 hours, the media was removed, and cells were fixed with 4% PFA. Next, cells were washed 3X with 1X PBS, and the cell nuclei were stained with DAPI. The coverslips were mounted using Vecta Mount (Vector Laboratories, USA). The cells were imaged using a Molecular Devices Imagexpress high content imaging confocal microscope, and image analysis was performed using ImageJ (v. 1.52q). Cell health was assessed by measuring the number of DAPI-stained nuclei per optic field of view, during which bright and condensed nuclei indicating cell death were excluded. NMed uptake was measured by quantifying intracellular Cy5 fluorescence intensity normalised for background fluorescence detected in untreated cells.

2.5.3 NMed uptake study in co-culture (C6 Glioblastoma/DI TNC1 Astrocytes)

C6 cells were grown in t12 flasks. For the Calcein-AM staining, the old F12K medium was removed, the flask was washed twice with 1X PBS, and F12K supplement/serum-free medium (2 mL) was added to the cells containing the dye (final concentration 2 μM). The cells were incubated at 37°C for 30 min, after which the medium with the dye was removed, the cells were washed twice with 1X PBS, and fresh F12K complete medium (+ supplements and FBS) was added. Subsequently, the cells were detached with Trypsin/EDTA and the C6 cells were seeded at low density in a 96 multi-well plate (2,000 cells/well, 100 μL per well). The DI TNC1 Astrocytes were grown in t12 flasks in parallel, detached with Trypsin/EDTA, and seeded at 4,000 cells/well (adding 100 μL per well). The co-cultures were grown overnight, and then the medium was removed from each well and replaced with 100 μl of complete F12K and 100 μL of complete DMEM. The NMeds were added to the co-culture at concentrations of 50 μg/mL and 100 μg/mL (either control NMeds (non-targeted) or each of the targeted NMeds (at 1 μg or 10 μg ligand in the post-modification reaction)). The co-culture was incubated for 3 hours at 37°C, the media was removed, and the cells were fixed with 4% PFA. Following fixation, the cells were washed 3X with 1X PBS, and the cell nuclei were stained with DAPI. Coverslips were mounted using Vecta Mount (Vector Laboratories, USA). Cells were imaged using a Molecular Devices Imagexpress high content imaging confocal microscope, and image analysis was performed using ImageJ (v. 1.52q). Cell health was assessed by measuring the number of all DAPI positive nuclei, and DAPI positive nuclei in Calcein-AM positive cells per optic field of view in which bright and condensed nuclei indicating cell death were excluded. NMed uptake was measured by quantifying intracellular Cy5 fluorescence intensity normalised for background fluorescence detected in untreated cells.

2.5.4 PXT NMed toxicity analysis

C6 cells were seeded at a density of 5,000 cells/well on a PLL-coated E-Plate VIEW 16 plate (ACEA Biosciences, San Diego, USA). The C6 cells were grown for 12.5 h before treatment with NMeds delivering the equivalent of 500 nM PTX and 500 nM free PTX and then monitored for another 14 h. Cell impedance was measured every 15 min using an ACEA xCELLigence RCTA DP system, where a decrease in impedance is associated with the detachment of cells and, therefore, a sign of cell death.

2.5.5 PXT NMed apoptosis assay

Healthy and apoptotic cells were measured using a healthy/apoptotic/necrotic cell detection kit (Promokine) according to the manufacturer's protocol. In brief, 30,000 C6 cells were seeded on PLL-coated glass coverslips inserted in a 24 well plate and grown overnight. NMeds were added to the cell media at concentrations to deliver the equivalent of 10, 50, 100, and 500 nM PTX. After 3 h of incubation, the medium was removed, cells were washed with 1X binding buffer, and incubated for 15 min at RT protected from light with a staining solution containing 100 μL of 1X binding buffer, 5 μL of FITC-Annexin V, and 5 μL of Hoechst 33342. Then, the cells were washed twice with 1X binding buffer and fixed in a solution containing 4% PFA in 1X PBS and 1.25 mM $CaCl_2$ at RT for 15 min. Coverslips were mounted using Vecta Mount (Vector Laboratories, USA), and the cells were imaged using an Olympus BX35 microscope. Image analysis detecting the total number of cells labelled by Hoechst and the number of Annexin V positive cells was performed using ImageJ (v. 1.52q).

*2.6. Statistical analysis*

Statistical analysis was performed using the Student's t-test for pairwise comparisons. A two-way repeated measures ANOVA followed by Tukey's Post

hoc test was performed for multiple comparisons over time. A one-way ANOVA analysis followed by Tukey's Post hoc test was used for multiple comparisons at one time point. Significance is indicated in the figures as * $p < 0.05$, ** $p < 0.01$, *** $p < 0.001$, **** $p < 0.0001$. Statistical analyses were done using GraphPad Prism 6 (GraphPad Holdings, San Diego, CA, USA). All samples were performed with at least n = 3 and expressed as an average with the standard error (SEM).

## 3. Results

### *3.1 NMed Optimisation*

The first step in creating a targeted NMed system is to optimise the formulation to be stable and reproducible. Starting from an already established protocol for formulating PLGA NMeds, the physical characteristics (size, Z-potential, PDI, and weight yield %) were used to optimise the amount of the fluorophore-conjugated polymer (PLGA-Cy5 0.1 - 4% w/w to the total polymer amount) and % Pluronic® F68 (0 - 3% w/v) used in the aqueous phase (Table S1, S2). The optimal values were chosen and held constant for all of the following experiments (0.2% PLGA-Cy5 and 1.5% Pluronic® F68) due to the NMed characteristics (size ~157 nm, PDI 0.07, Z-potential -46 mV), reproducibility, and high weight yield percent (87%) (Table 1, first line). Regarding the residual amount of Pluronic® F68 remaining in the matrix, no statistical differences were found when increasing the amount of surfactant used, remaining between 10 - 13% of the weight of the NMeds. This is in accordance with previously published results for PLGA-based NMeds and is an amount already demonstrated to be non-toxic (Table 1) [351,518].

With the matrix components established, the post-modification reaction to decorate the surface of the NMeds with each ligand was optimised. Mock reactions were performed to ensure that the peptide coupling reaction (EDC and NHS in MES 100 mM at pH 4.9) did not negatively influence the characteristics of the assembled NMeds. While the presence of the reagents and the buffer did not have any significant effect on the NMed characteristics, repetitive centrifugations led to a decreased weight yield from 90% to less than 30% with five cycles of centrifugation due to aggregation and poor resuspension (Table S3). To circumvent this problem, the first centrifugation step to purify the formed NMeds was removed, and the post-modification reaction was performed directly by adding concentrated 5X MES (500 mM) to the NMed formulation. This was possible because very little free PLGA was available, as suggested by the high weight yield (87%), and Pluronic® F68 lacks any free amine or acid groups which

could cause possible side reactions between the reagents and interfere in the surface modification. These reaction conditions had no significant effect on the size, PDI, or Z-potential of the NMeds (166 nm, 0.12, -32 mV) and, therefore, were used for surface modification with either 1 or 10 μg of each ligand (1 or 10 μg per 40 mg NMeds) which were then fully characterised. The addition of the different ligands had minor effects on the physical properties of the NMeds, maintaining the beneficial delivery characteristics ranging from 155 to 170 nm, PDI ~0.1, and a surface charge between -24 and -33 mV (Table 1). The high weight yields were maintained, although they exceeded 100%, which was probably due to residual salt from the reaction buffer that was not completely removed with the single centrifugation step. These physical characteristics were also supported by AFM microscopy, showing NMeds ranging from 100 - 200 nm, with good homogeneity and a spherical shape with no differences between the different ligand surface modifications (Figure 1).

**Table 1.** Physico-chemical characteristics of ligand modified NMeds. Results are given as the median plus/minus the standard deviation (SD).

| NMed formulation | Ligand Amount (μg) | Size (nm) | PDI | Z potential (mV) | % Residual surfactant | % Weight yield |
|---|---|---|---|---|---|---|
| Optimised NMed | 0 | 157 ± 8 | 0.07 ± 0.01 | -45.6 ± 4 | 12 ± 5 | 87 ± 9 |
| NMeds with mock reaction | 0 | 166 ± 10 | 0.12 ± 0.01 | -33 ± 10 | 10 ± 7 | 93 ± 6 |
| g7-NMeds | 1 | 155 ± 13 | 0.09 ± 0.03 | -34 ± 11 | 9 ± 8 | 92 ± 5 |
| PAAVF-NMeds | | 156 ± 9 | 0.08 ± 0.01 | -25 ± 9 | 10 ± 5 | 112 ± 10 |
| M08J-NMeds | | 161 ± 11 | 0.11 ± 0.02 | -31 ± 8 | 11 ± 5 | 102 ± 7 |
| M08-NMeds | | 164 ± 10 | 0.16 ± 0.01 | -26 ± 10 | 11 ± 6 | 97 ± 9 |
| g7-NMeds | 10 | 159 ± 10 | 0.08 ± 0.01 | -31 ± 13 | 8 ± 9 | 104 ± 5 |
| PAAVF-NMeds | | 156 ± 12 | 0.09 ± 0.02 | -29 ± 8 | 10 ± 5 | 96 ± 3 |
| M08J-NMeds | | 159 ± 11 | 0.10 ± 0.02 | -29 ± 11 | 9 ± 9 | 110 ± 4 |
| M08-NMeds | | 160 ± 14 | 0.18 ± 0.03 | -32 ± 9 | 11 ± 6 | 119 ± 4 |

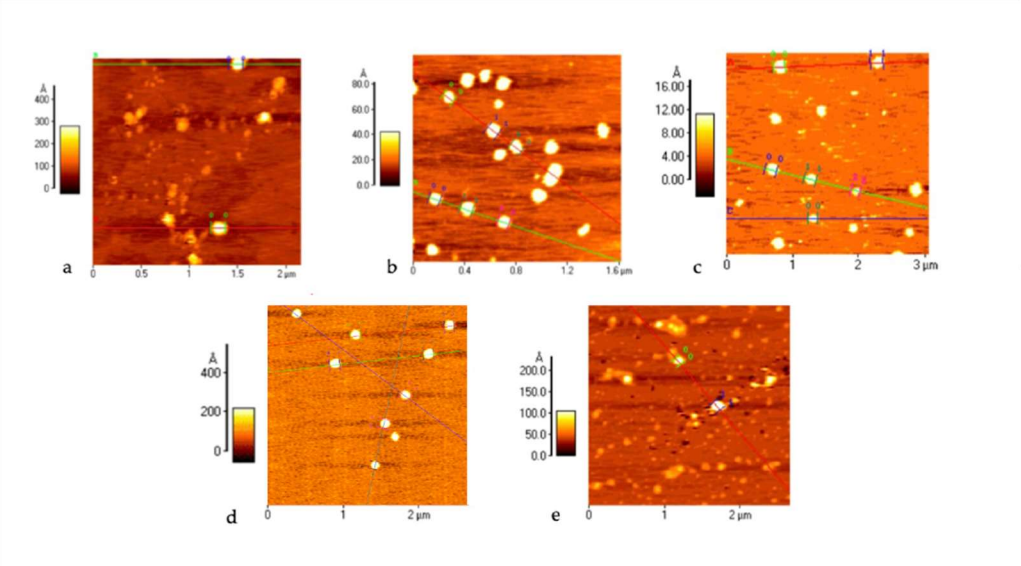


**Figure 1**. AFM Microscopy analysis of NMeds: a) non-modified NMeds; b) g7-NMeds; c) PAAVF-NMeds; d) M08J-NMeds; and e) M08-NMeds. All images were obtained with NMeds modified with 10 μg of ligand.

Finally, with the intent to create stable drug-loaded NMeds, storage stability optimisation studies were performed. NMeds formed with these optimised parameters remained stable under numerous storage conditions over three weeks, including at 4°C, under freeze-thaw conditions, and even when lyophilised (Table S4).

### *3.2 C6 Targeting Studies*

To investigate whether NMed uptake into GBM cells is ligand-dependent, targeting studies were performed using C6 GBM cell cultures. Imaging-based uptake studies were performed at both 3 and 24 hours post addition of the fluorescent Cy5 containing NMeds (50 μg/mL) using the formulations with 1 μg of ligand in the post-modification reaction. Significant differences were observed even after only 3 hours (Figure 2a), where all targeted NMeds, independent of the ligand, demonstrated higher cell uptake than the non-targeted control; however, after 24 hours, the difference in targeted and non-targeted NMeds lost significance with all samples having similar uptake even though the total uptake increased

compared to 3 hours. This could be explained by the fact that NMeds dispersed in the cell medium were not removed and remained disposed to nonspecific uptake caused by the division and metabolism of the rapidly growing cells (Figure 2b).

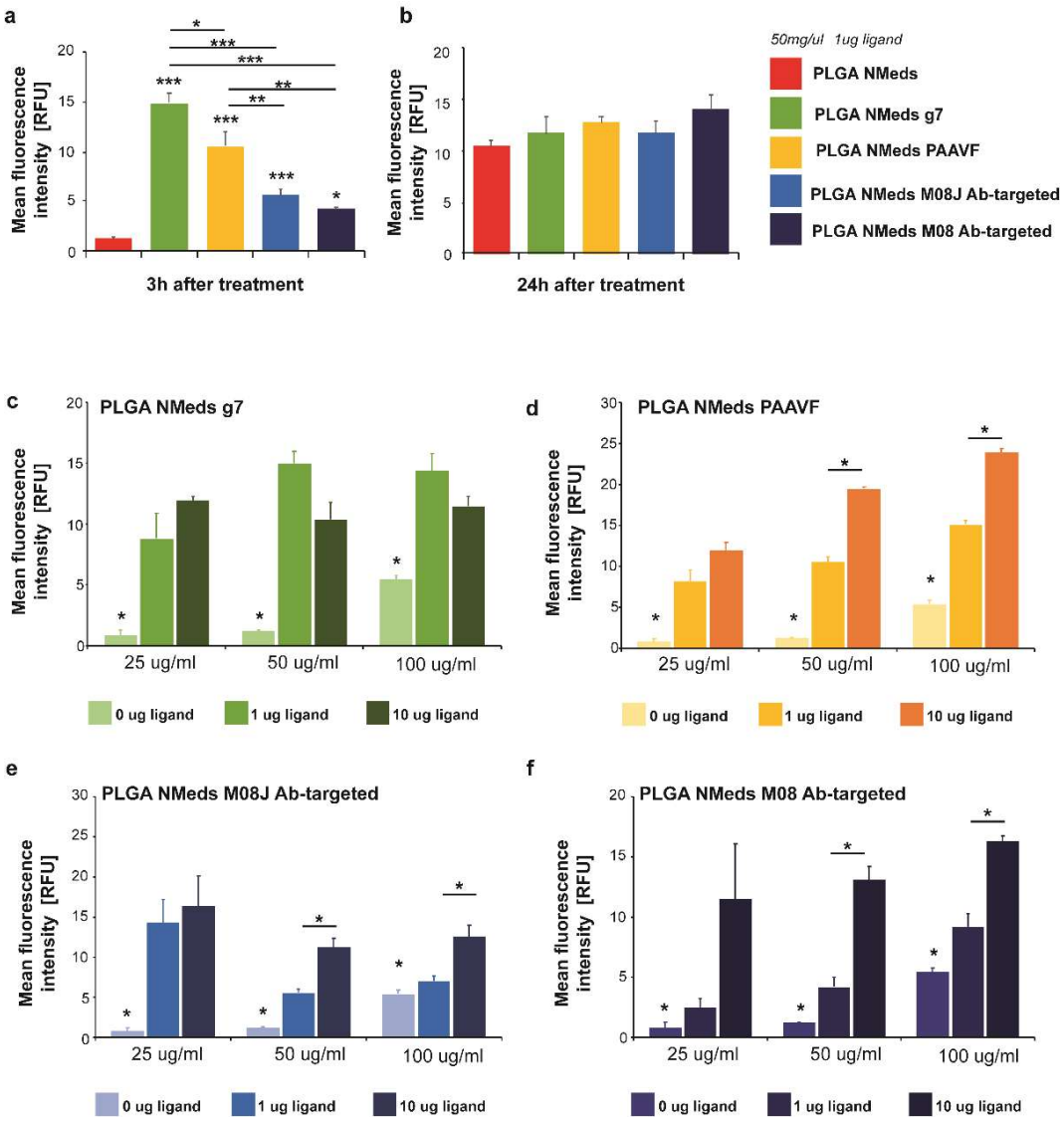


**Figure 2. C6 cell** uptake of 50 μg/mL targeted and non-targeted NMeds at a) 3 h and b) 24 h after administration. The relative fluorescence intensity of Cy5 intracellular signals (normalised to background fluorescence of untreated cells) was measured in 10 cells from n = 3 samples per condition. c-f) Uptake of non-modified and targeted NMeds surfaced modified with 0, 1, or 10 μg of each ligand and administered at concentrations of 25, 50, or 100 μg/mL. The relative fluorescence intensity of Cy5 intracellular signals (normalised to background fluorescence of untreated cells) was measured in 10 cells from n = 3 samples per condition. Statistical analysis was performed with one-way ANOVA and Post hoc test, * $p < 0.5$, ** $p < 0.1$, *** $p < 0.01$, *** $p < 0.001$. Full statistical analysis is available in Supplementary material Table S5.

To maximise targeted uptake and minimise the amount of non-specific cell internalization, 3-hour incubations were performed to test the dependence of ligand amount in the surface modification and NMed concentration on the uptake. NMeds modified with 0, 1, or 10 μg of each ligand were incubated for 3 hours at concentrations of 25, 50, or 100 μg/mL(Figure 2c-f). As previously observed in the time course experiment, all targeted NMeds showed increased uptake over non-targeted controls independent of both ligand amount and NMed concentration. Three observable trends could be reported when comparing these two variables between the different ligand-modified NMeds (concentration and ligand). First, the uptake of g7-targeted NMeds neither increased depending on ligand amount in the reaction nor the total NMed concentration (Figure 2c). For the M08J-modified NMeds, increasing the concentration from 25 to 100 μg did not lead to statistically increased uptake; however, there was a statistical difference at higher NMed concentrations when the amount of ligand in the post-modification reaction was increased from 1 to 10 μg (Figure 2e). Lastly, PAAVF and M08-modified NMeds showed statistical increases in uptake dependent on both the ligand amount and NMed concentration (Figure 2d,f).

Further analysis of cell uptake determined the cell viability based on the number of cells remaining per field of vision (Figure 3). Cells were treated with 50 or 100 μg/mL of NMeds surface modified with 10 μg of each ligand. It was apparent that at these concentrations, the unmodified and targeted NMeds did not affect cell proliferation. The only exception was the M08 modified NMeds. At 100 μg/mL, no variation in cell number was seen. This was probably due to the presence of larger NMed aggregates that inhibited the uptake; however, at 50 μg/mL, M08 targeted NMeds led to a statistical decrease in cell number.

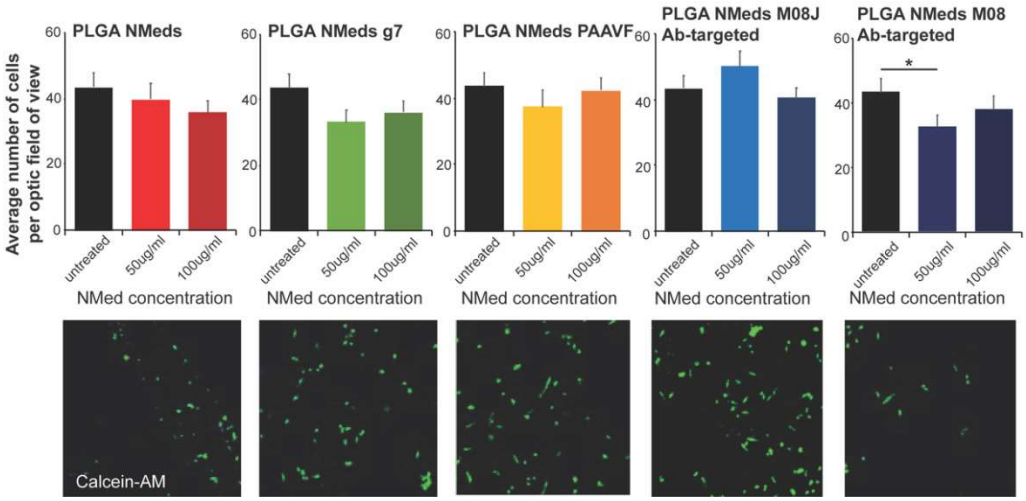


**Figure 3**. Cell growth inhibition studies. Quantification (top) of the number of cells per field analysed after incubating NMeds at a concentration of 50 or 100 μg/mL for 3 hours and visualised by confocal microscopy (bottom). The number of cells visualised by DAPI and Calcein-AM staining per optic fields of view (OFV) was measured by counting n = 10 OFV for each condition. Statistical analysis was performed with one-way ANOVA and Post hoc analysis, * $p < 0.05$.

### *3.3 Co-Culture Studies*

To investigate whether the ligands facilitated selective uptake into GBM cells, co-culture experiments were performed using both rat C6 GBM cells that are derived from astrocytes and "healthy" rat DI TNC1 astrocytes. The C6 GBM cells were labelled with Calcein-AM in the co-culture to distinguish the difference between the cells. The fluorescence of internalised NMeds in the co-cultured cells demonstrated that non-targeted, g7 and M08J-targeted NMeds showed comparable levels at 50 or 100 μg/mL. The similar results between non-targeted and targeted NMeds indicate a natural and non-specific uptake of these NMeds into both cell types that is not dependent on targeting. There was a slight, but not statistically significant, increase in C6 cell uptake of AAVF-targeted NMeds. Uniquely M08 targeted NMeds showed a statistically increased uptake into GBM cells over healthy astrocytes (Figure 4a,b).

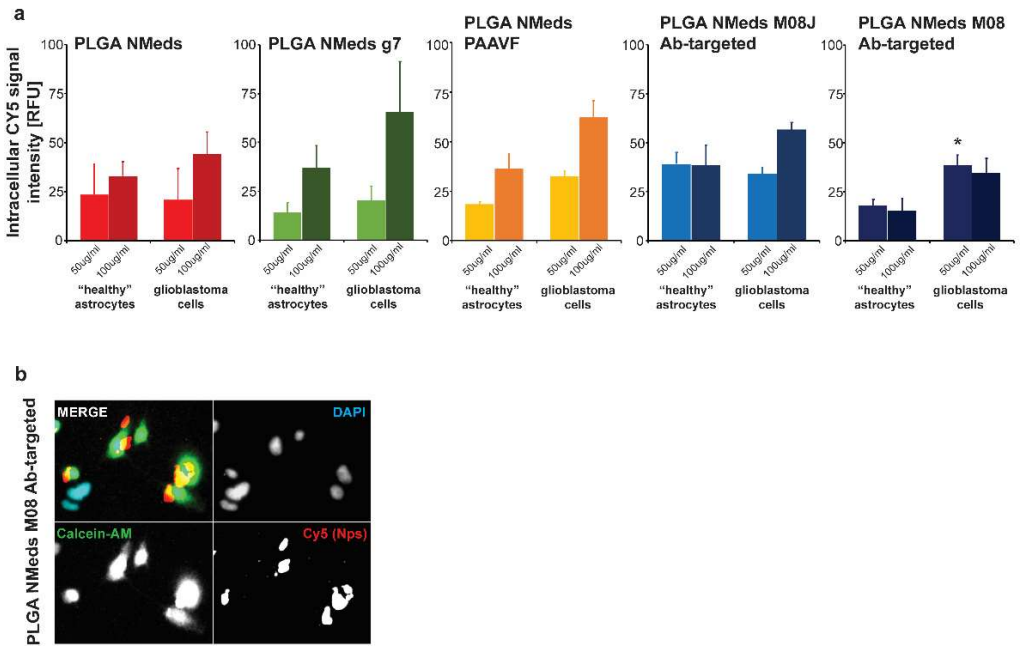


**Figure 4**: Cell uptake and growth inhibition studies. a) Uptake in C6 (GBM) and DI TNC1 ("Healthy" astrocytes) cells after the administration of 50 and 100 μg/mL of targeted and non-targeted NMeds with 10 μg of each ligand after 3 h. Statistical analysis was performed with one-way ANOVA and Post hoc analysis, * $p < 0.05$; $n = 8$. b) a representative image of M08 targeted NMeds, colocalizing with C6 but not DI TNC1 cells. Red: Cy5 (NMeds), blue: DAPI, green: Calcein-AM.

Moreover, the experiment was repeated to analyse the total number of each cell type (Figure 5). Untreated co-culture wells showed that the cell growth between the two cell lines led to a ~80:20 ratio of C6:DI TNC1 cells. This could be explained by the faster cell division rate of C6 cells over healthy astrocytes and the potentially invasive nature of C6 cells, which could lead to them spreading out and occupying more surface space in the well, "choking out" astrocyte growth. This growth ratio was maintained with non-targeted, AAVF, and g7-targeted NMeds, suggesting no effect on cell proliferation; however, M08J targeted NMeds did show a difference. Here, the "healthy" astrocytes increased to up to 40%, with a corresponding decrease in C6 cells to 60%.

Nevertheless, the most potent effects were seen with M08 targeted NMeds, which inverted this ratio with "healthy" astrocytes constituting 60% of the culture with only 40% GBM cells. Supporting other literature for CSV antibodies [506], this result demonstrates a biological effect of these antibodies to decrease GBM growth

and allowing the healthy astrocytes to grow more freely. This effect could further promote the delivery and efficacy of anticancer therapeutics using these types of targeted NMeds.

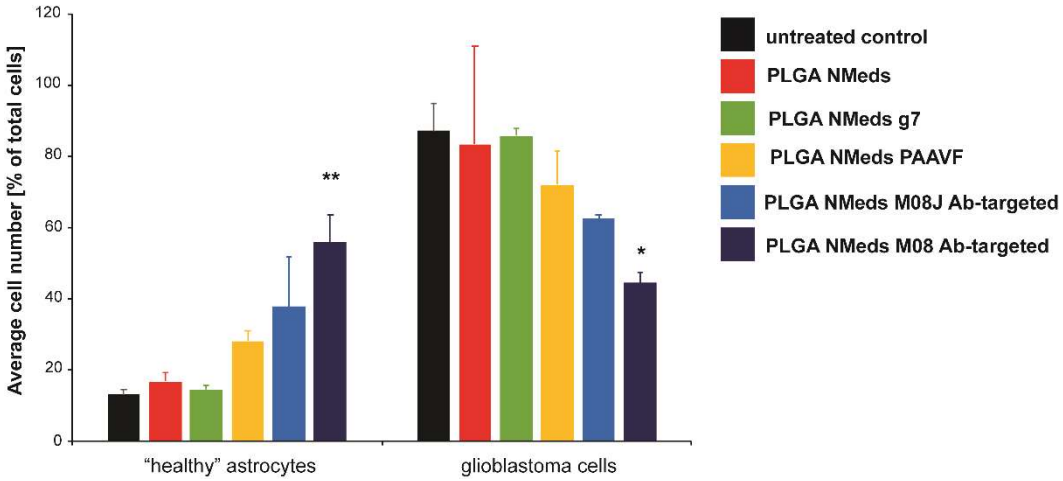


**Figure 5**: The confocal microscopy quantification ofC6 and DI TNC1 cell numbers per optic field of view (OFV) after a 3 h incubation with 50 μg/mL of NMeds modified with 10 μg of ligand. All experiments were performed in triplicate (n=3), and the number of cells visualised by DAPI and Calcein-AM staining per OFV was measured by counting 8 OFV for each condition. Statistical analysis was performed with one-way ANOVA, * $p < 0.05$, ** $p < 0.01$.

### *3.4 Chemotherapeutic Drug Delivery with Targeted NMeds*

Finally, if the GBM-specific delivery of targeted NMeds loaded with the chemotherapeutic drug paclitaxel (PTX) were tested compared to free drug. In the first set of experiments, C6 GBM cells were treated with NMeds delivering the equivalent of 10, 50, 100, and 500 nM with the same concentrations of free PTX used as controls-. By analysing FITC-Annexin V as an apoptotic cell marker, PTX-loaded NMeds (targeted and non-targeted) induced higher apoptosis rates than free PTX. Furthermore, M08-targeted NMeds outperformed free PTX and led to an increased number of apoptotic cells compared to non-targeted NMeds. While the toxicity of free PTX significantly increased from 50 to 500 nM, no further increase was observed for PTX-loaded M08-NMeds even at low concentrations, which already reached almost 100% of apoptotic cells at 50 nM. These results indicate the

high therapeutic potential of these targeted NMeds, which are much more toxic (100% compared to40%) even at drug concentrations 10x lower than the free drug (Figure 6a,b).

Next, a label-free cell health assay based on impedance measurements was performed to understand whether the increase in apoptotic cells translates to an increase in cell death (Figure 6c,d). C6 GBM cells were treated with NMeds delivering the equivalent of 500 nM PTX and compared to 500 nM of free PTX since a significant effect of free PTX was previously seen at this concentration. Cells were seeded and grown until confluent and monitored for 12.5 hours before treatment (Figure 6c). Cell impedance was measured every 15 minutes, and cell death was evaluated as a decrease in impedance. Before treatment, no significant difference between cells assigned to different treatment groups was observed. Cells were then treated with NMeds or free PTX and monitored for another 14 hours. A significant effect of treatment, time, and treatment x time interaction was observed comparing empty with PTX-loaded NMeds. Non-targeted and M08 PTX-loaded NMeds induced significantly more cell death than empty NMeds; however, over the time course, M08 targeted PTX-loaded M08 NMeds were significantly more toxic than all other samples, including the non-targeted PTX-loaded NMeds. This difference remained significant even at the endpoint measurement (Figure 6d).

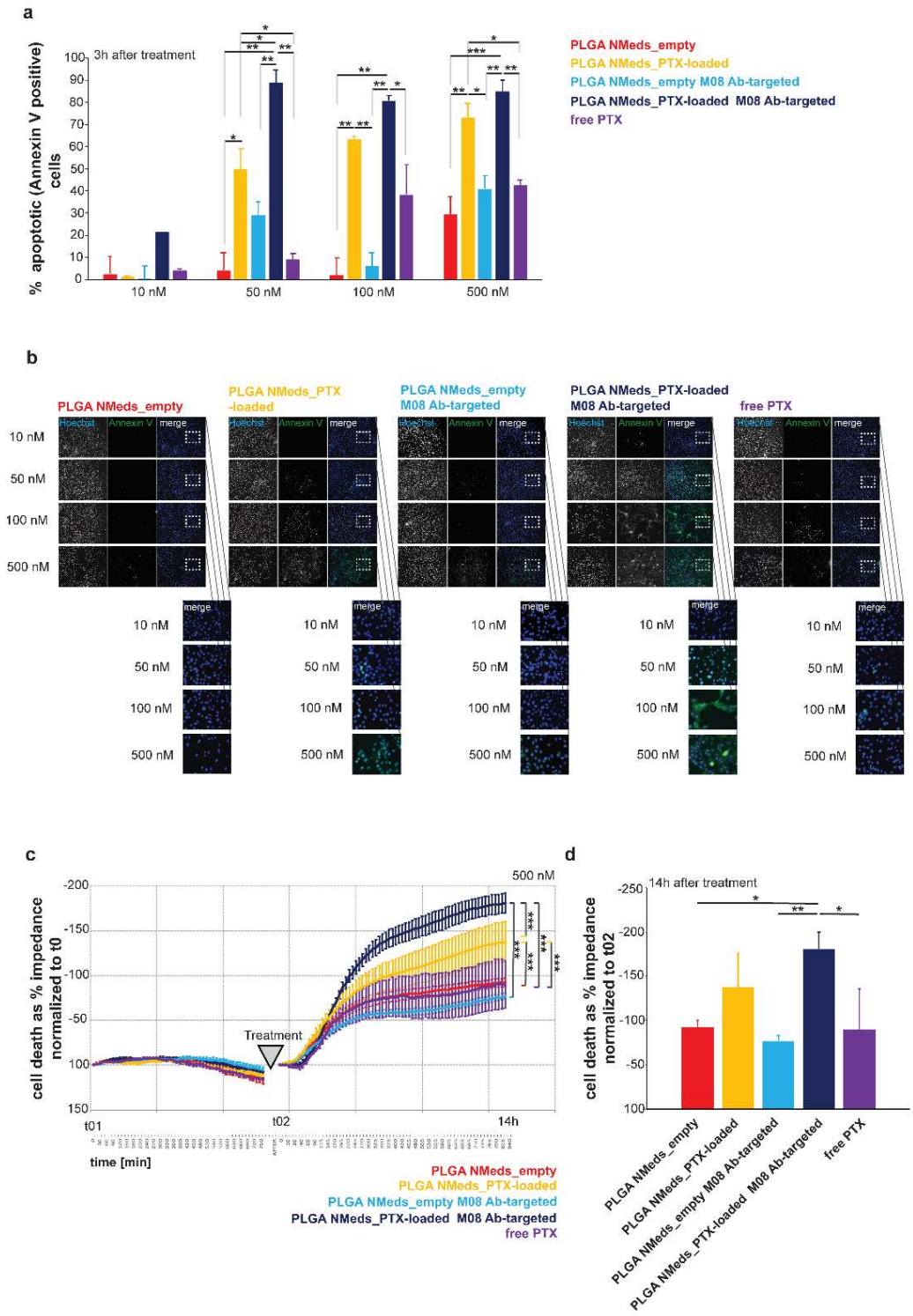


**Figure 6:** Effect of PTX-loaded NMeds on cell health of C6 glioblastoma cells. a) Quantification of apoptosis using FITC-Annexin V. The percent of Annexin V positive cells of total cells is shown as average from n = 3 OFV. C6 cells were treated for 3 h with empty non-targeted and M08-targeted NMeds, and non-targeted and M08-targeted NMeds delivering the equivalent of 10, 50, 100, and 500 nM PTX. Free PTX at the same concentrations was used as controls. b) Representative images showing all cells. The visualisation was achieved by labelling the nuclei with Hoechst staining and labelling apoptotic cells with Annexin V-FITC. c,d) Cell impedance measurement after treatment

with empty non-targeted and M08-targeted NMeds as well as their PTX loaded counterparts (the equivalent of 500 nM PTX) and compared with500 nM free PTX as a control treatment. Before treatment, cells were grown for 12.5 h ($t0_1$ – 750 min). n = 3 per treatment. Cell death was evaluated as a decrease in impedance and shown as % of t0. d) Cell death analysis at the 14 h endpoint of the treatment shown in (c). One-way ANOVA analysis and Tukey's Post hoc tests were performed, * $p < 0.05$, ** $p < 0.01$, *** $p < 0.001$, **** $p < 0.0001$.

## 4. Discussion

GBM is one of the most aggressive forms of brain cancer that affects thousands of people and is notable for its poor prognoses. Since current strategies lack specificity, which leads to toxicity in healthy tissues and does not inhibit recurrences, targeted nanomedicines (NMeds) are being widely investigated as promising new tools, as demonstrated by an abundance of reviews in the last two years [519–525]. One of the most important aspects to consider when optimising a targeted NMed is selecting an appropriate targeting ligand. In general, targeting strategies fall under three main categories [526,527]. Cell-penetrating peptides represent one first approach [528–531]. These peptides help deliver pharmaceutics into cancer cells but are often considered non-specific, as they promote indiscriminate NMed uptake. Secondly, upregulated cell pathways can be targeted [532–534], for example, using miRNAs that disrupt those pathways [535,536]. Similarly, the tumour microenvironment can be a site of therapeutic interest [537–541]: one example is exploiting the high concentration of Reactive Oxygen Species (ROS) with ROS-sensitive NMeds that would release the drug only in the presence of ROS [165,312]. However, major limitations to these strategies lay in the poor stability of sensitive molecules such as RNAs and the lack of cell specificity that could still lead to off-target effects.

The third strategy, and the focus of this work, consists in using cell-specific ligands, which take advantage of upregulated receptors on the cell surface. Due to the variations in the biochemical identity of tumour cells, a myriad of reviews and research papers have been dedicated to the different ligands for GBM targeting, ranging from small molecules to peptides to antibodies [234,526,542–545]. While having so many options is beneficial, and this targeting strategy is generally more effective compared to the previous two, it is important to remember that many of these have characteristics that could still limit their use, such as poor specificity, low affinity, incapacity to internalise or activate the receptor with nano-sized cargo, saturability etc. [546,547]. Thus, it is crucial to investigate novel ligands that

can improve the GBM-specific delivery of therapeutics. In this study, polymeric NMeds were surface coated with different ligands, peptides and antibodies and evaluated for their GBM targeting potential.

First, the standardisation of the formulation process to give reproducible and consistent NMeds was critical to be able to focus on the targeting ligand effects and avoid any differences due to size, morphology, or surface charge. NMeds modified with each of the four ligands showed a rapid and improved uptake in GBM cells even at short periods. Different trends in the NMed uptake arose when analysing the impact of the amount of ligand on the surface, or the concentration of NMeds, evidencing a unique behaviour for each ligand. Overall, the only ligand that showed GBM specificity over DI TNC1 cells was the antibody M08. M08 not only improved GBM specific uptake but also showed potential biological activity: analysing cell growth, M08-targeted NMeds led to decreased GBM cell growth in a single culture, while in co-culture, they did not affect the astrocytes, allowing them to grow more readily. When loaded with the chemotherapeutic PTX, higher cell death was observed after dosing M08-NMeds over both free PTX and non-targeted NMeds in GBM cells; also, at only 3 hours of incubation, M08-targeted NMeds significantly increased apoptotic markers in the cells, highlighting the anti-cancer potential of these systems. These results show the promise of a well optimized targeted NMed. At the same time, CSV is known to be upregulated to different extent in different cell lines, with C6 cells having a lower amount compared to other models [548,549]. Hence, these results could also evidence a severe underestimation of the true potential of CSV targeted NMeds.

Our results can be compared to a recent study by Ullah et al. [550] where PTX-loaded NMeds were surface modified with the cell-penetrating peptide RGD. This ligand is known to have specificity towards brain cancer, where the cells upregulate integrin $\alpha v\beta 3$ [531], and has been widely used to help deliver and increase the potency of chemotherapeutics such as temozolomide or PTX [551–553]. In their study, RGD-NMeds showed a similar effect to our M08 modified

NMeds in the arrest of cell growth, but the effect was solely due to the presence of PTX: in fact, there was no significant difference in cell viability between free drug, non-targeted NMeds, and RGD-targeted NMeds. Also, when analysing cell toxicity, no significant difference was evidenced between the free drug and RGD-targeted NMeds, even if the latter showed decreased tumour volumes when dosed *in vivo*. In the present study, the presence of M08 on the NMed surface led to higher PTX toxicity compared both to free drug and non-targeted NMeds, indicating improved uptake and enhanced synergistic effects of the drug and M08 when co-delivered *in vitro*.

Another point to address when considering GBM-targeted NMeds is distinguishing between targeting ligands that promote BBB crossing and others that improve GBM uptake [554–556]. Since the BBB is a major limitation to the effectiveness of brain cancer treatments, BBB-targeted NMeds are often effective in reducing tumour volume, but they lack specificity for diseased cells. For this reason, although not specific for GBM, NMeds decorated with g7 and AAVF can still be valuable players in the search for improved GBM treatments, as they are known to be effective for BBB crossing [495,497,557,558]. This brings up a major point in the field, described in great detail in a review by Luo et al. [559]. Here, the authors highlight that BBB-targeted NMeds are often considered GBM specific, but single targeting strategies cannot guarantee both the BBB infiltration and GBM specificity. Thus, various NMeds with two or more targeting ligands on their surface or bispecific antibodies are currently being investigated [560–562]. Although these systems show improved efficacy, combining several targeting ligands on the same NMed drastically increase the difficulty of production and characterisation [563,564]. Considering these issues, the M08 antibody can represent a step forward in the design of GBM-targeted NMeds: from our results, it is evident that M08 is a prime candidate thanks to its ability to cross the BBB, specifically target GBM cells, and exert biological anti-cancer activity. Furthermore, all these functions in a single antibody make producing and

characterising these systems easier, leading to better chances of translating these results into preclinical applications.

## 5. Conclusions

NMeds are one of the most promising medical tools for difficult-to-treat diseases such as GBM. Enhancing the solubility, biodistribution, and compatibility with chemotherapeutics are significant players in designing treatments; however, to have an effective NMed treatment against GBM, selective delivery into the brain and only to GBM cells is critical to lower doses, improve drug delivery, and lower collateral damage to healthy surrounding cells. This study demonstrated several promising ligands with the potential for BBB and/or GBM targeting. In addition, by optimising surface modifications, we have indicated a monoclonal antibody (M08) that can specifically enter GBM cells over healthy cells and cause synergistic effects when delivering the chemotherapeutic PTX. This improved cell uptake and GBM specificity is an important step to creating improved chemotherapeutic NMeds that could offer higher curative potential with lowered off-target toxicity to healthy cells.

## 6. Supplementary Material

**Table S1.** Physico-chemical characteristics of NMeds formulated with different percentages of PLGA-Cy5.

| PLGA-CY5 (% w/w) | Size (nm) | PDI | Z-potential (mV) | % Weight yield |
|---|---|---|---|---|
| 4 | 142 ± 23 | 0.21 ± 0.01 | -28.8 ± 12 | 28 ± 15 |
| 2 | 157 ± 15 | 0.07 ± 0.01 | -35.6± 10 | 34 ± 11 |
| 1 | 160 ± 25 | 0.13 ± 0.01 | -28.4 ± 4 | 41 ± 13 |
| 0.4 | 156 ± 20 | 0.08 ± 0.02 | -30.2 ± 7 | 82 ± 6 |
| 0.2 | 147 ± 18 | 0.06 ± 0.01 | -31.1 ± 3 | 90 ± 8 |
| 0.1 | 155 ± 12 | 0.19 ± 0.01 | -31.5 ± 5 | 93 ± 8 |

**Table S2**. The effects of Pluronic® F68 amount on physico-chemical characteristics of NMeds.

| NMed formulation | % w/v surfactant in Aqueous phase (12.5 mL) | Size (nm) | PDI | Z-potential (mV) | % Residual surfactant | % Weight yield |
|---|---|---|---|---|---|---|
| 1 | MilliQ water | 183 ± 12 | 0.14 ± 0.01 | -43.8 ± 5 | n/a | 25 ± 8 |
| 2 | 0.5% | 155 ± 7 | 0.08 ± 0.02 | -39.4 ± 6 | 10 ± 3 | 42 ± 10 |
| 3 | 1.5% | 157 ± 8 | 0.07 ± 0.01 | -45.6 ± 4 | 12 ± 5 | 87 ± 9 |
| 4 | 3% | 183 ± 10 | 0.20 ± 0.01 | -45.7 ± 7 | 14 ± 7 | 88 ± 4 |

**Table S3.** Physico-chemical characteristics of NMeds after mock reaction, submitted to several cycles of centrifugation.

| Centrifugation | Size (nm) | PDI | Z potential (mV) | % Weight yield |
|---|---|---|---|---|
| 1* | 147 ± 18 | 0.05 ± 0.01 | -31 ± 3 | 90 ± 8 |
| 2 | 166 ± 27 | 0.12 ± 0.01 | -32 ± 7 | 60 ± 7 |
| 3 | 170 ± 15 | 0.05 ± 0.01 | -31 ± 8 | 43 ± 12 |
| 4 | 160 ± 10 | 0.18 ± 0.03 | -29 ± 9 | 30 ± 15 |
| 5 | 156 ± 11 | 0.08 ± 0.01 | -25 ± 5 | 27 ± 13 |
| 1** | 166 ± 10 | 0.12 ± 0.01 | -32 ± 5 | 90 ± 1 |

* Centrifugation step after NMed formulation, followed by mock reaction without any further purification. Sample analysed in reaction buffer.

** Post-modification was run on NMeds directly from the formulation without purification. One centrifugation step was performed on the NMeds after the mock reaction.

**Table S4.** Stability results of non-modified NMeds and targeted NMeds after 3 weeks after storage at 4 - 8°C, freezing at -20°C without trehalose, freezing at -20 °C with trehalose at 3 w/w ratio and after lyophilisation.

| NMed formulation | Storage conditions | Size (nm) | PDI | Z potential (mV) |
|---|---|---|---|---|
| non-modified NMeds | Storage 4 - 8°C | 289 ± 10 | 0.29 ± 0.01 | -28 ± 11 |
| g7-NMeds | | 260 ± 14 | 0.33 ± 0.03 | -22.6 ± 8 |
| PAAVF-NMeds | | 180 ± 9 | 0.25 ± 0.03 | -27.4 ± 6 |
| M08J-NMeds | | 176 ± 11 | 0.19 ± 0.01 | -27.6 ± 9 |
| M08-NMeds | | 220 ± 10 | 0.26 ± 0.02 | -18.1 ± 8 |
| Non-modified NMeds | Freezing -20°C without trehalose | 560 ± 60 | 0.66 ± 0.04 | -10.8 ± 8 |
| g7-NMeds | | 340 ± 54 | 0.33 ± 0.04 | -28.7 ± 9 |
| PAAVF-NMeds | | 176 ± 9 | 0.13 ± 0.02 | -29.1 ± 6 |
| M08J-NMeds | | 182 ± 8 | 0.17 ± 0.03 | -27.1 ± 11 |
| M08-NMeds | | 230 ± 10 | 0.28 ± 0.02 | -28.7 ± 10 |
| Non-modified NMeds | Freezing -20°C with trehalose at 3 w/w ratio | 254 ± 10 | 0.33 ± 0.02 | -25.0 ± 6 |
| g7-NMeds | | 228 ± 8 | 0.21 ± 0.01 | -25.6 ± 8 |
| PAAVF-NMeds | | 181 ± 9 | 0.12 ± 0.01 | -31.9 ± 5 |
| M08J-NMeds | | 179 ± 11 | 0.18 ± 0.02 | -30.4 ± 6 |
| M08-NMeds | | 211 ± 14 | 0.19 ± 0.02 | -30.8 ± 6 |
| Non-modified NMeds | Lyophilisation | 350 ± 8 | 0.42 ± 0.03 | -20.4 ± 8 |
| g7-NMeds | | 288 ± 11 | 0.30 ± 0.02 | -18.8 ± 13 |
| PAAVF-NMeds | | 189 ± 12 | 0.23 ± 0.01 | -17.2 ± 13 |
| M08J-NMeds | | 202 ± 9 | 0.24 ± 0.02 | -22.4 ± 12 |
| M08-NMeds | | 240 ± 14 | 0.25 ± 0.01 | -21.4 ± 12 |

**Table S5**. Full statistical data for the *in vitro* results.

| | | | | | |
|---|---|---|---|---|---|
| | | | | | |
| 2-way ANOVA: effect of concentration, effect of treatment, concentration x treatment interaction | | | | | |
| | | | | | |
| Source of Variation | % of total variation | P value | | | |
| Interaction | 14.97 | <0.0001 | | | |
| concentration | 32.58 | <0.0001 | | | |
| treatment | 49.28 | <0.0001 | | | |
| **10 mM** | | | | | |
| ANOVA summary | | | | | |
| F | | | | 5.157 | |
| P value | | | | 0.0507 | |
| P value summary | | | | ns | |
| Significant diff. among means (P < 0.05)? | | | | No | |

| **50 mM** | | | |
|---|---|---|---|
| ANOVA summary | | | |
| F | 26.27 | | |
| P value | 0.0015 | | |
| P value summary | ** | | |
| Significant diff. among means (P < 0.05)? | Yes | | |
| R squared | 0.9546 | | |

| Tukey's multiple comparisons test | Significant? | Summary | Adjusted P Value |
|---|---|---|---|
| PLGA NPS_EMPTY vs. PLGA NPS_PTX-LOADED | Yes | * | 0.0248 |
| PLGA NPS_EMPTY vs. PLGA NPS_EMPTY M08 AB-TARGETED | No | ns | 0.2018 |
| PLGA NPS_EMPTY vs. PLGA NPS_PTX-LOADED M08 AB-TARGETED | Yes | ** | 0.0016 |
| PLGA NPS_EMPTY vs. PTX | No | ns | 0.9819 |
| PLGA NPS_PTX-LOADED vs. PLGA NPS_EMPTY M08 AB-TARGETED | No | ns | 0.3155 |
| PLGA NPS_PTX-LOADED vs. PLGA NPS_PTX-LOADED M08 AB-TARGETED | Yes | * | 0.0467 |
| PLGA NPS_PTX-LOADED vs. PTX | Yes | * | 0.0389 |
| PLGA NPS_EMPTY M08 AB-TARGETED vs. PLGA NPS_PTX-LOADED M08 AB- TARGETED | Yes | ** | 0.008 |
| PLGA NPS_EMPTY M08 AB-TARGETED vs. PTX | No | ns | 0.3437 |
| PLGA NPS_PTX-LOADED M08 AB-TARGETED vs. PTX | Yes | ** | 0.0021 |

| **100 mM** | | | |
|---|---|---|---|
| ANOVA summary | | | |
| F | 27.04 | | |

| | | | |
|---|---|---|---|
| P value | 0.0014 | | |
| P value summary | ** | | |
| Significant diff. among means (P < 0.05)? | Yes | | |
| R squared | 0.9558 | | |

| Tukey's multiple comparisons test | Significant? | Summary | Adjusted P Value |
|---|---|---|---|
| PLGA NPS_EMPTY vs. PLGA NPS_PTX-LOADED | Yes | ** | 0.0067 |
| PLGA NPS_EMPTY vs. PLGA NPS_EMPTY M08 AB-TARGETED | No | ns | 0.9921 |
| PLGA NPS_EMPTY vs. PLGA NPS_PTX-LOADED M08 AB-TARGETED | Yes | ** | 0.0022 |
| PLGA NPS_EMPTY vs. PTX | No | ns | 0.0579 |
| PLGA NPS_PTX-LOADED vs. PLGA NPS_EMPTY M08 AB-TARGETED | Yes | ** | 0.009 |
| PLGA NPS_PTX-LOADED vs. PLGA NPS_PTX-LOADED M08 AB-TARGETED | No | ns | 0.4452 |
| PLGA NPS_PTX-LOADED vs. PTX | No | ns | 0.1921 |
| PLGA NPS_EMPTY M08 AB-TARGETED vs. PLGA NPS_PTX-LOADED M08 AB- TARGETED | Yes | ** | 0.0027 |
| PLGA NPS_EMPTY M08 AB-TARGETED vs. PTX | No | ns | 0.0863 |
| PLGA NPS_PTX-LOADED M08 AB-TARGETED vs. PTX | Yes | * | 0.0321 |

| **500 mM** | | | | | |
|---|---|---|---|---|---|
| ANOVA summary | | | | | |

| | | | | |
|---|---|---|---|---|
| F | 37.35 | | | |
| P value | 0.0006 | | | |
| P value summary | *** | | | |
| Significant diff. among means (P < 0.05)? | Yes | | | |
| R squared | 0.9676 | | | |

| Tukey's multiple comparisons test | Significant? | Summary | Adjusted P Value |
|---|---|---|---|
| PLGA NPS_EMPTY vs. PLGA NPS_PTX-LOADED | Yes | ** | 0.0026 |
| PLGA NPS_EMPTY vs. PLGA NPS_EMPTY M08 AB-TARGETED | No | ns | 0.3416 |
| PLGA NPS_EMPTY vs. PLGA NPS_PTX-LOADED M08 AB-TARGETED | Yes | *** | 0.0009 |
| PLGA NPS_EMPTY vs. PTX | No | ns | 0.2479 |
| PLGA NPS_PTX-LOADED vs. PLGA NPS_EMPTY M08 AB-TARGETED | Yes | * | 0.0103 |
| PLGA NPS_PTX-LOADED vs. PLGA NPS_PTX-LOADED M08 AB-TARGETED | No | ns | 0.3312 |
| PLGA NPS_PTX-LOADED vs. PTX | Yes | * | 0.013 |
| PLGA NPS_EMPTY M08 AB-TARGETED vs. PLGA NPS_PTX-LOADED M08 AB- TARGETED | Yes | ** | 0.0026 |
| PLGA NPS_EMPTY M08 AB-TARGETED vs. PTX | No | ns | 0.9972 |
| PLGA NPS_PTX-LOADED M08 AB-TARGETED vs. PTX | Yes | ** | 0.0031 |

| **Tukey's multiple comparisons test** | **Significant?** | **Summary** | **Adjusted P Value** |
|---|---|---|---|
| | | | |
| 10:PLGA NPS_EMPTY vs. 10:PLGA NPS_PTX-LOADED | No | ns | >0.9999 |

| | | | |
|---|---|---|---|
| 10:PLGA NPS_EMPTY vs. 10:PLGA NPS_EMPTY M08 AB-TARGETED | No | ns | >0.9999 |
| 10:PLGA NPS_EMPTY vs. 10:PLGA NPS_PTX-LOADED M08 AB-TARGETED | No | ns | 0.6288 |
| 10:PLGA NPS_EMPTY vs. 10:PTX | No | ns | >0.9999 |
| 10:PLGA NPS_EMPTY vs. 50:PLGA NPS_EMPTY | No | ns | >0.9999 |
| 10:PLGA NPS_EMPTY vs. 50:PLGA NPS_PTX-LOADED | Yes | *** | 0.0006 |
| 10:PLGA NPS_EMPTY vs. 50:PLGA NPS_EMPTY M08 AB-TARGETED | No | ns | 0.1524 |
| 10:PLGA NPS_EMPTY vs. 50:PLGA NPS_PTX-LOADED M08 AB-TARGETED | Yes | **** | <0.0001 |
| 10:PLGA NPS_EMPTY vs. 50:PTX | No | ns | >0.9999 |
| 10:PLGA NPS_EMPTY vs. 100:PLGA NPS_EMPTY | No | ns | >0.9999 |
| 10:PLGA NPS_EMPTY vs. 100:PLGA NPS_PTX-LOADED | Yes | **** | <0.0001 |
| 10:PLGA NPS_EMPTY vs. 100:PLGA NPS_EMPTY M08 AB-TARGETED | No | ns | >0.9999 |
| 10:PLGA NPS_EMPTY vs. 100:PLGA NPS_PTX-LOADED M08 AB-TARGETED | Yes | **** | <0.0001 |
| 10:PLGA NPS_EMPTY vs. 100:PTX | Yes | * | 0.0146 |
| 10:PLGA NPS_EMPTY vs. 500:PLGA NPS_EMPTY | No | ns | 0.1379 |
| 10:PLGA NPS_EMPTY vs. 500:PLGA NPS_PTX-LOADED | Yes | **** | <0.0001 |
| 10:PLGA NPS_EMPTY vs. 500:PLGA NPS_EMPTY M08 AB-TARGETED | Yes | ** | 0.0071 |
| 10:PLGA NPS_EMPTY vs. 500:PLGA NPS_PTX-LOADED M08 AB-TARGETED | Yes | **** | <0.0001 |
| 10:PLGA NPS_EMPTY vs. 500:PTX | Yes | ** | 0.0045 |

| | | | |
|---|---|---|---|
| 10:PLGA NPS_PTX-LOADED vs. 10:PLGA NPS_EMPTY M08 AB-TARGETED | No | ns | >0.9999 |
| 10:PLGA NPS_PTX-LOADED vs. 10:PLGA NPS_PTX-LOADED M08 AB-TARGETED | No | ns | 0.5266 |
| 10:PLGA NPS_PTX-LOADED vs. 10:PTX | No | ns | >0.9999 |
| 10:PLGA NPS_PTX-LOADED vs. 50:PLGA NPS_EMPTY | No | ns | >0.9999 |
| 10:PLGA NPS_PTX-LOADED vs. 50:PLGA NPS_PTX-LOADED | Yes | *** | 0.0004 |
| 10:PLGA NPS_PTX-LOADED vs. 50:PLGA NPS_EMPTY M08 AB-TARGETED | No | ns | 0.1127 |
| 10:PLGA NPS_PTX-LOADED vs. 50:PLGA NPS_PTX-LOADED M08 AB-TARGETED | Yes | **** | <0.0001 |
| 10:PLGA NPS_PTX-LOADED vs. 50:PTX | No | ns | 0.9998 |
| 10:PLGA NPS_PTX-LOADED vs. 100:PLGA NPS_EMPTY | No | ns | >0.9999 |
| 10:PLGA NPS_PTX-LOADED vs. 100:PLGA NPS_PTX-LOADED | Yes | **** | <0.0001 |
| 10:PLGA NPS_PTX-LOADED vs. 100:PLGA NPS_EMPTY M08 AB-TARGETED | No | ns | >0.9999 |
| 10:PLGA NPS_PTX-LOADED vs. 100:PLGA NPS_PTX-LOADED M08 AB- TARGETED | Yes | **** | <0.0001 |
| 10:PLGA NPS_PTX-LOADED vs. 100:PTX | Yes | * | 0.0103 |
| 10:PLGA NPS_PTX-LOADED vs. 500:PLGA NPS_EMPTY | No | ns | 0.1016 |
| 10:PLGA NPS_PTX-LOADED vs. 500:PLGA NPS_PTX-LOADED | Yes | **** | <0.0001 |
| 10:PLGA NPS_PTX-LOADED vs. 500:PLGA NPS_EMPTY M08 AB-TARGETED | Yes | ** | 0.005 |
| 10:PLGA NPS_PTX-LOADED vs. 500:PLGA NPS_PTX-LOADED M08 AB- TARGETED | Yes | **** | <0.0001 |
| 10:PLGA NPS_PTX-LOADED vs. 500:PTX | Yes | ** | 0.0031 |
| 10:PLGA NPS_EMPTY M08 AB-TARGETED vs. 10:PLGA NPS_PTX-LOADED M08 AB-TARGETED | No | ns | 0.4544 |
| 10:PLGA NPS_EMPTY M08 AB-TARGETED vs. 10:PTX | No | ns | >0.9999 |

| | | | |
|---|---|---|---|
| 10:PLGA NPS_EMPTY M08 AB-TARGETED vs. 50:PLGA NPS_EMPTY | No | ns | >0.9999 |
| 10:PLGA NPS_EMPTY M08 AB-TARGETED vs. 50:PLGA NPS_PTX-LOADED | Yes | *** | 0.0003 |
| 10:PLGA NPS_EMPTY M08 AB-TARGETED vs. 50:PLGA NPS_EMPTY M08 AB- TARGETED | No | ns | 0.0897 |
| 10:PLGA NPS_EMPTY M08 AB-TARGETED vs. 50:PLGA NPS_PTX-LOADED M08 AB-TARGETED | Yes | **** | <0.0001 |
| 10:PLGA NPS_EMPTY M08 AB-TARGETED vs. 50:PTX | No | ns | 0.9993 |
| 10:PLGA NPS_EMPTY M08 AB-TARGETED vs. 100:PLGA NPS_EMPTY | No | ns | >0.9999 |
| 10:PLGA NPS_EMPTY M08 AB-TARGETED vs. 100:PLGA NPS_PTX-LOADED | Yes | **** | <0.0001 |
| 10:PLGA NPS_EMPTY M08 AB-TARGETED vs. 100:PLGA NPS_EMPTY M08 AB- TARGETED | No | ns | >0.9999 |
| 10:PLGA NPS_EMPTY M08 AB-TARGETED vs. 100:PLGA NPS_PTX-LOADED M08 AB-TARGETED | Yes | **** | <0.0001 |
| 10:PLGA NPS_EMPTY M08 AB-TARGETED vs. 100:PTX | Yes | ** | 0.0079 |
| 10:PLGA NPS_EMPTY M08 AB-TARGETED vs. 500:PLGA NPS_EMPTY | No | ns | 0.0806 |
| 10:PLGA NPS_EMPTY M08 AB-TARGETED vs. 500:PLGA NPS_PTX-LOADED | Yes | **** | <0.0001 |
| 10:PLGA NPS_EMPTY M08 AB-TARGETED vs. 500:PLGA NPS_EMPTY M08 AB- TARGETED | Yes | ** | 0.0038 |
| 10:PLGA NPS_EMPTY M08 AB-TARGETED vs. 500:PLGA NPS_PTX-LOADED M08 AB-TARGETED | Yes | **** | <0.0001 |
| 10:PLGA NPS_EMPTY M08 AB-TARGETED vs. 500:PTX | Yes | ** | 0.0024 |
| 10:PLGA NPS_PTX-LOADED M08 AB-TARGETED vs. 10:PTX | No | ns | 0.7427 |

| | | | |
|---|---|---|---|
| 10:PLGA NPS_PTX-LOADED M08 AB-TARGETED vs. 50:PLGA NPS_EMPTY | No | ns | 0.7618 |
| 10:PLGA NPS_PTX-LOADED M08 AB-TARGETED vs. 50:PLGA NPS_PTX-LOADED | No | ns | 0.0977 |
| 10:PLGA NPS_PTX-LOADED M08 AB-TARGETED vs. 50:PLGA NPS_EMPTY M08 AB-TARGETED | No | ns | 0.9999 |
| 10:PLGA NPS_PTX-LOADED M08 AB-TARGETED vs. 50:PLGA NPS_PTX-LOADED M08 AB-TARGETED | Yes | **** | <0.0001 |
| 10:PLGA NPS_PTX-LOADED M08 AB-TARGETED vs. 50:PTX | No | ns | 0.9784 |
| 10:PLGA NPS_PTX-LOADED M08 AB-TARGETED vs. 100:PLGA NPS_EMPTY | No | ns | 0.5958 |
| 10:PLGA NPS_PTX-LOADED M08 AB-TARGETED vs. 100:PLGA NPS_PTX- LOADED | Yes | ** | 0.0027 |
| 10:PLGA NPS_PTX-LOADED M08 AB-TARGETED vs. 100:PLGA NPS_EMPTY M08 AB-TARGETED | No | ns | 0.8691 |
| 10:PLGA NPS_PTX-LOADED M08 AB-TARGETED vs. 100:PLGA NPS_PTX- LOADED M08 AB-TARGETED | Yes | **** | <0.0001 |
| 10:PLGA NPS_PTX-LOADED M08 AB-TARGETED vs. 100:PTX | No | ns | 0.7729 |
| 10:PLGA NPS_PTX-LOADED M08 AB-TARGETED vs. 500:PLGA NPS_EMPTY | No | ns | 0.9998 |
| 10:PLGA NPS_PTX-LOADED M08 AB-TARGETED vs. 500:PLGA NPS_PTX- LOADED | Yes | *** | 0.0002 |
| 10:PLGA NPS_PTX-LOADED M08 AB-TARGETED vs. 500:PLGA NPS_EMPTY M08 AB-TARGETED | No | ns | 0.5701 |
| 10:PLGA NPS_PTX-LOADED M08 AB-TARGETED vs. 500:PLGA NPS_PTX- LOADED M08 AB-TARGETED | Yes | **** | <0.0001 |
| 10:PLGA NPS_PTX-LOADED M08 AB-TARGETED vs. 500:PTX | No | ns | 0.4399 |
| 10:PTX vs. 50:PLGA NPS_EMPTY | No | ns | >0.9999 |

| | | | |
|---|---|---|---|
| 10:PTX vs. 50:PLGA NPS_PTX-LOADED | Yes | *** | 0.0009 |
| 10:PTX vs. 50:PLGA NPS_EMPTY M08 AB-TARGETED | No | ns | 0.2116 |
| 10:PTX vs. 50:PLGA NPS_PTX-LOADED M08 AB-TARGETED | Yes | **** | <0.0001 |
| 10:PTX vs. 50:PTX | No | ns | >0.9999 |
| 10:PTX vs. 100:PLGA NPS_EMPTY | No | ns | >0.9999 |
| 10:PTX vs. 100:PLGA NPS_PTX-LOADED | Yes | **** | <0.0001 |
| 10:PTX vs. 100:PLGA NPS_EMPTY M08 AB-TARGETED | No | ns | >0.9999 |
| 10:PTX vs. 100:PLGA NPS_PTX-LOADED M08 AB-TARGETED | Yes | **** | <0.0001 |
| 10:PTX vs. 100:PTX | Yes | * | 0.0217 |
| 10:PTX vs. 500:PLGA NPS_EMPTY | No | ns | 0.1927 |
| 10:PTX vs. 500:PLGA NPS_PTX-LOADED | Yes | **** | <0.0001 |
| 10:PTX vs. 500:PLGA NPS_EMPTY M08 AB-TARGETED | Yes | * | 0.0106 |
| 10:PTX vs. 500:PLGA NPS_PTX-LOADED M08 AB-TARGETED | Yes | **** | <0.0001 |
| 10:PTX vs. 500:PTX | Yes | ** | 0.0067 |
| 50:PLGA NPS_EMPTY vs. 50:PLGA NPS_PTX-LOADED | Yes | ** | 0.001 |
| 50:PLGA NPS_EMPTY vs. 50:PLGA NPS_EMPTY M08 AB-TARGETED | No | ns | 0.2239 |
| 50:PLGA NPS_EMPTY vs. 50:PLGA NPS_PTX-LOADED M08 AB-TARGETED | Yes | **** | <0.0001 |
| 50:PLGA NPS_EMPTY vs. 50:PTX | No | ns | >0.9999 |
| 50:PLGA NPS_EMPTY vs. 100:PLGA NPS_EMPTY | No | ns | >0.9999 |
| 50:PLGA NPS_EMPTY vs. 100:PLGA NPS_PTX-LOADED | Yes | **** | <0.0001 |
| 50:PLGA NPS_EMPTY vs. 100:PLGA NPS_EMPTY M08 AB-TARGETED | No | ns | >0.9999 |

| | | | |
|---|---|---|---|
| 50:PLGA NPS_EMPTY vs. 100:PLGA NPS_PTX-LOADED M08 AB-TARGETED | Yes | **** | <0.0001 |
| 50:PLGA NPS_EMPTY vs. 100:PTX | Yes | * | 0.0233 |
| 50:PLGA NPS_EMPTY vs. 500:PLGA NPS_EMPTY | No | ns | 0.2041 |
| 50:PLGA NPS_EMPTY vs. 500:PLGA NPS_PTX-LOADED | Yes | **** | <0.0001 |
| 50:PLGA NPS_EMPTY vs. 500:PLGA NPS_EMPTY M08 AB-TARGETED | Yes | * | 0.0114 |
| 50:PLGA NPS_EMPTY vs. 500:PLGA NPS_PTX-LOADED M08 AB-TARGETED | Yes | **** | <0.0001 |
| 50:PLGA NPS_EMPTY vs. 500:PTX | Yes | ** | 0.0072 |
| 50:PLGA NPS_PTX-LOADED vs. 50:PLGA NPS_EMPTY M08 AB-TARGETED | No | ns | 0.4809 |
| 50:PLGA NPS_PTX-LOADED vs. 50:PLGA NPS_PTX-LOADED M08 AB-TARGETED | Yes | ** | 0.0065 |
| 50:PLGA NPS_PTX-LOADED vs. 50:PTX | Yes | ** | 0.0039 |
| 50:PLGA NPS_PTX-LOADED vs. 100:PLGA NPS_EMPTY | Yes | *** | 0.0006 |
| 50:PLGA NPS_PTX-LOADED vs. 100:PLGA NPS_PTX-LOADED | No | ns | 0.9492 |
| 50:PLGA NPS_PTX-LOADED vs. 100:PLGA NPS_EMPTY M08 AB-TARGETED | Yes | ** | 0.0016 |
| 50:PLGA NPS_PTX-LOADED vs. 100:PLGA NPS_PTX-LOADED M08 AB- TARGETED | No | ns | 0.0552 |
| 50:PLGA NPS_PTX-LOADED vs. 100:PTX | No | ns | 0.9876 |
| 50:PLGA NPS_PTX-LOADED vs. 500:PLGA NPS_EMPTY | No | ns | 0.5141 |
| 50:PLGA NPS_PTX-LOADED vs. 500:PLGA NPS_PTX-LOADED | No | ns | 0.3092 |
| 50:PLGA NPS_PTX-LOADED vs. 500:PLGA NPS_EMPTY M08 AB-TARGETED | No | ns | 0.9993 |
| 50:PLGA NPS_PTX-LOADED vs. 500:PLGA NPS_PTX-LOADED M08 AB- TARGETED | Yes | * | 0.0189 |
| 50:PLGA NPS_PTX-LOADED vs. 500:PTX | No | ns | >0.9999 |

| | | | |
|---|---|---|---|
| 50:PLGA NPS_EMPTY M08 AB-TARGETED vs. 50:PLGA NPS_PTX-LOADED M08 AB-TARGETED | Yes | **** | <0.0001 |
| 50:PLGA NPS_EMPTY M08 AB-TARGETED vs. 50:PTX | No | ns | 0.5428 |
| 50:PLGA NPS_EMPTY M08 AB-TARGETED vs. 100:PLGA NPS_EMPTY | No | ns | 0.1384 |
| 50:PLGA NPS_EMPTY M08 AB-TARGETED vs. 100:PLGA NPS_PTX-LOADED | Yes | * | 0.0222 |
| 50:PLGA NPS_EMPTY M08 AB-TARGETED vs. 100:PLGA NPS_EMPTY M08 AB- TARGETED | No | ns | 0.3156 |
| 50:PLGA NPS_EMPTY M08 AB-TARGETED vs. 100:PLGA NPS_PTX-LOADED M08 AB-TARGETED | Yes | *** | 0.0002 |
| 50:PLGA NPS_EMPTY M08 AB-TARGETED vs. 100:PTX | No | ns | 0.9989 |
| 50:PLGA NPS_EMPTY M08 AB-TARGETED vs. 500:PLGA NPS_EMPTY | No | ns | >0.9999 |
| 50:PLGA NPS_EMPTY M08 AB-TARGETED vs. 500:PLGA NPS_PTX-LOADED | Yes | ** | 0.0016 |
| 50:PLGA NPS_EMPTY M08 AB-TARGETED vs. 500:PLGA NPS_EMPTY M08 AB- TARGETED | No | ns | 0.9834 |
| 50:PLGA NPS_EMPTY M08 AB-TARGETED vs. 500:PLGA NPS_PTX-LOADED M08 AB-TARGETED | Yes | **** | <0.0001 |
| 50:PLGA NPS_EMPTY M08 AB-TARGETED vs. 500:PTX | No | ns | 0.9472 |
| 50:PLGA NPS_PTX-LOADED M08 AB-TARGETED vs. 50:PTX | Yes | **** | <0.0001 |
| 50:PLGA NPS_PTX-LOADED M08 AB-TARGETED vs. 100:PLGA NPS_EMPTY | Yes | **** | <0.0001 |
| 50:PLGA NPS_PTX-LOADED M08 AB-TARGETED vs. 100:PLGA NPS_PTX- LOADED | No | ns | 0.2032 |
| 50:PLGA NPS_PTX-LOADED M08 AB-TARGETED vs. 100:PLGA NPS_EMPTY M08 AB-TARGETED | Yes | **** | <0.0001 |

| | | | |
|---|---|---|---|
| 50:PLGA NPS_PTX-LOADED M08 AB-TARGETED vs. 100:PLGA NPS_PTX- LOADED M08 AB-TARGETED | No | ns | 0.9998 |
| 50:PLGA NPS_PTX-LOADED M08 AB-TARGETED vs. 100:PTX | Yes | *** | 0.0003 |
| 50:PLGA NPS_PTX-LOADED M08 AB-TARGETED vs. 500:PLGA NPS_EMPTY | Yes | **** | <0.0001 |
| 50:PLGA NPS_PTX-LOADED M08 AB-TARGETED vs. 500:PLGA NPS_PTX- LOADED | No | ns | 0.8618 |
| 50:PLGA NPS_PTX-LOADED M08 AB-TARGETED vs. 500:PLGA NPS_EMPTY M08 AB-TARGETED | Yes | *** | 0.0006 |
| | | | |

| | | | |
|---|---|---|---|
| 50:PLGA NPS_PTX-LOADED M08 AB-TARGETED vs. 500:PLGA NPS_PTX- LOADED M08 AB-TARGETED | No | ns | >0.9999 |
| 50:PLGA NPS_PTX-LOADED M08 AB-TARGETED vs. 500:PTX | Yes | *** | 0.0009 |
| 50:PTX vs. 100:PLGA NPS_EMPTY | No | ns | >0.9999 |
| 50:PTX vs. 100:PLGA NPS_PTX-LOADED | Yes | *** | 0.0001 |
| 50:PTX vs. 100:PLGA NPS_EMPTY M08 AB-TARGETED | No | ns | >0.9999 |
| 50:PTX vs. 100:PLGA NPS_PTX-LOADED M08 AB-TARGETED | Yes | **** | <0.0001 |
| 50:PTX vs. 100:PTX | No | ns | 0.0823 |
| 50:PTX vs. 500:PLGA NPS_EMPTY | No | ns | 0.509 |
| 50:PTX vs. 500:PLGA NPS_PTX-LOADED | Yes | **** | <0.0001 |
| 50:PTX vs. 500:PLGA NPS_EMPTY M08 AB-TARGETED | Yes | * | 0.0421 |
| 50:PTX vs. 500:PLGA NPS_PTX-LOADED M08 AB-TARGETED | Yes | **** | <0.0001 |
| 50:PTX vs. 500:PTX | Yes | * | 0.027 |
| 100:PLGA NPS_EMPTY vs. 100:PLGA NPS_PTX-LOADED | Yes | **** | <0.0001 |
| 100:PLGA NPS_EMPTY vs. 100:PLGA NPS_EMPTY M08 AB-TARGETED | No | ns | >0.9999 |
| 100:PLGA NPS_EMPTY vs. 100:PLGA NPS_PTX-LOADED M08 AB-TARGETED | Yes | **** | <0.0001 |
| 100:PLGA NPS_EMPTY vs. 100:PTX | Yes | * | 0.013 |
| 100:PLGA NPS_EMPTY vs. 500:PLGA NPS_EMPTY | No | ns | 0.1251 |
| 100:PLGA NPS_EMPTY vs. 500:PLGA NPS_PTX-LOADED | Yes | **** | <0.0001 |
| 100:PLGA NPS_EMPTY vs. 500:PLGA NPS_EMPTY M08 AB-TARGETED | Yes | ** | 0.0063 |
| 100:PLGA NPS_EMPTY vs. 500:PLGA NPS_PTX-LOADED M08 AB-TARGETED | Yes | **** | <0.0001 |
| 100:PLGA NPS_EMPTY vs. 500:PTX | Yes | ** | 0.004 |
| 100:PLGA NPS_PTX-LOADED vs. 100:PLGA NPS_EMPTY M08 AB-TARGETED | Yes | **** | <0.0001 |
| 100:PLGA NPS_PTX-LOADED vs. 100:PLGA NPS_PTX-LOADED M08 AB- TARGETED | No | ns | 0.7509 |

| | | | |
|---|---|---|---|
| 100:PLGA NPS_PTX-LOADED vs. 100:PTX | No | ns | 0.2154 |
| 100:PLGA NPS_PTX-LOADED vs. 500:PLGA NPS_EMPTY | Yes | * | 0.0249 |
| 100:PLGA NPS_PTX-LOADED vs. 500:PLGA NPS_PTX-LOADED | No | ns | 0.9979 |
| 100:PLGA NPS_PTX-LOADED vs. 500:PLGA NPS_EMPTY M08 AB-TARGETED | No | ns | 0.3642 |
| 100:PLGA NPS_PTX-LOADED vs. 500:PLGA NPS_PTX-LOADED M08 AB- TARGETED | No | ns | 0.4359 |
| 100:PLGA NPS_PTX-LOADED vs. 500:PTX | No | ns | 0.4857 |
| 100:PLGA NPS_EMPTY M08 AB-TARGETED vs. 100:PLGA NPS_PTX-LOADED M08 AB-TARGETED | Yes | **** | <0.0001 |
| 100:PLGA NPS_EMPTY M08 AB-TARGETED vs. 100:PTX | Yes | * | 0.0365 |
| 100:PLGA NPS_EMPTY M08 AB-TARGETED vs. 500:PLGA NPS_EMPTY | No | ns | 0.2901 |
| 100:PLGA NPS_EMPTY M08 AB-TARGETED vs. 500:PLGA NPS_PTX-LOADED | Yes | **** | <0.0001 |
| 100:PLGA NPS_EMPTY M08 AB-TARGETED vs. 500:PLGA NPS_EMPTY M08 AB- TARGETED | Yes | * | 0.0181 |
| 100:PLGA NPS_EMPTY M08 AB-TARGETED vs. 500:PLGA NPS_PTX-LOADED M08 AB-TARGETED | Yes | **** | <0.0001 |
| 100:PLGA NPS_EMPTY M08 AB-TARGETED vs. 500:PTX | Yes | * | 0.0114 |
| 100:PLGA NPS_PTX-LOADED M08 AB-TARGETED vs. 100:PTX | Yes | ** | 0.0025 |
| 100:PLGA NPS_PTX-LOADED M08 AB-TARGETED vs. 500:PLGA NPS_EMPTY | Yes | *** | 0.0002 |
| 100:PLGA NPS_PTX-LOADED M08 AB-TARGETED vs. 500:PLGA NPS_PTX- LOADED | No | ns | >0.9999 |
| 100:PLGA NPS_PTX-LOADED M08 AB-TARGETED vs. 500:PLGA NPS_EMPTY M08 AB-TARGETED | Yes | ** | 0.0051 |
| 100:PLGA NPS_PTX-LOADED M08 AB-TARGETED vs. 500:PLGA NPS_PTX- LOADED M08 AB-TARGETED | No | ns | >0.9999 |

| | | | |
|---|---|---|---|
| 100:PLGA NPS_PTX-LOADED M08 AB-TARGETED vs. 500:PTX | Yes | ** | 0.0082 |
| 100:PTX vs. 500:PLGA NPS_EMPTY | No | ns | 0.9994 |
| 100:PTX vs. 500:PLGA NPS_PTX-LOADED | Yes | * | 0.0193 |
| 100:PTX vs. 500:PLGA NPS_EMPTY M08 AB-TARGETED | No | ns | >0.9999 |
| 100:PTX vs. 500:PLGA NPS_PTX-LOADED M08 AB-TARGETED | Yes | *** | 0.0008 |
| 100:PTX vs. 500:PTX | No | ns | >0.9999 |
| 500:PLGA NPS_EMPTY vs. 500:PLGA NPS_PTX-LOADED | Yes | ** | 0.0018 |
| 500:PLGA NPS_EMPTY vs. 500:PLGA NPS_EMPTY M08 AB-TARGETED | No | ns | 0.9884 |
| 500:PLGA NPS_EMPTY vs. 500:PLGA NPS_PTX-LOADED M08 AB-TARGETED | Yes | **** | <0.0001 |
| 500:PLGA NPS_EMPTY vs. 500:PTX | No | ns | 0.9594 |
| 500:PLGA NPS_PTX-LOADED vs. 500:PLGA NPS_EMPTY M08 AB-TARGETED | Yes | * | 0.0389 |
| 500:PLGA NPS_PTX-LOADED vs. 500:PLGA NPS_PTX-LOADED M08 AB- TARGETED | No | ns | 0.9867 |
| 500:PLGA NPS_PTX-LOADED vs. 500:PTX | No | ns | 0.0602 |
| 500:PLGA NPS_EMPTY M08 AB-TARGETED vs. 500:PLGA NPS_PTX-LOADED M08 AB-TARGETED | Yes | ** | 0.0017 |
| 500:PLGA NPS_EMPTY M08 AB-TARGETED vs. 500:PTX | No | ns | >0.9999 |
| 500:PLGA NPS_PTX-LOADED M08 AB-TARGETED vs. 500:PTX | Yes | ** | 0.0027 |

| **After treatment** | **Two-way repeated measures ANOVA** | | | **with Tukey's post hoc test** | |
|---|---|---|---|---|---|
| | | | | | |
| Two-way RM ANOVA | Matching: Stacked | | | | |

| | | | | | |
|---|---|---|---|---|---|
| Assume sphericity? | No | | | | |
| Alpha | 0.05 | | | | |
| | | | | | |

| Source of Variation | % of total variation | P value | P value summary | Significant? | Geisser-Greenhouse's epsilon |
|---|---|---|---|---|---|
| Time x treatment | 8.904 | <0.0001 | **** | Yes | |
| Time | 55.76 | <0.0001 | **** | Yes | 1 |
| treatment | 22.79 | 0.0107 | * | Yes | |
| Subject | 9.697 | <0.0001 | **** | Yes | |
| | | | | | |
| ANOVA table | SS | DF | MS | F (DFn, DFd) | P value |
| Time x treatment | 222709 | 272 | 818.8 | F (272, 680) = 7.824 | P<0.0001 |
| Time | 1394625 | 68 | 20509 | F (68.00, 680.0) = 196.0 | P<0.0001 |
| treatment | 570109 | 4 | 142527 | F (4, 10) = 5.877 | P=0.0107 |
| Subject | 242522 | 10 | 24252 | F (10, 680) = 231.7 | P<0.0001 |
| Residual | 71162 | 680 | 104.7 | | |
| | | | | | |
| Data summary | | | | | |
| Number of columns (treatment) | 5 | | | | |
| Number of rows (Time) | 69 | | | | |
| Number of subjects (Subject) | 15 | | | | |
| Number of missing values | 0 | | | | |

**Repeated measures ANOVA, effect of treatment: (F4,10)=5.877; *P=0.0107, effect of time: (F68, 680)=196.0;**

******P<0.0001, treatment x time interaction: (F272,680)= 7,824; ****P<0.0001**

| Post hoc analysis | | | | | |
|---|---|---|---|---|---|
| Compare column means (main column effect) | | | | | |
| | | | | | |
| Number of families | 1 | | | | |
| Number of comparisons per family | 10 | | | | |
| Alpha | 0.05 | | | | |
| | | | | | |
| Tukey's multiple comparisons test | Mean Diff. | 95.00% CI of diff. | Significant? | Summar y | Adjusted P Value |
| | | | | | |
| PLGA NPS_EMPTY vs. PLGA NPS_PTX LOADED M08 AB-TARGETED | -51.66 | -65.05 to -38.27 | Yes | **** | <0.0001 |
| PLGA NPS_EMPTY vs. PLGA NPS_EMPTY M08 AB-TARGETED | 13.59 | 6.543 to 20.64 | Yes | **** | <0.0001 |
| PLGA NPS_EMPTY vs. PLGA NPS_PTX-LOADED | -23.7 | -34.36 to -13.04 | Yes | **** | <0.0001 |
| PLGA NPS_EMPTY vs. FREE PTX | 3.685 | -5.961 to 13.33 | No | ns | 0.8331 |
| PLGA NPS_PTX-LOADED M08 AB-<br>TARGETED vs. PLGA NPS_EMPTY M08 AB-TARGETED | 65.25 | 52.37 to 78.14 | Yes | **** | <0.0001 |
| PLGA NPS_PTX-LOADED M08 AB- TARGETED vs PLGANPS_PTX- LOADED | 27.96 | 12.83 to 43.10 | Yes | **** | <0.0001 |

| | | | | | |
|---|---|---|---|---|---|
| PLGA NPS_PTX-LOADED M08 AB- TARGETED vs. FREE PTX | 55.35 | 40.90 to 69.79 | Yes | **** | <0.0001 |
| PLGA NPS_EMPTY M08 AB- TARGETED vs PLGA NPS_PTX- LOADED | -37.29 | -47.31 to -27.27 | Yes | **** | <0.0001 |
| PLGA NPS_EMPTY M08 AB- TARGETED vs. FREE PTX | -9.908 | -18.84 to -0.9801 | Yes | * | 0.0211 |
| PLGA NPS_PTX-LOADED vs. FREE PTX | 27.38 | 15.41 to 39.35 | Yes | **** | <0.0001 |

# CHAPTER 4

# Controlled Release

# Optimization of an Injectable Hydrogel Depot System for the Controlled Release of Retinal-Targeted Hybrid Nanoparticles

**Ilaria Ottonelli [1,2], Andrea Bighinati [3], Elisa Adani [3], François Loll [4], Riccardo Caraffi [1,2], Maria Angela Vandelli [2], Frank Boury [5], Giovanni Tosi [2], Jason Thomas Duskey [2], Valeria Marigo [3,6], and Barbara Ruozi [2]**

[1] Clinical and Experimental Medicine PhD Program, University of Modena and Reggio Emilia, 41124 Modena, Italy

[2] Nanotech Lab, Te.Far.T.I., Department of Life Sciences, University of Modena and Reggio Emilia, 41125 Modena, Italy

[3] Department of Life Sciences, University of Modena and Reggio Emilia, 41125 Modena, Italy

[4] Nantes Université, Oniris, Univ Angers, CHU Nantes, INSERM, Regenerative Medicine and Skeleton, RMeS, UMR 1229, Nantes, France

[5] Inserm UMR 1307, CNRS UMR 6075, Université de Nantes, CRCI²NA, 49000 Angers, Université d'Angers France

[6] Center for Neuroscience and Neurotechnology, via Campi 287, 41125 Modena, Italy

Pharmaceutics 2023, 15(1), 25; https://doi.org/10.3390/pharmaceutics15010025

This article belongs to the Special Issue: "Polymer- and Lipid-Based Nanostructured Drug Delivery Systems for the Treatment of CNS Diseases: Recent Advances towards Clinical Application"

Received: 16 November 2022

Revised: 13 December 2022

Accepted: 15 December 2022

Published: 22 December 2022

## Abstract

A drawback in the development of treatments that can reach the retina is the presence of barriers in the eye that restrain compounds to reach the target. Intravitreal injections hold promise for retinal delivery, but the natural defenses in the vitreous can rapidly degrade or eliminate therapeutic molecules. Injectable hydrogel implants, which act as a reservoir, can allow for long-term drug delivery with a single injection into the eye, but still suffer due to the fast clearance of the released drugs when traversing the vitreous and random diffusion that leads to lower pharmaceutic efficacy. A combination with HA covered nanoparticles, which can be released from the gel and more readily pass through the vitreous to increase the delivery of therapeutic agents to the retina, represent an advanced and elegant way to overcome some of the limitation in eye drug delivery. In this article, we have developed hybrid PLGA-Dotap NPs, that due to their hyaluronic acid coating can improve in vivo distribution throughout the vitreous and delivery to retinal cells. Moreover, a hydrogel implant was developed to act as a depot for the hybrid NPs to better control and slow their release. These results are a first step to improve the treatment of retinal diseases by protecting and transporting the therapeutic across the vitreous, and to improve treatment options by creating a depot system for long term treatments.

## 1. Introduction

The retina, located in the posterior segment of the eye, is part of the Central Nervous System (CNS), and is responsible for light sensitivity, which is why retinal pathologies affecting different cell types in the retina are directly related to sight loss and blindness. Several multifactorial disorders can result in retinal impairments, such as diabetes, retinal detachment, age related retinal degenerations and tumors, or inherited forms of retinal degeneration. These are an important burden to society because almost 300 million people suffer from severe visual impairment and blindness worldwide [565–567]. The retina is well protected by both the blood-retinal barrier and the inner limiting membrane (at the retinal-vitreal interface), regulating the flux into and out of the retina which greatly limit administration routes. Eye drops are a common drug delivery system for the eye, but this administration route poorly reaches the retina [568]. Surgery is still the major treatment option to remove damaged tissues, administer therapeutic molecules, or place implants and scaffolds for the long term release of drugs, but it is poorly tolerated by patients despite recent advances in surgical techniques [569,570]. Subretinal injections are very effective in the administration of drugs to the retina, as demonstrated in the delivery of Luxturna™, an approved gene therapy for a severe form of retinal degeneration [571]; however this treatment requires a single injection and not repetitive administration. One of the most frequently used routes is intravitreal (IVT) injection, which is less invasive and more tolerated compared to other techniques, allowing repeated injections but increasing the risk of inflammatory reactions in the eye, and retinal detachment . Non-specific diffusion through the eye can lead to poor accumulation in the retina, and finally, free drugs often suffer short half-lives and poor biodistribution through the vitreous when attempting to deliver them to the retina [574,575].

An approach to overcome these limitations, reducing the frequency of administration and improving specific retinal targeting, could be to load therapeutic molecules into nanoparticles (NPs). NPs have emerged as effective tools to deliver therapeutics to specific cells [35,576,577]. In fact, NPs can be tuned

to vary their chemico-physical properties and engineered with specific surface modifications to specifically interact with target cells [234,314,578]. Moreover, NPs have the ability to encapsulate and protect sensitive molecules from degradation in the biological environment, such as peptides, enzymes, and genetic materials which have been proposed for their therapeutic effects but degrade rapidly *in vivo*, such as is often the case when delivering to the retina [341,472]. All these advantages can help reduce side effects to the surrounding healthy tissues and increase the overall therapeutic efficacy of drugs for retinal pathologies, while decreasing the necessary dose and lowering the number of injections. The size of the NPs can be tuned to have specific behavior after IVT injection: it has been demonstrated that NPs larger than 500 nm tend to be rapidly eliminated from the vitreous, while NPs between 200 – 250 nm are cleared less rapidly offering beneficial delivery potential [574,579]. Finally, the surface of NPs can be modified to improve their mobility and avoid clearance by immune cells, which is the starting point for an efficient drug delivery [580,581].

Despite their advantageous properties, when in the vitreous NPs can interact with anionic macromolecules, resulting in their retention at the injection site where they can be eliminated by hyalocytes or freely diffuse and be cleared from the vitreous, hampering their long term efficacy and still requiring multiple injections [582–586]. Moreover, direct injection of NPs might cause toxicity due to poor biomimetic properties of the medium, and poor control on drug release with high burst release [587]. To improve their therapeutic profile, reduce their clearance and therefore the needed number of administrations, while maintaining the advantageous properties of NPs, a depot system can be used. Hydrogels are currently on the rise as effective depot drug delivery systems thanks to their properties such as biocompatibility, biodegradability, high stability, and sensitivity to specific stimuli that can lead to gelification (pH and temperature) after *in vivo* administration [588,589]. Several studies have already shown the advantages of hydrogels for ocular delivery to improve the durability and slow release of large molecules that normally don't transfer through the vitreous, such as growth factors, antibiotics,

or anti-inflammatory drugs, and as scaffolds for wound healing, tissue regeneration after brain surgery, bone regeneration or spinal cord injuries [590–598]. For this reason, hydrogels have also been loaded with NPs, to promote drug loading and improve drug delivery strategies by exploiting the features of the NPs; however, most of these studies focus on inorganic NPs such as gold, silica, or silver NPs [599–601], that offer high stability and reproducibility but tend to accumulate in the tissues and can cause long term toxicity [22,602]. Finally, depending on the makeup of the hydrogel, their stability and degradation rate can be tuned from a few days to several weeks, as shown with other similar hydrogels in the literature [603–606]. This will become critical when deciding on the desired release kinetics for retinal treatment.

In this study, we present an injectable hydrogel loaded with retinal-targeted, biodegradable, hybrid NPs. This system can act as a depot to improve retinal delivery of therapeutics after IVT injection to both protect the therapeutic molecules and slow down their release for more long-term treatment options. Hybrid NPs were formulated with biodegradable components, such as poly(L-lactide-co-glycolic) acid and phospholipids which were fully characterized for their physical chemical properties. Retinal targeting was achieved through a surface functionalization of the NPs with hyaluronic acid and their endocytosis by retinal photoreceptors was assessed *in vitro*. To control the release of the NPs, they were embedded into a thermosensitive hydrogel composed of poloxamer 407 and hyaluronic acid, which showed a liquid behavior at 4°C but underwent gelification at 37°C. These results demonstrated that the hydrogel could delay the mobility of NPs for up to 36 h after administration. This complex delivery system could greatly improve the administration of sensitive therapeutic molecules to the retina by exploiting both the targeting ability and protective effect of NPs while prolonging their release, improving the potential therapeutic timeframe with injectable hydrogels.

## 2. Materials and Methods

### *2.1. Materials*

The Resomer® RG 503H Poly(D,L-lactide-co-glycolide) 50:50 (PLGA) MW 11,000-12,000 was purchased from Evonik (Essen, Germany). Dioleoyl trimethylammonium propane (DOTAP) was purchased by Avanti Polar Lipids (Alabaster, AL). Poloxamer 188; poloxamer 407; Extra Low molecular weight hyaluronic acid MW 8-12kDa (HA12); acetone; methanol; trifluoroacetic Acid (TFA); barium chloride ($BaCl_2$); iodine ($I_2$); and low gelation point agarose, were purchased from Sigma Aldrich (St. Louis, Missouri, USA). Hyaluronic acid, MW 330kDa (HA330), and 1100kDa (HA1100) were purchased from Contipro (Dolní Dobrouč, Czech Republic). Cy5-PLGA was purchased from CD-Bioparticles (Shirley, NY, USA). Dichloromethane (DCM) and potassium iodide (KI) were purchased from Carlo Erba (Cornaredo, Italy). MilliQ water was purified by a Millipore system (Millipore, Bedford, MA, USA). All chemicals used were of analytical grade. Avertin mixture (1.25% (w/v) 2,2,2-tribromoethanol and 2.5% (v/v) 2-methyl-2-butanol), Davidson's fixative (8% Formaldehyde, 31.5% Ethanol, 2 M Acetic Acid), Paraffin, Paraformaldehyde, 4',6-diamidino-2- phenylindole (DAPI), Mowiol 4-88 and 3-(4,5-dimethylthiazol-2-yl)-2,5-diphenyl tetrazolium bromide (MTT) were purchased from Sigma Aldrich. Anti β-Tubulin and anti-Rhodopsin clone 1D4 were purchased from Sigma Aldrich. Anti-Iba1 was purchased from Wako-Chemicals (Fujifilm-Wako, Neuss, Germany). Secondary antibodies anti-mouse and anti-rabbit AlexaFluor 488 were purchased from Invitrogen (Thermo Fisher Scientific, Waltham, MA, USA). 661W-A11 cells [607] were derived from 661W cells received from Dr. Muayyad Al-Ubaidi [608] and are a photoreceptor cell line. Dulbecco's Modified Eagle Medium, Trypsin, Fetal Bovine Serum, Glutamine, Penicillin-Streptomycin were purchased from Thermo Fisher Scientific (Waltham, MA, USA).

*2.2. Nanoparticles*

2.2.1. NP Formulation

NPs were produced following the nanoprecipitation protocol adapted from previously published literature [351,609]. Briefly, 17 mg PLGA, 1 mg Cy5-labeled PLGA, and 2 mg DOTAP were dissolved in 2 mL of acetone and were added dropwise to 20 mL of poloxamer 188 0.5% w/v. The organic phase was evaporated for 2 h under magnetic agitation (Multi-Stirrer, Magnetic Stirrer Velp® Scientifica, Usmate Velate, Italy). The NPs were then centrifuged at 9,700 RPM for 10 minutes to remove excess surfactant (ALC multispeed centrifuge PK 121, Camlab, Cambridge, UK), the pellet was resuspended in MilliQ and stored at 4°C until further use. Purified NPs were lyophilized (LyoLab 3000, Heto-Holten, ThermoFisher Scientific, Waltham, MA) in pre-weighed Eppendorf tubes, and the weight yield % (WY%) was calculated as follows:

WY % = (mg lyophilized product /mg total materials)* 100

2.2.2. Surface modification with HA12

Purified NPs were engineered on the surface by adding HA12 via charge interaction. Based on the amount of NPs recovered, the amount of cationic lipid in the formulation was calculated and used to determine the amount of HA12 to be added. In particular, solutions at different HA12 concentrations were prepared, and 50 μL of stock solutions were added to 300 μL of a prepared NP suspension under magnetic stirring. The concentration was calculated to achieve different N:O molar ratios (N = quaternary amines from the DOTAP molecules, O = acid residues on HA12) ranging from 1:0.025 to 1:2. The HA12 solution was added in 5 μL drops over 2 minutes. The suspension was left under stirring for 1 h and then characterized.

2.2.3. Chemico physical characterization

The size, Polydispersity Index (PDI), and Z-Potential of the NPs were measured by diluting 10 μL of purified NPs in 1 mL of MilliQ water (final concentration ~0.01 mg/mL) and analyzed using Photon Correlation Spectroscopy (PCS) (Zetasizer Nano ZS, Malvern, Malvern, UK). All samples were analyzed in triplicate at room temperature, and each measurement was made on three different NP formulations.

### 2.2.4. Morphological characterization

Morphology of NPs was evaluated using Atomic Force and Electron Microscopy. AFM analysis (AFM, Park Instruments, Sunnyvale, CA, USA) was performed at RT, operating in non-contact mode using triangular silicon tips. The resonant frequencies of the cantilever were found to be about 160 kHz. Before the analysis, NPs were diluted to 0.01 mg/mL in MilliQ water, and applied to a small mica disc. Excess water was removed before analysis. The topographical images were flattened using second-order fitting to remove sample tilt.

The structure of the samples was also analyzed by scanning transmission electron microscopy (STEM FEI Nova NanoSEM 450, Bruker, Billerica, MA, USA). Briefly, a drop of the same diluted suspension (0.01 mg/mL) used for AFM imaging was placed on a 200–mesh copper grid (TABB Laboratories Equipment, Berks, UK), allowed to adsorb, and the excess was removed by filter paper. All grids were analyzed using the transmission electron microscope operating at 25 kV using a STEM II detector in Field free mode.

### 2.2.5. Residual poloxamer 188

The residual surfactant in the NP matrix was evaluated by an already published colorimetric method [610,611]. About 2 mg of NPs were solubilized in 0.5 mL of DCM, and then added to 10 mL of water. After evaporation of DCM, the suspension was filtered through cellulose nitrate filter, porosity 0.45 m (Sartorius,

Firenze, Italy) to remove the precipitated PLGA. 2 mL of the aqueous solution were treated with 2 mL of 0.5% w/v $BaCl_2$ in HCl 1 N and 0.5 mL of $I_2$/KI (0.05 M/0.15 M), and incubated for 10 minutes in the dark. Poloxamer 188 concentration was calculated using a spectrophotometer (Model V530, Jasco, Cremella, Italy) measuring the absorbance at 540 nm, using a calibration curve from stock solutions of poloxamer 188 prepared under the same experimental conditions. Linearity was found in the range of 4 – 48 μg ($R^2 = 0.9927$). Due to the sensitivity to heat and light of the aqueous solution of $I_2$/KI, the calibration curve was calculated fresh before analysis. The analysis was performed in triplicate on three different NP formulations. The residual poloxamer 188 was calculated as follow:

% RP = (mg poloxamer 188 from quantification / mg NP) * 100

*2.3. In vivo biodistribution*

All procedures on mice were conducted at CSSI (Centro Servizi Stabulario Interdipartimentale) and approved by the Ethical Committee of University of Modena and Reggio Emilia (Prot. N. 106 22/11/2012) and by the Italian Ministero della Salute (346/2015-PR). *Rho*$^{P23H/+}$ mice [612] were obtained from Dr K. Palczewski and maintained in a 12 h light/dark cycle with free access to food and water. NPs were intravitreally injected in *Rho*$^{P23H/+}$ mice at the age of 14 days after birth (PN14). Mice were anesthetized with an intraperitoneal injection of avertin at a dose of 250 mg/kg body weight, a 34GA needle was inserted adjacent to the limbal border of the cornea and 0.5 μL of fluorescently labeled HA12-coated or uncoated NPs were injected into the vitreous at a concentration of 8 mg/mL. Twenty-four h after administration animals were sacrificed, eyes were removed, fixed in Davidson's fixative for 24 hours, embedded in paraffin and sectioned with a microtome [613]. For cell type identification, immunofluorescence was performed with anti-Rhodopsin clone 1D4 (1:500), anti-Iba1 (1:100) as primary antibodies and AlexaFluor 488 anti-mouse or anti-rabbit (1:1,000) as secondary antibodies. Nuclei were stained with 0.1 μg/ml DAPI. Slides were mounted using

Mowiol 4-88 and images were acquired using an SP8 confocal microscope (Leica, Heidelberg, Germany) with a 40X oil objective, equipped with white light laser.

### *2.4. In vitro tests*

#### 2.4.1. Cell viability

Toxicity of NPs was assessed as previously published [614]. Briefly, 661W-A11 cells were cultured in 96-well plates at a density of 6000 cells/well and increasing dilutions of NPs were added to the culture medium. After 48 or 72 h, the medium was aspirated and the cells in each well were incubated for 2 h at 37°C with 50 µL of 1 mg/mL 3-(4,5-dimethylthiazol-2-yl)-2,5-diphenyl tetrazolium bromide (MTT) diluted in the culture medium. The supernatant was removed and the purple formazan crystals were dissolved in 100 µL of isopropanol and shaken for 10 min. Lastly, the optical density (OD) was measured at 570 nm using a microplate reader (Labsystems Multiskan MCC/340, Fisher Scientific, Rodano, Italy).

#### 2.4.2. Cell uptake studies

661W-A11 cells were seeded onto laminin coated glass coverslips in a 24-well plate at a density of 20,000 cells/well and 8 µg/mL of NPs were added to the culture medium. After incubation for 1 or 24 h, cells were fixed with 2% paraformaldehyde for 10 min. Cell cytoskeleton was labelled by immunofluorescence. Briefly, the cells were blocked and permeabilized with 3% bovine serum albumin and 0.1% Triton X-100, then incubated with the primary antibody anti-$\alpha$-Tubulin (1:100) for 1 h and secondary antibody AlexaFluor 488 anti-mouse (1:1,000) for 1 h and nuclei were stained with 0.1 µg/ml DAPI. Slides were mounted using Mowiol 4-88 and images were acquired using the confocal microscope.

### *2.5. Thermosensitive hydrogel (TSH)*

The formulation of the TSH was optimized by changing the concentration of HA 330 kDa (HA330) and poloxamer 407 (P407). Empty TSH were formulated by dissolving different amounts of HA330 in MilliQ water at 50°C under magnetic stirring for about 30 seconds, ranging from 0.5 to 1% w/v. After complete dissolution, samples were cooled to 4°C. Then, different amounts of P407 were added from 5 to 15% w/v, and samples were left under agitation at 4°C overnight.

To formulate TSH loaded with NPs, the NP suspension was prepared and used instead of water during the formulation of the TSH. HA330 was added to the NP suspension, and samples were heated to 50°C for 30 seconds under stirring. Samples were immediately cooled to 4°C, P407 was added, and samples were left under agitation overnight at 4°C. The impact of NP concentration on the rheological properties of the resulting TSH was also evaluated by preparing hydrogels with NP suspensions ranging from 4 to 12 mg/mL.

### *2.6. Synthetic Vitreous (SV)*

To investigate the mobility of the NPs loaded in the TSH without the use of animal models, a model for synthetic vitreous (SV) was optimized and characterized starting from literature protocols [615]. Briefly, HA1100 was dissolved in MilliQ at 60°C under magnetic stirring. After complete dissolution, Agarose was added while keeping the temperature at 60°C. Eventually, samples were cooled and stored at 4°C until further use. Details on the formulated SVs and their characterization are provided in the Results.

### *2.7. Rheological measurements*

Rheological properties of the TSH and the SV samples were evaluated with a Haake Mars Rheometer (ThermoFisher Scientific, Waltham, MA), using a conic geometry (1°) of 35 mm diameter. The gap size was 52 μm, and the volume of the sample analyzed was 200 μL. All analyses were performed using the RheoWin

Data Manager software (version 4.82.0002, ThermoFisher Scientific, Waltham, MA).

Viscosity of synthetic vitreous (SV) samples was measured by applying a shear rate from 0.01 to 300 $sec^{-1}$ at 37 °C, and results were fitted with the Carreau-Yasuda mathematical model to obtain the absolute viscosity ($\eta_0$). An amplitude sweep from 10 to 600% was performed at constant parameters of 1 Hz and 37 °C to get the storage modulus G' of the gels, as a mean of values on the linear-viscoelastic regime (LVR). To measure the gelation temperature (Tgel) of the TSH samples, a 20-steps ramp in a range of 5-50 °C at a rate of 0,075 °C/sec was performed at a constant frequency f = 1 Hz and a constant shear stress $\tau$ = 1 Pa. G' and G'' were recorded at each step and the gelation temperature was obtained at the crossover.

*2.8. NP diffusion through TSH*

NP diffusion through the TSH was evaluated by confocal imaging using the optimized SV as a model. The SV was heated to room temperature, then 200 µL were put in the wells of a 8-well glass bottom plate (Ibidi, Gräfelfing, Germany), covered with Parafilm and incubated at 37°C for 1 h. After that, 20 µL of cold (4°C) Cy5-labeled NP suspension or NP-loaded TSH were injected into the SV. Confocal imaging started right after the injection, keeping the temperature at 37°C. The laser was set to acquire the signal of the Cy5 (ex. 650 nm; em. 670 nm), and images were acquired every 6 h for a total of 48 h using a 10x objective. Each time point consisted of 35 Z-stack images with a 5 µm Z-step. Two fields were imaged, i.e. the injection site, and the opposite corner of the well (5 mm distance) After acquisition, images were processed with Fiji ImageJ: Z-stacks were collapsed to maximum intensity per each time point. A threshold was set to remove background signal, and total fluorescent intensity was measured for each time point and for each field. Each sample was analyzed in triplicate. Fluorescence intensity % was calculated as follows:

FI% = FI in the analyzed field / (FI at injection site + FI opposite corner) * 100

*2.9 Statistical analysis*

Statistical analysis was performed using the Mann-Whitney test for pairwise comparisons using GraphPad Prism 6 (GraphPad Holdings, San Diego, CA, USA). Significances are indicated in the figures as * $p < 0.05$. All samples were performed with $n > 3$ and expressed as an average with standard deviation (SD).

## 3. Results

### *3.1. Formulation and Characterization of NPs*

Starting from an already published nanoprecipitation protocol, hybrid NPs composed of the biodegradable and biocompatible polymer poly(lactic-co-glycolic) acid (PLGA) and the cationic lipid dioleoyl-trimethylammonium propane (DOTAP) were formulated and characterized (Table 1). Dimensional analysis evidenced a monomodal population with a size ∽240 nm, with low dispersity demonstrated by a PDI < 0.2. The Z-potential was strongly positive, over +35 mV, as expected due to the presence of the cationic lipid. The weight yield was calculated to be 85 ± 6%. Moreover, the amount of residual poloxamer 188 was calculated and accounted for about 10% of the total weight of the NPs, which is in line with previous studies for similar polymeric and hybrid NPs [616].

**Table 1.** Chemico-physical characteristics of NPs.

| N:O ratio | Size (nm) | PDI | Z Potential (mV) |
|---|---|---|---|
| 1:0 † | 239 ± 18 | 0.16 ± 0.04 | +39 ± 2 |
| 1:0.025 | 306 ± 12 | 0.29 ± 0.05 | +38 ± 7 |
| 1:0.05 | > 1000 | / | / |
| 1:0.1 | > 1000 | / | / |
| 1:0.2 | > 1000 | / | / |
| 1:0.5 | 846 ± 147 | 0.78 ± 0.11 | -30 ± 7 |
| 1:1 | 257 ± 6 | 0.21 ± 0.04 | -35 ± 5 |
| 1:2 | 298 ± 16 | 0.25 ± 0.07 | -38 ± 6 |

† 1:0 ratio refers to uncoated NPs

The formation of the HA12 coating was optimized by evaluating the effects of adding different molar ratios based on the cationic nitrogen of the DOTAP and negative oxygen on the HA12 (N:O ratio) from 1:0.025 to 1:2 (Table 1). Starting from the sample with the lowest amount of HA12, no differences in the Z-potential were noticed with the NPs remaining cationic. This suggested that this amount of HA12 was too low to produce an effective coating. Increasing the amount of HA12 between 1:0.05 and 1:0.5 caused rapid aggregation which could be ascribed to the

incomplete formation of the coating, with the polyanionic molecules extending from one particle to another, causing aggregation between the molecules. Similar effects have been reported in the literature in which a low concentration of polyanion resulted in the entanglement of the polymeric chains, promoting their aggregation and hampering the colloidal stability [617,618]. Further increase of the N:O ratio over 1:1 resulted in the formation of stable and homogenous NPs with a size around 260 nm and a good homogeneity (PDI < 0.3). Notably, the Z-potential shifted to negative values ($\backsim$ −30 mV), suggesting the formation of the HA12 layer on the surface of the cationic NPs. Further addition of HA12 at a 1:2 ratio also resulted in homogeneous and stable NPs, with a size < 300 nm and low PDI, but the ratio of 1:1 was deemed the most promising as it could produce suitable NPs while using the minimum amount of HA12. The presence of this stable coating was also confirmed by Atomic Force (AFM) and Scanning Transmission Electron microscopy (STEM) analysis (Figure 1). AFM images showed the presence of flattened material surrounding the more rigid PLGA-based core, while STEM images revealed the presence of a lighter corona around an electron dense core, suggesting a distinct deposition of HA12 around the surface of the hybrid NPs.

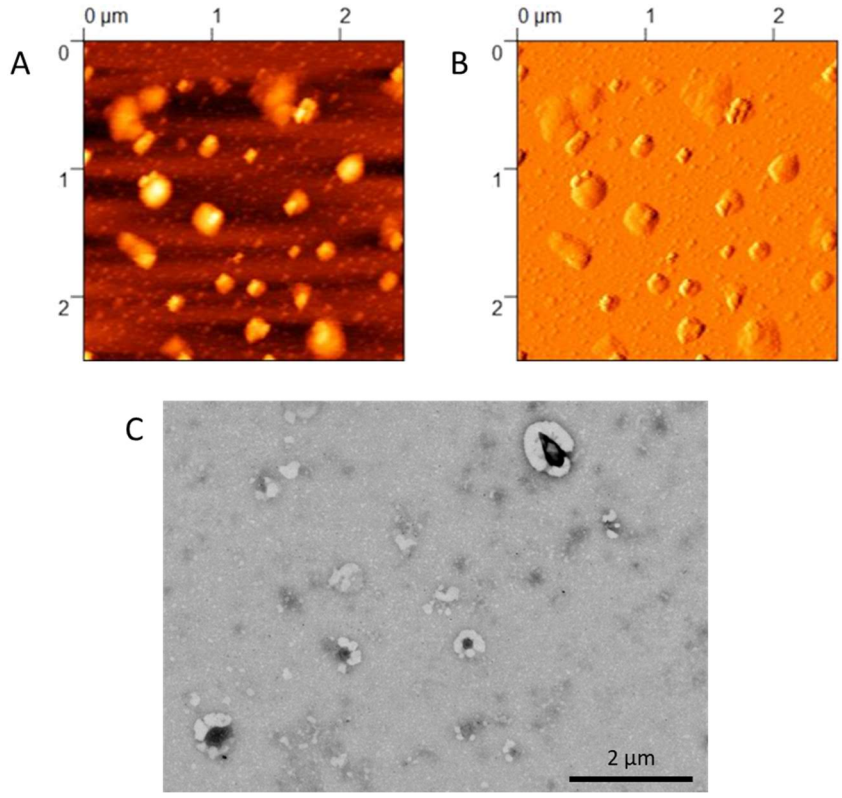


**Figure 1.** Morphological analysis of HA12-coated NPs, at N:O ratio 1:1. A) AFM "Topography" image, B) AFM "Error Signal" image. C) STEM images.

### *3.2. In vivo biodistribution and microglia colocalization*

To assess the retinal targeting potential of these hybrid NPs, an in vivo biodistribution study was performed. The experiment was performed using a murine line bearing a mutation in the rhodopsin gene (Rho) that causes slow-progression retinal degeneration, where photoreceptor cell death starts to be detected at PN15. The choice of a disease model allowed us to define whether the pathological environment may affect NP biodistribution. Mice were intravitreally injected at PN14 with 0.5 µL of a suspension of fluorescently labeled NPs with or without the HA12 coating and analyzed one day later. To assess the distribution of NPs in the retinal tissue, photoreceptor and microglia cells were labelled. Confocal imaging evidenced the different behavior of the two formulations: uncoated NPs were unable to disperse through the vitreous due to their cationic surface that strongly interacted with the anionic polymers in the vitreous matrix.

These NPs accumulated at the site of injection and were uptaken by cells in the vitreous (Figure 2A). On the other hand, HA12-coated NPs were abundantly found inside the retinal tissue up to the photoreceptor cell layer, indicating that the presence of the coating improved the mobility of NPs through the vitreous towards the retina (Figure 2B).

Microglia is activated in the degenerating retina and may promptly phagocytize the injected NPs. Thus, microglia cells were highlighted to investigate this possibility. Data evidenced no colocalization between NPs and microglia cells, suggesting a low in vivo uptake of these NPs at the concentration used (Figure 2C,D).

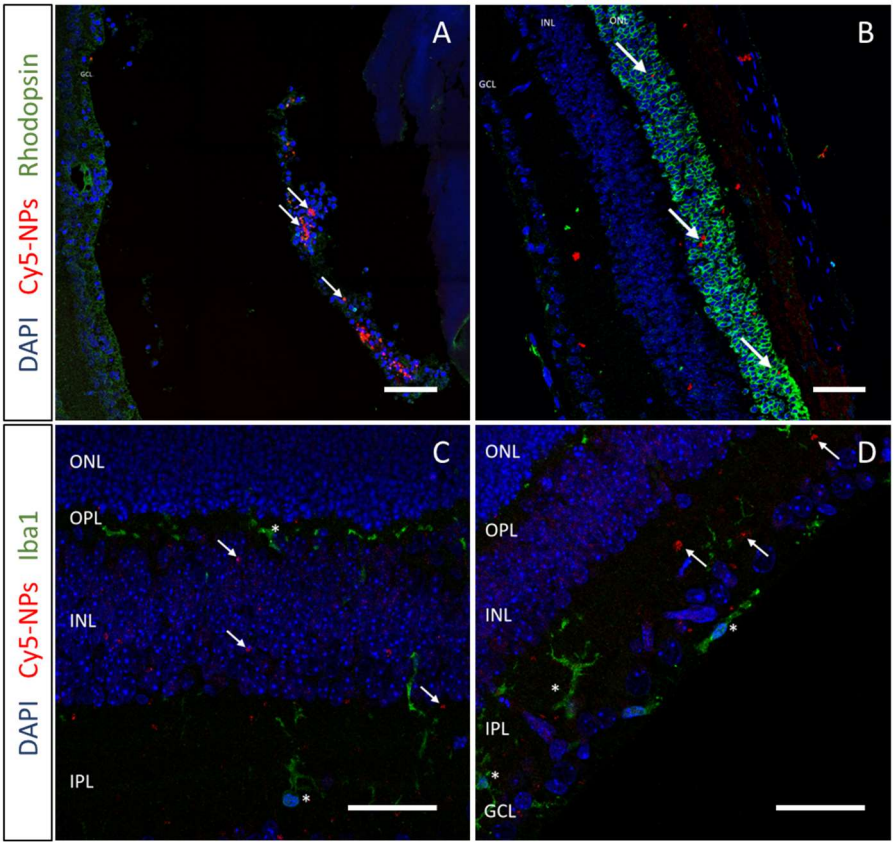


**Figure 2.** *In vivo* biodistribution study. Confocal images of sagittal eye sections after intravitreal injection of A) Uncoated NPs, B) HA12-coated NPs. Red: Cy5-labeled NPs; Blue: DAPI-labeled nuclei; Green: Rhodopsin labelling photoreceptors. C,D) Evaluation of microglia in retinal tissue after injection of HA12-coated NPs. Red: Cy5-labeled NPs; Blue: DAPI labeled nuclei; Green: Iba-1 labelling microglia cells. Scale bar 40 μm. Arrows indicate NPs, Stars indicate Iba-1 positive cells. ONL: Outer nuclear layer; OPL: Outer plexiform layer; INL: Inner nuclear layer; IPL: Inner plexiform layer; GCL: Ganglion cell layer.

*3.3. In vitro uptake studies*

Data collected *in vivo* suggested that HA12-coated NPs were the most promising NPs to deliver drugs to photoreceptor cells. Hence, HA12-coated NPs were further investigated with toxicity and uptake studies performed *in vitro* in a photoreceptor cell line, 661W-A11 [607].

Toxicity studies were performed to assess the tolerated concentration of coated NPs to be further used in the uptake studies (Figure 3). Reduction of cell viability was not observed with doses up to 8 μg/mL of NPs over 72 h of exposure. Increasing the concentration of NPs to 80 or 800 μg/mL induced a slight toxicity in cells, reducing the cell viability of about 25% with a dose-dependent trend. Thus, 8 μg/mL was chosen as the working dilution for further experiments, as this was the highest concentration that did not significantly affect cell viability.

To study the ability of photoreceptor cells to uptake the HA12-coated NPs, 661W-A11 cells were co-cultured with fluorescently labeled NPs. Cells were fixed at 1h and 24 h after administration and NP internalization was assessed by staining the nucleus and the cytoskeleton to distinguish the cytoplasmic and nuclear compartments. Images acquired at 1 h already showed the presence of NPs in the cytoplasm of some cells, which was confirmed after 24 h (Figure 4). Based on these results, together with the *in vivo* biodistribution study, we propose that these NPs can be a promising tool to deliver drugs to the retina.

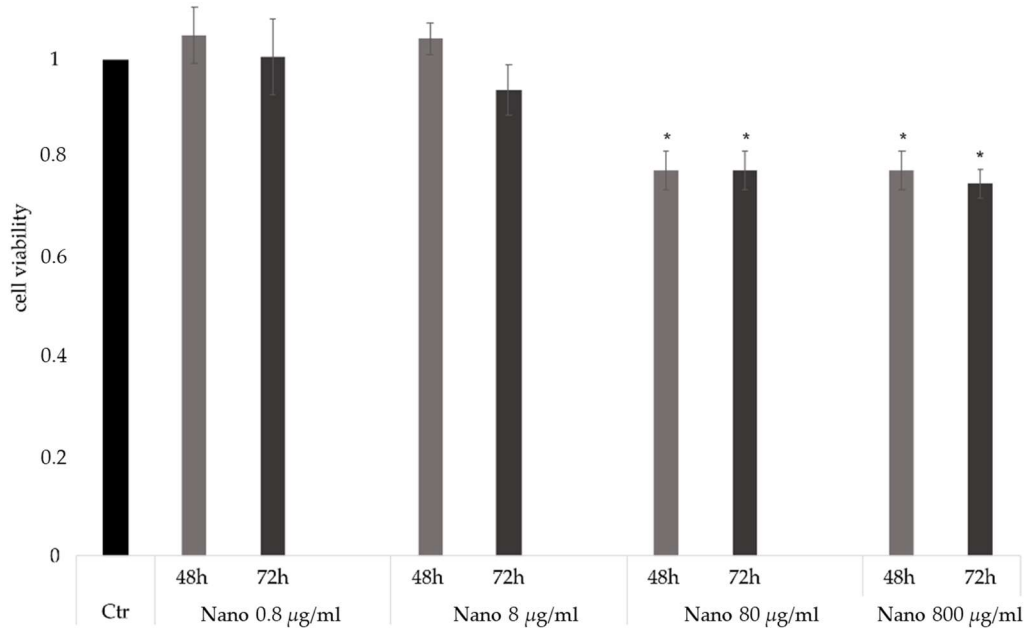


**Figure 3.** *In vitro* toxicity study. Cell viability of 661W-A11 cells after administration of HA12-coated NPs diluted in cell medium at 0.8, 8, 80, and 800 μg/mL. Mean and SD, n>3, with p = * < 0.05 calculated using the Mann-Whitney Comparison test.

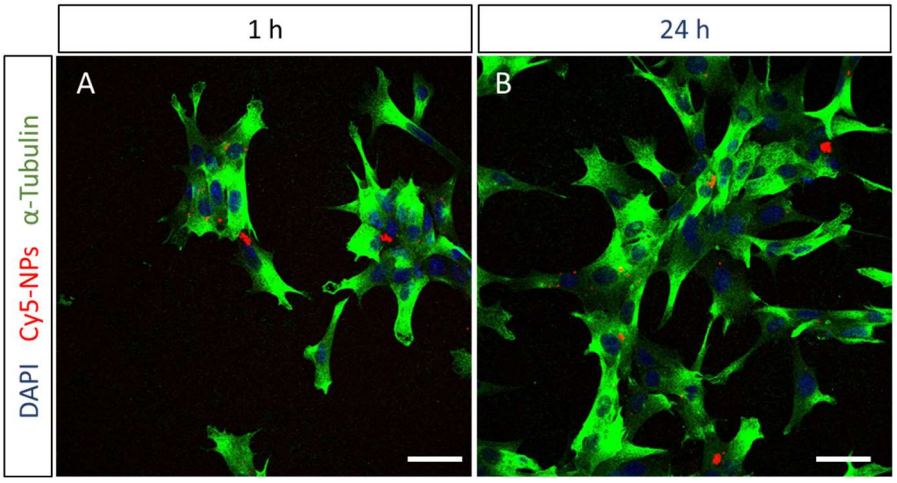


**Figure 4.** *In vitro* uptake study. Confocal images of 661W-A11 photoreceptor cells A) 1 h and B) 24 h after administration of HA12-coated NPs. Red: Cy5-labeled NPs; Blue: DAPI labelling nuclei; Green: α-Tubulin labelling the cytoskeleton. Scale bar 40 μm.

### *3.4. Formulation of the TSH*

After demonstrating the ability of HA12-coated NPs to reach the retina after IVT injection, the formulation of a NP-loaded thermosensitive hydrogel was optimized. The aim was to have a hydrogel with a liquid-like behavior at cold temperatures, promoting a good injectability, and a gelation point around 35°C, in

order to form a hydrogel in vivo. TSH formulations were produced with poloxamer 407 (P407) and hyaluronic acid 330kDa (HA330). A first screening was performed evaluating the effect of both polymers individually on the gelation temperature (Tgel). First, hydrogels with 15% P407 and HA330 from 0.1 to 1% were tested, showing that the Tgel is independent from the amount of HA330 (Table 2). Thus, 0.5% was chosen for further formulations, to balance the need for biocompatibility together with low viscosity of the formulation. Hydrogels were then formulated with 5-15% P407, evidencing the tight relationship between the concentration of P07 and the Tgel (Table 3): only formulations with 10 and 15% P407 showed a Tgel around 35°C, being respectively around 46 and 25 °C. While it would have been possible to further optimize the empty formulation of TSH to reach the Tgel of 35°C, the influence of NPs in the matrix of a hydrogel is also a crucial parameter to consider, as it can directly affect the Tgel. Therefore, the hydrogel with 10% P407 and 0.5% HA330 was formulated and loaded with either uncoated or HA12-coated NPs to investigate their impact on the gelation.

**Table 2**. Effect of the HA330 concentration on the Tgel of different empty TSH formulations with 15% P407.

| HA330 | Tgel °C (SD) |
|---|---|
| 0.1% | 27.2 (2.0) |
| 0.25% | 24.2 (0.3) |
| 0.5% | 25.7 (3.0) |
| 0.75% | 23.1 (0.1) |
| 1% | 26.6 (1.9) |

**Table 3**. Effect of the P407 concentration on the Tgel of different empty TSH formulations with 0.5% HA330

| P407 | Tgel °C (SD) |
|---|---|
| 5% | >50 |
| 10% | 46.2 (3.1) |
| 15% | 25.7 (3.0) |

Different concentrations of NPs were used to assess the loading capacity of the TSH and their impact on the Tgel. NPs at 4, 8, and 12 mg/mL were produced and characterized (Table 4). Data evidenced that 12 mg/mL NPs were too concentrated to have reproducible formulations: in fact, both coated and uncoated NPs showed the formation of aggregates with higher polydispersity compared to lower concentrations. This also resulted in poor reproducibility when testing the Tgel of the TSH formulations, as suggested by the high SD values of these samples. On the contrary, hydrogels prepared with NP suspensions at 8 and 4 mg/mL showed more reproducible results, all of them having a Tgel in the range 34 - 40 °C. Specifically, the formulation of TSH produced with uncoated or coated NPs at 8 mg/mL was deemed the most promising to be further tested: the Tgel of these hydrogels was around the desired temperature of 35°C, and at the same time NPs were at the highest concentration.

**Table 4**. Chemico-physical characteristics of NPs at different concentration, and effect of the concentration of NPs on the Tgel of a TSH formulation with 10% P407 and 0.5% HA330.

| | **Uncoated NPs** | | | **HA12-coated NPs** | | |
|---|---|---|---|---|---|---|
| **[NPs]** | **Size nm (SD)** | **PDI (SD)** | **Tgel °C (SD)** | **Size nm (SD)** | **PDI (SD)** | **Tgel °C (SD)** |
| 4 mg/mL | 228 (5) | 0.10 (0.05) | 40.4 (2.4) | 224 (13) | 0.16 (0.02) | 36.6 (0.9) |
| 8 mg/mL | 239 (18) | 0.16 (0.04) | 34.3 (0.5) | 257 (6) | 0.21 (0.04) | 35.1 (1.1) |
| 12 mg/mL | 460 (114) | 0.25 (0.18) | 39.2 (10.3) | 361 (24) | 0.30 (0.05) | 38.8 (9.4) |

*3.5. Mobility of NPs through the TSH in synthetic vitreous*

With the aim of evaluating the behavior of the TSH in a vitreous environment, an *in vitro* model of the vitreous was developed. The formulation of a model for synthetic vitreous (SV) was optimized by adapting literature protocols, based on hyaluronic acid HA1100 (MW 1100 kDa) and Agarose. Formulations with different amounts of these polymers were tested for viscosity and storage modulus G' to match with values reported for the human vitreous. In particular, the composition was modified in order to obtain a viscosity around 0.1 Pas and a G' < 3 Pa, and the optimal composition was found to be 0.25% w/v HA1100 and 0.05% w/v agarose

(Table 5) [619,620]. This formulation was used to simulate the vitreous in further experiments.

**Table 5**. Composition and rheological characteristics of synthetic vitreous models.

| Agarose | HA1100 | η (Pas) | G′ (Pa) |
|---|---|---|---|
| 0.5% w/V | 0.5% w/V | 11.0 ± 1.9 | 15.1 ± 3.2 |
| 0.1% w/V | 0.5% w/V | 5.1 ± 0.5 | 13.9 ± 2.3 |
| 0.1% w/V | 0.25% w/V | 0.5 ± 0.1 | 0.7 ± 0.1 |
| 0.05% w/V | 0.5% w/V | 0.7 ± 0.1 | 1.2 ± 0.2 |
| 0.05% w/V | 0.25% w/V | 0.1 ± 0.0 | 0.3 ± 0.1 |

The mobility of NPs loaded into TSH was evaluated using the optimized SV as a model. Comparisons were made between HA12-coated NPs embedded in the TSH formulation, and NPs as a suspension to simulate the direct injection. When NPs were embedded in the TSH, only 7 % of NPs were found at the opposite corner of the well after 36 h, and increased to around 15% after 48 h incubation (Figure 5A). This 36 h delay suggests that the hydrogel could help control the release of these retinal targeted NPs, enhancing the therapeutic efficacy. On the other hand, the suspension of coated NPs were expected to be highly mobile when in the SV, similarly to what was observed *in vivo*. Surprisingly, they rapidly precipitated to the bottom of the dish, and no fluorescence was observed after 48 h at the opposite corner (Figure 5B).

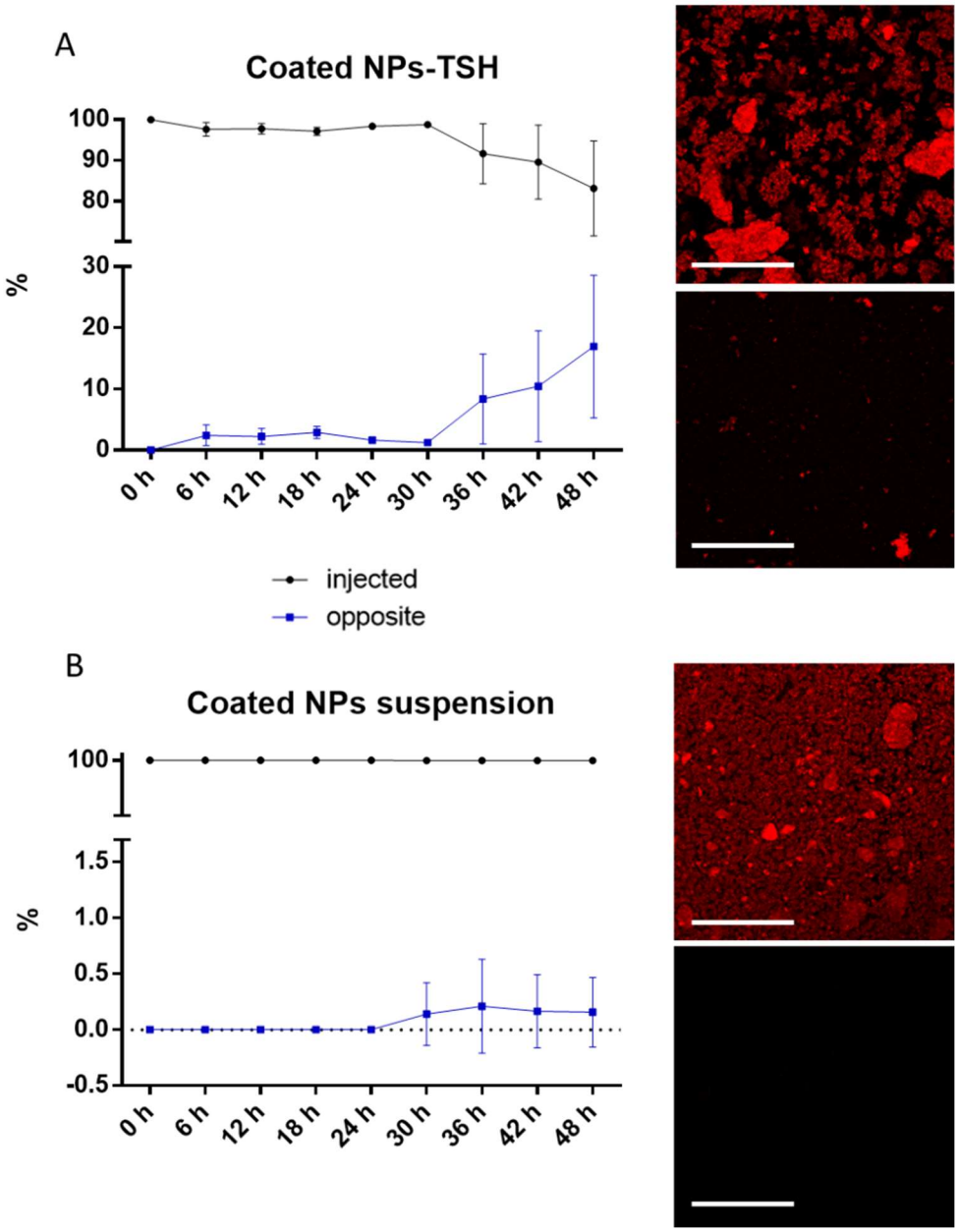


**Figure 5.** Fluorescence intensity % of NPs after administration in synthetic vitreous with representative confocal images at 48 h. Black line: fluorescence intensity at the injected site. Blue line: fluorescence intensity at the opposite corner. A) Mobility of HA12-coated NPs in the TSH formulation. B) Mobility of HA12-coated NPs in water suspension. Mean and SD, n = 3. Scale bar: 100 μm.

## 4. Discussion

The development of non-invasive delivery strategies is one of the major challenges in the field of treating retinal pathologies. The retina is well protected by the inner limiting membrane, which separates it from the vitreous, and the blood-retinal barrier, together limiting diffusion of therapeutics to the retinal cells. Moreover, free drugs injected in the vitreous are often rapidly degraded or eliminated, reducing their therapeutic efficacy. Finally, common administration routes for the retina are often invasive, producing inflammation and reducing the compliance of patients. In this work, we optimized an advanced drug delivery system, composed of coated hybrid nanoparticles embedded in an injectable hydrogel that undergoes gelation *in vivo*. This system can allow for the slow release of nanoparticles, and thanks to their HA coating, their passage towards the retina can be improved, which could positively affect their therapeutic efficacy and reduce the invasiveness of the approach.

Retinal targeted hybrid nanoparticles (NPs) have been demonstrated to have great promise when optimized to transport various biological molecules to the retina, as they combine the characteristics of lipidic and polymeric systems for improved stability, enhanced drug loading, lower degradation kinetics, and decreased cell toxicity [621–624], but they can still require repeat injections diminishing their overall efficacy and desirability. Here, hybrid NPs were successfully formulated with a single-step nanoprecipitation protocol, followed by surface modification via charge interaction between the core and the HA. The optimized NPs had a diameter of approximately 260 nm which can be beneficial for an extended half-life and delivery through the vitreous to the retina. The optimized biodegradable NPs, composed of PLGA, Dotap, and hyaluronic acid hold especially high potential to encapsulate, adsorb, or incorporate a variety of therapeutic molecules. The hydrophobic matrix of PLGA and Dotap will aid in the ability to incorporate small lipophilic molecules, [40,625,626] while the cationic charge of Dotap could be advantageous to enhance the loading efficiency of anionic molecules. Finally, the presence of HA enhanced the biocompatibility and mobility of NPs in the

vitreous humor, as demonstrated by the fact that uncoated NPs became trapped and did not move through the vitreous, while the HA coating allowed for the diffusion towards the retina. This ultimately improved cellular uptake in the retina, most likely due to the interaction with the CD44 receptors, as it has previously been suggested in the literature [627–629]. This nanosystem represents a highly versatile tool to deliver therapeutics to the retina, as demonstrated by its targeting potential, and its ability to diffuse throughout the vitreous and reach the retina, where NPs could be endocytosed by photoreceptor cells, while also representing a system that could be highly compatible with various drug types, if compared to the non-hybrid or non-coated systems alone, as the anionic HA layer on the surface is expected to help entrap cationic molecules [630–632].

Notwithstanding the possibility of using HA coated NPs to deliver therapeutics to the retina, strategies to reduce the number of intravitreal injections needed by prolonging the stability of the NPs were developed. With this aim, HA-coated NPs were embedded into an injectable thermosensitive hydrogel, which was optimized to have a gelation point of around 35°C. This temperature would allow it to be easily injectable in its liquid form but would form a scaffold when administered *in vivo* reaching biological temperatures in the eye. This was achieved by using 10% P407, 0.5% HA330, and 8 mg/mL NPs. These parameters were optimized for IVT injectable scaffold systems, requiring minimized injection volumes and maximized NP loading to be efficacious. This is because concerns arise that injecting a hydrogel would overly increase interocular pressure and cause damage [633,634]. While this is true, especially in such a small model such as in a mouse, advanced methodologies for higher order animals (i.e. rabbits) have already started to overcome this issue by performing a small vitrectomy before gel injection to reduce the overall pressure. This work showed that such a procedure in the rabbit retina did not lead to inflammation or other damage, opening the possibility for more detailed studies going forward [635].

To demonstrate the ability of the TSH to reduce the mobility of NPs in the vitreous, enhancing the timeframe of therapeutic efficacy, NP-loaded TSH and a NP suspension were compared after injection in a syagaronthetic vitreous model. Results evidenced that, contrary to the rapid diffusion of NPs observed *in vivo*, the THS was able to delay NPs mobility for up to 36 h after administration. Surprisingly, NPs in suspension rapidly sedimented at the bottom of the dish and were not able to move in the SV. This evidences a missing piece in the use of this *in vitro* model just for NP assessment, as the phenomenon could be explained by the different microenvironment formed at the interface between the sample and the SV. For the NPs alone, the aqueous phase, even if heated to the solidification temperature of the gel (37°C), dilutes the gel at the point of injection leading to a loss of viscosity and allowing the precipitation of the NPs down onto the surface, where they can no longer move throughout the gel. On the other hand, increasing the viscosity and osmotic pressure of the medium by adding the HA330 and P407 enhanced the colloidal stability, and the similarity between the hydrogel and the SV resulting in a reduced osmotic gradient that would favor suspension of the NPs [179,636–638]. While these results would closely mimic the results of the *in vivo* retinal injection of the loaded TSH, the artifact with the NPs alone demonstrated the need for for more advanced *in vivo* studies to precisely assess the impact of the hydrogel on the mobility of NPs.

Recent studies over the last two years address similar approaches based on hydrogels or NPs for ocular applications. The use of hydrogel alone has been investigated by López-Cano et al., demonstrating promising results; however, its efficacy was only tested with small molecules *in vitro*, therefore the stability and drug release could differ after *in vivo* injection, demonstrating rapid degradation or clearance as often seen for non-protected small molecules [639]. On the other hand, Suri et al. studied NPs of PLGA and Chitosan to protect and deliver sirolimus to the retina for the treatment of age-related macular degeneration [640]; however, NPs alone might not ensure a prolonged release of the drug as they are often rapidly cleared from the eye, requiring multiple injections. Thus, the

combination of NPs and hydrogels seems to be the most effective strategy going forward to achieve both prolonged release and protection of the drug. To this end, Hsu et al. developed a hydrogel based on hyaluronic acid loaded with PLGA NPs, using bovine serum albumin as a model drug. While showing promising results in terms of stability and drug release, the hydrogel required chemical cross-linking before administration. This led to a more stable system, but highly viscous cross-linked hydrogels cannot be injected and must be implanted, leading to a more invasive approach [641]. Finally, injectable thermosensitive hydrogels loaded with chitosan-based NPs were investigated by Taheri et al. This system required the addition of the semi-synthetic cellulose derivative HPMC to reach the desired gelation point, and higher concentrations of poloxamer 407 compared to our system [642].

Altogether, our thermosensitive NP-loaded hydrogel was optimized to be versatile to overcome many of these barriers: 1) hybrid NPs to load and protect a variety of molecules; 2) HA coating on NPs to improve mobility through the vitreous towards the retina; 3) thermosensitive hydrogel for sustained release; 4) gelation at physiological temperature allowing injectability with gel formation upon administration. This work is a first step in creating a more patient-friendly and new curative option for retinal diseases.

# CHAPTER 5

# Scalability Issues

# Microfluidic Technology for the Production of Hybrid Nanomedicines

**Ilaria Ottonelli [1,2], Jason Thomas Duskey [1], Arianna Rinaldi [1,2], Maria Vittoria Grazioli [1], Irene Parmeggiani [1], Maria Angela Vandelli [1], Leon Z. Wang [3], Robert K. Prud'homme [3], Giovanni Tosi [1,] and Barbara Ruozi [1]**

[1] Nanotech Lab, Te. Far.T.I., Department. Life Sciences, University of Modena and Reggio Emilia, 41125, Modena, Italy

[2] Clinical and Experimental Medicine PhD Program, University of Modena and Reggio Emilia, 41125, Modena, Italy

[3] Department of Chemical and Biological Engineering, Princeton University, Princeton, NJ 08544, USA

Pharmaceutics 2021, 13(9), 1495; doi: 10.3390/pharmaceutics13091495

This article belongs to the Special Issue: "Pharmaceutics and Drug Delivery in Italy"

Received: 5 August 2021

Revised: 6 September 2021

Accepted: 13 September 2021

Published: 17 September 2021

## Abstract

Microfluidic technologies have recently been applied as innovative methods for the production of a variety of nanomedicines (NMeds), demonstrating their potential on a global scale. The capacity to precisely control variables, such as the flow rate ratio, temperature, total flow rate, etc., allows for greater tunability of the NMed systems that are more standardized and automated than the ones obtained by well-known benchtop protocols. However, it is a crucial aspect to be able to obtain NMeds with the same characteristics of the previously optimized ones. In this study, we focused on the transfer of a production protocol for hybrid NMeds (H-NMeds) consisting of PLGA, Cholesterol, and Pluronic® F68 from a benchtop nanoprecipitation method to a microfluidic device. For this aim, we modified parameters such as the flow rate ratio, the concentration of core materials in the organic phase, and the ratio between PLGA and Cholesterol in the feeding organic phase. Outputs analysed were the chemico–physical properties, such as size, PDI, and surface charge, the composition in terms of %Cholesterol and residual %Pluronic® F68, their stability to lyophilization, and the morphology via atomic force and electron microscopy. On the basis of the results, even if microfluidic technology is one of the unique procedures to obtain industrial production of NMeds, we demonstrated that the translation from a benchtop method to a microfluidic one is not a simple transfer of already established parameters, with several variables to be taken into account and to be optimized.

## 1. Introduction

Nanomedicine has been the leading topic of interest for novel therapeutic approaches against difficult-to-treat diseases for the last decade [184] thanks to the possibility of loading drugs that are normally inaccessible for direct injection due to their poor solubility, increasing the pharmacokinetic half-life of drugs in the blood and even decreasing off-target effects or of exploiting targeting ligands to engineer NMed surfaces for selective and tailored treatments. In particular, the potential of NMeds has been recently highlighted by the development of the nanomedicine-based vaccine against COVID-19 [200,643,644]. This incredible scientific effort has pointed out more than before that the ability to control the design and production of nanomedicines (NMed) is a crucial aspect for their eventual success with strong chances of ameliorating therapeutic effects.

In fact, notwithstanding all of the promising results in the field, few NMeds have passed the rigorous selection required for commercial availability [645]. A major reason for this bottleneck in commercially available NMeds lies in the difficulty of making classic benchtop methods reproducible or automated in a way that can be directly translated to large-scale industrial use. This passage is vital to ensure that industrial nanoproduction will allow the obtainment of NMed with standardized features, thus allowing governing agencies, such as the FDA or EMA, to certify them for commercial human use. In fact, the variations in fundamental parameters of optimized small-scale benchtop methods to those that allow reproducibility at a large scale must not affect the critical NMed pharmaceutical characteristics that may define their success, such as: a size ranging from 100–400 nm for improved biodistribution, surface charge minimizing first past clearance as well as the potential aggregation process, and standard drug content [646–648].

To combat this issue, companies have increased the investigations and optimizations of microfluidic systems [649,650]. These devices allow the reproducible production of NMeds with increased consistency thanks to the automated and constant output of a standardized and certified machine [651,652]

resulting in NMeds with consistent physical characteristics and drug loading. Moreso, they open up a direct path for upscaling through higher yield, minimized production time, and much larger production volumes with minimal or no batch variability. The result of the application of microfluidics is a certifiable and FDA-approved vaccine rolled out worldwide, proving the potential of a successful NMed design that passed phase 4 clinical trials and entered production on a global scale [653,654].

Even with its several advantages, the use of microfluidic devices for the production of NMeds requires an in-depth optimization of the protocols and instrumentation settings. For any researh laboratory, but most of all for small university laboratories, far from the economic possibilities of big companies such as Pfizer or Moderna, the application of microfluidics opens two different scenarios: 1) the use of microfluidic devices for the design and optimization of NMeds directly from a small scale or 2) the adaptation of already established small-scale benchtop protocols to a microfluidic system. In the first case, the use of microfluidic devices from the beginning during the small-scale NMed design ensures that the protocols are compatible and always reproducible as the same technology is used throughout the process. At the same time, this approach has a high upfront cost linked to the cost of the machine, and the proprietary and often mono-use cartridges used for each individual sample; even non-commercialized, 3D-printed or home-made devices can have a difficult set-up and several requirements. More importantly, this first approach is only possible when considering the design of novel NMeds; it cannot be applied to the numerous well-established or already published successful NMeds. In an evolving scenario where microfluidic devices for NMed production are taking the spotlight as a new paradigm instead of classical nanoprecipitation [655], it would be wasteful to abandon all the previous optimization studies to restart completely with a microfluidic process and incur all the upfront costs. This second one is a more classical and maybe economical approach that is used to translate optimized small-scale production of NMeds to a microfluidic system; however, adapting benchtop

protocols to a microfluidic device to obtain NMeds similar to the well-known ones can be a difficult and time-consuming process [656,657].

Microfluidic systems have already been tested for the translation and automated production of already established polymeric [658–661] and lipidic [203,662–666] NMed systems, as well as some hybrid [667–670] nanomedicines consisting of a polymeric core and a lipidic shell, which are now abundant in the literature. However, some new and innovative hybrid NMeds are yet to be optimized to exploit microfluidics for their improved production. Therefore, in this work we studied the transfer to a microfluidic-based protocol of a well-optimized and recently published [314,671] formulation method for hybrid nanomedicines (H-NMeds), consisting of the FDA-approved polymer poly-lactide-co-glycolic acid (PLGA) and cholesterol (Chol), a biocompatible and ubiquitous molecule [672] widely used for NMed formulation [673–676]. To this end, attempts to translate the benchtop production of H-NMed to this automated and standardized technology were performed by exploiting a homemade 2–channel microfluidic device.

The aim was to assess whether this already optimized benchtop method was easily transferable to the microfluidic technology by comparing physical and compositional changes, as well as morphological features, between the well-known H-NMeds from benchtop protocols and those reproduced with the microfluidic device. The parameters varied to attempt and obtain comparable H-NMeds were 1) initial concentration of core materials in the organic phase; 2) the flow rate ratio (FRR, the ratio of the aqueous to organic phase); 3) the ratio of polymer to cholesterol. The resulting H-NMeds were then compared in terms of size and homogeneity, surface charge, morphology, composition, and storage stability.

## 2. Materials and Methods

### *2.1. Materials*

Poly (d,l-lactide-co-glycolide) (PLGA, RG503H,MW ≅ 11,000) was used as received from the manufacturer (Evonik, Essen, Germany). Isopropanol was purchased from Carlo Erba, Conraredo Milan, Italy. Cholesterol, Pluronic® F68, Acetonitrile, Ethanol, Acetone, Chloroform, Barium Chloride (BaCl2), Iodide (I2), and Potassium Iodide (KI) were purchased from Sigma Aldrich (Merck Life Sciences, Milan, Italy). All solvents and reagents purchased were of analytical purity and used as delivered.

### *2.2. H-NMed Formation by the Optimized Benchtop Method.*

H-NMeds were obtained by adapting an already optimized benchtop protocol [314,671] with minor modifications: 20 mg of Chol and 20 mg of PLGA were weighed and dissolved in 4 mL of acetone. This organic phase was then added dropwise into a beaker containing 50 mL of a 5 mg/mL Pluronic® F68 solution warmed at 45 °C and kept under magnetic stirring. After 15 min, the suspension was left for 1 h at room temperature and then the solvent was removed under vacuum via Rotavapor® for 30 min. The obtained H-NMeds were purified by centrifugation at 14,500 rpm for 10 min at 4 °C. The supernatant was discarded, and the pellet was resuspended in 4 mL of MilliQ. From the resulting suspension, 10 μL was diluted in 1 mL of MilliQ water for size, zeta potential, and microscopy studies. Another 500 μL aliquot of H-NMed suspension was lyophilized for weight yield and compositional analysis.

### *2.3. Optimization of H-NMed Formation by Microfluidics*

To optimize the microfluidic method, a similar protocol to the benchtop one was used: PLGA and Cholesterol were dissolved in acetone and mixed with a 5 mg/mL Pluronic® F68 solution at 45 °C in the microfluidic device to produce H-NMeds,

using a Total Flow Ratio of 10 mL/min. The temperature, composition of the aqueous phase, and Total Flow Ratio were maintained constant throughout the experiments, as well as the organic solvent, in order to ensure high diffusibility with the organic phase and therefore a fine mixing of the two in the device. The parameters changed to reach an optimization of this method included: 1) the ratio (v:v) of organic and aqueous solutions (from 12, 5:1 to 1:1) with final volume kept constant at 13 mL; 2) total concentration of PLGA and Cholesterol in the organic solution (from 5 to 30 mg/mL); 3) ratio of PLGA to Cholesterol in the organic phase (w:w, from totally polymeric 100:0 to totally lipidic 0:100), keeping a total concentration of materials of 20 mg/mL. After formulation through the microfluidic device, NMeds were left under magnetic stirring at room temperature for 2 h to allow solvent evaporation. The final suspension was centrifuged at 14,500 rpm for 10 min and resuspended in MilliQ, and aliquots of 2 mL of suspension were lyophilized for weight yield and compositional analysis.

*2.4. Size and Surface Charge Analysis.*

The mean particle size (Z-Average) and polydispersity index (PDI) of all samples were determined by PCS (Photon Correlation Spectroscopy) analysis, using a Zetasizer Nano ZS (Malvern, UK; Laser 4 mW He Ne, 633 nm, Laser attenuator Automatic, transmission 100–0.0003%, Detector Avalanche photodiode, Q.E. > 50% at 633 nm, T = 25 °C). All samples were diluted before being analyzed to arrive at a final concentration of ~ 0.1 mg/mL. All data are expressed as the means of at least three individual H-NMed preparations.

The zeta potential (ζ-pot) was measured using a Zetasizer Nano ZS (Malvern) with a combination of laser Doppler velocimetry and a patented phase analysis light scattering method (M3-PALS). The same samples subjected to PCS (0.1 mg/ mL) were analyzed using DTS1070 zeta potential cuvettes and expressed as the mean of at least three individual H-NMed preparations.

2.5. Weight Yield

*Aliquots of a water suspension of purified H-NMeds were freeze-dried (−60 °C, 1 × 10−3* mm/Hg; LyoLab 3000, x-Holten, Allerod, Denmark) for at least 8 h and weighed. The yield (WY %) was calculated as follows:

WY(%) = ((mg of freeze-dried sample)/(mg PLGA + mg cholesterol)) × 100

*2.6. Quantification of Cholesterol*

An aliquot of lyophilized H-NMeds (~1 mg) was dissolved in 300 μL of chloroform. After sonication and vortex for 60 s, 600 μL of isopropanol was added and the solution was vortexed again. The solvent mixture was put under magnetic stirring to evaporate the chloroform and precipitate the PLGA in the isopropanol phase. Isopropanol was eventually adjusted to a final volume of 1 mL. This solution was centrifuged at 13,000 rpm for 10 min. The supernatant was analysed by HPLC using a Syncronis C18 4.6 × 250 mm 5 μm reverse phase column using an isocratic gradient of 50:50 ethanol (EtOH) absolute and acetonitrile (ACN) and a flow rate of 1.2 mL/min. The retention time of cholesterol was 16 min and had a linear range from 50 to 1000 μg/mL at 210 nm (Curve: y = 2545.70*x–32555.1: R2 = 0.994596). The total cholesterol content was calculated based on three injections from different formulations.

The amount of cholesterol in the formulations was calculated as Chol Recovery % (CR %) and Cholesterol Content % (CC %) with the following formulas:

CR(%) = ((mg of Chol in the formulation)/(mg of Chol used for formulation)) × 100

CC(%) = ((mg of Chol in the formulation)/(mg of H-NMeds analysed)) × 100

*2.7. Quantification of Residual Pluronic® F68*

The residual amount of surfactant in the H-NMeds was determined by a colorimetric method [610]. Briefly, ~1 mg of a freeze-dried H-NMeds sample was

solubilized in 0.5 mL of dichloromethane. Then, 10 mL of distilled water was added and the organic solvent was evaporated at r.t. under stirring for 2 h. The suspension was filtered (cellulose acetate filter, porosity 0.45 μm, Sartorius, Florence, Italy) to obtain an aqueous solution (A).

To calculate the amount of Pluronic® F68 in the formulation, 2 mL of the aqueous solution (A) was treated with 2 mL of 0.5% (w/v) BaCl2 in HCl 1 N and 0.5 mL of an aqueous solution of I2/KI (0.05 M/0.15 M). The obtained solution was incubated at r.t. for exactly 10 min in the dark. Pluronic® F68 concentration was determined measuring the absorbance at 540 nm (Model V530, Jasco, Cremella, Italy). A calibration curve was calculated using the same method on stock solutions of Pluronic® F68, and linearity was found in the range of 2–18 μg/mL. All data are expressed as the mean of at least three determinations. The amount of surfactant in the formulation was expressed as the Pluronic® F68 Content % (PC %) and calculated using the following equation:

PC(%) = ((mg of Pluronic® F68 in the formulation)/(mg of H-NMeds analysed)) × 10

*2.8. Morphological Studies*

AFM observations were performed with an atomic force microscope (Park Instruments, Sunnyvale, CA, USA) at about 25 °C operating in air and in non-contact mode using a commercial silicon tip-cantilever (high-resolution noncontact "GOLDEN" Silicon Cantilevers NSG–11, NT-MDT, tip diameter 5–10 nm; Zelenograd, Moscow, Russia) with stiffness of about 40 Nm–1 and a resonance frequency of around 150 kHz. After the purification, the sample was dispersed in distilled water (0.01 mg/mL) before being applied to a freshly cleaved mica disk (1 cm × 1 cm); two minutes after the deposition, the excess water was removed using a blotting paper. The AFM images were obtained with a scan rate 1 Hz. Two kinds of images were obtained: the first one was a topographical image and the second one was indicated as "error signal". This error signal was obtained by comparing

two signals: the first one, direct, representing the amplitude of the vibrations of the cantilever, and the other one being the amplitude of a reference point. The images obtained by this method showed small superficial variations of the samples. Images were processed using ProScan Data Acquisition software.

The structure of the samples was also analyzed by scanning transmission electron microscopy (STEM). Briefly, a drop of the same water-diluted suspension (0.01 mg/mL) used for AFM imaging was placed on a 200–mesh copper grid (TABB Laboratories Equipment, Berks, UK), allowed to adsorb, and the suspension surplus was removed by filter paper. All grids were analyzed using a Nova NanoSEM 450 (FEI, City, OR, USA) transmission electron microscope operating at 25 kV using a STEM II detector in Field free mode.

*2.9. Storage Stability*

Aliquots of 10 uL of H-NMed formulation at a final concentration of 10 mg/mL were tested for stability to lyophilization and freezing. In particular, the microfluidic formulation that was found to be the most similar in composition and physical characteristics to the benchtop one was selected and used.

Samples were tested after addition to the suspension of different amounts of trehalose as a cryoprotectant, in w:w ratio with H-NMeds of 0:1 (no trehalose), 1:1, 3:1 and 6:1. Samples were vortexed for 60 s to allow solubilization of the sugar. Two freezing methods were used, namely, standard slow freezing at –19 °C and flash freezing by immersion of the aliquots in a dry ice and methanol bath until completely frozen. Once frozen, all these samples were lyophilized for 8 h and stored at + 4 °C until further analysis.

Another set of samples was prepared exactly as described above. Instead of lyophilization, samples were stored for one week at –19 °C independently from the freezing method used and then thawed at room temperature before further analysis.

Lyophilized or thawed samples were resuspended or diluted with 1 mL MilliQ, vortexed for 60 s, and eventually analyzed via PCS for size distribution and PDI, as previously described (Section 2.4).

### *2.10. Statistical Analysis*

Statistical analysis was performed using Student's T Test, where *$p < 0.05$ and **$p < 0.01$, using the software GraphPad Prism 6. All samples were performed with $n > 3$, and the error bars in graphs indicate the standard deviation (SD) from the average.

## 3. Results and Discussion

Microfluidic systems have been studied and optimized over the last 20 years for their application for the production of nanomedicines (NMeds), showing advantages over traditional benchtop methods, such as higher reproducibility, batch to batch standardization, and direct translation towards industrial scale-up, as strongly emphasised by the recent production of the COVID-19 vaccine. Notwithstanding the undoubted benefits of the increased use of microfluidic based systems for the optimization of novel NMeds, the passage from traditional methods to this novel technology requires the careful adaptation of already optimized and published successful platforms without losing the features of the original NMeds. In this study, we propose the first optimization steps to adapt the production protocol of a well-established hybrid NMed consisting of PLGA and Cholesterol (H-NMed) and analysing how changing crucial parameters of a microfluidic-based process affects the physical and compositional characteristics of the resulting H-NMeds.

As a point of reference, H-NMeds produced with the classical benchtop protocol were analysed for size, homogeneity, surface charge, and composition (Table 1). Hybrid NMeds produced by nanoprecipitation are known [671] to have a final composition of about 30% Chol and to incorporate within their matrix about 10% of surfactant from the formulation environment (Figure 1A). They display a homogeneous size around 250 nm, with a strong negative surface charge around–35 mV. The published nanoprecipitation protocol used for these H-NMeds was extensively optimized [351,671], allowing for a high yield of almost 80%.

**Table 1.** Physico chemical characterization of H-NMeds obtained by the nanoprecipitation benchtop protocol. Standard Deviation (SD) is reported in parentheses.

| [materials] | FRR | Size (SD) | PDI (SD) | Zeta (SD) | Weight Yield% (SD) | Pluronic% (SD) | Chol Recovery% (SD) | Chol Content% (SD) |
|---|---|---|---|---|---|---|---|---|
| 10mg/mL | 12.5:1 | 241 (14) | 0.24 (0.03) | -36 (3) | 77 (8) | 9 (3) | 50 (11) | 36 (7) |

To start the optimization process using microfluidic technology, the concentration of materials in the organic phase, 10 mg/mL corresponding to that for nanoprecipitation, and the total volume (13 mL) were held constant. Another point to be considered prior to optimization is the surfactant since the microfluidic technology for NMed preparations is based on the fine mixing of two different fluids, namely, an organic and an aqueous solution, and the type and concentration of surfactant are crucial parameters to be addressed. This is valid not only for droplet microfluidics, now widely applied to high-throughput screenings [677–681], but also for NMed preparations. Triblock polymers such as Pluronics® have been demonstrated to be safe and biocompatible [682,683] and are frequently used as stabilizers during the formation of NMeds both in benchtop [234,428,684,685] and in microfluidic based protocols [686–689]. For this reason, we standardized the use of Pluronic® F68 as already exploited in our optimized benchtop methods to be used with the microfluidic device. Literature showed that a Pluronic® F68 concentration between 0.1 and 1% leads to the successful formation of NMeds with microfluidic devices [690,691]; therefore, we fixed its concentration at 0.5% w/v, the same used in previous nanoprecipitation protocols.

### *3.1. Variation of the Flow Rate Ratio*

With these variables fixed, the impact of changing the ratio between the volume of the aqueous and organic phases (Flow Rate Ratio, FRR) from 12.5:1 to 1:1 was analysed (Table 2). Analysis of the physico chemical characteristics of these formulations showed an inverse trend in the average size of these H-NMeds, which increased from 170 to 250 nm when decreasing the FRR from 6:1 to 1:1 following literature reports for polymeric, lipidic, and other hybrid nanoparticles [656,658,692,693]. The only exception to this trend was represented by the formulation produced with the highest FRR of 12.5:1, where NMeds produced showed a higher poly-dispersity index (PDI > 0.3) and size over 250 nm. A deeper analysis of this formulation using Photon Correlation Spectroscopy prior to

purification revealed the presence of a second population of particles with an average size of 70 nm accounting for almost 10% of the total intensity. This abundant subpopulation was hypothesised to be surfactant micelles [694] that could interfere with the proper formation of the PLGA and Chol into an H-NMed, leading to the low weight yield of 24% after purification, due to the poor pelleting of the small surfactant micelles.

On the other hand, the size distribution, PDI, and surface charge of every other formulation demonstrated the possibility to successfully formulate H-NMeds with various FRRs with similar physical characteristics to those created with the benchtop method; however, evident differences were found in their composition. In particular, analysing the amount of surfactant stably connected to the H-NMeds, a decreasing trend could be observed with the decreased FRR ranging from over 70% to a minimum of about 15%. Specifically, the selection of an FRR of 6:1 and 3:1 resulted in structures with a very high amount of surfactant, hinting towards the formation of particles with a different architecture with respect to the H-NMeds obtained by nanoprecipitation. Formulations produced with FRRs lower than 2:1 were the most similar to the classic benchtop H-NMeds, with a Pluronic® F68 content of less than 20%, and 40–50% of the matrix being composed of Cholesterol (Figure 1B).

Nevertheless, the formulation with FRR 2:1 was the only one that showed the formation of homogeneous and monodispersed H-NMeds, as decreasing the FRR to 1.5:1 or 1:1 led to samples with a very high PDI > 0.4, which is generally considered a cutoff to determine whether a sample is homogeneous in size [695], and a higher variability in size. Additionally, the formulation with FRR or 2:1 also showed the highest recovery of Cholesterol, almost 80%, hinting towards a lower loss of materials, a crucial point for an industrially relevant environment. For these reasons, H-NMeds produced with an FRR of 2:1 were deemed to be the most promising to be further optimized.

**Table 2.** Physico chemical characterization of H-NMeds obtained with the microfluidic device varying the Flow Rate Ratio (FRR). Standard Deviation (SD) is reported in parentheses.

| [materials] | FRR | Size (SD) | PDI (SD) | Zeta (SD) | Weight Yield% (SD) | Pluronic% (SD) | Chol Recovery% (SD) | Chol Content% (SD) |
|---|---|---|---|---|---|---|---|---|
| 10mg/mL | 12.5:1 | 260 (45) | 0.34 (0.04) | -27 (7) | 24 (4) | / | / | / |
| 10mg/mL | 6:1 | 173 (6) | 0.27 (0.03) | -25 (5) | 56 (6) | 72 (13) | 31 (2) | 27 (1) |
| 10mg/mL | 3:1 | 185 (0) | 0.16 (0.02) | -26 (6) | 49 (6) | 42 (1) | 51 (1) | 52 (0) |
| 10mg/mL | 2:1 | 262 (15) | 0.19 (0.03) | -29 (5) | 71 (3) | 19 (3) | 77 (6) | 54 (4) |
| 10mg/mL | 1.5:1 | 254 (52) | 0.59 (0.04) | -28 (5) | 53 (4) | 16 (3) | 41 (5) | 46 (5) |
| 10mg/mL | 1:1 | 245 (48) | 0.57 (0.08) | -29 (6) | 51 (2) | 14 (1) | 42 (2) | 41 (2) |

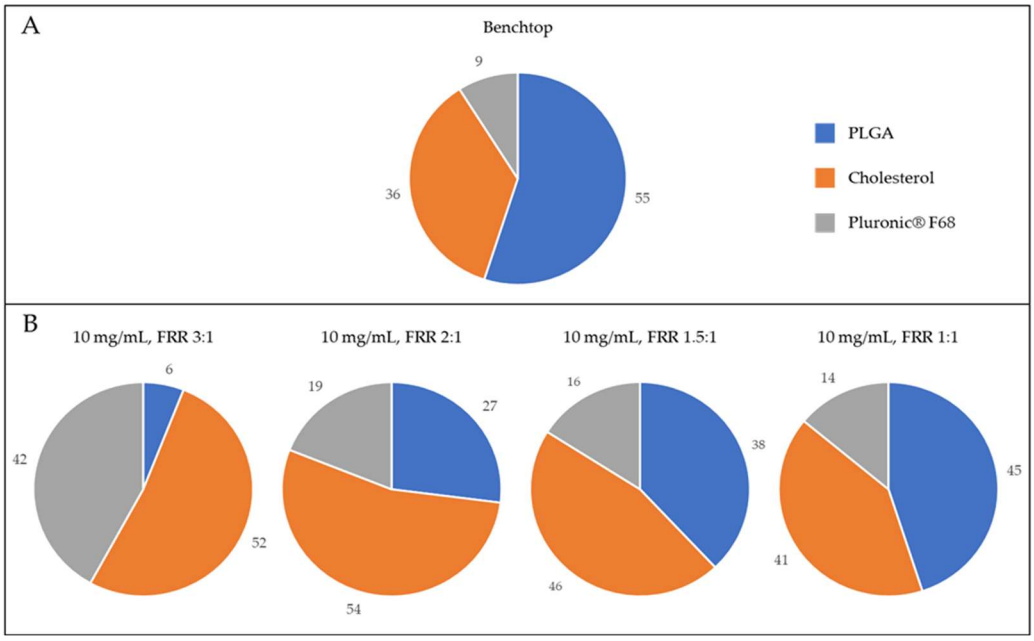


**Figure 1.** Graphical representation of the composition of H-NMeds. Blue: PLGA content. Orange: Cholesterol content. Grey: Pluronic® F68 content. (A) H-NMeds obtained with nanoprecipitation. (B) H-NMeds obtained with microfluidic-based protocols using a concentration of materials in the organic phase of 10 mg/mL and different FRRs, namely, 3:1 (left), 2:1 (center) and 1:1 (right).

### *3.2. Variation in the Total Concentration of the Starting Material in the Organic Phase*

The second step of the investigation on nanoproduction optimization was performed using a constant FRR of 2:1 and varying the total concentration of materials in the organic phase. Previous studies have pointed out an interesting

relationship between the concentration of polymers or lipids in the organic phase and the size of the resulting NMeds, where an increase in their concentration of starting materials produces bigger polymeric NMeds [656,690,695,696] but smaller liposomes [697]. Regarding other types of NMeds consisting of both polymer and lipids, it is difficult to find information in the literature data that could help predicting the behaviour of our H-NMeds, as those are often formulated with dissolving phospholipid derivatives in the aqueous phase, and separately modifying the concentration of the polymer or the lipid [652,667,698–702] eventually leads to the same trends reported for single components. As reported in Table 3, each formulation resulted in an average size between 250 and 300 nm, with PDI < 0.3 and strongly negative surface charges of almost–30 mV. Nonetheless, it was possible to observe an inverse trend where the size decreased with an increased concentration from 5 to 30 mg/mL. This behavior could be attributed to a stronger influence of the lipidic component, which was calculated to account for slightly more than 50% of the total composition of the H-NMeds. Looking at the composition of these formulations, the amount of Pluronic® F68 stably connected to the H-NMeds followed a trend where the Pluronic® F68 decreased from 35 to 10% when the concentration of the core materials in the organic phase was increased. As previously mentioned, the residual surfactant stably associated with the matrix of an NMed is a crucial parameter to be evaluated. As reported in the literature, the type and surfactant not only influence the formation of the NMeds depending on their characteristics, such as HLB, molecular structure, and critical micelle concentration, but can also determine colloid stability: in fact, the concentration of the surfactant in the medium has an optimum, over which colloid stability decreases. Lastly, it impacts the interaction of NMeds with biological environments, as it can induce the formation of a protein corona with a different composition [703–707]. Despite their important role, surfactants are often considered secondary components of NMeds and remain unquantified. Here, we report a significant reduction in the amount of residual surfactant in these H-NMeds (*$p < 0.02$) by only varying the concentration of other

core materials, underlining the importance of their quantification when optimizing a formulation protocol.

**Table 3.** Physico chemical characterization of H-NMeds obtained with the microfluidic device varying the initial concentration of core materials in the organic phase. Standard Deviation (SD) is reported in parentheses.

| [materials] | FRR | Size (SD) | PDI (SD) | Zeta (SD) | Weight Yield% (SD) | Pluronic% (SD) | Chol Recovery% (SD) | Chol Content% (SD) |
|---|---|---|---|---|---|---|---|---|
| 5mg/mL | 2:1 | 287 (11) | 0.22 (0.02) | -24 (6) | 69 (2) | 35 (3) | 76 (2) | 55 (1) |
| 10mg/mL | 2:1 | 262 (15) | 0.19 (0.03) | -29 (5) | 71 (3) | 19 (3) | 77 (6) | 54 (4) |
| 20mg/mL | 2:1 | 254 (3) | 0.22 (0.02) | -27 (7) | 69 (5) | 25 (6) | 69 (2) | 50 (1) |
| 30mg/mL | 2:1 | 248 (25) | 0.28 (0.08) | -28 (5) | 71 (9) | 10 (8) | 77 (12) | 54 (10) |

Globally, no critical differences were found among these formulations in weight yield, Cholesterol content or physical characteristics. Considering the composition, the most similar H-NMed to our reference was the one obtained at the highest concentration of 30 mg/mL. Nevertheless, this concentration was experimentally found to be at the solubility limit of the PLGA and Cholesterol mixture, leading to a higher variability both in physical characteristics and composition as evidenced by the higher SD values for these results. Therefore, we decided to subject to further optimization the formulation produced with an initial concentration of 20 mg/mL (Figure 2A).

### *3.3. Variation of the PLGA: Cholesterol Ratio*

The next step to optimize a microfluidic based protocol to produce H-NMeds was to test the possibility to use different ratios between PLGA and Cholesterol in the stock organic phase. To do this, H-NMeds were produced with a set FRR of 2:1 and a total concentration of materials of 20 mg/mL, ranging from a fully polymeric NMed of 100% PLGA to a fully lipidic one of 100% Cholesterol (Table 4).

**Table 4**. Physico chemical characterization of H-NMeds obtained with the microfluidic device varying the ratio between PLGA and Cholesterol. Standard Deviation (SD) is reported in parentheses.

| [materials] | FRR | PLGA:Chol ratio | Size (SD) | PDI (SD) | Zeta (SD) | Weight Yield% (SD) | Pluronic% (SD) | Chol Recovery% (SD) | Chol Content% (SD) |
|---|---|---|---|---|---|---|---|---|---|
| 20mg/mL | 2:1 | 0:100 | 402 (21) | 0.24 (0.10) | -24 (4) | 64 (6) | 20 (10) | 37 (3) | 67 (5) |
| 20mg/mL | 2:1 | 25:75 | 391 (27) | 0.20 (0.04) | -28 (6) | 54 (4) | 21 (5) | 35 (4) | 48 (6) |
| 20mg/mL | 2:1 | 50:50 | 254 (3) | 0.22 (0.02) | -27 (7) | 69 (5) | 25 (6) | 69 (2) | 50 (1) |
| 20mg/mL | 2:1 | 75:25 | 223 (2) | 0.26 (0.03) | -27 (6) | 70 (4) | 22 (10) | 82 (6) | 29 (2) |
| 20mg/mL | 2:1 | 100:0 | 154 (1) | 0.22 (0.00) | -32 (5) | 82 (4) | 20 (9) | / | / |

PCS analysis revealed that it was possible to formulate NMeds at each ratio tested, with average size less than 400 nm, low PDI, and a strongly negative surface charge. However, it is clearly evident that a high presence of lipid in the organic phase correlates with an increase in the size, while an increase in the polymeric concentration corresponds to a size reduction. This evidence is in contrast to the trends reported in the literature and described above, in which polymers or lipids are used alone or in separate phases. In fact, these data suggest, without any literature precedent, a unique behavior of these H-NMeds, different from more simple situations where the interaction between polymeric chains and lipidic molecules dissolved in the same organic phase produces a novel effect.

At the same time, WY % also showed a significantly decreasing trend ($^*p < 0.05$) related to an increase in the lipidic fraction used in the organic phase. This could be correlated with a different density of fully polymeric NMeds compared to fully lipidic ones, leading to a diverse reaction to the centrifugal forces applied during purification [708]. However, the lowest value of WY % reported was still not significantly different ($p = 0.09$) from that obtained with the original nanoprecipitation method ($64 \pm 6$ vs $77 \pm 8\%$).

Compositional analysis revealed that the amount of Pluronic® F68 that was stably recovered with the NMeds was independent from the variation of the organic phase composition and remained constant at around 20%, indicating that this value, from a process point of view, was more intimately linked to the FRR (Table 2) and total concentration of material in the organic phase (Table 3) during

microfluidic formulations. Interestingly an increase in the Chol concentration in the stock organic phase did not correlate with a significant increase in its final content. In fact, when 75% of Cholesterol was used in the initial phase, the recovered NMeds showed a composition of around 50% of Cholesterol, despite the much higher initial concentration. This finding is again describing a difference in comparison to previous reports [351] in which the H-NMed obtained with benchtop nanoprecipitation procedures was shown to roughly keep within the NMed composition the cholesterol content from starting to the final step, confirming that changing the technology of production (from benchtop to microfluidic) impacted the composition of produced NMeds [709].

Among the formulations in Table 4, interstingly the PLGA:Chol ratio of 75:25 revealed the composition most similar to the composition of the benchtop-derived H-NMeds (with a similar Chol content % [29 vs. 36% ($p = 0.17$)], Cholesterol recovery Figure 1A and Figure 2B), and residual Pluronic® F68 amounts ($p = 0.09$), although H-NMed obtained with microfluidics showed high variability in this last value (22 ± 10).

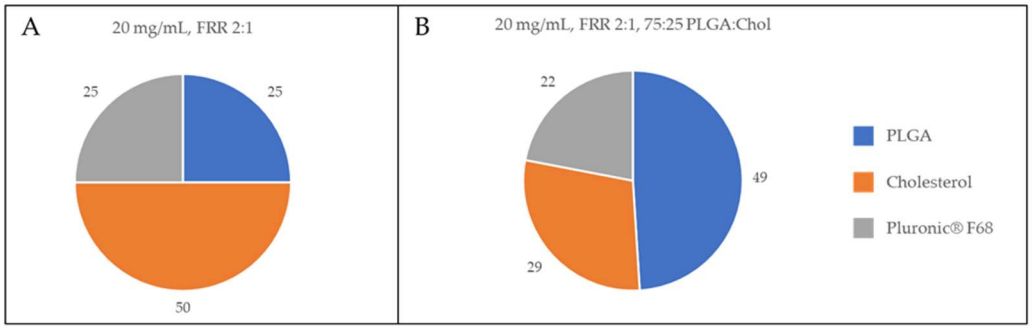


**Figure 2**. Graphical representation of the composition of H-NMeds. Blue: PLGA content. Orange: Cholesterol content (CC %). Grey: Pluronic® F68 content. (A) H-NMeds obtained with the microfluidic device at a concentration of 20 mg/mL and an FRR of 2:1. (B) H-NMeds obtained with microfluidic-based protocols using a ratio of PLGA:Chol of 75:25, using an initial concentration of 20 mg/mL, and an FRR of 2:1.

### *3.4. Stability Test and Morphology*

To further assess if the most similar formulation showed other similar characteristics, the two optimized H-NMeds were tested for storage stability. Storage stability is crucial for industrial and clinical use: a good storage stability allows for easier industrial production and transport of therapeutics, while the lack of storage stability implies that the product has to be formulated the same day of administration, increasing human error and variability. H-NMeds from benchtop protocols are known to be stable to lyophilization; therefore, samples of benchtop- and microfluidic-derived H-NMeds were lyophilized and tested for size and homogeneity analysis after resuspension. Moreover, different amounts of cryoprotectant were added, from 0 to 6 times the weight of the H-NMeds in the aliquots tested. The method of freezing was also varied, using a standard slow freezing method and flash freezing by immersion in a dry ice and methanol bath (Figure 3A).

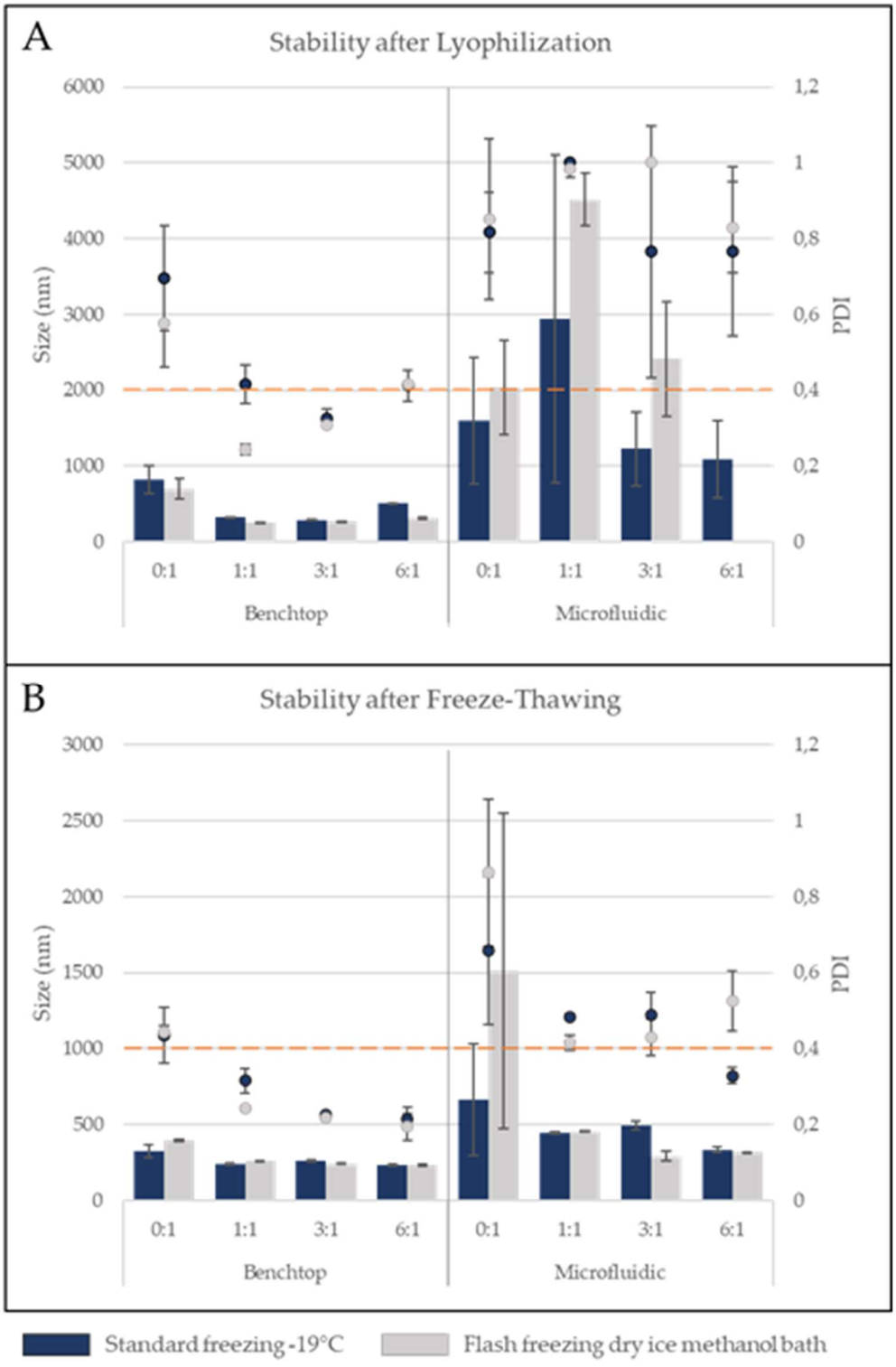


**Figure 3.** Size and homogeneity analysis of H-NMeds (A) after resuspension of lyophilized and (B) freeze-thawed aliquots. Bars: Size (nm), Dots: PDI. Blue bars and dots: standard freezing −19 °C, Grey bars and dots: flash freezing in a dry ice methanol bath. Each value is expressed as the Mean ± SD of three independent formulations.

Data analysed revealed an evident difference between the H-NMeds from the two formulation techniques. Benchtop-formulated NMeds showed little to no aggregation after resuspension, especially with the addition of trehalose at a 1:1 or 3:1 ratio, with a size remaining under 300 nm and PDI lower than 0.4 independently from the freezing method. On the other hand, H-NMeds obtained with the microfluidic technology showed poor resuspension, with the formation of aggregates in the micrometric range and PDI close to 1 in all cases tested. Due to the poor prospect of lyophilized storage, another set of aliquots was then tested with the same variables for storing the samples frozen to verify which of the two steps was so detrimental for H-NMeds stability (Figure 3B). In fact, this test revealed that freezing alone also led to the aggregation of microfluidic-derived H-NMeds, showing an increase in size over 1 μm and PDI higher than 0.4. Here too, H-NMeds produced via nanoprecipitation revealed a different behavior, with a smaller average size and most importantly a smaller PDI around 0.2, indicating good homogeneity, compared with their microfluidic counterparts. Moreover, these samples revealed a decreasing trend in PDI correlated with the increase in cryoprotectant used [710], as expected from literature data. Globally, these tests suggested that despite the two H-NMeds having a similar composition in material percentages, they still displayed crucial differences, probably in their architecture, that determined their different response to the same condition or process, especially in a stressing step as freezing and lyophilization.

In order to furnish a view of the morphology of samples, both atomic force (AFM) and transmission microscopy (STEM) were conducted on the two different H-NMeds produced (Figure 4).

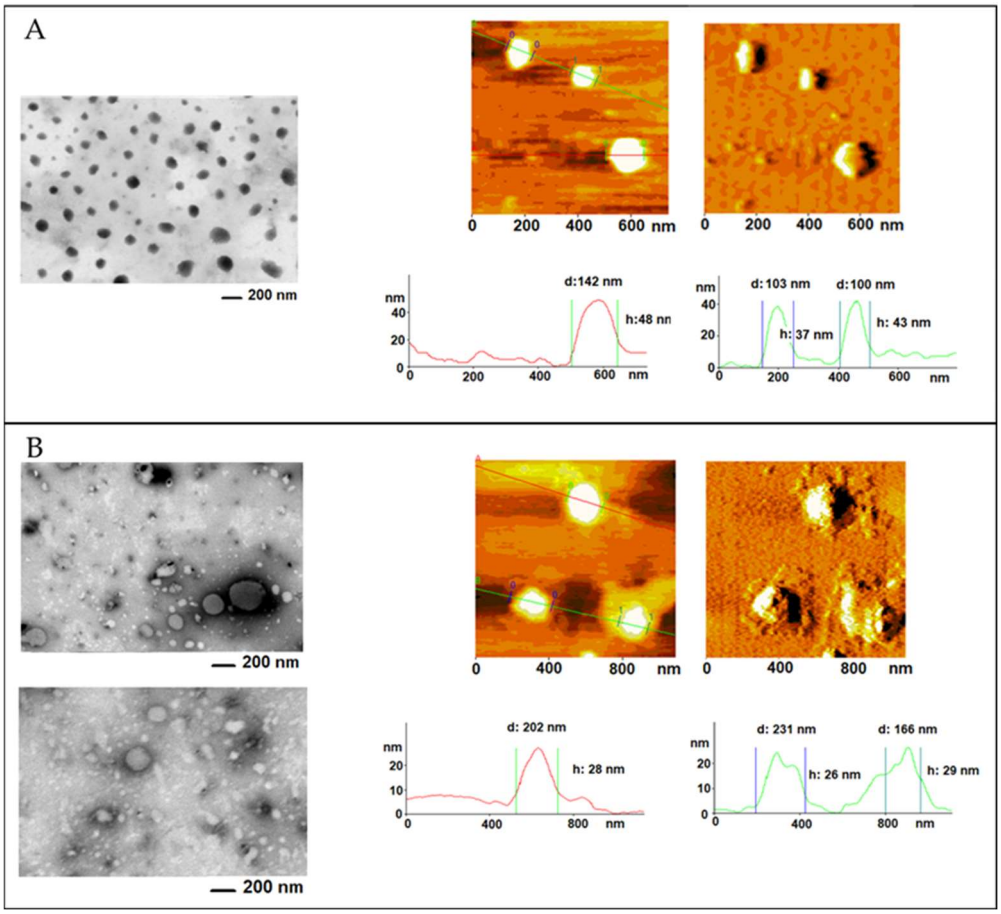


**Figure 4.** Microscopy images of H-NMeds produced via (A) nanoprecipitation or (B) the microfluidic device. Left panels: STEM imaging. Right panels: AFM imaging, topography, and error signal.

STEM analysis of benchtop-derived H-NMeds confirmed the presence of a homogeneous sample, as previously reported [351], where H-NMeds appeared spherical and monodisperse all across the sample. This was also confirmed by AFM images, where H-NMeds displayed a sharp border and a round shape, and it was possible to measure particle diameters of 100–150 nm. These images confirmed what was already demonstrated in previous studies [351], i.e., the formulation of a matrix of PLGA, Cholesterol, and Pluronic® F68, where all components were strongly interconnected.

On the other hand, STEM images of microfluidic-derived H-NMeds revealed a sample with high variability, as evidenced by the two images reported in Figure 4B (left panel). This high variability was not recorded by PCS analysis, as this

sample showed a low PDI of 0.26. Nevertheless, they appeared to not be broadly uniform and therefore apparently less reproducible than the H-NMeds produced via nanoprecipitation. This variability in shape and size was also confirmed by AFM analysis: not only did the H-NMeds appear to be compressed and flattened under the tip of the cantilever, suggesting a softer structure, but the presence of unformed material surrounding the surface of formed H-NMeds was also evident. It was hypothesized that this material consisted of excess surfactant not stably connected to the surface of H-NMeds that was lost after deposition on the mica. Indeed, this is supported by the previous discussion regarding the quantification of Pluronic® F68, which showed a higher presence of surfactant in this sample.

Taken together, these data suggest that the instability of the H-NMeds produced by microfluidics may be explained by an excess of Pluronic® F68 that is not stably associated with or incorporated into the matrix of H-NMeds. This hypothesis is supported by past literature cited above, which confirmed that the amount of surfactant in the medium of NMeds plays a pivotal role in NMed stability, as it displays an optimum range of concentration, and an excess, especially if not strongly connected to the NMeds, could lead to instability due to its rearrangement into different structures [711,712].

## 4. Conclusion

In recent years, microfluidic technologies have taken the spotlight as a promising tool for the successful production of NMeds up to a global scale, as recently highlighted by the production of an NMed-based COVID19 vaccine. Nevertheless, the transition from established small-scale benchtop protocols to microfluidic devices faces several issues to produce NMeds with analogous features of those already optimized with benchtop protocols. In particular, several microfluidic parameters have to be taken into consideration, such as the flow rate ratio, concentration of core materials, and type of materials used, each of which could have an impact on NMed characteristics. Therefore, in this study, we aimed to investigate the translation of a well-known multi-component H-NMed consisting of PLGA and Cholesterol stabilized with Pluronic® F68 from already established benchtop methods to a microfluidic device, in view of the possible exploitation of the unquestionable potential of microfluidic technology to standardize the production of these H-NMeds towards the high standards needed for GMP approval. Using an FRR of 2:1, a concentration of 20 mg/mL, and an initial ratio of PLGA:Cholesterol of 75:25, it was possible to reach the production of H-NMeds with statistically similar composition and chemico-physical properties to the benchtop ones, but still they displayed a critically different behavior when tested for storage stability. These data demonstrate that the translation of a multi-component system from an optimized benchtop method to a microfluidic-based system requires extensive efforts in terms of work and time in order to determine the optimal settings, not only during the microfluidic formulation, but also in the selection and amount of stabilizers, and methods for purification and storage, to ensure that the NMeds will have reproducible physico-chemical characteristics, composition, structures, and stabilities.

# CHAPTER 6

# Biological Fate

# Quantitative Comparison of the Protein Corona of Nanoparticles with Different Matrices

**Ilaria Ottonelli [1,2,†], Jason Thomas Duskey [1,†], Filippo Genovese [3], Francesca Pederzoli [1], Riccardo Caraffi [1], Marta Valenza [4], Giovanni Tosi [1], Maria Angela Vandelli [1] and Barbara Ruozi [1]**

[1] Nanotech Lab, Te.Far.T.I., Department of Life Sciences, Via Campi 103, University of Modena and Reggio Emilia, 41125, Modena, Italy;

[2] Clinical and Experimental Medicine PhD Program, Department of Biomedical, Metabolic, and Neural Sciences, Via Campi 287, University of Modena and Reggio Emilia, 41125, Modena, Italy

[3] CIGS, Centro Interdipartimentale Grandi Strumenti, Via Campi 213A, University of Modena and Reggio Emilia, 41125, Modena, Italy

[4] Department of Biosciences, Vi Giovanni Celoria 26, University of Milan, 20133, Milan, Italy

† These authors contributed equally to this work.

*International Journal of Pharmaceutics: X* 2022, *4*, 100136,
doi:10.1016/j.ijpx.2022.100136

Received 7 August 2022

Revised 18 October 2022

Accepted 19 October 2022

Available online 21 October 2022

Version of Record 23 October 2022

## Abstract

Nanoparticles (NPs) are paving the way for improved treatments for difficult to treat diseases diseases; however, much is unknown about their fate in the body. One important factor is the interaction between NPs and blood proteins leading to the formation known as the "protein corona" (PC). The PC, consisting of the Hard (HC) and Soft Corona (SC), varies greatly based on the NP composition, size, and surface properties. This highlights the need for specific studies to differentiate the PC formation for each individual NP system. This work focused on comparing the HC and SC of three NPs with different matrix compositions: a) polymeric NPs based on poly(lactic-co-glycolic) acid (PLGA), b) hybrid NPs consisting of PLGA and Cholesterol, and c) lipidic NPs made only of Cholesterol. NPs were formulated and characterized for their physico-chemical characteristics and composition, and then were incubated in human plasma. In-depth purification, identification, and statistical analysis were then performed to identify the HC and SC components. Finally, similar investigations demonstrated whether the presence of a targeting ligand on the NP surface would affect the PC makeup. These results highlighted the different PC fingerprints of these NPs, which will be critical to better understand the biological influences of the PC and improve future NP designs.


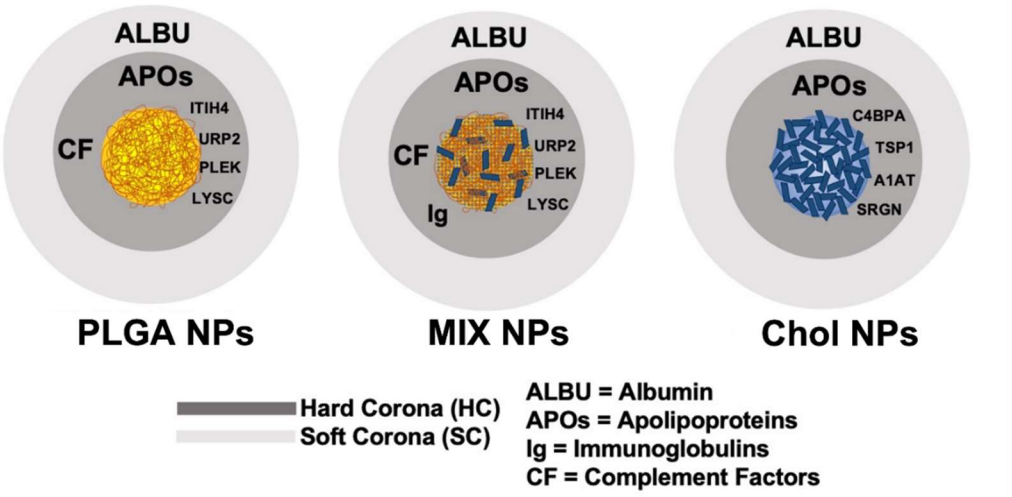

## 1. Introduction

Nanoparticles (NPs) represent one of the most innovative tools in the medical field. They can offer a wide range of potential advantages to drug delivery, such as the ability to a) incorporate a broad range of characteristically diverse active substances [232,320,713]; b) stabilize and protect molecules from degradation in different biological environments [341,472,714]; c) be surface-modified for specific targeted delivery (i.e. to tissue, cell types, or intra-cellular receptors) [234,241,715]; d) selectively modulate drug release (i.e. prolonged or retarded release) [237,716,717]. NPs used for medical applications should be non-toxic, cause a limited immune response activation, and be site-specific to limit negative off-target effects [718]. Nevertheless, once intravenously dosed, their biological effects can be very difficult to predict due to the various interactions of the NPs with proteins in the blood. These interactions lead to the formation of various layers around the NP surface, termed "the protein corona" (PC), made up of numerous blood proteins that can affect the fate of the NPs; moreover, the composition of this PC is usually hard to predict, necessitating thorough analyses for each NP system [719].

The PC absorbed on the surface of NPs is very complex, but can generally be broken down into two distinct layers: 1) the more stable and slowly exchanging Hard Corona (HC) which interacts more intimately with the surface of the NPs, and 2) the more dynamic and weakly associated Soft Corona (SC) [211,212,720,721]. The composition of the two PCs has been shown to influence circulation and biodistribution [722–727], drug targeting [728–730], cellular uptake [731–734], and toxicity [735–738] of both organic and inorganic NPs. These differences can be further complicated by biological parameters such as protein concentration [739–741], exposure time [742–744], and temperature [745,746], which could vary from patient to patient or be due to a pathological state. For these reasons, the study of the PC is considered an urgent issue in the field of NP characterization as a necessary requirement to better predict the biological identity, biological consequences, and therapeutic outcomes of NPs [747–750].

The formation of the PC, both the HC and SC, is influenced not only by the characteristics of the blood composition, but also by the NP characteristics. In particular, the composition [751], hydrophobicity [752–754], physical characteristics such as size and surface charge [755–758], shape [759,760], and surface modifications with targeting ligands or coatings [221,761–763]. All of these factors are interconnected and can influence critical variations in the PC fingerprint between delivery systems. This leads to the conclusion that there is no "universal" PC. Each individual factor ranging from the matrix, surfactant, size, and morphology can have important effects on the PC composition. Therefore, it is crucial to analyse the PC for each NP to determine which factors play the most important roles and which proteins lead to the strongest effects on the delivery of the NPs *in vivo*.

The present work aims to characterize the entire PC of three NPs with different compositions: 1) polymeric NPs that form solid matrix cores composed of poly-lactic co-glycolic acid (PLGA NPs), 2) hybrid NPs composed of a homogeneous matrix of PLGA and cholesterol (MIX NPs), and 3) solid-core lipidic NPs composed of cholesterol (Chol NPs) (Figure 1). PLGA is a well-known FDA approved polymer that has been extensively used for the encapsulation and delivery of pharmaceutics. Cholesterol is a natural, ubiquitous lipid that has been widely used to formulate liposomes and hybrid NPs [616,671,764] and has recently been adapted to form lipidic NPs without any helper component (patent pending). Finally, hybrid NPs which have gained promise in the literature with the capacity to combine the advantages of both polymeric and lipidic systems as improved delivery tools [40]. Therefore, these three NPs represent highly studied delivery systems that bridge the gap between the two extremes of polymeric and lipidic NPs.

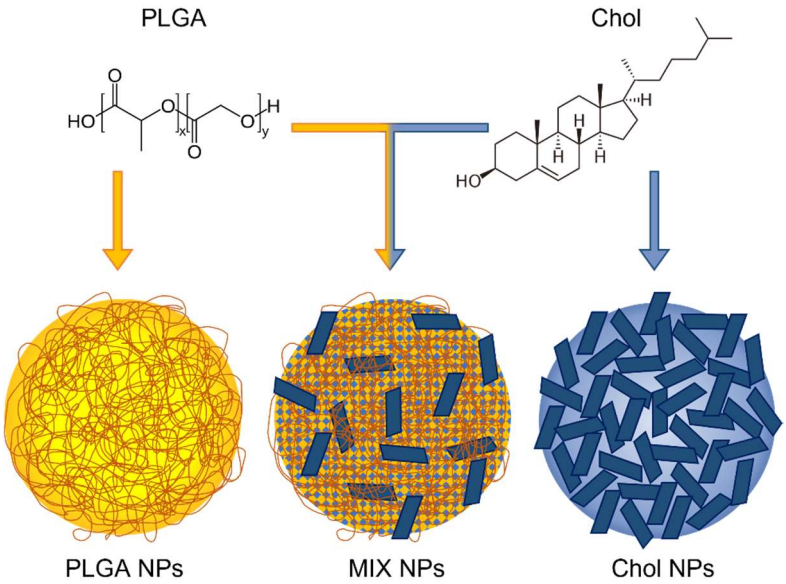


**Fig. 1**. The chemical structure of the polymer PLGA and Cholesterol and a schematic repre-sentation of the structure of PLGA, hybrid PLGA-Cholesterol (MIX), and Cholesterol NPs.

To evaluate the impact of the NP core composition on the formation of the HC and SC, NPs were incubated in plasma and the proteins absorbed were identified, evaluated, quantified, and compared. HPLC ms-ms analysis was used to identify the major proteins present and supported with statistical analysis (volcano plots) to determine the congruency between each NP type based on the proteins present in the HC or SC. A second set of NPs with the same composition was then produced and surfaced modified with the g7 peptide, known to promote BBB crossing *in vivo* and the HC and SC were analysed using identical methodologies to determine if the core composition or the surface engineering led to greater disparities in the PC layers. With this in-depth characterization of the PC of these 3 NPs (PLGA, MIX, and Chol), and determining the effect of surface modifications on the NPs, we hope to supplement the vast amount of similar research being performed on other types of NPs [747,765,766]. This will help to create a field-wide understanding of how the PC affects the *in vivo* behaviour of NPs, allowing for the intelligent design of NP systems based on the identity of their PCs and their potential biological effects and reduce unanticipated biological responses during translation to *in vivo* testing.

## 2. Materials and Methods

### *2.1. Materials*

Poly-(D,L-lactic-co-glycolic) acid RG503H (PLGA) 50:50, MW 11,000 Da, (Evonik, Essen, Germany), was used as received from the manufacturer. The g7 peptide was purchased from Mimotopes, Mulgrave, Australia: sequence GFtGFLS(O-β-Glc)-CONH2, MW 888.97. Cholesterol and Pluronic® F68 were purchased from Sigma Aldrich, Milan, Italy. Sterile filtered human K2EDTA plasma from a healthy donor (protein concentration estimated 6.4 g/dl; Gentaur, Bergamo, Italy), pre-stained Protein Sharp Mass V Plus (Euroclone, Milan, Italy), and Coomassie Brilliant Blue R-250 (Bio-Rad, Milan, Italy) were used as received from the manufacturers. All other solvents (analytical grade), products, and reagents were purchased from Sigma Aldrich (Milan, Italy) and used without any further purification (unless otherwise specified). High-purity water was supplied by a MilliQ water system (Millipore, MA, USA).

To ensure that samples were free of erroneous proteins, all multi-use glassware, plasticware, spatulas, and stir bars were pre-washed with 70% ethanol and then heated at 200 °C for at least 2 hours. Mono-use sterile, protein-free, DNAse free, RNAse free materials were used for all other experiments. Finally, to further avoid sample contamination, all preparation methods were performed under a sterile vertical laminar flow hood (Asalair Vertical 700, Asalair, Firenze, Italy).

### *2.2. Formulation of the NPs*

The g7 peptide was conjugated to PLGA or Cholesterol prior to NP formulation via a peptide coupling reaction as previously described [393,428]. PLGA, hybrid PLGA-Cholesterol (MIX), and Cholesterol (Chol) NPs were prepared using the nanoprecipitation procedure as previously reported [241,314,671]. Briefly, polymers and/or lipids were dissolved in the organic solvent and added dropwise to water

containing Pluronic® F68 and under magnetic stirring (1,300 rpms). The organic solvent was then removed at 30°C under reduced pressure (R 114 Rotavapor, Buchi, Cornaredo, Italy). The recovered NP suspensions were then ultracentrifuged (J21, Beckman, CA, USA; 16,000 rpms) for 10 min at 4°C and the supernatant was discarded to remove unformed polymer and or lipid and free surfactant. The NPs were resuspended in water, stored at 4°C, and used within a week.

*2.3. Chemico-physical characterization*

2.3.1. Weight yield

A measured amount (200 μl) of the purified NP suspension was transferred to a pre-weighed Eppendorf tube and freeze-dried (-60°C, 3 mm/Hg, for 48 h; LyoLab 3000, Heto-Holten, Allerod, Denmark) to calculate the Yield%:

Yield%=(mg of NPs recovered)/(Total initial components)*100

2.3.2. Size and Zeta Potential Analysis

Each NP sample was diluted in MilliQ water to a final concentration of 0.1 mg/mL to measure the size (Z-Average) and the polydispersity index (PDI) of the samples determined at room temperature by photon correlation spectroscopy using a Zetasizer Nano ZS (Malvern, Malvern, UK) equipped with a 4 mW He–Ne Laser at 633 nm, automatic Laser attenuator, Avalanche photodiode Detector, with a quantum efficiency (Q.E.) >50% at 633 nm.

The ζ potential (ζ-pot) was calculated starting from the electrophoretic mobility measured using the same sample and instrument equipped with a combination of laser Doppler velocimetry and phase analysis light scattering. For each preparation, the Z-Average, PDI, and ζ-pot were calculated as the mean of triplicate measurements from 3 distinct NP formulations.

2.3.3. The NP Morphology

The NP morphology was investigated using a scanning transmission electron microscopy (STEM). Samples were prepared by immersing a 200-mesh Cu grid (TABB Laboratories Equipment, Berks, UK) into the NP suspension (~ 0.1 mg/mL) and letting it air dry at room temperature. Images were then achieved using a Nova Nano SEM 450 (FEI Co., OR, USA) (acceleration voltage 30 KV, Spot 1.5) with a scanning transmission electron microscope II detector.

2.3.4. Residual Pluronic® F68

The residual Pluronic® F68 associated with the NPs was quantified following a previously published colorimetric reaction [517]. Briefly, the surfactant was extracted from 10 mg of lyophilized NPs by solubilisation in 2 mL of dichloromethane followed by the addition of 10 mL of MilliQ water. After the dichloromethane was completely evaporated, the solution was filtered through a 0.2 μm cellulose acetate filter to remove any insoluble components. An aliquot of the filtrate was treated with 1 mL of a 0.005 % (w/v) $BaCl_2$ solution in 0.1M HCl and 1 mL of an $I_2$/KI solution (0.05 M / 0.15 M). After a 15 min incubation at room temperature, the absorbance was measured at 540 nm using a UV/Vis Spectrophotometer V-530 (Jasco Europe, Cremella, Italy) and the amount of Pluronic® F68 was calculated using a standard curve created that day under the same conditions.

*2.4. PC Purification and Characterization*

Characterization of the PC was performed following previously published methods (thoroughly described in the Supplementary material) [761]. Briefly, NP samples were first incubated in human plasma. To isolate NPs with only the HC, samples were centrifuged to remove the unbound material and SC from the NP-

HC complex. In order to collect the NPs with the SC still intact, size exclusion chromatographic purification was used as a more gentle alternative [767]. Eluted fractions were monitored by SDS-PAGE to distinguish the free proteins in solution from the samples containing NP-PC complexes. Both samples, with only the HC or with the HC and SC, were then characterized in terms of total amount of proteins using the bicinchoninic acid (BCA) assay following the manufacturer's instructions. To identify the proteins present, these samples were processed with reducing and alkylating agents, and eventually trypsin, before being analysed by mass spectrometry. Plasma samples without NPs were treated similarly as controls.

*2.5. Software and statistical analysis*

Statistical analysis regarding the chemico-physical properties of NPs was performed using the Student's T Test, where * $p < 0.05$ and ** $p < 0.01$, included in the software GraphPad Prism 6 (GraphPad Holdings, San Diego, CA, USA). All results are the mean with standard deviation (SD) measuring at least 3 different samples: $n > 3$.

Protein identification was achieved by searching the protein databases Swiss-Prot (2018_05, Homo Sapiens 557,491 entries) for peptides, and c-RAP for contaminants (ftp://ftp.thegpm.org/fasta/cRAP, 116 entries), using the MASCOT protein identification software (Version 2.4, Matrix Science, London, UK). Once identified, proteins were semi-quantified by normalizing their presence to the total amount of proteins and expressed using the "exponentially modified Protein Abundance Index" (emPAI) [768].

Eventually, results were statistically evaluated with the MSStat tool [769] and graphed as volcano plots with the binary logarithm of the fold change between two samples in the x-axis and the –log2 of the adjusted *p* on the y-axis. Proteins present in the PC with a log fold change < -2 or > 2 and an adjusted $p < 0.05$ were considered statistically differently between samples.

## 3. Results

### *3.1. NP chemico-physical characterization*

The physico-chemical characteristics of NPs have been demonstrated to directly influence the PC formation. Therefore, a complete chemico-physical analysis of each different formulation was performed (Table 1, Figure S1). Independently of the NP matrix all three formulations formed homogenous and reproducible structures as evidenced by a low PDI (< 0.3) [695]. As expected from previous literature [234,472], PLGA NPs exhibited the smallest size compared to the other formulations (~ 150 nm), while MIX and Chol NPs displayed slightly larger structures of around 250 nm [314,351,671]. Regarding the Zeta potential, all formulations were statistically similar, ranging from -20 to -35 mV, with a trend towards more negative values correlating to the number of carboxylic moieties of PLGA present in the matrix (PLGA < MIX < Chol NPs). While all the NPs were recovered with high weight yields of almost 80%, differences were found in the amount of residual Pluronic® F68 between each NP type. PLGA NPs were found to have a lower percentage of surfactant compared to MIX and Chol NPs, in accordance with previous literature (14 vs 26%) [351,395,671]. This increase of residual Pluronic® F68 could be explained by its high affinity with cholesterol, leading to higher non-specific interactions and more being retained in the matrix [706,770]. This is important because contradicting literature suggests in some cases that the amount or location of the surfactant (in the matrix or absorbed on the surface) does not lead to interference of protein absorption and PC formation. Other sources claim that while it does not block PC formation, surfactants can influence its composition: this must be taken into consideration before conclusions are made about the importance of NP matrix on the PC proteins [771–773].

**Table 1.** Chemico-physical characteristics of the three NP formulations.

| NP sample | Size (SD), nm | PDI (SD) | Electrophoretic Mobility (SD), µmcm/Vs | ζ-pot (SD), mV | Weight Yield % w/w | Pluronic® F68 % w/w |
|---|---|---|---|---|---|---|
| **PLGA-NPs** | 152 (13) | 0.12 (0.02) | -2.52 (0.12) | -34.4 (6.2) | 74.9 (6.6) | 14 (4) |
| **MIX-NPs** | 237 (17) | 0.26 (0.01) | -2.00 (0.44) | -25.8 (5.3) | 76.7 (6.6) | 27 (3) |
| **Chol-NPs** | 257 (14) | 0.18 (0.05) | -1.55 (0.05) | -19.1 (6.8) | 78.7 (6.0) | 26 (9) |

The physical characteristics of the NPs recorded by light scattering were also confirmed by STEM microscopy. Images acquired evidenced the presence of homogeneous populations of NPs in each sample while defining differences previously described, such as PLGA yielding smaller, more dense NPs, while Chol NPs being slightly larger and less electron dense. MIX NPs displayed intermediate characteristics between the two, as MIX NPs are formed by the homogeneous mixture in the NP matrix of both PLGA and Chol [351] (Figure 2).

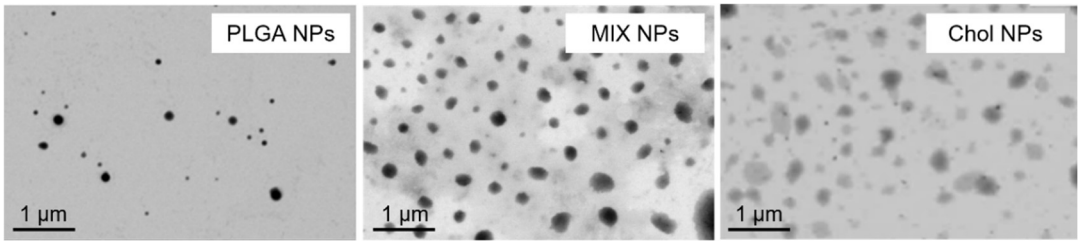


**Fig. 2.** STEM images of PLGA, MIX, and Chol NPs.

*3.2. Hard Corona Studies*

To study the HC, quantitative analysis of the major detectable proteins was compared between each NP matrix type (expressed as % normalized emPAI) while using pure plasma as a standard (Figure 3). Statistical analysis in the relative protein abundance was determined by group comparisons of each matrix using volcano plots: dots above the grey line have a p value < 0.05. To increase the confidence of the results, only proteins outside the range of -2 < Log2 fold change

< 2 (represented by a blue rectangle) were considered as representing significant differences not linked to possible measurement variations (Figure 4).

| | PLGA NPs | | | | MIX NPs | | | | Chol NPs | | | |
|---|---|---|---|---|---|---|---|---|---|---|---|---|
| | Protein | % normal emPAI | SD | Total | Protein | % normal emPAI | SD | Total | Protein | % normal emPAI | SD | Total |
| APOs | APOA1 | 51.79 | 4.14 | 87.06 | APOA1 | 53.7 | 1.07 | 71.91 | APOA1 | 56.68 | 7.52 | 90.13 |
| | APOE | 15.64 | 4.68 | | APOA4 | 8.38 | 5.12 | | APOA4 | 20.01 | 5.87 | |
| | APOA4 | 15.34 | 3.89 | | APOE | 6.67 | 1.42 | | APOE | 5.19 | 0.91 | |
| | APOC1 | 3.15 | 0.46 | | APOC1 | 4.40 | 1.33 | | APOA2 | 3.91 | 1.11 | |
| | APOA2 | 0.39 | 0.14 | | APOA2 | 2.16 | 0.81 | | APOC3 | 1.88 | 0.32 | |
| | APOH | 0.35 | 0.04 | | APOH | 0.65 | 0.17 | | APOC1 | 1.34 | 0.26 | |
| | APOC4 | 0.26 | 0.02 | | APOC3 | 0.18 | 0.03 | | APOC2 | 0.78 | 0.05 | |
| | APOC3 | 0.14 | 0.02 | | APOC4 | 0.17 | 0.04 | | APOC4 | 0.21 | 0.06 | |
| | | | | | | | | | APOD | 0.07 | 0.02 | |
| | | | | | | | | | APOL1 | 0.03 | 0.01 | |
| | | | | | | | | | APOF | 0.03 | 0.01 | |
| Complement Factors | CO3 | 1.32 | 0.1 | 4.02 | CO3 | 7.35 | 1.33 | 9.80 | C1QB | 1.14 | 0.22 | 1.64 |
| | C1QB | 0.66 | 0.23 | | CFAH | 0.78 | 0.01 | | C1QC | 0.42 | 0.11 | |
| | CFAH | 0.64 | 0.08 | | C1QB | 0.65 | 0.1 | | C1QA | 0.40 | 0.06 | |
| | C1QC | 0.55 | 0.04 | | CXCL7 | 0.51 | 0.08 | | CO3 | 0.08 | 0.02 | |
| | FHR1 | 0.37 | 0.07 | | C1QC | 0.40 | 0.08 | | | | | |
| | CXCL7 | 0.27 | 0.06 | | C1QA | 0.35 | 0.03 | | | | | |
| | C1QA | 0.21 | 0.05 | | CO4A | 0.16 | 0.02 | | | | | |
| Immunoglobulins | IGKC | 1.14 | 0.35 | 2.49 | IGKC | 1.44 | 0.38 | 4.24 | IGHM | 0.65 | 0.16 | 2.33 |
| | IGHG3 | 0.50 | 0.01 | | IGHG3 | 0.79 | 0.08 | | IGKC | 0.43 | 0.10 | |
| | IGLC2 | 0.40 | 0.02 | | IGLC2 | 0.65 | 0.11 | | IGJ | 0.39 | 0.06 | |
| | IGG1 | 0.33 | 0.04 | | IGHM | 0.50 | 0.16 | | IGHG3 | 0.25 | 0.03 | |
| | IGHA1 | 0.24 | 0.08 | | IGG1 | 0.45 | 0.06 | | IGLC2 | 0.25 | 0.15 | |
| | IGHM | 0.22 | 0.03 | | IGJ | 0.34 | 0.1 | | IGG1 | 0.14 | 0.02 | |
| | IGK | 0.21 | 0.07 | | IGHG2 | 0.30 | 0.03 | | IGK | 0.09 | 0.02 | |
| | IGHG2 | 0.17 | 0.03 | | IGK | 0.28 | 0.04 | | IGHA1 | 0.08 | 0.02 | |
| | IGL1 | 0.09 | 0.03 | | IGHA1 | 0.15 | 0.06 | | IGHG2 | 0.05 | 0.01 | |
| | IGJ | 0.09 | 0.02 | | IGL1 | 0.14 | 0.02 | | | | | |
| Unique | URP2 | 0.32 | 0.04 | | URP2 | 0.48 | 0.16 | | C4BPA | 0.23 | 0.05 | |
| | ITIH4 | 0.29 | 0.13 | | LYSC | 0.41 | 0.35 | | TSP1 | 0.15 | 0.01 | |
| | LYSC | 0.26 | 0.09 | | ITIH4 | 0.32 | 0.05 | | SRGN | 0.10 | 0.03 | |
| | PLEK | 0.17 | 0.04 | | PLEK | 0.23 | 0.14 | | A1AT | 0.04 | 0.01 | |
| | ALBU | 0.14 | 0.06 | | ALBU | 0.51 | 0.09 | | ALBU | 2.20 | 1.29 | |

**Fig. 3**. Qualitative and quantitative analysis of the HC. HC protein analysis of PLGA, MIX, and Chol NPs divided into the major subgroups and ordered by emPAI score. The standard devi-ation was determined by the analysis of three different NP formulations. The complete com-position analysis of the HC is reported in Fig. S2.

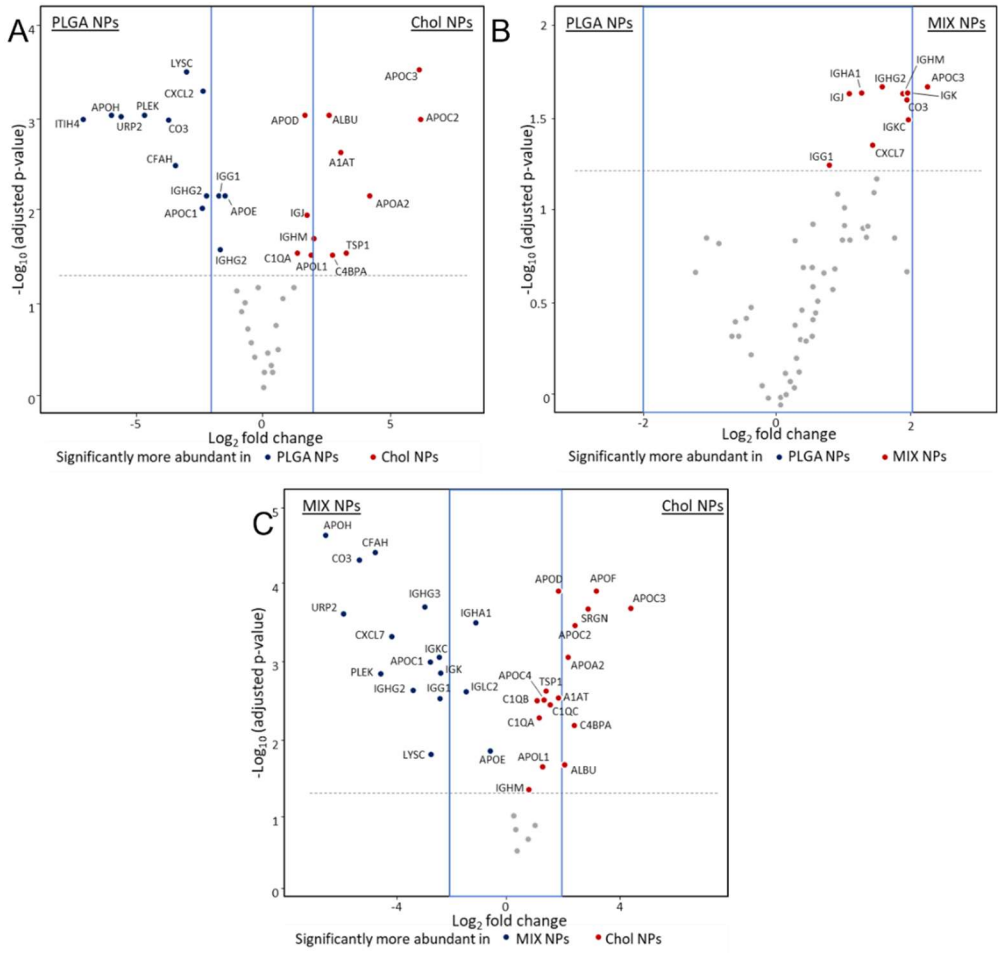


**Fig. 4**. Volcano plots representing relative abundance of the proteins detected in the HC comparing NPs of different matrices. A) PLGA vs MIX NPs. B) PLGA vs Chol NPs. C) MIX vs Chol NPs. The dotted line represents the limit of statistical significance; the blue square represents a secondary selection for those proteins that are at least 2-fold more present in one sample than its counterpart. The complete statistical analysis is reported in Fig. S3

Quantitative analysis of the plasma control sample showed albumin (HSA) as the most abundant protein, with the next highest proteins being transferrin (0.86%), Immunoglobulin H (0.17%), Haptoglobin (0.14%), and Vitamin D binding protein (0.10%), with a long list of below 0.10% (Figure S2A). Of these most prominent proteins in the plasma, only albumin was consistently detectable in the HC of the different NPs; however, while being the most abundant plasma protein it was always less than 3% of the NP HC composition. Interestingly, the albumin amount appeared to be directly related to the amount of Cholesterol in the NPs: Chol NPs (2.20%), MIX NPs (0.51%) NPs, and in a much minor fraction for PLGA NPs

(0.14%) (Figure 3, Figure S2B) [774–776]. These results demonstrate that the plasma abundance is not the critical determining factor for which proteins form the HC. Instead, the most abundant HC proteins, representing 95 – 99% of the total HC proteins according to emPAI calculations, could be separated into three distinct categories: apolipoproteins complement factors, and immunoglobulins (Figure 3). This categorization of the most abundant HC proteins is in accordance with studies for other NPs where similar observations were seen [212,749,777].

Even though apolipoproteins account for only 4.8% of the plasma proteins (when excluding albumin), they were the most abundant proteins in the HC for all of the NPs and accounted for approximately 70-90% of the HC. Comparing the three formulations, slight variations were evident. While APO_A1 accounts for approximately 53% of proteins across all of the formulations, APO_E, APO_A4, and other APOs are more variable, being most prevalent in PLGA and Chol NPs compared to MIX NPs. This high abundance of APOs in the HC is in accordance with numerous other studies of different nanomedicines and are probably linked to the hydrophobic nature of these structures, but is interesting as to why they were less abundant in the MIX NPs [778–780].

The other most abundant classes of proteins found in the HC consisted of a mix of complement factors and immunoglobulins. In the HC of all three NPs, CO3 was the most abundant complement factor, ranging from 1.3%, 0.1%, and 7.4% for PLGA, Chol, and MIX NPs respectively. This is followed prominently by C1QB, C1QC, and CFAH with only a small trace of numerous others. Immunoglobulins present in the HC represented 2-4% of the total proteins. In all three matrix types, IGKC was the major immunoglobulin protein followed by IGHG3, IGLC2, and various others. Altogether, a major difference can be seen in the amount of these proteins in the HC of the NP types. The HC of MIX NPs had the highest amount of complement factors and IG levels compared to PLGA and Chol NPs (14% vs 6.5% and 3% respectively).

Altogether, APOs, complement factors, and IGs added up to more than 90% of the total composition of the HC for each NP matrix type. Nevertheless, it is also important to consider other potentially important candidates that are unique to the HC of each matrix type whether they were quantifiable in the plasma control or not. In fact, several proteins that were too low to be detected in the plasma were detectable in the HC of the PLGA and MIX NPs, including URP2, LYSC, ITIH4, PLEK, and CYTC (Figure 3, yellow), but were not detected in the Chol NP HC. At the same time, numerous unique proteins were found in the HC of Chol NP but not in PLGA or MIX NPs, namely C4BPA, A1AT, SRGN, and TSP1 (Figure 3, blue).

After identifying the main proteins that compose the HC, a statistical analysis was performed to evaluate the significant differences in the protein abundance linked to each matrix type. Figure 4A represents the comparison between the two most different NPs in terms of characteristics and nature: PLGA and Chol NPs. The classes of proteins that were the most prominent in both the plasma and HC, discussed above, showed no significant difference in abundance between PLGA NPs and Chol NPs with a few exceptions. In particular, the HC of the PLGA NPs had significantly higher amounts of the complement factors (CO3, and CFAH), while Chol NPs had significantly higher levels of APO_C2, APO_C3, and albumin. This statistical analysis also supported previous observations regarding the proteins uniquely found in either the HC of Chol or PLGA NPs.

The comparison of PLGA NPs and MIX NPs highlighted little to no differences in the composition of the HC with the only difference being that APO_C3 was statistically more abundant in the HC of the MIX NPs (Figure 4B). On the contrary, a comparison between Chol and MIX NPs exhibited a surprisingly similar trend to the Chol vs PLGA NPs. MIX NPs showed statistically more proteins that were also seen in the polymeric PLGA NPs, such as URP2, PLEK, and LYSC, as well as the complement factors CO3 and CFAH. Interestingly, they also showed a significant predominance of immunoglobulins compared to Chol NPs, with IGKC, IGHG3,

and IGG1(Figure 4C). Both MIX and Chol NPs showed an abundance of a different variety of APOs.

These data could have important implications on the fate of these NPs. APOs were found to be more present in the HC of Chol NPs compared to the other two types. This effect could be expected, as this class of proteins is involved in the transport of lipidic and hydrophobic material in the bloodstream generally represented by high-density and low-density lipoproteins rich in cholesterol (HDL and LDL) [781–785]. At the same time, the total amount of complement factors and immunoglobulins is an important factor to be considered. Unlike APOs, complement factors have been linked to more negative biological repercussions, inciting both an inflammatory and immunogenic effect [786–788].

*3.3. Soft Corona*

While the HC is made up of proteins intimately associated with the surface of the NPs, the soft corona (SC) is much more dynamic and less intimately bound. This does not negate the need to characterize this entity as an equilibrium will still be reached in the plasma environment leading to effects on the biological fate of the NPs (Figure 5, Figure S4) [789]. One major difference seen in the emPAI scores is that the SC of both the PLGA and Chol NPs consisted of fewer proteins compared to the HC (30 vs 50 proteins). Of these, the most abundant proteins were albumin and haptoglobin, which ranged from 60-86%, with no statistical difference between the three matrix types (Figure 6). This was followed by low amounts of the three major categories previously seen in the HC: APOs, complement factors, and immunoglobulins. Chol and MIX NPs shared the highest variety of APOs compared to the few found in the PLGA NPs. This variety could be linked to the biological role of these proteins in transporting Chol as described previously in the section regarding the HC; however, it is also important to consider the amount of APOs present in the SC. In Chol NPs, APOs represented only 3% of the SC proteins while in MIX NPs they represented over 20%. Similarly, the SC of MIX NPs

consisted of a notably larger variety of complement factors compared to the other two NPs even though the total emPAI percentage was no different from that of PLGA NPs (2.11% and 1.87% respectively). On the other hand, Chol NPs showed the smallest amount of complement factors with a total of 0.48% of the total composition of the SC. Unlike what was reported for the HC, the SC of the different NPs did not contain "unique" proteins, but instead consisted of variations in the amount and number of the major proteins, suggesting the difference of the soft equilibrium formed.

| | PLGA NPs | | | | MIX NPs | | | | Chol NPs | | | |
|---|---|---|---|---|---|---|---|---|---|---|---|---|
| | Protein | % normal emPAI | SD | **Total** | Protein | % normal emPAI | SD | **Total** | Protein | % normal emPAI | SD | **Total** |
| | **ALBU** | 66.27 | 15.32 | 70.45 | **ALBU** | 59.93 | 18.47 | 63.31 | **ALBU** | 86.01 | 1.51 | 88.85 |
| | **HPT** | 4.18 | 0.71 | | **HPT** | 3.38 | 0.65 | | **HPT** | 2.84 | 0.61 | |
| **APOs** | **APOA2** | 7.62 | 2.98 | 15.10 | **APOA1** | 14.38 | 12.6 | 22.69 | **APOA2** | 1.56 | 0.68 | 3.35 |
| | **APOA1** | 7.48 | 3.56 | | **APOA2** | 7.23 | 3.09 | | **APOA1** | 1.18 | 0.12 | |
| | | | | | **APOE** | 0.40 | 0.06 | | **APOC3** | 0.52 | 0.01 | |
| | | | | | **APOC3** | 0.29 | 0.09 | | **APOE** | 0.15 | 0.03 | |
| | | | | | **APOA4** | 0.21 | 0.03 | | **APOL1** | 0.07 | 0.00 | |
| | | | | | **APOB** | 0.09 | 0.05 | | **APOA4** | 0.05 | 0.03 | |
| | | | | | **APOL1** | 0.09 | 0.05 | | | | | |
| **Complement Factors** | **CFAH** | 0.61 | 0.23 | 1.87 | **CO3** | 1.00 | 0.5 | 2.11 | **CO3** | 0.18 | 0.02 | 0.48 |
| | **C4BPA** | 0.54 | 0.18 | | **CO4B** | 0.26 | 0.15 | | **C4BPA** | 0.16 | 0.04 | |
| | **CO3** | 0.48 | 0.15 | | **C4BPA** | 0.24 | 0.05 | | **CFAH** | 0.14 | 0.02 | |
| | **CO4B** | 0.24 | 0.09 | | **CFAH** | 0.21 | 0.08 | | | | | |
| | | | | | **C1QC** | 0.11 | 0.05 | | | | | |
| | | | | | **C1QB** | 0.11 | 0.05 | | | | | |
| | | | | | **C1S** | 0.07 | 0.01 | | | | | |
| | | | | | **C1R** | 0.06 | 0.02 | | | | | |
| | | | | | **CO9** | 0.05 | 0.03 | | | | | |
| **Immunoglobulins** | **IGJ** | 3.57 | 0.89 | 6.77 | **IGHA1** | 0.95 | 0.38 | 2.26 | **IGHA1** | 1.47 | 0.19 | 1.83 |
| | **IGHA1** | 2.87 | 0.57 | | **IGJ** | 0.41 | 0.13 | | **IGJ** | 0.27 | 0.00 | |
| | **IGHM** | 0.26 | 0.05 | | **IGHM** | 0.35 | 0.30 | | **IGHG3** | 0.05 | 0.02 | |
| | **IGHG3** | 0.07 | 0.01 | | **IGHA2** | 0.31 | 0.12 | | **IGHM** | 0.04 | 0.02 | |
| | | | | | **IGHG3** | 0.12 | 0.09 | | | | | |
| | | | | | **IGG1** | 0.12 | 0.11 | | | | | |
| **Others** | **ITIH2** | 0.47 | 0.12 | | **ITIH2** | 0.39 | 0.05 | | **ITIH2** | 0.27 | 0.01 | |
| | **ITIH1** | 0.13 | 0.02 | | **ITIH1** | 0.24 | 0.09 | | **ITIH1** | 0.03 | 0.00 | |
| | | | | | **A1AG1** | 0.15 | 0.11 | | | | | |

**Fig. 5**. Qualitative analysis of the SC. SC protein analysis of PLGA, MIX and Chol NPs di-vided into the major subgroups and ordered by emPAI score. The standard deviation was de-termined by the analysis of three different NP formulations. The complete composition analysis of the SC is reported in Fig. S4.

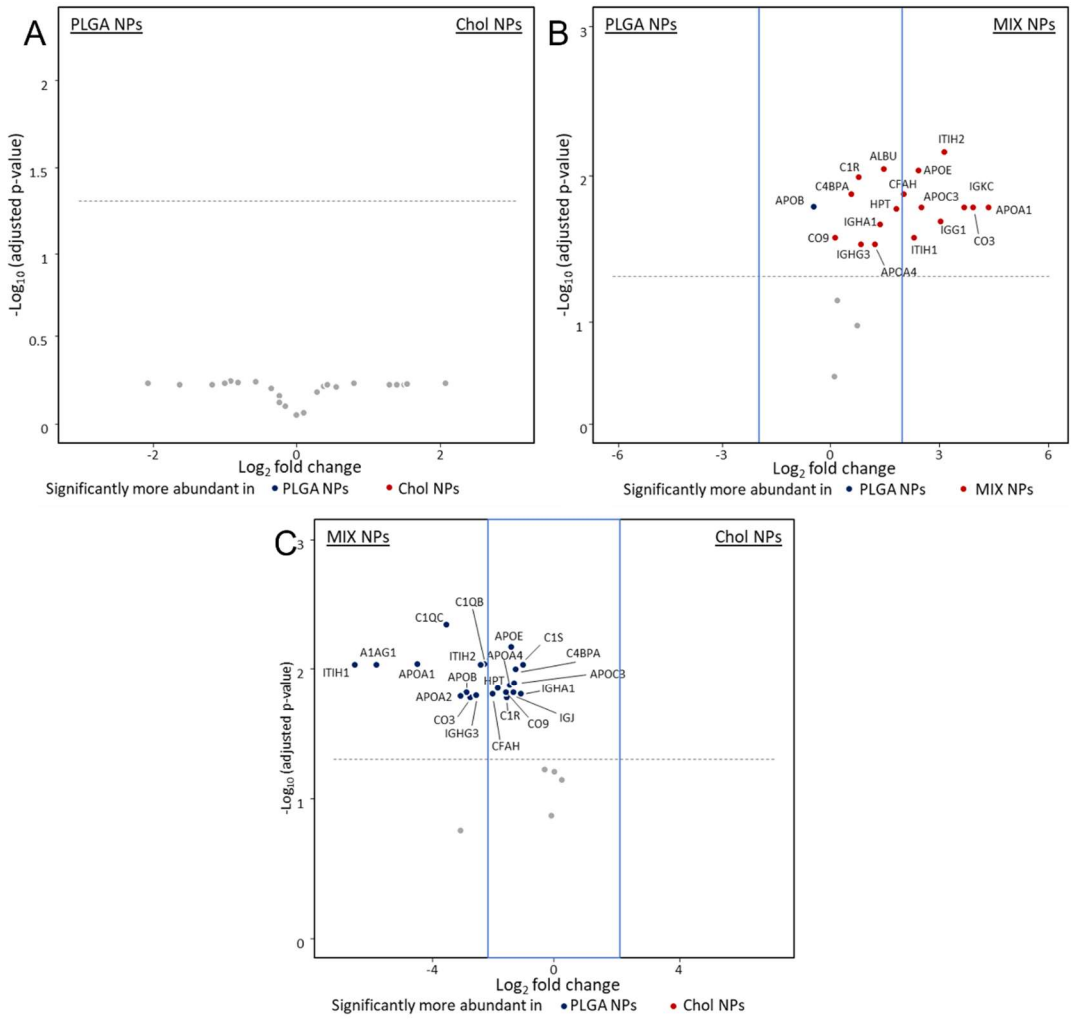


**Fig. 6**. Volcano plots representing relative abundance of the proteins detected in the SC com-paring NPs of different matrices. A) PLGA vs MIX NPs. B) PLGA vs Chol NPs. C) MIX vs Chol NPs. The dotted line represents the limit of statistical significance; the blue square rep-resents a secondary selection for those proteins that are present at least 2-fold higher in one sample compared to its counterpart. The complete statistical analysis is reported in Fig. S5.

Statistical analysis with volcano plots supported these results. PLGA and Chol NPs showed no statistical differences in the identity of the SC proteins (Figure 6A). On the contrary, MIX NPs showed statistically higher amounts of apolipoproteins (such as APO_A, APO_C, and APO_E), complement factors (CO5, CO3, C1QC), and immunoglobulins (IGKC, IGHM) compared to both other NP matrix types (Figure 6B and 6C).

### *3.4. The PC of NPs with targeting ligands*

The surface modification of NPs has been demonstrated to be critical for the composition of the PC. Therefore, the PC of NPs surface modified with a targeting ligand was analysed to test if the differences in PC linked to the matrix composition would be modified by the presence of a surface ligand. For this purpose, the g7 peptide was chosen: this is a well-known BBB targeting ligand proven to promote CNS targeting when conjugated onto the surface of NPs [138,314,395]. Overall, the emPAI scores for the HC and SC of each matrix were very similar for each NP type with or without the ligand present (Figure S6 and S7). Statistical analysis confirmed that all proteins forming the HC and SC remained under the significance threshold when comparing the g7-modified NPs to their unmodified counterparts (Figure 7). The only exception was an increased amount of C4BPA in the SC for unmodified Chol NPs. In opposition to many literature sources, these data suggest that the presence of the g7 ligand on the surface of these NPs did not significantly alter the HC or SC for any of the different matrix types of NPs and that the differences seen in previous sections are derived solely due to the different matrix compositions.

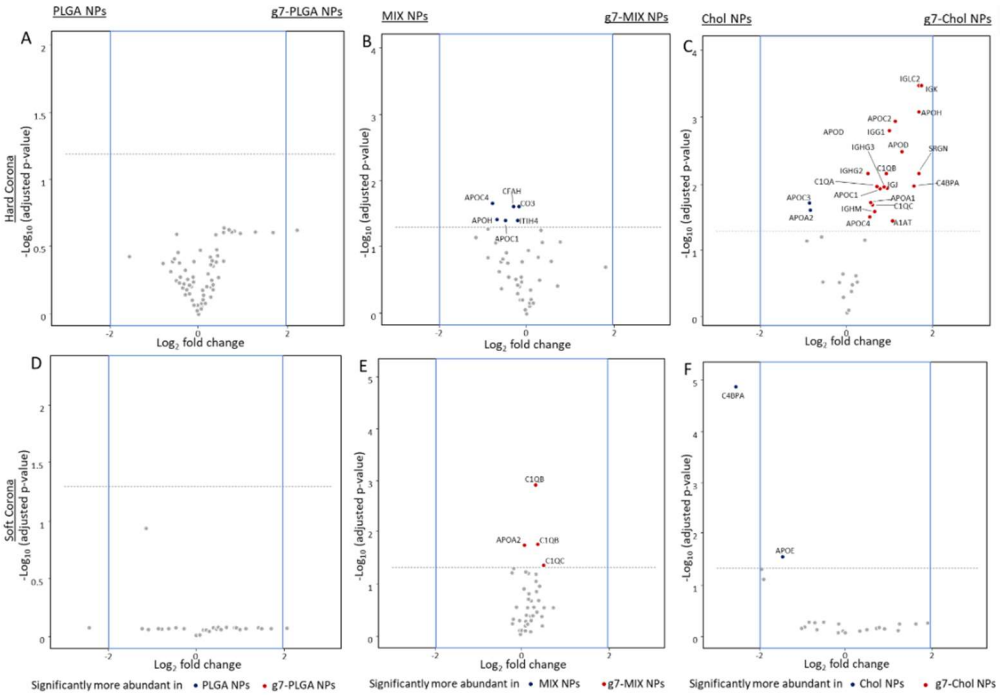

**Fig. 7**. Volcano plots representing relative abundance of the proteins detected in the HC and SC comparing NPs with or without the g7 peptide. A) HC and D) SC of PLGA vs g7-PLGA NPs. B) HC and E) SC of MIX vs g7-MIX NPs. C) HC and F) SC of Chol vs g7-Chol NPs. The dotted line represents the limit of statistical significance; the blue square represents a secondary selection for those proteins that are at least 2-fold more present in one sample than its counterpart. The complete statistical analysis is reported in Fig. S8.

## 4. Discussion

Analysis of the PC is crucial to understand the interactions between NPs and the biological environment [214,790]. In fact, the PC is known to affect the fate of NPs after administration by influencing their biodistribution, circulation time, surface properties, cell uptake dynamics, toxicity, and drug release profile [791–793]. At the same time, several chemico-physical features of the NPs, including their composition, size, charge, and hydrophobicity have been reported to strongly influence the composition of the PC, suggesting that PC should be investigated for each individual NP formulation [705,794]. Here we reported the investigation of the PC of three different NPs: polymeric PLGA NPs, fully lipidic Cholesterol NPs, and hybrid NPs (MIX) composed of PLGA and Chol. In-depth knowledge of the PC of different prominent NPs is critical for understanding their potential biological and pharmacological effects, in order to improve the specific design of NPs by taking into account the composition of their PC [795,796].

As reported in the literature, apolipoproteins are a major component of the PC independent of the matrix type for all NPs [756,757,797–800]. Previous literature has demonstrated that APOs can have a positive effect on the fate of NPs [750,801–803]. In fact, APOs can change the surface properties of NPs minimizing toxicity of the matrix, increasing blood circulation, and improving biodistribution. Moreover, many APOs have even been demonstrated to aid in BBB crossing, a crucial effect to consider when designing NPs [804–806]. On the other hand, complement factors and immunoglobulins represent a fundamental part of the immune system, and their presence in the HC of NPs must be taken into great consideration due to the negative effects they could have on early clearance and immunogenicity [750,807–812]. Quantification of these proteins with emPAI calculations showed their presence was 2-fold higher in MIX NPs compared to both PLGA and Chol NPs. This was also confirmed by statistical analysis, where several complement factors and immunoglobulins were found to be significantly more expressed in the HC of MIX NPs compared to the other two formulations.

When considering the potential biological effects of the PC, it is also important to look beyond the proteins found in abundance in both the plasma and on the NP surface: in fact, other potentially important candidates might be in such low concentrations in the plasma that they are unquantifiable, but could still play crucial roles when incorporated in the HC formation. This is what was observed for a series of "unique" proteins whose presence appeared to be completely dependent on the NP matrix. In fact, several proteins were too low to be detected in the plasma but were present in the HC of both PLGA and MIX NPs while being absent in the HC of the Chol NPs. This could suggest that the PLGA in both NP types is the cause of these proteins being present in the HC. At the same time, numerous proteins were found in the HC of Chol NPs but not in PLGA NPs. These considerations were supported also by statistical analysis, highlighting the significant difference in the composition of the HC for these NPs which would create unique protein profiles directly linked to the matrix composition.

It could be hypothesised that the lipidic and polymeric NPs had different PC characteristics due to their different chemical properties; however, statistical comparisons demonstrated near identical PCs between PLGA and MIX NPs, while variations were observed with Chol NPs. This difference could suggest that the polymeric portion of the MIX NPs plays a larger role in the composition of the minor proteins in the HC. Interestingly, a unique profile for MIX NPs was also reported in the composition of the SC. More specifically, MIX NPs showed higher variability in the type and total amount of complement factors forming the SC compared to the other NPs. This result could be linked to the composition of the HC in which the higher presence of immunoglobulins could lead to higher complement factor recruitment in the outer SC layer of the PC [813].

It is interesting to note that the proteins associated with the HC of PLGA and Chol NPs play very different biological roles. Proteins uniquely found in the polymeric and hybrid NPs, such as complement factors and immunoglobulins, were mainly linked to the immune response, and are involved in inflammatory and stress

response pathways. On the other hand, the HC of Chol NPs had higher levels of APOs which are involved in intracellular transport and storage and a smaller amount of immune response linked proteins. The HC profile could be easily explained through the high biocompatibility of cholesterol, which is a physiologic molecule normally present in the blood with high affinity to APOs. Altogether, these data suggest that the use of Chol NPs as drug delivery systems could be promising due to their potentially low immunogenicity, improved biodistribution and reduced toxicity compared to PLGA-based NPs.

As previously mentioned, the size of NPs as well as their surface composition are important factors that can affect the composition of the PC [755,757,758,771–773]; however, other studies report that a difference in size ranging 150-250 nm might not be enough to produce differences in terms of PC composition [756,814,815]. Our data support this literature precedence: in our study, MIX NPs (237 nm and 27% residual Pluronic® F68) were shown to have a HC with a more similar composition to PLGA NPs (152 nm and 14% residual Pluronic® F68) than Chol NPs (257 nm and 26% residual Pluronic® F68). Our data suggest that, for polymeric or lipidic NPs in this size range, the NP matrix composition had a larger impact on the formation and identity of the PC proteins respective of both the size or the amount of Pluronic® F68 that was either internalized or on the surface of the NPs. This highlights an important gap in the literature and emphasizes the need of thorough analysis of all the factors that affect the formation of the PC. In fact, most studies on the PC are now focused on evaluating the impact of single NP features, often leading to contradictory findings. Thus, an extensive and comprehensive study is still missing to understand which parameters play a predominant role in affecting the PC composition.

One of the most fascinating applications of NPs is the possibility to achieve targeted delivery to specific cells. Current approaches mainly depend on the modification of the NP surface with targeting ligands [134]. Because NP surface modifications are considered a major factor that can affect the formation of the PC, peptide targeted NPs of each matrix composition were analysed. Comparing the

ligand modified with the unmodified NPs, no significant differences were observed in the composition of both the HC and SC. This result is in contrast to what is found in the literature, however, it must be considered that the ligand density on the surface of these NPs is often so low that their presence do not change the physical characteristics, thus not affecting the PC [816]. It is important to note that several studies have linked the formation of the PC to a loss of targeting potential of NPs *in vitro* [804,817–819]. Nevertheless, recent findings evidence how the PC *in vivo* has different dynamics compared to *in vitro* studies which is supported by the successful targeted delivery results *in vivo* already published [818,820,821].

Research on the PC is crucial to better understand the biological implications of NPs. Although much research is being done to progress in this direction, some points still need to be addressed. While identifying and quantifying the proteins in the PC is important, it will be critical in future experiments to assess the effective concentration needed for these proteins to elicit a biological effect. This will help determine if the difference in the amount or variety of proteins facilitate a difference in biological effects. Another factor to be considered is the conformational state of the bound proteins. Literature precedence highlights that protein interaction with the surface of the NP could provoke a conformational change in the structure of adsorbed proteins resulting in a change or loss of activity. This calls for the need to not only quantify the proteins in the PC, but also to analyse their conformation after binding [822–826]. Such studies will further allow researchers to determine which key proteins need to be specifically evaluated and which can be considered innocent bystanders in the fate of the NPs. Intricate experiments both *in vitro* and *in vivo* will be required, but this information could lead to fascinating discoveries for the future of nanomedicine.

## 5. Conclusions

Research on the PC is rapidly growing despite the difficulty in accurately isolating, identifying, and quantifying the proteins in the HC and SC. While there are some general consistencies across the proteins found in the HC and SC of all NPs, each individual NP shows individual differences in the PC that will lead to drastic effects on the biodistribution, toxicity, immunogenicity, and general therapeutic potential making these individual studies critical for each NP system. Strong examples in this work include the seemingly small effect of both size and surfactant amount on the PC as stated in other literature works compared to the major differences in matrix composition, as well as the increase of immunoglobulins in the SC due to the higher presence of complement factors in the HC of MIX NPs. This work advanced this research by analysing the HC and SC composition of three types of NPs with different matrices that have recently shown great promise in the literature and evaluated if the matrix or the presence of a targeting ligand on the surface would have a more critical impact on the proteins present. Overall, this work represents a "piece of the puzzle" in the world of PC studies, where continuous research for different NPs would lead to more controlled and safe tools, thus paving the way for a brighter future for Nanomedicine.

## 6. Patents

PATENT: Italian patent application number 102020000025126 registered October 23rd 2020. PCT application PCT/IB2021/059750 registered October 21st 2021.

# 7. Supplementary Materials

## Methods for PC analysis

### *7.1.1. Incubation and purification of NP-HC and NP-SC complexes*

NPs (8 mg/mL) were incubated at 37°C under agitation (1600 rpm) in plasma for 20 minutes. To separate samples with HC, samples were centrifuged at 13,300 r.p.m. (Spectrafuge 24D, Labnet Int., Woodbridge, NJ, USA) for 10 min, and resuspended in $NH_4HCO_3$ buffer (25 mM, 100 μL). To evaluate the amount and composition of SC, 500 μL of incubated NPs were purified by size exclusion (Sepharose CL-2B, 20×1.3 cm) with Tris NaCl buffer pH 7.5. The eluate was collected in 2 mL fractions. To identify the fraction containing the complex NPs-PC, fractions were evaluated by SDS-PAGE gel (see section 3). In particular, samples were incubated 5 minutes at 95°C after addition of Laemmli sample buffer, and eventually loaded in 12% polyacrylamide gel for electrophoresis (MiniPROTEAN, Bio-Rad). Coomassie Brilliant Blue 0.1% in water:methanol:acetic acid (50:40:10 volume ratio) was used to visualize proteins in the gel.

### *7.1.2. Quantification of total protein amount*

The bicinchoninic acid assay (BCA) was performed to evaluate the total amount of proteins adsorbed on the surface of NPs after purification. Briefly, 150 μL of diluted purified samples (1:100) or standard solution were added to 150 μL of reagent mixture (Reagents A, B and C) and incubated 37°C for 2 h to allow the reaction. Absorbance at 570 nm was measured by means of Microplate Reader Multiscan (Spectrum Finstruments , MTX Lab system, FL, USA).

### *7.1.3 Mass spectrometry*

Prior to mass spectrometry analysis, samples were treated with trypsin (1:50 w/w enzyme:substrate) and incubated at 37°C under agitation at 500 r.p.m. for 18 h. A 2.5% v/v trifluoroacetic acid solution was used to stop the reaction. Samples were centrifuged at 13,300 r.p.m. for 30 minutes, and the supernatant was used for mass spectrometry analysis.

Peptide solutions were spiked with Glu-1-Fibrinopeptide B (sequence: EGVNDNEEGFFSAR) as an internal standard. An electrospray ionization quadrupole time-of-flight (ESI-Q-TOF) Accurate-Mass spectrometer (G6520AA, Agilent Technologies, CA, USA), controlled by MassHunter software (v. B.04.00) and interfaced with a Chip cube to an Agilent 1200 nanopump was used. Chromatographic separation was performed on a high-capacity loading chip (Agilent Technologies) with a 75 μm internal diameter (I.D.), 150 mm, 300 °A C18 column. Phase A: water:ACN:FA [96.9:3:0.1 v/v/v], Phase B: ACN:water:FA [94.5:5:0.1 v/v/v]. Ions were formed in a nano-ESI source operated in positive mode, 1850 V capillary voltage, with the source gas heated at 350°C and at a 3 L/min flow. Fragmentor was set to 170 V, skimmer lens operated at 65 V. Centroided MS and MS2 spectra were recorded from 350 to 1700 m/z and 50 to 1700 m/z, respectively, at scan rates of 6 and 3 Hz. The eight most intense multicharged ions were selected for MS2 nitrogen-promoted collision-induced dissociation. The collision energy was calculated according to the following expression: CE(V) = 3.6((m/z)/100)-3. A precursor active exclusion of 0.15 min was set, and the detector was operated at 2 GHz in extended dynamic range mode.

**Figure S1**: Correlogram and Intensity function of the PCS analysis on PLGA, MIX, and Chol NPs.

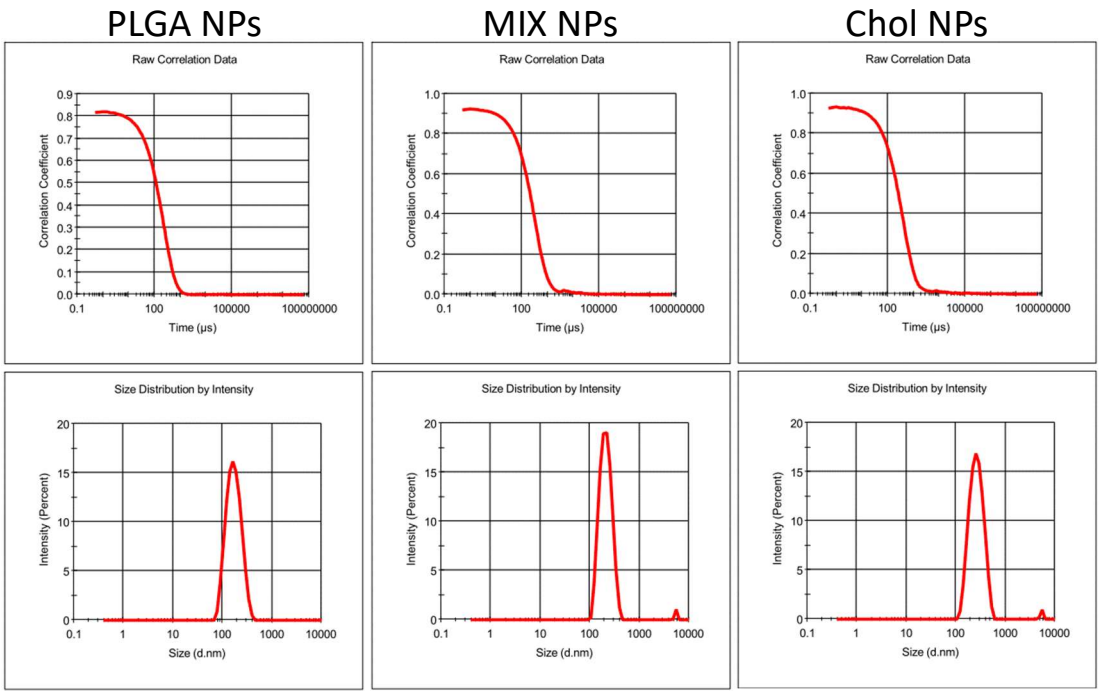

**Figure S2:** A) Total protein composition of plasma. B) Total composition of the HC of PLGA, MIX and Chol NPs.

A

| PLASMA | | |
|---|---|---|
| Protein | % normal emPAI | SD |
| ALBU | 97.56 | 0.66 |
| TRFE | 0.86 | 0.29 |
| IGHA1 | 0.17 | 0.04 |
| HPT | 0.14 | 0.01 |
| VTDB | 0.11 | 0.03 |
| HEMO | 0.09 | 0.01 |
| APOA2 | 0.07 | 0.05 |
| IGKC | 0.06 | 0.01 |
| IGJ | 0.06 | 0.01 |
| CO3 | 0.04 | 0.02 |
| FIBG | 0.04 | 0.01 |
| FETUA | 0.03 | 0.00 |
| FIBB | 0.03 | 0.00 |
| C1QA | 0.03 | 0.01 |
| IGHM | 0.02 | 0.00 |
| IGHG3 | 0.02 | 0.00 |
| THRB | 0.02 | 0.00 |
| APOA4 | 0.02 | 0.01 |
| ANT3 | 0.02 | 0.01 |
| CXCL7 | 0.02 | 0.00 |
| IGG1 | 0.02 | 0.01 |
| VTNC | 0.02 | 0.01 |
| ACTB | 0.02 | 0.00 |
| IGL1 | 0.02 | 0.01 |
| KNG1 | 0.02 | 0.00 |
| CD5L | 0.01 | 0.01 |
| ITIH2 | 0.01 | 0.00 |
| CLUS | 0.01 | 0.00 |
| AMBP | 0.01 | 0.00 |
| CO4A | 0.01 | 0.00 |
| CFAH | 0.01 | 0.00 |
| CERU | 0.01 | 0.00 |
| FIBA | 0.01 | 0.00 |
| C1QC | 0.01 | 0.00 |
| APOE | 0.01 | 0.00 |
| IGHG2 | 0.01 | 0.00 |
| PON1 | 0.01 | 0.00 |
| A2MG | 0.01 | 0.00 |

B

| PLGA NPs | | | MIX NPs | | | Chol NPs | | |
|---|---|---|---|---|---|---|---|---|
| Protein | % normal emPAI | SD | Protein | % normal emPAI | SD | Protein | % normal emPAI | SD |
| APOA1 | 51.79 | 4.14 | APOA1 | 53.70 | 1.07 | APOA1 | 56.68 | 7.52 |
| APOE | 15.64 | 4.68 | APOA4 | 8.38 | 5.12 | APOA4 | 20.01 | 5.87 |
| APOA4 | 15.34 | 3.89 | CO3 | 7.35 | 1.33 | APOE | 5.19 | 0.91 |
| APOC1 | 3.15 | 0.46 | APOE | 6.67 | 1.42 | APOA2 | 3.91 | 1.11 |
| CO3 | 1.32 | 0.10 | APOC1 | 4.40 | 1.33 | ALBU | 2.20 | 1.29 |
| IGKC | 1.14 | 0.35 | APOA2 | 2.16 | 0.81 | APOC3 | 1.88 | 0.32 |
| C1QB | 0.66 | 0.23 | IGKC | 1.44 | 0.38 | APOC1 | 1.34 | 0.26 |
| CFAH | 0.64 | 0.08 | G3P | 1.14 | 0.39 | C1QB | 1.14 | 0.22 |
| C1QC | 0.55 | 0.04 | IGHG3 | 0.79 | 0.08 | APOC2 | 0.78 | 0.05 |
| IGHG3 | 0.50 | 0.01 | CFAH | 0.78 | 0.01 | IGHM | 0.65 | 0.16 |
| CLUS | 0.49 | 0.13 | IGLC2 | 0.65 | 0.11 | IGKC | 0.43 | 0.10 |
| IGLC2 | 0.4 | 0.02 | APOH | 0.65 | 0.17 | C1QC | 0.42 | 0.11 |
| APOA2 | 0.39 | 0.14 | C1QB | 0.65 | 0.10 | C1QA | 0.40 | 0.06 |
| FHR1 | 0.37 | 0.07 | CXCL7 | 0.51 | 0.08 | CLUS | 0.39 | 0.05 |
| APOH | 0.35 | 0.04 | ALBU | 0.51 | 0.09 | IGJ | 0.39 | 0.06 |
| G3P | 0.34 | 0.01 | IGHM | 0.50 | 0.16 | G3P | 0.37 | 0.06 |
| IGG1 | 0.33 | 0.04 | URP2 | 0.48 | 0.16 | PLF4 | 0.35 | 0.05 |
| URP2 | 0.32 | 0.04 | IGG1 | 0.45 | 0.06 | IGHG3 | 0.25 | 0.03 |
| VTNC | 0.30 | 0.02 | CLUS | 0.45 | 0.07 | IGLC2 | 0.25 | 0.15 |
| PLF4 | 0.29 | 0.03 | LYSC | 0.41 | 0.35 | C4BPA | 0.23 | 0.05 |
| ITIH4 | 0.29 | 0.13 | C1QC | 0.40 | 0.08 | APOC4 | 0.21 | 0.06 |
| CXCL7 | 0.27 | 0.06 | PLF4 | 0.35 | 0.09 | CD5L | 0.21 | 0.02 |
| APOC4 | 0.26 | 0.02 | C1QA | 0.35 | 0.03 | TTHY | 0.19 | 0.06 |
| PON1 | 0.26 | 0.05 | IGJ | 0.34 | 0.10 | SAA4 | 0.16 | 0.06 |
| LYSC | 0.26 | 0.09 | ITIH4 | 0.32 | 0.05 | TSP1 | 0.15 | 0.01 |
| IGHA1 | 0.24 | 0.08 | IGHG2 | 0.30 | 0.03 | IGG1 | 0.14 | 0.02 |
| IGHM | 0.22 | 0.03 | ENOA | 0.30 | 0.09 | PON1 | 0.14 | 0.02 |
| IGK | 0.21 | 0.07 | IGK | 0.28 | 0.04 | SRGN | 0.10 | 0.03 |
| C1QA | 0.21 | 0.05 | FHR1 | 0.27 | 0.04 | IGK | 0.09 | 0.02 |
| IGHG2 | 0.17 | 0.03 | PROP | 0.26 | 0.04 | CO3 | 0.08 | 0.02 |
| PLEK | 0.17 | 0.04 | PLEK | 0.23 | 0.14 | IGHA1 | 0.08 | 0.02 |
| PROP | 0.17 | 0.01 | VTNC | 0.20 | 0.04 | PROP | 0.07 | 0.03 |
| RAP1B | 0.16 | 0.05 | APOC3 | 0.18 | 0.03 | APOD | 0.07 | 0.02 |
| ENOA | 0.15 | 0.10 | APOC4 | 0.17 | 0.04 | FIBG | 0.06 | 0.01 |
| SAA4 | 0.15 | 0.01 | CO4A | 0.16 | 0.02 | IGHG2 | 0.05 | 0.01 |
| ALBU | 0.14 | 0.06 | TLN1 | 0.15 | 0.05 | KV320 | 0.05 | 0.01 |
| APOC3 | 0.14 | 0.02 | IGHA1 | 0.15 | 0.06 | CFAH | 0.05 | 0.01 |
| IGL1 | 0.09 | 0.03 | VASP | 0.14 | 0.04 | HV307 | 0.05 | 0.01 |
| IGJ | 0.09 | 0.02 | COF1 | 0.14 | 0.04 | COL11 | 0.05 | 0.01 |
| VASP | 0.08 | 0.02 | IGL1 | 0.14 | 0.02 | TRFE | 0.05 | 0.03 |
| CD5L | 0.08 | 0.01 | CD5L | 0.12 | 0.03 | C4BPB | 0.05 | 0.01 |
| CYTC | 0.08 | 0.01 | CAP1 | 0.12 | 0.07 | A1AT | 0.04 | 0.01 |
| COF1 | 0.08 | 0.03 | PON1 | 0.11 | 0.03 | HPT | 0.04 | 0.02 |
| TLN1 | 0.08 | 0.02 | KPYM | 0.11 | 0.05 | ENOA | 0.04 | 0.01 |
| ANGI | 0.08 | 0.06 | RAP1B | 0.11 | 0.04 | FIBB | 0.04 | 0.00 |
| CAMP | 0.07 | 0.02 | HV307 | 0.10 | 0.01 | VTNC | 0.04 | 0.00 |
| ZPI | 0.07 | 0.02 | RARR2 | 0.10 | 0.06 | PROS | 0.04 | 0.01 |
| ACTB | 0.06 | 0.01 | APOC2 | 0.08 | 0.06 | TLN1 | 0.04 | 0.00 |
| HEMO | 0.06 | 0.02 | KV320 | 0.08 | 0.02 | APOL1 | 0.03 | 0.01 |
| RARR2 | 0.06 | 0.02 | SAA4 | 0.08 | 0.01 | RAP1B | 0.03 | 0.02 |
| KPYM | 0.06 | 0.01 | FA12 | 0.07 | 0.01 | APOF | 0.03 | 0.01 |

**Figure S3**: Volcano plots representing relative abundance of the proteins detected in the HC comparing NPs of different matrices. A) PLGA vs MIX NPs. B) PLGA vs Chol NPs. C) MIX vs Chol NPs. The dotted line represents the limit of statistical significance; the blue square represents a secondary selection for those proteins that are at least 2 fold more present in one sample than its counterpart. Yellow: APOs. Blue: Albumin. Green: complement factors. Red: IGs. Grey, orange: unique proteins for polymeric and lipidic NPs respectively.

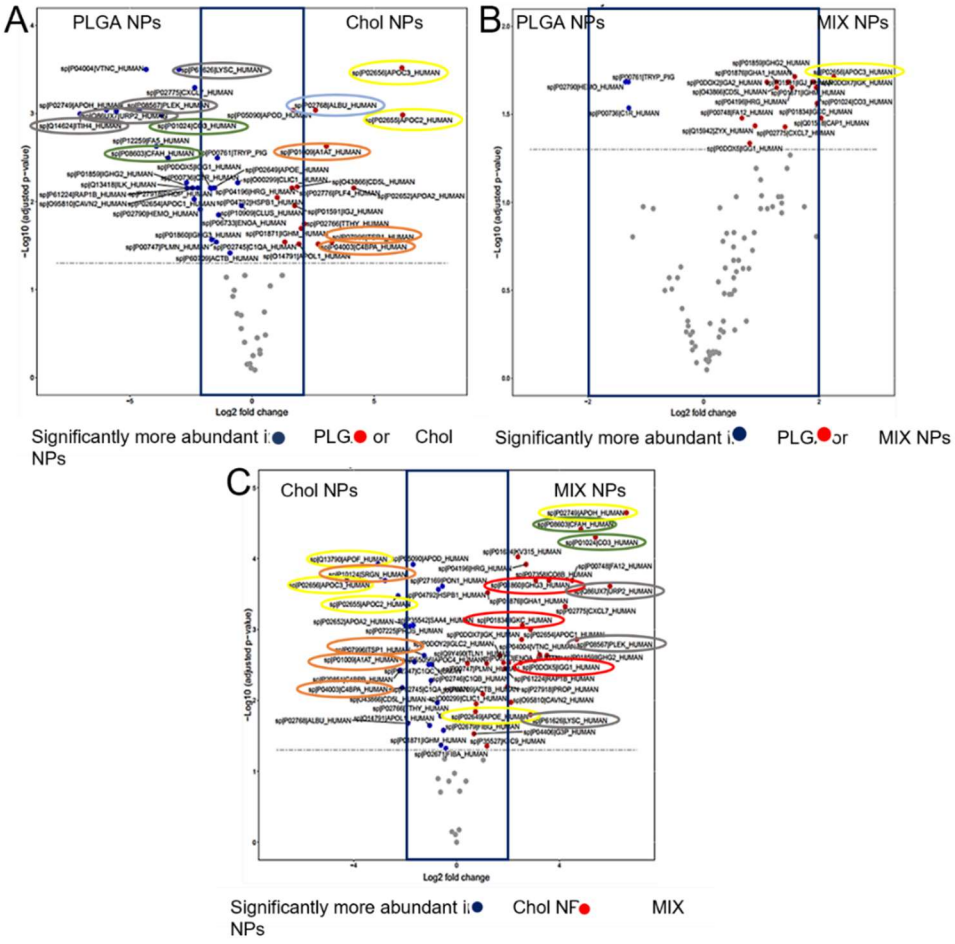

**Figure S4:** Total composition of the SC of PLGA, MIX and Chol NPs.

| PLGA NPs | | | MIX NPs | | | Chol NPs | | |
|---|---|---|---|---|---|---|---|---|
| Protein | % normal emPAI | SD | Protein | % normal emPAI | SD | Protein | % normal emPAI | SD |
| **ALBU** | 66.27 | 15.32 | **ALBU** | 59.93 | 18.47 | **ALBU** | 86.01 | 1.51 |
| **APOA2** | 7.62 | 2.98 | **APOA1** | 14.38 | 12.60 | **HPT** | 2.84 | 0.61 |
| **APOA1** | 7.48 | 3.56 | **APOA2** | 7.23 | 3.09 | **APOA2** | 1.56 | 0.68 |
| **HPT** | 4.18 | 0.71 | **HPT** | 3.38 | 0.65 | **IGHA1** | 1.47 | 0.19 |
| **IGJ** | 3.57 | 0.89 | **A2MG** | 1.39 | 0.70 | **APOA1** | 1.18 | 0.12 |
| **IGHA1** | 2.87 | 0.57 | **HPTR** | 1.02 | 0.32 | **HPTR** | 0.70 | 0.07 |
| **CD5L** | 0.81 | 0.25 | **CO3** | 1.00 | 0.50 | **APOC3** | 0.52 | 0.01 |
| **THRB** | 0.72 | 0.18 | **IGHA1** | 0.95 | 0.38 | **TRFE** | 0.51 | 0.18 |
| **VTDB** | 0.72 | 0.23 | **FIBA** | 0.92 | 0.38 | **FIBA** | 0.46 | 0.08 |
| **VTNC** | 0.62 | 0.14 | **FIBG** | 0.91 | 0.37 | **CLUS** | 0.37 | 0.09 |
| **CFAH** | 0.61 | 0.23 | **FIBB** | 0.88 | 0.29 | **THRB** | 0.33 | 0.00 |
| **C4BPA** | 0.54 | 0.18 | **CLUS** | 0.53 | 0.14 | **HEMO** | 0.33 | 0.04 |
| **CO3** | 0.48 | 0.15 | **THRB** | 0.46 | 0.16 | **A2MG** | 0.32 | 0.05 |
| **ITIH2** | 0.47 | 0.12 | **IGJ** | 0.41 | 0.13 | **FIBB** | 0.30 | 0.09 |
| **AMBP** | 0.44 | 0.04 | **APOE** | 0.40 | 0.06 | **IGJ** | 0.27 | 0.00 |
| **A2MG** | 0.37 | 0.08 | **CERU** | 0.40 | 0.08 | **ITIH2** | 0.27 | 0.01 |
| **FETUA** | 0.34 | 0.10 | **ITIH2** | 0.39 | 0.05 | **CO3** | 0.18 | 0.02 |
| **FIBA** | 0.33 | 0.09 | **IGHM** | 0.35 | 0.30 | **FETUA** | 0.16 | 0.04 |
| **KNG1** | 0.27 | 0.07 | **IGHA2** | 0.31 | 0.12 | **VTDB** | 0.16 | 0.02 |
| **IGHM** | 0.26 | 0.05 | **APOC3** | 0.29 | 0.09 | **C4BPA** | 0.16 | 0.04 |
| **CO4B** | 0.24 | 0.09 | **PON1** | 0.27 | 0.11 | **VTNC** | 0.15 | 0.02 |
| **FIBB** | 0.17 | 0.03 | **CO4B** | 0.26 | 0.15 | **FIBG** | 0.15 | 0.00 |
| **FINC** | 0.15 | 0.05 | **C4BPA** | 0.24 | 0.05 | **APOE** | 0.15 | 0.03 |
| **ITIH1** | 0.13 | 0.02 | **ITIH1** | 0.24 | 0.09 | **CFAH** | 0.14 | 0.02 |
| **CERU** | 0.11 | 0.01 | **VTDB** | 0.22 | 0.08 | **ANT3** | 0.13 | 0.02 |
| **IGHG3** | 0.07 | 0.01 | **IC1** | 0.21 | 0.03 | **CERU** | 0.12 | 0.03 |
| **ARP2** | 0.06 | 0.01 | **APOA4** | 0.21 | 0.03 | **KNG1** | 0.12 | 0.02 |
| **FIBG** | 0.06 | 0.00 | **CFAH** | 0.21 | 0.08 | **IC1** | 0.12 | 0.09 |
| **HRG** | 0.05 | 0.01 | **SAA4** | 0.20 | 0.04 | **CD5L** | 0.10 | 0.03 |
| | | | **CD5L** | 0.17 | 0.07 | **AMBP** | 0.10 | 0.03 |
| | | | **A1AG1** | 0.15 | 0.11 | **PON1** | 0.08 | 0.06 |
| | | | **AMBP** | 0.15 | 0.01 | **APOL1** | 0.07 | 0.00 |
| | | | **HEMO** | 0.14 | 0.03 | **IGHG3** | 0.05 | 0.02 |
| | | | **KNG1** | 0.13 | 0.00 | **PLMN** | 0.05 | 0.00 |
| | | | **IGHG3** | 0.12 | 0.09 | **APOA4** | 0.05 | 0.03 |
| | | | **IGG1** | 0.12 | 0.11 | **FCN3** | 0.04 | 0.00 |
| | | | **C1QC** | 0.11 | 0.05 | **IGHM** | 0.04 | 0.02 |
| | | | **C1QB** | 0.11 | 0.05 | **ITIH4** | 0.04 | 0.01 |
| | | | **PROS** | 0.11 | 0.02 | **FINC** | 0.03 | 0.00 |
| | | | **ANT3** | 0.10 | 0.05 | **ARP2** | 0.03 | 0.00 |
| | | | **VTNC** | 0.10 | 0.02 | **ITIH1** | 0.03 | 0.00 |
| | | | **APOB** | 0.09 | 0.05 | | | |
| | | | **APOL1** | 0.09 | 0.05 | | | |
| | | | **FINC** | 0.09 | 0.03 | | | |
| | | | **CPN2** | 0.08 | 0.02 | | | |
| | | | **C1S** | 0.07 | 0.01 | | | |
| | | | **C1R** | 0.06 | 0.02 | | | |
| | | | **ITIH4** | 0.06 | 0.02 | | | |
| | | | **HBA** | 0.05 | 0.01 | | | |
| | | | **KLKB1** | 0.05 | 0.03 | | | |
| | | | **CO9** | 0.05 | 0.03 | | | |

**Figure S5**: Volcano plots representing relative abundance of the proteins detected in the SC comparing NPs of different matrices. A) PLGA vs MIX NPs. B) PLGA vs Chol NPs. C) MIX vs Chol NPs. The dotted line represents the limit of statistical significance; the blue square represents a secondary selection for those proteins that are at least 2 fold more present in one sample than its counterpart. Yellow: APOs. Blue: Albumin. Green: complement factors. Red: IGs. Purple: unique proteins for MIX NPs.

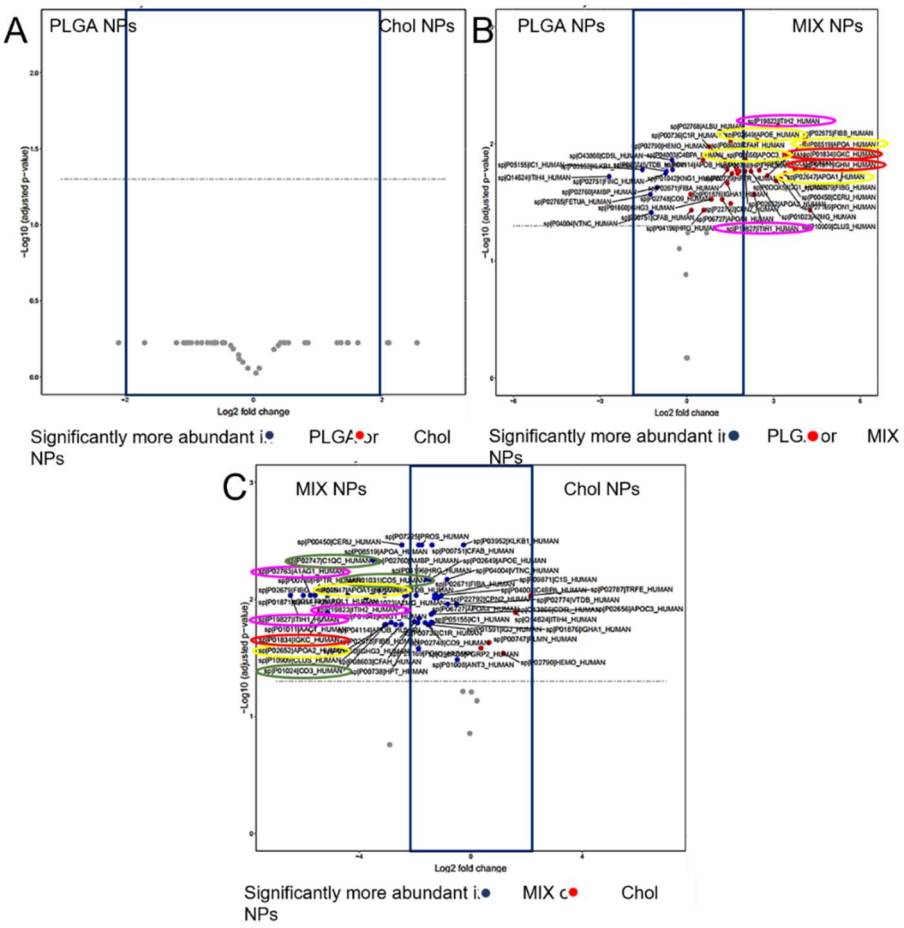

**Figure S6**: Total composition of the HC of g7-modified NPs.

| g7-PLGA NPs | | | g7-MIX NPs | | | g7-Chol NPs | | |
|---|---|---|---|---|---|---|---|---|
| Protein | % normal emPAI | SD | Protein | % normal emPAI | SD | Protein | % normal emPAI | SD |
| **APOA1** | 41.00 | 2.71 | **APOA1** | 47.60 | 4.49 | **APOA1** | 60.81 | 3.60 |
| **APOA4** | 29.48 | 2.19 | **APOA4** | 8.36 | 2.45 | **APOA4** | 14.45 | 2.45 |
| **APOE** | 14.47 | 2.15 | **APOE** | 7.90 | 1.01 | **APOA2** | 3.46 | 0.90 |
| **APOC1** | 2.27 | 0.41 | **CO3** | 6.40 | 0.39 | **APOE** | 2.33 | 0.21 |
| **CO3** | 1.21 | 0.05 | **APOC1** | 4.96 | 0.58 | **APOC1** | 2.01 | 0.11 |
| **IGKC** | 0.81 | 0.09 | **ALBU** | 3.69 | 3.38 | **ALBU** | 1.53 | 0.20 |
| **CFAH** | 0.52 | 0.09 | **APOA2** | 2.84 | 0.18 | **C1QB** | 1.17 | 0.18 |
| **CLUS** | 0.50 | 0.03 | **IGKC** | 2.80 | 0.78 | **C1QA** | 0.83 | 0.17 |
| **C1QB** | 0.46 | 0.05 | **G3P** | 1.16 | 0.13 | **APOC3** | 0.79 | 0.22 |
| **ITIH4** | 0.44 | 0.08 | **CFAH** | 0.88 | 0.14 | **IGKC** | 0.78 | 0.19 |
| **C1QC** | 0.39 | 0.06 | **IGHG3** | 0.80 | 0.07 | **IGHM** | 0.76 | 0.07 |
| **IGHG3** | 0.38 | 0.05 | **IGLC2** | 0.71 | 0.07 | **C4BPA** | 0.70 | 0.06 |
| **APOH** | 0.38 | 0.07 | **C1QB** | 0.70 | 0.23 | **C1QC** | 0.63 | 0.10 |
| **IGLC2** | 0.38 | 0.02 | **CLUS** | 0.57 | 0.06 | **PLF4** | 0.60 | 0.07 |
| **APOA2** | 0.35 | 0.11 | **APOH** | 0.56 | 0.11 | **IGJ** | 0.57 | 0.07 |
| **FHR1** | 0.31 | 0.03 | **IGHM** | 0.54 | 0.06 | **APOC2** | 0.56 | 0.21 |
| **PLF4** | 0.31 | 0.07 | **IGG1** | 0.51 | 0.09 | **CD5L** | 0.56 | 0.07 |
| **IGG1** | 0.28 | 0.03 | **IGJ** | 0.49 | 0.11 | **IGLC2** | 0.40 | 0.02 |
| **URP2** | 0.28 | 0.04 | **IGK** | 0.44 | 0.09 | **IGHG3** | 0.39 | 0.04 |
| **G3P** | 0.28 | 0.03 | **CXCL7** | 0.42 | 0.07 | **CLUS** | 0.38 | 0.07 |
| **CXCL7** | 0.26 | 0.08 | **IGHG2** | 0.39 | 0.06 | **CO3** | 0.35 | 0.03 |
| **ENOA** | 0.24 | 0.04 | **C1QC** | 0.39 | 0.07 | **APOC4** | 0.30 | 0.06 |
| **VTNC** | 0.22 | 0.03 | **PLF4** | 0.33 | 0.07 | **HV307** | 0.29 | 0.05 |
| **ALBU** | 0.22 | 0.11 | **ENOA** | 0.32 | 0.04 | **SRGN** | 0.27 | 0.07 |
| **IGHM** | 0.20 | 0.02 | **ITIH4** | 0.30 | 0.07 | **PON1** | 0.27 | 0.06 |
| **PON1** | 0.19 | 0.08 | **FHR1** | 0.28 | 0.05 | **G3P** | 0.26 | 0.05 |
| **C1QA** | 0.19 | 0.02 | **URP2** | 0.28 | 0.06 | **IGG1** | 0.24 | 0.03 |
| **IGHG2** | 0.18 | 0.02 | **C1QA** | 0.27 | 0.04 | **TSP1** | 0.24 | 0.03 |
| **IGK** | 0.16 | 0.01 | **PROP** | 0.26 | 0.03 | **PF4V** | 0.22 | 0.03 |
| **PF4V** | 0.16 | 0.02 | **APOC3** | 0.23 | 0.03 | **PROP** | 0.22 | 0.03 |
| **APOC3** | 0.15 | 0.03 | **LYSC** | 0.19 | 0.04 | **FIBB** | 0.19 | 0.06 |
| **PLEK** | 0.15 | 0.02 | **APOC2** | 0.19 | 0.08 | **SAA4** | 0.18 | 0.06 |
| **APOC4** | 0.14 | 0.07 | **IGHA1** | 0.18 | 0.03 | **IGK** | 0.17 | 0.03 |
| **PROP** | 0.14 | 0.02 | **VTNC** | 0.18 | 0.03 | **CFAH** | 0.17 | 0.01 |
| **CYTC** | 0.13 | 0.02 | **CD5L** | 0.15 | 0.02 | **TTHY** | 0.17 | 0.07 |
| **LYSC** | 0.13 | 0.04 | **APOC4** | 0.15 | 0.04 | **A1AT** | 0.16 | 0.03 |
| **SAA4** | 0.12 | 0.04 | **VASP** | 0.13 | 0.01 | **KV320** | 0.16 | 0.04 |
| **PEDF** | 0.12 | 0.04 | **COF1** | 0.12 | 0.03 | **PROS** | 0.15 | 0.01 |
| **IGHA1** | 0.12 | 0.02 | **IGL1** | 0.12 | 0.01 | **C4BPB** | 0.13 | 0.01 |
| **IGJ** | 0.11 | 0.02 | **PON1** | 0.11 | 0.03 | **HV374** | 0.13 | 0.03 |
| **COF1** | 0.10 | 0.01 | **TLN1** | 0.11 | 0.01 | **FIBG** | 0.12 | 0.03 |
| **CD5L** | 0.10 | 0.02 | **KV320** | 0.11 | 0.02 | **IGHG2** | 0.11 | 0.02 |
| **RAP1B** | 0.10 | 0.01 | **PLEK** | 0.10 | 0.01 | **KVD20** | 0.11 | 0.03 |
| **IGL1** | 0.09 | 0.01 | **CO4A** | 0.09 | 0.06 | **IGHA1** | 0.10 | 0.01 |
| **VASP** | 0.08 | 0.01 | **PLMN** | 0.09 | 0.02 | **CO4B** | 0.10 | 0.02 |
| **ANGI** | 0.06 | 0.00 | **FA12** | 0.08 | 0.00 | **CXCL7** | 0.09 | 0.02 |
| **HEMO** | 0.06 | 0.01 | **HV307** | 0.08 | 0.02 | **HPTR** | 0.09 | 0.03 |
| **FHR2** | 0.06 | 0.04 | **KPYM** | 0.08 | 0.02 | **COL11** | 0.08 | 0.02 |
| **ZYX** | 0.06 | 0.01 | **CYTC** | 0.07 | 0.02 | **FIBA** | 0.08 | 0.02 |
| **IGA2** | 0.05 | 0.01 | **IGA2** | 0.07 | 0.01 | **CO4A** | 0.07 | 0.05 |
| **FHR5** | 0.05 | 0.01 | **C4BPA** | 0.07 | 0.02 | **K2C1** | 0.07 | 0.07 |

**Figure S7**: Total composition of the SC of g7-modified NPs.

| g7-PLGA NPs | | | g7-MIX NPs | | | g7-Chol NPs | | |
|---|---|---|---|---|---|---|---|---|
| Protein | % normal emPAI | SD | Protein | % normal emPAI | SD | Protein | % normal emPAI | SD |
| **ALBU** | 77.62 | 5.09 | **ALBU** | 58.26 | 18.98 | **ALBU** | 80.28 | 0.94 |
| **APOA1** | 5.41 | 2.15 | **APOA1** | 14.42 | 10.77 | **IGHA1** | 2.62 | 0.63 |
| **APOA2** | 3.07 | 2.03 | **APOA2** | 5.74 | 2.60 | **HPT** | 2.33 | 0.33 |
| **IGHA1** | 2.78 | 0.14 | **HPT** | 3.46 | 0.79 | **APOC3** | 1.51 | 0.06 |
| **HPT** | 2.53 | 0.83 | **A2MG** | 1.52 | 0.97 | **APOA2** | 1.44 | 0.06 |
| **IGJ** | 1.34 | 0.23 | **HPTR** | 1.31 | 0.17 | **IGJ** | 1.37 | 0.74 |
| **THRB** | 0.80 | 0.02 | **FIBG** | 1.20 | 0.20 | **APOA1** | 1.06 | 0.42 |
| **VTDB** | 0.64 | 0.11 | **FIBA** | 1.12 | 0.20 | **THRB** | 1.03 | 0.04 |
| **FETUA** | 0.41 | 0.24 | **FIBB** | 1.10 | 0.43 | **FIBA** | 0.93 | 0.10 |
| **CO3** | 0.37 | 0.07 | **CO3** | 1.09 | 0.56 | **FETUA** | 0.77 | 0.03 |
| **CD5L** | 0.36 | 0.15 | **IGHA1** | 0.93 | 0.24 | **A2MG** | 0.75 | 0.09 |
| **AMBP** | 0.35 | 0.01 | **THRB** | 0.57 | 0.26 | **VTNC** | 0.63 | 0.30 |
| **ITIH2** | 0.33 | 0.06 | **IGJ** | 0.52 | 0.36 | **AMBP** | 0.58 | 0.02 |
| **C4BPA** | 0.33 | 0.03 | **APOE** | 0.50 | 0.20 | **CD5L** | 0.57 | 0.28 |
| **APOC3** | 0.30 | 0.01 | **IGHM** | 0.45 | 0.35 | **C4BPA** | 0.55 | 0.02 |
| **IC1** | 0.28 | 0.15 | **ITIH2** | 0.44 | 0.08 | **CO3** | 0.48 | 0.09 |
| **VTNC** | 0.28 | 0.05 | **CLUS** | 0.43 | 0.10 | **FIBB** | 0.40 | 0.20 |
| **A2MG** | 0.27 | 0.04 | **CERU** | 0.43 | 0.08 | **VTDB** | 0.34 | 0.12 |
| **CLUS** | 0.26 | 0.01 | **IGHA2** | 0.36 | 0.10 | **IGHG3** | 0.34 | 0.01 |
| **FIBA** | 0.25 | 0.05 | **APOC3** | 0.35 | 0.13 | **HEMO** | 0.26 | 0.01 |
| **KNG** | 0.18 | 0.08 | **CO4B** | 0.30 | 0.11 | **APOL1** | 0.26 | 0.13 |
| **ANT3** | 0.18 | 0.00 | **C4BPA** | 0.28 | 0.10 | **CO4B** | 0.19 | 0.26 |
| **CFAH** | 0.18 | 0.06 | **ITIH1** | 0.28 | 0.11 | **CFAH** | 0.16 | 0.23 |
| **CO4B** | 0.17 | 0.03 | **PON1** | 0.26 | 0.13 | **ARP2** | 0.14 | 0.01 |
| **HEMO** | 0.16 | 0.06 | **AACT** | 0.25 | 0.22 | **IGHM** | 0.14 | 0.20 |
| **ACTB** | 0.15 | 0.11 | **CFAH** | 0.24 | 0.09 | **CLUS** | 0.12 | 0.01 |
| **CO8G** | 0.14 | 0.00 | **SAA4** | 0.24 | 0.13 | **CO4A** | 0.11 | 0.16 |
| **IGHM** | 0.13 | 0.10 | **IC1** | 0.21 | 0.07 | **APOE** | 0.10 | 0.14 |
| **FIBB** | 0.12 | 0.00 | **CD5L** | 0.21 | 0.05 | **C1S** | 0.10 | 0.14 |
| **C1R** | 0.10 | 0.03 | **HEMO** | 0.18 | 0.07 | **PON1** | 0.08 | 0.12 |
| **ITIH4** | 0.10 | 0.04 | **FETUA** | 0.17 | 0.04 | **ITIH4** | 0.07 | 0.11 |
| **FINC** | 0.08 | 0.02 | **VTDB** | 0.16 | 0.06 | **FIBG** | 0.07 | 0.10 |
| **CERU** | 0.08 | 0.00 | **IGG1** | 0.16 | 0.12 | **ITIH2** | 0.70 | 0.10 |
| **IGHG3** | 0.08 | 0.00 | **C1QC** | 0.16 | 0.10 | **ANT3** | 0.06 | 0.09 |
| **ARP2** | 0.06 | 0.00 | **APOL1** | 0.16 | 0.07 | **CPN2** | 0.06 | 0.09 |
| **FIBG** | 0.06 | 0.00 | **PROS** | 0.15 | 0.05 | **IC1** | 0.06 | 0.08 |
| **ITIH1** | 0.06 | 0.00 | **KNG** | 0.15 | 0.03 | **PGRP2** | 0.06 | 0.08 |
| | | | **A1AG1** | 0.14 | 0.09 | | | |
| | | | **C1QB** | 0.14 | 0.07 | | | |
| | | | **TRFE** | 0.14 | 0.13 | | | |
| | | | **AMBP** | 0.14 | 0.05 | | | |
| | | | **CO8G** | 0.14 | 0.09 | | | |
| | | | **HRG** | 0.13 | 0.12 | | | |
| | | | **APOA4** | 0.13 | 0.05 | | | |
| | | | **APOC2** | 0.12 | 0.06 | | | |
| | | | **ANT3** | 0.12 | 0.04 | | | |
| | | | **IGHG3** | 0.11 | 0.11 | | | |
| | | | **APOB** | 0.11 | 0.08 | | | |
| | | | **VTNC** | 0.11 | 0.02 | | | |
| | | | **CPN2** | 0.10 | 0.05 | | | |
| | | | **C1S** | 0.08 | 0.02 | | | |

**Figure S8**: Volcano plots representing relative abundance of the proteins detected in the HC and SC comparing NPs with or without the g7 peptide. A) HC and D) SC of PLGA vs g7-PLGA NPs. B) HC and E) SC of MIX vs g7-MIX NPs. C) HC and F) SC of Chol vs g7-Chol NPs. The dotted line represents the limit of statistical significance; the blue square represents a secondary selection for those proteins that are at least 2 fold more present in one sample than its counterpart.

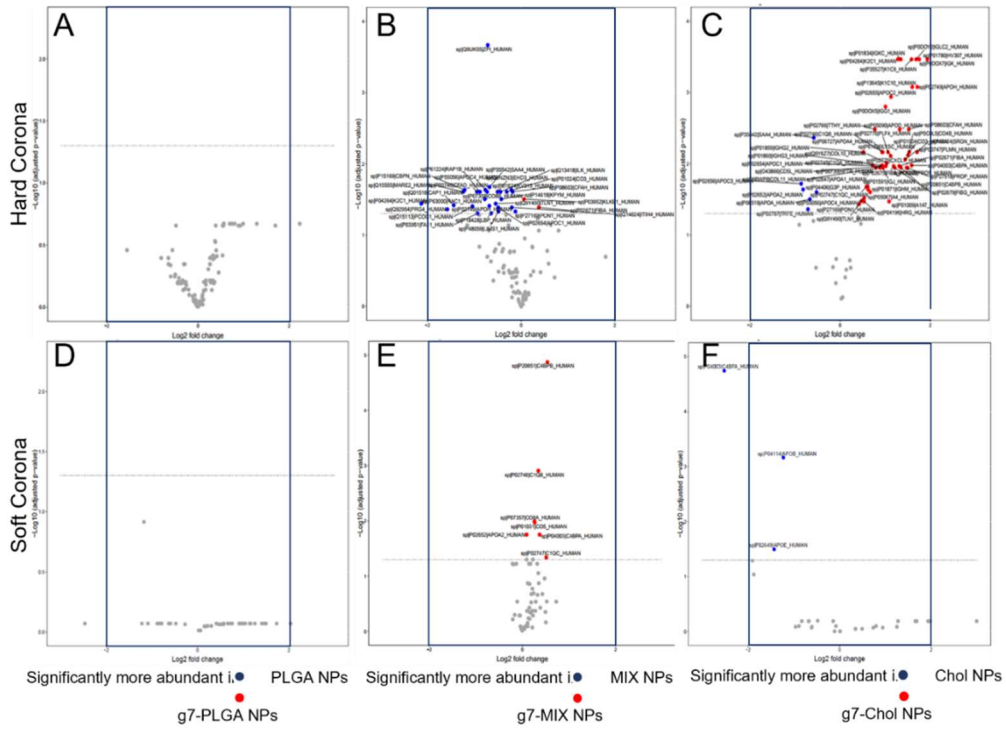

# Tunneling Nanotubes: A New Target for Nanomedicine?

**Ilaria Ottonelli [1,2], Riccardo Caraffi [2], Giovanni Tosi [2], Maria Angela Vandelli [2], Jason Thomas Duskey [2,*] and Barbara Ruozi [2]**

[1] Clinical and Experimental Medicine PhD Program, University of Modena and Reggio Emilia, 41125 Modena, Italy

[2] Nanotech Lab, Te.Far.T.I., Department of Life Sciences, University of Modena and Reggio Emilia, 41125 Modena, Italy

*Int. J. Mol. Sci.* 2022, 23(4), 2237; doi: 10.3390/ijms23042237

Received: 31 January 2022

Revised: 14 February 2022

Accepted: 15 February 2022

Published: 17 February 2022

## Abstract

Tunneling nanotubes (TNTs), discovered in 2004, are thin, long protrusions between cells utilized for intercellular transfer and communication. These newly discovered structures have been demonstrated to play a crucial role in homeostasis, but also in the spreading of diseases, infections, and metastases. Gaining much interest in the medical research field, TNTs have been shown to transport nanomedicines (NMeds) between cells. NMeds have been studied thanks to their advantageous features in terms of reduced toxicity of drugs, enhanced solubility, protection of the payload, prolonged release, and more interestingly, cell-targeted delivery. Nevertheless, their transfer between cells via TNTs makes their true fate unknown. If better understood, TNTs could help control NMed delivery. In fact, TNTs can represent the possibility both to improve the biodistribution of NMeds throughout a diseased tissue by increasing their formation, or to minimize their formation to block the transfer of dangerous material. To date, few studies have investigated the interaction between NMeds and TNTs. In this work, we will explain what TNTs are and how they form and then review what has been published regarding their potential use in nanomedicine research. We will highlight possible future approaches to better exploit TNT intercellular communication in the field of nanomedicine.

## 1. Tunneling Nanotubes

### *1.1. What Are Tunneling Nanotubes?*

Tunneling Nanotubes (TNTs), first described in the literature in 2004 by Rustom et al. [827], have gained growing interest from the scientific community. They are described as long and thin protrusions of the cytoskeleton and plasma membrane which connect two different cells, extending distances even up to several μm [828,829]. The composition of these bridges is simple as they are normally composed of actin and tubulin filaments surrounded by plasma membrane; however, the presence of tubulin has also been reported as variable, leading to the classification of two different types of TNTs: 1) "thin" TNTs, composed of only actin, which are usually more delicate and transient, and 2) "thick" TNTs, with both actin and tubulin, which are often associated with a more stable structure [830]. TNTs have peculiar features which distinguish them from other cell protrusions. TNTs differ from filopodia, cilia, or cytonemes, both in their structure and function: TNTs are very thin filaments which do not adhere to the substratum, but more importantly they present open endings in the plasma membrane of the two cells they are connecting. Moreover, these open endings allow for direct exchange of virtually any kind of cargo from one cytoplasm to another: they allow for the transport of not only of ions and neurotransmitters, but also whole organelles, proteins, and genetic material [228,828]. A more detailed explanation is included in a review by Pinto et al. with a comprehensive table explaining the differences and relevant citations [5]. In physiological conditions, these bridges have been demonstrated to be essential not only for embryonic development [225,831–833] of vertebrates, but also in their adult form to maintain a healthy status of their tissues. For example, TNTs have been demonstrated to be critical not only to preserve the differentiation potential of mesenchymal cells [834], but also to repair damages in other neighboring cells by exchanging intact organelles [835–837]. Moreover, TNTs are involved in the exchange of electrical and chemical signaling in different tissues, such as in the eye [838,839]. It was reported that an

insufficient communication via TNTs in trabecular meshwork is linked to an increase in intraocular pressure and consequently an increased risk of glaucoma [840]; at the same time, TNTs are involved in the transmission of calcium ions in the retina, determining good health and correct firing of retinal photoreceptors [841,842].

Notwithstanding their essential role in physiological conditions, TNTs are better known due to their involvement in pathological processes. As reported in several recent review works, TNTs play a key role in the spreading of several disease states such as neurodegeneration, infections, and cancer. In the case of neurodegenerative diseases, literature shows that cells can use TNTs to transport prions, misfolded huntingtin, Tau protein, $\alpha$-synuclein, and $\beta$-amyloid, promoting protein misfolding in other cells [843]. This additive effect increases the risk of developing Huntington's [844,845], Parkinson's [846,847], and Alzheimer's diseases [848–850]. Another field where TNTs play a pivotal role is cancer. The exchange of misfolded proteins and damaged genetic material through TNTs in cancers is considered one of the major phenomena that contribute to the transformation of healthy into tumoral cells and an increase in metastasis formation [228,851]. While TNTs have been linked to the communication and spreading in several types of cancer [852], such as prostate [853], bladder [854–856], pancreatic [857], breast cancer [858], as well as different types of leukemia [859–861], Glioblastoma Multiforme (GBM) is by far the most studied for the consequences of TNT activity [830,862]. GBM is one of the most aggressive, invasive, and fatal brain cancers [863], with a survival of less than 15 months after the diagnosis [864,865]. In fact, fast growth and invasiveness of GBM have been linked to TNT-mediated communication between GBM cells and towards and surrounding healthy astrocytes [866,867]. This could be linked to the reason why the vast majority of studies about TNTs are performed using GBM cells. The high rates of TNT formation in these cells makes them an optimal *in vitro* model to study their mechanics and dynamics [224].

The natural exchange of different materials from one cell to another is an evolutionary defensive strategy to reduce the risk of cell death: on one hand, a healthy cell could share its organelles with a diseased one to promote damage repair [868,869], or improve cell respiration by transfer of mitochondria in case of hypoxia [870]; on the other hand, this can also be used by cells in an attempt to dilute stressful inputs, leading to an increased number of stressed cells but lower stress level. However, these mechanisms are also exploited and enhanced by numerous viruses, such as HIV [871], herpesviruses [872,873], Influenza virus [874,875], and more recently SARS-CoV-2 [184,874,876]. After viral replication, the infected cell will be in an inflammatory state that causes the formation of a larger number of TNTs, in order to reduce the stress on the primary cell. With these mechanisms, viruses exploit this highway to increase the number of infected cells while also reducing the risk of recognition by the immune system outside the plasma membrane [877]. The same pattern was observed *in vitro* after the administration of cytotoxic drugs, where the cells were demonstrated to promote the efflux of toxic compounds and share it with neighboring cells [878], often with a linear correlation between the amount of cytotoxic drug administered and the number of TNTs formed by cells [857]. While this is a protective reaction of the cell to dilute the toxin, it could also be a pitfall leading to lethal levels of the drugs in all surrounding cells. Another consequence of this is that TNTs are considered one of the major mechanisms involved in the onset of chemoresistance [879], as the simultaneous transport via TNTs of drugs, P-glycoproteins, and microRNAs all contribute to multidrug resistance [880–882].

### *1.2. Exogenous Modulation of Tunneling Nanotubes*

It is clear that in order to take advantage of this intercellular cross-talk a deeper study of the physiological and pathological role of TNTs in different tissues is needed. As previously described, while the inhibition of TNTs could help reduce the spreading of tumors and diseases, in other cases promoting their formation

might improve the localized cellular distribution of therapeutic molecules. To date, inhibitors of the formation of TNTs mostly block the mobility of the whole cytoskeleton [883,884]. For example, latrunculin B, the most used compound to affect TNTs, is an inhibitor of actin polymerization that affects the whole cell. Similarly, other small molecules like metformin and everolimus are able to reduce the number of TNTs formed by cells due to their role as inhibitors on the mTOR pathway [885,886]. Nevertheless, most of these compounds are considered toxic for cells because their effect is not limited to reducing the formation of TNTs, but they affect the whole cytoskeleton mobility. This non-specific inhibition of physiological processes such as cell migration and mobility disrupts normal cell function and growth leading to devastating effects. Interestingly, tolytoxin was reported to have a selective effect of inhibition of the formation of TNTs without any general effects on the cytoskeleton, thus representing a valuable tool for limiting the intercellular transport via TNTs [887].

On the contrary, induction of TNTs seems to be easier to achieve. It has been abundantly demonstrated in the literature that the formation rate of TNTs *in vitro* can be increased by several inputs linked to the culture protocol. This includes variables such as low levels of oxygen or high presence of $CO_2$, acidic pH, serum starvation, or low glucose concentrations [228,853,866,868]. All these conditions represent situations of cellular stress in which cells tend to connect in order to improve their survival, as previously described. Another widely used technique to induce the formation of TNTs *in vitro* is also to transfect cells with proteins involved in cytoskeletal mobility and cell adhesion. The administration of mSEC [888,889], which triggers the formation of TNTs due to higher dynamicity of the cytoskeleton, is a primary example. Most drugs used and tested in cell cultures have been also linked to an increase in the connections between cells due to their stressful effect, especially considering anticancer and antibiotics [890–892].

This has raised the question of if the same effect is seen by the administration of nanomedicines (NMeds). NMeds as drug delivery systems have been studied for

more than 30 years, but when administered to cells they represent a source of stress and could increase the number of TNTs, facilitating the spreading in the tissue of the loaded drug. When designing a NMed-based therapeutic approach, it is crucial to take into account this piece of information, whether it is necessary to reduce or trigger TNT formation. Research in this direction has the potential to change the way we design therapeutic approaches, but could represent a great step forward in improving the efficacy and specificity of NMed treatments.

## 2. Nanomedicine

Nanomedicines (NMeds) are one of the most investigated tools in drug delivery due to their numerous advantages over traditional pharmaceuticals [40,233,296,893–896]. NMeds are defined as nanometric sized delivery systems with a vast range of types that, depending on their specific characteristics, can be optimized to encapsulate, protect, and specifically deliver virtually any kind of therapeutic agent. In particular, literature results of the last 20 years demonstrate NMeds intelligently designed to 1) improve the solubility of poorly soluble drugs [897,898], 2) stabilize and protect sensitive molecules like proteins [138,341,472,899], peptides [241,900,901], and genetic material [902,903] from degradation, 3) promote their accumulation into target cells or tissues [904,905], thereby 4) reduce drug toxicity outside the targeted tissue [906,907], 5) prolong and/or control the release of the drug over time (Figure 1) [908–911]. All these properties together make NMeds the perfect candidates in the treatment of a plethora of pathologies, especially those considered difficult to treat or that affect difficult-to-reach organs: neurodegenerative disorders, such as Alzheimer's [912], Parkinson's [913], or Huntington's [314], different types of cancer [914], e.g. breast cancer [915], leukemia [916], GBM, and numerous other diseases that require penetration of the Blood Brain Barrier (BBB) [232].

The main feature that allows these NMeds to be so widely applied to these pathologies is the possibility to engineer their surface with ligands, such as small molecules [917,918], peptides [233,234,428,919], antibodies [920–922], aptamers [923,924] etc., which specifically react with the cell surface to improve localized accumulation at the target site. Targeted delivery can also be achieved by modifying the surface with coating layers [925–929], or environmentally sensitive moieties that react to differences such as pH, ROS, temperature, light, enzymes etc. in order to promote the controlled release only in the relevant microenvironment, often created by a pathological change [312,930–937]. These different ligands have been developed and improved in the last decade to increase their specificity and thereby enhance the ability of NMeds to cross barriers (i.e. BBB or blood-retinal

barrier) and/or accumulation of NMeds only in the target cells [938,939]. Notwithstanding the great advancement in targeting specificity, TNTs are currently under investigation for their potential role in diminishing this targeting effect due to intercellular transport by exchanging NMeds from a correctly targeted cell towards a neighboring off-target one. Remarkably, despite the impact it could have, the topic has been poorly addressed. Here we review the work that has been done to demonstrate the interaction between TNTs and NMeds.

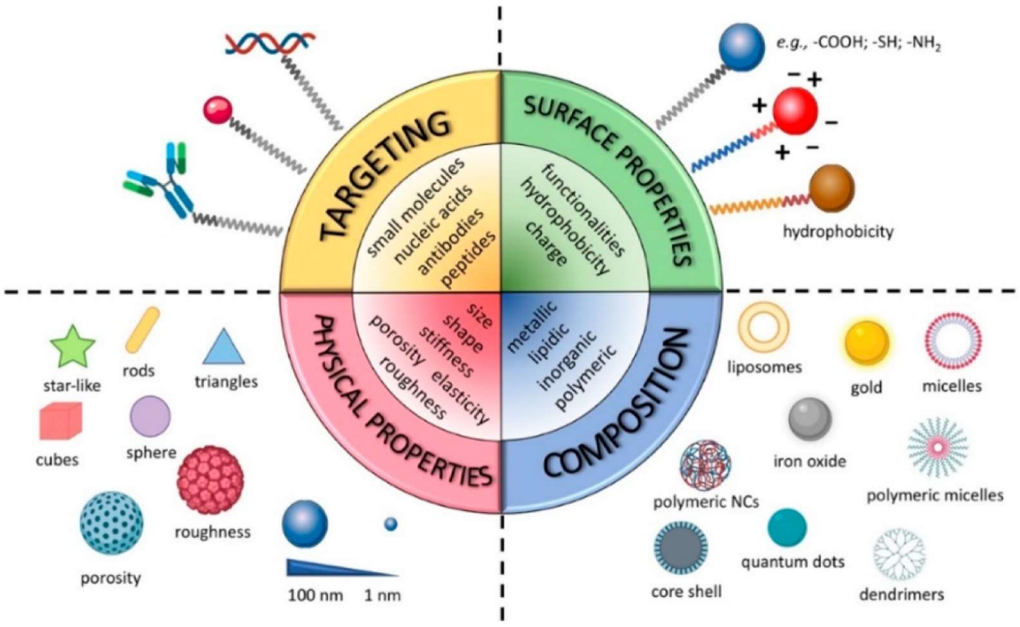


**Figure 1.** Graphical representation NMeds customization options and advantages. Reproduced with permission from Salvioni et al. [893]; Cancers; published by MDPI; 2019.

## 3. Nanomedicine and TNTs

### *3.1. Inorganic NMeds*

The first evidence in 2010 that NMeds travel along TNTs was reported by He et al. and involved the transfer of inorganic nanoparticles [940]. Here they visualized Quantum Dots (QD) of CdSe/ZnS being transported along "newly discovered nanotubular structures" formed between rat cardiac myoblast cells. In fact, this study pioneered the idea that NMeds could be transported via TNTs inside membrane vesicles, and that the exchange could be bidirectional, which would afterwards be confirmed by successive publications [226,941]. Similarly, the following year Mi et al. reported the intercellular transfer of CdTe QD along TNTs in human hepatocellular carcinoma cells [942]. Here the authors further distinguished that the transfer of these QD could be unidirectional or bidirectional depending on the composition of the TNT. It is important to clarify that this bidirectionality was possible only in the presence of tubulin, thus meaning in the more stable "thick" TNTs [849]. A more in depth analysis of the mechanism underlying the transport of these QD showed that they were not transported as single particles, but instead traveled inside lysosomes as aggregates. Although this was not specifically investigated in the study by He et al., it is safe to hypothesize that the QD were transported within lysosomes also in those cultures. Another interesting work was published by Domhan et al. regarding the trafficking of QD, in which the authors demonstrated the transport of two different QD-based fluorophores via TNTs among primary cultures of human tubular epithelial cells [943]. Remarkably, the TNTs were demonstrated to play a key role in the exchange of QD, as modulating their number with exogenous factors like stress, and administration of latrunculin B or zeocin resulted in different rates of NMeds exchange. In fact, these data were the first evidence of the possibility to directly impact the transport of NMeds through TNTs by influencing their formation with external stimuli, even if the precise mechanism has not been characterized. Another important aspect that can be highlighted by these reported examples is

that the trafficking of QDs, and of NMeds in general, is not limited to immortalized cells but is also present in primary cultures. This can also be extended further to 3D *in vitro* models such as organoids, and tissues which will be discussed in later sections. Further confirmation of this effect was reported by where Rehberg et al. detected and tracked the transportation of QD along TNTs *in vivo* in the cremaster muscle of mice, especially between tissue macrophages [944]. This represents one of the few reports of TNTs *in vivo* to date.

All the previously cited articles demonstrated the ability of TNTs to transfer NMeds between cells in a monoculture. Nevertheless, an important factor that was ignored in the previously reported works is that TNTs can create connections not only between cells of the same type (homotypical transfer), but also between cells of different types (heterotypical). Interestingly, NMeds can be shared with other cells by both types of transport. This effect was specifically noted in a study by Epperla et al. [945]. In this study, authors used fluorescent nanodiamonds (FNDs) in both human embryonic kidney cells and neuroblastoma cells. First, it was evidenced that both these cell types were able to form homotypical TNTs when separately cultured. The only difference arose from the thickness and composition of the TNTs naturally formed by each specific celltype. In particular, neuroblastoma cells mainly formed "thin" actin-based TNTs, while HEK cells predominantly formed "thick" TNTs containing both actin and tubulin. In both cell types, the FNDs were exchanged in single cultures, but more remarkably, the authors also documented heterotypical exchange of FNDs between the cells in co-cultures. The authors reported that FNDs spread from predosed HEK cells to neuroblastoma cells when added in the culture. Quantification reported that approximately 10% of the neuroblastoma cells tested positive for FNDs due to the transposition between cells by TNTs.

To further investigate heterotypical exchange of NMeds, an interesting TNT study by Franco et al. takes precedence [946]. The authors dosed mesoporous silica nanoparticles into mice macrophages. Results suggested that the presence of these

fluorescent NMeds along TNTs were localized in the so-called "gondola" structures, indicating the node where NMeds accumulated during transportation (Figure 2). This study led to a number of reported peculiarities regarding the formation of TNTs and in their ability to transport NMeds. First, researchers demonstrated the formation of TNTs between murine macrophages and HeLa cells, indicating that these structures can be formed even between murine and human cells. More importantly, the transfer of NMeds via TNTs was successfully modulated by exogenous factors. In particular, by adding cell stress by serum starvation, the trafficking of NMeds between the two cell lines increased significantly. On the contrary, hyperthermia reduced TNT formation and consequently NMed transfer. These results lead to two important points. On one hand, the possible transfer of NMeds to very different cell types calls for a deeper investigation on the dynamics and occurrence: it is crucial to determine incidence, extent and direction of transportation of drug loaded NMeds. On the other hand, these data were a first step towards controlling TNT formation to modulate NMed delivery. This response to hyperthermia could be critical to the formation of TNTs in other cell types. The idea of controlling TNTs in this simple way could help control NMed delivery to improve therapeutic efficacy and reduce toxicity of the loaded drug in a plethora of diseases, for which optimized NMeds are already produced [138,241,314]. The control over the fate of NMeds is necessary to increase pharmaceutical effects over off-target toxicity. This duality is an important part of TNT research that until this point has been poorly addressed and calls for more in-depth studies.

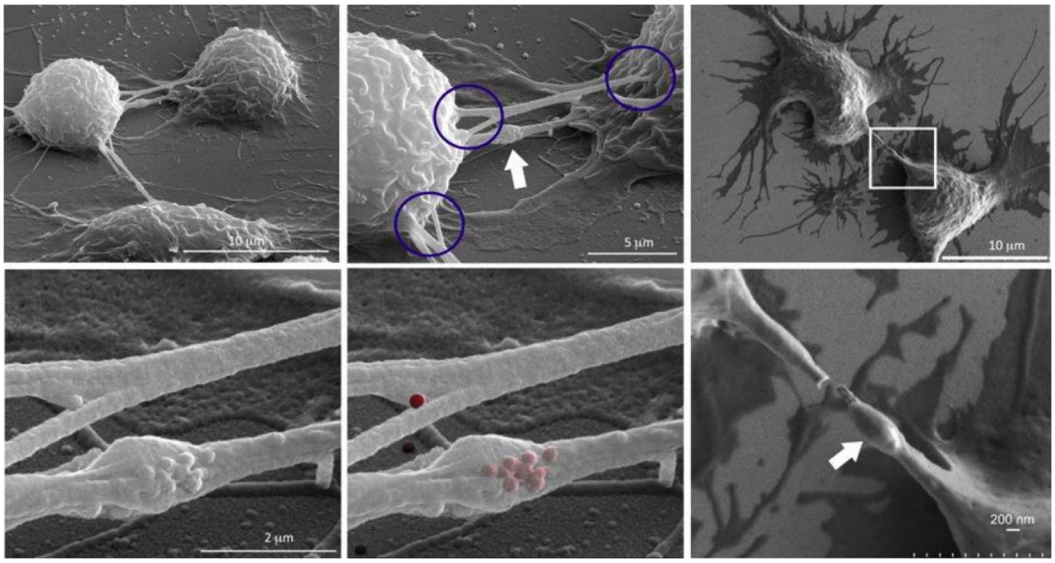


**Figure 2.** SEM images showing TNTs between macrophages emphasizing disparate sites of connectivity (circled) and the presence of a gondola (white arrow). NMeds are pseudo-colored red in the lower central image. Reproduced with permission from Franco et al. [946]; Cancers; published by MDPI; 2020.

### *3.2. Organic NMeds*

While inorganic NMeds are generally easier to produce and characterize, they are less frequently used in therapeutic approaches due to their low biodegradability and the fact that they accumulate unfavorably in the liver and kidney, leading to off-target toxicity [947]. Organic NMeds on the other hand are generally more biocompatible, highly versatile and easy to functionalize on the surface to obtain targeted delivery. For these reasons, polymeric and lipidic NMeds are generally preferred as promising tools for specific targeted delivery. Nevertheless, they also have been demonstrated to undergo intercellular trafficking via TNTs, thus representing a huge limitation to their efficacy. Here we gathered the works that have analyzed the interaction between polymeric or lipidic NMeds and the formation rate of TNTs.

#### 3.2.1. Polymeric NMeds

Polymeric NMeds have been leading the research field in recent years for their ability to encapsulate both hydrophilic and hydrophobic compounds, stability, and high potential in terms of scalability, ease of production, targeting ability, and low material cost. Notwithstanding their advantages, polymeric NMeds are transported along TNTs, thus implying the possibility of uncontrolled biodistribution. Ingle et al. recently reported the trafficking of polyplexes along TNTs in cultured HeLa cells [948]. In particular, they followed the transposition of fluorescently labelled Glycofect/DNA polyplexes in membranous bridges *in vitro*, showing the transport of these NMeds in vesicles along TNTs. Evidence of this kind of transport leads to the hypothesis of exploiting TNTs in diseased tissues, like tumors, as highways to increase the biodistribution of therapeutics like RNAs, enhancing currently used approaches to improve treatments against diseases such as cancer. Unfortunately, this study reported only preliminary results, and in-depth studies are still lacking. For example, whether the administration of polyplexes has an impact on the number of TNTs that cells form, as well as to compare their formation in tumoral and healthy cells.

Interesting results were also reported by Sáenz-de-Santa-María and coworkers [949]. In this study, the authors mainly focused on the biological mechanisms underlying the formation of TNTs in cultured squamous-cells carcinoma cells. To this end they monitored the transport of inert methacrylate NMeds along TNTs in cultured cells. They were able to inhibit the formation of TNTs using two different agents, namely the FAK inhibitors FRNK and PF-562271, the latter bein currently investigated for its anticancer activity [950]. Unfortunately, no comparison in the exchange rate of NMeds after modulation of TNTs was performed, which would be pivotal information. Nevertheless, the authors demonstrated the formation of TNTs in tumor spheroid models, making a first pass towards a model that more closely represents physiological conditions of *in vivo* experiments. In fact, these results represent a steppingstone to a novel therapeutic approach against cancer, but the correlation between TNTs and NMeds should be further investigated, in particular since it is possible to observe them in a complex 3D model like a

spheroid. This additional information represents the next critical step to assess the possibility for researchers to exploit TNT for the improved transfer and therapeutic effect of NMeds.

Another crucial parameter that is rarely taken into account when performing this type of study is the surface modifications of the NMeds. TNTs represent a major issue in the field of targeted delivery, and therefore it is crucial to understand how targeted NMeds interact with these structures and how they change the targeting capacity to influence the final localization of the NMed. In 2014, Tosi et al. demonstrated the transfer of BBB-targeted NMeds along TNTs [402]. The NMeds used were composed of the FDA-approved biocompatible and biodegradable polymer poly(L-lactic-co-glycolide) (PLGA) which was surface decorated with the g7 peptide [332,395], known to promote BBB crossing and CNS accumulation. These NMeds were administered to cultures of glial cells or to co-cultures of neuronal and glial cells. Remarkably, the authors were able to demonstrate both the homotypical transport of targeted NMeds between glial cells and also the heterotypical exchange from glial cells to neuronal cells. This piece of information holds great importance for therapies: often for neurodegenerative pathologies researchers search to have selective targeting to neurons, which is difficult to achieve. Promoting the formation of TNTs could therefore represent a possibility to enhance the transport of NMeds from glial cells to neurons. To pursue this hypothesis, the authors also demonstrated a 2-fold increase in the number of TNTs formed by glial and neuronal cells after transfection with the protein mSEC, known to enhance the formation of TNTs. Interestingly, the transport of NMeds among cells increased by almost 25% along with the increased number of TNTs. This study highlights how crucial it is to investigate how NMeds impact TNT formation in order to design ways to modulate their formation with transfection, other molecules that can be more easily administered with the NMeds, or even that could be co-encapsulated with the therapeutic pharmaco in the NMed formulation.

### 3.2.2. Lipidic NMeds

Lipid-based NMeds are now on the cutting edge of nanomedicine development. This has been largely due to the recent global pandemic caused by SARS-CoV-2 for which the primary vaccine is a lipidic NMed [201]. With the increase in NMed use on the global level, it is important to carefully study how TNTs will come into play for the biodistribution and biological response of these treatments. The first study to analyse lipidic NMeds interacting with TNTs was by Kristl et al. [951]. In this interesting study, the authors administered solid lipid nanoparticles (SLNs) composed of compritol to cultured keratinocytes revealing that the SLNs were actively transported along thick TNTs between cells. Notably, a comparison in the number of TNTs formed by SLN-treated and untreated keratinocytes was also performed. Experiments where the cells were treated with the SLNs showed an increased TNT formation rate compared to the controls. This highlights the stressful effect of the NMeds on cell cultures, but also the importance of studying how they interact with TNTs to decide their final fate and the significance of their biological effect. In fact, these data show that the presence of NMeds could directly affect the exchange of materials between cells even without any specific molecular trigger.

Astanina et al. also investigated the impact of TNT modulation by fatty acids on the exchange of lipid droplets [952]. In this study, they tested the effect of arachidonic and stearic acid on the formation rate of TNTs in a primary culture of endothelial cells dosed with NMeds. Authors reported that no difference was observed after administration of stearic acid, while arachidonic acid led to a 4-fold increase in the number of TNTs. This difference might lay in the role of arachidonic acid, which promotes migration and metabolic activity in the cells [953]. Remarkably, this increase in TNT formation led to a 3-fold increase in the exchange of NMeds compared to the control. These data highlight that the formation rate of

TNTs is not linearly correlated with the transport of NMeds, although they are influenced by each other.

A study by Formicola et al. recently highlighted that the type of TNTs formed by cells is also an important parameter to analyze [954]. In fact, "thick" TNTs are more efficient in the transport of material compared to "thin" ones. The authors here showed a difference in the composition of TNTs between two cell types: while GBM cells tended to form more stable "thick" TNTs, healthy astrocytes more frequently formed "thin" TNTs. Interestingly, the administration of free doxorubicin [955–958] induced a shift in this ratio between "thick" and "thin" TNTs for GBM cells while astrocytes were unaffected. In particular, the majority of TNTs formed by GBM cells after the administration of the drug was of the "thin" type, similar to healthy astrocytes. Interestingly, the administration of doxorubicin loaded liposomes produced the same effect on the composition of TNTs in both cell types (Figure 3A, 3B). This aspect needs to be properly investigated to assess the implications of this shift and understand how to possibly control this phenomenon accordingly. Moreover, groundbreaking results presented in this study further underlined the importance of investigating the impact of targeting ligands. In this study the authors decorated liposomes with ApoE and chlorotoxin, two moieties used for GBM targeting, and studied their trafficking via TNTs. In particular, they administered these NMeds to co-cultures of U87GM and human astrocytes cells (Figure 3C). Notably, the authors reported that targeted liposomes were actively transported via TNTs in co-cultures; however, a significant difference was seen in the direction of movement. In fact, homotypical transfer GBM→GBM and astrocyte→astrocytes was significantly more frequent compared to heterotypical transfer GBM→astrocyte (Figure 3D). These data demonstrate a pivotal point in the future design of NMeds for GBM treatment. This could be a good indication that the efficacy of targeted NMeds could be enhanced by the homotypic transfer of drugs between GBM cells while preserving the health of nearby healthy astrocytes. These various studies show the complexity of TNT research and their potential role in NMed therapeutics. On one side this could be

helpful to improve the spread of NMeds between localized cells, but on the other could be detrimental if the targeted cells spread the formulation to cells that were not the intended target.

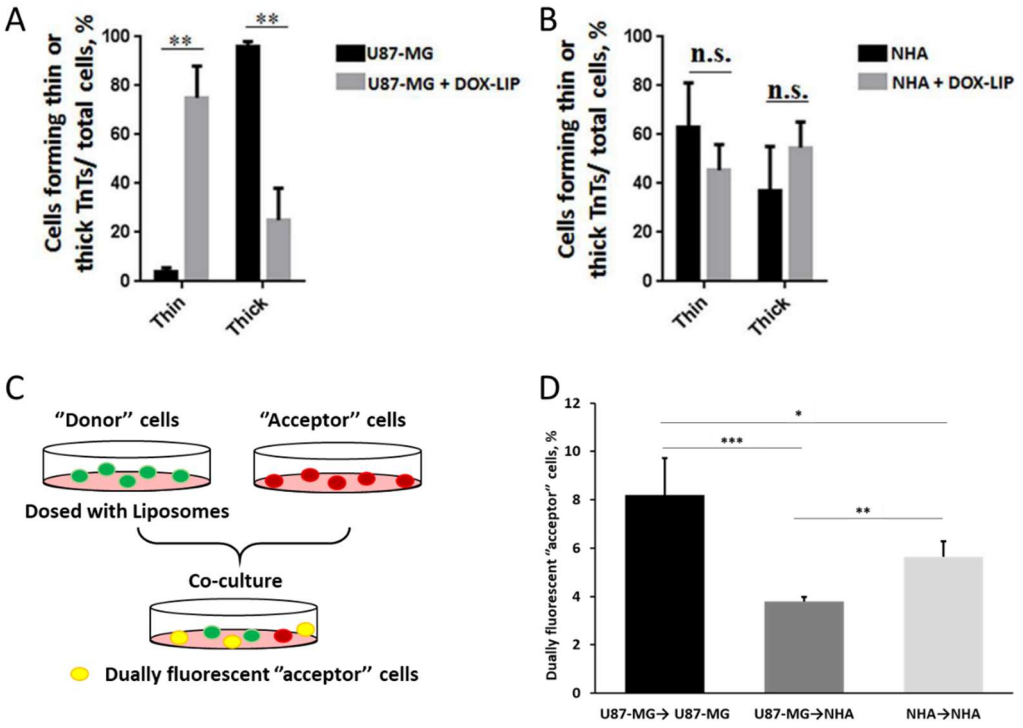


**Figure 3**. Type of TNTs in GBM and healthy astrocytes, and exchange of liposomes via TNTs. (A) Type of TNTs formed by GBM cells before and after administration of doxorubicin. (B) Type of TNTs formed by healthy astrocytes before and after administration of doxorubicin. Data are ex-pressed as mean ± SE from three independent experiments. Data were analyzed by two-way ANOVA followed by Sidak's multiple comparisons test; n.s., not significant; **p < 0.01 (C) Experimental protocol to study TNT formation in co-cultures using different fluorophores to distinguish cell types. (D) Homotypical vs. heterotypical transfer via TNTs of doxorubicin-loaded liposomes in co-cultures of GBM and healthy astrocytes. U87-MG: GBM cells; NHA: normal human astrocytes; DOX: doxorubicin. N = 3 independent experiments. *p < 0.05; **p < 0.01; ***p < 0.001 by Student t-test Reproduced with permission from Formicola et al. [954]; Frontiers in Bioengineering and Biotechnology; published by Frontiers; 2019.

## 4. Limitations in Tunneling Nanotubes Detection

As described in the previous chapters, TNTs have been detected in a plethora of models and shown to have an notable effect in NMed delivery. They have been found in immortalized or primary cell cultures [222], but also in spheroids [862,949] and organoids [959], as well as *in vivo* [857,960]; however, evidence of TNTs in tissues *in vivo* is less prominent when compared to the abundance of studies about TNTs *in vitro*. It is crucial though to highlight that the true number or rate of TNT formation *in vivo* is still probably underestimated. In fact, this possible misinterpretation of results could arise from the difficulty of detecting TNTs in samples, which is hampered by several problems in the imaging techniques available. These difficulties are predominantly linked to the fragile and transient structure of TNTs. These membranous tubules are often difficult to image even in cultured cells *in vitro* due to the numerous and arduous treatments necessary to prepare samples for imaging via electron, atomic force, or confocal microscopy which can damage or destroy the projections. These problems linked to sample processing are exacerbated when animal tissue samples are involved due to the fixation and preparation methods required. For these reasons, confocal microscopy is the preferred technique to visualize TNTs due to the less arduous sample preparation while maintaining high resolution at the nanoscale via STED (Stimulated Emission Depletion) and spinning disk imaging [961]. While confocal microscopy offers many advantages and is the preferred method to image TNTs, another difficulty arises in the fact that there are few viable methods to specifically image TNTs. To clarify, TNTs are composed of cytoskeletal components and cell membrane. This means that any staining with antibodies for actin, tubulin, or plasma membrane will most likely result in high background fluorescence throughout the whole sample with no distinction between different types of cell protrusions. Thus, one of the most used techniques to visualize TNTs both *in vitro* and *in vivo* is to combine a highly specific fluorescent staining for the object of interest combined with a transmitted light imaging. With this approach, it is possible to visualize the structure of the TNTs and the cargo transported along the

tubules simultaneously (Figure 4). It is important to note that this method is mainly applicable to cell cultures where ultrathin tissue sections of only a few μm are necessary to exploit the combination of fluorescence and light transmission images. This highlights the importance of investigating new techniques and protocols for TNT imaging, along with researching methods to tune their formation. In particular, a new antibody specific for TNTs would represent a huge improvement in TNT studies, with positive implications also for more complex samples from tissues. With all of the processing required, true *in vivo* experiments would ideally be able to track TNTs in real time, but up until now this has not been achieved and is a critical next step to understand their biological relevance.

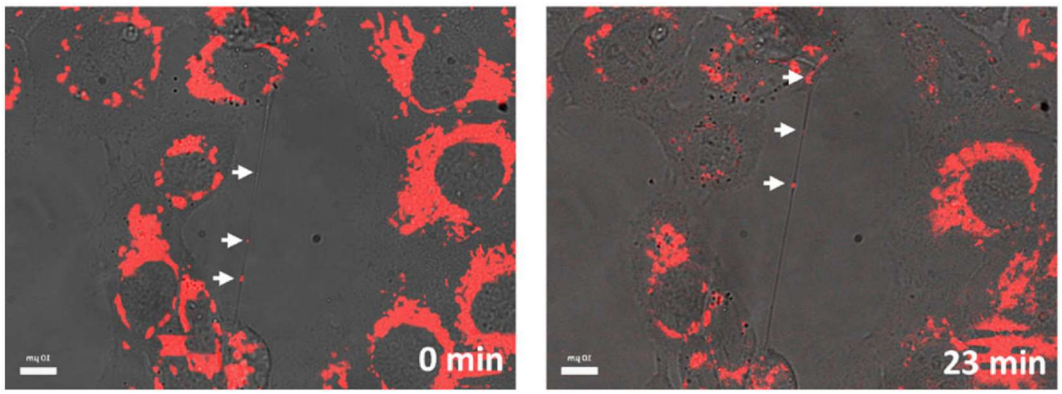


**Figure 4.** Representative imaging of TNTs using a combination of transmitted light and fluorescently labelled NMeds by confocal microscope. Reproduced with permission from Sáenz-de-Santa-María et al. [949]; Oncotarget; 2017.

## 5. Conclusions and Future Prospects

Cells have been biologically programmed to share material, both to benefit from shared material like proteins and organelles, and to dilute toxins. For this reason, cells naturally create connections such as TNTs to fulfill this need. While this can be a positive trait that allows for cell survival, they can represent a highway for the spreading of dangerous materials and even pathogens (viruses and bacteria), which take advantage of these connections to avoid the immune system. This opens up a Pandora's box for researchers to use these pathways to deliver NMeds in a more controlled way, blocking or exploiting these connections. In fact, starting from the knowledge that NMeds can be transferred to other cells after uptake, it is of crucial significance to understand the dynamics that trigger TNT trafficking in order to take advantage of it. Hampering the formation of TNTs can help increase drug accumulation in the target cell while avoiding off-target toxicity; however, increasing these connections could multiply the therapeutic effect of delivered pharmaceutics throughout a tissue. Either way, TNTs need to be deeply investigated in their interaction with targeted NMeds: if the NMeds arrive at the targeted cells but are then transferred to other cells, the targeting effect is minimized. On the other hand, these connections could be used to enhance delivery between cells and promote drug delivery to difficult-to-reach cell populations.

In this work, we reviewed the work that has been done in this direction focusing on the core material of the NMeds. Overall, we found that both inorganic and organic NMeds are trafficked along TNTs although differences in the rate of exchange were evidenced. Unfortunately, it is still unclear whether these differences are to be attributed to the NMeds or to the cell types, as it was demonstrated that different cells use TNTs with different rates. It would be therefore necessary to perform a more comprehensive investigation on the impact that different NMeds have on the same cell type, in terms of number of TNTs formed, extent of NMed exchange, and type of TNTs (“thick” or “thin”). At the

same time, literature is lacking to characterize the effect of a single type of NMed on TNT formation in different cell types. Information about this will be crucial for researchers to better understand how NMeds, both targeted and untargeted, can be exchanged between cells and predict whether TNTs are promoting or reducing the therapeutic efficacy of NMeds.

Besides the core material, there are several other parameters of NMeds that are to be considered when investigating their transport via TNTs, such as: size, hydrophilicity, surface engineering, stiffness, shape, surface charge, and the amount and type of drug loaded into the NMeds. Surface charge for example is one of the most important features for NMeds, as it can affect biodistribution, toxicity, and immunogenicity. It could be hypothesized that a positively charged NMed would trigger the formation of TNTs due to a higher toxicity compared to those that are negatively charged. This could potentially promote the spread of NMeds in the whole targeted tissue. Following the same rationale, the drug loaded into NMeds could also have a direct effect on TNT formation rate. A higher amount of drug, both from higher loading content or faster release, could in fact increase the stress level of the targeted cell, thus promoting the formation of a higher number of TNTs and the spreading of the drug to other cells. At the same time, co-encapsulation of an inhibitor of TNT formation such as metformin could determine an accumulation of drug in the target cell and/or reduction in the spreading of diseases.

The study of TNTs is still in its infancy, but results are already demonstrating the theoretical importance that they offer in NMed treatments. New methodology and further in-depth studies will be crucial to better understand and potentially control this currently un-utilized process of cell-to-cell transfer. Altogether these data will be pivotal to give researchers a clearer picture of how our technological tools, i.e. NMeds can be optimized and specialized using TNTs.

# CONCLUSIONS

The use of Nanotechnologies for biomedical applications represents a huge opportunity for the advancement of therapeutic strategies to treat a variety of diseases. Nanotechnology based therapies have demonstrated great improvements in increasing drug solubility, and bioavailability, improved drug loading, reduced toxicity and side effects, selective targeting, and the possibility for a controlled release. Advancing nanotechnologies, such as nanoparticles (NPs) and nanomedicines (NMeds), to clinical use is hampered by the numerous and difficult steps needed to strategically design a fully functional system. In fact, not only must the production of NPs be optimized, but an in-depth characterization is a crucial step to ensure reproducible and reliable results. In this thesis work, it was attempted to overcome some of the most important barriers to the design Nanotechnologies with the potential of for clinical success: the choice of the core material, the use of stabilizers to protect sensitive drugs, surface engineering for targeted delivery, strategies to have controlled release, issues linked to large-scale production, and investigation on their interaction with biological environment after administration.

In the first Chapter, a novel material for the production of NPs was synthesized by combining the biodegradable and biocompatible polymer poly(lactic-co-glycolic) acid and the natural polymer chitosan. The novel conjugate, with hybrid properties between the anionic, hydrophobic PLGA and the cationic, hydrophilic chitosan, presented dual properties that could help encapsulate both hydrophobic and hydrophilic molecules, including the incorporation of hydrophilic or highly negatively charged drugs (i.e. plasmid DNA, sirna etc).

After thoughtfully considering the core material used for the production of NPs, it is also of paramount importance to study the encapsulation strategy for the selected drug to ensure its stability throughout the formulation and administration processes. This topic was addressed in Chapter 2, where the encapsulation of a model enzyme into PLGA NPs was optimized by using two different stabilizers,

bovine serum albumin (BSA) and Tween. In both articles, the stabilizers were capable of preserving enzyme activity throughout the stresses of nanoparticle formulation. It was also noted that the two stabilizers worked under different mechanisms: BSA improved enzyme activity by improving enzyme encapsulation, while Tween only slightly improved encapsulation amounts but was better at maintaining higher levels of enzyme activity. In both cases, it was possible to obtain functional NPs, with enhanced enzyme content and higher enzyme activity. Moreover, the two mechanisms were synergistic when both stabilizers were combined and led to higher loading and even greater enzyme activity compared to each stabilizer alone. This highly increases the potential of creating an enzyme replacement therapy that could lead to clinical applications.

One of the most interesting advantages offered by the use of NPs as a therapeutic strategy is the possibility to engineer their surface with selective ligands to have an accumulation of therapeutic molecules at the target organs or cells. In Chapter 3, NPs were surface modified with novel ligands to achieve specific targeting. In the first section, the BBB-targeting efficacy of a novel peptide was evaluated. These peptides, derived from the opioid peptide deltorphin, were characterized and conjugated on the surface of PLGA NPs and demonstrated passage into the brain parenchyma after in vivo administration. Similarly, PLGA NPs were modified with ANG-2, which also enhanced the penetration and accumulation of the NPs in the brain. While demonstrating that targeted NPs arrive at the desired site is important, it is crucial to observe whether the NPs can exert a therapeutic effect. This was evaluated using hybrid NPs composed of PLGA and Cholesterol, surface modified with the well-known BBB targeting g7 peptide. Hybrid g7-modified NPs were administered to Huntington's Disease mouse models where impressive beneficial results on both the cognitive and motor impairment were observed. This result was possible thanks to the slow and prolonged release of cholesterol from the NPs in the brain, thus confirming the pivotal role of surface engineering of NPs in order to improve their therapeutic efficacy. In the last section of Chapter 3, the targeting ability of different ligands was further evaluated to achieve not only BBB

crossing, but also cell specificity in the brain. In this study, targeted PLGA NPs were tested for their ability to target glioblastoma cells over healthy cells in the brain. One ligand, a monoclonal antibody against cell surface vimentin, demonstrated high specificity for cancer cells over healthy astrocytes both in cell uptake and cell toxicity studies using paclitaxel as a chemotherapeutic agent. The three articles in this Chapter demonstrate the untapped potential of targeted NPs to improve the therapeutic options for a variety of hard-to-treat diseases by increasing specific uptake and reducing undesired side effects on healthy tissues.

To further advance these already astounding accomplishments, research into the regulation of drug release from NP systems was performed. While this can be achieved via several strategies, the study reported in Chapter 4 analyzed the formulation of an injectable scaffold for the controlled release of hybrid NPs for retinal delivery. Here, NPs were first optimized to be able to reach the retina after intravitreal injection and then were embedded into a hydrogel which was optimized to be liquid at 4 °C for injectability but which underwent gelation around 35°C after administration in vivo. This system demonstrated to be effective in delaying the mobility of NPs after administration and improving the prolonged release of therapeutic molecules. This is a major step to be able to reduce the number of injections that would be needed for patients, which represents one of the major limitations of therapeutic approaches for the retina.

In Chapter 5, issues linked to the scalability of NPs was addressed. In fact, a major factor hampering the marketability of NPs is linked to the inherent difficulty of transferring a benchtop protocol for lab-scale production to an industrial level. To overcome this limitation, the use of the microfluidic technique was investigated for hybrid NPs. The study highlighted that, although it was possible to obtain NPs with similar chemico-physical characteristics and composition to the NPs optimized by benchtop methods, the microfluidic NPs showed different morphological features and, more importantly, poor stability to common storage conditions. While this might not be an issue for newly optimized systems, these

differences might represent a problem for previous studies that demonstrated promising results with benchtop methods but become limited by poor reproduction on a large scale. Overall, this study evidenced that the use of microfluidics can be a huge help in the production of reproducible NPs, although several outcomes still need to be considered.

The last Chapter of this thesis is dedicated to the biological fate of NPs. After administration, NPs interact with the biological environment depending on both biological parameters and the features of NPs. For example, these interactions lead to the formation of the protein corona and the exchange of NPs via Tunneling Nanotubes (TNTs), both of which are still poorly understood despite the studies being performed and published in the literature. In this Chapter, two investigations are reported on the formation of the protein corona on different NPs, and on the current knowledge about the interactions between NPs and TNTs. Both studies highlight the importance of in-depth investigations about these two phenomena that are lacking in the literature, and which could both enhance and/or nullify the therapeutic efficacy of NPs.

Altogether, the studies reported highlight the complex path towards the formulation of a successful nanotechnology system, from the raw materials to the final fate of NPs. While previous studies have improved the fine control of some of these NP parameters, much is still to investigate, optimize, and understand. On one hand, it is important to always study novel materials, stabilizers, and targeting ligands to improve drug loading, selectivity, and overall efficacy of nano-based therapeutic approaches. On the other hand, future research will be needed to address topics such as the translation of benchtop protocols to a larger scale, in order to accelerate the transition towards clinical use of NPs. Another crucial aspect to elucidate will be the fate of NPs after administration. Specifically, it is important to analyze which parameters of the NPs can determine their quick removal from the bloodstream due to the presence of certain proteins in the protein corona, and what the critical concentration of these proteins is to exert this effect.

At the same time, a full understanding of which characteristics of NPs induce their transfer via TNTs is still missing, canceling the possibility to predict the diffusion of NPs via this route. In-depth understanding of these parameters would enable researchers to more intelligently design NPs that would produce a specific effect in vivo, enhancing their therapeutic efficacy and promoting their translation towards clinical trials. While each of these individual projects proved to be successful in elucidating a barrier towards efficient nanotechnology cures, incorporating them all into a single system and controlling how each factor interacts with the other is a huge undertaking that will require vast research hours and the brightest minds to push forward.

# REFERENCES


1. World Life Expectancy 1950-2022 Available online: https://www.macrotrends.net/countries/WLD/world/life-expectancy (accessed on 21 November 2022).
2. Silva, G.A. A New Frontier: The Convergence of Nanotechnology, Brain Machine Interfaces, and Artificial Intelligence. *Frontiers in Neuroscience* **2018**, *12*.
3. Contera, S. *Nano Comes to Life: How Nanotechnology Is Transforming Medicine and the Future of Biology*; Princeton University Press, 2019; ISBN 978-0-691-18928-4.
4. Awasthi, R.; Bhushan, B.; Kulkarni, G.T. Chapter 9 - Concepts of Nanotechnology in Nanomedicine: From Discovery to Applications. In *Targeting Chronic Inflammatory Lung Diseases Using Advanced Drug Delivery Systems*; Dua, K., Hansbro, P.M., Wadhwa, R., Haghi, M., Pont, L.G., Williams, K.A., Eds.; Academic Press, 2020; pp. 171–209 ISBN 978-0-12-820658-4.
5. Kargozar, S.; Mozafari, M. Nanotechnology and Nanomedicine: Start Small, Think Big. *Materials Today: Proceedings* **2018**, *5*, 15492–15500, doi:10.1016/j.matpr.2018.04.155.
6. Bayda, S.; Adeel, M.; Tuccinardi, T.; Cordani, M.; Rizzolio, F. The History of Nanoscience and Nanotechnology: From Chemical–Physical Applications to Nanomedicine. *Molecules* **2020**, *25*, 112, doi:10.3390/molecules25010112.
7. Saeedi, M.; Eslamifar, M.; Khezri, K.; Dizaj, S.M. Applications of Nanotechnology in Drug Delivery to the Central Nervous System. *Biomedicine & Pharmacotherapy* **2019**, *111*, 666–675, doi:10.1016/j.biopha.2018.12.133.
8. Hu, Q.; Li, H.; Wang, L.; Gu, H.; Fan, C. DNA Nanotechnology-Enabled Drug Delivery Systems. *Chem. Rev.* **2019**, *119*, 6459–6506, doi:10.1021/acs.chemrev.7b00663.
9. Kanwar, R.; Rathee, J.; Salunke, D.B.; Mehta, S.K. Green Nanotechnology-Driven Drug Delivery Assemblies. *ACS Omega* **2019**, *4*, 8804–8815, doi:10.1021/acsomega.9b00304.
10. Pradhan, D.; Biswasroy, P.; Goyal, A.; Ghosh, G.; Rath, G. Recent Advancement in Nanotechnology-Based Drug Delivery System Against Viral Infections. *AAPS PharmSciTech* **2021**, *22*, 47, doi:10.1208/s12249-020-01908-5.
11. Cevaal, P.M.; Ali, A.; Czuba-Wojnilowicz, E.; Symons, J.; Lewin, S.R.; Cortez-Jugo, C.; Caruso, F. In Vivo T Cell-Targeting Nanoparticle Drug Delivery Systems: Considerations for Rational Design. *ACS Nano* **2021**, *15*, 3736–3753, doi:10.1021/acsnano.0c09514.
12. Tian, H.; Zhang, T.; Qin, S.; Huang, Z.; Zhou, L.; Shi, J.; Nice, E.C.; Xie, N.; Huang, C.; Shen, Z. Enhancing the Therapeutic Efficacy of Nanoparticles for Cancer Treatment Using Versatile Targeted Strategies. *Journal of Hematology & Oncology* **2022**, *15*, 132, doi:10.1186/s13045-022-01320-5.
13. Adhikari, A.; Mondal, S.; Darbar, S.; Pal, S. Role of Nanomedicine in Redox Mediated Healing at Molecular Level. *Biomolecular Concepts* **2019**, *10*, 160–174, doi:10.1515/bmc-2019-0019.
14. Schneider, J.; Liu, J.X.; Lee, V.E.; Prud'homme, R.K.; Datta, S.S.; Priestley, R.D. Tuning Morphologies and Reactivities of Hybrid Organic–Inorganic Nanoparticles. *ACS Nano* **2022**, *16*, 16133–16142, doi:10.1021/acsnano.2c04585.
15. Huang, H.; Feng, W.; Chen, Y.; Shi, J. Inorganic Nanoparticles in Clinical Trials and Translations. *Nano Today* **2020**, *35*, 100972, doi:10.1016/j.nantod.2020.100972.
16. Fang, F.; Li, M.; Zhang, J.; Lee, C.-S. Different Strategies for Organic Nanoparticle Preparation in Biomedicine. *ACS Materials Lett.* **2020**, *2*, 531–549, doi:10.1021/acsmaterialslett.0c00078.

17. Kim, T.; Hyeon, T. Applications of Inorganic Nanoparticles as Therapeutic Agents. *Nanotechnology* **2014**, *25*, 012001, doi:10.1088/0957-4484/25/1/012001.
18. Meena, J.; Gupta, A.; Ahuja, R.; Singh, M.; Bhaskar, S.; Panda, A.K. Inorganic Nanoparticles for Natural Product Delivery: A Review. *Environ Chem Lett* **2020**, *18*, 2107–2118, doi:10.1007/s10311-020-01061-2.
19. Wang, M.; Thanou, M. Targeting Nanoparticles to Cancer. *Pharmacological Research* **2010**, *62*, 90–99, doi:10.1016/j.phrs.2010.03.005.
20. Varna, M.; Ratajczak, P.; Ferreira, I.; Leboeuf, C.; Bousquet, G.; Janin, A. <I>In Vivo</I> Distribution of Inorganic Nanoparticles in Preclinical Models. *JBNB* **2012**, *03*, 269–279, doi:10.4236/jbnb.2012.322033.
21. Arami, H.; Khandhar, A.; Liggitt, D.; Krishnan, K.M. In Vivo Delivery, Pharmacokinetics, Biodistribution and Toxicity of Iron Oxide Nanoparticles. *Chem. Soc. Rev.* **2015**, *44*, 8576–8607, doi:10.1039/C5CS00541H.
22. Yang, G.; Phua, S.Z.F.; Bindra, A.K.; Zhao, Y. Degradability and Clearance of Inorganic Nanoparticles for Biomedical Applications. *Advanced Materials* **2019**, *31*, 1805730, doi:10.1002/adma.201805730.
23. MÃ¼ller, R. Solid Lipid Nanoparticles (SLN) for Controlled Drug Delivery – a Review of the State of the Art. *European Journal of Pharmaceutics and Biopharmaceutics* **2000**, *50*, 161–177, doi:10.1016/S0939-6411(00)00087-4.
24. Paliwal, R.; Paliwal, S.R.; Kenwat, R.; Kurmi, B.D.; Sahu, M.K. Solid Lipid Nanoparticles: A Review on Recent Perspectives and Patents. *Expert Opinion on Therapeutic Patents* **2020**, *30*, 179–194, doi:10.1080/13543776.2020.1720649.
25. Maja, L.; Željko, K.; Mateja, P. Sustainable Technologies for Liposome Preparation. *The Journal of Supercritical Fluids* **2020**, *165*, 104984, doi:10.1016/j.supflu.2020.104984.
26. Filipczak, N.; Pan, J.; Yalamarty, S.S.K.; Torchilin, V.P. Recent Advancements in Liposome Technology. *Advanced Drug Delivery Reviews* **2020**, *156*, 4–22, doi:10.1016/j.addr.2020.06.022.
27. Lee, E.S.; Shin, J.M.; Son, S.; Ko, H.; Um, W.; Song, S.H.; Lee, J.A.; Park, J.H. Recent Advances in Polymeric Nanomedicines for Cancer Immunotherapy. *Adv. Healthcare Mater.* **2019**, 1801320, doi:10.1002/adhm.201801320.
28. George, A.; Shah, P.A.; Shrivastav, P.S. Natural Biodegradable Polymers Based Nano-Formulations for Drug Delivery: A Review. *International Journal of Pharmaceutics* **2019**, *561*, 244–264, doi:10.1016/j.ijpharm.2019.03.011.
29. Duncan, R. Polymer Therapeutics as Nanomedicines: New Perspectives. *Current Opinion in Biotechnology* **2011**, *22*, 492–501, doi:10.1016/j.copbio.2011.05.507.
30. Banik, B.L.; Fattahi, P.; Brown, J.L. Polymeric Nanoparticles: The Future of Nanomedicine. *WIREs Nanomed Nanobiotechnol* **2016**, *8*, 271–299, doi:10.1002/wnan.1364.
31. Tao, L.; Hu, W.; Liu, Y.; Huang, G.; Sumer, B.D.; Gao, J. Shape-Specific Polymeric Nanomedicine: Emerging Opportunities and Challenges. *Exp Biol Med (Maywood)* **2011**, *236*, 20–29, doi:10.1258/ebm.2010.010243.
32. Hernández-Parra, H.; Cortés C, H.; Avalos-Fuentes, A.; Del Prado, M.; Floran, B.; Leyva-Gómez, G.; Sharifi-Rad, M.; Cho, W. Repositioning of Drugs for Parkinson's Disease and Pharmaceutical Nanotechnology Tools for Their Optimization. *Journal of Nanobiotechnology* **2022**, *20*, doi:10.1186/s12951-022-01612-5.
33. El-Hammadi, M.M.; Arias, J.L. Recent Advances in the Surface Functionalization of PLGA-Based Nanomedicines. *Nanomaterials* **2022**, *12*, 354, doi:10.3390/nano12030354.
34. Feng, X.; Liu, J.; Xu, W.; Li, G.; Ding, J. Tackling Autoimmunity with Nanomedicines. *Nanomedicine* **2020**, *15*, 1585–1597, doi:10.2217/nnm-2020-0102.

35. Su, S.; Kang, P.M. Systemic Review of Biodegradable Nanomaterials in Nanomedicine. *Nanomaterials* **2020**, *10*, 656, doi:10.3390/nano10040656.
36. Arpagaus, C. PLA/PLGA Nanoparticles Prepared by Nano Spray Drying. *J. Pharm. Investig.* **2019**, *49*, 405–426, doi:10.1007/s40005-019-00441-3.
37. Operti, M.C.; Bernhardt, A.; Grimm, S.; Engel, A.; Figdor, C.G.; Tagit, O. PLGA-Based Nanomedicines Manufacturing: Technologies Overview and Challenges in Industrial Scale-Up. *International Journal of Pharmaceutics* **2021**, *605*, 120807, doi:10.1016/j.ijpharm.2021.120807.
38. Gangapurwala, G.; Vollrath, A.; De San Luis, A.; Schubert, U.S. PLA/PLGA-Based Drug Delivery Systems Produced with Supercritical CO2—A Green Future for Particle Formulation? *Pharmaceutics* **2020**, *12*, 1118, doi:10.3390/pharmaceutics12111118.
39. Jose, C.; Amra, K.; Bhavsar, C.; Momin, M.; Omri, A. Polymeric Lipid Hybrid Nanoparticles: Properties and Therapeutic Applications. *Crit Rev Ther Drug Carrier Syst* **2018**, *35*, 555–588, doi:10.1615/CritRevTherDrugCarrierSyst.2018024751.
40. Ghitman, J.; Biru, E.I.; Stan, R.; Iovu, H. Review of Hybrid PLGA Nanoparticles: Future of Smart Drug Delivery and Theranostics Medicine. *Materials & Design* **2020**, *193*, 108805, doi:10.1016/j.matdes.2020.108805.
41. Mohanty, A.; Uthaman, S.; Park, I.-K. Utilization of Polymer-Lipid Hybrid Nanoparticles for Targeted Anti-Cancer Therapy. *Molecules* **2020**, *25*, 4377, doi:10.3390/molecules25194377.
42. Rizwanullah, Md.; Alam, M.; Harshita; Mir, S.R.; Rizvi, Mohd.M.A.; Amin, S. Polymer-Lipid Hybrid Nanoparticles: A Next-Generation Nanocarrier for Targeted Treatment of Solid Tumors. *CPD* **2020**, *26*, 1206–1215, doi:10.2174/1381612826666200116150426.
43. Sivadasan, D.; Sultan, M.H.; Madkhali, O.; Almoshari, Y.; Thangavel, N. Polymeric Lipid Hybrid Nanoparticles (PLNs) as Emerging Drug Delivery Platform—A Comprehensive Review of Their Properties, Preparation Methods, and Therapeutic Applications. *Pharmaceutics* **2021**, *13*, 1291, doi:10.3390/pharmaceutics13081291.
44. Sánchez-López, E.; Ettcheto, M.; Egea, M.A.; Espina, M.; Cano, A.; Calpena, A.C.; Camins, A.; Carmona, N.; Silva, A.M.; Souto, E.B.; et al. Memantine Loaded PLGA PEGylated Nanoparticles for Alzheimer's Disease: In Vitro and in Vivo Characterization. *J Nanobiotechnol* **2018**, *16*, 32, doi:10.1186/s12951-018-0356-z.
45. Osman, G.; Rodriguez, J.; Chan, S.Y.; Chisholm, J.; Duncan, G.; Kim, N.; Tatler, A.L.; Shakesheff, K.M.; Hanes, J.; Suk, J.S.; et al. PEGylated Enhanced Cell Penetrating Peptide Nanoparticles for Lung Gene Therapy. *Journal of Controlled Release* **2018**, *285*, 35–45, doi:10.1016/j.jconrel.2018.07.001.
46. Reznickova, A.; Slavikova, N.; Kolska, Z.; Kolarova, K.; Belinova, T.; Hubalek Kalbacova, M.; Cieslar, M.; Svorcik, V. PEGylated Gold Nanoparticles: Stability, Cytotoxicity and Antibacterial Activity. *Colloids and Surfaces A: Physicochemical and Engineering Aspects* **2019**, *560*, 26–34, doi:10.1016/j.colsurfa.2018.09.083.
47. Pannuzzo, M.; Esposito, S.; Wu, L.-P.; Key, J.; Aryal, S.; Celia, C.; di Marzio, L.; Moghimi, S.M.; Decuzzi, P. Overcoming Nanoparticle-Mediated Complement Activation by Surface PEG Pairing. *Nano Lett.* **2020**, *20*, 4312–4321, doi:10.1021/acs.nanolett.0c01011.
48. Huckaby, J.T.; Lai, S.K. PEGylation for Enhancing Nanoparticle Diffusion in Mucus. *Advanced Drug Delivery Reviews* **2018**, *124*, 125–139, doi:10.1016/j.addr.2017.08.010.
49. Mohamed, M.; Abu Lila, A.S.; Shimizu, T.; Alaaeldin, E.; Hussein, A.; Sarhan, H.A.; Szebeni, J.; Ishida, T. PEGylated Liposomes: Immunological Responses. *Science and Technology of Advanced Materials* **2019**, *20*, 710–724, doi:10.1080/14686996.2019.1627174.

50. Li, P.Y.; Bearoff, F.; Zhu, P.; Fan, Z.; Zhu, Y.; Fan, M.; Cort, L.; Kambayashi, T.; Blankenhorn, E.P.; Cheng, H. PEGylation Enables Subcutaneously Administered Nanoparticles to Induce Antigen-Specific Immune Tolerance. *Journal of Controlled Release* **2021**, *331*, 164–175, doi:10.1016/j.jconrel.2021.01.013.
51. Shimizu, T.; Ishima, Y.; Ishida, T. [Induction of Anti-PEG Immune Responses by PEGylation of Proteins]. *Yakugaku Zasshi* **2020**, *140*, 163–169, doi:10.1248/yakushi.19-00187-5.
52. Huynh, V.A.; Janssen, C.; Beaumier, L. [ARN COVID-19 COMIRNATY Vaccine desensitization in a case of PEG Severe Immediate Hypersensitivity]. *Rev Fr Allergol (2009)* **2022**, *62*, 431–434, doi:10.1016/j.reval.2021.07.007.
53. Mohanraj, V.J.; Chen, Y. Nanoparticles - A Review. *Tropical Journal of Pharmaceutical Research* **2006**, *5*, 561–573, doi:10.4314/tjpr.v5i1.14634.
54. Aldewachi, H.; Al-Zidan, R.N.; Conner, M.T.; Salman, M.M. High-Throughput Screening Platforms in the Discovery of Novel Drugs for Neurodegenerative Diseases. *Bioengineering (Basel)* **2021**, *8*, 30, doi:10.3390/bioengineering8020030.
55. Potter, J.E.; Petts, G.; Ghosh, A.; White, F.J.; Kinsella, J.L.; Hughes, S.; Roberts, J.; Hodgkinson, A.; Brammeier, K.; Church, H.; et al. Enzyme Replacement Therapy and Hematopoietic Stem Cell Transplant: A New Paradigm of Treatment in Wolman Disease. *Orphanet J Rare Dis* **2021**, *16*, 235, doi:10.1186/s13023-021-01849-7.
56. Wikman-Jorgensen, P.E.; López Amorós, A.; Peris García, J.; Esteve Atienzar, P.J.; Cañizares Navarro, R.; Asensio Tomás, M.L.; Seguí Ripoll, J.M.; Bonet, D.; Esteban-Giner, M.J.; Robert, J.; et al. Enzyme Replacement Therapy for the Treatment of Hunter Disease: A Systematic Review with Narrative Synthesis and Meta-Analysis. *Molecular Genetics and Metabolism* **2020**, *131*, 206–210, doi:10.1016/j.ymgme.2020.07.005.
57. Spada, M.; Baron, R.; Elliott, P.M.; Falissard, B.; Hilz, M.J.; Monserrat, L.; Tøndel, C.; Tylki-Szymańska, A.; Wanner, C.; Germain, D.P. The Effect of Enzyme Replacement Therapy on Clinical Outcomes in Paediatric Patients with Fabry Disease – A Systematic Literature Review by a European Panel of Experts. *Molecular Genetics and Metabolism* **2019**, *126*, 212–223, doi:10.1016/j.ymgme.2018.04.007.
58. Active Site Available online: https://pmgbiology.com/tag/active-site/ (accessed on 26 November 2022).
59. Iglesia-García, D. de la; Huang, W.; Szatmary, P.; Baston-Rey, I.; Gonzalez-Lopez, J.; Prada-Ramallal, G.; Mukherjee, R.; Nunes, Q.M.; Domínguez-Muñoz, J.E.; Sutton, R.; et al. Efficacy of Pancreatic Enzyme Replacement Therapy in Chronic Pancreatitis: Systematic Review and Meta-Analysis. *Gut* **2017**, *66*, 1354–1355, doi:10.1136/gutjnl-2016-312529.
60. Sato, Y.; Okuyama, T. Novel Enzyme Replacement Therapies for Neuropathic Mucopolysaccharidoses. *IJMS* **2020**, *21*, 400, doi:10.3390/ijms21020400.
61. Germain, D.P.; Charrow, J.; Desnick, R.J.; Guffon, N.; Kempf, J.; Lachmann, R.H.; Lemay, R.; Linthorst, G.E.; Packman, S.; Scott, C.R.; et al. Ten-Year Outcome of Enzyme Replacement Therapy with Agalsidase Beta in Patients with Fabry Disease. *Journal of Medical Genetics* **2015**, *52*, 353–358, doi:10.1136/jmedgenet-2014-102797.
62. Solomon, M.; Muro, S. Lysosomal Enzyme Replacement Therapies: Historical Development, Clinical Outcomes, and Future Perspectives. *Advanced Drug Delivery Reviews* **2017**, *118*, 109–134, doi:10.1016/j.addr.2017.05.004.
63. McClements, D.J. Encapsulation, Protection, and Delivery of Bioactive Proteins and Peptides Using Nanoparticle and Microparticle Systems: A Review. *Advances in Colloid and Interface Science* **2018**, *253*, 1–22, doi:10.1016/j.cis.2018.02.002.
64. van Oers, M.; Rutjes, F.; van Hest, J. Cascade Reactions in Nanoreactors. *Current Opinion in Biotechnology* **2014**, *28*, 10–16, doi:10.1016/j.copbio.2013.10.011.

65. Chen, N.; Li, S.; Li, X.; Zhan, Q.; Li, L.; Long, L.; Zhao, J.; Hou, X.; Yuan, X. Construction of Enzymatic Nanoreactors with High Catalytic Activity in Millifluidic Systems for Cancer Therapy. *Chemical Engineering Journal* **2022**, *429*, 132305, doi:10.1016/j.cej.2021.132305.
66. Wilkerson, J.W.; Yang, S.-O.; Funk, P.J.; Stanley, S.K.; Bundy, B.C. Nanoreactors: Strategies to Encapsulate Enzyme Biocatalysts in Virus-like Particles. *New Biotechnology* **2018**, *44*, 59–63, doi:10.1016/j.nbt.2018.04.003.
67. Koyani, R.; Pérez-Robles, J.; Cadena-Nava, R.D.; Vazquez-Duhalt, R. Biomaterial-Based Nanoreactors, an Alternative for Enzyme Delivery. *Nanotechnology Reviews* **2017**, *6*, 405–419, doi:10.1515/ntrev-2016-0071.
68. Liu, X.; Hao, Y.; Popovtzer, R.; Feng, L.; Liu, Z. Construction of Enzyme Nanoreactors to Enable Tumor Microenvironment Modulation and Enhanced Cancer Treatment. *Adv. Healthcare Mater.* **2021**, *10*, 2001167, doi:10.1002/adhm.202001167.
69. Liao, R.; Pon, J.; Chungyoun, M.; Nance, E. Enzymatic Protection and Biocompatibility Screening of Enzyme-Loaded Polymeric Nanoparticles for Neurotherapeutic Applications. *Biomaterials* **2020**, *257*, 120238, doi:10.1016/j.biomaterials.2020.120238.
70. Ariga, K.; Ji, Q.; Hill, J.P. Enzyme-Encapsulated Layer-by-Layer Assemblies: Current Status and Challenges Toward Ultimate Nanodevices. In *Modern Techniques for Nano- and Microreactors/-reactions*; Caruso, F., Ed.; Advances in Polymer Science; Springer Berlin Heidelberg: Berlin, Heidelberg, 2010; Vol. 229, pp. 51–87 ISBN 978-3-642-12872-1.
71. El-Say, K.M.; El-Sawy, H.S. Polymeric Nanoparticles: Promising Platform for Drug Delivery. *International Journal of Pharmaceutics* **2017**, *528*, 675–691, doi:10.1016/j.ijpharm.2017.06.052.
72. Devi, G.R. SiRNA-Based Approaches in Cancer Therapy. *Cancer Gene Ther* **2006**, *13*, 819–829, doi:10.1038/sj.cgt.7700931.
73. Koutsilieri, E.; Rethwilm, A.; Scheller, C. The Therapeutic Potential of SiRNA in Gene Therapy of Neurodegenerative Disorders. In *Neuropsychiatric Disorders An Integrative Approach*; Gerlach, M., Deckert, J., Double, K., Koutsilieri, E., Eds.; Journal of Neural Transmission. Supplementa; Springer Vienna: Vienna, 2007; Vol. 72, pp. 43–49 ISBN 978-3-211-73573-2.
74. Li, S.; Ma, Z. Nonviral Gene Therapy. *CGT* **2001**, *1*, 201–226, doi:10.2174/1566523013348814.
75. Tavernier, G.; Andries, O.; Demeester, J.; Sanders, N.N.; De Smedt, S.C.; Rejman, J. MRNA as Gene Therapeutic: How to Control Protein Expression. *Journal of Controlled Release* **2011**, *150*, 238–247, doi:10.1016/j.jconrel.2010.10.020.
76. Ledley, F.D. Non-Viral Gene Therapy. *Current Opinion in Biotechnology* **1994**, *5*, 626–636, doi:10.1016/0958-1669(94)90085-X.
77. Yamamoto, A.; Kormann, M.; Rosenecker, J.; Rudolph, C. Current Prospects for MRNA Gene Delivery. *European Journal of Pharmaceutics and Biopharmaceutics* **2009**, *71*, 484–489, doi:10.1016/j.ejpb.2008.09.016.
78. Rai, R.; Alwani, S.; Badea, I. Polymeric Nanoparticles in Gene Therapy: New Avenues of Design and Optimization for Delivery Applications. *Polymers* **2019**, *11*, 745, doi:10.3390/polym11040745.
79. Aggarwal, P.; Hall, J.B.; McLeland, C.B.; Dobrovolskaia, M.A.; McNeil, S.E. Nanoparticle Interaction with Plasma Proteins as It Relates to Particle Biodistribution, Biocompatibility and Therapeutic Efficacy. *Adv Drug Deliv Rev* **2009**, *61*, 428–437, doi:10.1016/j.addr.2009.03.009.

80. Duran-Mota, J.A.; Yani, J.Q.; Almquist, B.D.; Borrós, S.; Oliva, N. Polyplex-Loaded Hydrogels for Local Gene Delivery to Human Dermal Fibroblasts. *ACS Biomater. Sci. Eng.* **2021**, *7*, 4347–4361, doi:10.1021/acsbiomaterials.1c00159.
81. Shen, L.; Li, B.; Qiao, Y. Fe3O4 Nanoparticles in Targeted Drug/Gene Delivery Systems. *Materials* **2018**, *11*, 324, doi:10.3390/ma11020324.
82. Abdelhamid, H.N.; Dowaidar, M.; Langel, Ü. Carbonized Chitosan Encapsulated Hierarchical Porous Zeolitic Imidazolate Frameworks Nanoparticles for Gene Delivery. *Microporous and Mesoporous Materials* **2020**, *302*, 110200, doi:10.1016/j.micromeso.2020.110200.
83. Proulx, J.; Joshi, C.; Vijayaraghavalu, S.; Saraswathy, M.; Labhasetwar, V.; Ghorpade, A.; Borgmann, K. Arginine-Modified Polymers Facilitate Poly (Lactide-Co-Glycolide)-Based Nanoparticle Gene Delivery to Primary Human Astrocytes. *Int J Nanomedicine* **2020**, *15*, 3639–3647, doi:10.2147/IJN.S250865.
84. Guimarães, D.; Cavaco-Paulo, A.; Nogueira, E. Design of Liposomes as Drug Delivery System for Therapeutic Applications. *International Journal of Pharmaceutics* **2021**, *601*, 120571, doi:10.1016/j.ijpharm.2021.120571.
85. Prabahar, K.; Alanazi, Z.; Qushawy, M. Targeted Drug Delivery System: Advantages, Carriers and Strategies. *Indian Journal of Pharmaceutical Education* **2021**, *55*, 346–353.
86. Synthesis of a Peptide Conjugated 5-Fluorouracil Gelator Prodrug for Photo-Controlled Release of the Antitumor Agent - Das - 2019 - ChemistrySelect - Wiley Online Library Available online: https://chemistry-europe.onlinelibrary.wiley.com/doi/full/10.1002/slct.201900905?casa_token=n6obJQoaTb0AAAAA%3AbwWzAFINexCRvZoOSIXLGa2NiLZ9yOt15UiuXjeM4EbY5p3Y1735dQLz6vEuWEjLPznkYlJHYQ1tYGE (accessed on 25 November 2022).
87. Price, P.M.; Mahmoud, W.E.; Al-Ghamdi, A.A.; Bronstein, L.M. Magnetic Drug Delivery: Where the Field Is Going. *Frontiers in Chemistry* **2018**, *6*.
88. Wang, Y.; Wang, L.; Guo, L.; Yan, M.; Feng, L.; Dong, S.; Hao, J. Photo-Responsive Magnetic Mesoporous Silica Nanocomposites for Magnetic Targeted Cancer Therapy. *New Journal of Chemistry* **2019**, *43*, 4908–4918, doi:10.1039/C8NJ06105J.
89. Peng, J.; Yang, Q.; Xiao, Y.; Shi, K.; Liu, Q.; Hao, Y.; Yang, F.; Han, R.; Qian, Z. Tumor Microenvironment Responsive Drug-Dye-Peptide Nanoassembly for Enhanced Tumor-Targeting, Penetration, and Photo-Chemo-Immunotherapy. *Advanced Functional Materials* **2019**, *29*, 1900004, doi:10.1002/adfm.201900004.
90. Liu, Y.; Bai, L.; Guo, K.; Jia, Y.; Zhang, K.; Liu, Q.; Wang, P.; Wang, X. Focused Ultrasound-Augmented Targeting Delivery of Nanosonosensitizers from Homogenous Exosomes for Enhanced Sonodynamic Cancer Therapy. *Theranostics* **2019**, *9*, 5261–5281, doi:10.7150/thno.33183.
91. Tekko, I.A.; Raj Singh, T.R. Microneedles for Ocular Drug Delivery and Targeting: Challenges and Opportunities. In *Microneedles for Drug and Vaccine Delivery and Patient Monitoring*; John Wiley & Sons, Ltd, 2018; pp. 283–306 ISBN 978-1-119-30510-1.
92. Cardoso, V.M. de O.; Ferreira, L.M.B.; Comparetti, E.J.; Sampaio, I.; Ferreira, N.N.; Miranda, R.R.; Zucolotto, V. Chapter 4 - Stimuli-Responsive Polymeric Nanoparticles as Controlled Drug Delivery Systems. In *Stimuli-Responsive Nanocarriers*; Gajbhiye, V., Gajbhiye, K.R., Hong, S., Eds.; Academic Press, 2022; pp. 87–117 ISBN 978-0-12-824456-2.
93. Narum, S.M.; Le, T.; Le, D.P.; Lee, J.C.; Donahue, N.D.; Yang, W.; Wilhelm, S. Chapter 4 - Passive Targeting in Nanomedicine: Fundamental Concepts, Body Interactions, and Clinical Potential. In *Nanoparticles for Biomedical Applications*; Chung, E.J., Leon, L.,

Rinaldi, C., Eds.; Micro and Nano Technologies; Elsevier, 2020; pp. 37–53 ISBN 978-0-12-816662-8.
94. Sharifi, M.; Cho, W.C.; Ansariesfahani, A.; Tarharoudi, R.; Malekisarvar, H.; Sari, S.; Bloukh, S.H.; Edis, Z.; Amin, M.; Gleghorn, J.P.; et al. An Updated Review on EPR-Based Solid Tumor Targeting Nanocarriers for Cancer Treatment. *Cancers* **2022**, *14*, 2868, doi:10.3390/cancers14122868.
95. Park, J.; Choi, Y.; Chang, H.; Um, W.; Ryu, J.H.; Kwon, I.C. Alliance with EPR Effect: Combined Strategies to Improve the EPR Effect in the Tumor Microenvironment. *Theranostics* **2019**, *9*, 8073–8090, doi:10.7150/thno.37198.
96. Maeda, H. The 35th Anniversary of the Discovery of EPR Effect: A New Wave of Nanomedicines for Tumor-Targeted Drug Delivery—Personal Remarks and Future Prospects. *Journal of Personalized Medicine* **2021**, *11*, 229, doi:10.3390/jpm11030229.
97. Torchilin, V. Tumor Delivery of Macromolecular Drugs Based on the EPR Effect. *Advanced Drug Delivery Reviews* **2011**, *63*, 131–135, doi:10.1016/j.addr.2010.03.011.
98. Kai Tee, J.; Xian Yip, L.; Sheau Tan, E.; Santitewagun, S.; Prasath, A.; Chun Ke, P.; Kiat Ho, H.; Tai Leong, D. Nanoparticles' Interactions with Vasculature in Diseases. *Chemical Society Reviews* **2019**, *48*, 5381–5407, doi:10.1039/C9CS00309F.
99. Kang, H.; Rho, S.; Stiles, W.R.; Hu, S.; Baek, Y.; Hwang, D.W.; Kashiwagi, S.; Kim, M.S.; Choi, H.S. Size-Dependent EPR Effect of Polymeric Nanoparticles on Tumor Targeting. *Advanced Healthcare Materials* **2020**, *9*, 1901223, doi:10.1002/adhm.201901223.
100. Durymanov, M.; Kamaletdinova, T.; Lehmann, S.E.; Reineke, J. Exploiting Passive Nanomedicine Accumulation at Sites of Enhanced Vascular Permeability for Non-Cancerous Applications. *Journal of Controlled Release* **2017**, *261*, 10–22, doi:10.1016/j.jconrel.2017.06.013.
101. Fang, J.; Islam, W.; Maeda, H. Exploiting the Dynamics of the EPR Effect and Strategies to Improve the Therapeutic Effects of Nanomedicines by Using EPR Effect Enhancers. *Advanced Drug Delivery Reviews* **2020**, *157*, 142–160, doi:10.1016/j.addr.2020.06.005.
102. Wu, J. The Enhanced Permeability and Retention (EPR) Effect: The Significance of the Concept and Methods to Enhance Its Application. *J Pers Med* **2021**, *11*, 771, doi:10.3390/jpm11080771.
103. Danhier, F. To Exploit the Tumor Microenvironment: Since the EPR Effect Fails in the Clinic, What Is the Future of Nanomedicine? *J Control Release* **2016**, *244*, 108–121, doi:10.1016/j.jconrel.2016.11.015.
104. Maeda, H.; Khatami, M. Analyses of Repeated Failures in Cancer Therapy for Solid Tumors: Poor Tumor-Selective Drug Delivery, Low Therapeutic Efficacy and Unsustainable Costs. *Clin Trans Med* **2018**, *7*, 11, doi:10.1186/s40169-018-0185-6.
105. Binnemars-Postma, K.; Storm, G.; Prakash, J. Nanomedicine Strategies to Target Tumor-Associated Macrophages. *International Journal of Molecular Sciences* **2017**, *18*, 979, doi:10.3390/ijms18050979.
106. Shekarian, T.; Valsesia-Wittmann, S.; Caux, C.; Marabelle, A. Paradigm Shift in Oncology: Targeting the Immune System Rather than Cancer Cells. *Mutagenesis* **2015**, *30*, 205–211, doi:10.1093/mutage/geu073.
107. Hoffmann, T.K.; Bier, H.; Whiteside, T.L. Targeting the Immune System: Novel Therapeutic Approaches in Squamous Cell Carcinoma of the Head and Neck. *Cancer Immunol Immunother* **2004**, *53*, 1055–1067, doi:10.1007/s00262-004-0530-z.
108. Li, C.; Li, J.; Li, Y.; Lang, S.; Yougbare, I.; Zhu, G.; Chen, P.; Ni, H. Crosstalk between Platelets and the Immune System: Old Systems with New Discoveries. *Advances in Hematology* **2012**, *2012*, e384685, doi:10.1155/2012/384685.

109. Bertrand, N.; Wu, J.; Xu, X.; Kamaly, N.; Farokhzad, O.C. Cancer Nanotechnology: The Impact of Passive and Active Targeting in the Era of Modern Cancer Biology. *Advanced Drug Delivery Reviews* **2014**, *66*, 2–25, doi:10.1016/j.addr.2013.11.009.
110. Chen, L.; Hong, W.; Ren, W.; Xu, T.; Qian, Z.; He, Z. Recent Progress in Targeted Delivery Vectors Based on Biomimetic Nanoparticles. *Sig Transduct Target Ther* **2021**, *6*, 1–25, doi:10.1038/s41392-021-00631-2.
111. Li, H.; Ham, A.; Ma, T.C.; Kuo, S.-H.; Kanter, E.; Kim, D.; Ko, H.S.; Quan, Y.; Sardi, S.P.; Li, A.; et al. Mitochondrial Dysfunction and Mitophagy Defect Triggered by Heterozygous GBA Mutations. *Autophagy* **2019**, *15*, 113–130, doi:10.1080/15548627.2018.1509818.
112. Woythe, L.; Tito, N.B.; Albertazzi, L. A Quantitative View on Multivalent Nanomedicine Targeting. *Advanced Drug Delivery Reviews* **2021**, *169*, 1–21, doi:10.1016/j.addr.2020.11.010.
113. Osswald, U.; Boneberg, J.; Wittmann, V. Photoswitching Affinity and Mechanism of Multivalent Lectin Ligands. *Chemistry – A European Journal* **2022**, *28*, e202200267, doi:10.1002/chem.202200267.
114. Wang, S.-C.; Cheng, K.-Y.; Fu, J.-H.; Cheng, Y.-C.; Chan, Y.-T. Conformational Regulation of Multivalent Terpyridine Ligands for Self-Assembly of Heteroleptic Metallo-Supramolecules. *J. Am. Chem. Soc.* **2020**, *142*, 16661–16667, doi:10.1021/jacs.0c06618.
115. Picault, L.; Laigre, E.; Gillon, E.; Tiertant, C.; Renaudet, O.; Imberty, A.; Goyard, D.; Dejeu, J. Characterization of the Interaction of Multivalent Glycosylated Ligands with Bacterial Lectins by Biolayer Interferometry. *Glycobiology* **2022**, *32*, 886–896, doi:10.1093/glycob/cwac047.
116. Tjandra, K.C.; Forest, C.R.; Wong, C.K.; Alcantara, S.; Kelly, H.G.; Ju, Y.; Stenzel, M.H.; McCarroll, J.A.; Kavallaris, M.; Caruso, F.; et al. Modulating the Selectivity and Stealth Properties of Ellipsoidal Polymersomes through a Multivalent Peptide Ligand Display. *Advanced Healthcare Materials* **2020**, *9*, 2000261, doi:10.1002/adhm.202000261.
117. Gullotti, E.; Yeo, Y. Extracellularly Activated Nanocarriers: A New Paradigm of Tumor Targeted Drug Delivery. *Mol. Pharmaceutics* **2009**, *6*, 1041–1051, doi:10.1021/mp900090z.
118. Allen, T.M. Ligand-Targeted Therapeutics in Anticancer Therapy. *Nat Rev Cancer* **2002**, *2*, 750–763, doi:10.1038/nrc903.
119. Ogris, M.; Steinlein, P.; Carotta, S.; Brunner, S.; Wagner, E. DNA/Polyethylenimine Transfection Particles: Influence of Ligands, Polymer Size, and PEGylation on Internalization and Gene Expression. *AAPS PharmSci* **2001**, *3*, 43, doi:10.1208/ps030321.
120. Gorden, Ph.; Carpentier, J.-L.; Freychet, P.; Orci, L. Internalization of Polypeptide Hormones. *Diabetologia* **1980**, *18*, 263–274, doi:10.1007/BF00251003.
121. Cubellis, M. v.; Wun, T. c.; Blasi, F. Receptor-Mediated Internalization and Degradation of Urokinase Is Caused by Its Specific Inhibitor PAI-1. *The EMBO Journal* **1990**, *9*, 1079–1085, doi:10.1002/j.1460-2075.1990.tb08213.x.
122. Wisler, J.W.; DeWire, S.M.; Whalen, E.J.; Violin, J.D.; Drake, M.T.; Ahn, S.; Shenoy, S.K.; Lefkowitz, R.J. A Unique Mechanism of β-Blocker Action: Carvedilol Stimulates β-Arrestin Signaling. *Proceedings of the National Academy of Sciences* **2007**, *104*, 16657–16662, doi:10.1073/pnas.0707936104.
123. Hicke, L.; Riezman, H. Ubiquitination of a Yeast Plasma Membrane Receptor Signals Its Ligand-Stimulated Endocytosis. *Cell* **1996**, *84*, 277–287, doi:10.1016/S0092-8674(00)80982-4.

124. Kenakin, T. Ligand-Selective Receptor Conformations Revisited: The Promise and the Problem. *Trends in Pharmacological Sciences* **2003**, *24*, 346–354, doi:10.1016/S0165-6147(03)00167-6.
125. Wells, A.; Welsh, J.B.; Lazar, C.S.; Wiley, H.S.; Gill, G.N.; Rosenfeld, M.G. Ligand-Induced Transformation by a Noninternalizing Epidermal Growth Factor Receptor. *Science* **1990**, *247*, 962–964, doi:10.1126/science.2305263.
126. Sapra, P.; Allen, T.M. Ligand-Targeted Liposomal Anticancer Drugs. *Progress in Lipid Research* **2003**, *42*, 439–462, doi:10.1016/S0163-7827(03)00032-8.
127. Saul, J.M.; Annapragada, A.V.; Bellamkonda, R.V. A Dual-Ligand Approach for Enhancing Targeting Selectivity of Therapeutic Nanocarriers. *Journal of Controlled Release* **2006**, *114*, 277–287, doi:10.1016/j.jconrel.2006.05.028.
128. Kettler, K.; Veltman, K.; van de Meent, D.; van Wezel, A.; Hendriks, A.J. Cellular Uptake of Nanoparticles as Determined by Particle Properties, Experimental Conditions, and Cell Type. *Environmental Toxicology and Chemistry* **2014**, *33*, 481–492, doi:10.1002/etc.2470.
129. Shi, Y.; van der Meel, R.; Chen, X.; Lammers, T. The EPR Effect and beyond: Strategies to Improve Tumor Targeting and Cancer Nanomedicine Treatment Efficacy. *Theranostics* **2020**, *10*, 7921–7924, doi:10.7150/thno.49577.
130. Wang, X.; Gao, B.; Ren, X.; Guo, J.; Xia, S.; Zhang, W.; Yang, C.; Feng, Y. A Two-Pronged Approach to Regulate the Behaviors of ECs and SMCs by the Dual Targeting-Nanoparticles. *Colloids and Surfaces B: Biointerfaces* **2021**, *208*, 112068, doi:10.1016/j.colsurfb.2021.112068.
131. Gao, X.; Li, L.; Cai, X.; Huang, Q.; Xiao, J.; Cheng, Y. Targeting Nanoparticles for Diagnosis and Therapy of Bone Tumors: Opportunities and Challenges. *Biomaterials* **2021**, *265*, 120404, doi:10.1016/j.biomaterials.2020.120404.
132. Kadkhoda, J.; Akrami-Hasan-Kohal, M.; Tohidkia, M.R.; Khaledi, S.; Davaran, S.; Aghanejad, A. Advances in Antibody Nanoconjugates for Diagnosis and Therapy: A Review of Recent Studies and Trends. *International Journal of Biological Macromolecules* **2021**, *185*, 664–678, doi:10.1016/j.ijbiomac.2021.06.191.
133. Loureiro, J.A.; Gomes, B.; Coelho, M.A.; Carmo Pereira, M. do; Rocha, S. Targeting Nanoparticles across the Blood–Brain Barrier with Monoclonal Antibodies. *Nanomedicine* **2014**, *9*, 709–722, doi:10.2217/nnm.14.27.
134. Yoo, J.; Park, C.; Yi, G.; Lee, D.; Koo, H. Active Targeting Strategies Using Biological Ligands for Nanoparticle Drug Delivery Systems. *Cancers* **2019**, *11*, 640, doi:10.3390/cancers11050640.
135. Haghiralsadat, F.; Amoabediny, G.; Naderinezhad, S.; Zandieh-Doulabi, B.; Forouzanfar, T.; Helder, M.N. Codelivery of Doxorubicin and JIP1 SiRNA with Novel EphA2-Targeted PEGylated Cationic Nanoliposomes to Overcome Osteosarcoma Multidrug Resistance. *Int J Nanomedicine* **2018**, *13*, 3853–3866, doi:10.2147/IJN.S150017.
136. Yakati, V.; Vangala, S.; Madamsetty, V.S.; Banerjee, R.; Moku, G. Enhancing the Anticancer Effect of Paclitaxel by Using Polymeric Nanoparticles Decorated with Colorectal Cancer Targeting CPKSNNGVC-Peptide. *Journal of Drug Delivery Science and Technology* **2022**, *68*, 103125, doi:10.1016/j.jddst.2022.103125.
137. Dosta, P.; Tamargo, I.; Ramos, V.; Kumar, S.; Kang, D.W.; Borrós, S.; Jo, H. Delivery of Anti-MicroRNA-712 to Inflamed Endothelial Cells Using Poly(β-Amino Ester) Nanoparticles Conjugated with VCAM-1 Targeting Peptide. *Advanced Healthcare Materials* **2021**, *10*, 2001894, doi:10.1002/adhm.202001894.
138. Rigon, L.; Salvalaio, M.; Pederzoli, F.; Legnini, E.; Duskey, J.T.; D'Avanzo, F.; De Filippis, C.; Ruozi, B.; Marin, O.; Vandelli, M.A.; et al. Targeting Brain Disease in MPSII:

Preclinical Evaluation of IDS-Loaded PLGA Nanoparticles. *International Journal of Molecular Sciences* **2019**, *20*, 2014, doi:10.3390/ijms20082014.
139. Zhang, C.; Wang, X.; Cheng, R.; Zhong, Z. A6 Peptide-Tagged Core-Disulfide-Cross-Linked Micelles for Targeted Delivery of Proteasome Inhibitor Carfilzomib to Multiple Myeloma In Vivo. *Biomacromolecules* **2020**, *21*, 2049–2059, doi:10.1021/acs.biomac.9b01790.
140. Go, G.; Lee, C.-S.; Yoon, Y.M.; Lim, J.H.; Kim, T.H.; Lee, S.H. PrPC Aptamer Conjugated–Gold Nanoparticles for Targeted Delivery of Doxorubicin to Colorectal Cancer Cells. *International Journal of Molecular Sciences* **2021**, *22*, 1976, doi:10.3390/ijms22041976.
141. Alibolandi, M.; Ramezani, M.; Abnous, K.; Hadizadeh, F. AS1411 Aptamer-Decorated Biodegradable Polyethylene Glycol-Poly(Lactic-Co-Glycolic Acid) Nanopolymersomes for the Targeted Delivery of Gemcitabine to Non-Small Cell Lung Cancer In Vitro. *J Pharm Sci* **2016**, *105*, 1741–1750, doi:10.1016/j.xphs.2016.02.021.
142. Pan, M.; Li, W.; Yang, J.; Li, Z.; Zhao, J.; Xiao, Y.; Xing, Y.; Zhang, X.; Ju, W. Plumbagin-Loaded Aptamer-Targeted Poly d,l-Lactic-Co-Glycolic Acid-b-Polyethylene Glycol Nanoparticles for Prostate Cancer Therapy. *Medicine (Baltimore)* **2017**, *96*, e7405, doi:10.1097/MD.0000000000007405.
143. Powell, D.; Chandra, S.; Dodson, K.; Shaheen, F.; Wiltz, K.; Ireland, S.; Syed, M.; Dash, S.; Wiese, T.; Mandal, T.; et al. Aptamer-Functionalized Hybrid Nanoparticle for the Treatment of Breast Cancer. *Eur J Pharm Biopharm* **2017**, *114*, 108–118, doi:10.1016/j.ejpb.2017.01.011.
144. Fang, Y.; Lin, S.; Yang, F.; Situ, J.; Lin, S.; Luo, Y. Aptamer-Conjugated Multifunctional Polymeric Nanoparticles as Cancer-Targeted, MRI-Ultrasensitive Drug Delivery Systems for Treatment of Castration-Resistant Prostate Cancer. *BioMed Research International* **2020**, *2020*, e9186583, doi:10.1155/2020/9186583.
145. Veiseh, O.; Gunn, J.W.; Zhang, M. Design and Fabrication of Magnetic Nanoparticles for Targeted Drug Delivery and Imaging. *Advanced Drug Delivery Reviews* **2010**, *62*, 284–304, doi:10.1016/j.addr.2009.11.002.
146. Gil-Garcia, M.; Ventura, S. Multifunctional Antibody-Conjugated Coiled-Coil Protein Nanoparticles for Selective Cell Targeting. *Acta Biomaterialia* **2021**, *131*, 472–482, doi:10.1016/j.actbio.2021.06.040.
147. Yook, S.; Cai, Z.; Lu, Y.; Winnik, M.A.; Pignol, J.-P.; Reilly, R.M. Radiation Nanomedicine for EGFR-Positive Breast Cancer: Panitumumab-Modified Gold Nanoparticles Complexed to the β-Particle-Emitter, 177Lu. *Mol. Pharmaceutics* **2015**, *12*, 3963–3972, doi:10.1021/acs.molpharmaceut.5b00425.
148. Weinstein, S.; Toker, I.A.; Emmanuel, R.; Ramishetti, S.; Hazan-Halevy, I.; Rosenblum, D.; Goldsmith, M.; Abraham, A.; Benjamini, O.; Bairey, O.; et al. Harnessing RNAi-Based Nanomedicines for Therapeutic Gene Silencing in B-Cell Malignancies. *Proceedings of the National Academy of Sciences* **2016**, *113*, E16–E22, doi:10.1073/pnas.1519273113.
149. Carroll, R.T.; Bhatia, D.; Geldenhuys, W.; Bhatia, R.; Miladore, N.; Bishayee, A.; Sutariya, V. Brain-Targeted Delivery of Tempol-Loaded Nanoparticles for Neurological Disorders. *J Drug Target* **2010**, *18*, 665–674, doi:10.3109/10611861003639796.
150. Klein, P.M.; Kern, S.; Lee, D.-J.; Schmaus, J.; Höhn, M.; Gorges, J.; Kazmaier, U.; Wagner, E. Folate Receptor-Directed Orthogonal Click-Functionalization of SiRNA Lipopolyplexes for Tumor Cell Killing in Vivo. *Biomaterials* **2018**, *178*, 630–642, doi:10.1016/j.biomaterials.2018.03.031.

151. Deshayes, S.; Cabral, H.; Ishii, T.; Miura, Y.; Kobayashi, S.; Yamashita, T.; Matsumoto, A.; Miyahara, Y.; Nishiyama, N.; Kataoka, K. Phenylboronic Acid-Installed Polymeric Micelles for Targeting Sialylated Epitopes in Solid Tumors. *J. Am. Chem. Soc.* **2013**, *135*, 15501–15507, doi:10.1021/ja406406h.
152. Song, M.-M.; Xu, H.-L.; Liang, J.-X.; Xiang, H.-H.; Liu, R.; Shen, Y.-X. Lactoferrin Modified Graphene Oxide Iron Oxide Nanocomposite for Glioma-Targeted Drug Delivery. *Mater Sci Eng C Mater Biol Appl* **2017**, *77*, 904–911, doi:10.1016/j.msec.2017.03.309.
153. Yi, Y.; Kim, H.J.; Zheng, M.; Mi, P.; Naito, M.; Kim, B.S.; Min, H.S.; Hayashi, K.; Perche, F.; Toh, K.; et al. Glucose-Linked Sub-50-Nm Unimer Polyion Complex-Assembled Gold Nanoparticles for Targeted SiRNA Delivery to Glucose Transporter 1-Overexpressing Breast Cancer Stem-like Cells. *Journal of Controlled Release* **2019**, *295*, 268–277, doi:10.1016/j.jconrel.2019.01.006.
154. Chen, Q.; Zheng, C.; Li, Y.; Bian, S.; Pan, H.; Zhao, X.; Lu, W.W. Bone Targeted Delivery of SDF-1 via Alendronate Functionalized Nanoparticles in Guiding Stem Cell Migration. *ACS Appl. Mater. Interfaces* **2018**, *10*, 23700–23710, doi:10.1021/acsami.8b08606.
155. Ahmad, M.; Mudgil, P.; Gani, A.; Hamed, F.; Masoodi, F.A.; Maqsood, S. Nano-Encapsulation of Catechin in Starch Nanoparticles: Characterization, Release Behavior and Bioactivity Retention during Simulated in-Vitro Digestion. *Food Chemistry* **2019**, *270*, 95–104, doi:10.1016/j.foodchem.2018.07.024.
156. Madheswaran, T.; Kandasamy, M.; Bose, R.J.; Karuppagounder, V. Current Potential and Challenges in the Advances of Liquid Crystalline Nanoparticles as Drug Delivery Systems. *Drug Discovery Today* **2019**, *24*, 1405–1412, doi:10.1016/j.drudis.2019.05.004.
157. Seidi, F.; Jenjob, R.; Crespy, D. Designing Smart Polymer Conjugates for Controlled Release of Payloads. *Chem. Rev.* **2018**, *118*, 3965–4036, doi:10.1021/acs.chemrev.8b00006.
158. Kamaly, N.; Yameen, B.; Wu, J.; Farokhzad, O.C. Degradable Controlled-Release Polymers and Polymeric Nanoparticles: Mechanisms of Controlling Drug Release. *Chem. Rev.* **2016**, *116*, 2602–2663, doi:10.1021/acs.chemrev.5b00346.
159. Patra, J.K.; Das, G.; Fraceto, L.F.; Campos, E.V.R.; Rodriguez-Torres, M. del P.; Acosta-Torres, L.S.; Diaz-Torres, L.A.; Grillo, R.; Swamy, M.K.; Sharma, S.; et al. Nano Based Drug Delivery Systems: Recent Developments and Future Prospects. *Journal of Nanobiotechnology* **2018**, *16*, 71, doi:10.1186/s12951-018-0392-8.
160. Corso, A.D.; Arosio, S.; Arrighetti, N.; Perego, P.; Belvisi, L.; Pignataro, L.; Gennari, C. A Trifunctional Self-Immolative Spacer Enables Drug Release with Two Non-Sequential Enzymatic Cleavages. *Chemical Communications* **2021**, *57*, 7778–7781, doi:10.1039/D1CC02895B.
161. Zhang, A.; Jung, K.; Li, A.; Liu, J.; Boyer, C. Recent Advances in Stimuli-Responsive Polymer Systems for Remotely Controlled Drug Release. *Progress in Polymer Science* **2019**, *99*, 101164, doi:10.1016/j.progpolymsci.2019.101164.
162. Zhao, W.; Zhao, Y.; Wang, Q.; Liu, T.; Sun, J.; Zhang, R. Remote Light-Responsive Nanocarriers for Controlled Drug Delivery: Advances and Perspectives. *Small* **2019**, *15*, 1903060, doi:10.1002/smll.201903060.
163. Zhang, Y.; Kim, I.; Lu, Y.; Xu, Y.; Yu, D.-G.; Song, W. Intelligent Poly(l-Histidine)-Based Nanovehicles for Controlled Drug Delivery. *Journal of Controlled Release* **2022**, *349*, 963–982, doi:10.1016/j.jconrel.2022.08.005.
164. Razavi, B.; Abdollahi, A.; Roghani-Mamaqani, H.; Salami-Kalajahi, M. Light- and Temperature-Responsive Micellar Carriers Prepared by Spiropyran-Initiated Atom Transfer Polymerization: Investigation of Photochromism Kinetics, Responsivities, and

Controlled Release of Doxorubicin. *Polymer* **2020**, *187*, 122046, doi:10.1016/j.polymer.2019.122046.
165. Rinaldi, A.; Caraffi, R.; Grazioli, M.V.; Oddone, N.; Giardino, L.; Tosi, G.; Vandelli, M.A.; Calzà, L.; Ruozi, B.; Duskey, J.T. Applications of the ROS-Responsive Thioketal Linker for the Production of Smart Nanomedicines. *Polymers* **2022**, *14*, 687, doi:10.3390/polym14040687.
166. Na, Y.; Lee, J.S.; Woo, J.; Ahn, S.; Lee, E.; Choi, W.I.; Sung, D. Reactive Oxygen Species (ROS)-Responsive Ferrocene-Polymer-Based Nanoparticles for Controlled Release of Drugs. *J. Mater. Chem. B* **2020**, *8*, 1906–1913, doi:10.1039/C9TB02533B.
167. Wan, W.; Qu, C.; Zhou, Y.; Zhang, L.; Chen, M.; Liu, Y.; You, B.; Li, F.; Wang, D.; Zhang, X. Doxorubicin and SiRNA-PD-L1 Co-Delivery with T7 Modified ROS-Sensitive Nanoparticles for Tumor Chemoimmunotherapy. *International Journal of Pharmaceutics* **2019**, *566*, 731–744, doi:10.1016/j.ijpharm.2019.06.030.
168. Xiong, R.; X. Xu, R.; Huang, C.; Smedt, S.D.; Braeckmans, K. Stimuli-Responsive Nanobubbles for Biomedical Applications. *Chemical Society Reviews* **2021**, *50*, 5746–5776, doi:10.1039/C9CS00839J.
169. Bu, X.; Alheshibri, M. The Effect of Ultrasound on Bulk and Surface Nanobubbles: A Review of the Current Status. *Ultrasonics Sonochemistry* **2021**, *76*, 105629, doi:10.1016/j.ultsonch.2021.105629.
170. Rizzo, F.; Kehr, N.S. Recent Advances in Injectable Hydrogels for Controlled and Local Drug Delivery. *Adv. Healthcare Mater.* **2021**, *10*, 2001341, doi:10.1002/adhm.202001341.
171. Ha, D.I.; Lee, S.B.; Chong, M.S.; Lee, Y.M.; Kim, S.Y.; Park, Y.H. Preparation of Thermo-Responsive and Injectable Hydrogels Based on Hyaluronic Acid and Poly(N-Isopropylacrylamide) and Their Drug Release Behaviors. *Macromol. Res.* **2006**, *14*, 87–93, doi:10.1007/BF03219073.
172. Ma, X.; Xu, T.; Chen, W.; Qin, H.; Chi, B.; Ye, Z. Injectable Hydrogels Based on the Hyaluronic Acid and Poly (γ-Glutamic Acid) for Controlled Protein Delivery. *Carbohydrate Polymers* **2018**, *179*, 100–109, doi:10.1016/j.carbpol.2017.09.071.
173. Sun, Y.; Nan, D.; Jin, H.; Qu, X. Recent Advances of Injectable Hydrogels for Drug Delivery and Tissue Engineering Applications. *Polymer Testing* **2020**, *81*, 106283, doi:10.1016/j.polymertesting.2019.106283.
174. Ornell, K.J.; Lozada, D.; Phan, N.V.; Coburn, J.M. Controlling Methacryloyl Substitution of Chondroitin Sulfate: Injectable Hydrogels with Tunable Long-Term Drug Release Profiles. *J. Mater. Chem. B* **2019**, *7*, 2151–2161, doi:10.1039/C8TB03020K.
175. Biondi, M.; Borzacchiello, A.; Mayol, L.; Ambrosio, L. Nanoparticle-Integrated Hydrogels as Multifunctional Composite Materials for Biomedical Applications. *Gels* **2015**, *1*, 162–178, doi:10.3390/gels1020162.
176. Palmese, L.L.; Thapa, R.K.; Sullivan, M.O.; Kiick, K.L. Hybrid Hydrogels for Biomedical Applications. *Current Opinion in Chemical Engineering* **2019**, *24*, 143–157, doi:10.1016/j.coche.2019.02.010.
177. Ye, E.; Loh, X.J. Polymeric Hydrogels and Nanoparticles: A Merging and Emerging Field. *Aust. J. Chem.* **2013**, *66*, 997, doi:10.1071/CH13168.
178. Gao, W.; Zhang, Y.; Zhang, Q.; Zhang, L. Nanoparticle-Hydrogel: A Hybrid Biomaterial System for Localized Drug Delivery. *Ann Biomed Eng* **2016**, *44*, 2049–2061, doi:10.1007/s10439-016-1583-9.
179. Jiang, Y.; Krishnan, N.; Heo, J.; Fang, R.H.; Zhang, L. Nanoparticle–Hydrogel Superstructures for Biomedical Applications. *Journal of Controlled Release* **2020**, *324*, 505–521, doi:10.1016/j.jconrel.2020.05.041.

180. Nunes, D.; Andrade, S.; Ramalho, M.J.; Loureiro, J.A.; Pereira, M.C. Polymeric Nanoparticles-Loaded Hydrogels for Biomedical Applications: A Systematic Review on In Vivo Findings. *Polymers* **2022**, *14*, 1010, doi:10.3390/polym14051010.
181. Shi, J.; Xiao, Z.; Kamaly, N.; Farokhzad, O.C. Self-Assembled Targeted Nanoparticles: Evolution of Technologies and Bench to Bedside Translation. *Acc. Chem. Res.* **2011**, *44*, 1123–1134, doi:10.1021/ar200054n.
182. Havel, H.; Finch, G.; Strode, P.; Wolfgang, M.; Zale, S.; Bobe, I.; Youssoufian, H.; Peterson, M.; Liu, M. Nanomedicines: From Bench to Bedside and Beyond. *AAPS J* **2016**, *18*, 1373–1378, doi:10.1208/s12248-016-9961-7.
183. Khairnar, S.V.; Pagare, P.; Thakre, A.; Nambiar, A.R.; Junnuthula, V.; Abraham, M.C.; Kolimi, P.; Nyavanandi, D.; Dyawanapelly, S. Review on the Scale-Up Methods for the Preparation of Solid Lipid Nanoparticles. *Pharmaceutics* **2022**, *14*, 1886, doi:10.3390/pharmaceutics14091886.
184. Zhang, C.; Yan, L.; Wang, X.; Zhu, S.; Chen, C.; Gu, Z.; Zhao, Y. Progress, Challenges, and Future of Nanomedicine. *Nano Today* **2020**, *35*, 101008, doi:10.1016/j.nantod.2020.101008.
185. Stavis, S.M.; Fagan, J.A.; Stopa, M.; Liddle, J.A. Nanoparticle Manufacturing – Heterogeneity through Processes to Products. *ACS Appl. Nano Mater.* **2018**, *1*, 4358–4385, doi:10.1021/acsanm.8b01239.
186. Rajsri, K.S.; McRae, M.P.; Simmons, G.W.; Christodoulides, N.J.; Matz, H.; Dooley, H.; Koide, A.; Koide, S.; McDevitt, J.T. A Rapid and Sensitive Microfluidics-Based Tool for Seroprevalence Immunity Assessment of COVID-19 and Vaccination-Induced Humoral Antibody Response at the Point of Care. *Biosensors* **2022**, *12*, 621, doi:10.3390/bios12080621.
187. Maeki, M.; Uno, S.; Niwa, A.; Okada, Y.; Tokeshi, M. Microfluidic Technologies and Devices for Lipid Nanoparticle-Based RNA Delivery. *Journal of Controlled Release* **2022**, *344*, 80–96, doi:10.1016/j.jconrel.2022.02.017.
188. Ramezankhani, R.; Solhi, R.; Chai, Y.C.; Vosough, M.; Verfaillie, C. Organoid and Microfluidics-Based Platforms for Drug Screening in COVID-19. *Drug Discovery Today* **2022**, *27*, 1062–1076, doi:10.1016/j.drudis.2021.12.014.
189. Lopes, C.; Cristóvão, J.; Silvério, V.; Lino, P.R.; Fonte, P. Microfluidic Production of MRNA-Loaded Lipid Nanoparticles for Vaccine Applications. *Expert Opinion on Drug Delivery* **2022**, *19*, 1381–1395, doi:10.1080/17425247.2022.2135502.
190. Dolomite Homepage Available online: https://www.dolomite-microfluidics.com/ (accessed on 19 November 2022).
191. NxGen - A Disruptive Technology Enabling Transformative Medicine Available online: https://www.precisionnanosystems.com/platform-technologies/nxgen (accessed on 19 November 2022).
192. Automated Nanoparticle System | ALFATEST Materials Science Available online: https://www.alfatest.it/prodotti/automated-nanoparticle-system (accessed on 19 November 2022).
193. Prabhakar, P.; Sen, R.K.; Dwivedi, N.; Khan, R.; Solanki, P.R.; Srivastava, A.K.; Dhand, C. 3D-Printed Microfluidics and Potential Biomedical Applications. *Frontiers in Nanotechnology* **2021**, *3*.
194. Ballacchino, G.; Weaver, E.; Mathew, E.; Dorati, R.; Genta, I.; Conti, B.; Lamprou, D.A. Manufacturing of 3D-Printed Microfluidic Devices for the Synthesis of Drug-Loaded Liposomal Formulations. *International Journal of Molecular Sciences* **2021**, *22*, 8064, doi:10.3390/ijms22158064.
195. Kotouček, J.; Hubatka, F.; Mašek, J.; Kulich, P.; Velínská, K.; Bezděková, J.; Fojtíková, M.; Bartheldyová, E.; Tomečková, A.; Stráská, J.; et al. Preparation of

Nanoliposomes by Microfluidic Mixing in Herring-Bone Channel and the Role of Membrane Fluidity in Liposomes Formation. *Sci Rep* **2020**, *10*, 5595, doi:10.1038/s41598-020-62500-2.
196. Shah, V.M.; Dorrell, C.; Al-Fatease, A.; Allen-Petersen, B.L.; Woo, Y.; Bortnyak, Y.; Gheewala, R.; Sheppard, B.C.; Sears, R.C.; Alani, A.W. Microfluidics Formulated Liposomes of Hypoxia Activated Prodrug for Treatment of Pancreatic Cancer. *Pharmaceutics* **2022**, *14*, 713, doi:10.3390/pharmaceutics14040713.
197. Xu, R.; Tomeh, M.A.; Ye, S.; Zhang, P.; Lv, S.; You, R.; Wang, N.; Zhao, X. Novel Microfluidic Swirl Mixers for Scalable Formulation of Curcumin Loaded Liposomes for Cancer Therapy. *International Journal of Pharmaceutics* **2022**, *622*, 121857, doi:10.1016/j.ijpharm.2022.121857.
198. Han, J.Y.; La Fiandra, J.N.; DeVoe, D.L. Microfluidic Vortex Focusing for High Throughput Synthesis of Size-Tunable Liposomes. *Nat Commun* **2022**, *13*, 6997, doi:10.1038/s41467-022-34750-3.
199. Zhang, G.; Sun, J. Lipid in Chips: A Brief Review of Liposomes Formation by Microfluidics. *Int J Nanomedicine* **2021**, *16*, 7391–7416, doi:10.2147/IJN.S331639.
200. Friedrichs, S.; Bowman, D.M. COVID-19 May Become Nanomedicine's Finest Hour yet. *Nat. Nanotechnol.* **2021**, *16*, 362–364, doi:10.1038/s41565-021-00901-8.
201. Schoenmaker, L.; Witzigmann, D.; Kulkarni, J.A.; Verbeke, R.; Kersten, G.; Jiskoot, W.; Crommelin, D.J.A. MRNA-Lipid Nanoparticle COVID-19 Vaccines: Structure and Stability. *Int J Pharm* **2021**, *601*, 120586, doi:10.1016/j.ijpharm.2021.120586.
202. Shepherd, S.J.; Issadore, D.; Mitchell, M.J. Microfluidic Formulation of Nanoparticles for Biomedical Applications. *Biomaterials* **2021**, *274*, 120826, doi:10.1016/j.biomaterials.2021.120826.
203. Shah, V.M.; Nguyen, D.X.; Patel, P.; Cote, B.; Al-Fatease, A.; Pham, Y.; Huynh, M.G.; Woo, Y.; Alani, A.W. Liposomes Produced by Microfluidics and Extrusion: A Comparison for Scale-up Purposes. *Nanomedicine: Nanotechnology, Biology and Medicine* **2019**, *18*, 146–156, doi:10.1016/j.nano.2019.02.019.
204. Carvalho, B.G.; Ceccato, B.T.; Michelon, M.; Han, S.W.; de la Torre, L.G. Advanced Microfluidic Technologies for Lipid Nano-Microsystems from Synthesis to Biological Application. *Pharmaceutics* **2022**, *14*, 141, doi:10.3390/pharmaceutics14010141.
205. Tengjisi; Hui, Y.; Fan, Y.; Zou, D.; Talbo, G.H.; Yang, G.; Zhao, C.-X. Influence of Nanoparticle Mechanical Property on Protein Corona Formation. *Journal of Colloid and Interface Science* **2022**, *606*, 1737–1744, doi:10.1016/j.jcis.2021.08.148.
206. Bilardo, R.; Traldi, F.; Vdovchenko, A.; Resmini, M. Influence of Surface Chemistry and Morphology of Nanoparticles on Protein Corona Formation. *WIREs Nanomedicine and Nanobiotechnology* **2022**, *14*, e1788, doi:10.1002/wnan.1788.
207. Kamaly, N.; Farokhzad, O.C.; Corbo, C. Nanoparticle Protein Corona Evolution: From Biological Impact to Biomarker Discovery. *Nanoscale* **2022**, *14*, 1606–1620, doi:10.1039/D1NR06580G.
208. Richtering, W.; Alberg, I.; Zentel, R. Nanoparticles in the Biological Context: Surface Morphology and Protein Corona Formation. *Small* **2020**, *16*, 2002162, doi:10.1002/smll.202002162.
209. Baimanov, D.; Cai, R.; Chen, C. Understanding the Chemical Nature of Nanoparticle–Protein Interactions. *Bioconjugate Chem.* **2019**, *30*, 1923–1937, doi:10.1021/acs.bioconjchem.9b00348.
210. Pareek, V.; Bhargava, A.; Bhanot, V.; Gupta, R.; Jain, N.; Panwar, J. Formation and Characterization of Protein Corona Around Nanoparticles: A Review. *j nanosci nanotechnol* **2018**, *18*, 6653–6670, doi:10.1166/jnn.2018.15766.

211. Lundqvist, M.; Cedervall, T. Three Decades of Research about the Corona Around Nanoparticles: Lessons Learned and Where to Go Now. *Small* **2020**, *16*, 2000892, doi:10.1002/smll.202000892.
212. García-Álvarez, R.; Vallet-Regí, M. Hard and Soft Protein Corona of Nanomaterials: Analysis and Relevance. *Nanomaterials* **2021**, *11*, 888, doi:10.3390/nano11040888.
213. Mishra, R.K.; Ahmad, A.; Vyawahare, A.; Alam, P.; Khan, T.H.; Khan, R. Biological Effects of Formation of Protein Corona onto Nanoparticles. *International Journal of Biological Macromolecules* **2021**, *175*, 1–18, doi:10.1016/j.ijbiomac.2021.01.152.
214. Mohammad-Beigi, H.; Hayashi, Y.; Zeuthen, C.M.; Eskandari, H.; Scavenius, C.; Juul-Madsen, K.; Vorup-Jensen, T.; Enghild, J.J.; Sutherland, D.S. Mapping and Identification of Soft Corona Proteins at Nanoparticles and Their Impact on Cellular Association. *Nat Commun* **2020**, *11*, 4535, doi:10.1038/s41467-020-18237-7.
215. Li, Y.; Lee, J.-S. Insights into Characterization Methods and Biomedical Applications of Nanoparticle–Protein Corona. *Materials* **2020**, *13*, 3093, doi:10.3390/ma13143093.
216. Yang, M.; Wu, E.; Tang, W.; Qian, J.; Zhan, C. Interplay between Nanomedicine and Protein Corona. *J. Mater. Chem. B* **2021**, *9*, 6713–6727, doi:10.1039/D1TB01063H.
217. Xiao, W.; Wang, Y.; Zhang, H.; Liu, Y.; Xie, R.; He, X.; Zhou, Y.; Liang, L.; Gao, H. The Protein Corona Hampers the Transcytosis of Transferrin-Modified Nanoparticles through Blood–Brain Barrier and Attenuates Their Targeting Ability to Brain Tumor. *Biomaterials* **2021**, *274*, 120888, doi:10.1016/j.biomaterials.2021.120888.
218. Mosquera, J.; García, I.; Henriksen-Lacey, M.; González-Rubio, G.; Liz-Marzán, L.M. Reducing Protein Corona Formation and Enhancing Colloidal Stability of Gold Nanoparticles by Capping with Silica Monolayers. *Chem. Mater.* **2019**, *31*, 57–61, doi:10.1021/acs.chemmater.8b04647.
219. Khramtsov, P.; Barkina, I.; Kropaneva, M.; Bochkova, M.; Timganova, V.; Nechaev, A.; Byzov, I.; Zamorina, S.; Yermakov, A.; Rayev, M. Magnetic Nanoclusters Coated with Albumin, Casein, and Gelatin: Size Tuning, Relaxivity, Stability, Protein Corona, and Application in Nuclear Magnetic Resonance Immunoassay. *Nanomaterials* **2019**, *9*, 1345, doi:10.3390/nano9091345.
220. Mahmoudi, M. The Need for Improved Methodology in Protein Corona Analysis. *Nat Commun* **2022**, *13*, 49, doi:10.1038/s41467-021-27643-4.
221. Ashby, J.; Pan, S.; Zhong, W. Size and Surface Functionalization of Iron Oxide Nanoparticles Influence the Composition and Dynamic Nature of Their Protein Corona. *ACS Appl. Mater. Interfaces* **2014**, *6*, 15412–15419, doi:10.1021/am503909q.
222. Austefjord, M.W.; Gerdes, H.-H.; Wang, X. Tunneling Nanotubes. *Communicative & Integrative Biology* **2014**, *7*, e27934, doi:10.4161/cib.27934.
223. Ljubojevic, N.; Henderson, J.M.; Zurzolo, C. The Ways of Actin: Why Tunneling Nanotubes Are Unique Cell Protrusions. *Trends in Cell Biology* **2021**, *31*, 130–142, doi:10.1016/j.tcb.2020.11.008.
224. Zurzolo, C. Tunneling Nanotubes: Reshaping Connectivity. *Current Opinion in Cell Biology* **2021**, *71*, 139–147, doi:10.1016/j.ceb.2021.03.003.
225. Gerdes, H.-H.; Rustom, A.; Wang, X. Tunneling Nanotubes, an Emerging Intercellular Communication Route in Development. *Mechanisms of Development* **2013**, *130*, 381–387, doi:10.1016/j.mod.2012.11.006.
226. Mittal, R.; Karhu, E.; Wang, J.-S.; Delgado, S.; Zukerman, R.; Mittal, J.; Jhaveri, V.M. Cell Communication by Tunneling Nanotubes: Implications in Disease and Therapeutic Applications. *Journal of Cellular Physiology* **2019**, *234*, 1130–1146, doi:10.1002/jcp.27072.

227. Hurtig, J.; Chiu, D.T.; Önfelt, B. Intercellular Nanotubes: Insights from Imaging Studies and beyond: Intercellular Nanotubes. *WIREs Nanomed Nanobiotechnol* **2010**, *2*, 260–276, doi:10.1002/wnan.80.
228. Pinto, G.; Brou, C.; Zurzolo, C. Tunneling Nanotubes: The Fuel of Tumor Progression? *Trends in Cancer* **2020**, S2405803320301552, doi:10.1016/j.trecan.2020.04.012.
229. Tantra, R.; Oksel, C.; Puzyn, T.; Wang, J.; Robinson, K.N.; Wang, X.Z.; Ma, C.Y.; Wilkins, T. Nano(Q)SAR: Challenges, Pitfalls and Perspectives. *Nanotoxicology* **2015**, *9*, 636–642, doi:10.3109/17435390.2014.952698.
230. Baig, M.H.; Ahmad, K.; Roy, S.; Ashraf, J.M.; Adil, M.; Siddiqui, M.H.; Khan, S.; Kamal, M.A.; Provazník, I.; Choi, I. Computer Aided Drug Design: Success and Limitations. *Curr Pharm Des* **2016**, *22*, 572–581, doi:10.2174/1381612822666151125000550.
231. Li, J.; Crowley, S.T.; Duskey, J.; Khargharia, S.; Wu, M.; Rice, K.G. Miniaturization of Gene Transfection Assays in 384- and 1536-Well Microplates. *Analytical Biochemistry* **2015**, *470*, 14–21, doi:10.1016/j.ab.2014.10.001.
232. Duskey, J.T.; Belletti, D.; Pederzoli, F.; Vandelli, M.A.; Forni, F.; Ruozi, B.; Tosi, G. Current Strategies for the Delivery of Therapeutic Proteins and Enzymes to Treat Brain Disorders. *Int Rev Neurobiol* **2017**, *137*, 1–28, doi:10.1016/bs.irn.2017.08.006.
233. Tosi, G.; Duskey, J.T.; Kreuter, J. Nanoparticles as Carriers for Drug Delivery of Macromolecules across the Blood-Brain Barrier. *Expert Opinion on Drug Delivery* **2020**, *17*, 23–32, doi:10.1080/17425247.2020.1698544.
234. Hoyos-Ceballos, G.P.; Ruozi, B.; Ottonelli, I.; Da Ros, F.; Vandelli, M.A.; Forni, F.; Daini, E.; Vilella, A.; Zoli, M.; Tosi, G.; et al. PLGA-PEG-ANG-2 Nanoparticles for Blood–Brain Barrier Crossing: Proof-of-Concept Study. *Pharmaceutics* **2020**, *12*, 72, doi:10.3390/pharmaceutics12010072.
235. Oddone, N.; Pederzoli, F.; Duskey, J.T.; De Benedictis, C.A.; Grabrucker, A.M.; Forni, F.; Angela Vandelli, M.; Ruozi, B.; Tosi, G. ROS-Responsive "Smart" Polymeric Conjugate: Synthesis, Characterization and Proof-of-Concept Study. *International Journal of Pharmaceutics* **2019**, *570*, 118655, doi:10.1016/j.ijpharm.2019.118655.
236. Liu, J.; Postupalenko, V.; Duskey, J.T.; Palivan, C.G.; Meier, W. PH-Triggered Reversible Multiple Protein-Polymer Conjugation Based on Molecular Recognition. *J Phys Chem B* **2015**, *119*, 12066–12073, doi:10.1021/acs.jpcb.5b06637.
237. Dinu, I.A.; Duskey, J.T.; Car, A.; Palivan, C.G.; Meier, W. Engineered Non-Toxic Cationic Nanocarriers with Photo-Triggered Slow-Release Properties. *Polym. Chem.* **2016**, *7*, 3451–3464, doi:10.1039/C6PY00343E.
238. Khargharia, S.; Baumhover, N.J.; Crowley, S.T.; Duskey, J.; Rice, K.G. The Uptake Mechanism of PEGylated DNA Polyplexes by the Liver Influences Gene Expression. *Gene Therapy* **2014**, *21*, 1021–1028, doi:10.1038/gt.2014.81.
239. Najer, A.; Thamboo, S.; Duskey, J.T.; Palivan, C.G.; Beck, H.-P.; Meier, W. Analysis of Molecular Parameters Determining the Antimalarial Activity of Polymer-Based Nanomimics. *Macromol Rapid Commun* **2015**, *36*, 1923–1928, doi:10.1002/marc.201500267.
240. Tosi, G.; Pederzoli, F.; Belletti, D.; Vandelli, M.A.; Forni, F.; Duskey, J.T.; Ruozi, B. Nanomedicine in Alzheimer's Disease: Amyloid Beta Targeting Strategy. *Prog Brain Res* **2019**, *245*, 57–88, doi:10.1016/bs.pbr.2019.03.001.
241. Pederzoli, F.; Ruozi, B.; Duskey, J.; Hagmeyer, S.; Sauer, A.K.; Grabrucker, S.; Coelho, R.; Oddone, N.; Ottonelli, I.; Daini, E.; et al. Nanomedicine Against Aβ Aggregation by β-Sheet Breaker Peptide Delivery: In Vitro Evidence. *Pharmaceutics* **2019**, *11*, E572, doi:10.3390/pharmaceutics11110572.

242. Danhier, F.; Ansorena, E.; Silva, J.M.; Coco, R.; Le Breton, A.; Préat, V. PLGA-Based Nanoparticles: An Overview of Biomedical Applications. *J Control Release* **2012**, *161*, 505–522, doi:10.1016/j.jconrel.2012.01.043.
243. Rezvantalab, S.; Drude, N.I.; Moraveji, M.K.; Güvener, N.; Koons, E.K.; Shi, Y.; Lammers, T.; Kiessling, F. PLGA-Based Nanoparticles in Cancer Treatment. *Front Pharmacol* **2018**, *9*, 1260, doi:10.3389/fphar.2018.01260.
244. Kim, K.-T.; Lee, J.-Y.; Kim, D.-D.; Yoon, I.-S.; Cho, H.-J. Recent Progress in the Development of Poly(Lactic-Co-Glycolic Acid)-Based Nanostructures for Cancer Imaging and Therapy. *Pharmaceutics* **2019**, *11*, E280, doi:10.3390/pharmaceutics11060280.
245. Li, X.; Jiang, X. Microfluidics for Producing Poly (Lactic-Co-Glycolic Acid)-Based Pharmaceutical Nanoparticles. *Advanced Drug Delivery Reviews* **2018**, *128*, 101–114, doi:10.1016/j.addr.2017.12.015.
246. Midoux, P.; Pichon, C.; Yaouanc, J.-J.; Jaffrès, P.-A. Chemical Vectors for Gene Delivery: A Current Review on Polymers, Peptides and Lipids Containing Histidine or Imidazole as Nucleic Acids Carriers. *British Journal of Pharmacology* **2009**, *157*, 166–178, doi:10.1111/j.1476-5381.2009.00288.x.
247. Chakravarthi, S.S.; Robinson, D.H. Enhanced Cellular Association of Paclitaxel Delivered in Chitosan-PLGA Particles. *International Journal of Pharmaceutics* **2011**, *409*, 111–120, doi:10.1016/j.ijpharm.2011.02.034.
248. Simon, L.C.; Stout, R.W.; Sabliov, C. Bioavailability of Orally Delivered Alpha-Tocopherol by Poly(Lactic-Co-Glycolic) Acid (PLGA) Nanoparticles and Chitosan Covered PLGA Nanoparticles in F344 Rats. *Nanobiomedicine (Rij)* **2016**, *3*, 8, doi:10.5772/63305.
249. Chung, Y.-I.; Kim, J.C.; Kim, Y.H.; Tae, G.; Lee, S.-Y.; Kim, K.; Kwon, I.C. The Effect of Surface Functionalization of PLGA Nanoparticles by Heparin- or Chitosan-Conjugated Pluronic on Tumor Targeting. *Journal of Controlled Release* **2010**, *143*, 374–382, doi:10.1016/j.jconrel.2010.01.017.
250. Nafee, N.; Taetz, S.; Schneider, M.; Schaefer, U.F.; Lehr, C.-M. Chitosan-Coated PLGA Nanoparticles for DNA/RNA Delivery: Effect of the Formulation Parameters on Complexation and Transfection of Antisense Oligonucleotides. *Nanomedicine: Nanotechnology, Biology and Medicine* **2007**, *3*, 173–183, doi:10.1016/j.nano.2007.03.006.
251. Li, A.D.; Sun, Z.Z.; Zhou, M.; Xu, X.X.; Ma, J.Y.; Zheng, W.; Zhou, H.M.; Li, L.; Zheng, Y.F. Electrospun Chitosan-Graft-PLGA Nanofibres with Significantly Enhanced Hydrophilicity and Improved Mechanical Property. *Colloids Surf B Biointerfaces* **2013**, *102*, 674–681, doi:10.1016/j.colsurfb.2012.09.035.
252. Cai, G.; Jiang, H.; Tu, K.; Wang, L.; Zhu, K. A Facile Route for Regioselective Conjugation of Organo-Soluble Polymers onto Chitosan. *Macromolecular Bioscience* **2009**, *9*, 256–261, doi:10.1002/mabi.200800153.
253. Thakur, C.K.; Thotakura, N.; Kumar, R.; Kumar, P.; Singh, B.; Chitkara, D.; Raza, K. Chitosan-Modified PLGA Polymeric Nanocarriers with Better Delivery Potential for Tamoxifen. *Int J Biol Macromol* **2016**, *93*, 381–389, doi:10.1016/j.ijbiomac.2016.08.080.
254. Branca, C.; D'Angelo, G.; Crupi, C.; Khouzami, K.; Rifici, S.; Ruello, G.; Wanderlingh, U. Role of the OH and NH Vibrational Groups in Polysaccharide-Nanocomposite Interactions: A FTIR-ATR Study on Chitosan and Chitosan/Clay Films. *Polymer* **2016**, *99*, 614–622, doi:10.1016/j.polymer.2016.07.086.
255. Vey, E.; Rodger, C.; Booth, J.; Claybourn, M.; Miller, A.F.; Saiani, A. Degradation Kinetics of Poly(Lactic-Co-Glycolic) Acid Block Copolymer Cast Films in Phosphate Buffer Solution as Revealed by Infrared and Raman Spectroscopies. *Polymer Degradation and Stability* **2011**, *96*, 1882–1889, doi:10.1016/j.polymdegradstab.2011.07.011.

256. Piyamongkala, K.; Mekasut, L.; Pongstabodee, S. Cutting Fluid Effluent Removal by Adsorption on Chitosan and Sds-Modified Chitosan. *Macromol. Res.* **2008**, *16*, 492–502, doi:10.1007/BF03218550.
257. Ma, F.K.; Li, J.; Kong, M.; Liu, Y.; An, Y.; Chen, X.G. Preparation and Hydrolytic Erosion of Differently Structured PLGA Nanoparticles with Chitosan Modification. *Int J Biol Macromol* **2013**, *54*, 174–179, doi:10.1016/j.ijbiomac.2012.12.019.
258. Heux, L.; Brugnerotto, J.; Desbrières, J.; Versali, M.F.; Rinaudo, M. Solid State NMR for Determination of Degree of Acetylation of Chitin and Chitosan. *Biomacromolecules* **2000**, *1*, 746–751, doi:10.1021/bm000070y.
259. Grabowski, G.A.; Leslie, N.; Wenstrup, R. Enzyme Therapy for Gaucher Disease: The First 5 Years. *Blood Rev.* **1998**, *12*, 115–133, doi:10.1016/s0268-960x(98)90023-6.
260. Eng, C.M.; Guffon, N.; Wilcox, W.R.; Germain, D.P.; Lee, P.; Waldek, S.; Caplan, L.; Linthorst, G.E.; Desnick, R.J. Safety and Efficacy of Recombinant Human $\alpha$-Galactosidase A Replacement Therapy in Fabry's Disease. *New England Journal of Medicine* **2001**, *345*, 9–16, doi:10.1056/NEJM200107053450102.
261. Van den Hout, H.; Reuser, A.J.; Vulto, A.G.; Loonen, M.C.; Cromme-Dijkhuis, A.; Van der Ploeg, A.T. Recombinant Human Alpha-Glucosidase from Rabbit Milk in Pompe Patients. *Lancet* **2000**, *356*, 397–398, doi:10.1016/s0140-6736(00)02533-2.
262. Safary, A.; Akbarzadeh Khiavi, M.; Mousavi, R.; Barar, J.; Rafi, M.A. Enzyme Replacement Therapies: What Is the Best Option? *Bioimpacts* **2018**, *8*, 153–157, doi:10.15171/bi.2018.17.
263. Barar, J.; Aghanejad, A.; Fathi, M.; Omidi, Y. Advanced Drug Delivery and Targeting Technologies for the Ocular Diseases. *Bioimpacts* **2016**, *6*, 49–67, doi:10.15171/bi.2016.07.
264. Muro, S. New Biotechnological and Nanomedicine Strategies for Treatment of Lysosomal Storage Disorders. *WIREs Nanomedicine and Nanobiotechnology* **2010**, *2*, 189–204, doi:10.1002/wnan.73.
265. Tam, V.H.; Sosa, C.; Liu, R.; Yao, N.; Priestley, R.D. Nanomedicine as a Non-Invasive Strategy for Drug Delivery across the Blood Brain Barrier. *Int J Pharm* **2016**, *515*, 331–342, doi:10.1016/j.ijpharm.2016.10.031.
266. Gasper, M.M.; Blanco, D.; Cruz, M.E.; Alonso, M.J. Formulation of L-Asparaginase-Loaded Poly(Lactide-Co-Glycolide) Nanoparticles: Influence of Polymer Properties on Enzyme Loading, Activity and in Vitro Release. *J Control Release* **1998**, *52*, 53–62, doi:10.1016/s0168-3659(97)00196-x.
267. Martins, M.B.F.; Simões, S.I.D.; Cruz, M.E.M.; Gaspar, R. Development of Enzyme-Loaded Nanoparticles: Effect of PH. *J Mater Sci: Mater Med* **1996**, *7*, 413–414, doi:10.1007/BF00122010.
268. Rietscher, R.; Czaplewska, J.A.; Majdanski, T.C.; Gottschaldt, M.; Schubert, U.S.; Schneider, M.; Lehr, C.-M. Impact of PEG and PEG-b-PAGE Modified PLGA on Nanoparticle Formation, Protein Loading and Release. *Int J Pharm* **2016**, *500*, 187–195, doi:10.1016/j.ijpharm.2016.01.021.
269. Crucho, C.I.C.; Barros, M.T. Polymeric Nanoparticles: A Study on the Preparation Variables and Characterization Methods. *Mater Sci Eng C Mater Biol Appl* **2017**, *80*, 771–784, doi:10.1016/j.msec.2017.06.004.
270. Crotts, G.; Park, T.G. Protein Delivery from Poly(Lactic-Co-Glycolic Acid) Biodegradable Microspheres: Release Kinetics and Stability Issues. *J Microencapsul* **1998**, *15*, 699–713, doi:10.3109/02652049809008253.
271. van de Weert, M.; Hennink, W.E.; Jiskoot, W. Protein Instability in Poly(Lactic-Co-Glycolic Acid) Microparticles. *Pharm Res* **2000**, *17*, 1159–1167, doi:10.1023/A:1026498209874.

272. Pérez, C.; Castellanos, I.J.; Costantino, H.R.; Al-Azzam, W.; Griebenow, K. Recent Trends in Stabilizing Protein Structure upon Encapsulation and Release from Bioerodible Polymers. *Journal of Pharmacy and Pharmacology* **2002**, *54*, 301–313, doi:10.1211/0022357021778448.
273. Taurozzi, J.S.; Hackley, V.A.; Wiesner, M.R. Ultrasonic Dispersion of Nanoparticles for Environmental, Health and Safety Assessment--Issues and Recommendations. *Nanotoxicology* **2011**, *5*, 711–729, doi:10.3109/17435390.2010.528846.
274. Roy, I.; Gupta, M.N. Freeze-Drying of Proteins: Some Emerging Concerns. *Biotechnology and Applied Biochemistry* **2004**, *39*, 165–177, doi:10.1042/BA20030133.
275. Shulgin, I.L.; Ruckenstein, E. Preferential Hydration and Solubility of Proteins in Aqueous Solutions of Polyethylene Glycol. *Biophysical Chemistry* **2006**, *120*, 188–198, doi:10.1016/j.bpc.2005.11.010.
276. Silva, C.; Martins, M.; Jing, S.; Fu, J.; Cavaco-Paulo, A. Practical Insights on Enzyme Stabilization. *Critical Reviews in Biotechnology* **2018**, *38*, 335–350, doi:10.1080/07388551.2017.1355294.
277. Han, J.; Wang, Q.; Zhang, Z.; Gong, T.; Sun, X. Cationic Bovine Serum Albumin Based Self-Assembled Nanoparticles as SiRNA Delivery Vector for Treating Lung Metastatic Cancer. *Small* **2014**, *10*, 524–535, doi:10.1002/smll.201301992.
278. Jain, N.; Bhargava, A.; Rathi, M.; Dilip, R.V.; Panwar, J. Removal of Protein Capping Enhances the Antibacterial Efficiency of Biosynthesized Silver Nanoparticles. *PLoS One* **2015**, *10*, doi:10.1371/journal.pone.0134337.
279. Prabhu, V.; Uzzaman, S.; Grace, V.M.B.; Guruvayoorappan, C. Nanoparticles in Drug Delivery and Cancer Therapy: The Giant Rats Tail. *Journal of Cancer Therapy* **2011**, *2*, 325–334, doi:10.4236/jct.2011.23045.
280. Sarett, S.M.; Werfel, T.A.; Lee, L.; Jackson, M.A.; Kilchrist, K.V.; Brantley-Sieders, D.; Duvall, C.L. Lipophilic SiRNA Targets Albumin in Situ and Promotes Bioavailability, Tumor Penetration, and Carrier-Free Gene Silencing. *Proc. Natl. Acad. Sci. U.S.A.* **2017**, *114*, E6490–E6497, doi:10.1073/pnas.1621240114.
281. Bs, C.; Rr, M. Enzyme Thermostabilization by Bovine Serum Albumin and Other Proteins: Evidence for Hydrophobic Interactions. *Biotechnology and Applied Biochemistry* **1995**, *22*, 203–214, doi:10.1111/j.1470-8744.1995.tb00346.x.
282. Hong, T.; Iwashita, K.; Shiraki, K. Viscosity Control of Protein Solution by Small Solutes: A Review. *Curr. Protein Pept. Sci.* **2018**, *19*, 746–758, doi:10.2174/1389203719666171213114919.
283. Jachimska, B.; Pajor, A. Physico-Chemical Characterization of Bovine Serum Albumin in Solution and as Deposited on Surfaces. *Bioelectrochemistry* **2012**, *87*, 138–146, doi:10.1016/j.bioelechem.2011.09.004.
284. Wang, L.; Yu, H. Chain Conformation of Linear Polyelectrolyte in Salt Solutions: Sodium Poly(Styrenesulfonate) in Potassium Chloride and Sodium Chloride. *Macromolecules* **1988**, *21*, 3498–3501, doi:10.1021/ma00190a026.
285. Belletti, D.; Tosi, G.; Riva, G.; Lagreca, I.; Galliania, M.; Luppi, M.; Vandelli, M.A.; Forni, F.; Ruozi, B. Nutlin-3 Loaded Nanocarriers: Preparation, Characterization and in Vitro Antineoplastic Effect against Primary Effusion Lymphoma. *Int J Pharm* **2015**, *490*, 85–93, doi:10.1016/j.ijpharm.2015.05.029.
286. Chhabra, R.; Grabrucker, A.M.; Veratti, P.; Belletti, D.; Boeckers, T.M.; Vandelli, M.A.; Forni, F.; Tosi, G.; Ruozi, B. Characterization of Lysosome-Destabilizing DOPE/PLGA Nanoparticles Designed for Cytoplasmic Drug Release. *Int J Pharm* **2014**, *471*, 349–357, doi:10.1016/j.ijpharm.2014.05.054.

287. Yoshioka, S.; Aso, Y.; Izutsu, K.; Terao, T. The Effect of Salts on the Stability of β-Galactosidase in Aqueous Solution, as Related to the Water Mobility. *Pharm Res* **1993**, *10*, 1484–1487, doi:10.1023/A:1018931527176.
288. Vilella, A.; Tosi, G.; Grabrucker, A.M.; Ruozi, B.; Belletti, D.; Vandelli, M.A.; Boeckers, T.M.; Forni, F.; Zoli, M. Insight on the Fate of CNS-Targeted Nanoparticles. Part I: Rab5-Dependent Cell-Specific Uptake and Distribution. *Journal of Controlled Release* **2014**, *174*, 195–201, doi:10.1016/j.jconrel.2013.11.023.
289. Vilella, A.; Ruozi, B.; Belletti, D.; Pederzoli, F.; Galliani, M.; Semeghini, V.; Forni, F.; Zoli, M.; Vandelli, M.A.; Tosi, G. Endocytosis of Nanomedicines: The Case of Glycopeptide Engineered PLGA Nanoparticles. *Pharmaceutics* **2015**, *7*, 74–89, doi:10.3390/pharmaceutics7020074.
290. Yoshioka, S.; Aso, Y.; Izutsu, K.; Terao, T. Stability of Beta-Galactosidase, a Model Protein Drug, Is Related to Water Mobility as Measured by 17O Nuclear Magnetic Resonance (NMR). *Pharm Res* **1993**, *10*, 103–108, doi:10.1023/a:1018933315538.
291. Yoshioka, S.; Aso, Y.; Izutsu, K.; Kojima, S. Is Stability Prediction Possible for Protein Drugs? Denaturation Kinetics of Beta-Galactosidase in Solution. *Pharm Res* **1994**, *11*, 1721–1725, doi:10.1023/a:1018955031042.
292. Cohen-Sela, E.; Chorny, M.; Koroukhov, N.; Danenberg, H.D.; Golomb, G. A New Double Emulsion Solvent Diffusion Technique for Encapsulating Hydrophilic Molecules in PLGA Nanoparticles. *J Control Release* **2009**, *133*, 90–95, doi:10.1016/j.jconrel.2008.09.073.
293. Iqbal, M.; Zafar, N.; Fessi, H.; Elaissari, A. Double Emulsion Solvent Evaporation Techniques Used for Drug Encapsulation. *International Journal of Pharmaceutics* **2015**, *496*, 173–190, doi:10.1016/j.ijpharm.2015.10.057.
294. Garti, N.; Bisperink, C. Double Emulsions: Progress and Applications. *Current Opinion in Colloid & Interface Science* **1998**, *3*, 657–667, doi:10.1016/S1359-0294(98)80096-4.
295. Gegg, M.E.; Burke, D.; Heales, S.J.R.; Cooper, J.M.; Hardy, J.; Wood, N.W.; Schapira, A.H.V. Glucocerebrosidase Deficiency in Substantia Nigra of Parkinson Disease Brains. *Ann Neurol* **2012**, *72*, 455–463, doi:10.1002/ana.23614.
296. Mulvihill, J.J.; Cunnane, E.M.; Ross, A.M.; Duskey, J.T.; Tosi, G.; Grabrucker, A.M. Drug Delivery across the Blood–Brain Barrier: Recent Advances in the Use of Nanocarriers. *Nanomedicine* **2020**, *15*, 205–214, doi:10.2217/nnm-2019-0367.
297. Li Mindy Enzyme Replacement Therapy: A Review and Its Role in Treating Lysosomal Storage Diseases. *Pediatric Annals* **2018**, *47*, e191–e197, doi:10.3928/19382359-20180424-01.
298. Eisengart, J.B.; Jarnes, J.; Ahmed, A.; Nestrasil, I.; Ziegler, R.; Delaney, K.; Shapiro, E.; Whitley, C. Long-Term Cognitive and Somatic Outcomes of Enzyme Replacement Therapy in Untransplanted Hurler Syndrome. *Molecular Genetics and Metabolism Reports* **2017**, *13*, 64–68, doi:10.1016/j.ymgmr.2017.07.012.
299. Gaffke, L.; Pierzynowska, K.; Piotrowska, E.; Węgrzyn, G. How Close Are We to Therapies for Sanfilippo Disease? *Metab Brain Dis* **2018**, *33*, 1–10, doi:10.1007/s11011-017-0111-4.
300. Wiseman, J.A.; Meng, Y.; Nemtsova, Y.; Matteson, P.G.; Millonig, J.H.; Moore, D.F.; Sleat, D.E.; Lobel, P. Chronic Enzyme Replacement to the Brain of a Late Infantile Neuronal Ceroid Lipofuscinosis Mouse Has Differential Effects on Phenotypes of Disease. *Molecular Therapy - Methods & Clinical Development* **2017**, *4*, 204–212, doi:10.1016/j.omtm.2017.01.004.
301. Solovyeva, V.V.; Shaimardanova, A.A.; Chulpanova, D.S.; Kitaeva, K.V.; Chakrabarti, L.; Rizvanov, A.A. New Approaches to Tay-Sachs Disease Therapy. *Front Physiol* **2018**, *9*, 1663, doi:10.3389/fphys.2018.01663.

302. Kumari, A.; Yadav, S.K.; Yadav, S.C. Biodegradable Polymeric Nanoparticles Based Drug Delivery Systems. *Colloids and Surfaces B: Biointerfaces* **2010**, *75*, 1–18, doi:10.1016/j.colsurfb.2009.09.001.
303. Wraith, J.E. Limitations of Enzyme Replacement Therapy: Current and Future. *Journal of Inherited Metabolic Disease* **2006**, *29*, 442–447, doi:10.1007/s10545-006-0239-6.
304. Concolino, D.; Deodato, F.; Parini, R. Enzyme Replacement Therapy: Efficacy and Limitations. *Italian Journal of Pediatrics* **2018**, *44*, 120, doi:10.1186/s13052-018-0562-1.
305. Ries, M. Enzyme Replacement Therapy and beyond—in Memoriam Roscoe O. Brady, M.D. (1923–2016). *J Inherit Metab Dis* **2017**, *40*, 343–356, doi:10.1007/s10545-017-0032-8.
306. Nelemans, L.C.; Gurevich, L. Drug Delivery with Polymeric Nanocarriers—Cellular Uptake Mechanisms. *Materials* **2020**, *13*, 366, doi:10.3390/ma13020366.
307. Alven, S.; Aderibigbe, B.A. Efficacy of Polymer-Based Nanocarriers for Co-Delivery of Curcumin and Selected Anticancer Drugs. *Nanomaterials* **2020**, *10*, 1556, doi:10.3390/nano10081556.
308. Abasian, P.; Ghanavati, S.; Rahebi, S.; Khorasani, S.N.; Khalili, S. Polymeric Nanocarriers in Targeted Drug Delivery Systems: A Review. *Polymers for Advanced Technologies* **2020**, *31*, 2939–2954, doi:10.1002/pat.5031.
309. Venditti, I. Morphologies and Functionalities of Polymeric Nanocarriers as Chemical Tools for Drug Delivery: A Review. *Journal of King Saud University - Science* **2019**, *31*, 398–411, doi:10.1016/j.jksus.2017.10.004.
310. Avramović, N.; Mandić, B.; Savić-Radojević, A.; Simić, T. Polymeric Nanocarriers of Drug Delivery Systems in Cancer Therapy. *Pharmaceutics* **2020**, *12*, 298, doi:10.3390/pharmaceutics12040298.
311. Duskey, J.T.; Baraldi, C.; Gamberini, M.C.; Ottonelli, I.; Da Ros, F.; Tosi, G.; Forni, F.; Vandelli, M.A.; Ruozi, B. Investigating Novel Syntheses of a Series of Unique Hybrid PLGA-Chitosan Polymers for Potential Therapeutic Delivery Applications. *Polymers* **2020**, *12*, 823, doi:10.3390/polym12040823.
312. Oddone, N.; Boury, F.; Garcion, E.; Grabrucker, A.M.; Martinez, M.C.; Da Ros, F.; Janaszewska, A.; Forni, F.; Vandelli, M.A.; Tosi, G.; et al. Synthesis, Characterization, and In Vitro Studies of an Reactive Oxygen Species (ROS)-Responsive Methoxy Polyethylene Glycol-Thioketal-Melphalan Prodrug for Glioblastoma Treatment. *Front. Pharmacol.* **2020**, *11*, doi:10.3389/fphar.2020.00574.
313. Belletti, D.; Riva, G.; Luppi, M.; Tosi, G.; Forni, F.; Vandelli, M.A.; Ruozi, B.; Pederzoli, F. Anticancer Drug-Loaded Quantum Dots Engineered Polymeric Nanoparticles: Diagnosis/Therapy Combined Approach. *European Journal of Pharmaceutical Sciences* **2017**, *107*, 230–239, doi:10.1016/j.ejps.2017.07.020.
314. Birolini, G.; Valenza, M.; Ottonelli, I.; Passoni, A.; Favagrossa, M.; Duskey, J.T.; Bombaci, M.; Vandelli, M.A.; Colombo, L.; Bagnati, R.; et al. Insights into Kinetics, Release, and Behavioral Effects of Brain-Targeted Hybrid Nanoparticles for Cholesterol Delivery in Huntington's Disease. *Journal of Controlled Release* **2021**, *330*, 587–598, doi:10.1016/j.jconrel.2020.12.051.
315. Musumeci, T.; Bonaccorso, A.; Carbone, C.; Impallomeni, G.; Ballistreri, A.; Duskey, J.T.; Puglisi, G.; Pignatello, R. Development and Biocompatibility Assessments of Poly(3-Hydroxybutyrate-Co-ε-Caprolactone) Microparticles for Diclofenac Sodium Delivery. *Journal of Drug Delivery Science and Technology* **2020**, *60*, 102081, doi:10.1016/j.jddst.2020.102081.
316. Puiggalí-Jou, A.; del Valle, L.J.; Alemán, C. Encapsulation and Storage of Therapeutic Fibrin-Homing Peptides Using Conducting Polymer Nanoparticles for

Programmed Release by Electrical Stimulation. *ACS Biomater. Sci. Eng.* **2020**, *6*, 2135–2145, doi:10.1021/acsbiomaterials.9b01794.
317. Du, A.W.; Stenzel, M.H. Drug Carriers for the Delivery of Therapeutic Peptides. *Biomacromolecules* **2014**, *15*, 1097–1114, doi:10.1021/bm500169p.
318. Elsabahy, M.; Song, Y.; Eissa, N.G.; Khan, S.; Hamad, M.A.; Wooley, K.L. Morphologic Design of Sugar-Based Polymer Nanoparticles for Delivery of Antidiabetic Peptides. *Journal of Controlled Release* **2021**, *334*, 1–10, doi:10.1016/j.jconrel.2021.04.006.
319. Cózar-Bernal, M.J.; Holgado, M.A.; Arias, J.L.; Muñoz-Rubio, I.; Martín-Banderas, L.; Álvarez-Fuentes, J.; Fernández-Arévalo, M. Insulin-Loaded PLGA Microparticles: Flow Focusing versus Double Emulsion/Solvent Evaporation. *Journal of Microencapsulation* **2011**, *28*, 430–441, doi:10.3109/02652048.2011.576786.
320. Sigg, S.J.; Postupalenko, V.; Duskey, J.T.; Palivan, C.G.; Meier, W. Stimuli-Responsive Codelivery of Oligonucleotides and Drugs by Self-Assembled Peptide Nanoparticles. *Biomacromolecules* **2016**, *17*, 935–945, doi:10.1021/acs.biomac.5b01614.
321. Nussbaumer, M.G.; Duskey, J.T.; Rother, M.; Renggli, K.; Chami, M.; Bruns, N. Chaperonin-Dendrimer Conjugates for SiRNA Delivery. *Adv Sci (Weinh)* **2016**, *3*, 1600046, doi:10.1002/advs.201600046.
322. Zou, W.; Liu, C.; Chen, Z.; Zhang, N. Preparation and Characterization of Cationic PLA-PEG Nanoparticles for Delivery of Plasmid DNA. *Nanoscale Res Lett* **2009**, *4*, 982–992, doi:10.1007/s11671-009-9345-3.
323. Martinez, Nelida.Y.; Andrade, P.F.; Durán, N.; Cavalitto, S. Development of Double Emulsion Nanoparticles for the Encapsulation of Bovine Serum Albumin. *Colloids and Surfaces B: Biointerfaces* **2017**, *158*, 190–196, doi:10.1016/j.colsurfb.2017.06.033.
324. Jahangiri, A.; Barghi, L. Polymeric Nanoparticles: Review of Synthesis Methods and Applications in Drug Delivery. *Journal of advanced chemical and pharmaceutical materials (JACPM)* **2018**, *1*, 38–47.
325. Mohanty, S.; Panda, S.; Purohit, D.; Si, S.C. A Comprehensive Review on PLGA-Based Nanoparticles Used for Rheumatoid Arthritis. *Rese. Jour. of Pharm. and Technol.* **2019**, *12*, 1481, doi:10.5958/0974-360X.2019.00245.2.
326. Xu, Y.; Kim, C.-S.; Saylor, D.M.; Koo, D. Polymer Degradation and Drug Delivery in PLGA-Based Drug–Polymer Applications: A Review of Experiments and Theories. *Journal of Biomedical Materials Research Part B: Applied Biomaterials* **2017**, *105*, 1692–1716, doi:10.1002/jbm.b.33648.
327. Yaghoobi, N.; Faridi Majidi, R.; Faramarzi, M. ali; Baharifar, H.; Amani, A. Preparation, Optimization and Activity Evaluation of PLGA/Streptokinase Nanoparticles Using Electrospray. *Adv Pharm Bull* **2017**, *7*, 131–139, doi:10.15171/apb.2017.017.
328. Hasanpour, A.; Esmaeili, F.; Hosseini, H.; Amani, A. Use of MPEG-PLGA Nanoparticles to Improve Bioactivity and Hemocompatibility of Streptokinase: In-Vitro and in-Vivo Studies. *Materials Science and Engineering: C* **2021**, *118*, 111427, doi:10.1016/j.msec.2020.111427.
329. Ding, D.; Zhu, Q. Recent Advances of PLGA Micro/Nanoparticles for the Delivery of Biomacromolecular Therapeutics. *Materials Science and Engineering: C* **2018**, *92*, 1041–1060, doi:10.1016/j.msec.2017.12.036.
330. Mohammadpour, F.; Hadizadeh, F.; Tafaghodi, M.; Sadri, K.; Mohammadpour, A.H.; Kalani, M.R.; Gholami, L.; Mahmoudi, A.; Chamani, J. Preparation, in Vitro and in Vivo Evaluation of PLGA/Chitosan Based Nano-Complex as a Novel Insulin Delivery Formulation. *International Journal of Pharmaceutics* **2019**, *572*, 118710, doi:10.1016/j.ijpharm.2019.118710.

331. Kaplan, M.A.; Sergienko, K.V.; Kolmakova, A.A.; Konushkin, S.V.; Baikin, A.S.; Kolmakov, A.G.; Sevostyanov, M.A.; Kulikov, A.V.; Ivanov, V.E.; Belosludtsev, K.N.; et al. Development of a Biocompatible PLGA Polymers Capable to Release Thrombolytic Enzyme Prourokinase. *Journal of Biomaterials Science, Polymer Edition* **2020**, *31*, 1405–1420, doi:10.1080/09205063.2020.1760699.
332. Salvalaio, M.; Rigon, L.; Belletti, D.; D'Avanzo, F.; Pederzoli, F.; Ruozi, B.; Marin, O.; Vandelli, M.A.; Forni, F.; Scarpa, M.; et al. Targeted Polymeric Nanoparticles for Brain Delivery of High Molecular Weight Molecules in Lysosomal Storage Disorders. *PLoS ONE* **2016**, *11*, e0156452, doi:10.1371/journal.pone.0156452.
333. Yun, X.; Maximov, V.D.; Yu, J.; Zhu, g; Vertegel, A.A.; Kindy, M.S. Nanoparticles for Targeted Delivery of Antioxidant Enzymes to the Brain after Cerebral Ischemia and Reperfusion Injury. *J Cereb Blood Flow Metab* **2013**, *33*, 583–592, doi:10.1038/jcbfm.2012.209.
334. Schuster, T.; Mühlstein, A.; Yaghootfam, C.; Maksimenko, O.; Shipulo, E.; Gelperina, S.; Kreuter, J.; Gieselmann, V.; Matzner, U. Potential of Surfactant-Coated Nanoparticles to Improve Brain Delivery of Arylsulfatase A. *Journal of Controlled Release* **2017**, *253*, 1–10, doi:10.1016/j.jconrel.2017.02.016.
335. Primavessy, D.; Günday Türeli, N.; Schneider, M. Influence of Different Stabilizers on the Encapsulation of Desmopressin Acetate into PLGA Nanoparticles. *Eur J Pharm Biopharm* **2017**, *118*, 48–55, doi:10.1016/j.ejpb.2016.12.003.
336. Fonte, P.; Soares, S.; Sousa, F.; Costa, A.; Seabra, V.; Reis, S.; Sarmento, B. Stability Study Perspective of the Effect of Freeze-Drying Using Cryoprotectants on the Structure of Insulin Loaded into PLGA Nanoparticles. *Biomacromolecules* **2014**, *15*, 3753–3765, doi:10.1021/bm5010383.
337. Taghipour, B.; Yakhchali, M.; Haririan, I.; Tamaddon, A.M.; Samani, S.M. The Effects of Technical and Compositional Variables on the Size and Release Profile of Bovine Serum Albumin from PLGA Based Particulate Systems. *Res Pharm Sci* **2014**, *9*, 407–420.
338. Imamura, K.; Murai, K.; Korehisa, T.; Shimizu, N.; Yamahira, R.; Matsuura, T.; Tada, H.; Imanaka, H.; Ishida, N.; Nakanishi, K. Characteristics of Sugar Surfactants in Stabilizing Proteins During Freeze–Thawing and Freeze–Drying. *Journal of Pharmaceutical Sciences* **2014**, *103*, 1628–1637, doi:10.1002/jps.23988.
339. Paillard-Giteau, A.; Tran, V.T.; Thomas, O.; Garric, X.; Coudane, J.; Marchal, S.; Chourpa, I.; Benoît, J.P.; Montero-Menei, C.N.; Venier-Julienne, M.C. Effect of Various Additives and Polymers on Lysozyme Release from PLGA Microspheres Prepared by an s/o/w Emulsion Technique. *Eur J Pharm Biopharm* **2010**, *75*, 128–136, doi:10.1016/j.ejpb.2010.03.005.
340. Rosa, G.D.; Iommelli, R.; La Rotonda, M.I.; Miro, A.; Quaglia, F. Influence of the Co-Encapsulation of Different Non-Ionic Surfactants on the Properties of PLGA Insulin-Loaded Microspheres. *Journal of Controlled Release* **2000**, *69*, 283–295, doi:10.1016/S0168-3659(00)00315-1.
341. Duskey, J.T.; da Ros, F.; Ottonelli, I.; Zambelli, B.; Vandelli, M.A.; Tosi, G.; Ruozi, B. Enzyme Stability in Nanoparticle Preparations Part 1: Bovine Serum Albumin Improves Enzyme Function. *Molecules* **2020**, *25*, 4593, doi:10.3390/molecules25204593.
342. Saraswat, M.; Reddy, P.Y.; Muthenna, P.; Reddy, G.B. Prevention of Non-Enzymic Glycation of Proteins by Dietary Agents: Prospects for Alleviating Diabetic Complications. *British Journal of Nutrition* **2008**, *101*, 1714–1721, doi:10.1017/S0007114508116270.
343. Pirooznia, N.; Hasannia, S.; Lotfi, A.S.; Ghanei, M. Encapsulation of Alpha-1 Antitrypsin in PLGA Nanoparticles: In Vitro Characterization as an Effective Aerosol Formulation in Pulmonary Diseases. *Journal of Nanobiotechnology* **2012**, *10*, 20, doi:10.1186/1477-3155-10-20.

344. Iwai, J.; Ogawa, N.; Nagase, H.; Endo, T.; Loftsson, T.; Ueda, H. Effects of Various Cyclodextrins on the Stability of Freeze-Dried Lactate Dehydrogenase. *Journal of Pharmaceutical Sciences* **2007**, *96*, 3140–3143, doi:10.1002/jps.20847.
345. Osman, R.; Kan, P.L.; Awad, G.; Mortada, N.; EL-Shamy, A.-E.; Alpar, O. Enhanced Properties of Discrete Pulmonary Deoxyribonuclease I (DNaseI) Loaded PLGA Nanoparticles during Encapsulation and Activity Determination. *International Journal of Pharmaceutics* **2011**, *408*, 257–265, doi:10.1016/j.ijpharm.2011.02.013.
346. Atkins, D.L.; Magana, J.R.; Sproncken, C.C.M.; van Hest, J.C.M.; Voets, I.K. Single Enzyme Nanoparticles with Improved Biocatalytic Activity through Protein Entrapment in a Surfactant Shell. *Biomacromolecules* **2021**, *22*, 1159–1166, doi:10.1021/acs.biomac.0c01663.
347. Hans, M.L.; Lowman, A.M. Biodegradable Nanoparticles for Drug Delivery and Targeting. *Current Opinion in Solid State and Materials Science* **2002**, *6*, 319–327, doi:10.1016/S1359-0286(02)00117-1.
348. Astete, C.E.; Sabliov, C.M. Synthesis and Characterization of PLGA Nanoparticles. *Journal of Biomaterials Science, Polymer Edition* **2006**, *17*, 247–289, doi:10.1163/156856206775997322.
349. Arsiccio, A.; McCarty, J.; Pisano, R.; Shea, J.-E. Effect of Surfactants on Surface-Induced Denaturation of Proteins: Evidence of an Orientation-Dependent Mechanism. *J. Phys. Chem. B* **2018**, *122*, 11390–11399, doi:10.1021/acs.jpcb.8b07368.
350. Michelin, K.; Wajner, A.; Goulart, L. da S.; Fachel, Â.A.; Pereira, M.L.S.; de Mello, A.S.; Souza, F.T.S.; Pires, R.F.; Giugliani, R.; Coelho, J.C. Biochemical Study on β-Glucosidase in Individuals with Gaucher's Disease and Normal Subjects. *Clinica Chimica Acta* **2004**, *343*, 145–153, doi:10.1016/j.cccn.2004.01.010.
351. Belletti, D.; Grabrucker, A.M.; Pederzoli, F.; Menrath, I.; Vandelli, M.A.; Tosi, G.; Duskey, T.J.; Forni, F.; Ruozi, B. Hybrid Nanoparticles as a New Technological Approach to Enhance the Delivery of Cholesterol into the Brain. *International Journal of Pharmaceutics* **2018**, *543*, 300–310, doi:10.1016/j.ijpharm.2018.03.061.
352. Nayak, V.S.; Tan, Z.; Ihnat, P.M.; Russell, R.J.; Grace, M.J. Evaporative Light Scattering Detection Based HPLC Method for the Determination of Polysorbate 80 in Therapeutic Protein Formulations. *Journal of Chromatographic Science* **2012**, *50*, 21–25, doi:10.1093/chromsci/bmr015.
353. Yoshii, H.; Buche, F.; Takeuchi, N.; Terrol, C.; Ohgawara, M.; Furuta, T. Effects of Protein on Retention of ADH Enzyme Activity Encapsulated in Trehalose Matrices by Spray Drying. *Journal of Food Engineering* **2008**, *87*, 34–39, doi:10.1016/j.jfoodeng.2007.03.014.
354. Bhatt, P.C.; Verma, A.; Al-Abbasi, F.A.; Anwar, F.; Kumar, V.; Panda, B.P. Development of Surface-Engineered PLGA Nanoparticulate-Delivery System of Tet1-Conjugated Nattokinase Enzyme for Inhibition of Aβ40 Plaques in Alzheimer's Disease. *Int J Nanomedicine* **2017**, *12*, 8749–8768, doi:10.2147/IJN.S144545.
355. Reddy, M.K.; Wu, L.; Kou, W.; Ghorpade, A.; Labhasetwar, V. Superoxide Dismutase-Loaded PLGA Nanoparticles Protect Cultured Human Neurons Under Oxidative Stress. *Appl Biochem Biotechnol* **2008**, *151*, 565, doi:10.1007/s12010-008-8232-1.
356. Parenti, G.; Pignata, C.; Vajro, P.; Salerno, M. New Strategies for the Treatment of Lysosomal Storage Diseases (Review). *International Journal of Molecular Medicine* **2013**, *31*, 11–20, doi:10.3892/ijmm.2012.1187.
357. Ratko, T.A.; Marbella, A.; Godfrey, S.; Aronson, N. *Enzyme-Replacement Therapies for Lysosomal Storage Diseases*; Agency for Healthcare Research and Quality (US), 2013;

358. Ullman, J.C.; Arguello, A.; Getz, J.A.; Bhalla, A.; Mahon, C.S.; Wang, J.; Giese, T.; Bedard, C.; Kim, D.J.; Blumenfeld, J.R.; et al. Brain Delivery and Activity of a Lysosomal Enzyme Using a Blood-Brain Barrier Transport Vehicle in Mice. *Science Translational Medicine* **2020**, *12*, doi:10.1126/scitranslmed.aay1163.
359. Tang, R.; Kim, C.S.; Solfiell, D.J.; Rana, S.; Mout, R.; Velázquez-Delgado, E.M.; Chompoosor, A.; Jeong, Y.; Yan, B.; Zhu, Z.-J.; et al. Direct Delivery of Functional Proteins and Enzymes to the Cytosol Using Nanoparticle-Stabilized Nanocapsules. *ACS Nano* **2013**, *7*, 6667–6673, doi:10.1021/nn402753y.
360. Johnson, A.K.; Zawadzka, A.M.; Deobald, L.A.; Crawford, R.L.; Paszczynski, A.J. Novel Method for Immobilization of Enzymes to Magnetic Nanoparticles. *J Nanopart Res* **2008**, *10*, 1009–1025, doi:10.1007/s11051-007-9332-5.
361. Naeem, M.; Kim, W.; Cao, J.; Jung, Y.; Yoo, J.-W. Enzyme/PH Dual Sensitive Polymeric Nanoparticles for Targeted Drug Delivery to the Inflamed Colon. *Colloids and Surfaces B: Biointerfaces* **2014**, *123*, 271–278, doi:10.1016/j.colsurfb.2014.09.026.
362. Han, C.; Goodwine, J.; Romero, N.; Steck, K.S.; Sauer, K.; Doiron, A. Enzyme-Encapsulating Polymeric Nanoparticles: A Potential Adjunctive Therapy in Pseudomonas Aeruginosa Biofilm-Associated Infection Treatment. *Colloids and Surfaces B: Biointerfaces* **2019**, *184*, 110512, doi:10.1016/j.colsurfb.2019.110512.
363. Seidel, Z.P.; Lee, C.T. Enhanced Activity of the Cellulase Enzyme β-Glucosidase upon Addition of an Azobenzene-Based Surfactant. *ACS Sustainable Chem. Eng.* **2020**, *8*, 1751–1761, doi:10.1021/acssuschemeng.9b05240.
364. Otsuka, F.A.M.; Chagas, R.S.; Almeida, V.M.; Marana, S.R. Homodimerization of a Glycoside Hydrolase Family GH1 β-Glucosidase Suggests Distinct Activity of Enzyme Different States. *Protein Science* **2020**, *29*, 1879–1889, doi:10.1002/pro.3908.
365. Caramia, S.; Gatius, A.G.M.; dal Piaz, F.; Gaja, D.; Hochkoeppler, A. Dual Role of Imidazole as Activator/Inhibitor of Sweet Almond (Prunus Dulcis) β-Glucosidase. *Biochemistry and Biophysics Reports* **2017**, *10*, 137–144, doi:10.1016/j.bbrep.2017.03.007.
366. Yusuf, M.; Khan, M.; Alrobaian, M.M.; Alghamdi, S.A.; Warsi, M.H.; Sultana, S.; Khan, R.A. Brain Targeted Polysorbate-80 Coated PLGA Thymoquinone Nanoparticles for the Treatment of Alzheimer's Disease, with Biomechanistic Insights. *Journal of Drug Delivery Science and Technology* **2021**, *61*, 102214, doi:10.1016/j.jddst.2020.102214.
367. Hodaei, D.; Baradaran, B.; Valizadeh, H.; Mohammadnejad, L.; Zakeri, P. The Effect of Tween Excipients on Expression and Activity of P-Glycoprotein in Caco-2 Cells. *Pharmazeutische Industrie* **2014**, *76*, 788–794.
368. Yang, S.; Liu, J.; Chen, Y.; Jiang, J. Reversal Effect of Tween-20 on Multidrug Resistance in Tumor Cells in Vitro. *Biomedicine & Pharmacotherapy* **2012**, *66*, 187–194, doi:10.1016/j.biopha.2011.10.007.
369. Dimitrijevic, D.; Shaw, A.J.; Florence, A.T. Effects of Some Non-Ionic Surfactants on Transepithelial Permeability in Caco-2 Cells. *Journal of Pharmacy and Pharmacology* **2000**, *52*, 157–162, doi:10.1211/0022357001773805.
370. Scherließ, R. The MTT Assay as Tool to Evaluate and Compare Excipient Toxicity in Vitro on Respiratory Epithelial Cells. *International Journal of Pharmaceutics* **2011**, *411*, 98–105, doi:10.1016/j.ijpharm.2011.03.053.
371. Farkas, W.R.; Lorch, V.; Conover, W.R.; Al-Ansari, H.M.H.; Abney, L.K.; Painter, P.C.; Reyniers, J.P.; Congdon, C.C. Polysorbate Toxicity in Neonatal Rats and Mice. *Pharmacology & Toxicology* **1991**, *68*, 154–156, doi:10.1111/j.1600-0773.1991.tb02057.x.
372. Chaturvedi, M.; Molino, Y.; Sreedhar, B.; Khrestchatisky, M.; Kaczmarek, L. Tissue Inhibitor of Matrix Metalloproteinases-1 Loaded Poly(Lactic-Co-Glycolic Acid)

Nanoparticles for Delivery across the Blood–Brain Barrier. *Int J Nanomedicine* **2014**, *9*, 575–588, doi:10.2147/IJN.S54750.

373. Gelperina, S.; Maksimenko, O.; Khalansky, A.; Vanchugova, L.; Shipulo, E.; Abbasova, K.; Berdiev, R.; Wohlfart, S.; Chepurnova, N.; Kreuter, J. Drug Delivery to the Brain Using Surfactant-Coated Poly(Lactide-Co-Glycolide) Nanoparticles: Influence of the Formulation Parameters. *European Journal of Pharmaceutics and Biopharmaceutics* **2010**, *74*, 157–163, doi:10.1016/j.ejpb.2009.09.003.

374. Pardridge, W.M. The Blood-Brain Barrier: Bottleneck in Brain Drug Development. *Neurotherapeutics* **2005**, *2*, 3–14, doi:10.1602/neurorx.2.1.3.

375. Dong, X. Current Strategies for Brain Drug Delivery. *Theranostics* **2018**, *8*, 1481–1493, doi:10.7150/thno.21254.

376. Teleanu, D.; Chircov, C.; Grumezescu, A.; Volceanov, A.; Teleanu, R. Blood-Brain Delivery Methods Using Nanotechnology. *Pharmaceutics* **2018**, *10*, 269, doi:10.3390/pharmaceutics10040269.

377. Rueda, F.; Cruz, L.J. Targeting the Brain with Nanomedicine. *CPD* **2017**, *23*, 1879–1896, doi:10.2174/1381612822666161221153228.

378. Tosi, G.; Pederzoli, F.; Belletti, D.; Vandelli, M.A.; Forni, F.; Duskey, J.T.; Ruozi, B. Chapter 2 - Nanomedicine in Alzheimer's Disease: Amyloid Beta Targeting Strategy. In *Progress in Brain Research*; Sharma, A., Sharma, H.S., Eds.; Nanoneuroprotection and Nanoneurotoxicology; Elsevier, 2019; Vol. 245, pp. 57–88.

379. Ruozi, B.; Belletti, D.; Pederzoli, F.; Forni, F.; Angela Vandelli, M.; Tosi, G. Potential Use of Nanomedicine for Drug Delivery Across the Blood-Brain Barrier in Healthy and Diseased Brain. *CNSNDDT* **2016**, *15*, 1079–1091, doi:10.2174/1871527315666160915112210.

380. Jones, E.M.; Polt, R. CNS Active O-Linked Glycopeptides. *Front. Chem.* **2015**, *3*, doi:10.3389/fchem.2015.00040.

381. Polt, R.; Dhanasekaran, M.; Keyari, C.M. Glycosylated Neuropeptides: A New Vista for Neuropsychopharmacology? *Med. Res. Rev.* **2005**, *25*, 557–585, doi:10.1002/med.20039.

382. Oller-Salvia, B.; Sánchez-Navarro, M.; Giralt, E.; Teixidó, M. Blood–Brain Barrier Shuttle Peptides: An Emerging Paradigm for Brain Delivery. *Chem. Soc. Rev.* **2016**, *45*, 4690–4707, doi:10.1039/C6CS00076B.

383. Oehlke, J.; Krause, E.; Wiesner, B.; Beyermann, M.; Bienert, M. Extensive Cellular Uptake into Endothelial Cells of an Amphipathic β-Sheet Forming Peptide. *FEBS Letters* **1997**, *415*, 196–199, doi:10.1016/S0014-5793(97)01123-X.

384. Egleton, R.D.; Davis, T.P. Development of Neuropeptide Drugs That Cross the Blood-Brain Barrier. *Neurotherapeutics* **2005**, *2*, 44–53, doi:10.1602/neurorx.2.1.44.

385. Valenza, M.; Chen, J.Y.; Di Paolo, E.; Ruozi, B.; Belletti, D.; Ferrari Bardile, C.; Leoni, V.; Caccia, C.; Brilli, E.; Di Donato, S.; et al. Cholesterol-loaded Nanoparticles Ameliorate Synaptic and Cognitive Function in H Untington's Disease Mice. *EMBO Mol Med* **2015**, *7*, 1547–1564, doi:10.15252/emmm.201505413.

386. Tosi, G.; Fano, R.A.; Bondioli, L.; Badiali, L.; Benassi, R.; Rivasi, F.; Ruozi, B.; Forni, F.; Vandelli, M.A. Investigation on Mechanisms of Glycopeptide Nanoparticles for Drug Delivery across the Blood–Brain Barrier. *Nanomedicine* **2011**, *6*, 423–436, doi:10.2217/nnm.11.11.

387. Fiori, A.; Cardelli, P.; Negri, L.; Savi, M.R.; Strom, R.; Erspamer, V. Deltorphin Transport across the Blood–Brain Barrier. *Proc. Natl. Acad. Sci. U.S.A.* **1997**, *94*, 9469–9474, doi:10.1073/pnas.94.17.9469.

388. Filira, F.; Biondi, B.; Biondi, L.; Giannini, E.; Gobbo, M.; Negri, L.; Rocchi, R. Opioid Peptides: Synthesis and Biological Properties of [(N $^{\gamma}$ -Glucosyl,N $^{\gamma}$ -Methoxy)-α,γ-

Diamino-(S)-Butanoyl] [4] -Deltorphin-1-Neoglycopeptide and Related Analogues. *Org. Biomol. Chem.* **2003**, *1*, 3059–3063, doi:10.1039/B306142F.
389. Brune, K. Opioid Analgesics, Chemistry and Receptors. *Trends in Pharmacological Sciences* **1987**, *8*, 39, doi:10.1016/0165-6147(87)90034-4.
390. Sodano, F.; Rolando, B.; Spyrakis, F.; Failla, M.; Lazzarato, L.; Gazzano, E.; Riganti, C.; Fruttero, R.; Gasco, A.; Sortino, S. Tuning the Hydrophobicity of a Mitochondria-Targeted NO Photodonor. *ChemMedChem* **2018**, *13*, 1238–1245, doi:10.1002/cmdc.201800088.
391. Erspamer, V.; Melchiorri, P.; Falconieri-Erspamer, G.; Negri, L.; Corsi, R.; Severini, C.; Barra, D.; Simmaco, M.; Kreil, G. Deltorphins: A Family of Naturally Occurring Peptides with High Affinity and Selectivity for Delta Opioid Binding Sites. *Proc. Natl. Acad. Sci. U.S.A.* **1989**, *86*, 5188–5192, doi:10.1073/pnas.86.13.5188.
392. Vergoni, A.V.; Tosi, G.; Tacchi, R.; Vandelli, M.A.; Bertolini, A.; Costantino, L. Nanoparticles as Drug Delivery Agents Specific for CNS: In Vivo Biodistribution. *Nanomedicine: Nanotechnology, Biology and Medicine* **2009**, *5*, 369–377, doi:10.1016/j.nano.2009.02.005.
393. Costantino, L.; Gandolfi, F.; Tosi, G.; Rivasi, F.; Vandelli, M.A.; Forni, F. Peptide-Derivatized Biodegradable Nanoparticles Able to Cross the Blood-Brain Barrier. *J Control Release* **2005**, *108*, 84–96, doi:10.1016/j.jconrel.2005.07.013.
394. Tosi, G.; Ruozi, B.; Belletti, D.; Vilella, A.; Zoli, M.; Vandelli, M.A.; Forni, F. Brain-Targeted Polymeric Nanoparticles: *In Vivo* Evidence of Different Routes of Administration in Rodents. *Nanomedicine* **2013**, *8*, 1373–1383, doi:10.2217/nnm.12.172.
395. Tosi, G.; Costantino, L.; Rivasi, F.; Ruozi, B.; Leo, E.; Vergoni, A.V.; Tacchi, R.; Bertolini, A.; Vandelli, M.A.; Forni, F. Targeting the Central Nervous System: In Vivo Experiments with Peptide-Derivatized Nanoparticles Loaded with Loperamide and Rhodamine-123. *Journal of Controlled Release* **2007**, *122*, 1–9, doi:10.1016/j.jconrel.2007.05.022.
396. Li, Y.; Lefever, M.R.; Muthu, D.; Bidlack, J.M.; Bilsky, E.J.; Polt, R. Opioid Glycopeptide Analgesics Derived from Endogenous Enkephalins and Endorphins. *Future Medicinal Chemistry* **2012**, *4*, 205–226, doi:10.4155/fmc.11.195.
397. Li, Y.; St. Louis, L.; Knapp, B.I.; Muthu, D.; Anglin, B.; Giuvelis, D.; Bidlack, J.M.; Bilsky, E.J.; Polt, R. Can Amphipathic Helices Influence the CNS Antinociceptive Activity of Glycopeptides Related to β-Endorphin? *J. Med. Chem.* **2014**, *57*, 2237–2246, doi:10.1021/jm400879w.
398. Kang, Y.S.; Bickel, U.; Pardridge, W.M. Pharmacokinetics and Saturable Blood-Brain Barrier Transport of Biotin Bound to a Conjugate of Avidin and a Monoclonal Antibody to the Transferrin Receptor. *Drug Metab Dispos* **1994**, *22*, 99–105.
399. Bickel, U.; Yoshikawa, T.; Pardridge, W.M. Delivery of Peptides and Proteins through the Blood-Brain Barrier. *Advanced Drug Delivery Reviews* **1993**, *10*, 205–245, doi:10.1016/0169-409X(93)90048-9.
400. Decherchi, S.; Bottegoni, G.; Spitaleri, A.; Rocchia, W.; Cavalli, A. BiKi Life Sciences: A New Suite for Molecular Dynamics and Related Methods in Drug Discovery. *J. Chem. Inf. Model.* **2018**, *58*, 219–224, doi:10.1021/acs.jcim.7b00680.
401. Hess, B.; Kutzner, C.; van der Spoel, D.; Lindahl, E. GROMACS 4: Algorithms for Highly Efficient, Load-Balanced, and Scalable Molecular Simulation. *J. Chem. Theory Comput.* **2008**, *4*, 435–447, doi:10.1021/ct700301q.
402. Tosi, G.; Vilella, A.; Chhabra, R.; Schmeisser, M.J.; Boeckers, T.M.; Ruozi, B.; Vandelli, M.A.; Forni, F.; Zoli, M.; Grabrucker, A.M. Insight on the Fate of CNS-Targeted Nanoparticles. Part II: Intercellular Neuronal Cell-to-Cell Transport. *Journal of Controlled Release* **2014**, *177*, 96–107, doi:10.1016/j.jconrel.2014.01.004.

403. Zoli, M.; Guidolin, D.; Agnati, L.F. Morphometric Evaluation of Populations of Neuronal Profiles (Cell Bodies, Dendrites, and Nerve Terminals) in the Central Nervous System. *Microsc. Res. Tech.* **1992**, *21*, 315–337, doi:10.1002/jemt.1070210408.
404. Beck-Broichsitter, M.; Nicolas, J.; Couvreur, P. Design Attributes of Long-Circulating Polymeric Drug Delivery Vehicles. *European Journal of Pharmaceutics and Biopharmaceutics* **2015**, *97*, 304–317, doi:10.1016/j.ejpb.2015.03.033.
405. Jokerst, J.V.; Lobovkina, T.; Zare, R.N.; Gambhir, S.S. Nanoparticle PEGylation for Imaging and Therapy. *Nanomedicine* **2011**, *6*, 715–728, doi:10.2217/nnm.11.19.
406. Xie, J.; Shen, Z.; Anraku, Y.; Kataoka, K.; Chen, X. Nanomaterial-Based Blood-Brain-Barrier (BBB) Crossing Strategies. *Biomaterials* **2019**, *224*, 119491, doi:10.1016/j.biomaterials.2019.119491.
407. Portioli, C.; Bovi, M.; Benati, D.; Donini, M.; Perduca, M.; Romeo, A.; Dusi, S.; Monaco, H.L.; Bentivoglio, M. Novel Functionalization Strategies of Polymeric Nanoparticles as Carriers for Brain Medications: PEPTIDIC MOIETIES ENABLE BBB TRAVERSAL OF THE NPs. *J. Biomed. Mater. Res.* **2017**, *105*, 847–858, doi:10.1002/jbm.a.35961.
408. Chen, Y.; Liu, L. Modern Methods for Delivery of Drugs across the Blood–Brain Barrier. *Advanced Drug Delivery Reviews* **2012**, *64*, 640–665, doi:10.1016/j.addr.2011.11.010.
409. Ramalho, M.J.; Sevin, E.; Gosselet, F.; Lima, J.; Coelho, M.A.N.; Loureiro, J.A.; Pereira, M.C. Receptor-Mediated PLGA Nanoparticles for Glioblastoma Multiforme Treatment. *International Journal of Pharmaceutics* **2018**, *545*, 84–92, doi:10.1016/j.ijpharm.2018.04.062.
410. Paka, G.D.; Ramassamy, C. Optimization of Curcumin-Loaded PEG-PLGA Nanoparticles by GSH Functionalization: Investigation of the Internalization Pathway in Neuronal Cells. *Mol. Pharmaceutics* **2017**, *14*, 93–106, doi:10.1021/acs.molpharmaceut.6b00738.
411. Bors, L.; Erdő, F. Overcoming the Blood–Brain Barrier. Challenges and Tricks for CNS Drug Delivery. *Sci. Pharm.* **2019**, *87*, 6, doi:10.3390/scipharm87010006.
412. Auderset, L.; Cullen, C.L.; Young, K.M. Low Density Lipoprotein-Receptor Related Protein 1 Is Differentially Expressed by Neuronal and Glial Populations in the Developing and Mature Mouse Central Nervous System. *PLoS ONE* **2016**, *11*, e0155878, doi:10.1371/journal.pone.0155878.
413. Tian, X.; Nyberg, S.; Sharp, P.S.; Madsen, J.; Daneshpour, N.; Armes, S.P.; Berwick, J.; Azzouz, M.; Shaw, P.; Abbott, N.J.; et al. LRP-1-Mediated Intracellular Antibody Delivery to the Central Nervous System. *Sci Rep* **2015**, *5*, 11990, doi:10.1038/srep11990.
414. Spuch, C.; Ortolano, S.; Navarro, C. LRP-1 and LRP-2 Receptors Function in the Membrane Neuron. Trafficking Mechanisms and Proteolytic Processing in Alzheimer's Disease. *Front. Physio.* **2012**, *3*, doi:10.3389/fphys.2012.00269.
415. Marzolo, M.-P.; Yuseff, M.I.; Retamal, C.; Donoso, M.; Ezquer, F.; Farfán, P.; Li, Y.; Bu, G. Differential Distribution of Low-Density Lipoprotein-Receptor-Related Protein (LRP) and Megalin in Polarized Epithelial Cells Is Determined by Their Cytoplasmic Domains: **Differential Polarized Distribution of LRP and Megalin**. *Traffic* **2003**, *4*, 273–288, doi:10.1034/j.1600-0854.2003.00081.x.
416. Wang, X.; Xiong, Z.; Liu, Z.; Huang, X.; Jiang, X. Angiopep-2/IP10-EGFRvIIIscFv Modified Nanoparticles and CTL Synergistically Inhibit Malignant Glioblastoma. *Sci Rep* **2018**, *8*, 12827, doi:10.1038/s41598-018-30072-x.
417. Wang, S.; Zhao, C.; Liu, P.; Wang, Z.; Ding, J.; Zhou, W. Facile Construction of Dual-Targeting Delivery System by Using Lipid Capped Polymer Nanoparticles for Anti-Glioma Therapy. *RSC Adv.* **2018**, *8*, 444–453, doi:10.1039/C7RA12376K.

418. Demeule, M.; Currie, J.-C.; Bertrand, Y.; Ché, C.; Nguyen, T.; Régina, A.; Gabathuler, R.; Castaigne, J.-P.; Béliveau, R. Involvement of the Low-Density Lipoprotein Receptor-Related Protein in the Transcytosis of the Brain Delivery Vector Angiopep-2. *Journal of Neurochemistry* **2008**, *106*, 1534–1544, doi:10.1111/j.1471-4159.2008.05492.x.
419. Xin, H.; Jiang, X.; Gu, J.; Sha, X.; Chen, L.; Law, K.; Chen, Y.; Wang, X.; Jiang, Y.; Fang, X. Angiopep-Conjugated Poly(Ethylene Glycol)-Co-Poly(ε-Caprolactone) Nanoparticles as Dual-Targeting Drug Delivery System for Brain Glioma. *Biomaterials* **2011**, *32*, 4293–4305, doi:10.1016/j.biomaterials.2011.02.044.
420. Ke, W.; Shao, K.; Huang, R.; Han, L.; Liu, Y.; Li, J.; Kuang, Y.; Ye, L.; Lou, J.; Jiang, C. Gene Delivery Targeted to the Brain Using an Angiopep-Conjugated Polyethyleneglycol-Modified Polyamidoamine Dendrimer. *Biomaterials* **2009**, *30*, 6976–6985, doi:10.1016/j.biomaterials.2009.08.049.
421. Wang, L.; Hao, Y.; Li, H.; Zhao, Y.; Meng, D.; Li, D.; Shi, J.; Zhang, H.; Zhang, Z.; Zhang, Y. Co-Delivery of Doxorubicin and SiRNA for Glioma Therapy by a Brain Targeting System: Angiopep-2-Modified Poly(Lactic-Co-Glycolic Acid) Nanoparticles. *Journal of Drug Targeting* **2015**, *23*, 832–846, doi:10.3109/1061186X.2015.1025077.
422. Chen, G.-J.; Su, Y.-Z.; Hsu, C.; Lo, Y.-L.; Huang, S.-J.; Ke, J.-H.; Kuo, Y.-C.; Wang, L.-F. Angiopep-Pluronic F127-Conjugated Superparamagnetic Iron Oxide Nanoparticles as Nanotheranostic Agents for BBB Targeting. *J. Mater. Chem. B* **2014**, *2*, 5666, doi:10.1039/C4TB00543K.
423. Tosi, G.; Vilella, A.; Veratti, P.; Belletti, D.; Pederzoli, F.; Ruozi, B.; Vandelli, M.A.; Zoli, M.; Forni, F. Exploiting Bacterial Pathways for BBB Crossing with PLGA Nanoparticles Modified with a Mutated Form of Diphtheria Toxin (CRM197): *In Vivo* Experiments. *Mol. Pharmaceutics* **2015**, *12*, 3672–3684, doi:10.1021/acs.molpharmaceut.5b00446.
424. Bi, C.; Wang, A.; Chu, Y.; Liu, S.; Mu, H.; Liu, W.; Wu, Z.; Sun, K.; Li, Y. Intranasal Delivery of Rotigotine to the Brain with Lactoferrin-Modified PEG-PLGA Nanoparticles for Parkinson’s Disease Treatment. *IJN* **2016**, *Volume 11*, 6547–6559, doi:10.2147/IJN.S120939.
425. Hoyos-Ceballos, G.P.; Sánchez-Giraldo, V.; Mendivil-Perez, M.; Jimenez-Del-Rio, M.; Sierra-Garcia, L.; Vélez-Pardo, C.; López-Osorio, B.L. Design of Epigallocatechin Gallate Loaded PLGA/PF127 Nanoparticles and Their Effect upon an Oxidative Stress Model. *Journal of Drug Delivery Science and Technology* **2018**, *48*, 152–160, doi:10.1016/j.jddst.2018.09.010.
426. Hao, Y.; Wang, L.; Zhao, Y.; Meng, D.; Li, D.; Li, H.; Zhang, B.; Shi, J.; Zhang, H.; Zhang, Z.; et al. Targeted Imaging and Chemo-Phototherapy of Brain Cancer by a Multifunctional Drug Delivery System: Targeted Imaging and Chemo-Phototherapy of Brain…. *Macromol. Biosci.* **2015**, *15*, 1571–1585, doi:10.1002/mabi.201500091.
427. Hao, Y.; Zhang, B.; Zheng, C.; Ji, R.; Ren, X.; Guo, F.; Sun, S.; Shi, J.; Zhang, H.; Zhang, Z.; et al. The Tumor-Targeting Core–Shell Structured DTX-Loaded PLGA@Au Nanoparticles for Chemo-Photothermal Therapy and X-Ray Imaging. *Journal of Controlled Release* **2015**, *220*, 545–555, doi:10.1016/j.jconrel.2015.11.016.
428. Duskey, J.T.; Ottonelli, I.; Da Ros, F.; Vilella, A.; Zoli, M.; Kovachka, S.; Spyrakis, F.; Vandelli, M.A.; Tosi, G.; Ruozi, B. Novel Peptide-Conjugated Nanomedicines for Brain Targeting: In Vivo Evidence. *Nanomedicine: Nanotechnology, Biology and Medicine* **2020**, *28*, 102226, doi:10.1016/j.nano.2020.102226.
429. Lowe, A.B. Thiol–Ene "Click" Reactions and Recent Applications in Polymer and Materials Synthesis: A First Update. *Polym. Chem.* **2014**, *5*, 4820–4870, doi:10.1039/C4PY00339J.

430. García, M.L.; Pérez, Y.; Gómara, M.J.; Vasconcelos, A.; Vega, E.; Haro, I. Conjugation of Cell-Penetrating Peptides with Poly(Lactic-Co-Glycolic Acid)-Polyethylene Glycol Nanoparticles Improves Ocular Drug Delivery. *IJN* **2015**, 609, doi:10.2147/IJN.S71198.
431. Hu, K.; Shi, Y.; Jiang, W.; Han, J.; Huang, S.; Jiang, X. Lactoferrin Conjugated PEG-PLGA Nanoparticles for Brain Delivery: Preparation, Characterization and Efficacy in Parkinson's Disease. *International Journal of Pharmaceutics* **2011**, *415*, 273–283, doi:10.1016/j.ijpharm.2011.05.062.
432. *Handbook of Biologically Active Peptides*; Kastin, A.J., Ed.; Second edition.; Elsevier/AP: Amsterdam, 2013; ISBN 978-0-12-385095-9.
433. Huang, N.; Lu, S.; Liu, X.-G.; Zhu, J.; Wang, Y.-J.; Liu, R.-T. PLGA Nanoparticles Modified with a BBB-Penetrating Peptide Co-Delivering Aβ Generation Inhibitor and Curcumin Attenuate Memory Deficits and Neuropathology in Alzheimer's Disease Mice. *Oncotarget* **2017**, *8*, 81001–81013, doi:10.18632/oncotarget.20944.
434. Tosi, G.; Vergoni, A.V.; Ruozi, B.; Bondioli, L.; Badiali, L.; Rivasi, F.; Costantino, L.; Forni, F.; Vandelli, M.A. Sialic Acid and Glycopeptides Conjugated PLGA Nanoparticles for Central Nervous System Targeting: In Vivo Pharmacological Evidence and Biodistribution. *Journal of Controlled Release* **2010**, *145*, 49–57, doi:10.1016/j.jconrel.2010.03.008.
435. Heggannavar, G.B.; Vijeth, S.; Kariduraganavar, M.Y. Development of Dual Drug Loaded PLGA Based Mesoporous Silica Nanoparticles and Their Conjugation with Angiopep-2 to Treat Glioma. *Journal of Drug Delivery Science and Technology* **2019**, *53*, 101157, doi:10.1016/j.jddst.2019.101157.
436. Shen, J.; Zhan, C.; Xie, C.; Meng, Q.; Gu, B.; Li, C.; Zhang, Y.; Lu, W. Poly(Ethylene Glycol)-Block-Poly( D , L -Lactide Acid) Micelles Anchored with Angiopep-2 for Brain-Targeting Delivery. *Journal of Drug Targeting* **2011**, *19*, 197–203, doi:10.3109/1061186X.2010.483517.
437. Gao, H. Progress and Perspectives on Targeting Nanoparticles for Brain Drug Delivery. *Acta Pharmaceutica Sinica B* **2016**, *6*, 268–286, doi:10.1016/j.apsb.2016.05.013.
438. Germain, M.; Caputo, F.; Metcalfe, S.; Tosi, G.; Spring, K.; Åslund, A.K.O.; Pottier, A.; Schiffelers, R.; Ceccaldi, A.; Schmid, R. Delivering the Power of Nanomedicine to Patients Today. *Journal of Controlled Release* **2020**, *326*, 164–171, doi:10.1016/j.jconrel.2020.07.007.
439. Hersh, D.S.; Wadajkar, A.S.; Roberts, N.B.; Perez, J.G.; Connolly, N.P.; Frenkel, V.; Winkles, J.A.; Woodworth, G.F.; Kim, A.J. Evolving Drug Delivery Strategies to Overcome the Blood Brain Barrier. *Current Pharmaceutical Design* **2016**, *22*, 1177–1193, doi:10.2174/1381612822666151221150733.
440. Saraiva, C.; Praça, C.; Ferreira, R.; Santos, T.; Ferreira, L.; Bernardino, L. Nanoparticle-Mediated Brain Drug Delivery: Overcoming Blood–Brain Barrier to Treat Neurodegenerative Diseases. *Journal of Controlled Release* **2016**, *235*, 34–47, doi:10.1016/j.jconrel.2016.05.044.
441. Tosi, G.; Bondioli, L.; Ruozi, B.; Badiali, L.; Severini, G.M.; Biffi, S.; De Vita, A.; Bortot, B.; Dolcetta, D.; Forni, F.; et al. NIR-Labeled Nanoparticles Engineered for Brain Targeting: In Vivo Optical Imaging Application and Fluorescent Microscopy Evidences. *J Neural Transm* **2011**, *118*, 145–153, doi:10.1007/s00702-010-0497-1.
442. Zuccato, C.; Valenza, M.; Cattaneo, E. Molecular Mechanisms and Potential Therapeutical Targets in Huntington's Disease. *Physiological Reviews* **2010**, *90*, 905–981, doi:10.1152/physrev.00041.2009.

443. Mauch, D.H.; Nägler, K.; Schumacher, S.; Göritz, C.; Müller, E.C.; Otto, A.; Pfrieger, F.W. CNS Synaptogenesis Promoted by Glia-Derived Cholesterol. *Science* **2001**, *294*, 1354–1357, doi:10.1126/science.294.5545.1354.
444. Ferris, H.A.; Perry, R.J.; Moreira, G.V.; Shulman, G.I.; Horton, J.D.; Kahn, C.R. Loss of Astrocyte Cholesterol Synthesis Disrupts Neuronal Function and Alters Whole-Body Metabolism. *Proceedings of the National Academy of Sciences* **2017**, *114*, 1189–1194, doi:10.1073/pnas.1620506114.
445. Valenza, M.; Rigamonti, D.; Goffredo, D.; Zuccato, C.; Fenu, S.; Jamot, L.; Strand, A.; Tarditi, A.; Woodman, B.; Racchi, M.; et al. Dysfunction of the Cholesterol Biosynthetic Pathway in Huntington's Disease. *Journal of Neuroscience* **2005**, *25*, 9932–9939, doi:10.1523/JNEUROSCI.3355-05.2005.
446. Valenza, M.; Leoni, V.; Tarditi, A.; Mariotti, C.; Björkhem, I.; Di Donato, S.; Cattaneo, E. Progressive Dysfunction of the Cholesterol Biosynthesis Pathway in the R6/2 Mouse Model of Huntington's Disease. *Neurobiology of Disease* **2007**, *28*, 133–142, doi:10.1016/j.nbd.2007.07.004.
447. Valenza, M.; Carroll, J.B.; Leoni, V.; Bertram, L.N.; Bjorkhem, I.; Singaraja, R.R.; Di Donato, S.; Lutjohann, D.; Hayden, M.R.; Cattaneo, E. Cholesterol Biosynthesis Pathway Is Disturbed in YAC128 Mice and Is Modulated by Huntingtin Mutation. *Human Molecular Genetics* **2007**, *16*, 2187–2198, doi:10.1093/hmg/ddm170.
448. Valenza, M.; Leoni, V.; Karasinska, J.M.; Petricca, L.; Fan, J.; Carroll, J.; Pouladi, M.A.; Fossale, E.; Nguyen, H.P.; Riess, O.; et al. Cholesterol Defect Is Marked across Multiple Rodent Models of Huntington's Disease and Is Manifest in Astrocytes. *Journal of Neuroscience* **2010**, *30*, 10844–10850, doi:10.1523/JNEUROSCI.0917-10.2010.
449. Valenza, M.; Cattaneo, E. Emerging Roles for Cholesterol in Huntington's Disease. *Trends in Neurosciences* **2011**, *34*, 474–486, doi:10.1016/j.tins.2011.06.005.
450. Shankaran, M.; Di Paolo, E.; Leoni, V.; Caccia, C.; Ferrari Bardile, C.; Mohammed, H.; Di Donato, S.; Kwak, S.; Marchionini, D.; Turner, S.; et al. Early and Brain Region-Specific Decrease of de Novo Cholesterol Biosynthesis in Huntington's Disease: A Cross-Validation Study in Q175 Knock-in Mice. *Neurobiology of Disease* **2017**, *98*, 66–76, doi:10.1016/j.nbd.2016.11.013.
451. Leoni, V.; Mariotti, C.; Tabrizi, S.J.; Valenza, M.; Wild, E.J.; Henley, S.M.D.; Hobbs, N.Z.; Mandelli, M.L.; Grisoli, M.; Björkhem, I.; et al. Plasma 24S-Hydroxycholesterol and Caudate MRI in Pre-Manifest and Early Huntington's Disease. *Brain* **2008**, *131*, 2851–2859, doi:10.1093/brain/awn212.
452. Leoni, V.; Long, J.D.; Mills, J.A.; Di Donato, S.; Paulsen, J.S. Plasma 24S-Hydroxycholesterol Correlation with Markers of Huntington Disease Progression. *Neurobiology of Disease* **2013**, *55*, 37–43, doi:10.1016/j.nbd.2013.03.013.
453. Karasinska, J.M.; Hayden, M.R. Cholesterol Metabolism in Huntington Disease. *Nat Rev Neurol* **2011**, *7*, 561–572, doi:10.1038/nrneurol.2011.132.
454. Birolini, G.; Valenza, M.; Di Paolo, E.; Vezzoli, E.; Talpo, F.; Maniezzi, C.; Caccia, C.; Leoni, V.; Taroni, F.; Bocchi, V.D.; et al. Striatal Infusion of Cholesterol Promotes Dose-Dependent Behavioral Benefits and Exerts Disease-Modifying Effects in Huntington's Disease Mice. *EMBO Molecular Medicine* **2020**, *12*, e12519, doi:10.15252/emmm.202012519.
455. Passoni, A.; Favagrossa, M.; Colombo, L.; Bagnati, R.; Gobbi, M.; Diomede, L.; Birolini, G.; Di Paolo, E.; Valenza, M.; Cattaneo, E.; et al. Efficacy of Cholesterol Nose-to-Brain Delivery for Brain Targeting in Huntington's Disease. *ACS Chem. Neurosci.* **2020**, *11*, 367–372, doi:10.1021/acschemneuro.9b00581.
456. Makadia, H.K.; Siegel, S.J. Poly Lactic-Co-Glycolic Acid (PLGA) as Biodegradable Controlled Drug Delivery Carrier. *Polymers* **2011**, *3*, 1377–1397, doi:10.3390/polym3031377.

457. Hines, D.J.; Kaplan, D.L. Poly(Lactic-Co-Glycolic) Acid-Controlled-Release Systems: Experimental and Modeling Insights. *Crit Rev Ther Drug Carrier Syst* **2013**, *30*, 257–276, doi:10.1615/CritRevTherDrugCarrierSyst.2013006475.
458. Mangiarini, L.; Sathasivam, K.; Seller, M.; Cozens, B.; Harper, A.; Hetherington, C.; Lawton, M.; Trottier, Y.; Lehrach, H.; Davies, S.W.; et al. Exon 1 of the HD Gene with an Expanded CAG Repeat Is Sufficient to Cause a Progressive Neurological Phenotype in Transgenic Mice. *Cell* **1996**, *87*, 493–506, doi:10.1016/S0092-8674(00)81369-0.
459. Pitto-Barry, A.; Barry, N.P.E. Pluronic® Block-Copolymers in Medicine: From Chemical and Biological Versatility to Rationalisation and Clinical Advances. *Polym. Chem.* **2014**, *5*, 3291–3297, doi:10.1039/C4PY00039K.
460. Rocha, B.N.P.; Colpo, G.D.; Teixeira, A.L.; Stimming, E.F. Clinical trials for Huntington disease. *Pract. Neurol.* **2020**, 69–74.
461. Nagatsu, T.; Mogi, M.; Ichinose, H.; Togari, A. Cytokines in Parkinson's Disease. In *Advances in Research on Neurodegeneration*; Mizuno, Y., Calne, D.B., Horowski, R., Poewe, W., Riederer, P., Youdim, M.B.H., Eds.; Springer Vienna: Vienna, 2000; pp. 143–151 ISBN 978-3-7091-7246-9.
462. Khaddour, K.; Johanns, T.; Ansstas, G. The Landscape of Novel Therapeutics and Challenges in Glioblastoma Multiforme: Contemporary State and Future Directions. *Pharmaceuticals* **2020**, *13*, 389, doi:10.3390/ph13110389.
463. Iwadate, Y. Epithelial-Mesenchymal Transition in Glioblastoma Progression. *Oncology Letters* **2016**, *11*, 1615–1620, doi:10.3892/ol.2016.4113.
464. Stensjøen, A.L.; Solheim, O.; Kvistad, K.A.; Håberg, A.K.; Salvesen, Ø.; Berntsen, E.M. Growth Dynamics of Untreated Glioblastomas in Vivo. *Neuro Oncol* **2015**, *17*, 1402–1411, doi:10.1093/neuonc/nov029.
465. Park, Y.; Park, M.; Kim, J.; Ahn, J.; Sim, J.; Bang, J.-I.; Heo, J.; Choi, H.; Cho, K.; Lee, M.; et al. NOX2-Induced High Glycolytic Activity Contributes to the Gain of COL5A1-Mediated Mesenchymal Phenotype in GBM. *Cancers* **2022**, *14*, 516, doi:10.3390/cancers14030516.
466. Cagney, D.N.; Alexander, B.M. The Cost and Value of Glioblastoma Therapy. *Expert Review of Anticancer Therapy* **2017**, *17*, 657–659, doi:10.1080/14737140.2017.1351355.
467. Norden, A.D.; Korytowsky, B.; You, M.; Kim Le, T.; Dastani, H.; Bobiak, S.; Singh, P. A Real-World Claims Analysis of Costs and Patterns of Care in Treated Patients with Glioblastoma Multiforme in the United States. *JMCP* **2019**, *25*, 428–436, doi:10.18553/jmcp.2019.25.4.428.
468. Hishii, M.; Matsumoto, T.; Arai, H. Diagnosis and Treatment of Early-Stage Glioblastoma. *Asian J Neurosurg* **2019**, *14*, 589, doi:10.4103/ajns.AJNS_18_19.
469. von Neubeck, C.; Seidlitz, A.; Kitzler, H.H.; Beuthien-Baumann, B.; Krause, M. Glioblastoma Multiforme: Emerging Treatments and Stratification Markers beyond New Drugs. *BJR* **2015**, *88*, 20150354, doi:10.1259/bjr.20150354.
470. Back, M.F.; Ang, E.L.L.; Ng, W.-H.; See, S.-J.; Lim, C.C.T.; Chan, S.P.; Yeo, T.-T. Improved Median Survival for Glioblastoma Multiforme Following Introduction of Adjuvant Temozolomide Chemotherapy. *Ann Acad Med Singap* **2007**, *36*, 338–342.
471. Lara-Velazquez, M.; Shireman, J.M.; Lehrer, E.J.; Bowman, K.M.; Ruiz-Garcia, H.; Paukner, M.J.; Chappell, R.J.; Dey, M. A Comparison Between Chemo-Radiotherapy Combined With Immunotherapy and Chemo-Radiotherapy Alone for the Treatment of Newly Diagnosed Glioblastoma: A Systematic Review and Meta-Analysis. *Frontiers in Oncology* **2021**, *11*.
472. Duskey, J.T.; Ottonelli, I.; Rinaldi, A.; Parmeggiani, I.; Zambelli, B.; Wang, L.Z.; Prud'homme, R.K.; Vandelli, M.A.; Tosi, G.; Ruozi, B. Tween® Preserves Enzyme Activity

and Stability in PLGA Nanoparticles. *Nanomaterials* **2021**, *11*, 2946, doi:10.3390/nano11112946.
473. Engelberg, S.; Lin, Y.; Assaraf, Y.G.; Livney, Y.D. Targeted Nanoparticles Harboring Jasmine-Oil-Entrapped Paclitaxel for Elimination of Lung Cancer Cells. *IJMS* **2021**, *22*, 1019, doi:10.3390/ijms22031019.
474. Jin, K.-T.; Lu, Z.-B.; Chen, J.-Y.; Liu, Y.-Y.; Lan, H.-R.; Dong, H.-Y.; Yang, F.; Zhao, Y.-Y.; Chen, X.-Y. Recent Trends in Nanocarrier-Based Targeted Chemotherapy: Selective Delivery of Anticancer Drugs for Effective Lung, Colon, Cervical, and Breast Cancer Treatment. *Journal of Nanomaterials* **2020**, *2020*, 1–14, doi:10.1155/2020/9184284.
475. Smith, J.D.; Cardwell, L.N.; Porciani, D.; Nguyen, J.A.; Zhang, R.; Gallazzi, F.; Tata, R.R.; Burke, D.H.; Daniels, M.A.; Ulery, B.D. Aptamer-Displaying Peptide Amphiphile Micelles as a Cell-Targeted Delivery Vehicle of Peptide Cargoes. *Phys. Biol.* **2018**, *15*, 065006, doi:10.1088/1478-3975/aadb68.
476. Ou, W.; Thapa, R.K.; Jiang, L.; Soe, Z.C.; Gautam, M.; Chang, J.-H.; Jeong, J.-H.; Ku, S.K.; Choi, H.-G.; Yong, C.S.; et al. Regulatory T Cell-Targeted Hybrid Nanoparticles Combined with Immuno-Checkpoint Blockage for Cancer Immunotherapy. *Journal of Controlled Release* **2018**, *281*, 84–96, doi:10.1016/j.jconrel.2018.05.018.
477. Wang, H.; Zhang, F.; Wen, H.; Shi, W.; Huang, Q.; Huang, Y.; Xie, J.; Li, P.; Chen, J.; Qin, L.; et al. Tumor- and Mitochondria-Targeted Nanoparticles Eradicate Drug Resistant Lung Cancer through Mitochondrial Pathway of Apoptosis. *J Nanobiotechnol* **2020**, *18*, 8, doi:10.1186/s12951-019-0562-3.
478. Gao, P.; Pan, W.; Li, N.; Tang, B. Boosting Cancer Therapy with Organelle-Targeted Nanomaterials. *ACS Appl. Mater. Interfaces* **2019**, *11*, 26529–26558, doi:10.1021/acsami.9b01370.
479. Zhao, H.; Xu, X.; Zhou, L.; Hu, Y.; Huang, Y.; Narita, A. Water-Soluble Nanoparticles with Twisted Double [7]Carbohelicene for Lysosome-Targeted Cancer Photodynamic Therapy. *Small* **2022**, *18*, 2105365, doi:10.1002/smll.202105365.
480. Georgieva, J.; Hoekstra, D.; Zuhorn, I. Smuggling Drugs into the Brain: An Overview of Ligands Targeting Transcytosis for Drug Delivery across the Blood–Brain Barrier. *Pharmaceutics* **2014**, *6*, 557–583, doi:10.3390/pharmaceutics6040557.
481. Cabezas, R.; Ã vila, M.; Gonzalez, J.; El-BachÃ¡, R.S.; BÃ¡ez, E.; GarcÃ-a-Segura, L.M.; Jurado Coronel, J.C.; Capani, F.; Cardona-Gomez, G.P.; Barreto, G.E. Astrocytic Modulation of Blood Brain Barrier: Perspectives on Parkinsonâ€™s Disease. *Front. Cell. Neurosci.* **2014**, *8*, doi:10.3389/fncel.2014.00211.
482. Lombardo, S.M.; Schneider, M.; Türeli, A.E.; Günday Türeli, N. Key for Crossing the BBB with Nanoparticles: The Rational Design. *Beilstein J. Nanotechnol.* **2020**, *11*, 866–883, doi:10.3762/bjnano.11.72.
483. Haumann, R.; Videira, J.C.; Kaspers, G.J.L.; van Vuurden, D.G.; Hulleman, E. Overview of Current Drug Delivery Methods Across the Blood–Brain Barrier for the Treatment of Primary Brain Tumors. *CNS Drugs* **2020**, *34*, 1121–1131, doi:10.1007/s40263-020-00766-w.
484. Ding, S.; Khan, A.I.; Cai, X.; Song, Y.; Lyu, Z.; Du, D.; Dutta, P.; Lin, Y. Overcoming Blood–Brain Barrier Transport: Advances in Nanoparticle-Based Drug Delivery Strategies. *Materials Today* **2020**, *37*, 112–125, doi:10.1016/j.mattod.2020.02.001.
485. Zhang, Y.; Yang, H.; Wei, D.; Zhang, X.; Wang, J.; Wu, X.; Chang, J. Mitochondria-targeted Nanoparticles in Treatment of Neurodegenerative Diseases. *Exploration* **2021**, *1*, 20210115, doi:10.1002/EXP.20210115.
486. Ricci, M.S.; Zong, W.-X. Chemotherapeutic Approaches for Targeting Cell Death Pathways. *The Oncologist* **2006**, *11*, 342–357, doi:10.1634/theoncologist.11-4-342.

487. Ahles, T.A. Brain Vulnerability to Chemotherapy Toxicities. *Psycho-Oncology* **2012**, *21*, 1141–1148, doi:10.1002/pon.3196.
488. Wefel, J.S.; Schagen, S.B. Chemotherapy-Related Cognitive Dysfunction. *Curr Neurol Neurosci Rep* **2012**, *12*, 267–275, doi:10.1007/s11910-012-0264-9.
489. Inagaki, M.; Yoshikawa, E.; Matsuoka, Y.; Sugawara, Y.; Nakano, T.; Akechi, T.; Wada, N.; Imoto, S.; Murakami, K.; Uchitomi, Y.; et al. Smaller Regional Volumes of Brain Gray and White Matter Demonstrated in Breast Cancer Survivors Exposed to Adjuvant Chemotherapy. *Cancer* **2007**, *109*, 146–156, doi:10.1002/cncr.22368.
490. Kovalchuk, A.; Kolb, B. Chemo Brain: From Discerning Mechanisms to Lifting the Brain Fog—An Aging Connection. *Cell Cycle* **2017**, *16*, 1345–1349, doi:10.1080/15384101.2017.1334022.
491. Gornstein, E.L.; Schwarz, T.L. Neurotoxic Mechanisms of Paclitaxel Are Local to the Distal Axon and Independent of Transport Defects. *Experimental Neurology* **2017**, *288*, 153–166, doi:10.1016/j.expneurol.2016.11.015.
492. Malinovskaya, Y.; Melnikov, P.; Baklaushev, V.; Gabashvili, A.; Osipova, N.; Mantrov, S.; Ermolenko, Y.; Maksimenko, O.; Gorshkova, M.; Balabanyan, V.; et al. Delivery of Doxorubicin-Loaded PLGA Nanoparticles into U87 Human Glioblastoma Cells. *International Journal of Pharmaceutics* **2017**, *524*, 77–90, doi:10.1016/j.ijpharm.2017.03.049.
493. Janes, P.W.; Slape, C.I.; Farnsworth, R.H.; Atapattu, L.; Scott, A.M.; Vail, M.E. EphA3 Biology and Cancer. *Growth Factors* **2014**, *32*, 176–189, doi:10.3109/08977194.2014.982276.
494. Chu, L.; Wang, A.; Ni, L.; Yan, X.; Song, Y.; Zhao, M.; Sun, K.; Mu, H.; Liu, S.; Wu, Z.; et al. Nose-to-Brain Delivery of Temozolomide-Loaded PLGA Nanoparticles Functionalized with Anti-EPHA3 for Glioblastoma Targeting. *Drug Delivery* **2018**, *25*, 1634–1641, doi:10.1080/10717544.2018.1494226.
495. Wang, D.; Li, S.; Gessler, D.J.; Xie, J.; Zhong, L.; Li, J.; Tran, K.; Van Vliet, K.; Ren, L.; Su, Q.; et al. A Rationally Engineered Capsid Variant of AAV9 for Systemic CNS-Directed and Peripheral Tissue-Detargeted Gene Delivery in Neonates. *Molecular Therapy - Methods & Clinical Development* **2018**, *9*, 234–246, doi:10.1016/j.omtm.2018.03.004.
496. Tang, Y.; Han, T.; Everts, M.; Zhu, Z.B.; Gillespie, G.Y.; Curiel, D.T.; Wu, H. Directing Adenovirus across the Blood–Brain Barrier via Melanotransferrin (P97) Transcytosis Pathway in an in Vitro Model. *Gene Ther* **2007**, *14*, 523–532, doi:10.1038/sj.gt.3302888.
497. Foust, K.D.; Nurre, E.; Montgomery, C.L.; Hernandez, A.; Chan, C.M.; Kaspar, B.K. Intravascular AAV9 Preferentially Targets Neonatal Neurons and Adult Astrocytes. *Nat Biotechnol* **2009**, *27*, 59–65, doi:10.1038/nbt.1515.
498. Hanlon, K.S.; Meltzer, J.C.; Buzhdygan, T.; Cheng, M.J.; Sena-Esteves, M.; Bennett, R.E.; Sullivan, T.P.; Razmpour, R.; Gong, Y.; Ng, C.; et al. Selection of an Efficient AAV Vector for Robust CNS Transgene Expression. *Molecular Therapy - Methods & Clinical Development* **2019**, *15*, 320–332, doi:10.1016/j.omtm.2019.10.007.
499. Bohn, L.M.; Belcheva, M.M.; Coscia, C.J. Evidence for κ- and μ-Opioid Receptor Expression in C6 Glioma Cells. *Journal of Neurochemistry* **2002**, *70*, 1819–1825, doi:10.1046/j.1471-4159.1998.70051819.x.
500. Brawanski, K.; Brockhoff, G.; Hau, P.; Vollmann-Zwerenz, A.; Freyschlag, C.; Lohmeier, A.; Riemenschneider, M.J.; Thomé, C.; Brawanski, A.; Proescholdt, M.A. Efficacy of D,L-Methadone in the Treatment of Glioblastoma *in Vitro*. *CNS Oncology* **2018**, *7*, CNS18, doi:10.2217/cns-2018-0006.

501. Friesen, C.; Hormann, I.; Roscher, M.; Fichtner, I.; Alt, A.; Hilger, R.; Debatin, K.-M.; Miltner, E. Opioid Receptor Activation Triggering Downregulation of CAMP Improves Effectiveness of Anti-Cancer Drugs in Treatment of Glioblastoma. *Cell Cycle* **2014**, *13*, 1560–1570, doi:10.4161/cc.28493.
502. Koerber, J.T.; Klimczak, R.; Jang, J.-H.; Dalkara, D.; Flannery, J.G.; Schaffer, D.V. Molecular Evolution of Adeno-Associated Virus for Enhanced Glial Gene Delivery. *Molecular Therapy* **2009**, *17*, 2088–2095, doi:10.1038/mt.2009.184.
503. Satelli, A.; Hu, J.; Xia, X.; Li, S. Potential Function of Exogenous Vimentin on the Activation of Wnt Signaling Pathway in Cancer Cells. *J. Cancer* **2016**, *7*, 1824–1832, doi:10.7150/jca.15622.
504. Ivaska, J. Vimentin: Central Hub in EMT Induction? *Small GTPases* **2011**, *2*, 51–53, doi:10.4161/sgtp.2.1.15114.
505. Steinmetz, N.F.; Cho, C.-F.; Ablack, A.; Lewis, J.D.; Manchester, M. Cowpea Mosaic Virus Nanoparticles Target Surface Vimentin on Cancer Cells. *Nanomedicine* **2011**, *6*, 351–364, doi:10.2217/nnm.10.136.
506. Paulin, D.; Lilienbaum, A.; Kardjian, S.; Agbulut, O.; Li, Z. Vimentin: Regulation and Pathogenesis. *Biochimie* **2022**, *197*, 96–112, doi:10.1016/j.biochi.2022.02.003.
507. Bozgeyik, E.; Ege, B.; Koparal, M.; Ceylan, O. Clinical Significance of Vimentin Antisense RNA 1 and Its Correlation with Other Epithelial to Mesenchymal Transition Markers in Oral Cancers. *Pathology - Research and Practice* **2022**, *232*, 153807, doi:10.1016/j.prp.2022.153807.
508. Gomez-Casal, R.; Bhattacharya, C.; Ganesh, N.; Bailey, L.; Basse, P.; Gibson, M.; Epperly, M.; Levina, V. Non-Small Cell Lung Cancer Cells Survived Ionizing Radiation Treatment Display Cancer Stem Cell and Epithelial-Mesenchymal Transition Phenotypes. *Mol Cancer* **2013**, *12*, 94, doi:10.1186/1476-4598-12-94.
509. Phiboonchaiyanan, P.P.; Puthongking, P.; Chawjarean, V.; Harikarnpakdee, S.; Sukprasansap, M.; Chanvorachote, P.; Priprem, A.; Govitrapong, P. Melatonin and Its Derivative Disrupt Cancer Stem-like Phenotypes of Lung Cancer Cells via AKT Downregulation. *Clin Exp Pharmacol Physiol* **2021**, *48*, 1712–1723, doi:10.1111/1440-1681.13572.
510. Trog, D.; Yeghiazaryan, K.; Schild, H.H.; Golubnitschaja, O. Up-Regulation of Vimentin Expression in Low-Density Malignant Glioma Cells as Immediate and Late Effects under Irradiation and Temozolomide Treatment. *Amino Acids* **2008**, *34*, 539–545, doi:10.1007/s00726-007-0007-4.
511. Grossen, A.; Smith, K.; Coulibaly, N.; Arbuckle, B.; Evans, A.; Wilhelm, S.; Jones, K.; Dunn, I.; Towner, R.; Wu, D.; et al. Physical Forces in Glioblastoma Migration: A Systematic Review. *IJMS* **2022**, *23*, 4055, doi:10.3390/ijms23074055.
512. Manzano, S.; Gutierrez-Uzquiza, A.; Bragado, P.; Sequera, C.; Herranz, Ó.; Rodrigo-Faus, M.; Jauregui, P.; Morgner, S.; Rubio, I.; Guerrero, C.; et al. C3G Downregulation Induces the Acquisition of a Mesenchymal Phenotype That Enhances Aggressiveness of Glioblastoma Cells. *Cell Death Dis* **2021**, *12*, 348, doi:10.1038/s41419-021-03631-w.
513. Noh, H.; Yan, J.; Hong, S.; Kong, L.-Y.; Gabrusiewicz, K.; Xia, X.; Heimberger, A.B.; Li, S. Discovery of Cell Surface Vimentin Targeting MAb for Direct Disruption of GBM Tumor Initiating Cells. *Oncotarget* **2016**, *7*, 72021–72032, doi:10.18632/oncotarget.12458.
514. Noh, H.; Zhao, Q.; Yan, J.; Kong, L.-Y.; Gabrusiewicz, K.; Hong, S.; Xia, X.; Heimberger, A.B.; Li, S. Cell Surface Vimentin-Targeted Monoclonal Antibody 86C Increases Sensitivity to Temozolomide in Glioma Stem Cells. *Cancer Letters* **2018**, *433*, 176–185, doi:10.1016/j.canlet.2018.07.008.

515. D'Alessio, A.; Proietti, G.; Lama, G.; Biamonte, F.; Lauriola, L.; Moscato, U.; Vescovi, A.; Mangiola, A.; Angelucci, C.; Sica, G. Analysis of Angiogenesis Related Factors in Glioblastoma, Peritumoral Tissue and Their Derived Cancer Stem Cells. *Oncotarget* **2016**, *7*, 78541–78556, doi:10.18632/oncotarget.12398.
516. Angelucci, C.; D'Alessio, A.; Lama, G.; Binda, E.; Mangiola, A.; Vescovi, A.L.; Proietti, G.; Masuelli, L.; Bei, R.; Fazi, B.; et al. Cancer Stem Cells from Peritumoral Tissue of Glioblastoma Multiforme: The Possible Missing Link between Tumor Development and Progression. *Oncotarget* **2018**, *9*, 28116–28130, doi:10.18632/oncotarget.25565.
517. Childs, C.E. The Determination of Polyethylene Glycol in Gamma Globulin Solutions. *Microchemical Journal* **1975**, *20*, 190–192, doi:10.1016/0026-265X(75)90038-7.
518. Yao, M.-Z.; Hu, Y.-L.; Sheng, X.-X.; Lin, J.; Ling, D.; Gao, J.-Q. Toxicity Analysis of Various Pluronic F-68-Coated Carbon Nanotubes on Mesenchymal Stem Cells. *Chemico-Biological Interactions* **2016**, *250*, 47–58, doi:10.1016/j.cbi.2016.03.013.
519. Taiarol, L.; Formicola, B.; Magro, R.D.; Sesana, S.; Re, F. An Update of Nanoparticle-Based Approaches for Glioblastoma Multiforme Immunotherapy. *Nanomedicine* **2020**, *15*, 1861–1871, doi:10.2217/nnm-2020-0132.
520. Luiz, M.T.; Delello Di Filippo, L.; Tofani, L.B.; de Araújo, J.T.C.; Dutra, J.A.P.; Marchetti, J.M.; Chorilli, M. Highlights in Targeted Nanoparticles as a Delivery Strategy for Glioma Treatment. *International Journal of Pharmaceutics* **2021**, *604*, 120758, doi:10.1016/j.ijpharm.2021.120758.
521. Hsu, J.-F.; Chu, S.-M.; Liao, C.-C.; Wang, C.-J.; Wang, Y.-S.; Lai, M.-Y.; Wang, H.-C.; Huang, H.-R.; Tsai, M.-H. Nanotechnology and Nanocarrier-Based Drug Delivery as the Potential Therapeutic Strategy for Glioblastoma Multiforme: An Update. *Cancers* **2021**, *13*, 195, doi:10.3390/cancers13020195.
522. Ahmad, E.; Ali, A.; Fatima, M.T.; Nimisha; Apurva; Kumar, A.; Sumi, M.P.; Sattar, R.S.A.; Mahajan, B.; Saluja, S.S. Ligand Decorated Biodegradable Nanomedicine in the Treatment of Cancer. *Pharmacological Research* **2021**, *167*, 105544, doi:10.1016/j.phrs.2021.105544.
523. Yasaswi, P.S.; Shetty, K.; Yadav, K.S. Temozolomide Nano Enabled Medicine: Promises Made by the Nanocarriers in Glioblastoma Therapy. *Journal of Controlled Release* **2021**, *336*, 549–571, doi:10.1016/j.jconrel.2021.07.003.
524. Wiwatchaitawee, K.; Quarterman, J.C.; Geary, S.M.; Salem, A.K. Enhancement of Therapies for Glioblastoma (GBM) Using Nanoparticle-Based Delivery Systems. *AAPS PharmSciTech* **2021**, *22*, 71, doi:10.1208/s12249-021-01928-9.
525. Amaral, M.; Cruz, N.; Rosa, A.; Nogueira, B.; Costa, D.; Santos, F.; Brazão, M.; Policarpo, P.; Mateus, R.; Kobozev, Y.; et al. An Update of Advanced Nanoplatforms for Glioblastoma Multiforme Management. *EXCLI J* **2021**, *20*, 1544–1570, doi:10.17179/excli2021-4393.
526. Raucher, D. Tumor Targeting Peptides: Novel Therapeutic Strategies in Glioblastoma. *Current Opinion in Pharmacology* **2019**, *47*, 14–19, doi:10.1016/j.coph.2019.01.006.
527. Tang, X.; Zuo, C.; Fang, P.; Liu, G.; Qiu, Y.; Huang, Y.; Tang, R. Targeting Glioblastoma Stem Cells: A Review on Biomarkers, Signal Pathways and Targeted Therapy. *Frontiers in Oncology* **2021**, *11*.
528. Chaix, A.; Griveau, A.; Defforge, T.; Grimal, V.; Le Borgne, B.; Gautier, G.; Eyer, J. Cell Penetrating Peptide Decorated Magnetic Porous Silicon Nanorods for Glioblastoma Therapy and Imaging. *RSC Adv.* **2022**, *12*, 11708–11714, doi:10.1039/D2RA00508E.

529. Silva, S.; Almeida, A.; Vale, N. Combination of Cell-Penetrating Peptides with Nanoparticles for Therapeutic Application: A Review. *Biomolecules* **2019**, *9*, 22, doi:10.3390/biom9010022.
530. Tripathi, P.P.; Arami, H.; Banga, I.; Gupta, J.; Gandhi, S. Cell Penetrating Peptides in Preclinical and Clinical Cancer Diagnosis and Therapy. *Oncotarget* **2018**, *9*, 37252–37267, doi:10.18632/oncotarget.26442.
531. Zhou, X.; Smith, Q.R.; Liu, X. Brain Penetrating Peptides and Peptide–Drug Conjugates to Overcome the Blood–Brain Barrier and Target CNS Diseases. *WIREs Nanomed Nanobiotechnol* **2021**, *13*, doi:10.1002/wnan.1695.
532. Ou, A.; Ott, M.; Fang, D.; Heimberger, A.B. The Role and Therapeutic Targeting of JAK/STAT Signaling in Glioblastoma. *Cancers* **2021**, *13*, 437, doi:10.3390/cancers13030437.
533. Maghrouni, A.; Givari, M.; Jalili-Nik, M.; Mollazadeh, H.; Bibak, B.; Sadeghi, M.M.; Afshari, A.R.; Johnston, T.P.; Sahebkar, A. Targeting the PD-1/PD-L1 Pathway in Glioblastoma Multiforme: Preclinical Evidence and Clinical Interventions. *International Immunopharmacology* **2021**, *93*, 107403, doi:10.1016/j.intimp.2021.107403.
534. Ottonelli, I.; Caraffi, R.; Tosi, G.; Vandelli, M.A.; Duskey, J.T.; Ruozi, B. Tunneling Nanotubes: A New Target for Nanomedicine? *International Journal of Molecular Sciences* **2022**, *23*, 2237, doi:10.3390/ijms23042237.
535. Yoo, J.Y.; Yeh, M.; Kaur, B.; Lee, T.J. Targeted Delivery of Small Noncoding RNA for Glioblastoma. *Cancer Letters* **2021**, *500*, 274–280, doi:10.1016/j.canlet.2020.11.004.
536. Mirzaei, S.; Mahabady, M.K.; Zabolian, A.; Abbaspour, A.; Fallahzadeh, P.; Noori, M.; Hashemi, F.; Hushmandi, K.; Daneshi, S.; Kumar, A.P.; et al. Small Interfering RNA (SiRNA) to Target Genes and Molecular Pathways in Glioblastoma Therapy: Current Status with an Emphasis on Delivery Systems. *Life Sciences* **2021**, *275*, 119368, doi:10.1016/j.lfs.2021.119368.
537. Uribe, D.; Niechi, I.; Rackov, G.; Erices, J.I.; San Martín, R.; Quezada, C. Adapt to Persist: Glioblastoma Microenvironment and Epigenetic Regulation on Cell Plasticity. *Biology* **2022**, *11*, 313, doi:10.3390/biology11020313.
538. Ali, S.; Borin, T.F.; Piranlioglu, R.; Ara, R.; Lebedyeva, I.; Angara, K.; Achyut, B.R.; Arbab, A.S.; Rashid, M.H. Changes in the Tumor Microenvironment and Outcome for TME-Targeting Therapy in Glioblastoma: A Pilot Study. *PLOS ONE* **2021**, *16*, e0246646, doi:10.1371/journal.pone.0246646.
539. Wang, H.; Zhou, H.; Xu, J.; Lu, Y.; Ji, X.; Yao, Y.; Chao, H.; Zhang, J.; Zhang, X.; Yao, S.; et al. Different T-Cell Subsets in Glioblastoma Multiforme and Targeted Immunotherapy. *Cancer Letters* **2021**, *496*, 134–143, doi:10.1016/j.canlet.2020.09.028.
540. Shi, Y.; Kong, Z.; Liu, P.; Hou, G.; Wu, J.; Ma, W.; Cheng, X.; Wang, Y. Oncogenesis, Microenvironment Modulation and Clinical Potentiality of FAP in Glioblastoma: Lessons Learned from Other Solid Tumors. *Cells* **2021**, *10*, 1142, doi:10.3390/cells10051142.
541. Zhu, H.; Yu, X.; Zhang, S.; Shu, K. Targeting the Complement Pathway in Malignant Glioma Microenvironments. *Front Cell Dev Biol* **2021**, *9*, 657472, doi:10.3389/fcell.2021.657472.
542. Ruan, S.; Xiao, W.; Hu, C.; Zhang, H.; Rao, J.; Wang, S.; Wang, X.; He, Q.; Gao, H. Ligand-Mediated and Enzyme-Directed Precise Targeting and Retention for the Enhanced Treatment of Glioblastoma. *ACS Appl. Mater. Interfaces* **2017**, *9*, 20348–20360, doi:10.1021/acsami.7b02303.
543. Gu, W.; Meng, F.; Haag, R.; Zhong, Z. Actively Targeted Nanomedicines for Precision Cancer Therapy: Concept, Construction, Challenges and Clinical Translation. *Journal of Controlled Release* **2021**, *329*, 676–695, doi:10.1016/j.jconrel.2020.10.003.

544. Liu, Y.; Wang, W.; Zhang, D.; Sun, Y.; Li, F.; Zheng, M.; Lovejoy, D.B.; Zou, Y.; Shi, B. Brain Co-delivery of First-line Chemotherapy Drug and Epigenetic Bromodomain Inhibitor for Multidimensional Enhanced Synergistic Glioblastoma Therapy. *Exploration* **2022**, 20210274, doi:10.1002/EXP.20210274.
545. Gao, X.; Xu, J.; Yao, T.; Liu, X.; Zhang, H.; Zhan, C. Peptide-Decorated Nanocarriers Penetrating the Blood-Brain Barrier for Imaging and Therapy of Brain Diseases. *Advanced Drug Delivery Reviews* **2022**, *187*, 114362, doi:10.1016/j.addr.2022.114362.
546. Gallego, L.; Ceña, V. **Nanoparticle-Mediated Therapeutic Compounds Delivery to Glioblastoma**. *Expert Opinion on Drug Delivery* **2020**, *17*, 1541–1554, doi:10.1080/17425247.2020.1810015.
547. Parveen, S.; Fatima, S.; Quadri, S.N.; Beg, S.; Abdin, M.Z. Surface-Decoration Strategies in Nanomedicine for Cancer Treatment. In *Nanoformulation Strategies for Cancer Treatment*; Elsevier, 2021; pp. 131–152 ISBN 978-0-12-821095-6.
548. Giakoumettis, D.; Kritis, A.; Foroglou, N. C6 Cell Line: The Gold Standard in Glioma Research. *Hippokratia* **2018**, *22*, 105–112.
549. Chou, Y.-H.; Khuon, S.; Herrmann, H.; Goldman, R.D. Nestin Promotes the Phosphorylation-Dependent Disassembly of Vimentin Intermediate Filaments During Mitosis. *Mol Biol Cell* **2003**, *14*, 1468–1478, doi:10.1091/mbc.E02-08-0545.
550. Ullah, I.; Chung, K.; Bae, S.; Li, Y.; Kim, C.; Choi, B.; Nam, H.Y.; Kim, S.H.; Yun, C.-O.; Lee, K.Y.; et al. Nose-to-Brain Delivery of Cancer-Targeting Paclitaxel-Loaded Nanoparticles Potentiates Antitumor Effects in Malignant Glioblastoma. *Mol. Pharmaceutics* **2020**, *17*, 1193–1204, doi:10.1021/acs.molpharmaceut.9b01215.
551. Song, S.; Mao, G.; Du, J.; Zhu, X. Novel RGD Containing, Temozolomide-Loading Nanostructured Lipid Carriers for Glioblastoma Multiforme Chemotherapy. *Drug Delivery* **2016**, *23*, 1404–1408, doi:10.3109/10717544.2015.1064186.
552. Zhang, J.; Xiao, X.; Zhu, J.; Gao, Z.; Lai, X.; Zhu, X.; Mao, G. Lactoferrin- and RGD-Comodified, Temozolomide and Vincristine-Coloaded Nanostructured Lipid Carriers for Gliomatosis Cerebri Combination Therapy. *IJN* **2018**, *Volume 13*, 3039–3051, doi:10.2147/IJN.S161163.
553. Wang, G.; Wang, Z.; Li, C.; Duan, G.; Wang, K.; Li, Q.; Tao, T. RGD Peptide-Modified, Paclitaxel Prodrug-Based, Dual-Drugs Loaded, and Redox-Sensitive Lipid-Polymer Nanoparticles for the Enhanced Lung Cancer Therapy. *Biomedicine & Pharmacotherapy* **2018**, *106*, 275–284, doi:10.1016/j.biopha.2018.06.137.
554. Ruan, H.; Chen, X.; Xie, C.; Li, B.; Ying, M.; Liu, Y.; Zhang, M.; Zhang, X.; Zhan, C.; Lu, W.; et al. Stapled RGD Peptide Enables Glioma-Targeted Drug Delivery by Overcoming Multiple Barriers. *ACS Appl. Mater. Interfaces* **2017**, *9*, 17745–17756, doi:10.1021/acsami.7b03682.
555. Miura, Y.; Takenaka, T.; Toh, K.; Wu, S.; Nishihara, H.; Kano, M.R.; Ino, Y.; Nomoto, T.; Matsumoto, Y.; Koyama, H.; et al. Cyclic RGD-Linked Polymeric Micelles for Targeted Delivery of Platinum Anticancer Drugs to Glioblastoma through the Blood–Brain Tumor Barrier. *ACS Nano* **2013**, *7*, 8583–8592, doi:10.1021/nn402662d.
556. Jena, L.; McErlean, E.; McCarthy, H. Delivery across the Blood-Brain Barrier: Nanomedicine for Glioblastoma Multiforme. *Drug Deliv. and Transl. Res.* **2020**, *10*, 304–318, doi:10.1007/s13346-019-00679-2.
557. Tosi, G.; Bortot, B.; Ruozi, B.; Dolcetta, D.; Vandelli, M.A.; Forni, F.; Severini, G.M. Potential Use of Polymeric Nanoparticles for Drug Delivery Across the Blood-Brain Barrier. *CMC* **2013**, *20*, 2212–2225, doi:10.2174/0929867311320170006.
558. Barbara, R.; Belletti, D.; Pederzoli, F.; Masoni, M.; Keller, J.; Ballestrazzi, A.; Vandelli, M.A.; Tosi, G.; Grabrucker, A.M. Novel Curcumin Loaded Nanoparticles

Engineered for Blood-Brain Barrier Crossing and Able to Disrupt Abeta Aggregates. *International Journal of Pharmaceutics* **2017**, *526*, 413–424, doi:10.1016/j.ijpharm.2017.05.015.
559. Luo, Y.; Yang, H.; Zhou, Y.-F.; Hu, B. Dual and Multi-Targeted Nanoparticles for Site-Specific Brain Drug Delivery. *Journal of Controlled Release* **2020**, *317*, 195–215, doi:10.1016/j.jconrel.2019.11.037.
560. Razpotnik, R.; Novak, N.; Čurin Šerbec, V.; Rajcevic, U. Targeting Malignant Brain Tumors with Antibodies. *Front. Immunol.* **2017**, *8*, 1181, doi:10.3389/fimmu.2017.01181.
561. Kloepper, J.; Riedemann, L.; Amoozgar, Z.; Seano, G.; Susek, K.; Yu, V.; Dalvie, N.; Amelung, R.L.; Datta, M.; Song, J.W.; et al. Ang-2/VEGF Bispecific Antibody Reprograms Macrophages and Resident Microglia to Anti-Tumor Phenotype and Prolongs Glioblastoma Survival. *Proc. Natl. Acad. Sci. U.S.A.* **2016**, *113*, 4476–4481, doi:10.1073/pnas.1525360113.
562. Choi, B.D.; Kuan, C.-T.; Cai, M.; Archer, G.E.; Mitchell, D.A.; Gedeon, P.C.; Sanchez-Perez, L.; Pastan, I.; Bigner, D.D.; Sampson, J.H. Systemic Administration of a Bispecific Antibody Targeting EGFRvIII Successfully Treats Intracerebral Glioma. *Proc. Natl. Acad. Sci. U.S.A.* **2013**, *110*, 270–275, doi:10.1073/pnas.1219817110.
563. Alkilany, A.M.; Zhu, L.; Weller, H.; Mews, A.; Parak, W.J.; Barz, M.; Feliu, N. Ligand Density on Nanoparticles: A Parameter with Critical Impact on Nanomedicine. *Advanced Drug Delivery Reviews* **2019**, *143*, 22–36, doi:10.1016/j.addr.2019.05.010.
564. Tietjen, G.T.; Bracaglia, L.G.; Saltzman, W.M.; Pober, J.S. Focus on Fundamentals: Achieving Effective Nanoparticle Targeting. *Trends in Molecular Medicine* **2018**, *24*, 598–606, doi:10.1016/j.molmed.2018.05.003.
565. Zetterberg, M. Age-Related Eye Disease and Gender. *Maturitas* **2016**, *83*, 19–26, doi:10.1016/j.maturitas.2015.10.005.
566. Klein, R.; Klein, B.E.K. The Prevalence of Age-Related Eye Diseases and Visual Impairment in Aging: Current Estimates. *Investigative Ophthalmology & Visual Science* **2013**, *54*, ORSF5–ORSF13, doi:10.1167/iovs.13-12789.
567. Kreft, D.; Doblhammer, G.; Guthoff, R.F.; Frech, S. Incidence, Individual, and Macro Level Risk Factors of Severe Binocular Visual Impairment and Blindness in Persons Aged 50 and Older. *PLOS ONE* **2021**, *16*, e0251018, doi:10.1371/journal.pone.0251018.
568. Himawan, E.; Ekström, P.; Buzgo, M.; Gaillard, P.; Stefánsson, E.; Marigo, V.; Loftsson, T.; Paquet-Durand, F. Drug Delivery to Retinal Photoreceptors. *Drug Discov Today* **2019**, *24*, 1637–1643, doi:10.1016/j.drudis.2019.03.004.
569. Vander Poorten, E.; Riviere, C.N.; Abbott, J.J.; Bergeles, C.; Nasseri, M.A.; Kang, J.U.; Sznitman, R.; Faridpooya, K.; Iordachita, I. 36 - Robotic Retinal Surgery. In *Handbook of Robotic and Image-Guided Surgery*; Abedin-Nasab, M.H., Ed.; Elsevier, 2020; pp. 627–672 ISBN 978-0-12-814245-5.
570. Loriga, B.; Di Filippo, A.; Tofani, L.; Signorini, P.; Caporossi, T.; Barca, F.; De Gaudio, A.R.; Rizzo, S.; Adembri, C. Postoperative Pain after Vitreo-Retinal Surgery Is Influenced by Surgery Duration and Anesthesia Conduction. *Minerva Anestesiol* **2019**, *85*, 731–737, doi:10.23736/s0375-9393.18.13078-1.
571. Trapani, I.; Auricchio, A. Has Retinal Gene Therapy Come of Age? From Bench to Bedside and Back to Bench. *Hum Mol Genet* **2019**, *28*, R108–R118, doi:10.1093/hmg/ddz130.
572. Meyer, C.H.; Krohne, T.U.; Issa, P.C.; Liu, Z.; Holz, F.G. Routes for Drug Delivery to the Eye and Retina: Intravitreal Injections. *Retinal Pharmacotherapeutics* **2016**, *55*, 63–70, doi:10.1159/000431143.
573. Ladha, R.; Caspers, L.E.; Willermain, F.; de Smet, M.D. Subretinal Therapy: Technological Solutions to Surgical and Immunological Challenges. *Front Med (Lausanne)* **2022**, *9*, 846782, doi:10.3389/fmed.2022.846782.

574. Kim, H.M.; Woo, S.J. Ocular Drug Delivery to the Retina: Current Innovations and Future Perspectives. *Pharmaceutics* **2021**, *13*, 108, doi:10.3390/pharmaceutics13010108.
575. Causin, P.; Malgaroli, F. Mathematical and Numerical Methods for Modeling Drug Delivery to the Posterior Segment of the Eye. **2017**.
576. van der Meel, R.; Sulheim, E.; Shi, Y.; Kiessling, F.; Mulder, W.J.M.; Lammers, T. Smart Cancer Nanomedicine. *Nat. Nanotechnol.* **2019**, *14*, 1007–1017, doi:10.1038/s41565-019-0567-y.
577. Beltrán-Gracia, E.; López-Camacho, A.; Higuera-Ciapara, I.; Velázquez-Fernández, J.B.; Vallejo-Cardona, A.A. Nanomedicine Review: Clinical Developments in Liposomal Applications. *Cancer Nano* **2019**, *10*, 11, doi:10.1186/s12645-019-0055-y.
578. Duskey, J.T.; Rinaldi, A.; Ottonelli, I.; Caraffi, R.; De Benedictis, C.A.; Sauer, A.K.; Tosi, G.; Vandelli, M.A.; Ruozi, B.; Grabrucker, A.M. Glioblastoma Multiforme Selective Nanomedicines for Improved Anti-Cancer Treatments. *Pharmaceutics* **2022**, *14*, 1450, doi:10.3390/pharmaceutics14071450.
579. Kim, H.M.; Ha, S.; Hong, H.K.; Hwang, Y.; Kim, P.; Yang, E.; Chung, J.Y.; Park, S.; Park, Y.J.; Park, K.H.; et al. Intraocular Distribution and Kinetics of Intravitreally Injected Antibodies and Nanoparticles in Rabbit Eyes. *Translational Vision Science & Technology* **2020**, *9*, 20, doi:10.1167/tvst.9.6.20.
580. Martens, T.F.; Remaut, K.; Deschout, H.; Engbersen, J.F.J.; Hennink, W.E.; van Steenbergen, M.J.; Demeester, J.; De Smedt, S.C.; Braeckmans, K. Coating Nanocarriers with Hyaluronic Acid Facilitates Intravitreal Drug Delivery for Retinal Gene Therapy. *Journal of Controlled Release* **2015**, *202*, 83–92, doi:10.1016/j.jconrel.2015.01.030.
581. Eriksen, A.Z.; Brewer, J.; Andresen, T.L.; Urquhart, A.J. The Diffusion Dynamics of PEGylated Liposomes in the Intact Vitreous of the Ex Vivo Porcine Eye: A Fluorescence Correlation Spectroscopy and Biodistribution Study. *International Journal of Pharmaceutics* **2017**, *522*, 90–97, doi:10.1016/j.ijpharm.2017.03.003.
582. Tawfik, M.; Chen, F.; Goldberg, J.L.; Sabel, B.A. Nanomedicine and Drug Delivery to the Retina: Current Status and Implications for Gene Therapy. *Naunyn-Schmiedeberg's Arch Pharmacol* **2022**, *395*, 1477–1507, doi:10.1007/s00210-022-02287-3.
583. Borodina, T.; Kostyushev, D.; Zamyatnin, A.A.; Parodi, A. Nanomedicine for Treating Diabetic Retinopathy Vascular Degeneration. *International Journal of Translational Medicine* **2021**, *1*, 306–322, doi:10.3390/ijtm1030018.
584. Devoldere, J.; Wels, M.; Peynshaert, K.; Dewitte, H.; De Smedt, S.C.; Remaut, K. The Obstacle Course to the Inner Retina: Hyaluronic Acid-Coated Lipoplexes Cross the Vitreous but Fail to Overcome the Inner Limiting Membrane. *European Journal of Pharmaceutics and Biopharmaceutics* **2019**, *141*, 161–171, doi:10.1016/j.ejpb.2019.05.023.
585. Shafaie, S.; Hutter, V.; Brown, M.B.; Cook, M.T.; Chau, D.Y.S. Diffusion through the Ex Vivo Vitreal Body – Bovine, Porcine, and Ovine Models Are Poor Surrogates for the Human Vitreous. *International Journal of Pharmaceutics* **2018**, *550*, 207–215, doi:10.1016/j.ijpharm.2018.07.070.
586. Romeo, A.; Bonaccorso, A.; Carbone, C.; Lupo, G.; Daniela Anfuso, C.; Giurdanella, G.; Caggia, C.; Randazzo, C.; Russo, N.; Luca Romano, G.; et al. Melatonin Loaded Hybrid Nanomedicine: DoE Approach, Optimization and in Vitro Study on Diabetic Retinopathy Model. *International Journal of Pharmaceutics* **2022**, *627*, 122195, doi:10.1016/j.ijpharm.2022.122195.
587. Xie, L.; Yue, W.; Ibrahim, K.; Shen, J. A Long-Acting Curcumin Nanoparticle/In Situ Hydrogel Composite for the Treatment of Uveal Melanoma. *Pharmaceutics* **2021**, *13*, 1335, doi:10.3390/pharmaceutics13091335.

588. Mathew, A.P.; Uthaman, S.; Cho, K.-H.; Cho, C.-S.; Park, I.-K. Injectable Hydrogels for Delivering Biotherapeutic Molecules. *International Journal of Biological Macromolecules* **2018**, *110*, 17–29, doi:10.1016/j.ijbiomac.2017.11.113.
589. Li, Y.; Yang, H.Y.; Lee, D.S. Advances in Biodegradable and Injectable Hydrogels for Biomedical Applications. *Journal of Controlled Release* **2021**, *330*, 151–160, doi:10.1016/j.jconrel.2020.12.008.
590. Rasool, A.; Ata, S.; Islam, A. Stimuli Responsive Biopolymer (Chitosan) Based Blend Hydrogels for Wound Healing Application. *Carbohydrate Polymers* **2019**, *203*, 423–429, doi:10.1016/j.carbpol.2018.09.083.
591. Han, L.; Zhang, Y.; Lu, X.; Wang, K.; Wang, Z.; Zhang, H. Polydopamine Nanoparticles Modulating Stimuli-Responsive PNIPAM Hydrogels with Cell/Tissue Adhesiveness. *ACS Appl. Mater. Interfaces* **2016**, *8*, 29088–29100, doi:10.1021/acsami.6b11043.
592. Deng, Z.; Guo, Y.; Zhao, X.; Ma, P.X.; Guo, B. Multifunctional Stimuli-Responsive Hydrogels with Self-Healing, High Conductivity, and Rapid Recovery through Host–Guest Interactions. *Chem. Mater.* **2018**, *30*, 1729–1742, doi:10.1021/acs.chemmater.8b00008.
593. Djoudi, A.; Molina-Peña, R.; Ferreira, N.; Ottonelli, I.; Tosi, G.; Garcion, E.; Boury, F. Hyaluronic Acid Scaffolds for Loco-Regional Therapy in Nervous System Related Disorders. *International Journal of Molecular Sciences* **2022**, *23*, 12174, doi:10.3390/ijms232012174.
594. Niemczyk, B.; Sajkiewicz, P.; Kolbuk, D. Injectable Hydrogels as Novel Materials for Central Nervous System Regeneration. *J. Neural Eng.* **2018**, *15*, 051002, doi:10.1088/1741-2552/aacbab.
595. Sood, N.; Bhardwaj, A.; Mehta, S.; Mehta, A. Stimuli-Responsive Hydrogels in Drug Delivery and Tissue Engineering. *Drug Delivery* **2016**, *23*, 748–770, doi:10.3109/10717544.2014.940091.
596. Echeverria, C.; Fernandes, S.N.; Godinho, M.H.; Borges, J.P.; Soares, P.I.P. Functional Stimuli-Responsive Gels: Hydrogels and Microgels. *Gels* **2018**, *4*, 54, doi:10.3390/gels4020054.
597. Chao, Y.; Chen, Q.; Liu, Z. Smart Injectable Hydrogels for Cancer Immunotherapy. *Advanced Functional Materials* **2020**, *30*, 1902785, doi:10.1002/adfm.201902785.
598. Liu, M.; Zeng, X.; Ma, C.; Yi, H.; Ali, Z.; Mou, X.; Li, S.; Deng, Y.; He, N. Injectable Hydrogels for Cartilage and Bone Tissue Engineering. *Bone Res* **2017**, *5*, 1–20, doi:10.1038/boneres.2017.14.
599. Nutan, B.; Chandel, A.K.S.; Biswas, A.; Kumar, A.; Yadav, A.; Maiti, P.; Jewrajka, S.K. Gold Nanoparticle Promoted Formation and Biological Properties of Injectable Hydrogels. *Biomacromolecules* **2020**, *21*, 3782–3794, doi:10.1021/acs.biomac.0c00889.
600. Lee, D.; Heo, D.N.; Nah, H.R.; Lee, S.J.; Ko, W.-K.; Lee, J.S.; Moon, H.-J.; Bang, J.B.; Hwang, Y.-S.; Reis, R.L.; et al. Injectable Hydrogel Composite Containing Modified Gold Nanoparticles: Implication in Bone Tissue Regeneration. *Int J Nanomedicine* **2018**, *13*, 7019–7031, doi:10.2147/IJN.S185715.
601. Baumann, B.; Wittig, R.; Lindén, M. Mesoporous Silica Nanoparticles in Injectable Hydrogels: Factors Influencing Cellular Uptake and Viability. *Nanoscale* **2017**, *9*, 12379–12390, doi:10.1039/C7NR02015E.
602. Hofmann-Amtenbrink, M.; Grainger, D.W.; Hofmann, H. Nanoparticles in Medicine: Current Challenges Facing Inorganic Nanoparticle Toxicity Assessments and Standardizations. *Nanomedicine: Nanotechnology, Biology and Medicine* **2015**, *11*, 1689–1694, doi:10.1016/j.nano.2015.05.005.

603. Cooper, R.C.; Yang, H. Hydrogel-Based Ocular Drug Delivery Systems: Emerging Fabrication Strategies, Applications, and Bench-to-Bedside Manufacturing Considerations. *Journal of Controlled Release* **2019**, *306*, 29–39, doi:10.1016/j.jconrel.2019.05.034.
604. Kim, M.R.; Park, T.G. Temperature-Responsive and Degradable Hyaluronic Acid/Pluronic Composite Hydrogels for Controlled Release of Human Growth Hormone. *Journal of Controlled Release* **2002**, *80*, 69–77, doi:10.1016/S0168-3659(01)00557-0.
605. Huh, H.W.; Zhao, L.; Kim, S.Y. Biomineralized Biomimetic Organic/Inorganic Hybrid Hydrogels Based on Hyaluronic Acid and Poloxamer. *Carbohydrate Polymers* **2015**, *126*, 130–140, doi:10.1016/j.carbpol.2015.03.033.
606. Lin, J.-Y.; Lai, P.-L.; Lin, Y.-K.; Peng, S.; Lee, L.-Y.; Chen, C.-N.; Chu, I.-M. A Poloxamer-Polypeptide Thermosensitive Hydrogel as a Cell Scaffold and Sustained Release Depot. *Polymer Chemistry* **2016**, *7*, 2976–2985, doi:10.1039/C5PY02067K.
607. Huang, L.; Kutluer, M.; Adani, E.; Comitato, A.; Marigo, V. New In Vitro Cellular Model for Molecular Studies of Retinitis Pigmentosa. *International Journal of Molecular Sciences* **2021**, *22*, 6440, doi:10.3390/ijms22126440.
608. Tan, E.; Ding, X.-Q.; Saadi, A.; Agarwal, N.; Naash, M.I.; Al-Ubaidi, M.R. Expression of Cone-Photoreceptor-Specific Antigens in a Cell Line Derived from Retinal Tumors in Transgenic Mice. *Invest Ophthalmol Vis Sci* **2004**, *45*, 764–768, doi:10.1167/iovs.03-1114.
609. Dave, V.; Tak, K.; Sohgaura, A.; Gupta, A.; Sadhu, V.; Reddy, K.R. Lipid-Polymer Hybrid Nanoparticles: Synthesis Strategies and Biomedical Applications. *Journal of Microbiological Methods* **2019**, *160*, 130–142, doi:10.1016/j.mimet.2019.03.017.
610. Joshi, D.P.; Lan-Chun-Fung, Y.L.; Pritchard, J.G. Determination of Poly(Vinyl Alcohol) via Its Complex with Boric Acid and Iodine. *Analytica Chimica Acta* **1979**, *104*, 153–160, doi:10.1016/S0003-2670(01)83825-3.
611. Ottonelli, I.; Duskey, J.T.; Genovese, F.; Pederzoli, F.; Caraffi, R.; Valenza, M.; Tosi, G.; Vandelli, M.A.; Ruozi, B. Quantitative Comparison of the Protein Corona of Nanoparticles with Different Matrices. *International Journal of Pharmaceutics: X* **2022**, *4*, 100136, doi:10.1016/j.ijpx.2022.100136.
612. Sakami, S.; Maeda, T.; Bereta, G.; Okano, K.; Golczak, M.; Sumaroka, A.; Roman, A.J.; Cideciyan, A.V.; Jacobson, S.G.; Palczewski, K. Probing Mechanisms of Photoreceptor Degeneration in a New Mouse Model of the Common Form of Autosomal Dominant Retinitis Pigmentosa Due to P23H Opsin Mutations♦. *J Biol Chem* **2011**, *286*, 10551–10567, doi:10.1074/jbc.M110.209759.
613. Sanges, D.; Comitato, A.; Tammaro, R.; Marigo, V. Apoptosis in Retinal Degeneration Involves Cross-Talk between Apoptosis-Inducing Factor (AIF) and Caspase-12 and Is Blocked by Calpain Inhibitors. *Proceedings of the National Academy of Sciences* **2006**, *103*, 17366–17371, doi:10.1073/pnas.0606276103.
614. Huang, L.; Himawan, E.; Belhadj, S.; Pérez García, R.O.; Paquet Durand, F.; Schipper, N.; Buzgo, M.; Simaite, A.; Marigo, V. Efficient Delivery of Hydrophilic Small Molecules to Retinal Cell Lines Using Gel Core-Containing Solid Lipid Nanoparticles. *Pharmaceutics* **2021**, *14*, 74, doi:10.3390/pharmaceutics14010074.
615. Thakur, S.S.; Shenoy, S.K.; Suk, J.S.; Hanes, J.S.; Rupenthal, I.D. Validation of Hyaluronic Acid-Agar-Based Hydrogels as Vitreous Humor Mimetics for in Vitro Drug and Particle Migration Evaluations. *European Journal of Pharmaceutics and Biopharmaceutics* **2020**, *148*, 118–125, doi:10.1016/j.ejpb.2020.01.008.
616. Ottonelli, I.; Duskey, J.T.; Rinaldi, A.; Grazioli, M.V.; Parmeggiani, I.; Vandelli, M.A.; Wang, L.Z.; Prud'homme, R.K.; Tosi, G.; Ruozi, B. Microfluidic Technology for the

Production of Hybrid Nanomedicines. *Pharmaceutics* **2021**, *13*, 1495, doi:10.3390/pharmaceutics13091495.
617. Zhao, L.; Skwarczynski, M.; Toth, I. Polyelectrolyte-Based Platforms for the Delivery of Peptides and Proteins. *ACS Biomater. Sci. Eng.* **2019**, *5*, 4937–4950, doi:10.1021/acsbiomaterials.9b01135.
618. Wakebayashi, D.; Nishiyama, N.; Itaka, K.; Miyata, K.; Yamasaki, Y.; Harada, A.; Koyama, H.; Nagasaki, Y.; Kataoka, K. Polyion Complex Micelles of PDNA with Acetal-Poly(Ethylene Glycol)-Poly(2-(Dimethylamino)Ethyl Methacrylate) Block Copolymer as the Gene Carrier System: Physicochemical Properties of Micelles Relevant to Gene Transfection Efficacy. *Biomacromolecules* **2004**, *5*, 2128–2136, doi:10.1021/bm040009j.
619. Nickerson, C.S.; Karageozian, H.L.; Park, J.; Kornfield, J.A. The Mechanical Properties of the Vitreous Humor. *Investigative Ophthalmology & Visual Science* **2004**, *45*, 37.
620. Nickerson, C.S.; Park, J.; Kornfield, J.A.; Karageozian, H. Rheological Properties of the Vitreous and the Role of Hyaluronic Acid. *Journal of Biomechanics* **2008**, *41*, 1840–1846, doi:10.1016/j.jbiomech.2008.04.015.
621. Crommelin, D.J.A.; van Hoogevest, P.; Storm, G. The Role of Liposomes in Clinical Nanomedicine Development. What Now? Now What? *Journal of Controlled Release* **2020**, *318*, 256–263, doi:10.1016/j.jconrel.2019.12.023.
622. Bachu, R.D.; Chowdhury, P.; Al-Saedi, Z.H.F.; Karla, P.K.; Boddu, S.H.S. Ocular Drug Delivery Barriers—Role of Nanocarriers in the Treatment of Anterior Segment Ocular Diseases. *Pharmaceutics* **2018**, *10*, 28, doi:10.3390/pharmaceutics10010028.
623. Salama, H.A.; Ghorab, M.; Mahmoud, A.A.; Abdel Hady, M. PLGA Nanoparticles as Subconjunctival Injection for Management of Glaucoma. *AAPS PharmSciTech* **2017**, *18*, 2517–2528, doi:10.1208/s12249-017-0710-8.
624. Zhang, E.; Zhukova, V.; Semyonkin, A.; Osipova, N.; Malinovskaya, Y.; Maksimenko, O.; Chernikov, V.; Sokolov, M.; Grigartzik, L.; Sabel, B.A.; et al. Release Kinetics of Fluorescent Dyes from PLGA Nanoparticles in Retinal Blood Vessels: In Vivo Monitoring and Ex Vivo Localization. *European Journal of Pharmaceutics and Biopharmaceutics* **2020**, *150*, 131–142, doi:10.1016/j.ejpb.2020.03.006.
625. Meikle, T.G.; Drummond, C.J.; Conn, C.E.; Meikle, T.G.; Drummond, C.J.; Conn, C.E. Microfluidic Synthesis of Rifampicin Loaded PLGA Nanoparticles and the Effect of Formulation on Their Physical and Antibacterial Properties. *Aust. J. Chem.* **2019**, *73*, 151–157, doi:10.1071/CH19359.
626. Markowski, A.; Jaromin, A.; Migdał, P.; Olczak, E.; Zygmunt, A.; Zaremba-Czogalla, M.; Pawlik, K.; Gubernator, J. Design and Development of a New Type of Hybrid PLGA/Lipid Nanoparticle as an Ursolic Acid Delivery System against Pancreatic Ductal Adenocarcinoma Cells. *International Journal of Molecular Sciences* **2022**, *23*, 5536, doi:10.3390/ijms23105536.
627. Mandal, A.; Pal, D.; Agrahari, V.; Trinh, H.M.; Joseph, M.; Mitra, A.K. Ocular Delivery of Proteins and Peptides: Challenges and Novel Formulation Approaches. *Advanced Drug Delivery Reviews* **2018**, *126*, 67–95, doi:10.1016/j.addr.2018.01.008.
628. Bisht, R.; Mandal, A.; Jaiswal, J.K.; Rupenthal, I.D. Nanocarrier Mediated Retinal Drug Delivery: Overcoming Ocular Barriers to Treat Posterior Eye Diseases: Nanocarrier Mediated Retinal Drug Delivery. *WIREs Nanomed Nanobiotechnol* **2018**, *10*, e1473, doi:10.1002/wnan.1473.
629. Laradji, A.; Karakocak, B.B.; Kolesnikov, A.V.; Kefalov, V.J.; Ravi, N. Hyaluronic Acid-Based Gold Nanoparticles for the Topical Delivery of Therapeutics to the Retina and the Retinal Pigment Epithelium. *Polymers* **2021**, *13*, 3324, doi:10.3390/polym13193324.

630. Yu, M.; Wang, K.; Zhang, H.; Liu, Q.; Wang, J.; Cao, L.; Li, W.; Wang, K.; Hong, Z. DOTAP-Incorporated PEG-PLGA Nanoparticles for Efficient In Vitro and In Vivo Gene Delivery. *Journal of Biomedical Nanotechnology* **2018**, *14*, 281–293, doi:10.1166/jbn.2018.2470.
631. Van Kampen, E.; Vandervelden, C.; Fakhari, A.; Qian, J.; Berkland, C.; Gehrke, S.H. Design of Hollow Hyaluronic Acid Cylinders for Sustained Intravitreal Protein Delivery. *Journal of Pharmaceutical Sciences* **2018**, *107*, 2354–2365, doi:10.1016/j.xphs.2018.04.024.
632. Sargazi, A.; Kamali, N.; Shiri, F.; Heidari Majd, M. Hyaluronic Acid/Polyethylene Glycol Nanoparticles for Controlled Delivery of Mitoxantrone. *Artificial Cells, Nanomedicine, and Biotechnology* **2018**, *46*, 500–509, doi:10.1080/21691401.2017.1324462.
633. Gómez-Mariscal, M.; Puerto, B.; Muñoz-Negrete, F.J.; de Juan, V.; Rebolleda, G. Acute and Chronic Optic Nerve Head Biomechanics and Intraocular Pressure Changes in Patients Receiving Multiple Intravitreal Injections of Anti-VEGF. *Graefes Arch Clin Exp Ophthalmol* **2019**, *257*, 2221–2231, doi:10.1007/s00417-019-04354-7.
634. Pacella, E.; Loffredo, L.; Malvasi, M.; Trovato Battagliola, E.; Messineo, D.; Pacella, F.; Arrico, L. Effects of Repeated Intravitreal Injections of Dexamethasone Implants on Intraocular Pressure: A 4-Year Study. *Clin Ophthalmol* **2020**, *14*, 3611–3617, doi:10.2147/OPTH.S265691.
635. Zhang, K.; Liu, Z.; Lin, Q.; Boo, Y.J.; Ow, V.; Zhao, X.; Wong, D.S.L.; Lim, J.Y.C.; Xue, K.; Su, X.; et al. Injectable PTHF-Based Thermogelling Polyurethane Implants for Long-Term Intraocular Application. *Biomaterials Research* **2022**, *26*, 70, doi:10.1186/s40824-022-00316-z.
636. Dannert, C.; Stokke, B.T.; Dias, R.S. Nanoparticle-Hydrogel Composites: From Molecular Interactions to Macroscopic Behavior. *Polymers* **2019**, *11*, 275, doi:10.3390/polym11020275.
637. Cheng, Y.-H.; Ko, Y.-C.; Chang, Y.-F.; Huang, S.-H.; Liu, C.J. Thermosensitive Chitosan-Gelatin-Based Hydrogel Containing Curcumin-Loaded Nanoparticles and Latanoprost as a Dual-Drug Delivery System for Glaucoma Treatment. *Experimental Eye Research* **2019**, *179*, 179–187, doi:10.1016/j.exer.2018.11.017.
638. Wang, X.; Liu, L.; Xia, S.; Muhoza, B.; Cai, J.; Zhang, X.; Duhoranimana, E.; Su, J. Sodium Carboxymethyl Cellulose Modulates the Stability of Cinnamaldehyde-Loaded Liposomes at High Ionic Strength. *Food Hydrocolloids* **2019**, *93*, 10–18, doi:10.1016/j.foodhyd.2019.02.004.
639. López-Cano, J.J.; Sigen A; Andrés-Guerrero, V.; Tai, H.; Bravo-Osuna, I.; Molina-Martínez, I.T.; Wang, W.; Herrero-Vanrell, R. Thermo-Responsive PLGA-PEG-PLGA Hydrogels as Novel Injectable Platforms for Neuroprotective Combined Therapies in the Treatment of Retinal Degenerative Diseases. *Pharmaceutics* **2021**, *13*, 234, doi:10.3390/pharmaceutics13020234.
640. Suri, R.; Neupane, Y.R.; Mehra, N.; Nematullah, M.; Khan, F.; Alam, O.; Iqubal, A.; Jain, G.K.; Kohli, K. Sirolimus Loaded Chitosan Functionalized Poly (Lactic-Co-Glycolic Acid) (PLGA) Nanoparticles for Potential Treatment of Age-Related Macular Degeneration. *International Journal of Biological Macromolecules* **2021**, *191*, 548–559, doi:10.1016/j.ijbiomac.2021.09.069.
641. Hsu, X.-L.; Wu, L.-C.; Hsieh, J.-Y.; Huang, Y.-Y. Nanoparticle-Hydrogel Composite Drug Delivery System for Potential Ocular Applications. *Polymers* **2021**, *13*, 642, doi:10.3390/polym13040642.
642. Taheri, S.L.; Rezazadeh, M.; Hassanzadeh, F.; Akbari, V.; Dehghani, A.; Talebi, A.; Mostafavi, S.A. Preparation, Physicochemical, and Retinal Anti-Angiogenic Evaluation of Poloxamer Hydrogel Containing Dexamethasone/Avastin-Loaded Chitosan-N-Acetyl-L-

Cysteine Nanoparticles. *International Journal of Biological Macromolecules* **2022**, *220*, 1605–1618, doi:10.1016/j.ijbiomac.2022.09.101.
643. Nanomedicine and the COVID-19 Vaccines. *Nat. Nanotechnol.* **2020**, *15*, 963–963, doi:10.1038/s41565-020-00820-0.
644. Let's Talk about Lipid Nanoparticles. *Nat Rev Mater* **2021**, *6*, 99–99, doi:10.1038/s41578-021-00281-4.
645. Zhong, H.; Chan, G.; Hu, Y.; Hu, H.; Ouyang, D. A Comprehensive Map of FDA-Approved Pharmaceutical Products. *Pharmaceutics* **2018**, *10*, 263, doi:10.3390/pharmaceutics10040263.
646. Bor, G.; Mat Azmi, I.D.; Yaghmur, A. Nanomedicines for Cancer Therapy: Current Status, Challenges and Future Prospects. *Therapeutic Delivery* **2019**, *10*, 113–132, doi:10.4155/tde-2018-0062.
647. Wei, Y.; Quan, L.; Zhou, C.; Zhan, Q. Factors Relating to the Biodistribution & Clearance of Nanoparticles & Their Effects on *in Vivo* Application. *Nanomedicine* **2018**, *13*, 1495–1512, doi:10.2217/nnm-2018-0040.
648. Raman, S.; Mahmood, S.; Hilles, A.R.; Javed, M.N.; Azmana, M.; Al-Japairai, K.A.S. Polymeric Nanoparticles for Brain Drug Delivery - A Review. *Curr Drug Metab* **2020**, *21*, 649–660, doi:10.2174/1389200221666200508074348.
649. Edel, J.B.; Fortt, R.; deMello, J.C.; deMello, A.J. Microfluidic Routes to the Controlled Production of NanoparticlesElectronic Supplementary Information ESI Available: Image of the Central Portion of the Micromixer Chip. See Http://Www.Rsc.Org/Suppdata/Cc/B2/B202998g/. *Chem. Commun.* **2002**, 1136–1137, doi:10.1039/b202998g.
650. Karnik, R.; Gu, F.; Basto, P.; Cannizzaro, C.; Dean, L.; Kyei-Manu, W.; Langer, R.; Farokhzad, O.C. Microfluidic Platform for Controlled Synthesis of Polymeric Nanoparticles. *Nano Lett.* **2008**, *8*, 2906–2912, doi:10.1021/nl801736q.
651. Shrimal, P.; Jadeja, G.; Patel, S. A Review on Novel Methodologies for Drug Nanoparticle Preparation: Microfluidic Approach. *Chemical Engineering Research and Design* **2020**, *153*, 728–756, doi:10.1016/j.cherd.2019.11.031.
652. Valencia, P.M.; Farokhzad, O.C.; Karnik, R.; Langer, R. Microfluidic Technologies for Accelerating the Clinical Translation of Nanoparticles. *Nature Nanotech* **2012**, *7*, 623–629, doi:10.1038/nnano.2012.168.
653. Thi, T.T.H.; Suys, E.J.A.; Lee, J.S.; Nguyen, D.H.; Park, K.D.; Truong, N.P. Lipid-Based Nanoparticles in the Clinic and Clinical Trials: From Cancer Nanomedicine to COVID-19 Vaccines. *Vaccines* **2021**, *9*, 359, doi:10.3390/vaccines9040359.
654. Milane, L.; Amiji, M. Clinical Approval of Nanotechnology-Based SARS-CoV-2 MRNA Vaccines: Impact on Translational Nanomedicine. *Drug Deliv Transl Res* **2021**, *11*, 1309–1315, doi:10.1007/s13346-021-00911-y.
655. Garg, S.; Heuck, G.; Ip, S.; Ramsay, E. Microfluidics: A Transformational Tool for Nanomedicine Development and Production. *Journal of Drug Targeting* **2016**, *24*, 821–835, doi:10.1080/1061186X.2016.1198354.
656. Chiesa, E.; Dorati, R.; Modena, T.; Conti, B.; Genta, I. Multivariate Analysis for the Optimization of Microfluidics-Assisted Nanoprecipitation Method Intended for the Loading of Small Hydrophilic Drugs into PLGA Nanoparticles. *International Journal of Pharmaceutics* **2018**, *536*, 165–177, doi:10.1016/j.ijpharm.2017.11.044.
657. Siavashy, S.; Soltani, M.; Ghorbani-Bidkorbeh, F.; Fallah, N.; Farnam, G.; Mortazavi, S.A.; Shirazi, F.H.; Tehrani, M.H.H.; Hamedi, M.H. Microfluidic Platform for Synthesis and Optimization of Chitosan-Coated Magnetic Nanoparticles in Cisplatin Delivery. *Carbohydrate Polymers* **2021**, *265*, 118027, doi:10.1016/j.carbpol.2021.118027.

658. Ding, S.; Anton, N.; Vandamme, T.F.; Serra, C.A. Microfluidic Nanoprecipitation Systems for Preparing Pure Drug or Polymeric Drug Loaded Nanoparticles: An Overview. *Expert Opinion on Drug Delivery* **2016**, *13*, 1447–1460, doi:10.1080/17425247.2016.1193151.
659. Streck, S.; Neumann, H.; Nielsen, H.M.; Rades, T.; McDowell, A. Comparison of Bulk and Microfluidics Methods for the Formulation of Poly-Lactic-Co-Glycolic Acid (PLGA) Nanoparticles Modified with Cell-Penetrating Peptides of Different Architectures. *International Journal of Pharmaceutics: X* **2019**, *1*, 100030, doi:10.1016/j.ijpx.2019.100030.
660. Shokoohinia, P.; Hajialyani, M.; Sadrjavadi, K.; Akbari, M.; Rahimi, M.; Khaledian, S.; Fattahi, A. Microfluidic-Assisted Preparation of PLGA Nanoparticles for Drug Delivery Purposes: Experimental Study and Computational Fluid Dynamic Simulation. *Res Pharm Sci* **2019**, *14*, 459–470, doi:10.4103/1735-5362.268207.
661. Xu, J.; Zhang, S.; Machado, A.; Lecommandoux, S.; Sandre, O.; Gu, F.; Colin, A. Controllable Microfluidic Production of Drug-Loaded PLGA Nanoparticles Using Partially Water-Miscible Mixed Solvent Microdroplets as a Precursor. *Sci Rep* **2017**, *7*, 4794, doi:10.1038/s41598-017-05184-5.
662. Yu, B.; Lee, R.J.; Lee, L.J. Chapter 7 - Microfluidic Methods for Production of Liposomes. In *Methods in Enzymology*; Methods in Enzymology; Academic Press, 2009; Vol. 465, pp. 129–141.
663. Jahn, A.; Vreeland, W.N.; DeVoe, D.L.; Locascio, L.E.; Gaitan, M. Microfluidic Directed Formation of Liposomes of Controlled Size. *Langmuir* **2007**, *23*, 6289–6293, doi:10.1021/la070051a.
664. Pradhan, P.; Guan, J.; Lu, D.; Wang, P.G.; Lee, L.J.; Lee, R.J. A Facile Microfluidic Method for Production of Liposomes. *Anticancer Research* **2008**, *28*, 943–947.
665. Arduino, I.; Liu, Z.; Rahikkala, A.; Figueiredo, P.; Correia, A.; Cutrignelli, A.; Denora, N.; Santos, H.A. Preparation of Cetyl Palmitate-Based PEGylated Solid Lipid Nanoparticles by Microfluidic Technique. *Acta Biomaterialia* **2021**, *121*, 566–578, doi:10.1016/j.actbio.2020.12.024.
666. Xia, H.M.; Seah, Y.P.; Liu, Y.C.; Wang, W.; Toh, A.G.G.; Wang, Z.P. Anti-Solvent Precipitation of Solid Lipid Nanoparticles Using a Microfluidic Oscillator Mixer. *Microfluid Nanofluid* **2015**, *19*, 283–290, doi:10.1007/s10404-014-1517-5.
667. Valencia, P.M.; Basto, P.A.; Zhang, L.; Rhee, M.; Langer, R.; Farokhzad, O.C.; Karnik, R. Single-Step Assembly of Homogenous Lipid−Polymeric and Lipid−Quantum Dot Nanoparticles Enabled by Microfluidic Rapid Mixing. *ACS Nano* **2010**, *4*, 1671–1679, doi:10.1021/nn901433u.
668. Bokare, A.; Takami, A.; Kim, J.H.; Dong, A.; Chen, A.; Valerio, R.; Gunn, S.; Erogbogbo, F. Herringbone-Patterned 3D-Printed Devices as Alternatives to Microfluidics for Reproducible Production of Lipid Polymer Hybrid Nanoparticles. *ACS Omega* **2019**, *4*, 4650–4657, doi:10.1021/acsomega.9b00128.
669. Feng, Q.; Zhang, L.; Liu, C.; Li, X.; Hu, G.; Sun, J.; Jiang, X. Microfluidic Based High Throughput Synthesis of Lipid-Polymer Hybrid Nanoparticles with Tunable Diameters. *Biomicrofluidics* **2015**, *9*, 052604, doi:10.1063/1.4922957.
670. Wang, J.; Song, Y. Microfluidic Synthesis of Nanohybrids. *Small* **2017**, *13*, 1604084, doi:10.1002/smll.201604084.
671. Belletti, D.; Grabrucker, A.M.; Pederzoli, F.; Menrath, I.; Cappello, V.; Vandelli, M.A.; Forni, F.; Tosi, G.; Ruozi, B. EXPLOITING THE VERSATILITY OF CHOLESTEROL IN NANOPARTICLES FORMULATION. *International Journal of Pharmaceutics* **2016**, *511*, 331–340, doi:10.1016/j.ijpharm.2016.07.022.

672. Krause, M.R.; Regen, S.L. The Structural Role of Cholesterol in Cell Membranes: From Condensed Bilayers to Lipid Rafts. *Acc. Chem. Res.* **2014**, *47*, 3512–3521, doi:10.1021/ar500260t.
673. Liu, W.; Wei, F.; Ye, A.; Tian, M.; Han, J. Kinetic Stability and Membrane Structure of Liposomes during in Vitro Infant Intestinal Digestion: Effect of Cholesterol and Lactoferrin. *Food Chemistry* **2017**, *230*, 6–13, doi:10.1016/j.foodchem.2017.03.021.
674. Briuglia, M.-L.; Rotella, C.; McFarlane, A.; Lamprou, D.A. Influence of Cholesterol on Liposome Stability and on in Vitro Drug Release. *Drug Deliv. and Transl. Res.* **2015**, *5*, 231–242, doi:10.1007/s13346-015-0220-8.
675. Lim, E.-B.; Haam, S.; Lee, S.-W. Sphingomyelin-Based Liposomes with Different Cholesterol Contents and Polydopamine Coating as a Controlled Delivery System. *Colloids and Surfaces A: Physicochemical and Engineering Aspects* **2021**, *618*, 126447, doi:10.1016/j.colsurfa.2021.126447.
676. Coderch, L.; Fonollosa, J.; De Pera, M.; Estelrich, J.; De La Maza, A.; Parra, J.L. Influence of Cholesterol on Liposome Fluidity by EPR: Relationship with Percutaneous Absorption. *Journal of Controlled Release* **2000**, *68*, 85–95, doi:10.1016/S0168-3659(00)00240-6.
677. Rosenfeld, L.; Lin, T.; Derda, R.; Tang, S.K.Y. Review and Analysis of Performance Metrics of Droplet Microfluidics Systems. *Microfluid Nanofluid* **2014**, *16*, 921–939, doi:10.1007/s10404-013-1310-x.
678. Brouzes, E. Droplet Microfluidics for Single-Cell Analysis. In *Single-Cell Analysis*; Lindström, S., Andersson-Svahn, H., Eds.; Methods in Molecular Biology; Humana Press: Totowa, NJ, 2012; Vol. 853, pp. 105–139 ISBN 978-1-61779-566-4.
679. Gach, P.C.; Iwai, K.; Kim, P.W.; Hillson, N.J.; Singh, A.K. Droplet Microfluidics for Synthetic Biology. *Lab Chip* **2017**, *17*, 3388–3400, doi:10.1039/C7LC00576H.
680. Baret, J.-C. Surfactants in Droplet-Based Microfluidics. *Lab Chip* **2012**, *12*, 422–433, doi:10.1039/C1LC20582J.
681. Riechers, B.; Maes, F.; Akoury, E.; Semin, B.; Gruner, P.; Baret, J.-C. Surfactant Adsorption Kinetics in Microfluidics. *Proc Natl Acad Sci USA* **2016**, *113*, 11465–11470, doi:10.1073/pnas.1604307113.
682. Kabanov, A.V.; Batrakova, E.V.; Alakhov, V.Y. Pluronic Block Copolymers as Novel Polymer Therapeutics for Drug and Gene Delivery. *J Control Release* **2002**, *82*, 189–212, doi:10.1016/s0168-3659(02)00009-3.
683. Singh-Joy, S.D.; McLain, V.C. Safety Assessment of Poloxamers 101, 105, 108, 122, 123, 124, 181, 182, 183, 184, 185, 188, 212, 215, 217, 231, 234, 235, 237, 238, 282, 284, 288, 331, 333, 334, 335, 338, 401, 402, 403, and 407, Poloxamer 105 Benzoate, and Poloxamer 182 Dibenzoate as Used in Cosmetics. *Int J Toxicol* **2008**, *27 Suppl 2*, 93–128, doi:10.1080/10915810802244595.
684. Moura, S.; Noro, J.; Cerqueira, P.; Silva, C.; Cavaco-Paulo, A.; Loureiro, A. Poloxamer 407 Based-Nanoparticles for Controlled Release of Methotrexate. *International Journal of Pharmaceutics* **2020**, *575*, 118924, doi:10.1016/j.ijpharm.2019.118924.
685. Li, D.X.; Han, M.J.; Balakrishnan, P.; Yan, Y.D.; Oh, D.H.; Joe, J.H.; Seo, Y.; Kim, J.O.; Park, S.M.; Yong, C.S.; et al. Enhanced Oral Bioavailability of Flurbiprofen by Combined Use of Micelle Solution and Inclusion Compound. *Arch. Pharm. Res.* **2010**, *33*, 95–101, doi:10.1007/s12272-010-2231-9.
686. Donno, R.; Gennari, A.; Lallana, E.; De La Rosa, J.M.R.; d'Arcy, R.; Treacher, K.; Hill, K.; Ashford, M.; Tirelli, N. Nanomanufacturing through Microfluidic-Assisted Nanoprecipitation: Advanced Analytics and Structure-Activity Relationships. *International Journal of Pharmaceutics* **2017**, *534*, 97–107, doi:10.1016/j.ijpharm.2017.10.006.

687. Shrimal, P.; Jadeja, G.; Patel, S. Microfluidics Nanoprecipitation of Telmisartan Nanoparticles: Effect of Process and Formulation Parameters. *Chem. Pap.* **2021**, *75*, 205–214, doi:10.1007/s11696-020-01289-w.
688. Hong, L.; Dong, Y.-D.; Boyd, B.J. Preparation of Nanostructured Lipid Drug Delivery Particles Using Microfluidic Mixing. *PNT* **2019**, *7*, 484–495, doi:10.2174/2211738507666191004123545.
689. Dev, S.; Iyer, K.S.; Raston, C.L. Nanosized Drug Formulations under Microfluidic Continuous Flow. *Lab Chip* **2011**, *11*, 3214, doi:10.1039/c1lc20666d.
690. Lababidi, N.; Sigal, V.; Koenneke, A.; Schwarzkopf, K.; Manz, A.; Schneider, M. Microfluidics as Tool to Prepare Size-Tunable PLGA Nanoparticles with High Curcumin Encapsulation for Efficient Mucus Penetration. *Beilstein J. Nanotechnol.* **2019**, *10*, 2280–2293, doi:10.3762/bjnano.10.220.
691. Morikawa, Y.; Tagami, T.; Hoshikawa, A.; Ozeki, T. The Use of an Efficient Microfluidic Mixing System for Generating Stabilized Polymeric Nanoparticles for Controlled Drug Release. *Biological & Pharmaceutical Bulletin* **2018**, *41*, 899–907, doi:10.1248/bpb.b17-01036.
692. Carugo, D.; Bottaro, E.; Owen, J.; Stride, E.; Nastruzzi, C. Liposome Production by Microfluidics: Potential and Limiting Factors. *Sci Rep* **2016**, *6*, 25876, doi:10.1038/srep25876.
693. Panneerselvam, K.; Lynge, M.E.; Riber, C.F.; Mena-Hernando, S.; Smith, A.A.A.; Goldie, K.N.; Zelikin, A.N.; Städler, B. Phospholipid—Polymer Amphiphile Hybrid Assemblies and Their Interaction with Macrophages. *Biomicrofluidics* **2015**, *9*, 052610, doi:10.1063/1.4929405.
694. Song, Y.; Tian, Q.; Huang, Z.; Fan, D.; She, Z.; Liu, X.; Cheng, X.; Yu, B.; Deng, Y. Self-Assembled Micelles of Novel Amphiphilic Copolymer Cholesterol-Coupled F68 Containing Cabazitaxel as a Drug Delivery System. *Int J Nanomedicine* **2014**, *9*, 2307–2317, doi:10.2147/IJN.S61220.
695. Shao, X.-R.; Wei, X.-Q.; Song, X.; Hao, L.-Y.; Cai, X.-X.; Zhang, Z.-R.; Peng, Q.; Lin, Y.-F. Independent Effect of Polymeric Nanoparticle Zeta Potential/Surface Charge, on Their Cytotoxicity and Affinity to Cells. *Cell Proliferation* **2015**, *48*, 465–474, doi:10.1111/cpr.12192.
696. Bramosanti, M.; Chronopoulou, L.; Grillo, F.; Valletta, A.; Palocci, C. Microfluidic-Assisted Nanoprecipitation of Antiviral-Loaded Polymeric Nanoparticles. *Colloids and Surfaces A: Physicochemical and Engineering Aspects* **2017**, *532*, 369–376, doi:10.1016/j.colsurfa.2017.04.062.
697. Joshi, S.; Hussain, M.T.; Roces, C.B.; Anderluzzi, G.; Kastner, E.; Salmaso, S.; Kirby, D.J.; Perrie, Y. Microfluidics Based Manufacture of Liposomes Simultaneously Entrapping Hydrophilic and Lipophilic Drugs. *International Journal of Pharmaceutics* **2016**, *514*, 160–168, doi:10.1016/j.ijpharm.2016.09.027.
698. Webb, C.; Khadke, S.; Tandrup Schmidt, S.; Roces, C.B.; Forbes, N.; Berrie, G.; Perrie, Y. The Impact of Solvent Selection: Strategies to Guide the Manufacturing of Liposomes Using Microfluidics. *Pharmaceutics* **2019**, *11*, 653, doi:10.3390/pharmaceutics11120653.
699. Gdowski, A.; Johnson, K.; Shah, S.; Gryczynski, I.; Vishwanatha, J.; Ranjan, A. Optimization and Scale up of Microfluidic Nanolipomer Production Method for Preclinical and Potential Clinical Trials. *Journal of Nanobiotechnology* **2018**, *16*, 12, doi:10.1186/s12951-018-0339-0.
700. Rezvantalab, S.; Moraveji, M.K. Microfluidic Assisted Synthesis of PLGA Drug Delivery Systems. *RSC Advances* **2019**, *9*, 2055–2072, doi:10.1039/C8RA08972H.

701. Kim, Y.; Lee Chung, B.; Ma, M.; Mulder, W.J.M.; Fayad, Z.A.; Farokhzad, O.C.; Langer, R. Mass Production and Size Control of Lipid–Polymer Hybrid Nanoparticles through Controlled Microvortices. *Nano Lett.* **2012**, *12*, 3587–3591, doi:10.1021/nl301253v.
702. Lundqvist, M.; Stigler, J.; Cedervall, T.; Berggård, T.; Flanagan, M.B.; Lynch, I.; Elia, G.; Dawson, K. The Evolution of the Protein Corona around Nanoparticles: A Test Study. *ACS Nano* **2011**, *5*, 7503–7509, doi:10.1021/nn202458g.
703. Shkodra-Pula, B.; Grune, C.; Traeger, A.; Vollrath, A.; Schubert, S.; Fischer, D.; Schubert, U.S. Effect of Surfactant on the Size and Stability of PLGA Nanoparticles Encapsulating a Protein Kinase C Inhibitor. *Int J Pharm* **2019**, *566*, 756–764, doi:10.1016/j.ijpharm.2019.05.072.
704. Heinz, H.; Pramanik, C.; Heinz, O.; Ding, Y.; Mishra, R.K.; Marchon, D.; Flatt, R.J.; Estrela-Lopis, I.; Llop, J.; Moya, S.; et al. Nanoparticle Decoration with Surfactants: Molecular Interactions, Assembly, and Applications. *Surface Science Reports* **2017**, *72*, 1–58, doi:10.1016/j.surfrep.2017.02.001.
705. Rahman, M.; Laurent, S.; Tawil, N.; Yahia, L.; Mahmoudi, M. Nanoparticle and Protein Corona. In *Protein-Nanoparticle Interactions*; Springer Series in Biophysics; Springer Berlin Heidelberg: Berlin, Heidelberg, 2013; Vol. 15, pp. 21–44 ISBN 978-3-642-37554-5.
706. Owens, D.E.; Peppas, N.A. Opsonization, Biodistribution, and Pharmacokinetics of Polymeric Nanoparticles. *International Journal of Pharmaceutics* **2006**, *307*, 93–102, doi:10.1016/j.ijpharm.2005.10.010.
707. Soppimath, K.S.; Aminabhavi, T.M.; Kulkarni, A.R.; Rudzinski, W.E. Biodegradable Polymeric Nanoparticles as Drug Delivery Devices. *Journal of Controlled Release* **2001**, *70*, 1–20, doi:10.1016/S0168-3659(00)00339-4.
708. Miller, J.B.; Harris, J.M.; Hobbie, E.K. Purifying Colloidal Nanoparticles through Ultracentrifugation with Implications for Interfaces and Materials. *Langmuir* **2014**, *30*, 7936–7946, doi:10.1021/la404675v.
709. Streck, S.; Hong, L.; Boyd, B.J.; McDowell, A. Microfluidics for the Production of Nanomedicines: Considerations for Polymer and Lipid-Based Systems. *PNT* **2019**, *7*, 423–443, doi:10.2174/2211738507666191019154815.
710. Jain, S.; Mittal, A.; K. Jain, A.; R. Mahajan, R.; Singh, D. Cyclosporin A Loaded PLGA Nanoparticle: Preparation, Optimization, In-Vitro Characterization and Stability Studies. *CNANO* **2010**, *6*, 422–431, doi:10.2174/157341310791658937.
711. Zaccone, A.; Wu, H.; Lattuada, M.; Morbidelli, M. Correlation between Colloidal Stability and Surfactant Adsorption/Association Phenomena Studied by Light Scattering. *J. Phys. Chem. B* **2008**, *112*, 1976–1986, doi:10.1021/jp0776210.
712. Jódar-Reyes, A.B.; Martín-Rodríguez, A.; Ortega-Vinuesa, J.L. Effect of the Ionic Surfactant Concentration on the Stabilization/Destabilization of Polystyrene Colloidal Particles. *Journal of Colloid and Interface Science* **2006**, *298*, 248–257, doi:10.1016/j.jcis.2005.12.035.
713. Zu, M.; Ma, Y.; Cannup, B.; Xie, D.; Jung, Y.; Zhang, J.; Yang, C.; Gao, F.; Merlin, D.; Xiao, B. Oral Delivery of Natural Active Small Molecules by Polymeric Nanoparticles for the Treatment of Inflammatory Bowel Diseases. *Advanced Drug Delivery Reviews* **2021**, *176*, 113887, doi:10.1016/j.addr.2021.113887.
714. Fornaguera, C.; García-Celma, M.J. Personalized Nanomedicine: A Revolution at the Nanoscale. *J Pers Med* **2017**, *7*, E12, doi:10.3390/jpm7040012.
715. Amini, M.A.; Ahmed, T.; Liu, F.-C.F.; Abbasi, A.Z.; Soeandy, C.D.; Zhang, R.X.; Prashad, P.; Cummins, C.L.; Rauth, A.M.; Henderson, J.T.; et al. Exploring the Transformability of Polymer-Lipid Hybrid Nanoparticles and Nanomaterial-Biology Interplay to Facilitate Tumor Penetration, Cellular Uptake and Intracellular Targeting of

Anticancer Drugs. *Expert Opinion on Drug Delivery* **2021**, *18*, 991–1004, doi:10.1080/17425247.2021.1902984.
716. Warsi, M.H. Development and Optimization of Vitamin E TPGS Based PLGA Nanoparticles for Improved and Safe Ocular Delivery of Ketorolac. *Journal of Drug Delivery Science and Technology* **2021**, *61*, 102121, doi:10.1016/j.jddst.2020.102121.
717. Bagheri, E.; Alibolandi, M.; Abnous, K.; Taghdisi, S.M.; Ramezani, M. Targeted Delivery and Controlled Release of Doxorubicin to Cancer Cells by Smart ATP-Responsive Y-Shaped DNA Structure-Capped Mesoporous Silica Nanoparticles. *J. Mater. Chem. B* **2021**, *9*, 1351–1363, doi:10.1039/D0TB01960G.
718. Tewabe, A.; Abate, A.; Tamrie, M.; Seyfu, A.; Abdela Siraj, E. Targeted Drug Delivery — From Magic Bullet to Nanomedicine: Principles, Challenges, and Future Perspectives. *J Multidiscip Healthc* **2021**, *14*, 1711–1724, doi:10.2147/JMDH.S313968.
719. How Does "Protein Corona" Affect the In Vivo Efficiency of Polymeric Nanoparticles? State of Art. In *Frontiers in Nanomedicine*; Tosi, G., Ed.; BENTHAM SCIENCE PUBLISHERS, 2017; pp. 199–238 ISBN 978-1-68108-493-0.
720. Milani, S.; Baldelli Bombelli, F.; Pitek, A.S.; Dawson, K.A.; Rädler, J. Reversible versus Irreversible Binding of Transferrin to Polystyrene Nanoparticles: Soft and Hard Corona. *ACS Nano* **2012**, *6*, 2532–2541, doi:10.1021/nn204951s.
721. Tenzer, S.; Docter, D.; Kuharev, J.; Musyanovych, A.; Fetz, V.; Hecht, R.; Schlenk, F.; Fischer, D.; Kiouptsi, K.; Reinhardt, C.; et al. Rapid Formation of Plasma Protein Corona Critically Affects Nanoparticle Pathophysiology. *Nature Nanotech* **2013**, *8*, 772–781, doi:10.1038/nnano.2013.181.
722. Bertrand, N.; Grenier, P.; Mahmoudi, M.; Lima, E.M.; Appel, E.A.; Dormont, F.; Lim, J.-M.; Karnik, R.; Langer, R.; Farokhzad, O.C. Mechanistic Understanding of in Vivo Protein Corona Formation on Polymeric Nanoparticles and Impact on Pharmacokinetics. *Nat Commun* **2017**, *8*, 777, doi:10.1038/s41467-017-00600-w.
723. Tekie, F.S.M.; Hajiramezanali, M.; Geramifar, P.; Raoufi, M.; Dinarvand, R.; Soleimani, M.; Atyabi, F. Controlling Evolution of Protein Corona: A Prosperous Approach to Improve Chitosan-Based Nanoparticle Biodistribution and Half-Life. *Sci Rep* **2020**, *10*, 9664, doi:10.1038/s41598-020-66572-y.
724. Chinen, A.B.; Guan, C.M.; Ko, C.H.; Mirkin, C.A. The Impact of Protein Corona Formation on the Macrophage Cellular Uptake and Biodistribution of Spherical Nucleic Acids. *Small* **2017**, *13*, 1603847, doi:10.1002/smll.201603847.
725. Ke, P.C.; Lin, S.; Parak, W.J.; Davis, T.P.; Caruso, F. A Decade of the Protein Corona. *ACS Nano* **2017**, *11*, 11773–11776, doi:10.1021/acsnano.7b08008.
726. Shanwar, S.; Liang, L.; Nechaev, A.V.; Bausheva, D.K.; Balalaeva, I.V.; Vodeneev, V.A.; Roy, I.; Zvyagin, A.V.; Guryev, E.L. Controlled Formation of a Protein Corona Composed of Denatured BSA on Upconversion Nanoparticles Improves Their Colloidal Stability. *Materials* **2021**, *14*, 1657, doi:10.3390/ma14071657.
727. Falahati, M.; Attar, F.; Sharifi, M.; Haertlé, T.; Berret, J.-F.; Khan, R.H.; Saboury, A.A. A Health Concern Regarding the Protein Corona, Aggregation and Disaggregation. *Biochim Biophys Acta Gen Subj* **2019**, *1863*, 971–991, doi:10.1016/j.bbagen.2019.02.012.
728. Prapainop, K.; Witter, D.P.; Wentworth, P. A Chemical Approach for Cell-Specific Targeting of Nanomaterials: Small-Molecule-Initiated Misfolding of Nanoparticle Corona Proteins. *J. Am. Chem. Soc.* **2012**, *134*, 4100–4103, doi:10.1021/ja300537u.
729. Mahmoudi, M.; Sheibani, S.; Milani, A.S.; Rezaee, F.; Gauberti, M.; Dinarvand, R.; Vali, H. Crucial Role of the Protein Corona for the Specific Targeting of Nanoparticles. *Nanomedicine* **2015**, *10*, 215–226, doi:10.2217/nnm.14.69.

730. Dai, Q.; Yan, Y.; Ang, C.-S.; Kempe, K.; Kamphuis, M.M.J.; Dodds, S.J.; Caruso, F. Monoclonal Antibody-Functionalized Multilayered Particles: Targeting Cancer Cells in the Presence of Protein Coronas. *ACS Nano* **2015**, *9*, 2876–2885, doi:10.1021/nn506929e.
731. Lesniak, A.; Fenaroli, F.; Monopoli, M.P.; Åberg, C.; Dawson, K.A.; Salvati, A. Effects of the Presence or Absence of a Protein Corona on Silica Nanoparticle Uptake and Impact on Cells. *ACS Nano* **2012**, *6*, 5845–5857, doi:10.1021/nn300223w.
732. De Paoli, S.H.; Diduch, L.L.; Tegegn, T.Z.; Orecna, M.; Strader, M.B.; Karnaukhova, E.; Bonevich, J.E.; Holada, K.; Simak, J. The Effect of Protein Corona Composition on the Interaction of Carbon Nanotubes with Human Blood Platelets. *Biomaterials* **2014**, *35*, 6182–6194, doi:10.1016/j.biomaterials.2014.04.067.
733. Yan, Y.; Gause, K.T.; Kamphuis, M.M.J.; Ang, C.-S.; O'Brien-Simpson, N.M.; Lenzo, J.C.; Reynolds, E.C.; Nice, E.C.; Caruso, F. Differential Roles of the Protein Corona in the Cellular Uptake of Nanoporous Polymer Particles by Monocyte and Macrophage Cell Lines. *ACS Nano* **2013**, *7*, 10960–10970, doi:10.1021/nn404481f.
734. Francia, V.; Yang, K.; Deville, S.; Reker-Smit, C.; Nelissen, I.; Salvati, A. Corona Composition Can Affect the Mechanisms Cells Use to Internalize Nanoparticles. *ACS Nano* **2019**, *13*, 11107–11121, doi:10.1021/acsnano.9b03824.
735. Nyström, A.M.; Fadeel, B. Safety Assessment of Nanomaterials: Implications for Nanomedicine. *Journal of Controlled Release* **2012**, *161*, 403–408, doi:10.1016/j.jconrel.2012.01.027.
736. Dobrovolskaia, M.A.; Neun, B.W.; Man, S.; Ye, X.; Hansen, M.; Patri, A.K.; Crist, R.M.; McNeil, S.E. Protein Corona Composition Does Not Accurately Predict Hematocompatibility of Colloidal Gold Nanoparticles. *Nanomedicine: Nanotechnology, Biology and Medicine* **2014**, *10*, 1453–1463, doi:10.1016/j.nano.2014.01.009.
737. Shannahan, J.H.; Podila, R.; Aldossari, A.A.; Emerson, H.; Powell, B.A.; Ke, P.C.; Rao, A.M.; Brown, J.M. Formation of a Protein Corona on Silver Nanoparticles Mediates Cellular Toxicity via Scavenger Receptors. *Toxicological Sciences* **2015**, *143*, 136–146, doi:10.1093/toxsci/kfu217.
738. Bélteky, P.; Rónavári, A.; Igaz, N.; Szerencsés, B.; Tóth, I.Y.; Pfeiffer, I.; Kiricsi, M.; Kónya, Z. <p>Silver Nanoparticles: Aggregation Behavior in Biorelevant Conditions and Its Impact on Biological Activity</P>. *IJN* **2019**, *14*, 667–687, doi:10.2147/IJN.S185965.
739. Caracciolo, G.; Pozzi, D.; Capriotti, A.L.; Cavaliere, C.; Foglia, P.; Amenitsch, H.; Laganà, A. Evolution of the Protein Corona of Lipid Gene Vectors as a Function of Plasma Concentration. *Langmuir* **2011**, *27*, 15048–15053, doi:10.1021/la202912f.
740. Monopoli, M.P.; Walczyk, D.; Campbell, A.; Elia, G.; Lynch, I.; Baldelli Bombelli, F.; Dawson, K.A. Physical–Chemical Aspects of Protein Corona: Relevance to in Vitro and in Vivo Biological Impacts of Nanoparticles. *J. Am. Chem. Soc.* **2011**, *133*, 2525–2534, doi:10.1021/ja107583h.
741. Partikel, K.; Korte, R.; Mulac, D.; Humpf, H.-U.; Langer, K. Serum Type and Concentration Both Affect the Protein-Corona Composition of PLGA Nanoparticles. *Beilstein J. Nanotechnol.* **2019**, *10*, 1002–1015, doi:10.3762/bjnano.10.101.
742. Barrán-Berdón, A.L.; Pozzi, D.; Caracciolo, G.; Capriotti, A.L.; Caruso, G.; Cavaliere, C.; Riccioli, A.; Palchetti, S.; Laganà, A. Time Evolution of Nanoparticle–Protein Corona in Human Plasma: Relevance for Targeted Drug Delivery. *Langmuir* **2013**, *29*, 6485–6494, doi:10.1021/la401192x.
743. Natte, K.; Friedrich, J.F.; Wohlrab, S.; Lutzki, J.; von Klitzing, R.; Österle, W.; Orts-Gil, G. Impact of Polymer Shell on the Formation and Time Evolution of Nanoparticle–Protein Corona. *Colloids and Surfaces B: Biointerfaces* **2013**, *104*, 213–220, doi:10.1016/j.colsurfb.2012.11.019.

744. Ren, J.; Andrikopoulos, N.; Velonia, K.; Tang, H.; Cai, R.; Ding, F.; Ke, P.C.; Chen, C. Chemical and Biophysical Signatures of the Protein Corona in Nanomedicine. *J. Am. Chem. Soc.* **2022**, *144*, 9184–9205, doi:10.1021/jacs.2c02277.
745. Mahmoudi, M.; Abdelmonem, A.M.; Behzadi, S.; Clement, J.H.; Dutz, S.; Ejtehadi, M.R.; Hartmann, R.; Kantner, K.; Linne, U.; Maffre, P.; et al. Temperature: The "Ignored" Factor at the NanoBio Interface. *ACS Nano* **2013**, *7*, 6555–6562, doi:10.1021/nn305337c.
746. Mahmoudi, M.; Lohse, S.E.; Murphy, C.J.; Fathizadeh, A.; Montazeri, A.; Suslick, K.S. Variation of Protein Corona Composition of Gold Nanoparticles Following Plasmonic Heating. *Nano Lett.* **2014**, *14*, 6–12, doi:10.1021/nl403419e.
747. Nguyen, V.H.; Lee, B.-J. Protein Corona: A New Approach for Nanomedicine Design. *Int J Nanomedicine* **2017**, *12*, 3137–3151, doi:10.2147/IJN.S129300.
748. Monopoli, M.P.; Åberg, C.; Salvati, A.; Dawson, K.A. Biomolecular Coronas Provide the Biological Identity of Nanosized Materials. *Nature Nanotech* **2012**, *7*, 779–786, doi:10.1038/nnano.2012.207.
749. Kopac, T. Protein Corona, Understanding the Nanoparticle-Protein Interactions and Future Perspectives: A Critical Review. *Int J Biol Macromol* **2021**, *169*, 290–301, doi:10.1016/j.ijbiomac.2020.12.108.
750. Ahsan, S.M.; Rao, C.M.; Ahmad, M.F. Nanoparticle-Protein Interaction: The Significance and Role of Protein Corona. *Adv Exp Med Biol* **2018**, *1048*, 175–198, doi:10.1007/978-3-319-72041-8_11.
751. Caracciolo, G.; Pozzi, D.; Capriotti, A.L.; Cavaliere, C.; Piovesana, S.; Amenitsch, H.; Laganà, A. Lipid Composition: A "Key Factor" for the Rational Manipulation of the Liposome–Protein Corona by Liposome Design. *RSC Adv.* **2015**, *5*, 5967–5975, doi:10.1039/C4RA13335H.
752. Lindman, S.; Lynch, I.; Thulin, E.; Nilsson, H.; Dawson, K.A.; Linse, S. Systematic Investigation of the Thermodynamics of HSA Adsorption to N-Iso-Propylacrylamide/N-Tert-Butylacrylamide Copolymer Nanoparticles. Effects of Particle Size and Hydrophobicity. *Nano Lett.* **2007**, *7*, 914–920, doi:10.1021/nl062743+.
753. Gessner, A.; Waicz, R.; Lieske, A.; Paulke, B.; Mäder, K.; Müller, R.H. Nanoparticles with Decreasing Surface Hydrophobicities: Influence on Plasma Protein Adsorption. *Int J Pharm* **2000**, *196*, 245–249, doi:10.1016/s0378-5173(99)00432-9.
754. Moyano, D.F.; Goldsmith, M.; Solfiell, D.J.; Landesman-Milo, D.; Miranda, O.R.; Peer, D.; Rotello, V.M. Nanoparticle Hydrophobicity Dictates Immune Response. *J Am Chem Soc* **2012**, *134*, 3965–3967, doi:10.1021/ja2108905.
755. Lacerda, S.H.D.P.; Park, J.J.; Meuse, C.; Pristinski, D.; Becker, M.L.; Karim, A.; Douglas, J.F. Interaction of Gold Nanoparticles with Common Human Blood Proteins. *ACS Nano* **2010**, *4*, 365–379, doi:10.1021/nn9011187.
756. Lundqvist, M.; Stigler, J.; Elia, G.; Lynch, I.; Cedervall, T.; Dawson, K.A. Nanoparticle Size and Surface Properties Determine the Protein Corona with Possible Implications for Biological Impacts. *Proc Natl Acad Sci U S A* **2008**, *105*, 14265–14270, doi:10.1073/pnas.0805135105.
757. Tenzer, S.; Docter, D.; Rosfa, S.; Wlodarski, A.; Kuharev, J.; Rekik, A.; Knauer, S.K.; Bantz, C.; Nawroth, T.; Bier, C.; et al. Nanoparticle Size Is a Critical Physicochemical Determinant of the Human Blood Plasma Corona: A Comprehensive Quantitative Proteomic Analysis. *ACS Nano* **2011**, *5*, 7155–7167, doi:10.1021/nn201950e.
758. Dobrovolskaia, M.A.; Patri, A.K.; Zheng, J.; Clogston, J.D.; Ayub, N.; Aggarwal, P.; Neun, B.W.; Hall, J.B.; McNeil, S.E. Interaction of Colloidal Gold Nanoparticles with Human Blood: Effects on Particle Size and Analysis of Plasma Protein Binding Profiles.

*Nanomedicine: Nanotechnology, Biology and Medicine* **2009**, *5*, 106–117, doi:10.1016/j.nano.2008.08.001.
759. Chakraborty, S.; Joshi, P.; Shanker, V.; Ansari, Z.A.; Singh, S.P.; Chakrabarti, P. Contrasting Effect of Gold Nanoparticles and Nanorods with Different Surface Modifications on the Structure and Activity of Bovine Serum Albumin. *Langmuir* **2011**, *27*, 7722–7731, doi:10.1021/la200787t.
760. García-Álvarez, R.; Hadjidemetriou, M.; Sánchez-Iglesias, A.; Liz-Marzán, L.M.; Kostarelos, K. In Vivo Formation of Protein Corona on Gold Nanoparticles. The Effect of Their Size and Shape. *Nanoscale* **2018**, *10*, 1256–1264, doi:10.1039/C7NR08322J.
761. Pederzoli, F.; Tosi, G.; Genovese, F.; Belletti, D.; Vandelli, M.A.; Ballestrazzi, A.; Forni, F.; Ruozi, B. Qualitative and Semiquantitative Analysis of the Protein Coronas Associated to Different Functionalized Nanoparticles. *Nanomedicine (Lond)* **2018**, *13*, 407–422, doi:10.2217/nnm-2017-0250.
762. Saha, K.; Rahimi, M.; Yazdani, M.; Kim, S.T.; Moyano, D.F.; Hou, S.; Das, R.; Mout, R.; Rezaee, F.; Mahmoudi, M.; et al. Regulation of Macrophage Recognition through the Interplay of Nanoparticle Surface Functionality and Protein Corona. *ACS Nano* **2016**, *10*, 4421–4430, doi:10.1021/acsnano.6b00053.
763. Almalik, A.; Benabdelkamel, H.; Masood, A.; Alanazi, I.O.; Alradwan, I.; Majrashi, M.A.; Alfadda, A.A.; Alghamdi, W.M.; Alrabiah, H.; Tirelli, N.; et al. Hyaluronic Acid Coated Chitosan Nanoparticles Reduced the Immunogenicity of the Formed Protein Corona. *Sci Rep* **2017**, *7*, 10542, doi:10.1038/s41598-017-10836-7.
764. Zhang, L.; Lin, Z.; Chen, Y.; Gao, D.; Wang, P.; Lin, Y.; Wang, Y.; Wang, F.; Han, Y.; Yuan, H. Co-Delivery of Docetaxel and Resveratrol by Liposomes Synergistically Boosts Antitumor Efficiency against Prostate Cancer. *European Journal of Pharmaceutical Sciences* **2022**, *174*, 106199, doi:10.1016/j.ejps.2022.106199.
765. Bing, J.; Xiao, X.; McClements, D.J.; Biao, Y.; Chongjiang, C. Protein Corona Formation around Inorganic Nanoparticles: Food Plant Proteins-TiO2 Nanoparticle Interactions. *Food Hydrocolloids* **2021**, *115*, 106594, doi:10.1016/j.foodhyd.2021.106594.
766. Zhang, W.; Cho, W.C.; Bloukh, S.H.; Edis, Z.; Du, W.; He, Y.; Hu, H.Y.; Hagen, T.L.M. ten; Falahati, M. An Overview on the Exploring the Interaction of Inorganic Nanoparticles with Microtubules for the Advancement of Cancer Therapeutics. *International Journal of Biological Macromolecules* **2022**, *212*, 358–369, doi:10.1016/j.ijbiomac.2022.05.150.
767. Cedervall, T.; Lynch, I.; Lindman, S.; Berggård, T.; Thulin, E.; Nilsson, H.; Dawson, K.A.; Linse, S. Understanding the Nanoparticle–Protein Corona Using Methods to Quantify Exchange Rates and Affinities of Proteins for Nanoparticles. *Proc. Natl. Acad. Sci. U.S.A.* **2007**, *104*, 2050–2055, doi:10.1073/pnas.0608582104.
768. Arike, L.; Peil, L. Spectral Counting Label-Free Proteomics. *Methods Mol Biol* **2014**, *1156*, 213–222, doi:10.1007/978-1-4939-0685-7_14.
769. Choi, M.; Chang, C.-Y.; Clough, T.; Broudy, D.; Killeen, T.; MacLean, B.; Vitek, O. MSstats: An R Package for Statistical Analysis of Quantitative Mass Spectrometry-Based Proteomic Experiments. *Bioinformatics* **2014**, *30*, 2524–2526, doi:10.1093/bioinformatics/btu305.
770. Maskarinec, S.A.; Hannig, J.; Lee, R.C.; Lee, K.Y.C. Direct Observation of Poloxamer 188 Insertion into Lipid Monolayers. *Biophys J* **2002**, *82*, 1453–1459, doi:10.1016/S0006-3495(02)75499-4.
771. Petry, R.; Saboia, V.M.; Franqui, L.S.; Holanda, C. de A.; Garcia, T.R.R.; de Farias, M.A.; de Souza Filho, A.G.; Ferreira, O.P.; Martinez, D.S.T.; Paula, A.J. On the Formation

of Protein Corona on Colloidal Nanoparticles Stabilized by Depletant Polymers. *Materials Science and Engineering: C* **2019**, *105*, 110080, doi:10.1016/j.msec.2019.110080.
772. Neagu, M.; Piperigkou, Z.; Karamanou, K.; Engin, A.B.; Docea, A.O.; Constantin, C.; Negrei, C.; Nikitovic, D.; Tsatsakis, A. Protein Bio-Corona: Critical Issue in Immune Nanotoxicology. *Arch Toxicol* **2017**, *91*, 1031–1048, doi:10.1007/s00204-016-1797-5.
773. Akhter, M.H.; Khalilullah, H.; Gupta, M.; Alfaleh, M.A.; Alhakamy, N.A.; Riadi, Y.; Md, S. Impact of Protein Corona on the Biological Identity of Nanomedicine: Understanding the Fate of Nanomaterials in the Biological Milieu. *Biomedicines* **2021**, *9*, 1496, doi:10.3390/biomedicines9101496.
774. Teir, M.M.A.; Ghithan, J.; Darwish, S.; Abu-Hadid, M.M. Multi-Spectroscopic Investigation of the Interactions between Cholesterol and Human Serum Albumin. **2012**, 11.
775. Peng, L.; Minbo, H.; Fang, C.; Xi, L.; Chaocan, Z. The Interaction Between Cholesterol and Human Serum Albumin. *Protein and Peptide Letters* **2008**, *15*, 360–364, doi:10.2174/092986608784246542.
776. Meierhofer, T.; van den Elsen, J.M.H.; Cameron, P.J.; Muñoz-Berbel, X.; Jenkins, A.T.A. The Interaction of Serum Albumin with Cholesterol Containing Lipid Vesicles. *J Fluoresc* **2010**, *20*, 371–376, doi:10.1007/s10895-009-0522-7.
777. Walkey, C.D.; Chan, W.C.W. Understanding and Controlling the Interaction of Nanomaterials with Proteins in a Physiological Environment. *Chem Soc Rev* **2012**, *41*, 2780–2799, doi:10.1039/c1cs15233e.
778. Pozzi, D.; Colapicchioni, V.; Caracciolo, G.; Piovesana, S.; Capriotti, A.L.; Palchetti, S.; De Grossi, S.; Riccioli, A.; Amenitsch, H.; Laganà, A. Effect of Polyethyleneglycol (PEG) Chain Length on the Bio-Nano-Interactions between PEGylated Lipid Nanoparticles and Biological Fluids: From Nanostructure to Uptake in Cancer Cells. *Nanoscale* **2014**, *6*, 2782–2792, doi:10.1039/c3nr05559k.
779. Sempf, K.; Arrey, T.; Gelperina, S.; Schorge, T.; Meyer, B.; Karas, M.; Kreuter, J. Adsorption of Plasma Proteins on Uncoated PLGA Nanoparticles. *Eur J Pharm Biopharm* **2013**, *85*, 53–60, doi:10.1016/j.ejpb.2012.11.030.
780. Pozzi, D.; Caracciolo, G.; Digiacomo, L.; Colapicchioni, V.; Palchetti, S.; Capriotti, A.L.; Cavaliere, C.; Chiozzi, R.Z.; Puglisi, A.; Laganà, A. The Biomolecular Corona of Nanoparticles in Circulating Biological Media. *Nanoscale* **2015**, *7*, 13958–13966, doi:10.1039/C5NR03701H.
781. Lai, W.; Li, D.; Wang, Q.; Nan, X.; Xiang, Z.; Ma, Y.; Liu, Y.; Chen, J.; Tian, J.; Fang, Q. A Protein Corona Adsorbed to a Bacterial Magnetosome Affects Its Cellular Uptake. *IJN* **2020**, *Volume 15*, 1481–1498, doi:10.2147/IJN.S220082.
782. Mahley, R.W. Apolipoprotein E: Cholesterol Transport Protein with Expanding Role in Cell Biology. *Science* **1988**, *240*, 622–630, doi:10.1126/science.3283935.
783. Bolanos-Garcia, V.M.; Miguel, R.N. On the Structure and Function of Apolipoproteins: More than a Family of Lipid-Binding Proteins. *Prog Biophys Mol Biol* **2003**, *83*, 47–68, doi:10.1016/s0079-6107(03)00028-2.
784. Reschly, E.J.; Sorci-Thomas, M.G.; Davidson, W.S.; Meredith, S.C.; Reardon, C.A.; Getz, G.S. Apolipoprotein A-I $\alpha$-Helices 7 and 8 Modulate High Density Lipoprotein Subclass Distribution *. *Journal of Biological Chemistry* **2002**, *277*, 9645–9654, doi:10.1074/jbc.M107883200.
785. Fielding, C.J.; Fielding, P.E. Molecular Physiology of Reverse Cholesterol Transport. *J Lipid Res* **1995**, *36*, 211–228.

786. Moghimi, S.M.; Andersen, A.J.; Ahmadvand, D.; Wibroe, P.P.; Andresen, T.L.; Hunter, A.C. Material Properties in Complement Activation. *Adv Drug Deliv Rev* **2011**, *63*, 1000–1007, doi:10.1016/j.addr.2011.06.002.
787. Xiao, W.; Gao, H. The Impact of Protein Corona on the Behavior and Targeting Capability of Nanoparticle-Based Delivery System. *Int J Pharm* **2018**, *552*, 328–339, doi:10.1016/j.ijpharm.2018.10.011.
788. Goldberg, B.S.; Ackerman, M.E. Antibody-Mediated Complement Activation in Pathology and Protection. *Immunology & Cell Biology* **2020**, *98*, 305–317, doi:10.1111/imcb.12324.
789. Caracciolo, G.; Farokhzad, O.C.; Mahmoudi, M. Biological Identity of Nanoparticles In Vivo : Clinical Implications of the Protein Corona. *Trends in Biotechnology* **2017**, *35*, 257–264, doi:10.1016/j.tibtech.2016.08.011.
790. Bai, X.; Wang, J.; Mu, Q.; Su, G. In Vivo Protein Corona Formation: Characterizations, Effects on Engineered Nanoparticles' Biobehaviors, and Applications. *Frontiers in Bioengineering and Biotechnology* **2021**, *9*.
791. Godara, S.; Lather, V.; Kirthanashri, S.V.; Awasthi, R.; Pandita, D. Lipid-PLGA Hybrid Nanoparticles of Paclitaxel: Preparation, Characterization, in Vitro and in Vivo Evaluation. *Materials Science and Engineering: C* **2020**, *109*, 110576, doi:10.1016/j.msec.2019.110576.
792. Behzadi, S.; Serpooshan, V.; Sakhtianchi, R.; Müller, B.; Landfester, K.; Crespy, D.; Mahmoudi, M. Protein Corona Change the Drug Release Profile of Nanocarriers: The "Overlooked" Factor at the Nanobio Interface. *Colloids and Surfaces B: Biointerfaces* **2014**, *123*, 143–149, doi:10.1016/j.colsurfb.2014.09.009.
793. Rampado, R.; Crotti, S.; Caliceti, P.; Pucciarelli, S.; Agostini, M. Recent Advances in Understanding the Protein Corona of Nanoparticles and in the Formulation of "Stealthy" Nanomaterials. *Frontiers in Bioengineering and Biotechnology* **2020**, *8*.
794. Singh, N.; Marets, C.; Boudon, J.; Millot, N.; Saviot, L.; Maurizi, L. In Vivo Protein Corona on Nanoparticles: Does the Control of All Material Parameters Orient the Biological Behavior? *Nanoscale Advances* **2021**, *3*, 1209–1229, doi:10.1039/D0NA00863J.
795. Rezaei, G.; Daghighi, S.M.; Haririan, I.; Yousefi, I.; Raoufi, M.; Rezaee, F.; Dinarvand, R. Protein Corona Variation in Nanoparticles Revisited: A Dynamic Grouping Strategy. *Colloids and Surfaces B: Biointerfaces* **2019**, *179*, 505–516, doi:10.1016/j.colsurfb.2019.04.003.
796. Wang, H.; Lin, Y.; Nienhaus, K.; Nienhaus, G.U. The Protein Corona on Nanoparticles as Viewed from a Nanoparticle-Sizing Perspective. *WIREs Nanomedicine and Nanobiotechnology* **2018**, *10*, e1500, doi:10.1002/wnan.1500.
797. Yu, Q.; Zhao, L.; Guo, C.; Yan, B.; Su, G. Regulating Protein Corona Formation and Dynamic Protein Exchange by Controlling Nanoparticle Hydrophobicity. *Frontiers in Bioengineering and Biotechnology* **2020**, *8*.
798. Cedervall, T.; Lynch, I.; Foy, M.; Berggård, T.; Donnelly, S.C.; Cagney, G.; Linse, S.; Dawson, K.A. Detailed Identification of Plasma Proteins Adsorbed on Copolymer Nanoparticles. *Angew. Chem. Int. Ed.* **2007**, *46*, 5754–5756, doi:10.1002/anie.200700465.
799. Charbgoo, F.; Nejabat, M.; Abnous, K.; Soltani, F.; Taghdisi, S.M.; Alibolandi, M.; Thomas Shier, W.; Steele, T.W.J.; Ramezani, M. Gold Nanoparticle Should Understand Protein Corona for Being a Clinical Nanomaterial. *Journal of Controlled Release* **2018**, *272*, 39–53, doi:10.1016/j.jconrel.2018.01.002.
800. Huang, W.; Xiao, G.; Zhang, Y.; Min, W. Research Progress and Application Opportunities of Nanoparticle–Protein Corona Complexes. *Biomedicine & Pharmacotherapy* **2021**, *139*, 111541, doi:10.1016/j.biopha.2021.111541.

801. Martínez-Negro, M.; González-Rubio, G.; Aicart, E.; Landfester, K.; Guerrero-Martínez, A.; Junquera, E. Insights into Colloidal Nanoparticle-Protein Corona Interactions for Nanomedicine Applications. *Advances in Colloid and Interface Science* **2021**, *289*, 102366, doi:10.1016/j.cis.2021.102366.
802. Kreuter, J.; Shamenkov, D.; Petrov, V.; Ramge, P.; Cychutek, K.; Koch-Brandt, C.; Alyautdin, R. Apolipoprotein-Mediated Transport of Nanoparticle-Bound Drugs Across the Blood-Brain Barrier. *Journal of Drug Targeting* **2002**, *10*, 317–325, doi:10.1080/10611860290031877.
803. Wagner, S.; Zensi, A.; Wien, S.L.; Tschickardt, S.E.; Maier, W.; Vogel, T.; Worek, F.; Pietrzik, C.U.; Kreuter, J.; Briesen, H. von Uptake Mechanism of ApoE-Modified Nanoparticles on Brain Capillary Endothelial Cells as a Blood-Brain Barrier Model. *PLOS ONE* **2012**, *7*, e32568, doi:10.1371/journal.pone.0032568.
804. Li, H.; Wang, Y.; Tang, Q.; Yin, D.; Tang, C.; He, E.; Zou, L.; Peng, Q. The Protein Corona and Its Effects on Nanoparticle-Based Drug Delivery Systems. *Acta Biomater* **2021**, *129*, 57–72, doi:10.1016/j.actbio.2021.05.019.
805. Ju, Y.; Dai, Q.; Cui, J.; Dai, Y.; Suma, T.; Richardson, J.J.; Caruso, F. Improving Targeting of Metal–Phenolic Capsules by the Presence of Protein Coronas. *ACS Appl. Mater. Interfaces* **2016**, *8*, 22914–22922, doi:10.1021/acsami.6b07613.
806. Michaelis, K.; Hoffmann, M.M.; Dreis, S.; Herbert, E.; Alyautdin, R.N.; Michaelis, M.; Kreuter, J.; Langer, K. Covalent Linkage of Apolipoprotein E to Albumin Nanoparticles Strongly Enhances Drug Transport into the Brain. *J Pharmacol Exp Ther* **2006**, *317*, 1246–1253, doi:10.1124/jpet.105.097139.
807. Sobczynski, D.J.; Eniola-Adefeso, O. IgA and IgM Protein Primarily Drive Plasma Corona-Induced Adhesion Reduction of PLGA Nanoparticles in Human Blood Flow. *Bioeng Transl Med* **2017**, *2*, 180–190, doi:10.1002/btm2.10064.
808. Wang, G.; Chen, F.; Banda, N.K.; Holers, V.M.; Wu, L.; Moghimi, S.M.; Simberg, D. Activation of Human Complement System by Dextran-Coated Iron Oxide Nanoparticles Is Not Affected by Dextran/Fe Ratio, Hydroxyl Modifications, and Crosslinking. *Frontiers in Immunology* **2016**, *7*.
809. Chen, F.; Wang, G.; Griffin, J.I.; Brenneman, B.; Banda, N.K.; Holers, V.M.; Backos, D.S.; Wu, L.; Moghimi, S.M.; Simberg, D. Complement Proteins Bind to Nanoparticle Protein Corona and Undergo Dynamic Exchange in Vivo. *Nature Nanotech* **2017**, *12*, 387–393, doi:10.1038/nnano.2016.269.
810. Buchman, J.T.; Hudson-Smith, N.V.; Landy, K.M.; Haynes, C.L. Understanding Nanoparticle Toxicity Mechanisms To Inform Redesign Strategies To Reduce Environmental Impact. *Acc. Chem. Res.* **2019**, *52*, 1632–1642, doi:10.1021/acs.accounts.9b00053.
811. Barbero, F.; Russo, L.; Vitali, M.; Piella, J.; Salvo, I.; Borrajo, M.L.; Busquets-Fité, M.; Grandori, R.; Bastús, N.G.; Casals, E.; et al. Formation of the Protein Corona: The Interface between Nanoparticles and the Immune System. *Semin Immunol* **2017**, *34*, 52–60, doi:10.1016/j.smim.2017.10.001.
812. Ehrenstein, M.R.; Notley, C.A. The Importance of Natural IgM: Scavenger, Protector and Regulator. *Nat Rev Immunol* **2010**, *10*, 778–786, doi:10.1038/nri2849.
813. Fischinger, S.; Fallon, J.K.; Michell, A.R.; Broge, T.; Suscovich, T.J.; Streeck, H.; Alter, G. A High-Throughput, Bead-Based, Antigen-Specific Assay to Assess the Ability of Antibodies to Induce Complement Activation. *Journal of Immunological Methods* **2019**, *473*, 112630, doi:10.1016/j.jim.2019.07.002.
814. Partikel, K.; Korte, R.; Stein, N.C.; Mulac, D.; Herrmann, F.C.; Humpf, H.-U.; Langer, K. Effect of Nanoparticle Size and PEGylation on the Protein Corona of PLGA

Nanoparticles. *European Journal of Pharmaceutics and Biopharmaceutics* **2019**, *141*, 70–80, doi:10.1016/j.ejpb.2019.05.006.
815. Zhang, H.; Burnum, K.E.; Luna, M.L.; Petritis, B.O.; Kim, J.-S.; Qian, W.-J.; Moore, R.J.; Heredia-Langner, A.; Webb-Robertson, B.-J.M.; Thrall, B.D.; et al. Quantitative Proteomics Analysis of Adsorbed Plasma Proteins Classifies Nanoparticles with Different Surface Properties and Size. *PROTEOMICS* **2011**, *11*, 4569–4577, doi:10.1002/pmic.201100037.
816. Segets, D.; Marczak, R.; Schäfer, S.; Paula, C.; Gnichwitz, J.-F.; Hirsch, A.; Peukert, W. Experimental and Theoretical Studies of the Colloidal Stability of Nanoparticles−A General Interpretation Based on Stability Maps. *ACS Nano* **2011**, *5*, 4658–4669, doi:10.1021/nn200465b.
817. Salvati, A.; Pitek, A.S.; Monopoli, M.P.; Prapainop, K.; Bombelli, F.B.; Hristov, D.R.; Kelly, P.M.; Åberg, C.; Mahon, E.; Dawson, K.A. Transferrin-Functionalized Nanoparticles Lose Their Targeting Capabilities When a Biomolecule Corona Adsorbs on the Surface. *Nature Nanotech* **2013**, *8*, 137–143, doi:10.1038/nnano.2012.237.
818. Su, G.; Jiang, H.; Xu, B.; Yu, Y.; Chen, X. Effects of Protein Corona on Active and Passive Targeting of Cyclic RGD Peptide-Functionalized PEGylation Nanoparticles. *Mol. Pharmaceutics* **2018**, *15*, 5019–5030, doi:10.1021/acs.molpharmaceut.8b00612.
819. Varnamkhasti, B.S.; Hosseinzadeh, H.; Azhdarzadeh, M.; Vafaei, S.Y.; Esfandyari-Manesh, M.; Mirzaie, Z.H.; Amini, M.; Ostad, S.N.; Atyabi, F.; Dinarvand, R. Protein Corona Hampers Targeting Potential of MUC1 Aptamer Functionalized SN-38 Core–Shell Nanoparticles. *International Journal of Pharmaceutics* **2015**, *494*, 430–444, doi:10.1016/j.ijpharm.2015.08.060.
820. Hadjidemetriou, M.; Al-Ahmady, Z.; Mazza, M.; Collins, R.F.; Dawson, K.; Kostarelos, K. In Vivo Biomolecule Corona around Blood-Circulating, Clinically Used and Antibody-Targeted Lipid Bilayer Nanoscale Vesicles. *ACS Nano* **2015**, *9*, 8142–8156, doi:10.1021/acsnano.5b03300.
821. Zhang, H.; Wu, T.; Yu, W.; Ruan, S.; He, Q.; Gao, H. Ligand Size and Conformation Affect the Behavior of Nanoparticles Coated with in Vitro and in Vivo Protein Corona. *ACS Appl. Mater. Interfaces* **2018**, *10*, 9094–9103, doi:10.1021/acsami.7b16096.
822. Linse, S.; Cabaleiro-Lago, C.; Xue, W.-F.; Lynch, I.; Lindman, S.; Thulin, E.; Radford, S.E.; Dawson, K.A. Nucleation of Protein Fibrillation by Nanoparticles. *Proceedings of the National Academy of Sciences* **2007**, *104*, 8691–8696, doi:10.1073/pnas.0701250104.
823. Smith, J.R.; Cicerone, M.T.; Meuse, C.W. Tertiary Structure Changes in Albumin upon Surface Adsorption Observed via Fourier Transform Infrared Spectroscopy. *Langmuir* **2009**, *25*, 4571–4578, doi:10.1021/la802955w.
824. Tsai, D.-H.; DelRio, F.W.; Keene, A.M.; Tyner, K.M.; MacCuspie, R.I.; Cho, T.J.; Zachariah, M.R.; Hackley, V.A. Adsorption and Conformation of Serum Albumin Protein on Gold Nanoparticles Investigated Using Dimensional Measurements and in Situ Spectroscopic Methods. *Langmuir* **2011**, *27*, 2464–2477, doi:10.1021/la104124d.
825. Roach, P.; Farrar, D.; Perry, C.C. Interpretation of Protein Adsorption: Surface-Induced Conformational Changes. *J. Am. Chem. Soc.* **2005**, *127*, 8168–8173, doi:10.1021/ja042898o.
826. Park, S.J. Protein–Nanoparticle Interaction: Corona Formation and Conformational Changes in Proteins on Nanoparticles. *Int J Nanomedicine* **2020**, *15*, 5783–5802, doi:10.2147/IJN.S254808.

827. Rustom, A.; Saffrich, R.; Markovic, I.; Walther, P.; Gerdes, H.-H. Nanotubular Highways for Intercellular Organelle Transport. *Science* **2004**, *303*, 1007–1010, doi:10.1126/science.1093133.
828. Korenkova, O.; Pepe, A.; Zurzolo, C. Fine Intercellular Connections in Development: TNTs, Cytonemes, or Intercellular Bridges? *Cell Stress 4*, 30–43, doi:10.15698/cst2020.02.212.
829. Dubois, F.; Bénard, M.; Jean-Jacques, B.; Schapman, D.; Roberge, H.; Lebon, A.; Goux, D.; Monterroso, B.; Elie, N.; Komuro, H.; et al. Investigating Tunneling Nanotubes in Cancer Cells: Guidelines for Structural and Functional Studies through Cell Imaging. *BioMed Research International* **2020**, *2020*, 1–16, doi:10.1155/2020/2701345.
830. Taiarol, L.; Formicola, B.; Fagioli, S.; Sierri, G.; D'Aloia, A.; Kravicz, M.; Renda, A.; Viale, F.; Dal Magro, R.; Ceriani, M.; et al. The 3.0 Cell Communication: New Insights in the Usefulness of Tunneling Nanotubes for Glioblastoma Treatment. *Cancers* **2021**, *13*, 4001, doi:10.3390/cancers13164001.
831. Pyrgaki, C.; Trainor, P.; Hadjantonakis, A.-K.; Niswander, L. Dynamic Imaging of Mammalian Neural Tube Closure. *Developmental Biology* **2010**, *344*, 941–947, doi:10.1016/j.ydbio.2010.06.010.
832. Caneparo, L.; Pantazis, P.; Dempsey, W.; Fraser, S.E. Intercellular Bridges in Vertebrate Gastrulation. *PLOS ONE* **2011**, *6*, e20230, doi:10.1371/journal.pone.0020230.
833. McKinney, M.C.; Stark, D.A.; Teddy, J.; Kulesa, P.M. Neural Crest Cell Communication Involves an Exchange of Cytoplasmic Material through Cellular Bridges Revealed by Photoconversion of KikGR. *Developmental Dynamics* **2011**, *240*, 1391–1401, doi:10.1002/dvdy.22612.
834. Jhala, D.; Rather, H.A.; Vasita, R. Extracellular Matrix Mimicking Polycaprolactone-Chitosan Nanofibers Promote Stemness Maintenance of Mesenchymal Stem Cells via Spheroid Formation. *Biomed. Mater.* **2020**, *15*, 035011, doi:10.1088/1748-605X/ab772e.
835. Liu, K.; Ji, K.; Guo, L.; Wu, W.; Lu, H.; Shan, P.; Yan, C. Mesenchymal Stem Cells Rescue Injured Endothelial Cells in an in Vitro Ischemia–Reperfusion Model via Tunneling Nanotube like Structure-Mediated Mitochondrial Transfer. *Microvascular Research* **2014**, *92*, 10–18, doi:10.1016/j.mvr.2014.01.008.
836. Hsu, M.-J.; Karkossa, I.; Schäfer, I.; Christ, M.; Kühne, H.; Schubert, K.; Rolle-Kampczyk, U.E.; Kalkhof, S.; Nickel, S.; Seibel, P.; et al. Mitochondrial Transfer by Human Mesenchymal Stromal Cells Ameliorates Hepatocyte Lipid Load in a Mouse Model of NASH. *Biomedicines* **2020**, *8*, 350, doi:10.3390/biomedicines8090350.
837. Boukelmoune, N.; Chiu, G.S.; Kavelaars, A.; Heijnen, C.J. Mitochondrial Transfer from Mesenchymal Stem Cells to Neural Stem Cells Protects against the Neurotoxic Effects of Cisplatin. *Acta Neuropathologica Communications* **2018**, *6*, 139, doi:10.1186/s40478-018-0644-8.
838. Li, X. Gap Junction Protein Connexin43 and Tunneling Nanotubes in Human Trabecular Meshwork Cells. *Int J Physiol Pathophysiol Pharmacol* **2019**, *11*, 212–219.
839. Chinnery, H.R.; Keller, K.E. Tunneling Nanotubes and the Eye: Intercellular Communication and Implications for Ocular Health and Disease. *BioMed Research International* **2020**, *2020*, 1–15, doi:10.1155/2020/7246785.
840. Keller, K. Tunneling Nanotubes and Actin Cytoskeleton Dynamics in Glaucoma. *Neural Regen Res* **2020**, *15*, 2031, doi:10.4103/1673-5374.282254.
841. Wittig, D.; Wang, X.; Walter, C.; Gerdes, H.-H.; Funk, R.H.W.; Roehlecke, C. Multi-Level Communication of Human Retinal Pigment Epithelial Cells via Tunneling Nanotubes. *PLoS One* **2012**, *7*, e33195, doi:10.1371/journal.pone.0033195.

842. Alarcon-Martinez, L.; Villafranca-Baughman, D.; Quintero, H.; Kacerovsky, J.B.; Dotigny, F.; Murai, K.K.; Prat, A.; Drapeau, P.; Di Polo, A. Interpericyte Tunnelling Nanotubes Regulate Neurovascular Coupling. *Nature* **2020**, *585*, 91–95, doi:10.1038/s41586-020-2589-x.
843. Victoria, G.S.; Zurzolo, C. The Spread of Prion-like Proteins by Lysosomes and Tunneling Nanotubes: Implications for Neurodegenerative Diseases. *J Cell Biol* **2017**, *216*, 2633–2644, doi:10.1083/jcb.201701047.
844. Costanzo, M.; Abounit, S.; Marzo, L.; Danckaert, A.; Chamoun, Z.; Roux, P.; Zurzolo, C. Transfer of Polyglutamine Aggregates in Neuronal Cells Occurs in Tunneling Nanotubes. *Journal of Cell Science* **2013**, *126*, 3678–3685, doi:10.1242/jcs.126086.
845. Sharma, M.; Subramaniam, S. Rhes Travels from Cell to Cell and Transports Huntington Disease Protein via TNT-like Protrusion. *Journal of Cell Biology* **2019**, *218*, 1972–1993, doi:10.1083/jcb.201807068.
846. Dieriks, B.V.; Park, T.I.-H.; Fourie, C.; Faull, R.L.M.; Dragunow, M.; Curtis, M.A. $\alpha$-Synuclein Transfer through Tunneling Nanotubes Occurs in SH-SY5Y Cells and Primary Brain Pericytes from Parkinson's Disease Patients. *Sci Rep* **2017**, *7*, 42984, doi:10.1038/srep42984.
847. Rajasekaran, S.; Witt, S.N. Trojan Horses and Tunneling Nanotubes Enable $\alpha$-Synuclein Pathology to Spread in Parkinson Disease. *PLOS Biology* **2021**, *19*, e3001331, doi:10.1371/journal.pbio.3001331.
848. Zhang, K.; Sun, Z.; Chen, X.; Zhang, Y.; Guo, A.; Zhang, Y. Intercellular Transport of Tau Protein and β-Amyloid Mediated by Tunneling Nanotubes. *Am J Transl Res* **2021**, *13*, 12509–12522.
849. Sisakhtnezhad, S.; Khosravi, L. Emerging Physiological and Pathological Implications of Tunneling Nanotubes Formation between Cells. *European Journal of Cell Biology* **2015**, *94*, 429–443, doi:10.1016/j.ejcb.2015.06.010.
850. Wang, X.-T.; Sun, H.; Chen, N.-H.; Yuan, Y.-H. Tunneling Nanotubes: A Novel Pharmacological Target for Neurodegenerative Diseases? *Pharmacological Research* **2021**, *170*, 105541, doi:10.1016/j.phrs.2021.105541.
851. Hanna, S.J.; McCoy-Simandle, K.; Leung, E.; Genna, A.; Condeelis, J.; Cox, D. Tunneling Nanotubes, a Novel Mode of Tumor Cell–Macrophage Communication in Tumor Cell Invasion. *Journal of Cell Science* **2019**, *132*, jcs223321, doi:10.1242/jcs.223321.
852. Matejka, N.; Reindl, J. Perspectives of Cellular Communication through Tunneling Nanotubes in Cancer Cells and the Connection to Radiation Effects. *Radiat Oncol* **2019**, *14*, 218, doi:10.1186/s13014-019-1416-8.
853. Kretschmer, A.; Zhang, F.; Somasekharan, S.P.; Tse, C.; Leachman, L.; Gleave, A.; Li, B.; Asmaro, I.; Huang, T.; Kotula, L.; et al. Stress-Induced Tunneling Nanotubes Support Treatment Adaptation in Prostate Cancer. *Sci Rep* **2019**, *9*, 7826, doi:10.1038/s41598-019-44346-5.
854. Lu, J.J.; Yang, W.M.; Li, F.; Zhu, W.; Chen, Z. Tunneling Nanotubes Mediated MicroRNA-155 Intercellular Transportation Promotes Bladder Cancer Cells' Invasive and Proliferative Capacity. *IJN* **2019**, *Volume 14*, 9731–9743, doi:10.2147/IJN.S217277.
855. Lu, J.; Zheng, X.; Li, F.; Yu, Y.; Chen, Z.; Liu, Z.; Wang, Z.; Xu, H.; Yang, W. Tunneling Nanotubes Promote Intercellular Mitochondria Transfer Followed by Increased Invasiveness in Bladder Cancer Cells. *Oncotarget* **2017**, *8*, 15539–15552, doi:10.18632/oncotarget.14695.
856. D'Aloia, A.; Arrigoni, E.; Costa, B.; Berruti, G.; Martegani, E.; Sacco, E.; Ceriani, M. RalGPS2 Interacts with Akt and PDK1 Promoting Tunneling Nanotubes Formation in

Bladder Cancer and Kidney Cells Microenvironment. *Cancers* **2021**, *13*, 6330, doi:10.3390/cancers13246330.
857. Desir, S.; O'Hare, P.; Vogel, R.I.; Sperduto, W.; Sarkari, A.; Dickson, E.L.; Wong, P.; Nelson, A.C.; Fong, Y.; Steer, C.J.; et al. Chemotherapy-Induced Tunneling Nanotubes Mediate Intercellular Drug Efflux in Pancreatic Cancer. *Sci Rep* **2018**, *8*, 9484, doi:10.1038/s41598-018-27649-x.
858. Franchi, M.; Piperigkou, Z.; Riti, E.; Masola, V.; Onisto, M.; Karamanos, N.K. Long Filopodia and Tunneling Nanotubes Define New Phenotypes of Breast Cancer Cells in 3D Cultures. *Matrix Biology Plus* **2020**, *6–7*, 100026, doi:10.1016/j.mbplus.2020.100026.
859. Polak, R.; de Rooij, B.; Pieters, R.; den Boer, M.L. B-Cell Precursor Acute Lymphoblastic Leukemia Cells Use Tunneling Nanotubes to Orchestrate Their Microenvironment. *Blood* **2015**, *126*, 2404–2414, doi:10.1182/blood-2015-03-634238.
860. Omsland, M.; Andresen, V.; Gullaksen, S.; Ayuda-Durán, P.; Popa, M.; Hovland, R.; Brendehaug, A.; Enserink, J.; McCormack, E.; Gjertsen, B.T. Tyrosine Kinase Inhibitors and Interferon-$\alpha$ Increase Tunneling Nanotube (TNT) Formation and Cell Adhesion in Chronic Myeloid Leukemia (CML) Cell Lines. *FASEB j.* **2020**, *34*, 3773–3791, doi:10.1096/fj.201802061RR.
861. de Rooij, B.; Polak, R.; Stalpers, F.; Pieters, R.; den Boer, M.L. Tunneling Nanotubes Facilitate Autophagosome Transfer in the Leukemic Niche. *Leukemia* **2017**, *31*, 1651–1654, doi:10.1038/leu.2017.117.
862. Civita, P.; M. Leite, D.; Pilkington, G.J. Pre-Clinical Drug Testing in 2D and 3D Human In Vitro Models of Glioblastoma Incorporating Non-Neoplastic Astrocytes: Tunneling Nano Tubules and Mitochondrial Transfer Modulates Cell Behavior and Therapeutic Respons. *IJMS* **2019**, *20*, 6017, doi:10.3390/ijms20236017.
863. Wu, W.; Klockow, J.L.; Zhang, M.; Lafortune, F.; Chang, E.; Jin, L.; Wu, Y.; Daldrup-Link, H.E. Glioblastoma Multiforme (GBM): An Overview of Current Therapies and Mechanisms of Resistance. *Pharmacological Research* **2021**, *171*, 105780, doi:10.1016/j.phrs.2021.105780.
864. Grech, N.; Dalli, T.; Mizzi, S.; Meilak, L.; Calleja, N.; Zrinzo, A. Rising Incidence of Glioblastoma Multiforme in a Well-Defined Population. *Cureus 12*, e8195, doi:10.7759/cureus.8195.
865. Hanif, F.; Muzaffar, K.; Perveen, K.; Malhi, S.M.; Simjee, S.U. Glioblastoma Multiforme: A Review of Its Epidemiology and Pathogenesis through Clinical Presentation and Treatment. *Asian Pac J Cancer Prev* **2017**, *18*, 3–9, doi:10.22034/APJCP.2017.18.1.3.
866. Valdebenito, S.; Malik, S.; Luu, R.; Loudig, O.; Mitchell, M.; Okafo, G.; Bhat, K.; Prideaux, B.; Eugenin, E.A. Tunneling Nanotubes, TNT, Communicate Glioblastoma with Surrounding Non-Tumor Astrocytes to Adapt Them to Hypoxic and Metabolic Tumor Conditions. *Sci Rep* **2021**, *11*, 14556, doi:10.1038/s41598-021-93775-8.
867. Venkatesh, V.S.; Lou, E. Tunneling Nanotubes: A Bridge for Heterogeneity in Glioblastoma and a New Therapeutic Target? *Cancer Reports* **2019**, *2*, e1185, doi:10.1002/cnr2.1185.
868. Nasoni, M.G.; Carloni, S.; Canonico, B.; Burattini, S.; Cesarini, E.; Papa, S.; Pagliarini, M.; Ambrogini, P.; Balduini, W.; Luchetti, F. Melatonin Reshapes the Mitochondrial Network and Promotes Intercellular Mitochondrial Transfer via Tunneling Nanotubes after Ischemic-like Injury in Hippocampal HT22 Cells. *J Pineal Res* **2021**, *71*, e12747, doi:10.1111/jpi.12747.
869. Damodaran, N.; Dilna, A.; Kielkopf, C.S.; Kagedal, K.; Ollinger, K.; Nath, S. *Amyloid-β Induced Membrane Damage Instigates Tunneling Nanotubes by Exploiting PAK1 Dependent Actin Remodulation*; 2020; p. 655340;.

870. Zou, X.; Hou, Y.; Xu, J.; Zhong, L.; Zhou, J.; Zhang, G.; Sun, J. Mitochondria Transfer via Tunneling Nanotubes Is an Important Mechanism by Which CD133+ Scattered Tubular Cells Eliminate Hypoxic Tubular Cell Injury. *Biochemical and Biophysical Research Communications* **2020**, *522*, 205–212, doi:10.1016/j.bbrc.2019.11.006.
871. Dupont, M.; Souriant, S.; Balboa, L.; Vu Manh, T.-P.; Pingris, K.; Rousset, S.; Cougoule, C.; Rombouts, Y.; Poincloux, R.; Ben Neji, M.; et al. Tuberculosis-Associated IFN-I Induces Siglec-1 on Tunneling Nanotubes and Favors HIV-1 Spread in Macrophages. *eLife* **2020**, *9*, e52535, doi:10.7554/eLife.52535.
872. Okura, T.; Taneno, A.; Oishi, E. Cell-to-Cell Transmission of Turkey Herpesvirus in Chicken Embryo Cells via Tunneling Nanotubes. *Avian Diseases* **2021**, *65*, 335–339, doi:10.1637/aviandiseases-D-21-00022.
873. Panasiuk, M.; Rychłowski, M.; Derewońko, N.; Bieńkowska-Szewczyk, K. Tunneling Nanotubes as a Novel Route of Cell-to-Cell Spread of Herpesviruses. *Journal of Virology* **2018**, doi:10.1128/JVI.00090-18.
874. Tiwari, V.; Koganti, R.; Russell, G.; Sharma, A.; Shukla, D. Role of Tunneling Nanotubes in Viral Infection, Neurodegenerative Disease, and Cancer. *Frontiers in Immunology* **2021**, *12*, 2256, doi:10.3389/fimmu.2021.680891.
875. Kumar, A.; Kim, J.H.; Ranjan, P.; Metcalfe, M.G.; Cao, W.; Mishina, M.; Gangappa, S.; Guo, Z.; Boyden, E.S.; Zaki, S.; et al. Influenza Virus Exploits Tunneling Nanotubes for Cell-to-Cell Spread. *Sci Rep* **2017**, *7*, 40360, doi:10.1038/srep40360.
876. Pepe, A.; Pietropaoli, S.; Vos, M.; Barba-Spaeth, G.; Zurzolo, C. *Tunneling Nanotubes Provide a Novel Route for SARS-CoV-2 Spreading between Permissive Cells and to Non-Permissive Neuronal Cells*; 2021; p. 2021.11.15.468633;
877. Jansens, R.J.J.; Tishchenko, A.; Favoreel, H.W. Bridging the Gap: Virus Long-Distance Spread via Tunneling Nanotubes. *J Virol* **2020**, *94*, e02120-19, /jvi/94/8/JVI.02120-19.atom, doi:10.1128/JVI.02120-19.
878. Guo, L.; Zhang, Y.; Yang, Z.; Peng, H.; Wei, R.; Wang, C.; Feng, M. Tunneling Nanotubular Expressways for Ultrafast and Accurate M1 Macrophage Delivery of Anticancer Drugs to Metastatic Ovarian Carcinoma. *ACS Nano* **2019**, *13*, 1078–1096, doi:10.1021/acsnano.8b08872.
879. Pasquier, J.; Guerrouahen, B.S.; Al Thawadi, H.; Ghiabi, P.; Maleki, M.; Abu-Kaoud, N.; Jacob, A.; Mirshahi, M.; Galas, L.; Rafii, S.; et al. Preferential Transfer of Mitochondria from Endothelial to Cancer Cells through Tunneling Nanotubes Modulates Chemoresistance. *J Transl Med* **2013**, *11*, 94, doi:10.1186/1479-5876-11-94.
880. Pasquier, J.; Galas, L.; Boulangé-Lecomte, C.; Rioult, D.; Bultelle, F.; Magal, P.; Webb, G.; Le Foll, F. Different Modalities of Intercellular Membrane Exchanges Mediate Cell-to-Cell P-Glycoprotein Transfers in MCF-7 Breast Cancer Cells. *J Biol Chem* **2012**, *287*, 7374–7387, doi:10.1074/jbc.M111.312157.
881. Bao, L.; Hazari, S.; Mehra, S.; Kaushal, D.; Moroz, K.; Dash, S. Increased Expression of P-Glycoprotein and Doxorubicin Chemoresistance of Metastatic Breast Cancer Is Regulated by MiR-298. *Am J Pathol* **2012**, *180*, 2490–2503, doi:10.1016/j.ajpath.2012.02.024.
882. Abad, E.; Lyakhovich, A. Movement of Mitochondria with Mutant DNA through Extracellular Vesicles Helps Cancer Cells Acquire Chemoresistance. *ChemMedChem n/a*, doi:10.1002/cmdc.202100642.
883. Dash, C.; Saha, T.; Sengupta, S.; Jang, H.L. Inhibition of Tunneling Nanotubes between Cancer Cell and the Endothelium Alters the Metastatic Phenotype. *International Journal of Molecular Sciences* **2021**, *22*, 6161, doi:10.3390/ijms22116161.

884. Sun, Y.Y.; Yang, Y.-F.; Keller, K.E. Myosin-X Silencing in the Trabecular Meshwork Suggests a Role for Tunneling Nanotubes in Outflow Regulation. *Investigative Ophthalmology & Visual Science* **2019**, *60*, 843–851, doi:10.1167/iovs.18-26055.
885. Lou, E.; Fujisawa, S.; Morozov, A.; Barlas, A.; Romin, Y.; Dogan, Y.; Gholami, S.; Moreira, A.L.; Manova-Todorova, K.; Moore, M.A.S. Tunneling Nanotubes Provide a Unique Conduit for Intercellular Transfer of Cellular Contents in Human Malignant Pleural Mesothelioma. *PLOS ONE* **2012**, *7*, e33093, doi:10.1371/journal.pone.0033093.
886. Sahu, P.; Jena, S.R.; Samanta, L. Tunneling Nanotubes: A Versatile Target for Cancer Therapy. *CCDT* **2018**, *18*, 514–521, doi:10.2174/1568009618666171129222637.
887. Dilsizoglu Senol, A.; Pepe, A.; Grudina, C.; Sassoon, N.; Reiko, U.; Bousset, L.; Melki, R.; Piel, J.; Gugger, M.; Zurzolo, C. Effect of Tolytoxin on Tunneling Nanotube Formation and Function. *Sci Rep* **2019**, *9*, 5741, doi:10.1038/s41598-019-42161-6.
888. Pergu, R.; Dagar, S.; Kumar, H.; Kumar, R.; Bhattacharya, J.; Mylavarapu, S.V.S. The Chaperone ERp29 Is Required for Tunneling Nanotube Formation by Stabilizing MSec. *Journal of Biological Chemistry* **2019**, *294*, 7177–7193, doi:10.1074/jbc.RA118.005659.
889. Barutta, F.; Kimura, S.; Hase, K.; Bellini, S.; Corbetta, B.; Corbelli, A.; Fiordaliso, F.; Barreca, A.; Papotti, M.G.; Ghiggeri, G.M.; et al. Protective Role of the M-Sec–Tunneling Nanotube System in Podocytes. *JASN* **2021**, *32*, 1114–1130, doi:10.1681/ASN.2020071076.
890. Yasuda, K.; Park, H.-C.; Ratliff, B.; Addabbo, F.; Hatzopoulos, A.K.; Chander, P.; Goligorsky, M.S. Adriamycin Nephropathy: A Failure of Endothelial Progenitor Cell-Induced Repair. *The American Journal of Pathology* **2010**, *176*, 1685–1695, doi:10.2353/ajpath.2010.091071.
891. Kato, K.; Nguyen, K.T.; Decker, C.W.; Silkwood, K.H.; Eck, S.M.; Hernandez, J.B.; Garcia, J.; Han, D. Tunneling Nanotube Formation Promotes Survival against 5-Fluorouracil in MCF-7 Breast Cancer Cells. *FEBS Open Bio* **2022**, *12*, 203–210, doi:10.1002/2211-5463.13324.
892. Hekmatshoar, Y.; Nakhle, J.; Galloni, M.; Vignais, M.-L. The Role of Metabolism and Tunneling Nanotube-Mediated Intercellular Mitochondria Exchange in Cancer Drug Resistance. *Biochemical Journal* **2018**, *475*, 2305–2328, doi:10.1042/BCJ20170712.
893. Salvioni, L.; Rizzuto, M.A.; Bertolini, J.A.; Pandolfi, L.; Colombo, M.; Prosperi, D. Thirty Years of Cancer Nanomedicine: Success, Frustration, and Hope. *Cancers* **2019**, *11*, 1855, doi:10.3390/cancers11121855.
894. Shi, Z.; Zhou, Y.; Fan, T.; Lin, Y.; Zhang, H.; Mei, L. Inorganic Nano-Carriers Based Smart Drug Delivery Systems for Tumor Therapy. *Smart Materials in Medicine* **2020**, *1*, 32–47, doi:10.1016/j.smaim.2020.05.002.
895. Mitchell, M.J.; Billingsley, M.M.; Haley, R.M.; Wechsler, M.E.; Peppas, N.A.; Langer, R. Engineering Precision Nanoparticles for Drug Delivery. *Nat Rev Drug Discov* **2021**, *20*, 101–124, doi:10.1038/s41573-020-0090-8.
896. Sur, S.; Rathore, A.; Dave, V.; Reddy, K.R.; Chouhan, R.S.; Sadhu, V. Recent Developments in Functionalized Polymer Nanoparticles for Efficient Drug Delivery System. *Nano-Structures & Nano-Objects* **2019**, *20*, 100397, doi:10.1016/j.nanoso.2019.100397.
897. Righeschi, C.; Coronnello, M.; Mastrantoni, A.; Isacchi, B.; Bergonzi, M.C.; Mini, E.; Bilia, A.R. Strategy to Provide a Useful Solution to Effective Delivery of Dihydroartemisinin: Development, Characterization and in Vitro Studies of Liposomal Formulations. *Colloids Surf B Biointerfaces* **2014**, *116*, 121–127, doi:10.1016/j.colsurfb.2013.12.019.
898. He, Y.; Liang, S.; Long, M.; Xu, H. Mesoporous Silica Nanoparticles as Potential Carriers for Enhanced Drug Solubility of Paclitaxel. *Materials Science and Engineering: C* **2017**, *78*, 12–17, doi:10.1016/j.msec.2017.04.049.

899. Volpatti, L.R.; Matranga, M.A.; Cortinas, A.B.; Delcassian, D.; Daniel, K.B.; Langer, R.; Anderson, D.G. Glucose-Responsive Nanoparticles for Rapid and Extended Self-Regulated Insulin Delivery. *ACS Nano* **2020**, *14*, 488–497, doi:10.1021/acsnano.9b06395.
900. Cao, S.; Xu, S.; Wang, H.; Ling, Y.; Dong, J.; Xia, R.; Sun, X. Nanoparticles: Oral Delivery for Protein and Peptide Drugs. *AAPS PharmSciTech* **2019**, *20*, 190, doi:10.1208/s12249-019-1325-z.
901. Huang, D.; Chen, Y.-S.; Green, C.R.; Rupenthal, I.D. Hyaluronic Acid Coated Albumin Nanoparticles for Targeted Peptide Delivery in the Treatment of Retinal Ischaemia. *Biomaterials* **2018**, *168*, 10–23, doi:10.1016/j.biomaterials.2018.03.034.
902. Dowaidar, M.; Nasser Abdelhamid, H.; Hällbrink, M.; Langel, Ü.; Zou, X. Chitosan Enhances Gene Delivery of Oligonucleotide Complexes with Magnetic Nanoparticles–Cell-Penetrating Peptide. *J Biomater Appl* **2018**, *33*, 392–401, doi:10.1177/0885328218796623.
903. Zhou, Y.; Quan, G.; Wu, Q.; Zhang, X.; Niu, B.; Wu, B.; Huang, Y.; Pan, X.; Wu, C. Mesoporous Silica Nanoparticles for Drug and Gene Delivery. *Acta Pharmaceutica Sinica B* **2018**, *8*, 165–177, doi:10.1016/j.apsb.2018.01.007.
904. Lu, J.; Wang, J.; Ling, D. Surface Engineering of Nanoparticles for Targeted Delivery to Hepatocellular Carcinoma. *Small* **2018**, *14*, 1702037, doi:10.1002/smll.201702037.
905. Xiao, Y.; Shi, K.; Qu, Y.; Chu, B.; Qian, Z. Engineering Nanoparticles for Targeted Delivery of Nucleic Acid Therapeutics in Tumor. *Molecular Therapy - Methods & Clinical Development* **2019**, *12*, 1–18, doi:10.1016/j.omtm.2018.09.002.
906. Hussain, S.; Joo, J.; Kang, J.; Kim, B.; Braun, G.B.; She, Z.-G.; Kim, D.; Mann, A.P.; Mölder, T.; Teesalu, T.; et al. Antibiotic-Loaded Nanoparticles Targeted to the Site of Infection Enhance Antibacterial Efficacy. *Nat Biomed Eng* **2018**, *2*, 95–103, doi:10.1038/s41551-017-0187-5.
907. Han, X.; Su, R.; Huang, X.; Wang, Y.; Kuang, X.; Zhou, S.; Liu, H. Triphenylphosphonium-Modified Mitochondria-Targeted Paclitaxel Nanocrystals for Overcoming Multidrug Resistance. *Asian Journal of Pharmaceutical Sciences* **2019**, *14*, 569–580, doi:10.1016/j.ajps.2018.06.006.
908. Fam, S.Y.; Chee, C.F.; Yong, C.Y.; Ho, K.L.; Mariatulqabtiah, A.R.; Tan, W.S. Stealth Coating of Nanoparticles in Drug-Delivery Systems. *Nanomaterials* **2020**, *10*, 787, doi:10.3390/nano10040787.
909. Kundu, M.; Chatterjee, S.; Ghosh, N.; Manna, P.; Das, J.; Sil, P.C. Tumor Targeted Delivery of Umbelliferone via a Smart Mesoporous Silica Nanoparticles Controlled-Release Drug Delivery System for Increased Anticancer Efficiency. *Materials Science and Engineering: C* **2020**, *116*, 111239, doi:10.1016/j.msec.2020.111239.
910. Salehiabar, M.; Nosrati, H.; Javani, E.; Aliakbarzadeh, F.; Kheiri Manjili, H.; Davaran, S.; Danafar, H. Production of Biological Nanoparticles from Bovine Serum Albumin as Controlled Release Carrier for Curcumin Delivery. *International Journal of Biological Macromolecules* **2018**, *115*, 83–89, doi:10.1016/j.ijbiomac.2018.04.043.
911. Jiang, P.; Choi, A.; Swindle-Reilly, K.E. Controlled Release of Anti-VEGF by Redox-Responsive Polydopamine Nanoparticles. *Nanoscale* **2020**, *12*, 17298–17311, doi:10.1039/D0NR03710A.
912. Cano, A.; Turowski, P.; Ettcheto, M.; Duskey, J.T.; Tosi, G.; Sánchez-López, E.; García, M.L.; Camins, A.; Souto, E.B.; Ruiz, A.; et al. Nanomedicine-Based Technologies and Novel Biomarkers for the Diagnosis and Treatment of Alzheimer's Disease: From Current to Future Challenges. *J Nanobiotechnol* **2021**, *19*, 122, doi:10.1186/s12951-021-00864-x.
913. Baskin, J.; Jeon, J.E.; Lewis, S.J.G. Nanoparticles for Drug Delivery in Parkinson's Disease. *J Neurol* **2021**, *268*, 1981–1994, doi:10.1007/s00415-020-10291-x.

914. Shi, J.; Kantoff, P.W.; Wooster, R.; Farokhzad, O.C. Cancer Nanomedicine: Progress, Challenges and Opportunities. *Nat Rev Cancer* **2017**, *17*, 20–37, doi:10.1038/nrc.2016.108.
915. Wu, D.; Si, M.; Xue, H.-Y.; Wong, H.-L. Nanomedicine Applications in the Treatment of Breast Cancer: Current State of the Art. *Int J Nanomedicine* **2017**, *12*, 5879–5892, doi:10.2147/IJN.S123437.
916. Tatar, A.-S.; Nagy-Simon, T.; Tomuleasa, C.; Boca, S.; Astilean, S. Nanomedicine Approaches in Acute Lymphoblastic Leukemia. *Journal of Controlled Release* **2016**, *238*, 123–138, doi:10.1016/j.jconrel.2016.07.035.
917. Naserifar, M.; Hosseinzadeh, H.; Abnous, K.; Mohammadi, M.; Taghdisi, S.M.; Ramezani, M.; Alibolandi, M. Oral Delivery of Folate-Targeted Resveratrol-Loaded Nanoparticles for Inflammatory Bowel Disease Therapy in Rats. *Life Sciences* **2020**, *262*, 118555, doi:10.1016/j.lfs.2020.118555.
918. Yan, F.; Zhong, Z.; Wang, Y.; Feng, Y.; Mei, Z.; Li, H.; Chen, X.; Cai, L.; Li, C. Exosome-Based Biomimetic Nanoparticles Targeted to Inflamed Joints for Enhanced Treatment of Rheumatoid Arthritis. *Journal of Nanobiotechnology* **2020**, *18*, 115, doi:10.1186/s12951-020-00675-6.
919. Kim, B.; Sun, S.; Varner, J.A.; Howell, S.B.; Ruoslahti, E.; Sailor, M.J. Securing the Payload, Finding the Cell, and Avoiding the Endosome: Peptide-Targeted, Fusogenic Porous Silicon Nanoparticles for Delivery of SiRNA. *Advanced Materials* **2019**, *31*, 1902952, doi:10.1002/adma.201902952.
920. Bu, J.; Nair, A.; Iida, M.; Jeong, W.; Poellmann, M.J.; Mudd, K.; Kubiatowicz, L.J.; Liu, E.W.; Wheeler, D.L.; Hong, S. An Avidity-Based PD-L1 Antagonist Using Nanoparticle-Antibody Conjugates for Enhanced Immunotherapy. *Nano Lett.* **2020**, *20*, 4901–4909, doi:10.1021/acs.nanolett.0c00953.
921. Marques, A.C.; Costa, P.J.; Velho, S.; Amaral, M.H. Functionalizing Nanoparticles with Cancer-Targeting Antibodies: A Comparison of Strategies. *Journal of Controlled Release* **2020**, *320*, 180–200, doi:10.1016/j.jconrel.2020.01.035.
922. Johnston, M.C.; Scott, C.J. Antibody Conjugated Nanoparticles as a Novel Form of Antibody Drug Conjugate Chemotherapy. *Drug Discovery Today: Technologies* **2018**, *30*, 63–69, doi:10.1016/j.ddtec.2018.10.003.
923. Ucak, S.; Sudagidan, M.; Borsa, B.A.; Mansuroglu, B.; Ozalp, V.C. Inhibitory Effects of Aptamer Targeted Teicoplanin Encapsulated PLGA Nanoparticles for Staphylococcus Aureus Strains. *World J Microbiol Biotechnol* **2020**, *36*, 69, doi:10.1007/s11274-020-02845-y.
924. Zununi Vahed, S.; Fathi, N.; Samiei, M.; Maleki Dizaj, S.; Sharifi, S. Targeted Cancer Drug Delivery with Aptamer-Functionalized Polymeric Nanoparticles. *Journal of Drug Targeting* **2019**, *27*, 292–299, doi:10.1080/1061186X.2018.1491978.
925. Cai, J.; Fu, J.; Li, R.; Zhang, F.; Ling, G.; Zhang, P. A Potential Carrier for Anti-Tumor Targeted Delivery-Hyaluronic Acid Nanoparticles. *Carbohydrate Polymers* **2019**, *208*, 356–364, doi:10.1016/j.carbpol.2018.12.074.
926. Huang, D.; Chen, Y.-S.; Rupenthal, I.D. Hyaluronic Acid Coated Albumin Nanoparticles for Targeted Peptide Delivery to the Retina. *Mol. Pharmaceutics* **2017**, *14*, 533–545, doi:10.1021/acs.molpharmaceut.6b01029.
927. Liu, L.; Cao, F.; Liu, X.; Wang, H.; Zhang, C.; Sun, H.; Wang, C.; Leng, X.; Song, C.; Kong, D.; et al. Hyaluronic Acid-Modified Cationic Lipid–PLGA Hybrid Nanoparticles as a Nanovaccine Induce Robust Humoral and Cellular Immune Responses. *ACS Appl. Mater. Interfaces* **2016**, *8*, 11969–11979, doi:10.1021/acsami.6b01135.
928. Sabri, T.; Pawelek, P.D.; Capobianco, J.A. Dual Activity of Rose Bengal Functionalized to Albumin-Coated Lanthanide-Doped Upconverting Nanoparticles:

Targeting and Photodynamic Therapy. *ACS Appl. Mater. Interfaces* **2018**, *10*, 26947–26953, doi:10.1021/acsami.8b08919.
929. Rao, L.; Yu, G.-T.; Meng, Q.-F.; Bu, L.-L.; Tian, R.; Lin, L.-S.; Deng, H.; Yang, W.; Zan, M.; Ding, J.; et al. Cancer Cell Membrane-Coated Nanoparticles for Personalized Therapy in Patient-Derived Xenograft Models. *Advanced Functional Materials* **2019**, *29*, 1905671, doi:10.1002/adfm.201905671.
930. Jiang, H.; Shi, X.; Yu, X.; He, X.; An, Y.; Lu, H. Hyaluronidase Enzyme-Responsive Targeted Nanoparticles for Effective Delivery of 5-Fluorouracil in Colon Cancer. *Pharm Res* **2018**, *35*, 73, doi:10.1007/s11095-017-2302-4.
931. Zhang, C.Y.; Gao, J.; Wang, Z. Bioresponsive Nanoparticles Targeted to Infectious Microenvironments for Sepsis Management. *Advanced Materials* **2018**, *30*, 1803618, doi:10.1002/adma.201803618.
932. Gao, Y.; Wang, J.; Chai, M.; Li, X.; Deng, Y.; Jin, Q.; Ji, J. Size and Charge Adaptive Clustered Nanoparticles Targeting the Biofilm Microenvironment for Chronic Lung Infection Management. *ACS Nano* **2020**, *14*, 5686–5699, doi:10.1021/acsnano.0c00269.
933. Yang, M.; Li, J.; Gu, P.; Fan, X. The Application of Nanoparticles in Cancer Immunotherapy: Targeting Tumor Microenvironment. *Bioactive Materials* **2021**, *6*, 1973–1987, doi:10.1016/j.bioactmat.2020.12.010.
934. Liu, C.-M.; Chen, G.-B.; Chen, H.-H.; Zhang, J.-B.; Li, H.-Z.; Sheng, M.-X.; Weng, W.-B.; Guo, S.-M. Cancer Cell Membrane-Cloaked Mesoporous Silica Nanoparticles with a PH-Sensitive Gatekeeper for Cancer Treatment. *Colloids and Surfaces B: Biointerfaces* **2019**, *175*, 477–486, doi:10.1016/j.colsurfb.2018.12.038.
935. Fathi, M.; Sahandi Zangabad, P.; Barar, J.; Aghanejad, A.; Erfan-Niya, H.; Omidi, Y. Thermo-Sensitive Chitosan Copolymer-Gold Hybrid Nanoparticles as a Nanocarrier for Delivery of Erlotinib. *International Journal of Biological Macromolecules* **2018**, *106*, 266–276, doi:10.1016/j.ijbiomac.2017.08.020.
936. Dariva, C.G.; Coelho, J.F.J.; Serra, A.C. Near Infrared Light-Triggered Nanoparticles Using Singlet Oxygen Photocleavage for Drug Delivery Systems. *Journal of Controlled Release* **2019**, *294*, 337–354, doi:10.1016/j.jconrel.2018.12.042.
937. Oddone, N.; Pederzoli, F.; Duskey, J.T.; De Benedictis, C.A.; Grabrucker, A.M.; Forni, F.; Angela Vandelli, M.; Ruozi, B.; Tosi, G. ROS-Responsive "Smart" Polymeric Conjugate: Synthesis, Characterization and Proof-of-Concept Study. *International Journal of Pharmaceutics* **2019**, *570*, 118655, doi:10.1016/j.ijpharm.2019.118655.
938. Ceña, V.; Játiva, P. Nanoparticle Crossing of Blood–Brain Barrier: A Road to New Therapeutic Approaches to Central Nervous System Diseases. *Nanomedicine* **2018**, *13*, 1513–1516, doi:10.2217/nnm-2018-0139.
939. Ranganath, S.H.; Thanuja, M.Y.; Anupama, C.; Manjunatha, T.D. Systemic Drug Delivery to the Posterior Segment of the Eye: Overcoming Blood–Retinal Barrier Through Smart Drug Design and Nanotechnology. In *Immobilization Strategies : Biomedical, Bioengineering and Environmental Applications*; Tripathi, A., Melo, J.S., Eds.; Gels Horizons: From Science to Smart Materials; Springer: Singapore, 2021; pp. 219–269 ISBN 9789811579981.
940. He, K.; Luo, W.; Zhang, Y.; Liu, F.; Liu, D.; Xu, L.; Qin, L.; Xiong, C.; Lu, Z.; Fang, X.; et al. Intercellular Transportation of Quantum Dots Mediated by Membrane Nanotubes. *ACS Nano* **2010**, *4*, 3015–3022, doi:10.1021/nn1002198.
941. Dagar, S.; Pathak, D.; Oza, H.V.; Mylavarapu, S.V.S. Tunneling Nanotubes and Related Structures: Molecular Mechanisms of Formation and Function. *Biochem J* **2021**, *478*, 3977–3998, doi:10.1042/BCJ20210077.

942. Mi, L.; Xiong, R.; Zhang, Y.; Yang, W.; Chen, J.-Y.; Wang, P.-N. Microscopic Observation of the Intercellular Transport of CdTe Quantum Dot Aggregates through Tunneling-Nanotubes. *Journal of Biomaterials and Nanobiotechnology* **2011**, *02*, 172, doi:10.4236/jbnb.2011.22022.
943. Domhan, S.; Ma, L.; Tai, A.; Anaya, Z.; Beheshti, A.; Zeier, M.; Hlatky, L.; Abdollahi, A. Intercellular Communication by Exchange of Cytoplasmic Material via Tunneling Nano-Tube Like Structures in Primary Human Renal Epithelial Cells. *PLOS ONE* **2011**, *6*, e21283, doi:10.1371/journal.pone.0021283.
944. Rehberg, M.; Nekolla, K.; Sellner, S.; Praetner, M.; Mildner, K.; Zeuschner, D.; Krombach, F. Intercellular Transport of Nanomaterials Is Mediated by Membrane Nanotubes In Vivo. *Small* **2016**, *12*, 1882–1890, doi:10.1002/smll.201503606.
945. Epperla, C.P.; Mohan, N.; Chang, C.-W.; Chen, C.-C.; Chang, H.-C. Nanodiamond-Mediated Intercellular Transport of Proteins through Membrane Tunneling Nanotubes. *Small* **2015**, *11*, 6097–6105, doi:10.1002/smll.201502089.
946. Franco, S.; Noureddine, A.; Guo, J.; Keth, J.; Paffett, M.L.; Brinker, C.J.; Serda, R.E. Direct Transfer of Mesoporous Silica Nanoparticles between Macrophages and Cancer Cells. *Cancers* **2020**, *12*, 2892, doi:10.3390/cancers12102892.
947. Lamberti, M.; Zappavigna, S.; Sannolo, N.; Caraglia, M. Advantages and Risks of Nanotechnologies in Cancer Patients and Occupationally Exposed Workers. *Expert opinion on drug delivery* **2014**, *11*, doi:10.1517/17425247.2014.913568.
948. Ingle, N.P.; Hexum, J.K.; Reineke, T.M. Polyplexes Are Endocytosed by and Trafficked within Filopodia. *Biomacromolecules* **2020**, *21*, 1379–1392, doi:10.1021/acs.biomac.9b01610.
949. Sáenz-de-Santa-María, I.; Bernardo-Castiñeira, C.; Enciso, E.; García-Moreno, I.; Chiara, J.L.; Suarez, C.; Chiara, M.-D. Control of Long-Distance Cell-to-Cell Communication and Autophagosome Transfer in Squamous Cell Carcinoma via Tunneling Nanotubes. *Oncotarget* **2017**, *8*, 20939–20960, doi:10.18632/oncotarget.15467.
950. Lee, B.Y.; Timpson, P.; Horvath, L.G.; Daly, R.J. FAK Signaling in Human Cancer as a Target for Therapeutics. *Pharmacol Ther* **2015**, *146*, 132–149, doi:10.1016/j.pharmthera.2014.10.001.
951. Kristl, J.; Plajnšek, K.T.; Kreft, M.E.; Janković, B.; Kocbek, P. Intracellular Trafficking of Solid Lipid Nanoparticles and Their Distribution between Cells through Tunneling Nanotubes. *European Journal of Pharmaceutical Sciences* **2013**, *50*, 139–148, doi:10.1016/j.ejps.2013.04.013.
952. Astanina, K.; Koch, M.; Jüngst, C.; Zumbusch, A.; Kiemer, A.K. Lipid Droplets as a Novel Cargo of Tunnelling Nanotubes in Endothelial Cells. *Sci Rep* **2015**, *5*, 11453, doi:10.1038/srep11453.
953. Rossen, N.S.; Hansen, A.J.; Selhuber-Unkel, C.; Oddershede, L.B. Arachidonic Acid Randomizes Endothelial Cell Motion and Regulates Adhesion and Migration. *PLOS ONE* **2011**, *6*, e25196, doi:10.1371/journal.pone.0025196.
954. Formicola, B.; D'Aloia, A.; Dal Magro, R.; Stucchi, S.; Rigolio, R.; Ceriani, M.; Re, F. Differential Exchange of Multifunctional Liposomes Between Glioblastoma Cells and Healthy Astrocytes via Tunneling Nanotubes. *Front. Bioeng. Biotechnol.* **2019**, *7*, 403, doi:10.3389/fbioe.2019.00403.
955. Qin, H.; Jiang, Y.; Zhang, J.; Deng, C.; Zhong, Z. Oncoprotein Inhibitor Rigosertib Loaded in ApoE-Targeted Smart Polymersomes Reveals High Safety and Potency against Human Glioblastoma in Mice. *Mol. Pharmaceutics* **2019**, *16*, 3711–3719, doi:10.1021/acs.molpharmaceut.9b00691.

956. Ouyang, J.; Jiang, Y.; Deng, C.; Zhong, Z.; Lan, Q. Doxorubicin Delivered via ApoE-Directed Reduction-Sensitive Polymersomes Potently Inhibit Orthotopic Human Glioblastoma Xenografts in Nude Mice. *Int J Nanomedicine* **2021**, *16*, 4105–4115, doi:10.2147/IJN.S314895.
957. Costa, P.M.; Cardoso, A.L.; Mendonça, L.S.; Serani, A.; Custódia, C.; Conceição, M.; Simões, S.; Moreira, J.N.; Pereira de Almeida, L.; Pedroso de Lima, M.C. Tumor-Targeted Chlorotoxin-Coupled Nanoparticles for Nucleic Acid Delivery to Glioblastoma Cells: A Promising System for Glioblastoma Treatment. *Molecular Therapy - Nucleic Acids* **2013**, *2*, e100, doi:10.1038/mtna.2013.30.
958. Cohen-Inbar, O.; Zaaroor, M. Glioblastoma Multiforme Targeted Therapy: The Chlorotoxin Story. *Journal of Clinical Neuroscience* **2016**, *33*, 52–58, doi:10.1016/j.jocn.2016.04.012.
959. Pinto, G.; Saenz-de-Santa-Maria, I.; Chastagner, P.; Perthame, E.; Delmas, C.; Toulas, C.; Moyal-Jonathan-Cohen, E.; Brou, C.; Zurzolo, C. Patient-Derived Glioblastoma Stem Cells Transfer Mitochondria through Tunneling Nanotubes in Tumor Organoids. *Biochemical Journal* **2021**, *478*, 21–39, doi:10.1042/BCJ20200710.
960. Chinnery, H.R.; Pearlman, E.; McMenamin, P.G. Cutting Edge: Membrane Nanotubes In Vivo: A Feature of MHC Class II+ Cells in the Mouse Cornea. *J Immunol* **2008**, *180*, 5779–5783.
961. Li, H.; Ye, S.; Guo, J.; Wang, H.; Yan, W.; Song, J.; Qu, J. Biocompatible Carbon Dots with Low-Saturation-Intensity and High-Photobleaching-Resistance for STED Nanoscopy Imaging of the Nucleolus and Tunneling Nanotubes in Living Cells. *Nano Res.* **2019**, *12*, 3075–3084, doi:10.1007/s12274-019-2554-x.

**Titre :** Advanced Nanotechnologies for the Central Nervous System : Conception, optimisation, application et mise à l'échelle

**Mots clés :** Nanotechnologies, microfluidiques, maladies difficiles à traiter

**Résumé :** Les nanotechnologies montrent un grand potentiel pour le traitement et le diagnostic des maladies du système nerveux central grâce à des caractéristiques comme la taille modulable, la haute capacité de charge des médicaments et la cible spécifique. Cependant, il est crucial d'optimiser ces technologies de la conception à la production pour leur application clinique.
Le matériau de base des NP, généralement des polymères et des lipides, doit être biocompatible, biodégradable et compatible avec le médicament chargé. Les NMeds protègent les molécules thérapeutiques sensibles, comme les peptides et les acides nucléiques, de la dégradation, augmentant ainsi leur efficacité. La délivrance des NMeds à travers la barrière hémato-encéphalique (BHE) est un défi, mais les concevoir avec des ligands spécifiques peut faciliter le passage de la BHE et la délivrance ciblée.
Malgré ces promesses, le passage des protocoles de laboratoire à la production à grande échelle est difficile. La technologie microfluidique offre une solution en automatisant et en adaptant les protocoles aux normes GMP, bien qu'assurer des propriétés nano-systèmes cohérentes reste un défi.
Mon travail de doctorat aborde ces défis par la synthèse et l'optimisation de nouveaux matériaux hybrides PLGA-chitosane, l'amélioration de la stabilité des enzymes dans les NP de PLGA, le ciblage de la BHE et du glioblastome, la libération contrôlée des médicaments avec des échafaudages en gel et la mise à l'échelle en utilisant des microfluidiques. Ces avancées améliorent notre compréhension des nanotechnologies et aident à surmonter les obstacles à la production de traitements commercialisables pour les maladies difficiles à traiter.

**Title :** Advanced Nanotechnologies for the Central Nervous System: Design, Optimization, Application, and Scale-up

**Keywords :** nanomedicine, microfluidics, hard-to-treat diseases

**Abstract :** Nanotechnologies, such as nanoparticles (NPs) and nanomedicines (NMeds), show great promise for treating and diagnosing central nervous system diseases due to features like tunable size, high drug loading capacity, and specific targeting. However, optimizing these technologies from design to production is crucial for clinical application. The core material of NPs, typically polymers and lipids, must be biocompatible, biodegradable, and compatible with the loaded drug. NMeds protect sensitive therapeutic molecules, such as peptides and nucleic acids, from degradation, enhancing their efficacy. Delivering NMeds across the blood-brain barrier (BBB) is challenging, but engineering them with specific targeting ligands can facilitate BBB crossing and targeted delivery.
Despite the promise, scaling up from lab protocols to larger production processes is difficult. Microfluidic technology offers a solution by automating and adapting protocols to GMP standards, though ensuring consistent nano system properties remains challenging.
My PhD work addresses these challenges through the synthesis and optimization of novel PLGA-chitosan materials, improving [illegible] stability in PLGA NPs, targeting glioblastoma, controlling drug release from scaffolds, and scaling up using microfluidics. These advancements improve our understanding of nanotechnology and help overcome barriers to producing marketable treatments for difficult diseases.